NTNU – Trondheim
Norwegian University of
Science and Technology

Development and Evaluation of an Effective Stress Based Model for Soft Clays

Jesper Bjerre

Civil and Environmental Engineering (2 year)
Submission date: June 2015
Supervisor: Steinar Nordal, BAT
Co-supervisor: Gustav Grimstad, BAT
Jon A. Rønningen, BAT
Varvara Zania, DTU Byg

Norwegian University of Science and Technology
Department of Civil and Transport Engineering

NORWEGIAN UNIVERSITY OF SCIENCE AND TECHNOLOGY
DEPARTMENT OF CIVIL AND TRANSPORT ENGINEERING

Report Title: Development and Evaluation of an Effective Stress Based Model for Soft Clays	**Date:** 10.06.2015 **Number of pages:** 278			
	Master Thesis	x	Project Work	
Name: Jesper Bjerre				
Professor in charge/supervisor: Steinar Nordal (NTNU) and Varvara Zania (DTU)				
Other external professional contacts/supervisors: Gustav Grimstad (NTNU) and Ph.D. Candidate Jon A. Rønningen (NTNU)				

Abstract: The term, natural soft clay, is commonly used to describe a normal or slightly overconsolidated clay. This soil type may be encountered in e.g. Scandinavia, Eastern Canada and South East Asia. The mechanical response of natural soft clay may be relatively complex and more research is still required to understand the entire process with respect to short and long time aspects. The observed mechanical behaviour in the field and in the laboratory has been investigated through a literature study to outline the main characteristic features which dominate the mechanical response. This study has shown that the viscous and ageing effects are the dominating features in natural soft clay. The observed features have made a foundation of a new constitutive model based on effective stresses. The model utilizes the theory behind the Modified Cam Clay model and invariants as framework.

The model requires 17 input parameters to access all its implemented features. Three additional input parameters are available to switch between different methods of simulating the stress history, evolution of anisotropy, and failure criteria in the general stress space. The model assumes associated flow and utilizes three hardening laws which introduce eight state (hardening) parameters in total. The model is implemented in the commercial software PLAXIS as a user defined soil model through the interface between PLAXIS and FORTRAN. The FORTRAN code is supported by additional MATLAB coding where the differential equations controlling the mechanical response are assembled. The initializing of the state parameters is performed in the FORTRAN code.

The model has been verified against laboratory tests such as constant rate of strain and undraind tri-axial tests and shows acceptable performance with respect to the implemented features. The performance of the suggested model has been investigated during a full scale boundary value problem for the test embankment located at Onsøy, Norway. The model shows fairly good predictions of the soil response and the dissipation of excess pore water with respect to field measurements. These predictions have further been compared to other known soil models.

Keywords:

1. Natural soft clay
2. Creep
3. Anisotropy
4. Destructuration
5. Recovery

Preface

The work presented in this report covers the main outcome of my master thesis attached to my civil engineering degree at the Technical University of Denmark (DTU). The work was produced in collaboration with the Norwegian University of Science and Technology (NTNU) and was conducted during the period: 14.01-2015 - 10.06-2015. The primary supervision was given by the division of Geotechnical Engineering at NTNU where the daily work took place. The report including an oral defence corresponds to a total work load of 30 ECTS points equivalent to one semester of study.

I personally hope that this master thesis may transfer knowledge between the universities. Hence, the format of the report is constructed in a manner which requires the reader to have a basic knowledge of soil mechanics.

Acknowledgements

Firstly, I would like to send my respect and deepest gratitude to the division of Geotechnical Engineering at NTNU whom has offered excellent supervision and contributed to a pleasant study environment during my stay in Trondheim.

I would like to give a special recognition to Jon A. Rønningen for his support and guidance, at a weekly basis, which has been related to his Ph.D. research attached to the GeoFuture project. Without his encouragement the final product would never have reached this stage. I send my gratitude to my main supervisor, Professor Steinar Nordal, for all his support and interesting discussions related to the project. Furthermore, Professor Gustav Grimstad has contributed to interesting discussions regarding the general stress space and his work related to implementation of creep in constitutive models which I would like to thank him for.

In addition, the guidance related to interpretation of soil parameters has been given by Assistant Professor Arnfinn Emdal and Helene Alexandra Amundsen (Ph.D. student) which has been very helpful during my master thesis and I would like to thank them for their help.

The Norwegian Geotechnical Institute (NGI) was granted access to huge amounts of data related to the test fill located at Onsøy. This has improved verification of my model and the comparison process which I am very grateful for. I would especially like to thank Magne Mehli, who has been the contact person and shared his work related to the embankment at Onsøy.

At the DTU I would like to thank my supervisor, Varvara Zania for her flexibility related to the working procedure. Furthermore, for her interest in my topic which has encouraged me and ensured that I followed the guidelines required by DTU. I would also like to thank Grunde Jomaas[1] for helping with the arrangement of the collaboration between NTNU and DTU.

Finally, I would like to express my gratitude to Louis Moe Christoffersen and Katrine Skjelanger Kvinge for proofreading and correcting the report.

[1] Associate Professor and head of studies related to the civil engineering study at DTU.

Abstract

The term, **natural soft clay**, is commonly used to describe a normal or slightly overconsolidated clay. This soil type may be encountered in e.g. Scandinavia, Eastern Canada and South East Asia. The mechanical response of natural soft clay may be relatively complex and more research is still required to understand the entire process with respect to short and long time aspects. The observed mechanical behaviour in the field and in the laboratory has been investigated through a literature study to outline the main characteristic features which dominate the mechanical response. This study has shown that the viscous and ageing effects are the dominating features in natural soft clay. The observed features have made a foundation of a new constitutive model based on effective stresses. The model utilizes the theory behind the Modified Cam Clay model and invariants as framework.

The model requires 17 input parameters to access all its implemented features. Three additional input parameters are available to switch between different methods of simulating the stress history, evolution of anisotropy, and failure criteria in the general stress space. The model assumes associated flow and utilizes three hardening laws which introduce eight state (hardening) parameters in total. The model is implemented in the commercial software PLAXIS as a user defined soil model through the interface between PLAXIS and FORTRAN. The FORTRAN code is supported by additional MATLAB coding where the differential equations controlling the mechanical response are assembled. The initializing of the state parameters is performed in the FORTRAN code.

The model has been verified against laboratory tests such as constant rate of strain and undraind tri-axial tests and shows acceptable performance with respect to the implemented features. The performance of the suggested model has been investigated during a full scale boundary value problem for the test embankment located at Onsøy, Norway. The model shows fairly good predictions of the soil response and the dissipation of excess pore water with respect to field measurements. These predictions have further been compared to other known soil models.

Keywords: Natural soft clay, creep, anisotropy, destructuration, recovery, Onsøy.

Sammendrag

Betegnelsen, **naturlig blødt ler**, er ofte anvendt til at betegne normalt eller svagt konsolideret ler. Denne jordart kan bl.a. findes i Skandinavien, det østlige Canada og det sydøstlige Asien. I henhold til Dansk jordartsklassifikationssystem vil jordarten falde ind under jordartstypen "Senglacialt marint og ferskvand ler".

De mekaniske egenskaber og reaktioner som følge af påførte laster på blødt normal konsolideret ler kan være relative komplekse, og supplerende forskning er påkrævet for at belyse og forstå processen mht. kort- og langtids aspekter. De mekaniske egenskaber observeret i felten og gennem forsøg i laboratoriet er blevet tilegnet igennem et litteraturstudie, med henblik på at opsummere de generelle karakteristiske egenskaber som dominerer den mekaniske opførsel. Dette studium har vist at viskos og aldersbetinget effekter er de dominerende karaktertræk i normalt konsolideret ler. Disse karaktertræk har skabt et grundlag for en ny konstitutiv model baseret på effektive spændinger. Den generelle struktur af modellen er baseret på teorien bag Modified Cam Clay modellen samt anvendelsen af invarianter.

Modellen kræver 17 input parametre for at anvende samtlige implementerede egenskaber. Derudover tilbyder modellen et valg om hvordan spændingshistorien skal initialiseres, udviklingen af anisotropien samt to forskellige brudkriterier i det generelle spændingsrum. Modellen antager associeret flydning og anvender tre hærdnings regler, hvilket medfører otte hærdnings paramtre totalt. Modellen er implementeret i det kommercielle program PLAXIS som en bruger defineret jord model igennem brugergrænseflade mellem PLAXIS og FORTRAN. FORTRAN koden er støttet af supplerende kodning i MATLAB, hvor de generelle differentielle ligninger, der styrer den mekaniske opførsel, er opstillet. Initialiseringen af hærdnings parametrene er foretaget i FORTRAN koden.

Modellen er verificeret igennem forskellige laboratorium forsøg, såsom konstant tøjningshastighed og udrænet tri-axial forsøg. Disse tilbage udregneringer viser en acceptabel ydeevne mht. de implementerede egenskaber. Modellens ydeevne under et fuldskala randværdiproblem er blevet undersøgt på testfyldning lokaliseret ved Onsøy i Norge. Modellen udviser forholdsvise gode forudsigelser af jordens opførsel samt af uddrivelsen af det genererede vandovertryk. Disse forudsigelser er blevet sammenlignet med andre kendte jord modeller.

Nøgleord: Naturlig blødt ler, krybning, anisotropi, ødelæggelse af bindinger, gendannelse af bindinger, Onsøy.

Contents

Foreword i

Preface v

Abstract vii

Sammendrag ix

List of Figures xv

List of Tables xxi

Nomenclature and Abridgment xxiii

1 Introduction 1

1.1 Background . . . 1
1.2 Motivation . . . 1
1.3 Challenges . . . 2
1.4 Objective . . . 2
1.5 Outline of Thesis . . . 3
1.6 Used Software . . . 3
1.7 Onsøy Test Fill . . . 4
1.7.1 Site Conditions . . . 5

2 Background Theory 7

2.1 General . . . 7
2.2 Continuum Mechanics . . . 7
2.3 Elastic Theory . . . 8
2.3.1 Linear Isotropic Elasticity . . . 9
2.4 Elasto-Plastic Theory . . . 10
2.5 Plasticity and Yielding . . . 11
2.6 Elasto-Plastic Model . . . 12
2.6.1 Elastic Volumetric Strain . . . 12
2.6.2 Plastic Volumetric Strain . . . 14
2.6.3 Plastic Devitoric Strain . . . 15
2.7 Three ingredients . . . 16
2.7.1 The Flow Rule . . . 16

2.7.2 Yield Criterion . . . 18
2.7.3 Hardening Rule . . . 19
2.8 The General Elasto-Plastic Model . . . 19
2.9 Modified Cam Clay . . . 21
2.9.1 General . . . 21
2.9.2 Stress Strain Relationship . . . 21

3 Natural Soft Clay **23**
3.1 General . . . 23
3.2 Characteristics of Natural Soft Clays . . . 24
3.3 Reference State . . . 24
3.4 Fabric . . . 25
3.4.1 Deposition Process . . . 26
3.5 Anisotropy . . . 28
3.5.1 Stress Induced Anisotropy . . . 31
3.6 Time dependent Behaviour . . . 33
3.6.1 Classification of Time Dependent Behaviour . . . 33
3.7 Viscous Effects . . . 34
3.7.1 Creep . . . 34
3.7.2 Stress Relaxation . . . 38
3.7.3 Strain Rate Effects . . . 39
3.8 Ageing Effects . . . 41
3.8.1 Bonding and Cementation . . . 42
3.8.2 Thixotropy . . . 44
3.9 Sample Disturbance . . . 46
3.10 Temperature . . . 47
3.11 Environment . . . 48

4 Visco-Plastic Model **49**
4.1 Introduction . . . 49
4.2 How to Model Anisotropy . . . 50
4.2.1 Second Hardening Law . . . 50
4.2.2 Anisotropy in Elastic Domain . . . 53
4.3 How to Model Bondings . . . 53
4.3.1 The Third Hardening Law . . . 54
4.4 How to Model Creep . . . 55
4.5 How to Model Recovery . . . 58
4.6 General Stress Space . . . 58
4.6.1 LMN Dependence . . . 59
4.6.2 Effect of Fabric in the Lode angle Dependency . . . 60
4.7 Initializing . . . 61
4.7.1 Initial Anisotropy . . . 61
4.7.2 Rotational Parameter $\boldsymbol{\beta}$ . . . 62
4.7.3 Rotational Parameter $\boldsymbol{\mu}$ . . . 63

4.7.4 Rotational Parameter s and z . . . 63
4.7.5 Destructuration Parameters a and b . . . 64
4.7.6 Amount of Structure x_0 . . . 64
4.7.7 Intrinsic Effective Pressure p'_{mi} . . . 65

5 Implementation **67**
5.1 General . . . 67
5.2 PLAXIS . . . 68
5.2.1 Field Equations . . . 68
5.2.2 Global Iterative Procedure . . . 70
5.2.3 Local Iterative Procedure . . . 71
5.3 Constitutive Model . . . 73
5.4 PLAXIS - User Defined Soil Model . . . 74
5.4.1 Modular Programming . . . 75

6 Verification of the Model **77**
6.1 General . . . 77
6.2 Basic Input Parameters . . . 78
6.2.1 Inclinations of the NCL and URL . . . 79
6.2.2 Inclination of the Critical State Line . . . 79
6.2.3 Unloading Reloading . . . 80
6.3 Advanced Features . . . 82
6.3.1 Anisotropy in the Elastic Region . . . 82
6.3.2 Anisotropy Evolution . . . 83
6.3.3 Destructuration . . . 87
6.3.4 Amount of Structure . . . 88
6.3.5 Creep . . . 89
6.3.6 Influence of Creep on Yielding Point . . . 89
6.3.7 Strain Rate . . . 90
6.3.8 Change Strain Rate . . . 91
6.3.9 Recovering of Structure . . . 92
6.3.10 Coupling Effect . . . 93
6.4 Additional Verification . . . 94
6.4.1 Compression vs. Extension . . . 94
6.4.2 Modified Cam Clay Response . . . 96

7 Soil Parameters **99**
7.1 General . . . 99
7.2 Available Data . . . 101
7.3 Interpreted Parameters . . . 101
7.3.1 Permeability Parameters . . . 101
7.3.2 Compressibility Parameters λ, κ and r_{si} . . . 103
7.3.3 Initial Stresses . . . 108
7.3.4 Strength Parameters . . . 109
7.4 Back-calculation . . . 111

8 Predictions and Performance **115**
8.1 Finite Element Model in PLAXIS . . . 115
8.1.1 Staged Construction . . . 116
8.2 General Observations . . . 117
8.3 First Prediction . . . 118
8.4 Final Prediction . . . 121
8.4.1 Sensitivity Analysis of Creep . . . 121
8.4.2 Modifications . . . 122
8.4.3 Settlement and Displacement . . . 124
8.4.4 Pore Pressure . . . 126
8.4.5 State Parameters . . . 129
8.5 Comparison with other Soil Models . . . 133
8.6 Evolution of OCR_τ . . . 137
8.7 Visco-Plastic Strains . . . 140
8.8 Mesh Analysis . . . 141
8.9 Implicit vs. Explicit . . . 142
8.10 Prediction - Recovery . . . 146
8.11 Coupling Effect - Reconstituted Response . . . 149
8.11.1 Ageing Effect during Loading . . . 150

9 Conclusion **151**
9.1 Summary and Conclusion . . . 151
9.2 Suggestions for Further work . . . 152

List of Figures **iv**

List of Tables **v**

List of Figures

1.1 Map showing the location of the test fill at Onsøy. Taken from (Berre, 2013). . . . 4

1.2 Plan view of the embankment showing trenches through the weathered crust, and positions of the boreholes for sampling. Figure 7.5 shows the bore profile taken by a 54 mm piston sampler. . . . 5

2.1 Soils model vs. real soil response. . . . 10

2.2 Investigation of yielding behaviour from three different soil tests. (1) Isotropic compression test: Specific volume (v) and mean effective stress (p'), (2) One-dimensional compression test: Specific volume (v) and vertical effective stress (σ'_v), (3) Undrained tri-axial compression test: Deviatoric stress (q) and deviatoric strain (ε_q). Inspired by (Wood, 1990). . . . 11

2.3 Different types of yielding. Inspired by (Leroueil and Vaughan, 1993). . . . 11

2.4 Normal Compression Line (ncl) and Unloading-Reloading Line (url) on the compression plane ($\ln p' : v$). . . . 13

2.5 Concept of plastic deformation. . . . 14

2.6 (a) Frictional block under normal load P and shear load T_x. (b) Frictional block under normal load P and shear loads T_x and T_y. (c) Interpretation of sliding in ($T_x : T_y$)-space. Inspired by (Rouainia and Muir Wood, 2000). . . . 15

2.7 Plastic strain increment vectors normal to the plastic potential surface: Plastic potential (- -) yield surface (-). Taken from Graham et al. (1984) and notice notation difference ($\delta = d$). . . . 16

2.8 Normalized yield surface and plastic strain increment. Taken from (Graham et al., 1984) notice notation difference ($\sigma'_{vc} = p'_c$). . . . 17

2.9 Associated flow rule illustrated by yield patterns in plane strain. . . . 18

2.10 MCC: Hardening and softening of the yield surface. . . . 22

3.1 Physical, chemical and biological processes which may influence the mechanical response of natural soft clay. Taken from (Perret et al., 1995). . . . 23

3.2 One-dimensional compression showing the difference between reconstituted and natural soil. . . . 25

3.3 Idealized clay structures. Taken from (Sides and Barden, 1970). . . . 26

3.4 Experimental data showing a rotated and/or skewed yield surface of different natural clays collected and presented by Länsivaara (1999). Notice notation difference ($\sigma'_{vc} = p'_c$). . . . 27

3.5 Five soil samples taken with respect to a Cartesian Coordinate system. . . . 28

3.6 Coaxiality of principal stresses and principal strains. . . . 29

3.7 Determining the elastic elastic anisotropic stiffness parameter and its influence on the stiffness. . . . 31

3.8 Classification of common time effects in natural soft clays. The dashed part of this figure and the temperature effect are beyond the scope of this work. . . . 33

3.9 Major types of fluids. (1) Newtonian (2) Thickening (3) Fluidizing (4) Casson (5) Bingham. Taken from (Locat and Demers, 1988). 34

3.10 Geological history and compressibility of a "young" and an "aged" normally consolidated clay (Bjerrum, 1973). 35

3.11 Typical values of $\left(\frac{p_c}{p_0}\right)$ and $\left(\frac{s_u}{p_0}\right)$ observed in normally consolidated late glacial and post glacial clays. The solid lines are associated to the left axis and the dashed are associated to the right axis. Notice, that the young dashed line is placed at the x-axis since $\frac{p_c}{p_0} = 1.0$. Inspired by (Bjerrum, 1973). 35

3.12 Illustration of creep characteristics. Notice that the total strain is plotted which should not be confused with the pure creep strain. Taken from (Sorensen, 2006). . 36

3.13 Characteristic features of creep strain related to time. 37

3.14 Influence of creep stress intensity on creep rate. 37

3.15 Constant stress creep showing the variation of creep rate with time. Notice, that Yoginder et al. (1977) utilized q for the symbol of normalized deviatoric stress. Taken from (Yoginder et al., 1977). 38

3.16 Behaviour of creep and stress relaxation during undrained tri-axial testing for a NC soil. 39

3.17 Experimental data from undrained tri-axial testing showing the effect of changing the strain rate. Taken from (Länsivaara, 1999). 39

3.18 Illustration of isotach and non-isotach behaviour for CRS. 40

3.19 Illustration of isotach and non-isotach behaviour for undrained tri-axial testing. The two upper Figures show the behaviour of creep and stress relaxation. The two lower figures show the effect of changing the strain rate during the test. 40

3.20 Influence of viscous effects and ageing effects on the effective stress path in undrained tri-axial compression of reconstituted Magnus clay. Taken from (Burland, 1990 after Jardine, 1985). 41

3.21 Effect of slow rate of straining on the one-dimensional compression behaviour of artificially sedimented Jonquiere clay. Taken from (Leroueil et al., 1996). Notice notation difference $\dot{\varepsilon}_v = \dot{\varepsilon}_p$. 42

3.22 Combined effect of bonding and creep. 43

3.23 Testing three Norwegian clays in tri-axial testing. Taken from (Lacasse et al., 1985). 44

3.24 Thixotropy hardening as a function of time for a reversible situation. 45

3.25 Principle of thixotropic in a fine grained soil. Taken from (Mitchell, 1960). 45

3.26 Comparing the degree of disturbance in tube sampling relative to block sampling for three different types of Norwegian clays. Taken from (Lacasse et al., 1985) . . . 46

3.27 Experimental data from a CRS test illustrating the similarities of changing the temperature or strain rate. Taken from (Laloui et al., 2008). 47

4.1 Incorporating bondings in the MCC model. Notice that the rotation of the yield surface is associated to the fabric (anisotropy) and the expanded yield surface is caused by bondings. 54

4.2 Difference between the "rate" and "Creep" model where the dashed line represent the "Creep-swelling". Taken from (Grimstad et al., 2010). 56

4.3 The intrinsic yield surface, its associated surface through the structure and the reference surface representing the stress condition. 57

4.4 Concept of isotaches effected by structure. Notice difference in notation $\varepsilon_v = \varepsilon_p$. . 57

4.5 Failure surface in the deviatoric plane. Taken from (Potts and Zdravkovic, 1999). . 59

4.6 Mohr-Coulomb criteria in the general stress space. 60

4.7 LMN dependency in the general stress space. 60

4.8 Value of β using $\nu_{ur} = 0.20$, λ_i=0.25, and κ=0.05. 62
4.9 Concept of destructuration with respect to the creep number. Taken from (Grimstad and Degago, 2010). 64
4.10 Incremental oedometer test for Eberg clay verifying Figure 4.9. Taken from (Grimstad et al., 2010). 64
4.11 Concept of initializing the SCA-R model. Notice that p^{eq} is a function of M,$\boldsymbol{\alpha}$ and the initial stresses. 65

5.1 The global iterative procedure in a FE analysis. 68
5.2 An arbitrary body affected by a load. 69
5.3 Principle of the computational framework. 73
5.4 General framework in FORTRAN. Notice that some less necessary subroutines and all the functions are left out for simplicity. 76

6.1 Theoretical oedometer path. See explanation of point A, B, C and D in the paragraph to the left. 77
6.2 General option in Soil Test showing the standard input parameters. 78
6.3 Interpretation of the inclination of the NCL and URL to verify λ_i, κ, and e_0 from the compression plane. The standard input parameters may be seen on Figure 6.2. 79
6.4 Interpretation of the inclination of the CSL to verify φ_{cs} for tri-axial simulations in compression. The standard input parameters may be seen on Figure 6.2. Notice that $\varphi_{cs} = 25.38 \longrightarrow M = 1.0$. 80
6.5 ESP in the $(p' : q)$-space to verify the input parameter ν_{ur} during one-dimensional compression. The standard input parameters may be seen on Figure 6.2. 81
6.6 Transverse anisotropic elastic response in undrained tri-axial scenario to verify the input parameter α_e. The standard input parameters may be seen on Figure 6.2 and $OCR = 4.0$ has been utilized. 82
6.7 Simulations of the rotation towards critical state in an undrained tri-axial test. Notice that the sample is compressed 100% to ensure theoretical critical state. The rate of rotation (μ and c) is set to 200. The standard input parameters may be seen on Figure 6.2. 85
6.8 Evolution of α during isotropic compression (Wheeler 2003). 86
6.9 Effect of destructuration parameters a and b during oedometer conditions. The standard soil parameters may be seen in Figure 6.2. Note, $OCR = 2.0$ and $r_{si,min} = 100$. 87
6.10 Influence of x_0 with respect to the yielding point during oedomenter conditions keeping p'_{mi} constant. The standard soil parameters may be seen on Figure 6.2 and Table 6.6. Notice, $a = b = 15.0$. 88
6.11 Oedometer condition under constant effective stresses for a period of 1095 Days (3 years). Notice that $r_{si} = r_{si,min}$ and the standard input parameters may be seen on Figure 6.2. 89
6.12 Influence of intrinsic creep number on the apparent yielding point by keeping the structure constant ($x = 5.0$). The solid line represent a scenario where $r_{si} = 100$ and $r_{si,min} = 16.66$. The standard soil parameters may be seen in Figure 6.2 besides the initial stress condition ($\sigma'_{11} = \sigma'_{22} = \sigma'_{33} = 100$ kPa). 90
6.13 Strain rate effects from viscous-plastic response. $r_{si} = 100$ and $OCR = 1.2$. The rest of the parameters may be seen on Figure 6.2. Notice, the test without creep corresponds to elasto-plastic response. 91
6.14 Effect of changing the strain rate in different tests. $r_{si} = 100$ and $OCR = 1.2$, the rest of the parameters may be seen on Figure 6.2. 91

6.15 Recovering of structure (x) over time. Notice, Reference time 0..100 symbolize a shearing phase of 1 day destroying the structure. Reference time 101..200 symbolize constant effective stresses over a period of 2000 days. For all four cases, R_t=0.001. The soil parameters may be seen in Figure 6.2. 92

6.16 Influence of recovering of structure with respect to creep under constant stress conditions. The standard soil parameters may be seen in Figure 6.2. The initial structure of the test is equal to $x_0 = 1$ going towards the boundary value of $x_b = \frac{r_{si}-r_{si,min}}{r_{si,min}} R = 9R$, since $r_{si,min} = 100$ and $r_{si} = 1000$. 93

6.17 Setup to control the soil response during compression and extension in undrained tri-axial. 94

6.18 Influence of K_0^{NC} with respect to compression and tension during undrained tri-axial conditions. The standard soil parameters may be seen on Figure 6.2. Notice that q becomes negative since it is computed as the vertical minus the horizontal effective stress. 95

6.19 Comparing the mobilisation of shear strength in a tri-axial test from MCC models. Red line symbolise MATLAB model, blue line symbolise visco-plastic model in PLAXIS. 96

6.20 Comparing the volumetric change and development of excess pore pressure for the drained and undrained cases in tri-axial simulation. Red line symbolise MATLAB model, blue line symbolise visco-plastic model in PLAXIS. 97

6.21 Comparing the stress path in $(p' : q)$-space in tri-axial simulation from MCC models. Red line symbolise MATLAB model, blue line symbolise visco-plastic model in FORTRAN. 97

7.1 Procedure to interpret hydraulic conductivity and its evolution from **Block-28-B-11**.102

7.2 Interpreted compression and swelling parameter from **Block-19-A1-O1** through the CRS. 104

7.3 Interpreted creep number from **Block-19-A1-O1** through the CRS. 105

7.4 Interpreted compression and swelling index from CRS. 105

7.5 Bore profile from a 54 mm standard tube sampler. The locations from the sampling may be seen on Figure 1.2. The bore profile is taken from (Berre, 2013). The black solid lines seperates the strata and the red dashes lines yields an average undrained remoulded and undistributed shear strength from the fallen cone in each layer. . . 107

7.6 Overconsolidation stress obtained from primary loading and unloading. 108

7.7 Evolution of K_0' during CAK_0UC testing. 109

7.8 ESP for seven tri-axial tests approaching critical state. K_0 means CAK_0UC (K_0-stage). 109

7.9 ESP for two tri-axial tests near the surface. 110

7.10 Principal sketch of the boundary value problem setup in PLAXIS used to back-calculate the CRS oedometer tests. 111

7.11 Back-calculation of the CRS response for **Block-19-A1-O1**. 112

7.12 Comparison of tri-axial measurements from **Block-18-A-30** to the SCA-R model and the SSC soil model. Utilizing $\mu = 4.0$ and α_e = -0.12. 114

8.1 Finite element model in PLAXIS of the embankment at Onsøy. 116

8.2 Ratio between the horizontal and vertical strains below the centreline of the embankment from field measurements. Taken from (Berre, 2013). 117

8.3 Measurements and predictions of the embankment (SCA-R: First prediction). . . . 119

8.4 Measurements of the embankment (SCA-R: First prediction). 120

8.5 Sensitivity analysis of the input parameters related to time evolution of the plastic multiplier. The utilized parameters may be seen in Table 8.5 122

8.6 Definition of OCR_τ and POP. 123
8.7 Estimated settlement just beneath the center of the embankment (SCA-R: Best-fit). 124
8.8 Estimated surface settlement of the embankment (SCA-R model best-fit). 124
8.9 Estimated displacement and strain of the embankment (SCA-R: Best-fit). 125
8.10 Estimated excess pore pressure of the embankment (SCA-R: Best-fit). 126
8.11 Excess pore pressure 8.0 meters below the ground surface (SCA-R: Best-fit). 127
8.12 Excess pore pressure distribution at day No. 36 (SCA-R: Best-fit). 128
8.13 Excess pore pressure distribution at day No. 1220 (SCA-R: Best-fit). 128
8.14 Evolution of plastic multiplier ($d\lambda$) - (SCA-R: Best-fit). 129
8.15 Destruction of structure (x) - (SCA-R: Best-fit). 130
8.16 Increase in intrinsic pressure (p'_{mi}) - (SCA-R: Best-fit). 131
8.17 Plastic multiplier at day No. 1120 using OCR_τ. 132
8.18 Comparison of soil models to estimate the settlement just beneath the center of the embankment. 133
8.19 Comparison of different soil models ability to estimate the surface settlement. . . . 134
8.20 Comparison of different soil models ability to estimate the excess pore pressure at the centreline of the embankment. 135
8.21 Comparison of different soil models ability to estimate the horizontal displacement 5.0 m from the centreline of the embankment. 135
8.22 Comparison of different soil models ability to estimate the vertical strain at the centreline of the embankment. 136
8.23 Evolution of OCR_τ and its associated parameters during construction of the fill (centreline). Note the black, violet, cyan, and green are located on top of each other or very close in Figure b and c. 138
8.24 Evolution of OCR_τ and its associated parameters at the long term. 139
8.25 Comparing elasto-plastic and visco-plastic response (SCA-R: Best-fit). 140
8.26 New mesh for the finite element model used to model the embankment at Onsøy. . 141
8.27 Mesh analysis I of the embankment. 141
8.28 Mesh analysis II for the embankment. 142
8.29 Performance for an explicit and implicit scheme in the local iteration. 143
8.30 Investigation of explicit and implicit scheme for layer 2 (2.0 - 5.0 m). 145
8.31 Effect of recovery of structure during creep test. The utilized input parameters are similar to the properties of layer 2 (2.0 - 5.0 m) and an isotropic stress condition of $\sigma' = 100$ kPa. 146
8.32 Influence of recovery on the settlement just beneath the center for the embankment. 147
8.33 Structure (x) for scenario 3. 148
8.34 Reconstituted response during drained creep and compression affected by recovery. The utilized input parameters are similar to soil layer 3 (5.0 - 10.0 m) in the final prediction. 149
8.35 Evolution of x during drained creep and compression for a reconstituted sample. The soil parameters is similar to layer 3 (5.0 - 10.0 m) in the final prediction and $POP = x = 0.0$. 149
8.36 Reconstituted response during compression affected by recovery. The utilized input parameters are similar to soil layer 3 (5.0 - 10.0 m) in the final prediction. 150

9.1 Suggested extensions to the SCA-R model. 153

List of Tables

2.1 Influence of η with respect to the plastic response. 18
2.2 Definition of the current state by the yield criterion. 18

3.1 Number of moduli in the stiffness matrix. 28

4.1 Value of K_0^{NC} to find zero initial rotation for different methods. 61

6.1 Basic input parameters and methods associated to interpretation. 78
6.2 Overview of the advanced features and related parameters. 82
6.3 Extracted values of the rotated yield surface during oedometer conditions. 84
6.4 Analytical values for the rotated yield surface for different K_0^{NC} related to oedometer conditions. 84
6.5 Controlling the boundary value of α_b towards critical state. 85
6.6 OCR values demanding p'_{mi} constant with a change of x. Reference: $x = 0.0$ and $OCR = 1.0$ 88
6.7 Verifying the creep parameter in oedometer scenario during constant effective stress. 89
6.8 Convention of strain rate into PLAXIS's time step for a chosen axial deformation of 10 %. 90
6.9 Theoretical and numerical results to verify the MATLAB model and visco-plastic model. 96

7.1 An overview of the input parameters used in the SCA-R model and related laboratory tests associated to interpretation methods. 100
7.2 List of available data related to the test fill at Onsøy. 101
7.3 Interpreted permeability parameters from CRS tests. 103
7.4 Determined sensitivity of the clay at Onsøy. 106
7.5 Interpreted data from the laboratory curves for the nine CRS oedometer tests. . . 107
7.6 Interpreted values of the elastic anisotropy parameter (α_e). 110
7.7 Overview of the input data used in the back-calculations of the CRS tests. The second row shows the interpreted values from laboratory tests. 113
7.8 Calibrated values of μ and α_e from the tri-axial tests. Brackets are the interpreted values. 113

8.1 Overview of the construction process and measured readings (Mehli, 2015b). . . . 116
8.2 Input data for material layer modelled with Soft Soil. 118
8.3 Input data for material layers modelled with Mohr-Coulomb. 118
8.4 First prediction of input data for material layers modelled with SCA-R. 118
8.5 Standard input parameters used in the sensitivity analysis for creep development. . 121

8.6 Final prediction of input data for material layers modelled with SCA-R. Number in brackets shows earlier values. 124
8.7 Constitutive models and their characteristics. Modified version of (Ashrafi, 2014). 133
8.8 Different scenarios with recovery of structure. The input parameters (R and R_t) are used for all layers. 147

Nomenclature and Abridgement

Greek letters:

$\boldsymbol{\alpha}$	State parameters	ε_p	Volume strain
$\boldsymbol{\alpha}$	Fabric tensor	ε_q	Deviatoric strain
$\boldsymbol{\alpha}_d$	Deviatoric fabric tensor	ε^e	Elastic strain
α	Scalar - Rotation of YS	ε^p	Plastic strain
α_b	Boundary value of rotation	ε^{vp}	Visco-Plastic strain
α_e	Elastic anisotropy parameter	ζ_i	Internal irrecoverable compressibility
α_h	Houlsby anisotropy parameter	η	Stress ratio
$\alpha_{K_0^{NC}}$	Inclination associated to K_0^{NC}	$\eta_{K_0^{NC}}$	Stress ratio associated to K_0^{NC}
α_0	Initial rotation of YS	θ	Lode angle
α_1	Fabric in x_1-direction	θ^α	Lode angle (fabric)
α_2	Fabric in x_2-direction	$\boldsymbol{\kappa}$	State parameters
α_3	Fabric in x_3-direction	κ	Swelling/unloading parameter
$\boldsymbol{\beta}$	State parameters	κ^*	Modified swelling/unloading parameter
β	Rotational hardening parameter	$d\lambda$	Plastic multiplier
γ	Unit weight	λ	Compression parameter
γ	Thermal coefficient	λ^*	Modified compression parameter
γ_i	Body forces	λ_i	Intrinsic compression parameter
γ_{12}	Shear strain on x_1- and x_2-surface	μ	Rotational hardening parameter
γ_{13}	Shear strain on x_1- and x_3-surface	μ_f	Friction coefficient
γ_{23}	Shear strain on x_2- and x_3-surface	ν	Poission's ratio
δ_{11}	Vertical displacement	ν'	Drained Poission's ratio
δ_{22}	Horizontal displacement	ν_u	Undrained Poission's ratio
δ_{33}	Horizontal displacement	ν_{ur}	Unloading/Reloading Poission's ratio
δu_i	Virtual displacement	ν_{water}	Viscosity of water
$\boldsymbol{\varepsilon}$	Strain tensor	ρ_s	Density of solid grains
ε_{11}	Normal Strain on x_1-surface	ρ_w	Density of water
ε_{22}	Normal Strain on x_2-surface	$\boldsymbol{\sigma}$	Stress tensor
ε_{33}	Normal Strain on x_3-surface	$\boldsymbol{\sigma}_d$	Deviatoric stress tensor
ε_{12}	Shear Strain on x_1- and x_2-surface	$\boldsymbol{\sigma}_d^\alpha$	Deviatoric stress tensor (fabric)
ε_{13}	Shear Strain on x_1- and x_3-surface	σ'_{ij}	Cauchy stress tensor
ε_{23}	Shear Strain on x_2- and x_3-surface	σ'_{ij}	Cauchy stress tensor.

σ'_v	Vertical effective stress
σ'_y	Vertical effective stress
σ'_c	Pre-consolidation pressure (PLAXIS)
σ'_{xx}	Horizontal effective stress (PLAXIS)
σ'_{yy}	Vertical effective stress (PLAXIS)
σ'_{1c}	Isotropic consolidation pressure
σ'_1	First effective principle stress
σ'_2	Second effective principle stress
σ'_3	Third effective principle stress
σ'_{11}	Normal effective stress on x_1-surface
σ'_{22}	Normal effective stress on x_2-surface
σ'_{33}	Normal effective stress on x_3-surface
σ'_{12}	Shear effective stress on x_1-,x_2-surface
σ'_{13}	Shear effective stress on x_1-,x_3-surface
σ'_{23}	Shear effective stress on x_2-,x_3-surface
τ	Reference time
τ_f	Shear strength
τ_i	Boundary traction components
φ	Friction angle
φ_{cs}	Friction angle (critical state)
φ_{inter}	Interface friction angle
ψ_{inter}	Interface parameter
χ_p	Target value, volume
χ_d	Target value, deviatoric
Ψ	Dilatancy angle

Latin letters:

A	Plastic resistance
A	Area
a	Attraction
a	Destructuration parameter
$\boldsymbol{B}$	Strain interpolation matrix
b	Destructuration parameter
C_A	Related to λ and κ
C_c	Compression index
C_s	Swelling index
c	Rotational hardening parameter
c	Coefficient
$c_{1..4}$	Coefficient
c_k	Change in k
$\boldsymbol{D}$	Elastic stiffness matrix
$\boldsymbol{D}(\sigma_n, \kappa_n)$	Tangential stiff. (previous iter. n)
D	Janbu's pore pressure parameter
D_{ep}	Elastic-Plastic constitutive matrix
d	Depth
d_s	Relative density
e	Void ratio
e_0	Initial void ratio
e^*_{100}	Void ratio at 100 kPa
e^*_{1000}	Void ratio at 1000 kPa
E	Young's modulus
E'	Drained Young's modulus
E_u	Undrained Young's modulus
E^*	Young's modulus (Reference)
$E^{\text{ref}}_{\text{oed}}$	Interface stiffness (oedometeer)
F	Yield surface
$\boldsymbol{f}_{ex}$	External force
$\boldsymbol{f}_{in}$	Internal reaction vector
G	Shear modulus
G'	Drained Shear modulus
g	Dimensionless constant
$\boldsymbol{h}$	Vector containing state parameters
$\boldsymbol{I}$	Identity matrix
I_1	First full stress invariant
I_2	Second full stress invariant
I_3	Third full stress invariant
I^ε_1	First full strain invariant
I^ε_2	Second full strain invariant
I^ε_3	Third full strain invariant
I_p	The plasticity index
I_v	Void index
J	Coupling stiffness
$\boldsymbol{J}$	Jacobi matrix
J_1	First deviatoric stress invariant
J_2	Second deviatoric stress invariant
J_3	Third deviatoric stress invariant
J^ε_1	First deviatoric strain invariant
J^ε_2	Second deviatoric strain invariant
J^ε_3	Third deviatoric strain invariant
J^α_1	First deviatoric fabric invariant
J^α_2	Second deviatoric fabric invariant
J^α_3	Third deviatoric fabric invariant
$\boldsymbol{K}$	Global stiffness matrix

K	Bulk modulus	R	Recovery parameter
K'	Drained bulk modulus	R_t	Recovery pace
K_w	Bulk modulus of water	R	Resistance number
K_0^{NC}	Stress ratio in NC	$\boldsymbol{r}$	Residual vector
K_0'	Initial stress ratio	r	Pre-consolidation pressure exponent
$K_{0,x}'$	Initial stress ratio (PLAXIS)	r_s	Creep number
k	Dimensionless constant	r_{si}	Intrinsic creep number
k	Hydraulic conductivity	$r_{si,min}$	Minimum creep number
k_x	Hydraulic conductivity	S	External boundary
	horizontal direction	S_A	Aged shear strength
k_y	Hydraulic conductivity	S_R	Remoulded shear strength
	vertical direction	$S_{Thi,t}$	Thixotropic regaining
k_0	Initial hydraulic conductivity	S_r	Degree of saturation
$\boldsymbol{L}$	Partial derivative matrix	S_t	Sensitive
M	Inclination of CSL	s	Model constant RH III
M_c	Inclination of CSL in compression	$\boldsymbol{s}$	Deviatoric stress tensor
m	Secant modulus	s_r	Remoulded shear strength
$m_{K_0^{NC}}$	Plastic flow direction	s_u	Undrained shear strength
	during oedometer condition	s_1	First principal deviatoric stress
$\boldsymbol{N}(\xi,\eta,\zeta)$	Shape functions	s_2	Second principal deviatoric stress
n	Pressure exponent	s_3	Third principal deviatoric stress
OCR	Over consolidation ratio	s_{11}	Deviatoric stress on x_1-surface
OCR_τ	Over consolidation ratio	s_{22}	Deviatoric stress on x_2-surface
	with reference τ	s_{33}	Deviatoric stress on x_3-surface
P	Force	s_{12}	Deviatoric stress on x_1- and x_2-surface
POP	Overburden pressure	s_{13}	Deviatoric stress on x_1- and x_3-surface
p	Total mean pressure	s_{23}	Deviatoric stress on x_2- and x_3-surface
p'	Effective mean pressure	T_x	Force in x-direction
p^{eq}	Equivalent reference surface	T_y	Force in y-direction
p_a	Reference pressure 100 kPa	T_z	Force in z-direction
p_{at}	Atmospheric pressure	T	Temperature
p_m'	Apparent yielding pressure	t	Time
p_{mi}'	Intrinsic pressure	$U(\varepsilon)$	Specific internal energy density
p_c'	Pre-consolidation pressure	$\boldsymbol{u}$	Displacement field
	or quasi-overconsolidation pressure	u	Displacement
p_0'	Sedimentation pressure	V	Volume
p_{01}'	Stress state	$\boldsymbol{v}$	Nodal displacement
p_{02}'	Stress state	v	Specific volume
Q	Plastic potential	$v_\lambda = N$	Reference void ratio
q	Deviatoric stress	v_κ	Reference void ratio
q^α	Deviatoric stress (fabric)	W	Internal work
q^*	Normalized deviatoric stress	w	Water content

w_l	Liquid limit
x	Demand of max strain increment
x	Structure
x	Cartesian coordinate
x^α	Model parameter RH III
x_0	Initial amount of structure
x_1	Cartesian coordinate
x_2	Cartesian coordinate
x_3	Cartesian coordinate
y	Cartesian coordinate
Y	Yield point
z	Cartesian coordinate
z	Model constant RH III

Mathematical Notation:

∂	Partial differentiate
d	Increment change
Δ	Change
$\dot{()}$	$\frac{\partial}{\partial t}$
$\langle\rangle$	Macaulayy brackets
T	Transposed
Tr	Trace

Abridgement:

CC	Cam Clay
CRS	Constant Rate of Strain
CS	Critical state
CSL	Critical State Line
CS-SSCG	Critical State Soft Soil Creep with Shear Stiffness
DLL	Digital Link Library
EE	Edge to Edge
EF	Edge to Face
ESP	Effective Stress Path
FEM	Finite Element Method
FF	Face to Face
MCC	Modified Cam Clay
NC	Normal Consolidated
NCL	Normal Compression Line
n-SAC	non-associated - Structure Anisotropic Creep
OC	Over Consolidated
P	Primary consolidation
RH	Rotational Hardening
S	Secondary compression
SBS	State Boundary Surface
SCA-R	Structure Creep Anisotropic - Recovery
SCL	Sedimentation Compression Line
SRS	Step-wise change in the Rate of Strain
SS	Soft Soil
SSC	Soft Soil Creep
T	Tertiary compression
TSP	Total Stress Path
UDSM	User Defined Soil Model
URL	Unloading Reloading Line
YS	Yield Surface

Subscript:

ani	Anisotropic
c	Compression
e	Extension
ij	Einstein notation
i	Intrinsic properties
iso	Isotropic
ort	Orthotropic
p	Volume
q	Deviatoric
S	Surface
u	Pore pressure
V	Volume
0	Initial
A	Active
cs	Critical stage
d	Devaitoric
f	Failure
H	Horizontal
P	Passive
V	Vertical

Superscript:

α	Fabric
$\Delta t + t$	Integer (current stage)
$\Delta n + n$	Integer (current stage)
e	Elastic
i	Integer (step number)
j	Integer (step number)
n	Integer (previous stage)
p	Plastic
t	Integer (previous stage)
vp	Visco-plastic

Chapter 1

Introduction

1.1 Background

The general understanding of soil behaviour has increased gradually over the last decades. However, deposits of natural soft clays may still be categorized as a research subject and may lead to huge geotechnical challenges (Karstunen et al., 2005). The focus on natural soft clay began in the early 1900's when the academic society initiated their research of this particular soil. At that time most of the observed behaviour were related directly or indirectly to the water content of the clay. However, as the performance of the sample technique and laboratory testing increased the understanding of natural soft clay improved and it turned out to be very complex.

Nowadays, the main features related to natural soft clay are associated to the viscous and aging effects which have a dominating influence of the soil response with respect to their reconstituted equivalents. Some of these effects are known as secondary compression (creep), rate dependence and the influence of structure in the natural soft clay. All these aspects need to be taken into consideration if a higher accuracy of estimating the response of natural soft clay is desired.

Additionally, the understanding of the natural soft clay is a growing demand from sectors outside the academic society caused by the expansion of infrastructure and large structures in areas where large deposits of natural soft clays are significant and cannot be avoided, (Karstunen et al., 2005). These deposits are mainly associated to places such as Scandinavia, Eastern Canada and South East Asia.

Hence, the scope of this master thesis will be to clarify some of the most important features related to natural soft clay, through a literature study. From the literature study and a study of existing soil models a constitutive model will be assembled into commercial software which may be used to estimate a more detailed behaviour of the complex natural soft clay.

1.2 Motivation

Nowadays, geotechnical engineers often design structures through analysis utilizing the Serviceability Limit State (SLS) and the Ultimate Limit State (ULS) which may be based on conservative assumptions often supported by traditional practice. The numerical modelling has applied a significant improvement and has narrowed the high conservativeness. However, the available soil models in commercial software may not be able to capture all the special features related to, for instance, natural soft clay due to their simplicity.

Through an advanced soil model the conservativeness may be reduced even more and a better estimation of the soil behaviour may be given. For instance, it would allow the geotechnical engineer to design structures utilizing the peak strength instead of the residual strength which

may be significantly higher. However, one should keep in mind that the maximum strength is a peak value and it will be progressively reduced towards the residual strength as a function of strain. If this aspect is taken into consideration, resources may be saved by utilizing a higher design strength. In general, a potential economical profit may be gained through a better understanding and modelling of natural soft clay which creates the platform for this master thesis.

1.3 Challenges

The main challenges when designing a constitutive formulation for soil are to design a model which is able to capture the observed behaviour in laboratory tests and full scale projects. In addition, to extend the model to general stress space and thereby simulate real soil response in the three dimensional stress space. The main challenges related to numerical modelling of soil response has been formulated by Muir Wood (1994) and may be listed as:

(a) **General stress space** - Appropriate use of invariants

(b) **Non-monotonic loading**

(c) **Anisotropic materials** - Deposition process

(d) **Structured materials** - Strain softening

(e) **Non-classical soils**

(f) **Particulate approaches**

(g) **Time effects** - Viscosity

Various models have been suggested to simulate some of these features. A notable drawback related to several of the suggested models are related to the numbers of input parameters. Some of input parameters are missing a direct physical meaning, or are impossible to identify from standard laboratory tests (Grimstad, 2009). Hence, the suggested model would try to minimize the input parameters and utilize methods where the input parameters may be determined through standard laboratory tests.

1.4 Objective

The aim of the study is listed as:

1. **Assemble the theory to develop a constitutive model involving the issue (a) mentioned in Section 1.3.**
    - i Involving the necessary mathematical formulations, procedures and numerical algorithms related to the soil model utilizing continuum mechanics as a platform.
2. **Literature study of the characteristics observed in natural soft clay related to (c), (d), and (g) mentioned in Section 1.3**.
3. **Develop a user-friendly effective stress based model for natural soft clays.**
    - i An advanced soil model which may be implemented into commercial software using a suitable finite element approach.
    - ii The robustness of the implementation should be such that it is possible to effectively use the implemented model on practical examples.
4. **Investigate the performance of the suggested model.**
    - i Model calibration against laboratory test.
    - ii Full scale boundary value problems involving water dissipation.

The suggested constitutive model would be restricted to monotonic loading conditions. Hence, cyclic and dynamic loading conditions are not taken into account and the effect of small stiffness is not considered as well in the model.

1.5 Outline of Thesis

The main report will consist of the following chapters:

- **Chapter 2** - Background theory
  - This chapter assembles the theory to develop an effective stress based constitutive model, similar to the Modified Cam Clay model, which creates a platform for the final constitutive model.
- **Chapter 3** - Natural soft clay
  - This chapter contains a literature study of natural soft clay and thereby yields the general understanding of the aims for the constitutive model.
- **Chapter 4** - Visco-plastic model
  - This chapter describes the chosen methods to implement the features observed in Chapter 3 to the constitutive model assembled in Chapter 2.
- **Chapter 5** - Implementation
  - This chapter describes how the constitutive model is implemented into commercial software.
- **Chapter 6** - Verification
  - This chapter performs a verification process of the constitutive model to insure that the model works as expected and that the input parameters may be interpreted from the output.
- **Chapter 7** - Soil parameters
  - This chapter contains a interpretation process to determine the necessary input parameters from laboratory tests. Furthermore, back-calculations of these laboratory tests are performed to calibrate the input parameters.
- **Chapter 8** - Predictions
  - This chapter contain a performance analysis, results and discussion related to the embankment located at Onsøy, Norway.
- **Chapter 9** - Conclusion and further work

As a supplement to the main report an appendix report has been constructed. The appendix report consists of related theory, coding in MATLAB and FORTRAN along with results related to the embankment at Onsøy. The additional theory is added so that the reader is more capable of following the utilized approach. The appendix report is attached as an additional report after the bibliography.

1.6 Used Software

Throughout this master's thesis the following software have been used:

- MATLAB R2014b
- PLAXIS 2D AE 2.0
- FORTRAN 90
- Latex (Text platform)

1.7 Onsøy Test Fill

The performance of the suggested constitutive model will be investigated through a boundary value problem of the test fill located at Onsøy in Norway. The test fill was constructed in 1966 by the Norwegian Geotechnical Institute (NGI) as a part of an investigation project in Thailand (Berre, 2013). The location of the test site is approximately 4 km north of the centre of Fredrikstad in Norway, see Figure 1.1. The purpose of the test fill was to investigate the deformations on soft plastic marine clay (natural soft clay). The test fill was constructed by five layers, yielding a total height of 2.3 meters, in 14 days. The dimensions of the fill are 20 m x 60 m, see Figure 1.2.

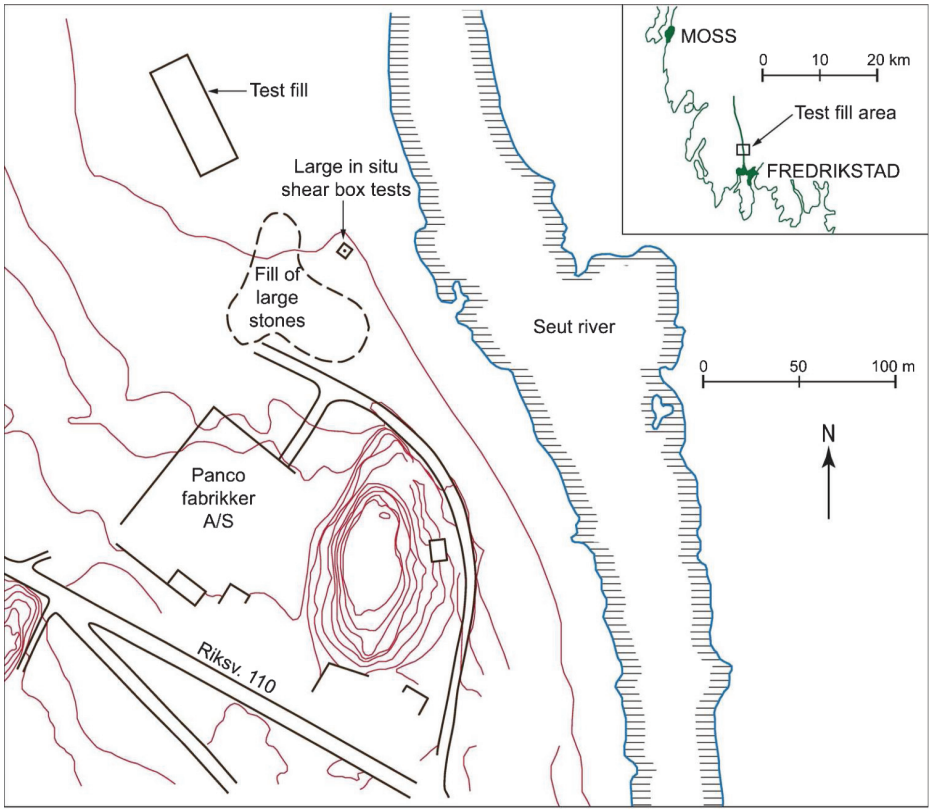

Figure 1.1: *Map showing the location of the test fill at Onsøy. Taken from (Berre, 2013).*

The safety factor of the embankment was estimated to 1.35 by undrained strength from in situ shear vane (Berre, 2013). After 3 years, the test fill was brought to failure by raising the height. The site was heavily instrumented and high quality samples have been taken by block samplers. An overview of the different instrumentations and their locations at the site may be seen in Appendix B.1. For further information regarding the block sampling at Onsøy, see e.g. (Lacasse et al., 1985).

1.7.1 Site Conditions

The Onsøy clay is a marine clay and was deposited during the deglaciation at the early postglacial period. The thickness of the clay deposit varies and is measured to 53 m beneath the test fill to the bedrock. The clay fraction varies between 40% to 60%. The ground water level is located around 0.2 m to 0.3 m below ground surface and the pore pressure is artesian (ca. 5% at 20 m depth). The clay is saturated from the dry crust and downwards and the height of the weather crust varies from 0.8 to 1.5 m. The water content (w) varies between 57% to 67%. The plasticity index (I_p) varies from 34 in the upper 9 m, to 44 between 9 m and 15 m and to 51 between 15 m to 20 m. Hence, the clay may be classified as highly plastic. The salt content is stable at 30 g/l from about 8 m and downwards. Black spots in the clay and pores with humus was found down to 10 m.

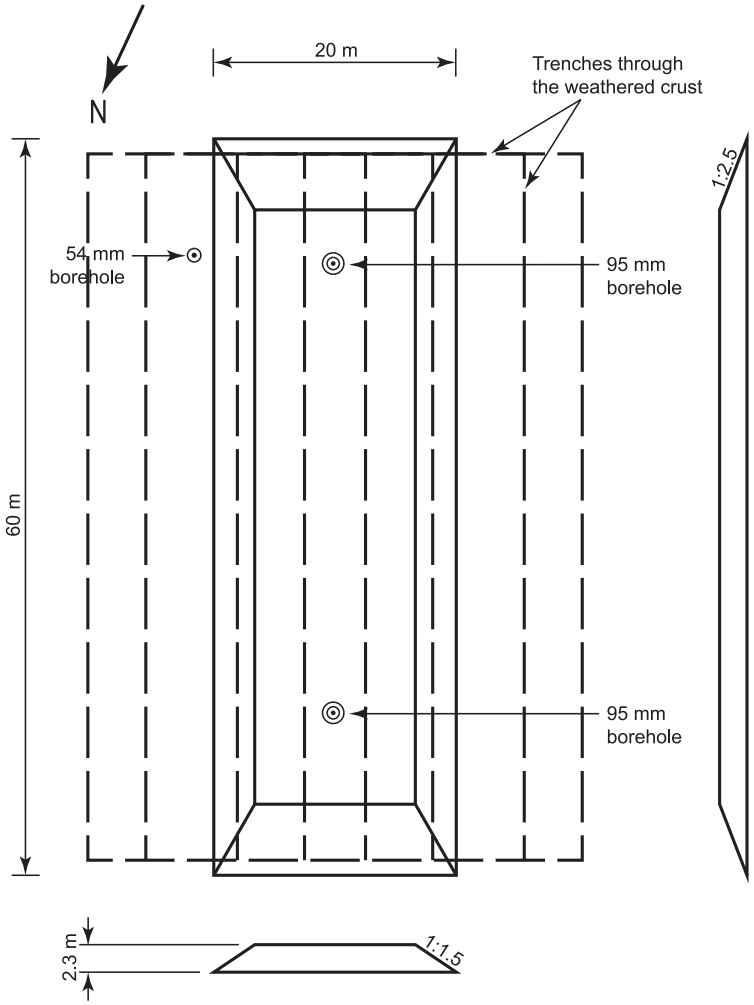

Figure 1.2: *Plan view of the embankment showing trenches through the weathered crust, and positions of the boreholes for sampling. Figure 7.5 shows the bore profile taken by a 54 mm piston sampler.*

For further information about the test fill and the field measurements, please see (Berre, 2013).

Chapter 2

Background Theory

The purpose of this chapter is to present the Modified Cam Clay (MCC) model and the elasto-plastic theory which is utilized to assembled it. The MCC model will establish a platform for the final constitutive model.

2.1 General

In order to predict the material behaviour, constitutive models that relate stresses and strains must be established. Several material models have been develop over the last decades aiming to increase the accuracy when predicting the stress-strain relationship of real materials.

To develop an visco-plastic model, it is necessary to have a basic understanding of the general elasto-plastic theory and the continuum mechanics behind constitutive models. Additionally, the concept and methodology of the critical state soil mechanics have underlined the majority of the isotropic soil models within the framework of elasto-plastic (Dafalias, 1986) and will also be the case in this work. Hence, the main concepts in critical state soil mechanics and the Modified Cam Clay (MCC) model will be presented in this chapter.

2.2 Continuum Mechanics

In order to describe the soil response, it is common to utilize the theory of continuum mechanics. Applying continuum mechanics, when estimating the soil response, may be considered as an assumption since the term **soil** consist of three phases: Particles, liquid, and gas which do not describe a continuum. Furthermore, each of these phases will consist of atoms and molecules which may not be described as a continuum themselves. However, regarding the macro behaviour for a soil the assumption of continuum mechanics is often utilized (Grimstad, 2009). The general concept of continuum mechanics utilize four basic principles which are used to establish the kinematic relation between stresses and strains (Grimstad and Benz, 2014):

- Conservation of mass
- Linear momentum
- Moment of momentum
- Conservation of energy

A short summary of continuum mechanics and the associated invariants may be found in Appendix C.1. In addition, Appendix C.1.8 shows a compact format of the utilized tensors: stresses, strains and fabrics in the principle and deviatoric format.

2.3 Elastic Theory

Elastic materials are characterized by reversible deformations meaning no dissipation of mechanical energy, path independence, and rate independence. In other words, the material will return to its original shape if an applied load is removed. If any work is performed on the material it will be stored as internal energy in the material without loss. Considering a unit cube the internal work per unit volume may be formulated as:

$$dW = \sigma'_{11}\varepsilon_{11} + \sigma'_{22}\varepsilon_{22} + \sigma'_{33}\varepsilon_{33} + \sigma'_{12}\varepsilon_{12} + \sigma'_{23}\varepsilon_{23} + \sigma'_{13}\varepsilon_{13} = \boldsymbol{\sigma} d\boldsymbol{\varepsilon} \tag{2.1}$$

where σ represent the stresses and ε represent the strains. Notice that the first index refer to the surface where the stress/strain component acts and the second index refer to the direction of the stress/strain component according to the Cartesian coordinate system, see Appendix C.1 for further explanation. Furthermore, bold letters will indicate vectors or matrices[1]. Through the specific internal energy density ($U(\varepsilon)$) it is possible to represent the internal energy per unit volume, at a deformed state, by the strain component ε. If a change in the state of strain occurs then the external work must be equal to the change in internal work:

$$dW = dU(\varepsilon) = \frac{\partial U}{\partial \varepsilon} d\varepsilon \tag{2.2}$$

Combining Eq. (2.1) and Eq. (2.2) a relationship between the stress components and the partial derivative of the internal energy function can be found as:

$$\boldsymbol{\sigma}^T = \frac{\partial U}{\partial \varepsilon} \tag{2.3}$$

Note, that the symmetry of the stresses and strains are the same, i.e. the stresses and strains have the same orientation. The relation between a small change in stress and the corresponding change in strain is found by differentiation:

$$d\boldsymbol{\sigma} = d\left(\frac{\partial U}{\partial \varepsilon}\right) = \frac{\partial^2 U}{\partial \varepsilon^T \partial \varepsilon} d\varepsilon \qquad \longrightarrow \qquad d\boldsymbol{\sigma} = \boldsymbol{D} d\varepsilon \tag{2.4}$$

where $\boldsymbol{D}$ is a 6×6 component elastic stiffness matrix. It should be mentioned that since matrix $\boldsymbol{D}$ is a double derivative of the internal energy potential ($U(\varepsilon)$) it implies symmetry, meaning:

$$\boldsymbol{D}^T = \boldsymbol{D} \tag{2.5}$$

With respect to symmetry, the stiffness matrix consists of 21 independent stiffness components. In a linear elastic material the stiffness will be constant and the stress-strain relationship is simply found by integrating from an incremental relation to a relation between current stress and strains:

$$\boldsymbol{\sigma} = \boldsymbol{D}\boldsymbol{\varepsilon} \quad , \quad \begin{bmatrix} \sigma'_{11} \\ \sigma'_{22} \\ \sigma'_{33} \\ \sigma'_{12} \\ \sigma'_{13} \\ \sigma'_{23} \end{bmatrix} = \begin{bmatrix} D_{11} & D_{12} & D_{13} & D_{14} & D_{15} & D_{16} \\ D_{21} & D_{22} & D_{23} & D_{24} & D_{25} & D_{26} \\ D_{31} & D_{32} & D_{33} & D_{34} & D_{35} & D_{36} \\ D_{41} & D_{42} & D_{43} & D_{44} & D_{45} & D_{46} \\ D_{51} & D_{52} & D_{53} & D_{54} & D_{55} & D_{56} \\ D_{61} & D_{62} & D_{63} & D_{64} & D_{65} & D_{66} \end{bmatrix} \begin{bmatrix} \varepsilon_{11} \\ \varepsilon_{22} \\ \varepsilon_{33} \\ 2\varepsilon_{12} \\ 2\varepsilon_{13} \\ 2\varepsilon_{23} \end{bmatrix} \tag{2.6}$$

Note, several engineers prefer to rename the shear strain into $\gamma_{ij} = 2\varepsilon_{ij}$, where i and j indicate different directions. This will not be the case here.

[1] This have been chosen instead of Einsteins notation see Appendix C.1

2.3.1 Linear Isotropic Elasticity

Isotropic materials are characterized by material properties which are independent of the particular orientation of the material relative to the load and deformation states. The material stiffness given in Eq. (2.6) may be reduced to only two independent elastic parameters in an isotropic condition. Firstly, considering a small cube which is affected only by normal stresses. According to the symmetry of the material properties about the coordinate planes the cube must deform without any increasing shear strains or shear stresses. To satisfy that requirement Eq. (2.6) can be reduced:

$$\begin{bmatrix} \sigma'_{11} \\ \sigma'_{22} \\ \sigma'_{33} \\ \sigma'_{12} \\ \sigma'_{13} \\ \sigma'_{23} \end{bmatrix} = \begin{bmatrix} D_{11} & D_{12} & D_{13} & 0 & 0 & 0 \\ D_{21} & D_{22} & D_{23} & 0 & 0 & 0 \\ D_{31} & D_{32} & D_{33} & 0 & 0 & 0 \\ 0 & 0 & 0 & D_{44} & D_{45} & D_{46} \\ 0 & 0 & 0 & D_{54} & D_{55} & D_{56} \\ 0 & 0 & 0 & D_{64} & D_{65} & D_{66} \end{bmatrix} \begin{bmatrix} \varepsilon_{11} \\ \varepsilon_{22} \\ \varepsilon_{33} \\ 2\varepsilon_{12} \\ 2\varepsilon_{13} \\ 2\varepsilon_{23} \end{bmatrix} \tag{2.7}$$

Next step in reducing Eq. (2.7) is done by considering a pure uniaxial tension and pure shear case. Through a uniaxial tension (for instance $\sigma'_{33} \neq 0$, $\sigma'_{11} = \sigma'_{22} = 0$) and as a result of symmetry the following relation can be obtained:

$$\varepsilon_{11} = \varepsilon_{22} = -\nu\varepsilon_{33} \tag{2.8}$$

where ν is Poisson's ratio. This may be used to reduce the upper block of 3×3 stiffness parameters. Lastly, by considering a shear state, the shear stress and deformation must be symmetric with respect to the same plane. Therefore, by considering shear individually in each of the coordinate planes the lower block of 3×3 stiffness parameters may be rewritten. Thereby, Eq. (2.7) can finally be reduced to:

$$\begin{bmatrix} \sigma'_{11} \\ \sigma'_{22} \\ \sigma'_{33} \\ \sigma'_{12} \\ \sigma'_{13} \\ \sigma'_{23} \end{bmatrix} = \begin{bmatrix} \frac{1}{E} & -\frac{\nu}{E} & -\frac{\nu}{E} & 0 & 0 & 0 \\ -\frac{\nu}{E} & \frac{1}{E} & -\frac{\nu}{E} & 0 & 0 & 0 \\ -\frac{\nu}{E} & -\frac{\nu}{E} & \frac{1}{E} & 0 & 0 & 0 \\ 0 & 0 & 0 & \frac{1}{G} & 0 & 0 \\ 0 & 0 & 0 & 0 & \frac{1}{G} & 0 \\ 0 & 0 & 0 & 0 & 0 & \frac{1}{G} \end{bmatrix} \begin{bmatrix} \varepsilon_{11} \\ \varepsilon_{22} \\ \varepsilon_{33} \\ 2\varepsilon_{12} \\ 2\varepsilon_{13} \\ 2\varepsilon_{23} \end{bmatrix} \tag{2.9}$$

Note that this relation is known as Hooke's law. In soil mechanics it is preferred to use the bulk (K) and shear (G) modulus (see Appendix C.1.7 for explanation) which are defined by:

$$K = \frac{E}{3\,(1-2\nu)} \qquad \text{and} \qquad G = \frac{E}{2\,(1+\nu)} \tag{2.10}$$

In respect to K and G, Eq. (2.9) may be formulated as:

$$\boldsymbol{D} = \begin{bmatrix} K+\frac{4}{3}G & K-\frac{2}{3}G & K-\frac{2}{3}G & 0 & 0 & 0 \\ K-\frac{2}{3}G & K+\frac{4}{3}G & K-\frac{2}{3}G & 0 & 0 & 0 \\ K-\frac{2}{3}G & K-\frac{2}{3}G & K+\frac{4}{3}G & 0 & 0 & 0 \\ 0 & 0 & 0 & G & 0 & 0 \\ 0 & 0 & 0 & 0 & G & 0 \\ 0 & 0 & 0 & 0 & 0 & G \end{bmatrix} \tag{2.11}$$

Anisotropic elasticity will be discussed in Section 3.5. An elastic material model and solution based on elastic theory may be used in geotechnical engineering for small deformations (Nordal, 2014c). However, for larger deformations the soil response will leave the elastic region. Therefore, the elastic model needs to be more advanced to describe the response of the soil if major overestimations are to be avoided. It should be mentioned that Section 2.3 has been created by inspiration from Nordal (2014c) and Krenk and Hoegsberg (2013).

2.4 Elasto-Plastic Theory

In elasto-plastic theory the material response is partly reversible and partly irreversible. Hence, the strains can be decomposed into recoverable elastic strains (ε^e) and irrecoverable plastic strains (ε^p). Note that e denotes **elastic** and p denotes **plastic**. Thus, the total strains in elasto-plastic theory can be rewritten as (Nordal, 2014a):

$$d\boldsymbol{\varepsilon} = d\boldsymbol{\varepsilon}^e + d\boldsymbol{\varepsilon}^p \tag{2.12}$$

This may also be illustrated for a one-dimensional linear elastic perfect-plastic material model as illustrated on Figure 2.1(a). One could argue how good a linear elastic perfect-plastic material model will represent a real soil response. Figure 2.1(b) shows how a real stress-strain response from a soil may look like.

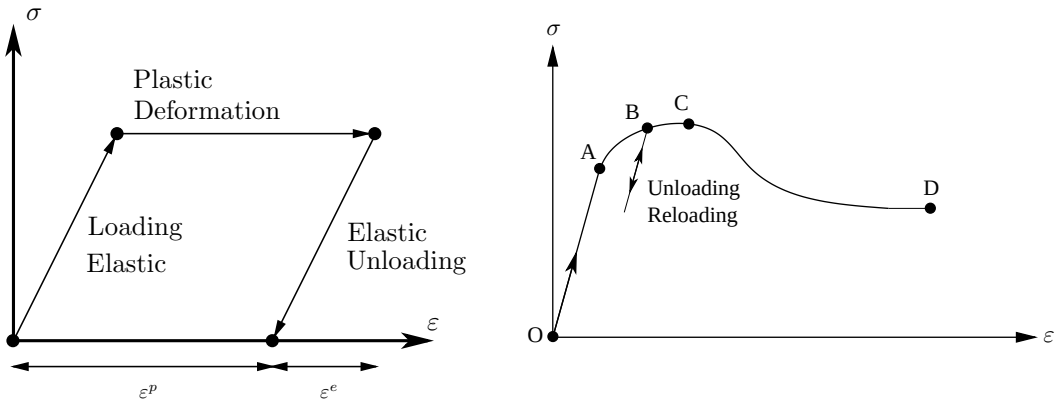

(a) Decompostion of total strains for a linear elastic perfect-plastic material model.

(b) Stress-strain path for a real soil.

Figure 2.1: *Soils model vs. real soil response.*

Comparing Figure 2.1(a) and Figure 2.1(b) it can be seen that a such a model may lead to under/over estimation of the soil response. Analysing the stress-strain path in Figure 2.1(b) following observations may be made:

A : The yielding point or the first yielding point (Permanent strains starts to occur)
B : Unloading reloading (Often assumed to be purely elastic process)
C : Failure at maximum stress
O $\rightarrow$ **A** : Initial part of the curve is linear (Linear elastic)
A $\rightarrow$ **C** : Elasto-plastic response, Hardening process (Plastic stiffness is continuously reduced)
C $\rightarrow$ **D** : Elasto-plastic response, Softening process (Negative stiffness)

These characteristics will be explained in the following sections to give a better understanding of the soil response with respect to critical soil mechanics.

2.5 Plasticity and Yielding

As mentioned in Section 2.4, elastic strains are recoverable and plastic strains irrecoverable. The transition between the elastic and plastic region is defined as yielding. In plasticity theory, a simplification is utilized to define the yielding, as a single point between the elastic and plastic region. In reality, it may be expected to observe a gradual transition from the elastic region to plastic region (Wong, 1975).

In contrast to elastic theory, plasticity is characterized by path dependence and energy dependence. The physical meaning of plastic yielding, with respect to geotechnical engineering, represent a slippage of grain contacts to obtain a closer or more loose packing of the grain structure. These phenomena are described as dilative or contractive soil behaviour. With respect to the terms softening and hardening, each of them occur in the plastic domain and are strain controlled processes. The theory of plasticity was originally developed for metals but despite the many differences relative to soil it may still be applied in geotechnical engineering (Roenningen et al., 2014). The definition of a yielding soil can be rather complex since a soil may yield in several stress combinations. An investigation of the yielding behaviour may be done by different soil tests and observing the soil response. Figure 2.2 shows the soil response from three different soil tests; Isotropic compression, one-dimensional compression, and conventional undrained compression (typically tri-axial testing).

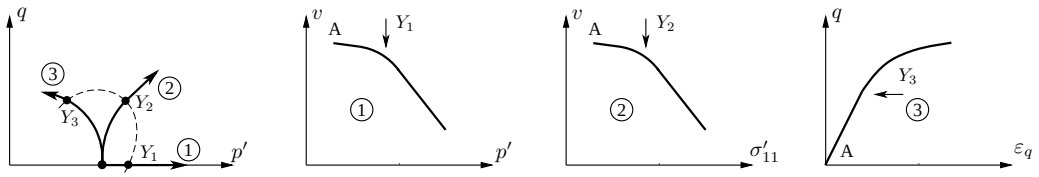

Figure 2.2: *Investigation of yielding behaviour from three different soil tests. (1) Isotropic compression test: Specific volume (v) and mean effective stress (p′), (2) One-dimensional compression test: Specific volume (v) and vertical effective stress (σ'_v), (3) Undrained tri-axial compression test: Deviatoric stress (q) and deviatoric strain (ε_q). Inspired by (Wood, 1990).*

It appears from Figure 2.2 that yielding may occur for different stress combinations. These yield points may be referred to as a surface boundary which separates the elastic and plastic region. The boundary is typically named as the yield surface but other names such as yield envelope or yield locus may be found in other literature. A general definition of a yield surface has been given by Wood (1990):

Definition 1. *A yield surface marks the boundary between the region of purely elastic strain to the region with combined elastic and plastic strain.*

Yielding may be divided into different categories. It has been suggested by Leroueil and Vaughan (1993) to divide yielding into three types as indicated on Figure 2.3.

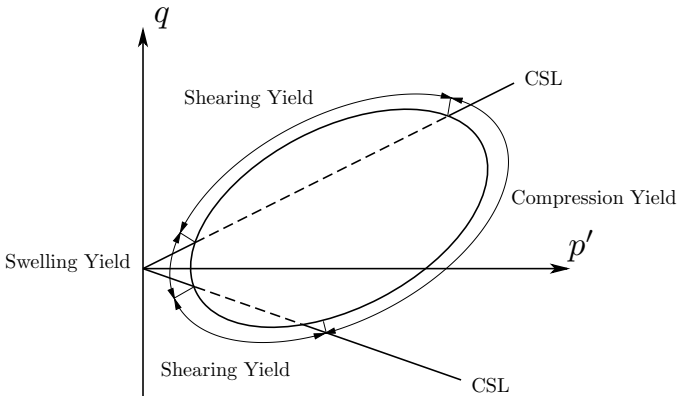

Figure 2.3: *Different types of yielding. Inspired by (Leroueil and Vaughan, 1993).*

The shape and location of the yield surface in the $(p' : q)$-space will be explained in Section 2.9 and Section 3.4.1, respectively. It should be mentioned that in reality, plastic deformation may occur inside the yield surface (Graham et al., 1982). This phenomena will often appear during cyclic loading. Still, the phenomena is often neglected and purely elastic response is assumed inside the yield surface for simplicity reasons.

2.6 Elasto-Plastic Model

An elasto-plastic model combines the concepts of elasticity, plasticity and yielding to predict the relationship between stresses and strains. The main concept in the model is to separate the relationship into two regions:

- Any stress changes inside the yield surface are associated by pure elastic strains.
- Any stress changes at edge of the yield surface are associated by a combination of elastic and plastic strains.

As a result of plastic strains the yield surface will change in shape. To establish an elasto-plastic constitutive soil model three ingredients are required (Nordal, 2014c):

- Yield Criterion
- Flow Rule
- Hardening rule(s)

To understand the elasto-plastic model in details, it is necessary to formulate the responses of elastic and plastic strain. In the following subsections, the strain development due to stress changes will be explained and the three "ingredients" will be described in Section 2.7.

2.6.1 Elastic Volumetric Strain

According to Section 2.4 and Section 2.5, deformations inside the yield surface are purely elastic. If the elastic properties are known the relationship between stresses and strains can be found by:

$$\begin{bmatrix} d\varepsilon_p \\ d\varepsilon_q \end{bmatrix} = \begin{bmatrix} K' & 0 \\ 0 & 3G' \end{bmatrix} = \begin{bmatrix} dp' \\ dq \end{bmatrix} \tag{2.13}$$

where ε_p are strains associated to changes in effective mean stresses (p') and ε_q are strains associated to changes in deviator stresses (q). Notice that changes in the volume are only associated with changes in p' and changes in shape are only associated to changes in q which explains the chosen notation. The prime on G' and K' refers to drained condition. Eq. (2.13) represents an isotropic situation and for convenience it is assumed that the soil behaves isotropically during elastic loading or unloading. It should be mentioned that since the deformations inside the yield surface are reversible, moving from one stress state to another is dependent of the stress path. In other words, in elastic region the change has no memory and only uses the change in stress not the current stress state.

The concept of elastic volumetric strain can be derived by looking at the compression plane from an arbitrary sample during a compression test, see Figure 2.4. In the compression plane $(p' : v)$, the Normal Compression Line (ncl) is obtained when loading past the effective pre-consolidation stress (p'_c), hence yielding. Plotting the volumetric response against the logarithmic to the effective mean stress $(\ln p')$, the response will approach linearity. The change in specific volume (v) beyond the yielding point may be associated to the compression parameter (λ) corresponding to the inclination of the ncl line:

$$v = v_\lambda - \lambda \ln(p') \tag{2.14}$$

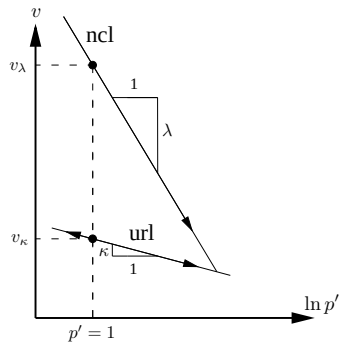

Figure 2.4: *Normal Compression Line (ncl) and Unloading-Reloading Line (url) on the compression plane* $(\ln p' : v)$.

For the Unloading/Reloading Line (url), the response was entirely elastic and the relationship between volume and effective mean stress can be described by the unloading parameter κ[2] which represent the inclination of the url:

$$v = v_\kappa - \kappa \ln(p') = v^e \tag{2.15}$$

Note that v_λ and v_κ are defined as the volume by intersection with the line of $p' = 1$, see Figure 2.4. These values (v_λ, v_κ) depend on the on the unit of p' and is chosen to be 1 kPa as suggested by Wood (1990). Rewriting Eq. (2.15) into its increment format the incremental change in volume, in the elastic region, may be formulated as:

$$dv^e = -\kappa \frac{-dp'}{p'} \tag{2.16}$$

As stated in Eq. (2.13) the change in volume is only associated to the change in effective mean stress in the elastic region. Therefore, the incremental relationship between the effective mean stress and volume may be written as:

$$d\varepsilon_p = \frac{-dv}{v} \tag{2.17}$$

Combining Eq. (2.16) and Eq. (2.17) the volumetric elastic strain may be formulated as:

$$d\varepsilon_p^e = \kappa \frac{dp'}{vp'} \tag{2.18}$$

The bulk modulus can be determined by combining Eq. (2.18) with Eq. (2.13) in the elastic region:

$$K' = \frac{vp'}{\kappa} \qquad \longrightarrow \qquad d\varepsilon_p^e = \frac{dp'}{K'} \tag{2.19}$$

Changes in deviatoric stress may occur inside the yield surface and create deviatoric strain. Therefore, the shear modulus is needed but it can be discussed if it is able to assume a constant value in the elastic region (Wood, 1990). In practice, a constant Poisson ratio is often assumed and a relationship between the bulk modulus and the shear modulus can be expressed:

$$G' = \frac{3(1-2\nu)K'}{2(1+\nu)} \tag{2.20}$$

The associated deviatoric strains may be determined as:

$$d\varepsilon_q^e = \frac{dq}{3G'} \tag{2.21}$$

[2] Also called the swelling parameter.

2.6.2 Plastic Volumetric Strain

The generation of plastic strains, as a result of changing the yield surface, is a function of the pre-consolidation pressure. As mentioned earlier, the expansion of the yield surface consists of both elastic and plastic deformation:

$$dv = dv^e + dv^p \tag{2.22}$$

The permanent deformation (plastic strains) can be found by visualizing the same compression plane as in Section 2.6.1 and adding one more unloading/reloading loop. It can be observed from Figure 2.5 that changing the stress state from point A to C and then unloading to point B with the same stress state as in point A would lead to a change in volume.

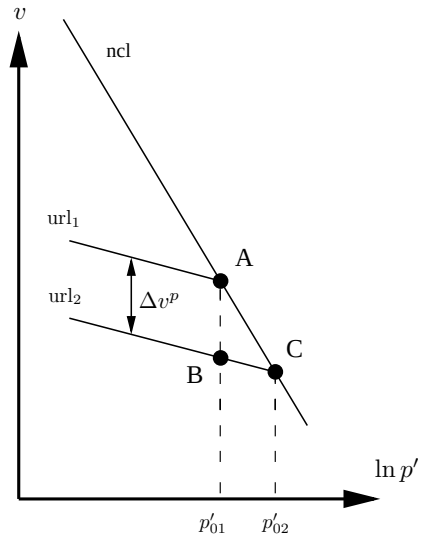

Figure 2.5: *Concept of plastic deformation.*

The change in volume corresponds to the plastic deformation and can be found as the total volume change minus the elastic contribution:

$$dv^p = dv - dv^e \tag{2.23}$$

Using Eq. (2.14) and Eq. (2.15) along with the stress states p'_{01} and p'_{02} representing point A and point B, respectively, the change in plastic volume can be determined as:

$$dv^p = -\lambda \ln\left(\frac{p'_{02}}{p'_{01}}\right) + \kappa \ln\left(\frac{p'_{02}}{p'_{01}}\right) = -(\lambda - \kappa) \ln\left(\frac{p'_{02}}{p'_{01}}\right) \tag{2.24}$$

The incremental form of Eq. (2.24) may be found by utilizing the limit states:

$$dv^p = -(\lambda - \kappa)\frac{dp'_c}{p'_c} \tag{2.25}$$

Using Eq. (2.17) the change in incremental plastic strain may be expressed by:

$$d\varepsilon_p^p = (\lambda - \kappa)\frac{dp'_c}{vp'_c} \tag{2.26}$$

According to the assumption that volumetric changes are only associated to changes in the effective mean stress the total strain can be determined by:

$$d\varepsilon_p = d\varepsilon_p^e + d\varepsilon_p^p \tag{2.27}$$

Thereby, the total strain cause by volumetric strains may be determined by Eq. (2.27).

2.6.3 Plastic Devitoric Strain

The plastic volumetric strains are only a part of the total plastic deformation since the contribution from plastic deviatoric strains should be taken into account. In order to fully understand the concept of the plastic deviatoric strains, it is important to realize that the direction of the plastic strain vector is path independent in contrast to the elastic strains which are stress dependent. The direction of the plastic strain vectors are determined from the specific combination of stresses at the specific yield point and not the stress path of which the yield point was reached. Hence, plastic strain vectors depend on the magnitude of the actual stress state where elastic strains are determined from stress increments. To describe the plastic shear strain an example of a frictional block is used. It should be mentioned that this example is inspired from (Wood, 1990).

A frictional block is subjected to an increasing shear load in both horizontal directions (T_x, T_y) as illustrated on Figure 2.6 and the necessary forces for sliding are analysed. In elasto-plastic terms, sliding of the block will correspond to yielding of the soil. In order for the block to slide, the applied shear forces must equal the friction force. In the situation of two shear forces the resultant force to obtain sliding is given by:

$$\sqrt{T_x^2 + T_y^2} = \mu_f P \tag{2.28}$$

where μ_f is the coefficient of friction for the rough interface[3]. From Eq. (2.28) it can be observed that the left hand side of the equation will represent a circle in the $(T_x : T_y)$-space with center at origo and the periphery symbolizes the limit to sliding (similar to the yield surface), see Figure 2.8.

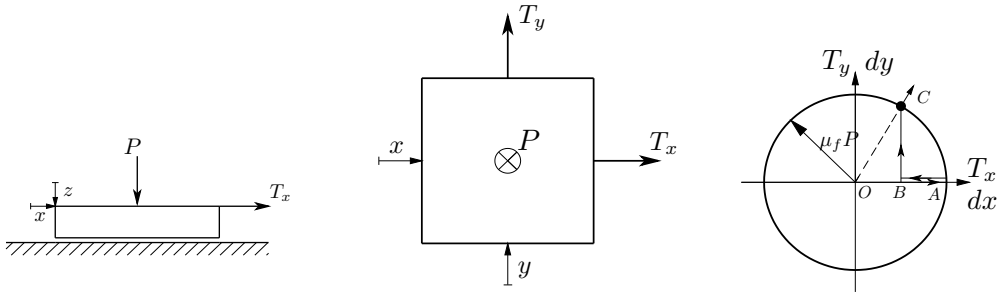

(a) Plan view. (b) Vertical view. (c) $T_x : T_y$-space.

Figure 2.6: *(a) Frictional block under normal load P and shear load T_x. (b) Frictional block under normal load P and shear loads T_x and T_y. (c) Interpretation of sliding in $(T_x : T_y)$-space. Inspired by (Rouainia and Muir Wood, 2000).*

From Figure 2.6(c) it can be seen that for any combination of T_x and T_y (causing sliding) the resulting force will always be perpendicular to the yield surface. The taken path to reach failure has no influence on the direction of the resulting force. The relative amount of sliding in each direction can be determined by introducing the plastic potential (Q) as:

$$Q = T_x^2 + T_y^2 - k^2 = 0 \qquad \text{where} \qquad k = \mu_f P \tag{2.29}$$

The relative amount of sliding can be found by differentiating Q with respect to each of the loads:

$$dx = d\lambda \frac{\partial Q}{\partial T_x} \quad , \quad dy = d\lambda \frac{\partial Q}{\partial T_y} \quad , \quad dz = d\lambda \frac{\partial Q}{\partial T_z} \tag{2.30}$$

where $d\lambda$ is a scalar multiplier also referred to as the plastic multiplier. This representation of the plastic strains is directly transferred to the $(p' : q)$-space, hence:

[3] Static and dynamic friction is assumed to be equal.

$$d\varepsilon_p^p = d\lambda \frac{\partial Q}{\partial p'} \tag{2.31}$$

$$d\varepsilon_q^p = d\lambda \frac{\partial Q}{\partial q} \tag{2.32}$$

Plastic potential

Yielding is associated with the occurrence of plastic irrecoverable volumetric and deviatoric strains. Plotting the magnitude of these components, as defined in Eq. (2.32), in a graph having parallel axes to a $(p' : q)$-plot, the plastic potential to a given stress state can be observed. As indicated on Figure 2.7, yielding may occur under many combinations. If the magnitude of the created plastic strains are drawn for these stress combinations a surface may be drawn which is referred to as the plastic potential. Notice that the plastic strain increment vectors always are orthogonal to the plastic potential.

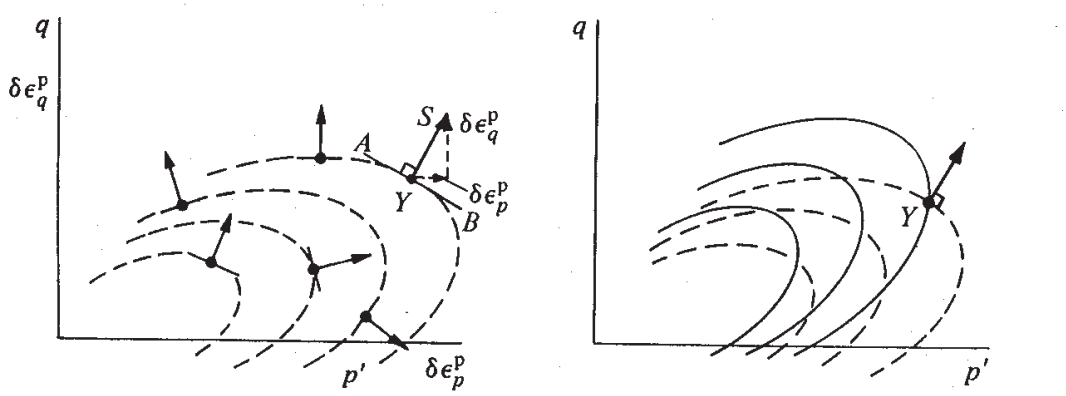

Figure 2.7: *Plastic strain increment vectors normal to the plastic potential surface: Plastic potential (- -) yield surface (-). Taken from Graham et al. (1984) and notice notation difference (δ = d).*

As indicated in Figure (2.7) the plastic potential surface may be different from the yield surface. This phenomenon will be explained in Section 2.7.1.

2.7 Three ingredients

As mentioned in Section 2.4, three ingredients are needed to define a constitutive model. These three ingredients will be described in the next sections.

2.7.1 The Flow Rule

The flow rule describes the relationship between the plastic strains to the plastic potential as introduced in Section 2.6.3. In general, two types of flow rules will be exist:

- Associated flow
- Non associated flow

The associated flow was postulated by Drucker in year 1951 and represent material stability of work hardening material. The non associated flow was postulated by Von Mises in year 1928 and represents "unstable" materials (Nordal, 2014c).

The associated flow rule is fulfilled if:

- The stress increment vector, which takes the sample beyond yielding, and the corresponding plastic strain increment is directed perpendicular to the yield surface.

In other words, the yield and the plastic potential surface should have the same shape and size. If associated flow may be assumed the number of equations to describe the plastic response can be reduced to one:

$$d\varepsilon^p = d\lambda \frac{\partial Q}{\partial \boldsymbol{\sigma}} = d\lambda \frac{\partial F}{\partial \boldsymbol{\sigma}} \tag{2.33}$$

where F represent the yield surface. If the yield surface and plastic potential is equal for a material it is said that the material obey the postulate of normality. The normality and associated flow are defined by Wood (1990) as:

Definition 2. *Normality: The plastic strain increment vector is in the direction of the outward normal to the yield surface.*

Definition 3. *Associated flow: The nature of the plastic deformations, or flow, is associated with the yield surface of the material.*

The practical method of visualizing and examining if associated flow is a suitable choice for the soil response is performed by the following method.

1. Aligning the $d\varepsilon_p$ and p' axes and the $d\varepsilon_q$ and q axes, respectively.
2. Plotting the plastic strain increments ($d\varepsilon_p^p$ and $d\varepsilon_q^p$) as a strain vector from the corresponding stress field.
3. If the strain vector is orthogonal to the yield surface the requirements for the associated flow rule are fulfilled.

A theoretical example of non associated flow may be seen in Figure 2.7 utilizing the approach mentioned above. Figure 2.8 shows the normalized yield surface and the direction of the plastic strain increments for test data presented by Graham et al. (1984). For this test data, the assumption of associated flow would be a suitable choice since the plastic strain vectors are almost orthogonal to the yield surface.

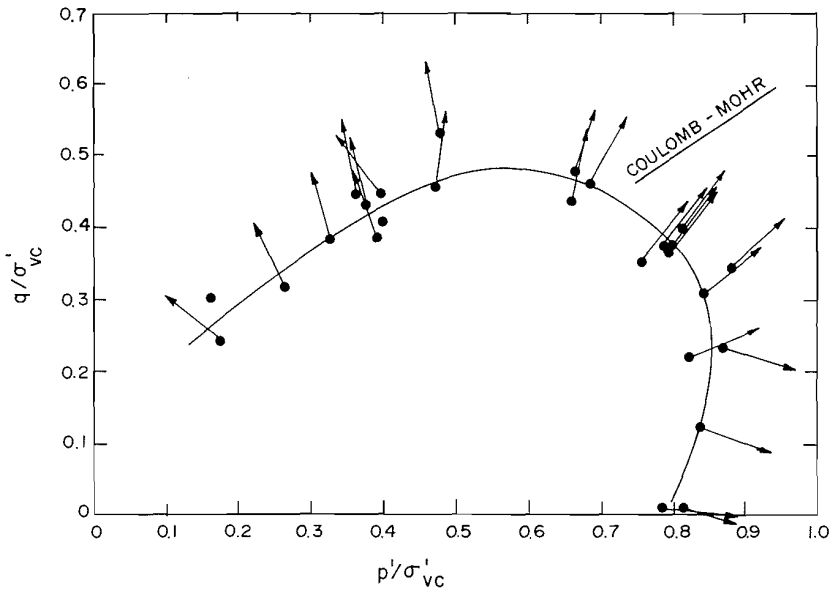

Figure 2.8: *Normalized yield surface and plastic strain increment. Taken from (Graham et al., 1984) notice notation difference ($\sigma'_{vc} = p'_c$).*

It have been shown from experimental data that the assumption of normality yields relatively minor deviations for several natural soft clays (Wood, 1990). However, it has been proved from other experimental data, that other soils (sand for instance) the assumption of associated flow is not a suitable choice (Wong, 1975). The purpose of this work is to create a model which should be able to simulate the soil response of natural soft clay. Hence, the associated flow rule is assumed to be sufficient.

With respect to the assumption of associated flow, the plastic deformation is purely associated to the stress ratio (η) at which yielding occurs and changes continuously as the stress ratio changes. Thereby, several points on the plastic potential surface are of interest and are marked on Figure 2.9.

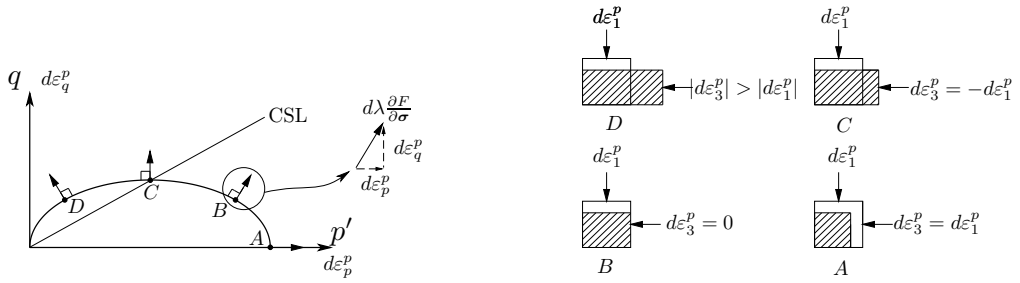

Figure 2.9: *Associated flow rule illustrated by yield patterns in plane strain.*

The marked points in Figure 2.7 illustrate different phenomena where the soil response is dominated by the magnitude of the stress ratio and the inclination of the CSL M (Wood, 2004):

Table 2.1: *Influence of η with respect to the plastic response.*

Point	Criteria	Dilation	Response	Condition
A	$\eta = 0$	$d\varepsilon_p^p/d\varepsilon_q^p = \infty$	Compression without distortion	(Isotropic compression)
B	$\eta < M^{(2)}$	$d\varepsilon_p^p/d\varepsilon_q^p > 0$	Compression and distortion	(Oedometer)
C	$\eta = M^{(1)}$	$d\varepsilon_p^p/d\varepsilon_q^p = 0$	Distortion without compression	(Critical state)
D	$\eta > M^{(1)}$	$d\varepsilon_p^p/d\varepsilon_q^p < 0$	Expansion plus distortion	(Dilative)

*High value
(2)Low value

The these points will be utilized in the report and be referred to as: isotropic compression, one-dimension compression, critical state and dilative behaviour as seen in Table 2.1.

2.7.2 Yield Criterion

The yield criterion will decide if any plastic strains will develop according to an incremental stress change relative to the plastic potential surface. Hence, three scenarios may be listed in Table 2.2:

Table 2.2: *Definition of the current state by the yield criterion.*

Situation	State	Development of strains
$F(\boldsymbol{\sigma}, \boldsymbol{\kappa}) > 0$	Is not allowed	(-)
$F(\boldsymbol{\sigma}, \boldsymbol{\kappa}) < 0$	Purely Elastic	$(d\boldsymbol{\varepsilon} = d\boldsymbol{\varepsilon}^e)$
$F(\boldsymbol{\sigma}, \boldsymbol{\kappa}) = 0$	Elasto Plastic	$(d\boldsymbol{\varepsilon} = d\boldsymbol{\varepsilon}^e + d\boldsymbol{\varepsilon}^p)$

Notice that associated flow is assumed ($Q = F$)

where $\boldsymbol{\kappa}$ is a suitable set of material variables also known as state variables. During yielding the surface may move along by the induced incremental stress change by either isotropic or/and kinematic hardening.

2.7.3 Hardening Rule

The hardening rule is the last "ingredient" which is required to assembled an elasto-plastic model. The hardening rule is associated to the development of plastic strains with respect to the evolution of the yield surface through the plastic multiplier ($d\lambda$). In terms of evolution, the yield surface may either expand, do a kinematic translation, behave rotationally, or a combination of these phenomena. The relation between plastic strain and evolution in the plastic potential is given by:

$$d\boldsymbol{\varepsilon}^p = d\lambda \frac{\partial Q}{\partial \boldsymbol{\sigma}} \tag{2.34}$$

As mentioned in Section 2.7.1, utilizing the associated flow, the development of plastic strains may be associated to the yield surface and the stress increment through the plastic multiplier. Recalling the yield criterion $F(\boldsymbol{\sigma}, \kappa) = 0$, the statement must be true for the given stress state and for any stress state introduced by incremental stresses:

$$F(\boldsymbol{\sigma}, \kappa) = 0 \tag{2.35a}$$

$$F(\boldsymbol{\sigma} + d\boldsymbol{\sigma}, \boldsymbol{\kappa} + d\boldsymbol{\kappa}) = 0 \tag{2.35b}$$

Utilizing the above condition during hardening, the consistency equation may be formulated as:

$$dF = \left\{ \frac{\partial F}{\partial \boldsymbol{\sigma}} \right\} d\boldsymbol{\sigma} + \left\{ \frac{\partial F}{\partial \boldsymbol{\kappa}} \right\} d\boldsymbol{\kappa} = 0 \tag{2.36}$$

Eq. (2.36) may also be referred to as the consistency condition and may be rewritten to:

$$\left\{ \frac{\partial F}{\partial \boldsymbol{\sigma}} \right\} d\boldsymbol{\sigma} - A d\lambda = 0 \tag{2.37}$$

where A is the plastic resistance number also known as the plastic modulus:

$$A = -\left(\left\{ \frac{\partial F}{\partial \boldsymbol{\kappa}} \right\}^T \cdot \left\{ \frac{d\boldsymbol{\kappa}}{d\lambda} \right\} \right) = -\left(\left\{ \frac{\partial F}{\partial \boldsymbol{\kappa}} \right\}^T \cdot \boldsymbol{h}(\boldsymbol{\sigma}, \boldsymbol{\kappa}) \right) \tag{2.38}$$

Notice, the plastic multiplier may be found analytically if all the derivatives in Eq. (2.38) are constant or linear functions in stress (Grimstad and Benz, 2014). Another way to express plastic resistance is by extending the term $\boldsymbol{h}(\boldsymbol{\sigma}, \boldsymbol{\kappa})$:

$$\boldsymbol{h}(\boldsymbol{\sigma}, \boldsymbol{\kappa}) = \left\{ \frac{d\boldsymbol{\kappa}}{d\varepsilon^p} \right\} \left\{ \frac{d\varepsilon^p}{d\lambda} \right\} \tag{2.39}$$

Utilizing Eq. (2.34), the term $\dfrac{d\varepsilon^p}{d\lambda} = \left\{ \dfrac{\partial Q}{\partial \boldsymbol{\sigma}} \right\}$ may be used. Thereby, the plastic resistance can be rewritten as:

$$A = -\left(\left\{ \frac{\partial F}{\partial \boldsymbol{\kappa}} \right\}^T \left\{ \frac{d\boldsymbol{\kappa}}{d\varepsilon^p} \right\} \left\{ \frac{d\varepsilon^p}{d\lambda} \right\} \right) = -\left(\left\{ \frac{\partial F}{\partial \boldsymbol{\kappa}} \right\}^T \left\{ \frac{d\boldsymbol{\kappa}}{d\varepsilon^p} \right\} \left\{ \frac{\partial Q}{\partial \boldsymbol{\sigma}} \right\} \right) \tag{2.40}$$

2.8 The General Elasto-Plastic Model

Utilizing the theory outlined in Sections 2.3-2.7.3 a constitutive model may be assembled to estimate the soil response as a result of elastic and plastic strains. Recalling the definition of strains in an elasto-plastic model:

$$d\boldsymbol{\varepsilon} = d\boldsymbol{\varepsilon}^e + d\boldsymbol{\varepsilon}^p \tag{2.41}$$

To summarize, the delimiter between the elastic and plastic behaviour is associated by the yield surface and the development of plastic strains are governed by the plastic potential surface. The yield and plastic potential surface are functions of:

$$Q(\boldsymbol{\sigma}, \boldsymbol{\beta}) = 0 \qquad , \qquad F(\boldsymbol{\sigma}, \boldsymbol{\kappa}) = 0 \tag{2.42}$$

where $\boldsymbol{\sigma}$ expresses the stress state, and $\boldsymbol{\kappa}$ and $\boldsymbol{\beta}$ are two state parameters controlling the size of the yield and plastic potential surface, respectively. Utilizing the flow rule along with an assumed relationship between the elastic strains and corresponding stresses, the strain response in Eq. (2.41) may be formulated as:

$$d\boldsymbol{\varepsilon} = \boldsymbol{D}^{-1} d\boldsymbol{\sigma} + d\lambda \left\{ \frac{\partial Q}{\partial \boldsymbol{\sigma}} \right\} \qquad \text{Using} \qquad \begin{cases} d\boldsymbol{\varepsilon}^e &= \boldsymbol{D}^{-1} d\boldsymbol{\sigma} \\ d\boldsymbol{\varepsilon}^p &= d\lambda \dfrac{\partial Q}{\partial \boldsymbol{\sigma}} \end{cases} \tag{2.43}$$

Rewriting the consistency conditions (see Eq. (2.37)) the plastic multiplier may be formulated as:

$$d\lambda = \frac{1}{A} \left\{ \frac{\partial F}{\partial \boldsymbol{\sigma}} \right\}^T d\boldsymbol{\sigma} \tag{2.44}$$

Substituting the expression for plastic multiplier, see Eq.(2.44), into Eq. (2.43) yields:

$$d\boldsymbol{\varepsilon} = \boldsymbol{D}^{-1} d\boldsymbol{\sigma} + \frac{1}{A} \left\{ \frac{\partial Q}{\partial \boldsymbol{\sigma}} \right\} \left\{ \frac{\partial F}{\partial \boldsymbol{\sigma}} \right\}^T d\boldsymbol{\sigma} \tag{2.45}$$

Which may be formulated in compact form as:

$$d\boldsymbol{\varepsilon} = \boldsymbol{D}_{ep}^{-1} d\boldsymbol{\sigma} \qquad \text{where} \qquad \boldsymbol{D}_{ep}^{-1} = \boldsymbol{D}^{-1} + \frac{1}{A} \left\{ \frac{\partial Q}{\partial \boldsymbol{\sigma}} \right\} \left\{ \frac{\partial F}{\partial \boldsymbol{\sigma}} \right\}^T \tag{2.46}$$

where A it the plastic resistance given in Eq. (2.40). With respect to numerical models it is often favourable to determine the incremental stresses through the strain and stiffness matrix:

$$d\boldsymbol{\sigma} = \boldsymbol{D}_{ep} d\boldsymbol{\varepsilon} \tag{2.47}$$

where

$$\boldsymbol{D}_{ep} = \boldsymbol{D} - \frac{\boldsymbol{D} \left\{ \dfrac{\partial Q}{\partial \boldsymbol{\sigma}} \right\} \left\{ \dfrac{\partial F}{\partial \boldsymbol{\sigma}} \right\}^T \boldsymbol{D}}{A + \left\{ \dfrac{\partial F}{\partial \boldsymbol{\sigma}} \right\}^T \boldsymbol{D} \left\{ \dfrac{\partial Q}{\partial \boldsymbol{\sigma}} \right\}} \tag{2.48}$$

The deriveration of $\boldsymbol{D}_{ep}$ may be seen in Appendix C.4. In terms of p' and q Eq. (2.46) may be written as

$$\begin{bmatrix} d\varepsilon_p^e \\ d\varepsilon_q^e \end{bmatrix} = \begin{bmatrix} \dfrac{1}{K'} & 0 \\ 0 & \dfrac{1}{3G'} \end{bmatrix} \begin{bmatrix} dp' \\ dq \end{bmatrix} \qquad \text{where} \qquad K' = \frac{vp'}{\kappa} \tag{2.49a}$$

$$\begin{bmatrix} d\varepsilon_p^p \\ d\varepsilon_q^p \end{bmatrix} = \frac{-1}{\dfrac{\partial F}{\partial \kappa} \left(\dfrac{\partial \kappa}{\partial \varepsilon_p^p} \dfrac{\partial Q}{\partial p'} + \dfrac{\partial \kappa}{\partial \varepsilon_q^p} \dfrac{\partial Q}{\partial q} \right)} \begin{bmatrix} \dfrac{\partial F}{\partial p'} \dfrac{\partial Q}{\partial p'} & \dfrac{\partial F}{\partial q} \dfrac{\partial Q}{\partial p'} \\ \dfrac{\partial F}{\partial p'} \dfrac{\partial Q}{\partial q} & \dfrac{\partial F}{\partial q} \dfrac{\partial Q}{\partial q} \end{bmatrix} \begin{bmatrix} dp' \\ dq \end{bmatrix} \tag{2.49b}$$

The reason to introduce Eq. (2.46) in terms of p' and q is done since next section will represent the well known MCC model. This model is an elasto-plastic model originally designed for tri-axial tests. The feature of axis symmetry is associated to tri-axial testing which makes the use of p' and q favourable.

2.9 Modified Cam Clay

The MCC model is a elastic-plastic model developed to estimate the soil response during tri-axial test. The original Cam Clay (CC) model was introduced back in 1963 by Roscoe and Schofield and was modified in 1968 by Roscoe and Burland (Wood, 1990). The difference between the CC and MCC will be described in Appendix C.2. The concept behind the MCC will be presented here.

2.9.1 General

The MCC model utilize the three ingredient required by an elasto-plastic model along with elastic properties of the medium (Wood, 1990). The model is formulated by utilizing fundamental principles and assumptions for simplification, where the main assumptions are listed here:

1. Recoverable volumetric strain due to change in p' may be determined by Eq. (2.18).
2. Recoverable shear strains due to changes in q can be expressed by Eq. (2.21).
3. Combination of Eq. (2.18) and Eq. (2.21) implies a variation of Poission's ratio with the mean effective stress but is assumed to be a constant value.
4. The law of associated flow ($Q = F$) is a fundamental part of the model.

The state parameters in the MCC model are purely associated to the pre-consolidation pressure, thereby $\kappa = p'_c$. Hence, the yield function may be written as:

$$F(\boldsymbol{\sigma}, p'_c) = 0 \qquad \text{or} \qquad F(p', q, p'_c) = 0 \tag{2.50}$$

A derivation of the yield surface related to MCC model may be seen in Appendix C.2.1 and may be formulated as:

$$0 = F = q^2 - M^2(p'(p'_c - p')) \tag{2.51}$$

Notice that the yield surface illustrates an ellipse in the $(p' : q)$-space.

2.9.2 Stress Strain Relationship

Applying the assumption of associated flow ($G = F$), the plastic strains may be determined from the yield function using Eq. (2.32):

$$d\varepsilon_p^p = d\lambda \frac{\partial Q}{\partial p'} = d\lambda \frac{\partial F}{\partial p'} = d\lambda M^2(2p' - p'_c) = (\lambda - \kappa)\frac{dp'_c}{vp_c} \tag{2.52a}$$

$$d\varepsilon_q^p = d\lambda \frac{\partial Q}{\partial q} = d\lambda \frac{\partial F}{\partial q} = 2qd\lambda \tag{2.52b}$$

According to the consistency equation (see Eq. (2.37)) the current stress state must be within the yield surface or at the boundary and may be formulated in terms of p' and q as:

$$dF = \frac{\partial F}{\partial p'}dp' + \frac{\partial F}{\partial q}dq + \frac{\partial F}{\partial p'_c}dp'_c = 0 \tag{2.53}$$

Recalling the definition on the hardening law, the change in pre-consolidation pressure was associated by the development of plastic strains:

$$d\boldsymbol{\kappa} = \frac{\partial \boldsymbol{\kappa}}{\partial \varepsilon^p}d\varepsilon^p \qquad \longrightarrow \qquad dp'_c = \frac{\partial p'_c}{\partial \varepsilon_p^p}d\varepsilon_p^p + \frac{\partial p'_c}{\partial \varepsilon_q^p}d\varepsilon_q^p \tag{2.54}$$

By comparing Eq. (2.54) to the ellipse shape of the yield surface, it may be concluded that the contribution of plastic deviatoric strains must be equal to zero since the plastic deviatoric strain will be equal to zero at p'_c during hardening. Therefore, only the purely plastic volumetric will contribute to the hardening. Hence, the MCC is known as a volumetric hardening model. By rearranging Eq. (2.52) yields:

$$\frac{dp'_c}{d\varepsilon_p^p} = \frac{vp'_c}{(\lambda - \kappa)} \qquad \text{and} \qquad \frac{dp'_c}{d\varepsilon_q^p} = 0 \tag{2.55}$$

It is common to reformulate the yield function by use of the parameter η which is the ratio between the shear stress and effective mean stress ($\eta = q/p'$):

$$\frac{p'}{p'_c} = \frac{M^2}{M^2 + \eta^2} \tag{2.56}$$

Combining Eq. (2.56) and (2.54) and substituting this into the general plastic constitutive relation (see Eq. 2.49) the plastic constitutive relation may be expressed by:

$$\begin{bmatrix} d\varepsilon_p^p \\ d\varepsilon_q^p \end{bmatrix} = \frac{(\lambda - \kappa)}{vp'(M^2 - \eta^2)} \begin{bmatrix} (M^2 + \eta^2) & 2\eta \\ 2\eta & \dfrac{4\eta^2}{(M^2 - \eta^2)} \end{bmatrix} \begin{bmatrix} dp' \\ dq \end{bmatrix} \tag{2.57}$$

The input parameters, M, v, λ and κ are constants in the $(p' : q)$-space. It should be mentioned that the compliance matrix is symmetric due to the assumption of associated flow.

Three scenarios may have interest regarding Eq. (2.57): $\eta < M$, $\eta = M$, and $\eta > M$ due to the term in the numerator. For the case, $\eta \longrightarrow M$, the development of plastic volumetric strains reduces. Since the plastic hardening only depends on development of plastic volumetric strains the change in pre-consolidation pressure may reduces. The shear stiffness will go to zero, as defined in the critical state. This may be formulated as:

$$\eta \longrightarrow M \quad , \quad d\varepsilon_p^p \longrightarrow 0 \quad , \quad dp'_c \longrightarrow 0 \quad , \quad \frac{d\varepsilon_q^p}{dq} \longrightarrow \infty \tag{2.58}$$

This may relate the soil parameter M to the ultimate value of the angle of shearing resistance φ_{cs} which is given in Section 4.6. For the case $\eta < M$, a stable response is observed and an expansion of the yield surface will occur which may be driven by stress changes or strain changes (Wood, 2004). For the case $\eta > M$ the distortional compliance is negative and continuing shearing will occur:

$$d\varepsilon_q^p > 0 \quad , \quad d\varepsilon_p^p < 0 \quad , \quad dq < 0 \tag{2.59}$$

This implies strain softening. These scenarios may be seen on Figure 2.10.

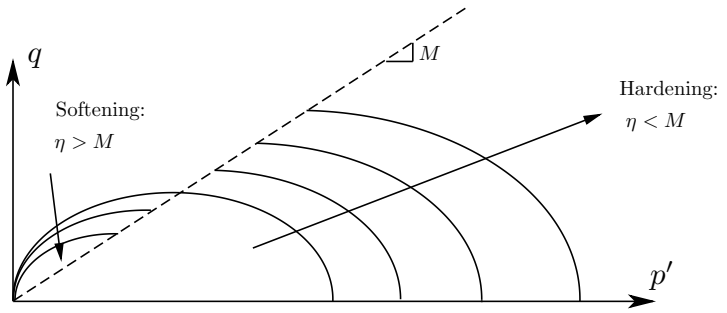

Figure 2.10: *MCC: Hardening and softening of the yield surface.*

Hence, the evolution of the yield surface depends on the magnitude of η related to M. A discussion of drained and undrained response associated to tri-axial scenarios may be found in Appendix C.3

Chapter 3

Natural Soft Clay

The purpose of this chapter is to provide information regarding the observed behaviour in natural soft clays with respect to laboratory testing and field measurements. The chapter will explain the main observations and the coupled processes between these. The characteristic features which have been chosen to be implemented in the constitutive model will be described in greater detail.

3.1 General

In order to establish a unified framework for a constitutive model it is necessary to describe the special characteristics which dominate the mechanical response for a natural soft clay. To understand the essence of these features, one may go back to the deposit process to investigate the initial structure of the natural soft clay. During the deposit several physical, chemical, and biological processes may influence the initial structure. Figure 3.1 yields an overview of several processes influencing the mechanical response of a natural soft clay deposit in a fjord.

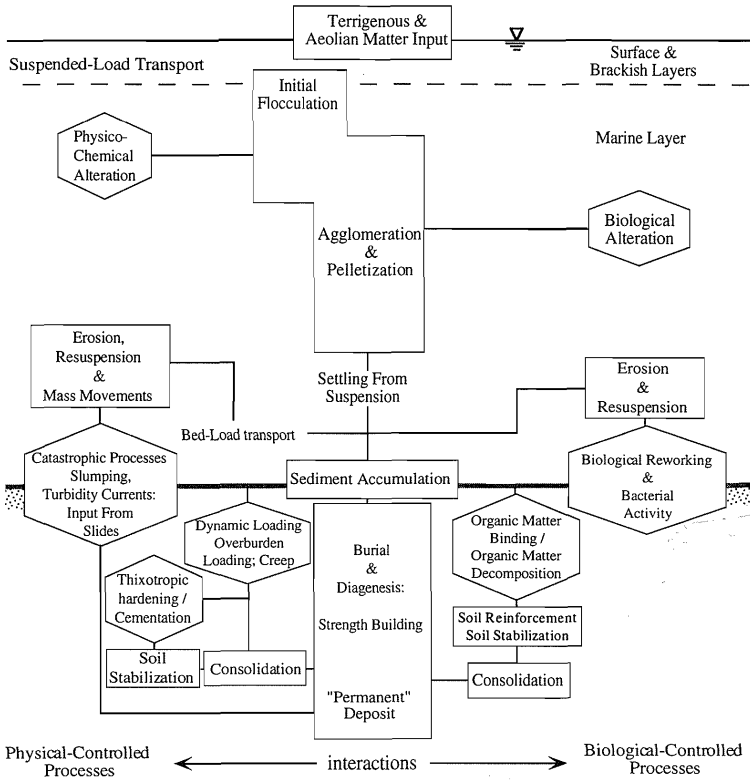

Figure 3.1: *Physical, chemical and biological processes which may influence the mechanical response of natural soft clay. Taken from (Perret et al., 1995).*

After the deposition, the time-dependent effects initiate which may be divided into two different main categories; viscous and ageing effects. These categories may further be divided into several phenomena. These phenomena are rather complex and may dominate the mechanical response of a soft natural soft clay.

Explaining the entire cycle on Figure 3.1 will be beyond the scope of this work. Hence, the chemical and biological processes have been left out and the physical processes will be the main focus.

3.2 Characteristics of Natural Soft Clays

The mechanical response of most natural sedimentary clays may differ from their reconstituted equivalents with respect to the observed behaviour in the laboratory (Leroueil and Vaughan, 1993). The additional strength and stiffness in natural clays have been defined, by many researchers, as the structure. A definition of the structure has been suggested by Burland (1990):

Definition 4. *The structure of a natural soil consist of the combination between the fabric, representing the arrangement of the particles and pore space, and the bonding representing the inter-particle forces between the clay particles and the water.*

Comparing the additional strength and resistance gained by the structural effect to their reconstituted equivalents, significant differences may be observed (Karstunen et al., 2005). It has been stated that the structural effect for natural clays has the same importance, when determining engineering behaviour, as the effects of initial porosity and stress history (Leroueil and Vaughan, 1993). Hence, it was of great importance to understand these features in order to incorporate them into a constitutive model which may predict the mechanical response of a natural clay.

The evolution of the structure may be effected by several time effects and the newest research has shown a possible coupling between these time effects (Sorensen, 2006). In addition, the fabric may contribute with significant influence to the soil response as a part of the structure. Before describing the structure in further details it is important to understand the term, **reconstituted equivalents** which may be used as a measure of the amount of structure in the soil.

3.3 Reference State

A reference state has been suggested by Burland (1990) through the term, **reconstituted soil** and may be defined as:

Definition 5. *A reconstituted soil is defined as one which has been thoroughly mixed at a water content equal to or greater than the liquid limit (w_l).*

See (Burland, 1990) for further details. Hence, this stage will not represent any additional stiffness or strength from the sedimentation or the time-dependent effects, since the structure and stress history are completely destructed[1]. The soil properties at this particular stage may be referred to as the intrinsic properties since they are independent of the state of the soil. It was originally denoted by the symbol, asterisk (*) see Eq. (3.1). However, to avoid confusion with other notation, subscript i will refer to intrinsic properties as indicated on Figure 3.2(a). Hence, by comparing the intrinsic and natural properties it is possible to evaluate the amount of structure in the soil.

Plotting the response for a reconstituted clay with respect to an one-dimension compression test, a linear relationship between the void ratio (e) to the logarithm of effective vertical stress ($\ln(\sigma'_v)$) may be found. This line is referred to as the Intrinsic Compression Line (ICL), see Figure 3.2(b). Burland (1990) presented the void index (I_v) whereby the compression characteristics of various reconstituted clays may be presented by the same ICL. The void index is determined through the intrinsic properties as:

[1] According to the definition: A reconstituted soil has isotropic stiffness.

$$I_v = \frac{e - e^*_{100}}{e^*_{100} - e^*_{1000}} \tag{3.1}$$

where e^*_{100} and e^*_{1000} refers to the intrinsic void ratio at 100 kPa and 1000 kPa. Testing a natural clay, in the same manner, the response will most likely deviate from the ICL due to the additional mechanical properties gained from the sedimentation and/or the viscous effects. A Sedimentation Compression Line (SCL) may be drawn parallel to ICL, as indicated on Figure 3.2(b). The SCL will be located above the ICL caused by the fabric which has been created during the deposition. Notice, the SCL is not associated to any viscous effects (no bonding effects).

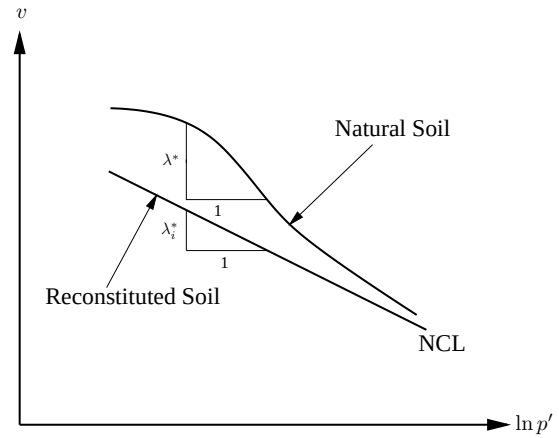

(a) Different inclination of (λ^*) for reconstituted and natural clay. Notice that (*) refers to modified MCC parameter.

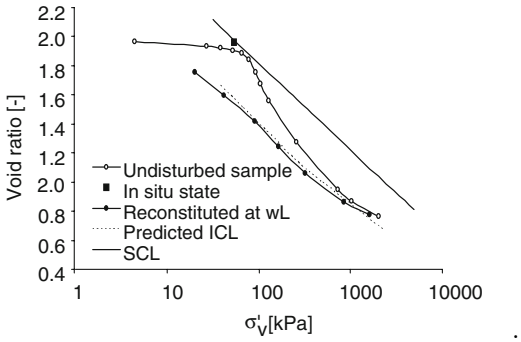

(b) Undisturbed and reconstituted clay. Taken from (Grimstad et al., 2010), original by (Burland, 1990).

Figure 3.2: *One-dimensional compression showing the difference between reconstituted and natural soil.*

As seen on Figure 3.2(b), the path of the natural clay starts to bend down towards the ICL when approaching the SCL. The physical meaning of this tendency is a rearranging of the fabric, created by the sedimentation, towards a reconstituted state corresponding to isotropic properties. If the response from the natural sample goes above the SCL it is caused by inter-particle bondings between the soil particles. Hence, the existence of structure in the soil yields a higher effective stress for a given void ratio which is allowed according to the unique relationship presented by Bjerrum (1967). This will be discussed more in Section 3.8. As seen on Figure 3.2(b), the fabric may contribute to a significant influence regarding the one-dimensional compression. The next section will explain the fabric and the initial fabric created under the deposit process.

3.4 Fabric

The term, **fabric** is associated to the orientation, distribution and shape of the individual clay particles in the clay deposit. The clay particles are normally assumed to have a plate-like shape in order to describe the fabric of the clay deposit in a relatively simple manner. Hence, the contact between the clay particles may either be Edge to Edge (EE), Edge to Face (EF), or Face to Face (FF), (Sides and Barden, 1970). Some of the first attempts to classify the fabric have be done by dividing the fabric into flocculated and dispersed structures. These terms refer to the condition during the deposition where the net electrical force between the adjacent particles could either be attraction or repulsion. A flocculated structure will normally be associated with an open structure where the contact between the clay particles would be EE and EF. The compaction would normally be in a relatively dry condition during a net attractive force. On the other hand, a dispersed structure would rather have a denser structure and tend to have a more orientated tendency. The net electrical force between adjacent particles during deposition has been repulsion which requires a large or expanded double layer effect. The typical rearrangement will be FF for a dispersed structure. Another classification has been formulated by Sides and Barden (1970) which suggests six possible types of fabric, see Figure 3.3. The ideal clay structures may be defined as:

- **Cardhouse**: Single particles in an open structure ($EE + EF$).
- **Bookhouse**: Arranged particles in an open structure ($EE + EF$).
- **Honeycomb**: Large open structure with a significant slit/sand content ($EE + EF$).
- **Dispersed**: Orientated single particles in a dense structure (FF).
- **Turbustratic**: Orientated arranged particles in a dense structure (FF).
- **Stack**: Highly oriented particles and dense structure (FF).

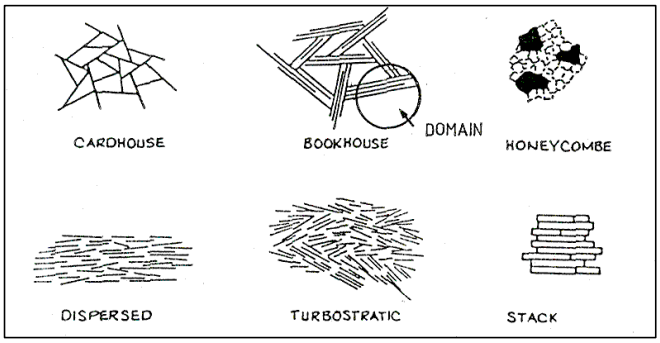

Figure 3.3: *Idealized clay structures. Taken from (Sides and Barden, 1970).*

As seen on Figure 3.3 the three lower cases of fabric would yield higher tendency of anisotropic stiffness relative to the three upper cases. To understand the creation of fabric, the deposition process much be clarified in greater detail.

3.4.1 Deposition Process

During deposition of clay particles, two main aspects will influence the creation of fabric. These two main aspects have been classified as: (1) The rate of deposition and, (2) The stillness (kinematic motion) of the water. Burland (1990) stated the following scenarios with respect to the creation of the fabric:

- **Still water + slow deposition:** Open and random fabric with high magnitude of void index laying. Thereby, the soil would be located on or above the SCL.
- **Current + fast deposition:** Orientated fabric yielding a more compact state with low void index.

The initial fabric formed during the deposition is often termed as the primary fabric. The fabric may change during the geological time though several effects. However, according to Burland (1990) the fabric does not change easily by a pure changes in overburden stresses but other phenomena are required if major changes will happen.

The influence of the fabric may be so significant that it violates the common assumption of isotropic response. Hence, the consequence of fabric may yield the necessity of implementing anisotropic conditions to ensure a more realistic soil response. The anisotropic stiffness has been observed for a wide range of soft soils as a rotated and/or skewed yield surface in the $(p' : q)$-space which may be seen on Figure 3.4. This tendency is commonly associated to typical natural clays found in Norway. However, the rotation of the yield surface may only describe the anisotropic response in the plastic domain with respect to a constitutive model. The approach of incorporating elastic anisotropic response will be discussed in Section 3.5.

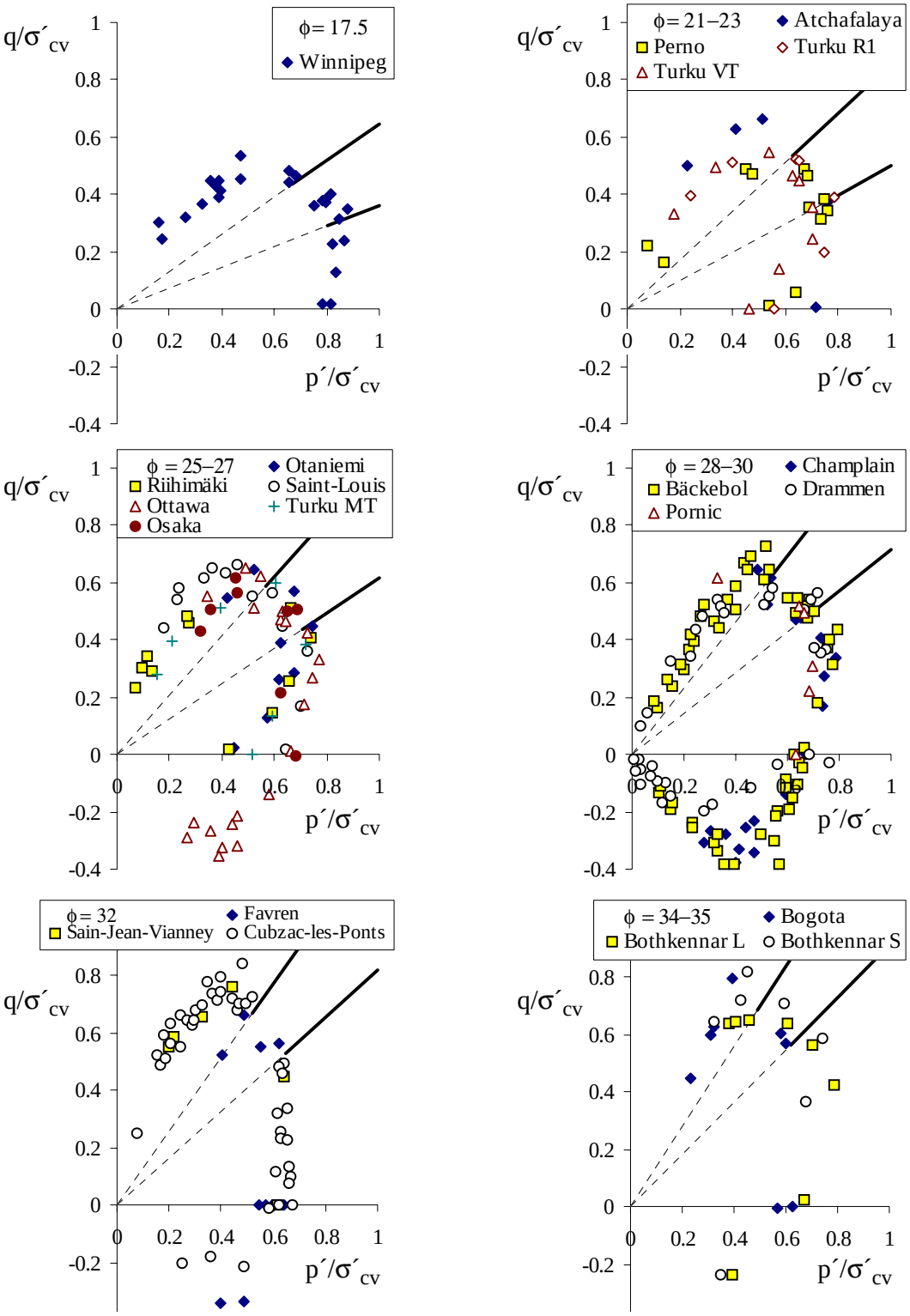

Figure 3.4: *Experimental data showing a rotated and/or skewed yield surface of different natural clays collected and presented by Länsivaara (1999). Notice notation difference ($\sigma'_{vc} = p'_c$).*

As a last comment on the term fabric, it should be known that two clays may have the same fabric and stress history but different mechanical properties. This may be caused by the inter-particle forces which are associated to time-effects and will be explained in Section 3.8.1.

3.5 Anisotropy

Section 2.3 presented an ideal case where the soil response was associated to pure isotropic elastic response. In reality, the response of natural soft clay may not behave isotropic and the assumption may be crucial according to the fabric, see Section 3.4. Hence, an anisotropic elastic stiffness matrix may be utilized to estimate a more realistic response of the natural soft clay. The general stiffness matrix consists of 36 moduli and may be reduced through different assumptions, see Table 3.1.

Table 3.1: *Number of moduli in the stiffness matrix.*

Scenario	Number of moduli	Characteristic feature
General	36	
Full Anisotropy	21	Symmetry associated to strain energy
Orthotropic	9	Three mutually perpendicular planes of symmetry
Transverse-anisotropy[(1)]	5	Equal stiffness in two directions[(2)]
Isotropic	2	Equal stiffness in all directions

[(1)] Also known as axis- or cross anisotropic

[(2)] Assuming the same stiffness in the horizontal plane

The deposited history and the shape of the clay particles may have a great influence with respect to the stiffness matrix. As mentioned in Section 3.4, the shape of the clay particles may be assumed to have a plate-like shape with a large specific area. During the deposition, the particles often tend to move downwards with relatively little lateral movement. Hence, the soil deposit would obtain different properties in the vertical and horizontal direction. The tendency would be a smaller stiffness in the vertical direction relative to the horizontal direction. Hence, transverse anisotropy may represent a natural soft clay deposit in a fairly good manner. Figure 3.5 illustrates five different soil samples taken with respect to a Cartesian Coordinate system. With respect to transverse anisotropy it may be assumed that the stiffness in sample B, C, D and E will be equal.

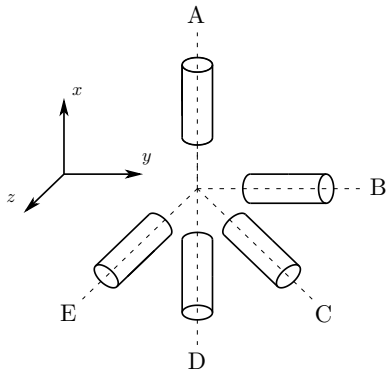

Figure 3.5: *Five soil samples taken with respect to a Cartesian Coordinate system.*

This may be assemble into a stiffness matrix given as:

$$\begin{bmatrix} \varepsilon_{11} \\ \varepsilon_{22} \\ \varepsilon_{33} \\ 2\varepsilon_{12} \\ 2\varepsilon_{13} \\ 2\varepsilon_{23} \end{bmatrix} = \underbrace{\begin{bmatrix} \frac{1}{E'_H} & -\frac{\nu_{HV}}{E'_H} & -\frac{\nu_{HH}}{E'_H} & 0 & 0 & 0 \\ -\frac{\nu_{HV}}{E'_H} & \frac{\nu_{HV}}{E'_H \nu_{VH}} & -\frac{\nu_{HV}}{E'_H} & 0 & 0 & 0 \\ -\frac{\nu_{HH}}{E'_H} & -\frac{\nu_{HV}}{E'_H} & \frac{1}{E'_H} & 0 & 0 & 0 \\ 0 & 0 & 0 & \frac{1}{G'_{HV}} & 0 & 0 \\ 0 & 0 & 0 & 0 & \frac{2(1+\nu_{HH})}{H'_H} & 0 \\ 0 & 0 & 0 & 0 & 0 & \frac{1}{G'_{HV}} \end{bmatrix}}_{\boldsymbol{D}_{Transverse}} \begin{bmatrix} \sigma_{11} \\ \sigma_{22} \\ \sigma_{33} \\ \sigma_{12} \\ \sigma_{13} \\ \sigma_{23} \end{bmatrix} \tag{3.2}$$

where H and V denote horizontal and vertical direction, respectively. Implementing of anisotropic stiffness yields no coaxiality response. The term, **coaxiality** refers to the fact that the principal directions of stress and strain are coinciding for isotropic elasticity, see Figure 3.6.

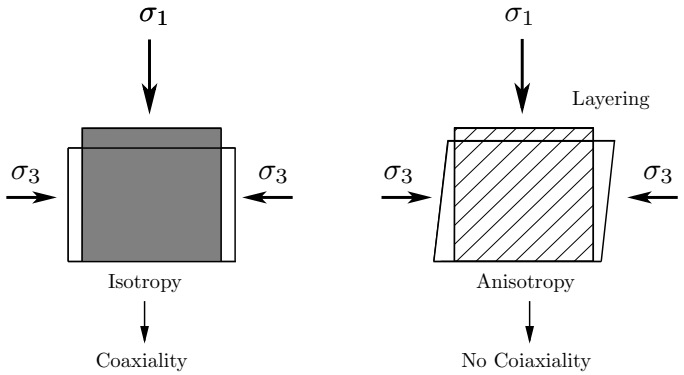

Figure 3.6: *Coaxiality of principal stresses and principal strains.*

Hence, the decomposition of the soil response into a purely volumetric and a deviatoric contribution cannot be done according to anisotropic conditions since a cross coupling term in the stiffness matrix will be present.

A method to incorporate the influence from fabric was presented by Houlsby and Graham (1983). Utilizing a normal sampling and testing approach only sample A, see Figure 3.5, would be tested in the laboratory. As stated by Houlsby and Graham (1983), only three elastic parameters may be interpreted from the sample in the laboratory. Two of these parameters are needed to determine the isotropic elastic response. Hence, Houlsby and Graham (1983) choose to incorporate the anisotropic response by utilizing the last parameter to increase/decrease the stiffness in either the horizontal or the vertical direction by an anisotropy factor α_h defined as:

$$\alpha_h = \sqrt{\frac{\nu_{HV}}{\nu_{VH}}} = \sqrt{\frac{E'_H}{E'_V}} = \frac{\nu_{HH}}{\nu_{VH}} = \frac{\nu_{HV}}{\nu_{HH}} = \frac{E'_H}{2(1+\nu_{HH})G_{HV}} \tag{3.3}$$

Thereby, the elastic relation between stresses and strains may be formulated as:

$$\begin{bmatrix} \varepsilon_{11} \\ \varepsilon_{22} \\ \varepsilon_{33} \\ 2\varepsilon_{12} \\ 2\varepsilon_{13} \\ 2\varepsilon_{23} \end{bmatrix} = \frac{1}{E'_H} \begin{bmatrix} 1 & -\alpha_h\nu_{HH} & -\nu_{HH} & 0 & 0 & 0 \\ -\alpha_h\nu_{HH} & \alpha_h^2 & -\alpha_h\nu_{HH} & 0 & 0 & 0 \\ -\nu_{HH} & -\alpha_h\nu_{HH} & 1 & 0 & 0 & 0 \\ 0 & 0 & 0 & 2\alpha_h(1-\nu_{HH}) & 0 & 0 \\ 0 & 0 & 0 & 0 & 2(1-\nu_{HH}) & 0 \\ 0 & 0 & 0 & 0 & 0 & 2\alpha_h(1-\nu_{HH}) \end{bmatrix} \begin{bmatrix} \sigma_{11} \\ \sigma_{22} \\ \sigma_{33} \\ \sigma_{12} \\ \sigma_{13} \\ \sigma_{23} \end{bmatrix} \tag{3.4}$$

A modified version of the anisotropic stiffness is given by Grimstad (2009) through a more complete formulation utilizing a general rotated orthotropic fabric matrix. The method utilizes the same principle as Houlsby and Graham (1983) and extends the formulation by an additional fabric matrix ($\boldsymbol{\alpha}$), see Appendix C.7 for further details. Hence, the orthotropic stiffness matrix may be found through:

$$\boldsymbol{D}_{ort} = \boldsymbol{\alpha}\boldsymbol{D}_{iso}\boldsymbol{\alpha} \tag{3.5}$$

Where *ort* refers to orthotropic and *iso* refers to isotropic. The orthotropic stiffness matrix may be assembled as:

$$\boldsymbol{D}_{ort} = \frac{E^*}{(1+\nu^*)(1-2\nu^*)} \begin{bmatrix} \alpha_1^2 D_{11} & \alpha_1\alpha_2 D_{12} & \alpha_1\alpha_z D_{13} & 0 & 0 & 0 \\ \alpha_2\alpha_1 D_{21} & \alpha_2^2 D_{22} & \alpha_2\alpha_3 D_{23} & 0 & 0 & 0 \\ \alpha_3\alpha_1 D_{31} & \alpha_3\alpha_2 D_{32} & \alpha_3^2 D_{33} & 0 & 0 & 0 \\ 0 & 0 & 0 & \alpha_1\alpha_2 \frac{1}{2}(D_{11} - D_{12}) & 0 & 0 \\ 0 & 0 & 0 & 0 & \alpha_1\alpha_3 \frac{1}{2}(D_{11} - D_{12}) & 0 \\ 0 & 0 & 0 & 0 & 0 & \alpha_2\alpha_3 \frac{1}{2}(D_{11} - D_{12}) \end{bmatrix} \tag{3.6}$$

where $(^*)$ denotes the reference direction and α_1, α_1, and α_1 refer to fabric directions. Transforming into the principle axis of the fabric may be done through:

$$\boldsymbol{D} = \boldsymbol{A}^{-1}\boldsymbol{D}_{ort}\boldsymbol{A} \tag{3.7}$$

where A is a rotational matrix containing elements of the rotation tensor $\boldsymbol{\alpha}$, see Appendix C.7. As a demand for introduced the fabric tensor, following requirement must be fulfilled:

$$\alpha_1 + \alpha_2 + \alpha_3 = 3 \tag{3.8}$$

In the case of transverse anisotropic an additional parameter may be introduced to simplify the relation which is similar to the anisotropic factor suggested by Houlsby and Graham (1983):

$$\alpha_e = \alpha_1 - \alpha_3 \qquad \text{and} \qquad \alpha_2 = \alpha_3 \tag{3.9}$$

Notice that α_e is not exactly the same as α_h since $\alpha_e = 0$ would yield isotropic conditions, whereas $\alpha_h = 1$ would yield isotropic conditions. Thereby, the relationship between stresses and strains with respect to $(p' : q)$-space may be assembled as:

$$\begin{bmatrix} dp' \\ dq \end{bmatrix} = \begin{bmatrix} K_{ani} & J_{ani} \\ J_{ani} & 3G_{ani} \end{bmatrix} \begin{bmatrix} d\varepsilon_v \\ d\varepsilon_q \end{bmatrix} \tag{3.10}$$

where *ani* refers to anisotropic conditions and J_{ani} represents the coupling term yielding no coaxiality. Eq. 3.10 may be rewritten in the full form as:

$$\begin{bmatrix} dp' \\ dq \end{bmatrix} = \begin{bmatrix} K_{iso} + \frac{4}{27}\alpha_e^2 G_{iso} & \alpha_e\left(K_{iso} + \frac{2}{3}G_{iso}\left(1 + \frac{1}{3}\alpha_e\right)\right) \\ \alpha_e\left(K_{iso} + \frac{2}{3}G_{iso}\left(1 + \frac{1}{3}\alpha_e\right)\right) & \alpha_e^2 K_{iso} + 3G_{iso}\left(1 + \frac{1}{3}\alpha_e\right)^2 \end{bmatrix} \begin{bmatrix} d\varepsilon_p \\ d\varepsilon_q \end{bmatrix} \tag{3.11}$$

Recalling that $\alpha_e = 0$ yields isotropic conditions. The elastic anisotropic stiffness parameter (α_e) may be determined through the pore pressure parameter (D) suggested by Janbu (1985):

$$du = dp - Ddq \qquad \longrightarrow \qquad D = \frac{dq}{dp'} \tag{3.12}$$

where du is the change in pore pressure. The relationship may be assembled though Eq. (3.11) during undrained tri-axial testing. Hence, no volume change may occur and thereby the following expression may be obtained:

$$D = \frac{\alpha_e\left(K_{iso} + \frac{2}{3}G_{iso}\left(1 + \frac{1}{3}\alpha_e\right)\right)}{\alpha_e^2 K_{iso} + 3G_{iso}\left(1 + \frac{1}{3}\alpha_e\right)^2} = \frac{\alpha_e\left(\frac{1+\nu^*}{1-2\nu^*} + 1 + \frac{1}{3}\alpha_e\right)}{\alpha_e^2\frac{1+\nu^*}{1-2\nu^*} + \frac{9}{2}\left(1 + \frac{1}{3}\alpha_e\right)^2} \tag{3.13}$$

The relationship is illustrated graphically on Figure 3.7(a) where it may be seen that $\alpha_e = D = 0$.

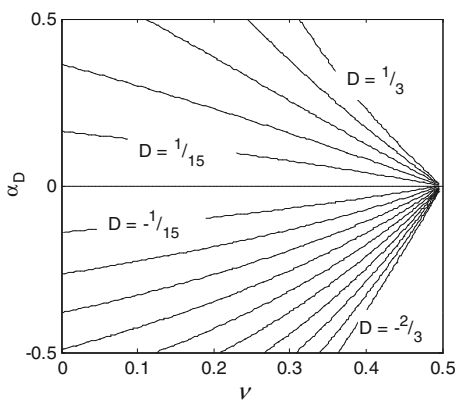

(a) Relationship between the elastic stiffness parameter (α_e), Poisson's ratio (ν) and Janbu's pore pressure parameter (D). The illustration is taken from (Grimstad et al., 2010) and α_D is equal to α_e.

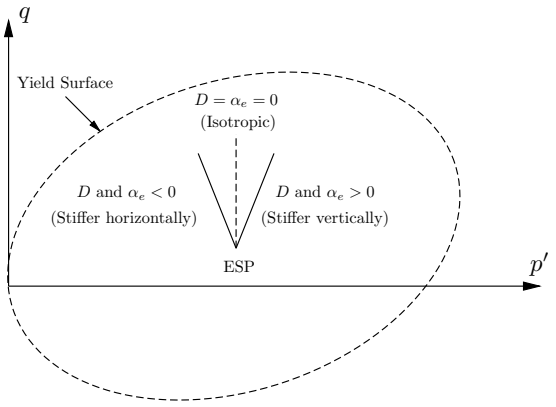

(b) Graphical illustration of ESP for different values of α_e in undrained tri-axial test.

Figure 3.7: *Determining the elastic elastic anisotropic stiffness parameter and its influence on the stiffness.*

Figure 3.7(b) shows how the elastic anisotropic stiffness parameter (α_e) influence the ESP in the $(p' : q)$-space with respect to the horizontal and vertical stiffness.

3.5.1 Stress Induced Anisotropy

It has been shown through experimental data that the small-strain stiffness of soils tend to be a non-linear function of stress. In addition, other aspects such as the void ratio and the pre-consolidation pressure may influence the stiffness (Houlsby et al., 2005). Thereby, if the non-linearity is neglected it may yield a significant violation of the thermodynamic laws regarding the storage of energy.

The MCC introduce the non-linearity by adopting a hypo-elastic formulation by varying the tangent moduli. The relationship between the bulk and shear modulus is determined by assuming a constant Possion's ratio (ν). The relationship yields a non-conservative elastic response and may generate continuous production of energy during multiple cycles. Houlsby et al. (2005) have suggested an approach without violating the thermodynamic laws by combining the hypo-elastic approach and the existence of an energy potential. The suggested method assembles the compliance matrix as:

$$\begin{bmatrix} d\varepsilon_p^e \\ d\varepsilon_q^e \end{bmatrix} = \begin{bmatrix} c_1 & c_3 \\ c_3 & c_2 \end{bmatrix} \begin{bmatrix} dp' \\ dq \end{bmatrix} \tag{3.14}$$

where:

$$c_1 = \frac{3G}{3KG - J^2} = \frac{\partial \varepsilon_p}{\partial p'} = \frac{\partial^2 U}{\partial p'^2} \tag{3.15a}$$

$$c_2 = \frac{K}{3KG - J^2} = \frac{\partial \varepsilon_q}{\partial q} = \frac{\partial^2 U}{\partial q^2} \tag{3.15b}$$

$$c_3 = \frac{-J}{3KG - J^2} = \frac{\partial \varepsilon_p}{\partial q} = \frac{\partial \varepsilon_q}{\partial p'} = \frac{\partial^2 U}{\partial p' \partial q} \tag{3.15c}$$

where U represents the internal energy mentioned in Section 2.3 and J to the coupling stiffness. Isotropic stiffness may be found by utilizing an internal energy function of:

$$U = \frac{1}{p_a}\left(\frac{1}{2k}p'^2 + \frac{1}{6g}q\right) \tag{3.16}$$

where k and g are dimensionless constants and p_a is a reference pressure. The relationship to the bulk and the shear modulus is given by:

$$K = kp_a \tag{3.17a}$$
$$G = gp_a \tag{3.17b}$$

Experimental data has shown that the relationship between the bulk modulus and the effective mean pressure for some soil may be presented better by the power function suggested by Houlsby et al. (2005). Thereby, stress induced anisotropy may be generated through the power function:

$$\frac{K}{p_a} = k\left(\frac{p'}{p_a}\right)^n \tag{3.18}$$

where n is the pressure exponent. In addition, Houlsby et al. (2005) stated that the previous stress history experienced by the material contributed to the internal energy. Hence, the internal energy will therefore be a function of:

$$U(\boldsymbol{\sigma}, \varepsilon) = U(q, p', \varepsilon) \tag{3.19}$$

Introducing a coupling term through the pre-consolidation pressure. Thereby, in terms of p' and q (tri-axial conditions) the relation between the stresses and strains may be found by:

$$d\varepsilon_p^e = \frac{\partial^2 U}{\partial p'^2}dp' + \frac{\partial^2 U}{\partial p' \partial q}dq + \frac{\partial^2 U}{\partial p \partial p'_c}dp'_c \tag{3.20a}$$

$$d\varepsilon_q^e = \frac{\partial^2 U}{\partial q^2}dp + \frac{\partial^2 U}{\partial q \partial p'}dp' + \frac{\partial^2 U}{\partial q \partial p'_c}dp'_c \tag{3.20b}$$

where the last term in Eq. (3.20) corresponds to the elastic-plastic coupling. The suggested extended hypo-elastic potential energy for clays is given as:

$$U = \left(\frac{p_a}{p'_c}\right)^r \left[\frac{p_1^{2-n}}{p_a^{1-n}k(1-n)(2-n)} - \frac{p'}{k(1-n)}\right] \tag{3.21}$$

where r is the pre-consolidation pressure exponent and p_1 is given by:

$$p_1^2 = p'^2 + \frac{k(1-n)q^2}{3g} \tag{3.22}$$

This secondary effect of stress induced anisotropy will not be incorporated in the model but has been chosen to be highlighted so the limitations for the suggested model is clear. In addition, if $n \neq 1$ the model will not be consistent and will yield a logarithmic function where issues regarding the subtraction of $\lambda^* - \kappa^*$ will occur.

3.6 Time dependent Behaviour

The time dependent behaviour is rather complex and the phenomenon has been investigated over the last decades. The attention began during the 1950s where the sensitivity and time dependent structuration of natural soft clays became of interest to the researchers. Other aspects of the time dependent behaviour, such as the time-delayed deformation, took off after the presentation by Bjerrum (1967) in the seventh Rankine lecture regarding the long time settlement of foundations. Today, the understanding of time dependent behaviour is still in a stage where further research is needed to fully understand the influence of time with respect to the soil response.

3.6.1 Classification of Time Dependent Behaviour

By reviewing the literature some confusion of terminology has occurred during the last decades caused by the lack of knowledge and limitations of testing equipment. However, nowadays the understanding of time-effects in natural soft clay have improved so the majority of researchers agree on the terminology and aspects associated to time-effects (Sorensen, 2006). The time dependent behaviour may be divided into viscous and ageing effects as seen on Figure 3.8.

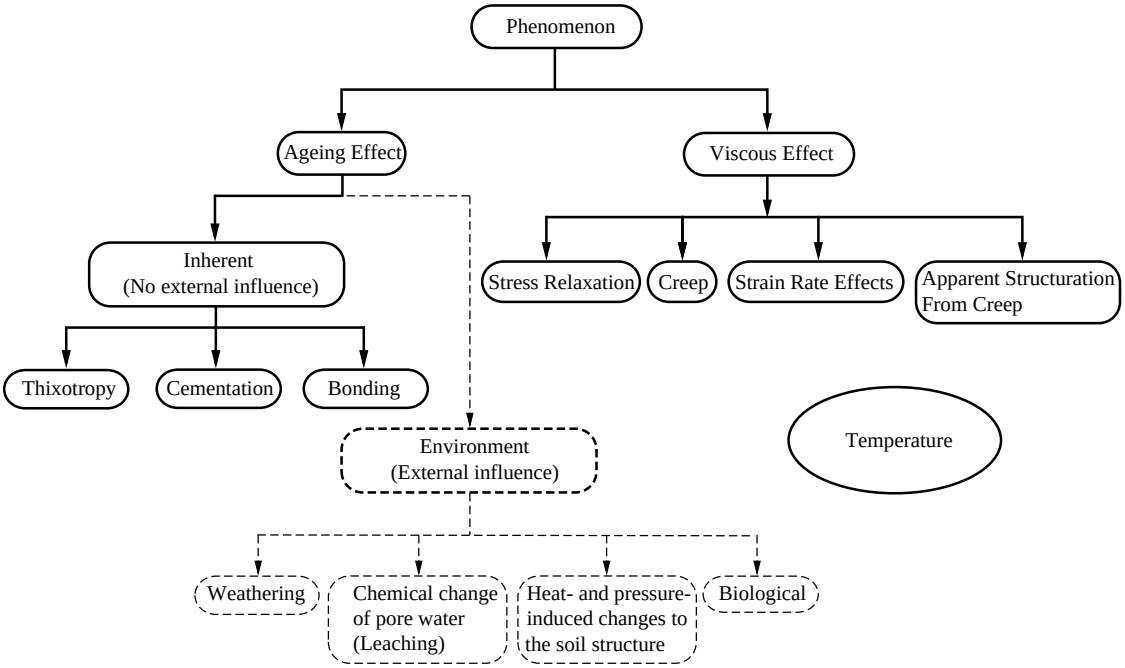

Figure 3.8: *Classification of common time effects in natural soft clays. The dashed part of this figure and the temperature effect are beyond the scope of this work.*

As indicated on Figure 3.8 the viscous and ageing effects may be divided into several other processes and will be described in the following sections.

3.7 Viscous Effects

The term, **viscosity** will normally be associated with liquids and gasses by symbolizing the measure of shear resistance to an applied shear force. Hence, the relationship between resistance and shear force may describe the characteristics of the matter. With respect to soil mechanics, a granular material yields a higher resistance to shear forces compared to clay for a given strain rate. Hence, granular materials would be defined as more viscous materials relative to clays. However, it is well known that the magnitude of creep is significant in clays relative to granular materials. Clays may therefore be characterised by a reducing viscosity with increasing shear rates and may be classified as a pseudoplastic or shear thickening matter (Sorensen, 2006). A shear thickening behaviour may be seen on Figure 3.9.

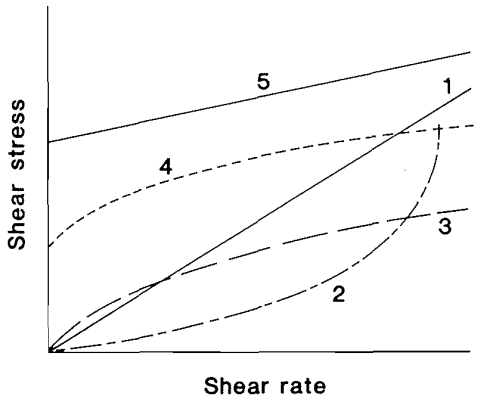

Figure 3.9: *Major types of fluids. (1) Newtonian (2) Thickening (3) Fluidizing (4) Casson (5) Bingham. Taken from (Locat and Demers, 1988).*

The general understanding of viscous effects are related to the consequence of sliding at inter-particle contacts and thereby associated to a rearrangement of particles in the soil medium. It has been shown that the presence of water in the soil medium only contributes by minor effects to the rearrangement process related to the viscous effects (Sorensen, 2006).

As indicated on Figure 3.8 it has been chosen to divide the viscous effects into four parts. Other aspects which may influence the viscous effects will not be presented in this work.

3.7.1 Creep

One of the first to encounter long-term deformation was Bjerrum (1967) during a research project regarding the soft clay found nearby Drammen in Norway. Bjerrum (1967) suggested to divide the deformation into two separate stages known as the instant and delayed compression:

Definition 6. *An 'instant compression' which occurred simultaneously with the increase in effective pressure and caused a reduction in void ratio until an equilibrium value was reached at which the structure effectively supported the overburden pressure.*

Definition 7. *A 'delayed compression' representing the reduction in volume at unchanged effective stresses.*

The two terms 'instant' and 'delayed' are more known as primary and secondary consolidation/-compression in modern literature. In addition, Bjerrum stated that the age of natural soft clays may have great importance with respect to its strength and stiffness properties. To distinguish between a young and aged normally consolidated clay Bjerrum (1973) defined a young clay as:

Definition 8. *A clay which has been recently deposited and has just reached equilibrium under its own weight can be classified as a young normally consolidated clay. Such a clay is characterised by the fact that it is just capable of carrying the overburden weight of soil, and additional load will result in relatively large settlements.*

Hence, after sedimentation, deformation in the clay deposit will initiate during constant effective stresses which will influence the mechanical properties due to a reduction in the void ratio (e). Bjerrum (1967) suggested a concept of isochrones or time lines in the one-dimensional compression plane to represent the increase in the apparent yielding point caused by the changed void ratio, see Figure 3.10.

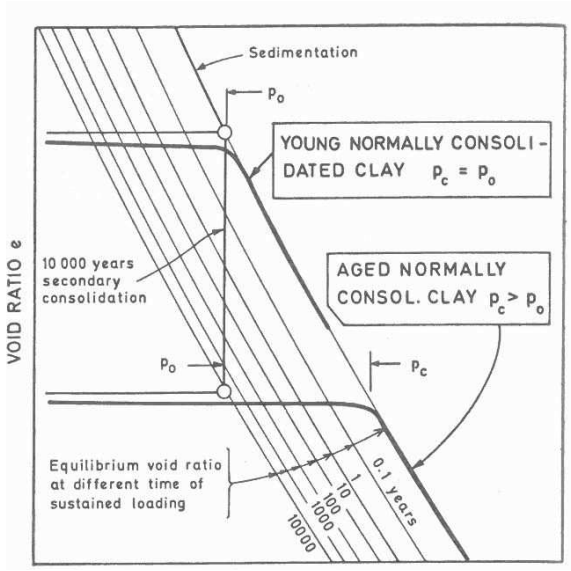

Figure 3.10: *Geological history and compressibility of a "young" and an "aged" normally consolidated clay (Bjerrum, 1973).*

Bjerrum's concept of unique parallel lines represents an equilibrium void ratio for specific times at various stress levels. Hence, a young normal consolidated clay may be located at the sedimentation line by p'_0 which corresponds to overburden weight (effective stress) of the overlaying soil. Associated to secondary compression, an increase in the apparent yielding stress will occur as illustrated in Figure 3.10 by moving down to another isochrone which is parallel to the virgin curve. The increased yield stress is often referred to as the quasi-overconsolidation (p_c). This phenomenon may be referred to as the apparent structuration related to creep caused by the expansion of the yield surface as a function of time. The expansion of the yield surface over time may be very similar to the ageing effects which will be discussed in Section 3.8. The unique relationship of isochrones has later been shown by Tavenas et al. (1978) to be extended to the entire yield surface. In other words, a unique stress path may be found. The undrained shear strength would increase as a consequence of the decrease in void ratio (e). The increasing strength is a function of the plasticity index (I_p) which may be seen on Figure 3.11.

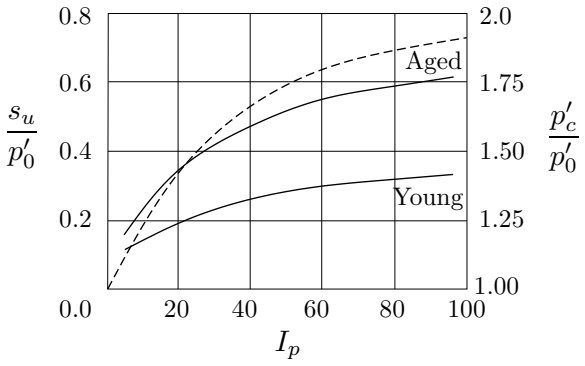

Figure 3.11: *Typical values of* $\left(\frac{p_c}{p_0}\right)$ *and* $\left(\frac{s_u}{p_0}\right)$ *observed in normally consolidated late glacial and post glacial clays. The solid lines are associated to the left axis and the dashed are associated to the right axis. Notice, that the young dashed line is placed at the x-axis since* $\frac{p_c}{p_0} = 1.0$. *Inspired by (Bjerrum, 1973).*

Creep is often assumed to be the same as the secondary compression, but is not entirely correct. The importance of distinguishing between secondary compression and creep has been stated by Tavenas et al. (1978). It is true that secondary compression is caused by pure creep. However, creep may also occur outside the secondary compression. The term **creep** is defined[2] as:

Definition 9. *A process in which deformation of the soil will happen as a function of time and the rate of creep is controlled by the viscous resistance.*

The reason why creep often is referred to as the secondary compression is because of the minor contribution of creep strains relative to the total strain during the primary consolidation. Thereby, people tend to neglect the creep strains in the primary consolidation. The viscous resistance, controlling the rate, is mainly governed by the effective stress level along with the soil properties such as the plasticity and water content. An increase of these factors would lead to a reduction in viscous resistance, resulting in larger deformations. The general characteristics of creep behaviour have shown to be similar for all types of soils, irrespectively of the grain size, mineralogy, degree of saturation and type of soil structure (Sorensen, 2006). It is common to divide the creep process into three separate stages to differentiate the contribution from creep with respect to the total strain:

- **Primary**[3]: The main deformation is associated to dissipation of excess pore water pressure where the contribution from creep is minor. The total strain rate decreases rapidly with time.
- **Secondary**[4]: A steady evolution of creep strain which reduces with time and is only associated to pure creep.
- **Tertiary Stage**: Approaching failure yielding an acceleration in the creep rate. If failure occurs it is known as creep rupture.

The total strain and its rate are presented for the three stages on Figure 3.12.

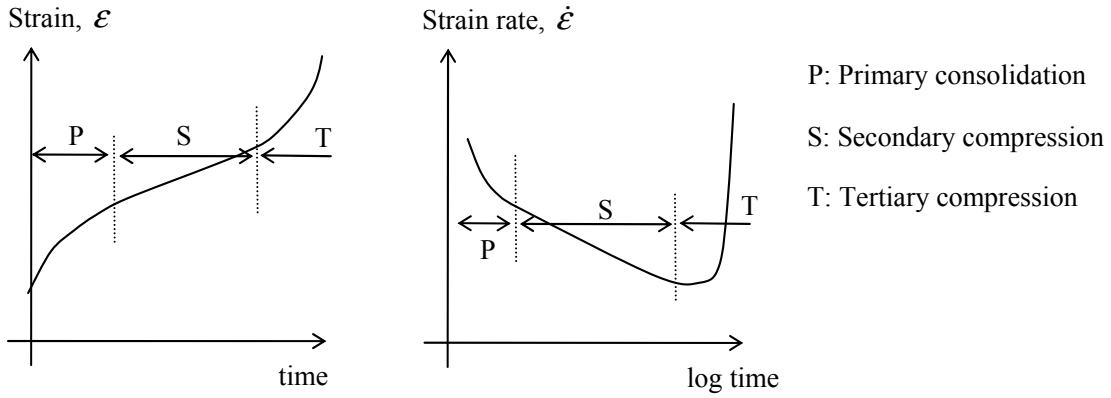

Figure 3.12: *Illustration of creep characteristics. Notice that the total strain is plotted which should not be confused with the pure creep strain. Taken from (Sorensen, 2006).*

The secondary compression shown on Figure 3.12, indicates a steady evolution of creep strains which is often approximated as linear with respect to a logarithmic time-scale. The linear relationship is commonly utilized when determining the magnitude of the secondary compression. However, the linear relationship may not be suitable for all kinds of soils, see Figure 3.13(a).

[2] The same terminology as in (Sorensen, 2006) will be utilized in this thesis.
[3] Also known as the primary consolidation/compression
[4] Also known as the secondary consolidation/compression

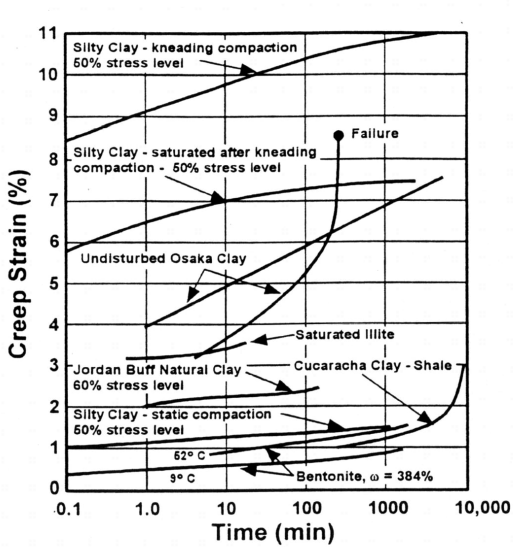

(a) General creep characteristics. Taken from (Singh and Mitchell, 1968).

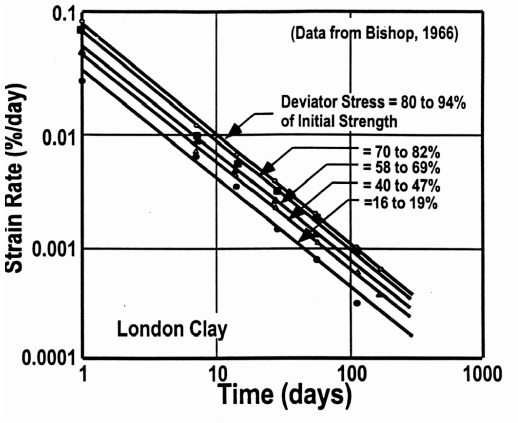

(b) Strain rate vs. time relationships during drained tri-axial creep of London Clay (Mitchell et al., 1997, replotted data from Bishop, 1966).

Figure 3.13: *Characteristic features of creep strain related to time.*

Figure 3.13(b) shows the relationship between the logarithm of strain rate to the logarithm of time where a linear relationship may be observed. It may be observed that the inclination of the relationship is essentially independent of the creep stress and an increase in stress only results in shifting the line vertically upwards (Singh and Mitchell, 1968). In addition, Singh and Mitchell (1968) has shown a linear relationship between the deviatoric stress and the logarithm to the strain rate for several clays subjected to loadings within the range of engineering interest, for instance 30% to 90 % of its strength, which are illustrated on Figure 3.14.

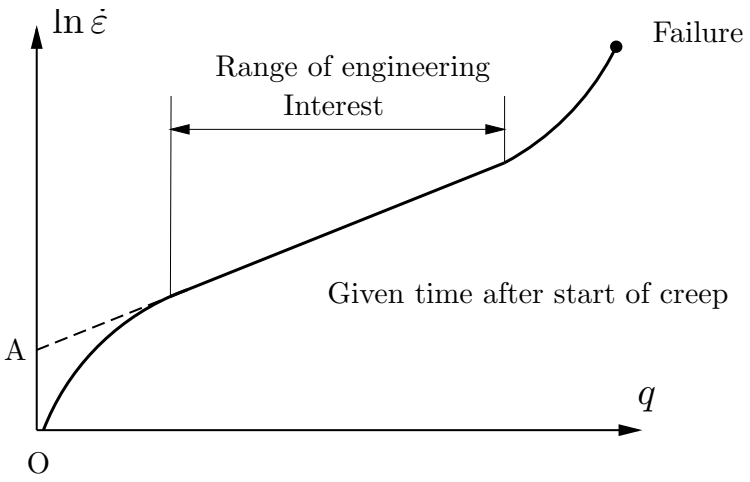

Figure 3.14: *Influence of creep stress intensity on creep rate.*

The rupture creep has been investigated by Yoginder et al. (1977) during isotropic consolidated tri-axial tests. The investigations showed that the occurrence of creep rupture was dependent on the normalized deviatoric stress which was defined as:

$$q^* = \frac{\sigma_1' - \sigma_3'}{\sigma_{1c}'} \tag{3.23}$$

where σ_{1c}' represents the isotropic consolidation pressure. Figure 3.15 shows the experimental data and shows a transition region between $q^* = 0.500 - 0.518$ going from no rupture to rupture, where a further increase ensured creep rupture.

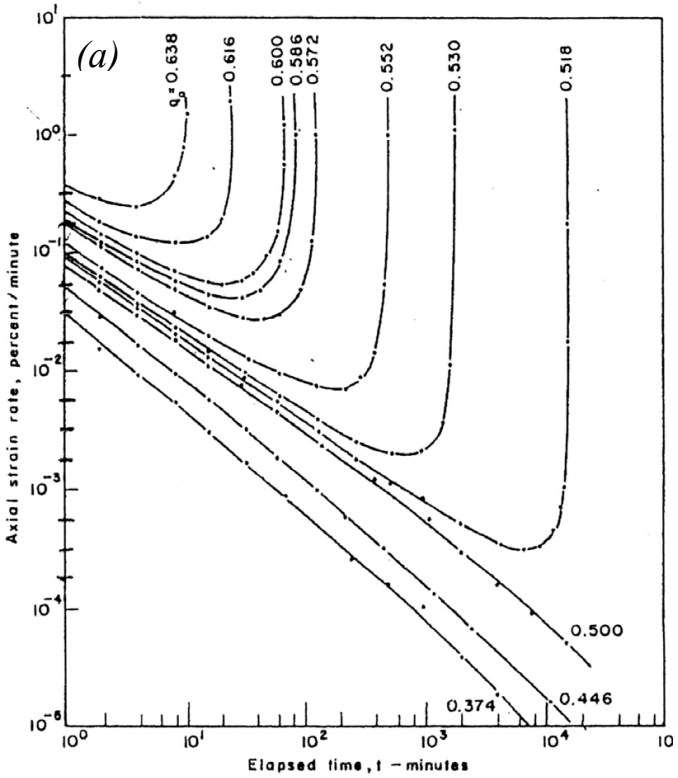

Figure 3.15: *Constant stress creep showing the variation of creep rate with time. Notice, that Yoginder et al. (1977) utilized q for the symbol of normalized deviatoric stress. Taken from (Yoginder et al., 1977).*

The phenomenon, creep rupture may not occur in one-dimensional compression or in isotropic compression since it requires relatively high magnitude of deviatoric stress to initiate. This phenomenon will not be simulated by the suggested model, but is highlighted to inform the user of the limitations of the model.

3.7.2 Stress Relaxation

The term, **stress relaxation** represent a situation where a time dependent reduction in stress occurs during constant shape and volume. In general, the stress relaxation shows similar patterns as for the creep deformation during constant effective stress and for cases not close to failure[5]. Hence, a link between stress relaxation and creep at fixed effective stress states may be assembled. During a creep test the elastic strains would be zero since the effective stresses are kept constant during the test. Thereby, the total strain may be associated to the visco-plastic strains:

$$\dot{\varepsilon} = \dot{\varepsilon}^e + \dot{\varepsilon}^{vp} = \dot{\varepsilon}^{vp} \qquad \text{since} \qquad \Delta\sigma' = 0 \quad \longrightarrow \quad \Delta\varepsilon^e = 0 \tag{3.24}$$

During a relaxation test the change in total strain is equal to zero. However, creep strains may still contribute by positive visco-plastic strains and should be counteracted by the same magnitude of negative elastic strains. Thereby, the change in total strain is kept zero. Negative elastic strains would be associated to a negative change in effective stress and thereby the rate of stress reduction may be linked to the creep rate.

Figure 3.16 shows the difference between creep during constant effective stresses and stress relaxation for a normal consolidation soil during an undrained tri-axial test. The strain effect will be discussed in Section 3.7.3.

[5] The creep rupture deviates from any observed behaviour with respect to stress relaxation.

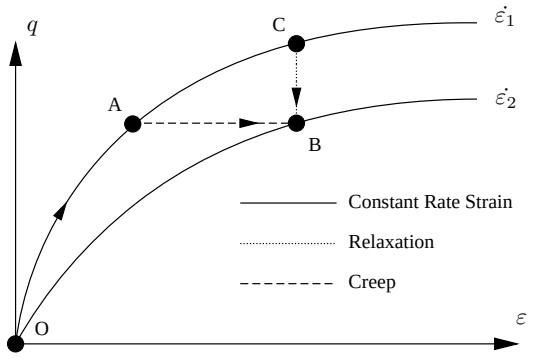

Figure 3.16: *Behaviour of creep and stress relaxation during undrained tri-axial testing for a NC soil.*

It may be concluded from Figure 3.16 that point B may be achieved through a stress relaxation or a creep phase when initiating the test with a constant strain rate of $\dot{\varepsilon}_1$.

3.7.3 Strain Rate Effects

Laboratory experiments have shown that the chosen strain rate influences the soil response. During undrained tri-axial testing, the strain rate will influence the stress path which has been reported for Norwegian clays by Lunne et al. (2006). The general tendency may be concluded as: An increase in strain rate may be associated to an increase in the undrained shear strength, see Figure 3.17(a).

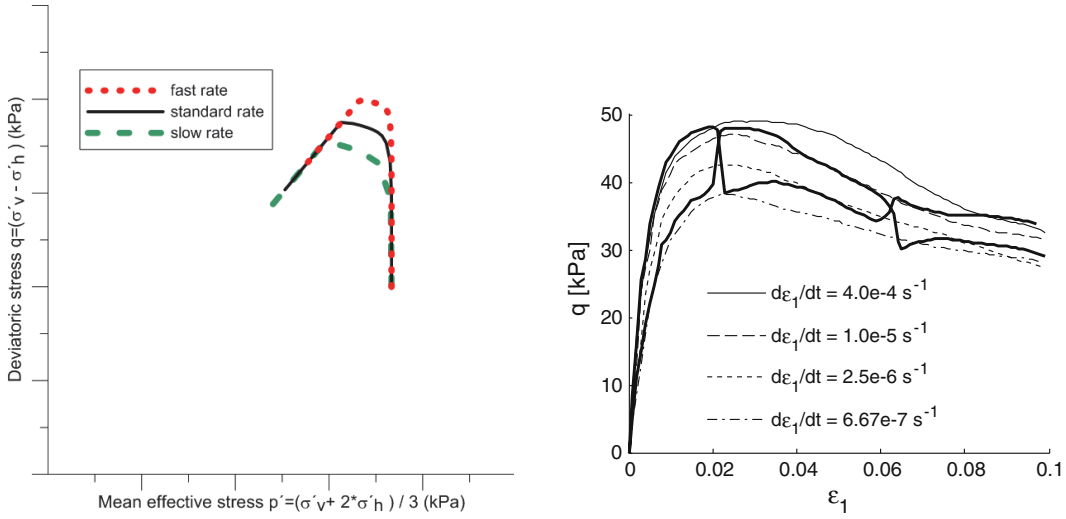

(a) Effective stress path.

(b) Deviatoric strain vs. deviatoric stress.

Figure 3.17: *Experimental data from undrained tri-axial testing showing the effect of changing the strain rate. Taken from (Länsivaara, 1999).*

Casagrande and Wilson (1951) suggested that the strain rate effect may be related to the evolution of excess pore pressure which is generated by the shearing in a undrained tri-axial test. Richardson and Whitman (1963) has verified this hypothesis by collecting experimental data from other researchers and by themselves by introducing a technique where the strain rate was changed during testing. The Step-wise change in the Rate of Strain (SRS) may be used to investigate the immediate strain rate effect, see Figure 3.17(b). Hence, it was concluded that the change in undrained shear strength of both NC and OC clays were associated to creep driven pore pressure.

Several studies have shown a unique relationship between void ratio and effective stresses for a given strain rate for clays. Thereby, the concept of isochrones suggested by Bjerrum (1967) may be replaced by the concept of isotach (same rate). Hence, by increasing the strain rate the apparent yielding point increase. However, other materials such as sand and gravel may not show isotach tendency (Augustesen, 2006). Figure 3.18 shows the characteristics for soil under one-dimensional compression with and without isotach behaviour.

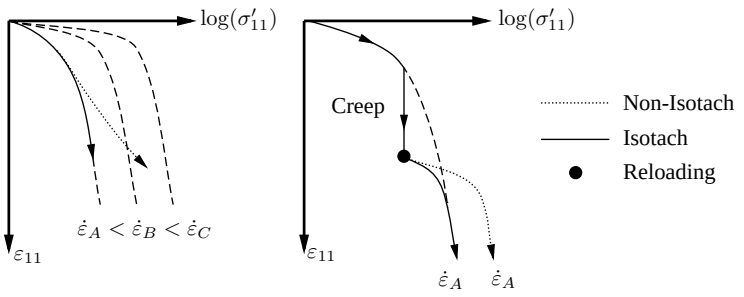

Figure 3.18: *Illustration of isotach and non-isotach behaviour for CRS.*

Figure 3.18 shows the characteristics for soils in tri-axial tests with and without isotach behaviour.

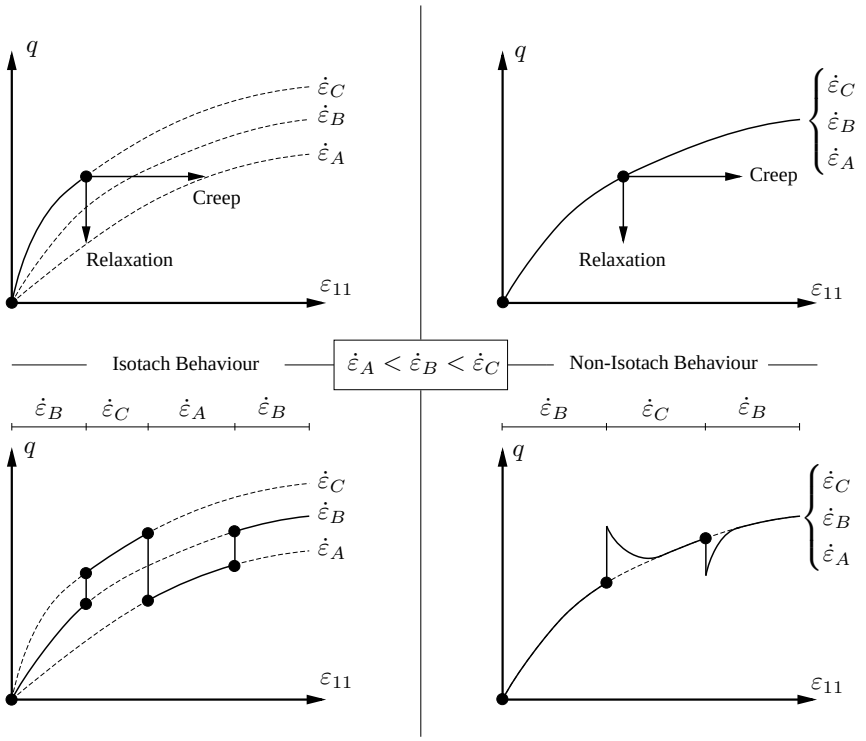

Figure 3.19: *Illustration of isotach and non-isotach behaviour for undrained tri-axial testing. The two upper Figures show the behaviour of creep and stress relaxation. The two lower figures show the effect of changing the strain rate during the test.*

It may be observed from Figure 3.19 that the SRS method is a fairly good tool to investigate the isotach behaviour of a soil. Yoginder et al. (1977) investigated the soil response of natural soft clays and concluded that the increase in undrained shear strength, induced by an increase in strain rate, is more pronounced in clays with higher plasticity index (I_p). In addition, the axial strain at the peak deviatoric stress and the critical state were essentially independent of the rate of the strain. Furthermore, Yoginder et al. (1977) stated that a lower limit regarding the undrained strength (named the upper yield) was approached when lowering the strain rate. At this stage, further reduction in strain rate did not result in additional loss in strength.

3.8 Ageing Effects

As indicated on Figure 3.8 the ageing effects may consist for several different phenomena. As presented by Sorensen (2006), these phenomena may be divided into two categories depending on the influence of the surroundings which may influence the intrinsic properties:

- **Inherent:** Does not require any interaction with the surrounding environment and may not necessarily lead to any significant changes in the intrinsic properties.
- **Environment:** Requires interaction with the surroundings and may lead to changes in the soil composition and most likely to changes in the intrinsic properties of the soil.

Concerning the scope of this thesis, only the inherent phenomenon will be explained in greater details. The ageing effects is a function of time as well as the viscous effects. Hence, in most cases a coupling between these two phenomena may be present. The viscous effects are a consequence of sliding at inter-particle contact. Thereby, if ageing effects induce a stronger bond between the particles over time a relationship must be present between the two effects. As mentioned in Section 3.7.1, the viscous effects would give rise to apparent ageing effect in form of extending the yield surface by drained creep strains. Several studies confuse the phenomenon of apparent ageing effects with the real ageing effects such as bonding, thixotropy and cementation. The confusion arise since many conclusions related to real ageing effects have been drawn without normalising their results with respect to the change in void ratio that occurs under the sustained stress (Sorensen, 2006). In other words, the influence of creep has not been removed when analysing the effect of ageing. Figure 3.20 shows two samples of the same reconstituted clay which has been tested in undrained tri-axial compression. A waiting period of either 3 or 20 days before shearing distinguish the samples. During the shearing phase, a larger brittleness and higher undrained shear strength may be observed for the 20 days sample relative to the sample of only 3 days of waiting.

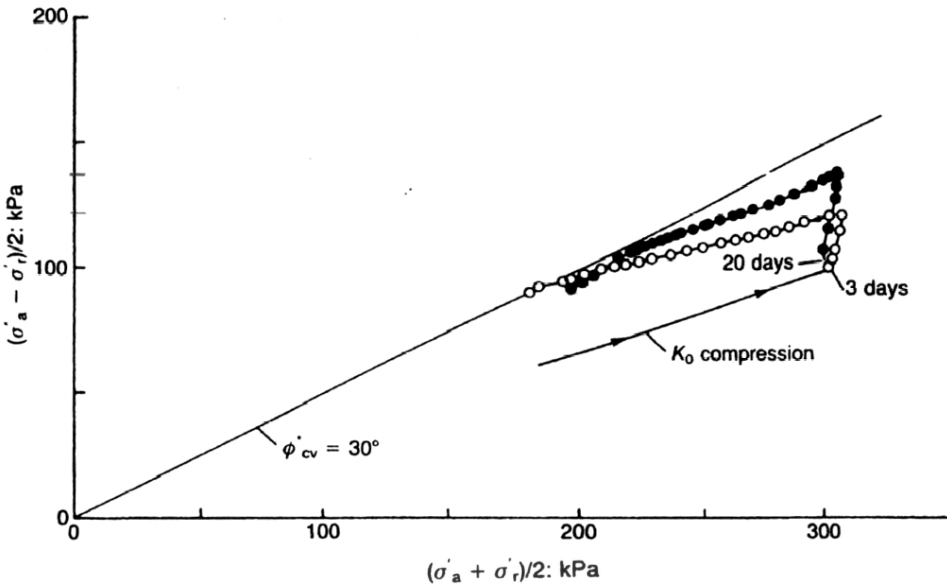

Figure 3.20: *Influence of viscous effects and ageing effects on the effective stress path in undrained tri-axial compression of reconstituted Magnus clay. Taken from (Burland, 1990 after Jardine, 1985).*

Figure 3.20 shows a clear difference between the sample of 3 and 20 days which are related to time dependent effects. However, it is not possible to measure the magnitude of either the viscous and ageing effects since the results have not been normalised with respect to the changes in void ratio. Another approach to investigate the ageing effects has been proposed by Leroueil et al.(1996) in one-dimensional compression through a conventional 24 hrs. incremental loading and two CRS, see Figure 3.21.

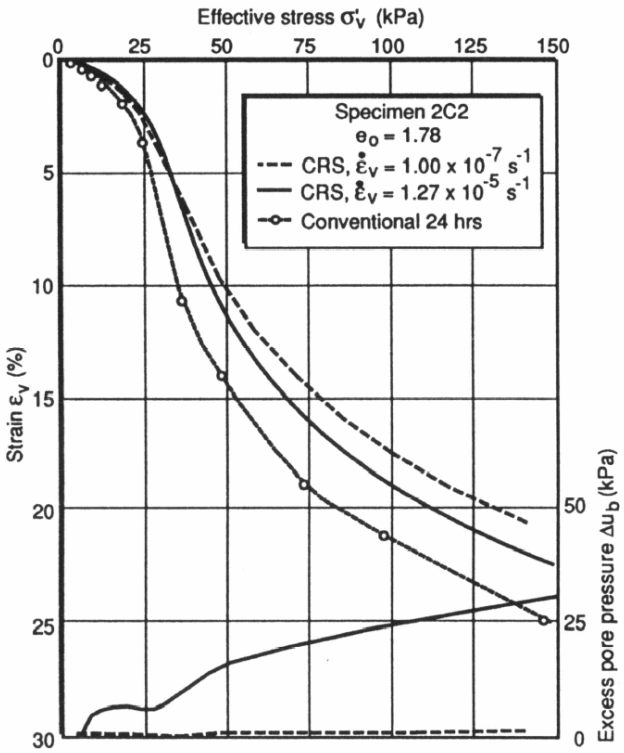

Figure 3.21: *Effect of slow rate of straining on the one-dimensional compression behaviour of artificially sedimented Jonquiere clay. Taken from (Leroueil et al., 1996). Notice notation difference* $\dot{\varepsilon}_v = \dot{\varepsilon}_p$.

The strain rate at the end of the last loading step was measured for the conventional 24 hrs incremental loading to approximate 10^{-7} s^{-1}. Hence, the CRS test with a strain rate of 10^{-7} s^{-1} should approach the same volume at the same effective stress according to the unique relationship. However, a clear difference may be observed when comparing the conventional 24 hrs. and the CRS. This phenomenon is caused by time effects where the ageing effects have increased the stiffness in the CRS, i.e. a smaller void ratio at higher effective stresses. The unique relationship is only true for pure viscous effects without any influence from the ageing effects. Hence, it may be concluded that during the slow CRS test, ageing effects have time to develop and influence the mechanical response.

In general, the inherent ageing effects will result in an expansion of the yield surface as indicated by an increase in the apparent yielding point in one-dimensional compression. Several studies have further shown that the critical state and the failure strain do not appear to be dependent on the ageing effects (Sorensen, 2006).

3.8.1 Bonding and Cementation

The term, **bonding** includes all the inter-particle forces which are not generated by pure friction between the grains. These forces may consist of electrostatic or electromagnetic nature, Van der Wall forces and viscous stresses within the absorbed water layers (Gasparre, 2005). Additional forces from instance organic content or non-clay minerals may be defined within the term cementation. Several of these effects are associated to the tiny dimension and large surface area which characterise the clay particles. By definition, clay particles are categorized as particles below 2 μm (Emdal et al., 2014) which allow these bondings to develop between the particles.

The bonding phenomenon in natural soft clay may initiate just after the deposition and develop over the geological life time of the clay until it reaches an equilibrium. During deposition the chemistry of the water may have a significant influence since particular ions tend to react more

with the clay minerals than others. The evolution of the bondings is a function of the mineralogy, electrostatic and magnetic interactions between the crystals, ion concentration, osmotic pressure, temperature and organic content (Gasparre, 2005).

It has been stated by Karstunen et al. (2005) that the natural inter-particle bonding, which originates from the type of minerals and pore water composition at the time of deposition, gives the soil extra strength and additional resistance to apparent yielding. However, after yielding the additional strength may be lost as a function of strain. It was stated by Leroueil and Vaughan (1993) that the characteristics of bonded structure are similar to those of porous weak rocks. The concept of combined creep and bonding effects for one-dimensional compression may be seen on Figure 3.22.

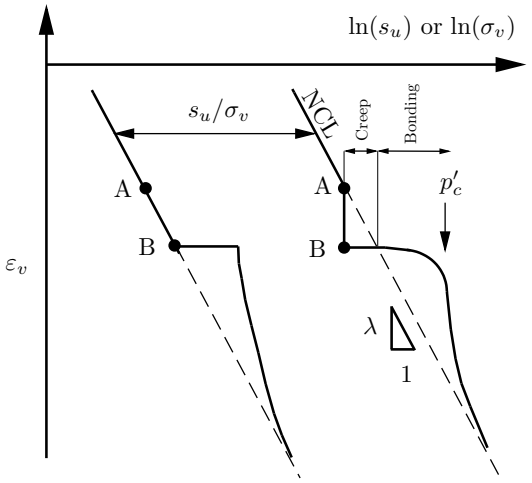

Figure 3.22: *Combined effect of bonding and creep.*

Figure 3.22 shows a young clay at point A which moves down to point B with a lower void ratio as a consequence of creep. At the same time ageing effects, in form of bondings between the clay particles, increase the apparent yield stress even further. However, if the clay is tested beyond the apparent yielding point it would loose the strength which it has gained from the bonding as a function of strain.

Destructuration

The term, **destructuration** is associated to destruction of the bondings in the soil. The bondings are not removed immediately after the apparent yielding but rather as a progressive process which is associated with the development of strains (Leroueil and Vaughan, 1993). The process is mainly driven by the development of plastic strains since the magnitude of elastic strains is relative small with respect to plastic strains.

Leroueil and Vaughan (1993) has investigated the destructuring process of the structure in one-dimensional compression for natural and reconstituted clay. Recalling that the structure consists of the bondings as well as the fabric. The oedemeter curves clearly indicated that the natural soft clays had a higher void ratio which is possible for soils without structure. In addition, during apparent yielding, natural soft clay has a higher compressibility compared to the reconstituted clay as a consequence of the structure. At the stage where the bondings are completely removed the compressibility of the compressed natural soft clay may still not have the same compressibility as the reconstituted soil. Further strains may be required to establish similar fabric and particle packing which is gained approaching the critical state (Leroueil and Vaughan, 1993). Carter and Liu (1999) have stated that in a theoretical point of view: Two samples (natural and reconstituted) should be identical when enough strains have been applied to the sample with respect to critical state soil mechanics. This conclusion is supported by the observations of the critical state strengths

and the critical state void ratios, for both natural and reconstituted soils, which only depends on the effective stress at the critical state. In general, the behaviour of a natural soft clay moves closer to the reconstituted clay as a function of the destructuring process. Figure 3.23 shows three Norwegian natural soft clays which have been sampled with either a block sampler[6] or a 95 mm piston sampler. All three clays have been tested in undrained tri-axial testing.

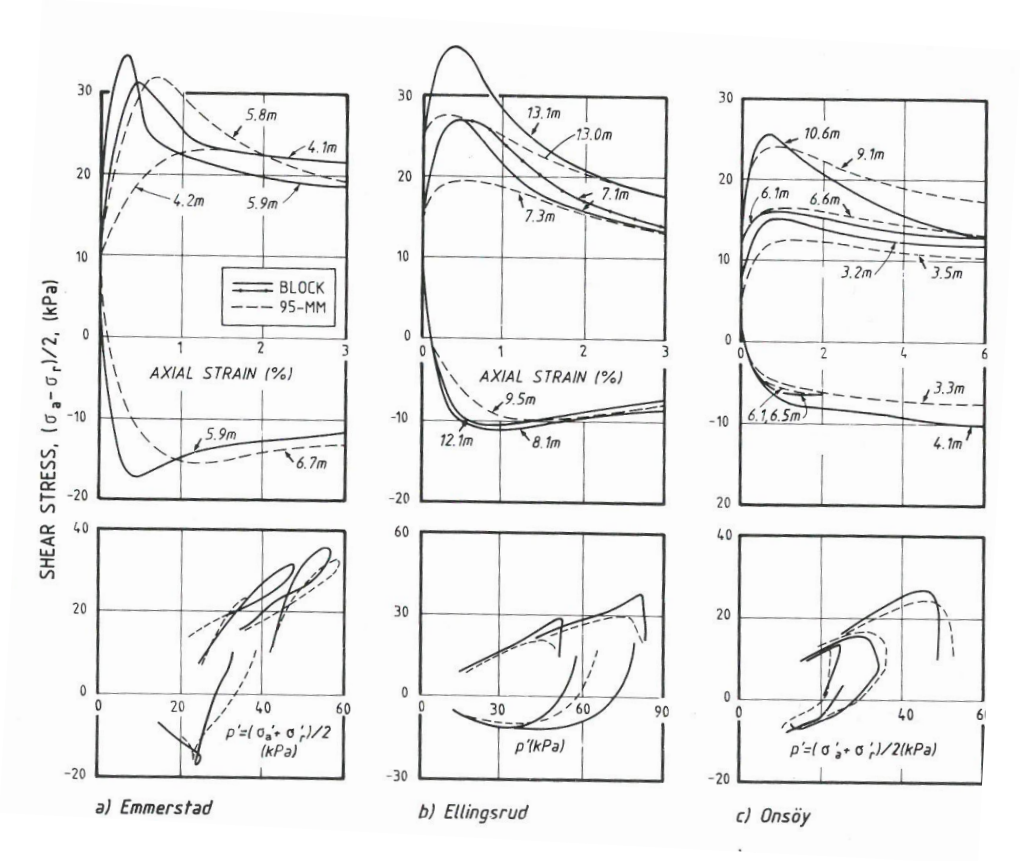

Figure 3.23: *Testing three Norwegian clays in tri-axial testing. Taken from (Lacasse et al., 1985).*

The samples disturbance will be discussed in Section 3.9. The magnitude of the structure may roughly be seen as the difference between the peak and residual undrained shear strength for the block samplers. The destructuration is associated with the path from the apparent yield towards the residual strength. The peak strength is associated with the structure and yields very brittle response. At larger strains the material tends to go towards the critical state where no structure is presented. The Emmerstad clay indicates a relatively high amount of structure which may also may be seen on the ESP which forms a special "hook" path. The Onsøy clay also indicates some amount of structure which will be analysed further in Section 7.3.2.

3.8.2 Thixotropy

Thixotropy is a phenomenon occurring as a consequence of remoulding the clay and thereby destroying the structure of clay also known as softening. After remoulding, the fabric may be in chemical disequilibrium and would approach equilibrium by changing the fabric as a function of time, see Figure 3.24. This phenomenon is known as thixotropy hardening and is essentially a reversible effect.

[6] This sampling technique is most likely the best to give high quality samples in natural soft clays.

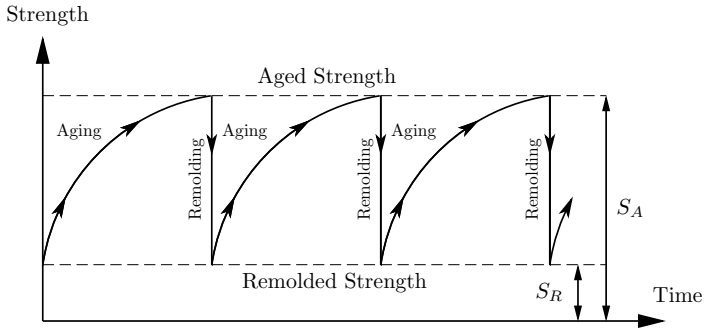

Figure 3.24: *Thixotropy hardening as a function of time for a reversible situation.*

After remoulding, the fabric will tend to be flocculated and gradually rearranged itself due to the attractive forces from the clay particles, and generate a structure until an equilibrium state is obtained, see Figure 3.25.

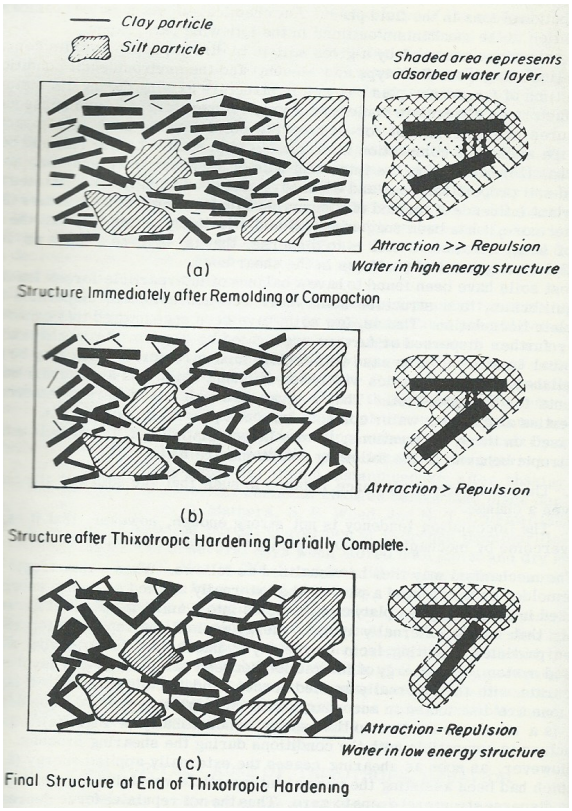

Figure 3.25: *Principle of thixotropic in a fine grained soil. Taken from (Mitchell, 1960).*

The recovery of the strength may either be partially or fully regained depending on the structure of the undisturbed clay and the contribution from micro- and macrostructure processes (Seng and Tanaka, 2012). Skempton and Northey (1952) investigated the thixotropic regaining effect and concluded that moderate sensitive clays may regain all the lost strength while it is most unlikely that sensitive and extra-sensititive clays regain the whole unremoulded strength back by thixotropic hardening. The following expression was proposed regarding the thixotropic regaining:

$$S_{Thi,t} = \frac{S_A}{S_R} \tag{3.25}$$

where S_A and S_R is the shear strength at the aged and at the remoulded state, respectively. It has been shown by Seng and Tanaka (2012) that the magnitude of thixotropy is a function of water content regardless of the soil type. They concluded that the influence of thixotropy is greatest around the liquid limit state (w_l) and the effect is less remarkable at lower and higher water

contents. As a matter of fact, thixotropic regaining will almost be insignificant in clays at water contents approaching the plastic limit. It has been proposed that the energy imbalance within the soil structure (thixotropy effect) takes place in the primary consolidation (Seng and Tanaka, 2012).

Sorensen (2006) stated that the thixotropic hardening will be less significant in natural soft clays at typical foundation stress levels (defined as $\sigma = 50$ kPa to 1000 kPa) due to the reduction in void content. The rearrangement of particles will be restricted at the low void ratios, and therefore the thixotropic hardening may be insignificant at higher stress levels and lower void ratios. Thereby, it may be concluded that the primary ageing effect is associated with bonding and cementation of the soil structure.

3.9 Sample Disturbance

Natural soft clay is very sensitive to sample disturbance. The sample disturbance may yield a significant change in soil properties obtained by laboratory tests. Therefore, the effect of sample disturbance will shortly be discussed since the constitutive model will utilize laboratory data to interpret the input parameters.

It has been proven that even for the best tube sampling technique the structure may suffer significant damage which results in a major difference in the mechanical properties (Lacasse et al., 1985). Hence, the destructuration phenomenon will only be present in high quality samples or in the field. Figure 3.26 shows three different Norwegian clays where sampling have been done by a 95 mm piston and a 300 mm diameter block sampler. The response during tri-axial testing may be seen on Figure 3.23.

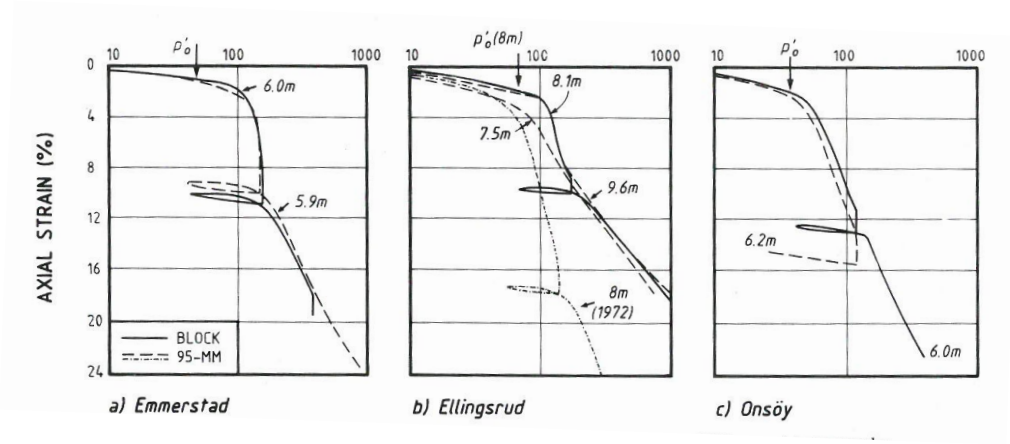

Figure 3.26: *Comparing the degree of disturbance in tube sampling relative to block sampling for three different types of Norwegian clays. Taken from (Lacasse et al., 1985)*

Depending on the type of clay, the tube sampler indicate various degrees of disturbance compared to the high quality block sampler. The degree of disturbance may be related to the higher plasticity, but sand and gravel particles may also have a negative influence since lateral straining may occur during sampling. The mechanical disturbance is the primary source of the destruction of the original structure in the natural soft clay. The aspects such as, overstressing and overstraining related to the penetration of the sampler, cutting of the sample along with the withdrawal of the sampler, and removal of the sample from the sampler should be minimized to obtain high quality samples. The clay samples are generally more sensitive to disturbance for low plasticity index and high sensitivity.

In general, disturbed samples tend to show a lower pre-consolidation pressure and smaller amount of structure than less disturbed samples. The disturbance may be compensated by the effect of higher strain rates in laboratory testing. However, the sample disturbance may change the soil response completely as it may lead to a lower void ratio after reconsolidation (Grimstad, 2009).

3.10 Temperature

As mentioned in Section 3.7.3 the strain rate may influence the soil response. It has been stated by Laloui et al. (2008) that for a non-organic clay-like soil an increase in the apparent yielding pressure of 10 % may be expected if the strain rate is changed by one order of magnitude. However, the same increase may be found if the temperature is increased by 12^{o}C (in the range of 5^{o}C to 40^{o}C). Hence, a coupled effect between the strain rate and the temperature will be present through the viscosity of pore water. The main aspects regarding temperature effects may be divided into two topics (Leroueil and Marques, 1996):

- The viscosity of water.
- The thermal expansion of solid particles and liquid particles.

However, the thermal expansion may be ignored in several types of soils, see (Tsutsumi and Tanaka, 2012). The amount of organic content in the soil would normally tend to increase the temperature sensitivity. Figure 3.27(a) shows two CRS tests with different rates and temperature.

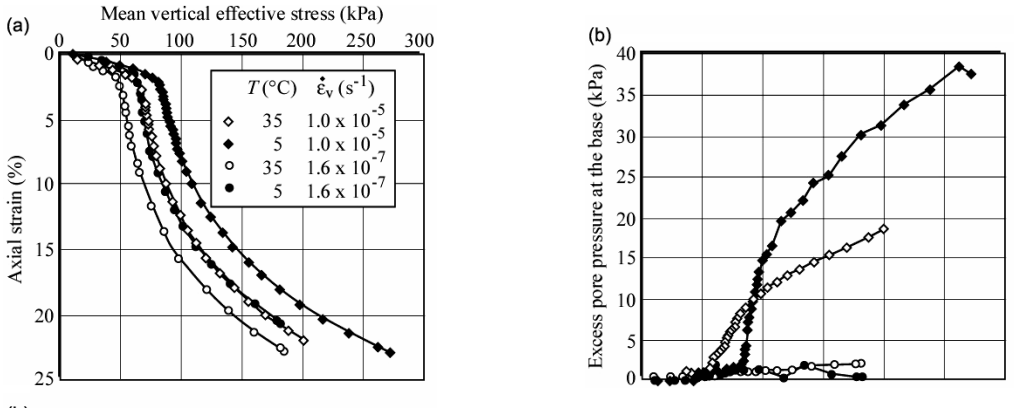

(a) Compression plane.

(b) Development of excess pore pressure. Notice that the x-axis is the same as in Figure 3.27(a).

Figure 3.27: *Experimental data from a CRS test illustrating the similarities of changing the temperature or strain rate. Taken from (Laloui et al., 2008).*

The tested Berthierville clay indicates that a change of temperature of 30^{o}C yields similar response as for a change in strain rate by two orders of magnitude. However, as seen on Figure 3.27(b) the excess pore pressure does not show the same tendency. This is caused by the difference in viscosity of pore water at each temperature. The viscosity of water at 5^{o}C has a viscosity which is 2.1 larger than for 35^{o}C. Hence, the hydraulic conductivity of the clay at 5^{o}C is smaller than the hydraulic conductivity at 35^{o}C at the same void ratio. The relationship between the hydraulic conductivity (k) and the viscosity of pore water (ν_{water}) at different temperatures may be formulated as:

$$\frac{k_{50}}{k_{10}} = \frac{\nu_{\text{water},10}}{\nu_{\text{water},50}} \tag{3.26}$$

Laloui et al. (2008) has proposed a model to simulate the coupled effect of strain rate and temperature effects for one-dimensional compression utilizing the proposed coupling formulation:

$$\sigma'_{y,\varepsilon_v^{vp},T} = \sigma'_{y,\varepsilon_v^{vp},T_0} \left(\frac{\dot{\varepsilon}_v^{vp}}{\dot{\varepsilon}_{v0}^{vp}}\right)^{C_A} \left(1 - \gamma \log\left(\frac{T}{T_0}\right)\right) \tag{3.27}$$

where C_A is a soil parameter which may be related to λ, and κ, T is the temperature, and γ are thermal soil parameters, which have been shown to vary with the liquid limit.

The constitutive model will not incorporate the temperature effect. However, it has been highlighted to inform the user about the limitations of the proposed model.

3.11 Environment

The environment effects are not included in the scope of this thesis, but the reader should be aware of these processes. A common environment effect in Norway is the leaching phenomenon, which creates a weakness of the bonds in the soil skeleton. The leaching process is often associated with the creation of quick clay. Leached clay will be very sensitive to soil disturbance since the swelling index is increased and a reduction in the structure is present. In addition, leached clay tend to change the fabric to a dispersed structure during consolidation (Kim and Do, 2010).

Chapter 4

Visco-Plastic Model

The purpose of this chapter is to provide general information regarding the development and implementation of the visco-plastic model. The chapter gives a detailed description of the mathematical formulations associated to the special features in natural soft clay and how the model is initialized. In addition, comparison to similar models found in the literature will shortly be discussed.

4.1 Introduction

From this point, the visco-plastic model will be known as the SCA-R model which has the ability to simulate some of the features regarding natural soft clay (Structure Creep Anisotropic - Recovering of structure). The model is based on principles similar to those used in: CREEP-SCLAY1S, n-SAC and MAC-s suggested by: Karstunen et al. (2005), Grimstad and Degago (2010), and Olsson (2013), respectively. A short description of these soil models among others may be found in Olsson (2013). The SCA-R model can be very similar to CREEP-SCLAY1S[1] where it deviates from the n-SAC and MAC-s by assuming associated flow[2]. The feature of recovering structure over time is an extension from the three models which yields a side effect of one extra feature to control the development of creep through the recovering of structure over time.

The SCA-R model is based on the MCC model and utilizing the theory given in Section 2.6 to assemble an elasto-plastic model which is extended to a visco-plastic model by introducing viscous effects described in Chapter 3. The model can use up to 15 input parameters[3] if all four features must operate. The model is able to simulate MCC behaviour utilizing six input parameters. In addition, two additional input parameters are available in the model which allows the user to choose between three different rotational hardening laws and two different failure criteria in the general stress space. In Chapter 8 another two input parameters are added to the model to preform better predictions. These additional parameters will not be highlighted here.

The SCA-R model is implemented into the commercial software PLAXIS as a user-defined soil model. The code is generated in FORTRAN supported by coding from MATLAB and utilize a simple explicit scheme to determine the stress-strain-time relationship. Further details may be found in Chapter 5.

[1] Selecting the same rotation law and failure criteria.
[2] Other minor deviations such as difference in the formulation of the yield surface may be found.
[3] 16 if the reference time is taken into account.

4.2 How to Model Anisotropy

The existence of anisotropy in the natural soft clay has been discussed in Section 3.4 and Section 3.5. In respect to modelling the effect of anisotropy in the plastic region various suggestions have been given of how to incorporate anisotropy into an elasto-plastic or visco-plastic model. The traditional approach is dividing the anisotropy into an initial anisotropy caused by sedimentation, and an evolution law describing the change of anisotropy during loading. One of the first suggestions was given by Sekiguchi and Ohta (1977) through an initial rotated yield surface without any kinematic hardening. This method is similar to a rotated CC model. Afterwards, other similar approaches have been suggested of how to model the yield and the plastic potential surface with respect to initial anisotropy and how the evolution of these surfaces should behave. In general, the majority of the proposed models are based on the MCC model and tends to go back to a standard MCC model by setting the anisotropic parameters to zero. The modelling of the initial fabric is generally accepted by a rotation of the yield and plastic potential surface, see Figure 4.1[4]. However, the formulation regarding the evolution differs from several models.

Dafalias (1986) proposed an extension of the MMC from isotropic to anisotropic response. The proposal is often applied to various models today since it may be the simplest possible energetic extension of the MCC model. The formulation introduce the rate of plastic work through a coupling between the volumetric and deviatoric plastic strain rates (Dafalias et al., 2006). The formulation of the yield surface was originally formulated as:

$$F = p'^2 - p'p'_c + \frac{1}{M^2}\left[(q - p'\alpha)^2 + (p'_c - p')\, p\alpha^2\right] = 0 \tag{4.1}$$

but is more commonly recognisable by the format presented by M. Koskinen, M. Karstunen (2002):

$$F = (q - \alpha p')^2 - \left(M^2 - \alpha^2\right)(p'_c - p')\, p' = 0 \tag{4.2}$$

In general, the yield surface consists of a rotated and distorted ellipse, where the degree of rotation and distortion is determined by the value of α. The rotation parameter (α) is a scalar and the value corresponds to the rotation in radians utilizing standard rotation with respect to a Cartesian Coordinate system. Notice that the above formulation requires that $|\alpha| < M$ in order to have real roots for q. In addition, compression corresponds to $q/p' \geq \alpha$ and extension $q/p' \leq \alpha$. Do to its simplicity, Eq. (4.2) will be used to model the anisotropic response. According to the general space Eq. (4.2) may be reformulated to:

$$F = \frac{3}{2}\left\{\boldsymbol{\sigma_d} - p'\boldsymbol{\alpha_d}\right\}\left\{\boldsymbol{\sigma_d} - p'\boldsymbol{\alpha_d}\right\}^T - \left(M^2 - \frac{3}{2}\boldsymbol{\alpha_d}^T\boldsymbol{\alpha_d}\right)(p'_m - p')\, p' = 0 \tag{4.3}$$

where p'_m refers to the apparent yielding pressure with incorporated structure (bondings)[5] , $\boldsymbol{\alpha_d}$ refers to the deviatoric fabric tensor, and $\boldsymbol{\sigma}_d$ is the deviatoric stress tensor. The initializing of the anisotropy will be described in Section 4.7.1. It should be mentioned that the initial rotation and evolution law only describes the anisotropic conditions during plastic strains. Applying anisotropic conditions in the elastic region will be described in Section 4.2.2.

4.2.1 Second Hardening Law

The next step is to define the evolution law for the yield and plastic potential surface. It has been stated by Dafalias and Taiebat (2013) that the rotational hardening (evolution of α) is a constitutive feature of anisotropic clay plasticity models. The purpose of the law is to introduce a rotation of the yield and plastic surface to simulate more realistic material response relative to isotropic models. These models should be verified under various loading scenarios to ensure that the response fulfils all requirements. The rotational hardening law should fulfil the following three requirements:

[4] Associated flow is assumed.
[5] Will be discussed in Section 4.3.

- The rotational hardening yields an unique critical state line in $(e : p')$-space.
- Restrictions of the model parameters to prevent unrealistic rotation of the yield and plastic potential surface.

The evolution of anisotropy is normally represented by changes in the inclination or position of yield and potential surface with respect to rotational and/or kinematic hardening. The evolution is driven by the development of plastic strains and are commonly assumed either to be purely volumetric or purely deviatoric plastic strains (Karstunen et al., 2008). In reality, both volumetric and deviatoric plastic strains contribute to the change in anisotropy and should therefore be incorporated in the model.

To simplify the model one could choose to set the evolution of anisotropy to zero and still keeping the initial anisotropy. By this, the input parameters will reduce by two[6]. The effect of this can be discussed, but some results have shown better fits to experimental data by setting the change in rotation to zero (Leoni et al., 2008). However, as stated by Dafalias and Taiebat (2013) these conclusions are often drawn without investigating the true influence of the evolution and the error may be introduced by for instance the choice of yield surface or assumptions regarding associated flow. Dafalias and Taiebat (2013) stated the great importance of incorporating the evolution law if a better estimate of natural soft clay is wanted.

In Appendix C.9 four rotational laws are listed up and they are briefly discussed according to the above mentioned characteristics[7]. Three of the four evolution laws have been chosen to be implemented in the SCA-R model. The three evolution laws are suggested by Wheeler et al. (2003), Dafalias (1986), and Dafalias and Taiebat (2013). These evolution laws will be described shortly in the next subsections.

Wheeler 2003

The rotational hardening presented by Wheeler et al. (2003) is a function of both plastic volumetric and plastic shear strains. The evolution of α is based on an assumption regarding a specific combination of the plastic strains to fulfil the criteria of a unique critical state line. The evolution of rotation is given by:

$$\frac{d\alpha}{d\lambda} = \mu\Big[\big(\chi_p(\eta) - \alpha\big)\langle d\varepsilon_p^p\rangle + \beta\big(\chi_d(\eta) - \alpha\big)|d\varepsilon_q^p|\Big] \tag{4.4}$$

where β controls the relative effectiveness of deviatoric and volumetric plastic strains by determining the boundary value (α_b), and μ controls the absolute rate at which α approaches its boundary value (α_b). The brackets $\langle\rangle$ are Macaulay brackets[8] and χ is targets values.

As stated by Wheeler et al. (2003), the plastic volumetric strains will attempt to drag the value of α towards an instantaneous target value $(\chi_p(\eta))$ which is dependent on the current stress ratio η. The physical meaning represent a slippage of the inter-particles contacts between the grains and may result in rearrangement of the soil fabric associated to the development of plastic volumetric strains. Thereby, the rearrangement regarding the fabric will change towards a structure which has a degree of anisotropy controlled by the stress state under which this plastic straining is occurring. Simultaneously, plastic shear strains are assumed to attempt to drag α towards a different instantaneous target value $(\chi_d(\eta))$. It is assumed that volumetric and deviatoric plastic strains results in a different rearrangements of the fabric. Hence, a procedure to determine the target values $\chi_p(\eta)$ and $\chi_d(\eta)$ may be assembled as:

$$\begin{aligned} &\text{Plastic volumetric strains dominate (low } \eta) \quad \longrightarrow \quad \alpha \text{ very close to } \chi_p(\eta) \\ &\text{Plastic shear strains dominate (high } \eta) \quad \longrightarrow \quad \alpha \text{ very close to } \chi_d(\eta) \end{aligned}$$

[6] If one parameter is determined theoretically it would only reduce by one, see Section 4.7.1.
[7] The discussion is a summary of the discussion presented by Dafalias and Taiebat (2013).
[8] Meaning: $\langle d\varepsilon_p^p\rangle = d\varepsilon_p^p$ for $d\varepsilon_p^p \geq 0$ else $\langle d\varepsilon_p^p\rangle = 0.0$

It should be mentioned that for a stress path where η is varying, α would continuously vary as well. Näätänen et al. (1999) have utilized this procedure mentioned above to estimate the values of $\chi_p(\eta)$ and $\chi_d(\eta)$. Näätänen et al. (1999) suggested the values on the basis of the experimental data:

$$\chi_p(\eta) = \frac{3}{4}\eta \qquad \text{and} \qquad \chi_d(\eta) = \frac{\eta}{3}$$

The soil parameter β and μ in Eq. (4.4) may be determined through calibration during laboratory testing. If laboratory testing is not possible, empirical and theoretical relations can be used to determine the two soil parameters, see Section 4.7.1. In respect to the general stress space Eq. (4.4) may be rewritten into:

$$\frac{d\boldsymbol{\alpha_d}}{d\lambda} = \mu \left[\left(\frac{3\boldsymbol{\sigma}_d}{4p'} - \boldsymbol{\alpha_d} \right) \langle d\varepsilon_p^p \rangle + \beta \left(\frac{\boldsymbol{\sigma}_d}{3p'} - \boldsymbol{\alpha_d} \right) |d\varepsilon_q^p| \right] \tag{4.5a}$$

This evolution law has been utilizing in CREEP-SCLAY1S, n-SAC and MAC-s suggested by: Karstunen et al. (2005), Grimstad and Degago (2010), and Olsson (2013), respectively.

Dafalias 1986

The evolution law suggested by Dafalias (1986) is the simplest of the three implemented laws. The evolution law ensure the correct stress ratio (K_0) during one-dimensional compression and may be formulated as:

$$\frac{d\alpha}{d\lambda} = cp_{at}\frac{p'}{p'_c}(\alpha_b - \alpha) \qquad \text{where} \qquad \alpha_b = \frac{\eta}{x^\alpha} \tag{4.6}$$

where p_{at} is the atmospheric pressure introduced for dimensional consistency[9], c is a model parameter controlling the pace of evolution, and x^α is another model parameter defining the equilibrium or boundary value α_b under fixed stress-ratio η loading. The boundary value depends of the earth coefficient (K_0^{NC}). In the general stress space $d\alpha = d\boldsymbol{\alpha_d}$ and $\eta = \frac{\boldsymbol{\sigma}_d}{p'}$.

Dafalias 2013

The third evolution law presented by Dafalias and Taiebat (2013) is a modification of the evolution law suggested by Dafalias (1986). The boundary value of α_b is substituted by an exponential function implemented through the parameter x^α:

$$x^\alpha = |\eta| \left(\frac{M}{z} \left[1 - \exp\left(-s\frac{|\eta|}{M} \right) \right] \right)^{-1} \tag{4.7}$$

By introducing the exponential dependence of x^α it has been shown that the output fit better to experimental data, see Appendix C.9. Hence, the formulation may be given as:

$$\frac{d\alpha}{d\lambda} = cp_{at}\frac{p'}{p'_c}(\alpha_b - \alpha) \qquad \text{where} \qquad \alpha_b = \pm\frac{M}{z}\left[1 - \exp\left(-s\frac{|\eta|}{M} \right) \right] \tag{4.8}$$

where z and s are positive model constants defining the equilibrium or boundary value α_b under fixed stress-ratio η loading. Furthermore, M will take the value either of M_c or M_e[10] and the $\pm$ sign becomes positive or negative for $\eta \geq 0$ or $\eta \leq 0$, respectively. The boundary value depends of the earth coefficient (K_0^{NC}). In the general stress space $d\alpha = d\boldsymbol{\alpha_d}$ and $\eta = \frac{\boldsymbol{\sigma}_d}{p'}$.

[9] See Appendix C.9
[10] c refers to compression and e refers to extension

4.2.2 Anisotropy in Elastic Domain

The anisotropy in the elastic region is modelled by implementing Eq. (3.6) in the SCA-R model. Assuming transverse anisotropy the fabric may be determined by one anisotropy parameter:

$$\alpha_1 = 1 + \frac{2}{3}\alpha_e \tag{4.9a}$$

$$\alpha_2 = 1 - \frac{\alpha_e}{3} \tag{4.9b}$$

$$\alpha_3 = 1 - \frac{\alpha_e}{3} \tag{4.9c}$$

where α_1 symbolizes the direction with different stiffness with respect to other directions. As mentioned in Section 2.6.1, the elastic bulk modulus in clays shows a tendency of stress dependency which is incorporated in the model by:

$$K = \frac{(1+e_0)p'}{\kappa} \tag{4.10}$$

where e_0 is the initial void ratio. Regarding anisotropy conditions, the bulk modulus is associated to $K = K_{ani}$. Hence, utilizing the expression for K_{ani} given in Eq. (3.11), a stress dependent formulation may be assembled as:

$$K_{ani} = \frac{(1+e_0)p'}{\kappa} = K_{iso} + \frac{4}{27}\alpha_e^2 G_{iso} \tag{4.11}$$

According to Eq. (3.6), the reference E^*-modulus is needed which may be found by inserting the formulations for the K_{iso} and G_{iso} given by Eq. (2.10) into Eq. (4.11) and rearranging with respect to E^*. Thereby a stress dependent stiffness in terms of the E^*-modulus may be given by:

$$E^* = \frac{27}{4}\frac{(1+e_0)p}{\kappa} \cdot \frac{(1+\nu)(2\nu-1)}{4\alpha_e^2\nu - 2\alpha_e^2 - 9(\nu+1)} \tag{4.12}$$

Notice, if $\alpha_e = 0$ yields isotropic conditions. In addition to the simplified transverse anisotropy, the model could easily be extended to simulated a more complex condition of anisotropy since it has been chosen to implement Eq. (3.6) in the SCA-R model. However, this requires more input parameters and has therefore been omitted.

4.3 How to Model Bondings

The existence of bondings in the natural soft clay has been discussed in Section 3.8, and the destructuration has been mentioned in Section 3.8.1. The MCC model may be extended to included bonded materials and thereby be able to simulate the destructuration phenomenon by introducing intrinsic properties (Wood, 2004). The intrinsic properties refers to the soil properties without any structure, see Section 3.3. A relation between the intrinsic yields surface and the apparent yield surface associated to the amount of bondings may be formulated as:

$$p'_m = (1+x)p'_{mi} \tag{4.13}$$

where x refers to amount of structure (bonding) as the ratio between the yield surface of the natural soft clay and the yield surface of the reconstituted clays (notice that i denotes intrinsic). Eq. (4.13) may be visualized in the $(p'-q)$-space and may be seen on Figure 4.1.

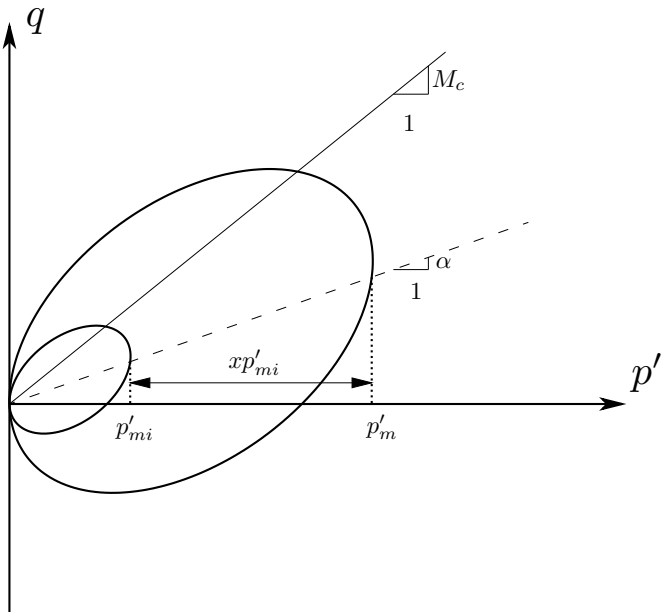

Figure 4.1: *Incorporating bondings in the MCC model. Notice that the rotation of the yield surface is associated to the fabric (anisotropy) and the expanded yield surface is caused by bondings.*

Introducing bondings in the MCC model yields a modification regarding the first hardening law. The isotropic hardening rule may be rewritten into intrinsic properties by:

$$dp'_{mi} = \frac{vp'_{mi}}{\lambda_i - \kappa} d\varepsilon_p^p \tag{4.14}$$

Notice that only λ is substituted to λ_i since the structure does not influence the reloading.

4.3.1 The Third Hardening Law

The third hardening law describes the degradation of bondings in the clay due to plastic straining. It is convenient to ignore the elastic strains since plastic strains are dominating in normal and slightly overconsolidated clay[11]. An expression related to the degradation of structure has been suggested by M. Koskinen, M. Karstunen (2002):

$$\frac{dx}{d\lambda} = -ax\Big[|d\varepsilon_p^p| + b|d\varepsilon_q^p|\Big] \tag{4.15}$$

where a controls the absolute rate of destructuration and b controls the relative effectiveness of plastic volumetric and deviatoric strains in destroying the bonding. Eq. (4.15) was original proposed by Gens and Nova (1993) in a modified format including the loss of attraction or tensile strength. However, since natural soft clay is not capable to withstand tension strength the simpler version given by Eq. (4.15) has been implemented. This hardening rule is commonly used in many advanced soil models which simulate the destructuration phenomenon: n-SAC (Grimstad and Degago, 2010) and S-CLAY1S (Karstunen et al., 2005). However, some slightly modifications may be seen in some of the other models through the location of the destructuration constants. Other methods to simulate the destructuration has been proposed by Liu and Carter (2002) in The Structured Cam Clay model. The utilized method (Eq. (4.15)) has been chosen due to its simplicity and its existence in the newest proposed models.

[11] In OC soil the stress path in the elastic region may be dominant and even if the contribution is small.

4.4 How to Model Creep

As mentioned in Section 3.7.1, creep is associated to deformation over time. Hence, a elasto-plastic model do not incorporate any times aspects and a visco-plastic model must be assembled. However, the SCA-R model would be assembled in a way where the time effects may be neglected and thereby converge towards an elasto-plastic model.

The traditional way of implementing viscous effects is commonly split into two different approaches depending on the utilized theory. The two methods known as the "rate" or "creep" model:

- **Rate:** Models the viscous behaviour directly and thereby model creep indirectly based on the theory suggested by Perzyna (1963).
- **Creep:** Models creep directly and may be categorized by non-stationary flow surface theory, see e.g. (Liingaard et al., 2004).

The development of visco-plastic strains in the "rate" model is restricted and may be seen as a disadvantage. The "rate" model utilizes over-stress theory which only generate visco-plastic strains for stress conditions above a static yield surface. On the other hand, the "creep" model generates visco-plastic strains on both sides of the yield surface and may be seen as an advantage. The two models have been discussed by Grimstad (2009) where the main conclusion was that the "creep" model is better suited to predict the behaviour of normal consolidated clay.

Several models have implemented viscous effects by utilizing the concept behind "rate" model. For instance: Soft Soil Creep (SSC), S-CLAY1S and ACM[12] suggested by Vermeer and Neher (1999), M. Koskinen, M. Karstunen (2002), and Leoni et al. (2008). These models experiences a numerical problem when approaching the critical state caused by the method to determine the visco-plastic strains in the general stress space:

$$\frac{d\boldsymbol{\varepsilon}^{vp}}{dt} = \frac{d\varepsilon_p^{vp}}{\dfrac{\partial p^{eq}}{\partial p'}} \frac{\partial p^{eq}}{\partial \boldsymbol{\sigma}} \tag{4.16}$$

The term $\dfrac{\partial p^{eq}}{\partial p'} \longrightarrow 0$ for $q/p' \longrightarrow M$. Hence, Eq. (4.16) goes towards infinity. This is solved in a practical way by utilizing a smaller inclination relative to M for obtaining failure (Olsson, 2013). This restricts the "rate" models to simulate visco-plastic strains in the wet region. Grimstad (2009) introduced the time evolution of plastic multiplier which utilizes the theory within the "creep" model. Hence, by utilizing the time evolution of the plastic multiplier one may simulate creep swelling and thereby the model would not be restricted to wet side of the CSL. The difference between the two formulations may be seen on Figure 4.2 where method using the time evolution of the plastic multiplier allows the model to simulate creep strains above the CSL. One drawback of utilizing the visco-plastic multiplier is with respect to the undrained shear strength in OC soil. It may suffer to overpredict the undrained shear strength as for the MCC model (Olsson, 2013). Nevertheless, the advantage of simulating swelling creep and the relative easy implementation are seen as huge advantages. Hence, it has by chosen to simulate viscous effects through the visco-plastic multiplier. The formulation suggested by Grimstad et al. (2010) may be formulated as:

$$\frac{d\lambda}{dt} = \dot{\lambda} = \frac{1}{r_{si}\tau}\left(\frac{p^{eq}}{(1+x)p'_{mi}}\right)^{r_{si}\zeta_i} m_{K_0^{NC}} \qquad \text{where} \qquad m_{K_0^{NC}} = \frac{M_c^2 - \alpha_{K_0^{NC}}}{M_c^2 - \eta_{K_0^{NC}}} \tag{4.17}$$

where $\zeta_i = \frac{\lambda_i - \kappa}{1+e_0}$ represent the internal irrecoverable compressibility, M_c represent the critical state line in compression, p^{eq} is the equivalent stress condition see Eq. (4.19), r_{si} refers to the intrinsic creep parameter associated by no structural effects see Figure 4.9, and τ is the reference time see Figure 4.4. The parameter $m_{K_0^{NC}}$ defines the plastic flow during one-dimension compression where $\alpha_{K_0^{NC}}$ and $\eta_{K_0^{NC}}$ is associated to K_0^{NC}, see Appendix C.8.

[12] The ACM model is a combination of SSC and S-CLAY1S

The time evolution of the plastic multiplier is based on the time resistance concept presented by Janbu (1969). The time resistance concept is based on one-dimensional compression which is extended to the general stress space. Notice that Eq. (4.17) does not depend on the time itself but rather an evolution in pre-consolidation pressure.

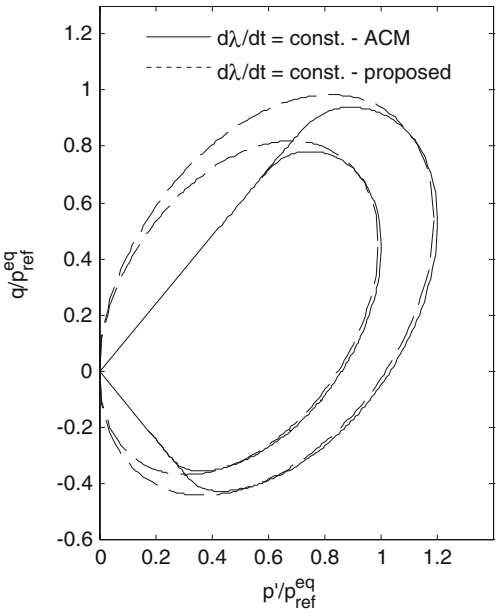

Figure 4.2: *Difference between the "rate" and "Creep" model where the dashed line represent the "Creep-swelling". Taken from (Grimstad et al., 2010).*

Eq. (4.17) may be applied by utilizing the chain rule:

$$\frac{d\boldsymbol{\varepsilon}^{\boldsymbol{vp}}}{dt} = \frac{d\boldsymbol{\varepsilon}^{\boldsymbol{vp}}}{d\lambda}\frac{d\lambda}{dt} \tag{4.18}$$

Introducing the viscous effects it is common to formulated the stress conditions by a reference surface presenting the equivalent stress condition:

$$p^{eq} = p' + \frac{\frac{3}{2}\left\{\boldsymbol{\sigma}_d - p'\boldsymbol{\alpha}_d\right\}^T\left\{\boldsymbol{\sigma}_d - p'\boldsymbol{\alpha}_d\right\}}{\left(M^2 - \frac{3}{2}\boldsymbol{\alpha}_d^T\boldsymbol{\alpha}_d\right)p'} \tag{4.19}$$

Hence, the yield surface and the Over Consolidation Ratio (OCR_τ) may be defined as:

$$F = p^{eq} - \underbrace{(1+x)p'_{mi}}_{p'_m} \qquad , \qquad OCR_\tau = \frac{p'_m}{p^{eq}} \tag{4.20}$$

Notice that OCR_τ is determined as the ratio between the equivalent stress and the stress condition representing the apparent yielding point associated with the chosen reference time (τ), e.g. the OCR_τ is rate dependent. The associated flow rule may be rewritten into visco-plastic strains utilizing the reference surface:

$$d\varepsilon^{vp} = d\lambda\frac{\partial p^{eq}}{\partial \boldsymbol{\sigma}'} \tag{4.21}$$

The reference, intrinsic and its associated surface with respect to the bondings may be visualized in the $(p' : q)$-space and may be seen on Figure 4.3.

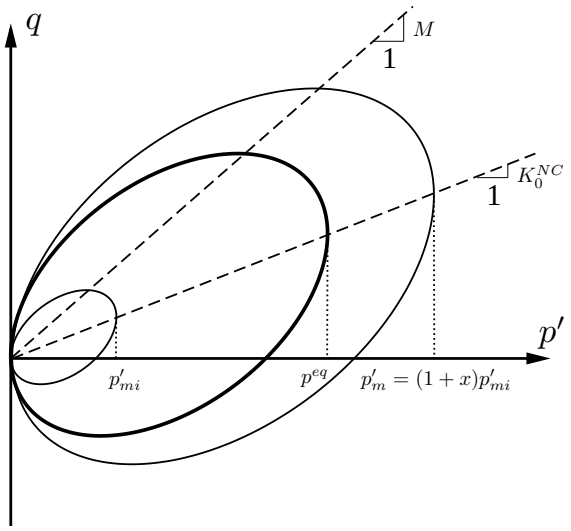

Figure 4.3: *The intrinsic yield surface, its associated surface through the structure and the reference surface representing the stress condition.*

In addition, the three hardening rules should be reformulated with respect to the new reference surface and with respect to the general stress space:

$$\frac{dp'_{mi}}{d\lambda} = \frac{vp'_{mi}}{\lambda_i - \kappa}\frac{\partial p^{eq}}{\partial p'} \tag{4.22a}$$

$$\frac{d\boldsymbol{\alpha_d}}{d\lambda} = \mu\left[\left(\frac{3\boldsymbol{\sigma}_d}{4p'} - \boldsymbol{\alpha_d}\right)\left\langle\frac{\partial p^{eq}}{\partial p'}\right\rangle + \beta\left(\frac{\boldsymbol{\sigma}_d}{3p'} - \boldsymbol{\alpha_d}\right)\sqrt{\frac{2}{3}\left\{\frac{\partial p^{eq}}{\partial \boldsymbol{\sigma}_d}\right\}^T\frac{\partial p^{eq}}{\partial \boldsymbol{\sigma}_d}}\right] \tag{4.22b}$$

$$\frac{dx}{d\lambda} = -ax\left(\left|\frac{\partial p^{eq}}{\partial p'}\right| + b\sqrt{\frac{2}{3}\left\{\frac{\partial p^{eq}}{\partial \boldsymbol{\sigma}_d}\right\}^T\frac{\partial p^{eq}}{\partial \boldsymbol{\sigma}_d}}\right) \tag{4.22c}$$

Extending the model to a viscous-plastic model will modify the method to assemble the incremental change in the visco-plastic multiplier which will be explained in Section 5.3. The concept of isotaches affected by structure may be seen on Figure 4.4.

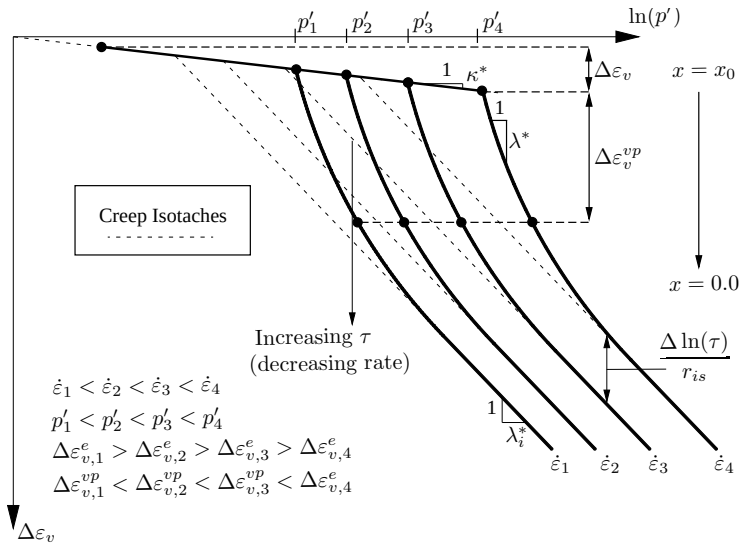

Figure 4.4: *Concept of isotaches effected by structure. Notice difference in notation $\varepsilon_v = \varepsilon_p$.*

4.5 How to Model Recovery

The creation of structure (bondings) is associated to ageing effects and has be discussed in Section 3.8. The destruction of the initial amount of bondings may be simulated through various models through the destructuration phenomenon. However, the regaining of structure over time or creation of structure for a young clay are not covered by any visco-plastic model known by the Author.

The initial structure found in natural soft clays is developed over its geologic life time and may have been influenced by physical and chemical factors. However, tri-axial testing on reconstituted clay have shown a comparable increase in undrained shear strength due to ageing effects of few days before shearing the sample[13] (Sorensen, 2006). It should be mentioned that the deviatoric stress has been normalized with respect to the changed void ratio to remove the effect of creep. Hence, an attempt to capture the ageing effects through a recovering of the structure over time has been made.

Due to simplicity reasons, it has been chosen only to simulate the recovery of destroyed structure and not the development of structure in young clays[14]. It is expected that various factors such as: plastic index, overburden stress, temperature, chemical composition etc. would influence the recovery process. However, for the sake of simplicity a simple procedure has been chosen which requires two additional input parameters. The recovery is implemented as a differential equation utilizing the same principle as the anisotropic evolution suggested by Dafalias (1986). The idea is, after the destruction process the recovery initiates as an exponential function towards a boundary value. The boundary value is controlled by the initial amount of structure and a new input parameter determining how much recovery is allowed with respect to the initial amount. Such a formulation may be formulated as:

$$\frac{dx}{dt} = (Rx_0 - x)R_t \cdot \langle Rx_0 - x \rangle \tag{4.23}$$

where R represent the amount of recovery allowed[15] and R_t is associated to the pace of recovery. To ensure that the recovery does not initiate before the amount of structure is below the boundary value ($x_0 \cdot R$) the macauley brackets are used. The recovery process may influence the creep rate caused by the increase in x which yields a lower creep rate, see Eq. (4.17). This effect has been verified, see Section 6.3.10 and introduces an extra tool to control the creep rates.

4.6 General Stress Space

As mentioned in Section 2.9, the MCC model was original formulated to conventional tri-axial testing. Thereby, the intermediate principle stress (σ_2) is either equal to the minor (σ_3) or major (σ_1) principle stress dependent on the type of test. The extension to a general stress space is done by introducing some assumptions according to the shape of the yield and plastic potential surface with respect to the deviatoric plane:

- Replacing the deviatoric stress (q) by the second deviatoric invariant (J_2) in the yield surface.
- Introducing another failure criterion which is more appropriate to represent soil failure.

Notice that the replacement of q means that the yield surface corresponds to a circle in the deviatoric plane, hence the failure surface. According to the poor representation of the soil failure by J_2 it may be changed to another failure criterion which is more appropriate. It have been proven experimentally that both the yield surface and the critical state is a function of the Lode angle (Coombs et al., 2009). The definition on the Lode angle, it was assembled through a combination of the second deviatoric stress invariant (J_2) and the third stress variant (I_3) to determine the principle stresses, see Appendix C.1.6 for further details. The Mohr-Coulomb failure criteria is a function of the Lode angle which may be seen on Figure 4.5.

[13] After the consolidation process.
[14] Generation of x may be simulated through a manual value implemented in initializing of the state parameters.
[15] From 0.00 to 1.00.

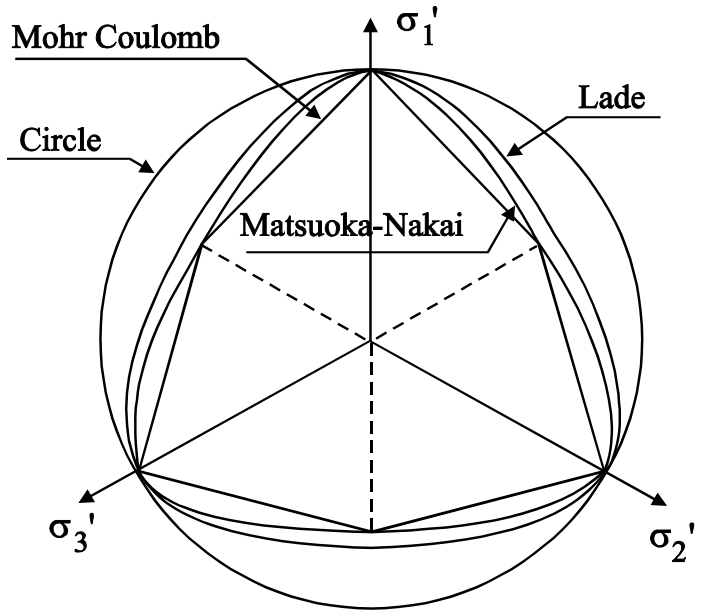

Figure 4.5: *Failure surface in the deviatoric plane. Taken from (Potts and Zdravkovic, 1999).*

It has been chosen to implement the Mohr-Coulomb criteria as the default option in the SCA-R model. The Mohr Coulomb failure criteria represent a hexagon in the deviatoric stress space and is given by (Grimstad, 2009):

$$M(\theta) = \frac{3\sin\varphi_{cs}}{\sqrt{3}\cos\theta - \sin\theta\sin\varphi_{cs}} \tag{4.24}$$

where φ_{cs} is the friction angle at the critical state and the Lode angle (θ) is given by:

$$\theta = \frac{1}{3}\cos^{-1}\left(\frac{3}{2}\frac{\sqrt{3}J_3}{\sqrt{J_2^3}}\right) = \frac{1}{3}\cos^{-1}\left(\frac{27}{2}\frac{J_3}{q^3}\right) \tag{4.25}$$

where J_3 is the third deviatoric stress invariant and see Appendix C.1.6 for derivation of Eq. (4.25). It should be mentioned that the critical state condition occurs with a constant φ_{cs} (Potts and Zdravkovic, 1999). In a simple tri-axial test the inclination of the critical state can be determined by:

$$M_c = \frac{6\sin\varphi_{cs}}{3 - \sin\varphi_{cs}} \tag{4.26a}$$

$$M_e = \frac{6\sin\varphi_{cs}}{3 + \sin\varphi_{cs}} \tag{4.26b}$$

Note that c denotes compression and e denotes extension.

4.6.1 LMN Dependence

In addition to the Mohr-Coulomb failure criteria another criteria has been implemented in the SCA-R known as the LMN dependence. The LMN dependence has been proposed by Bardet (1990) and is based on the failure surfaces suggested by Lade and Duncan (1975) and Matsuoka and Nakai (1974), see Figure 4.5. The formulation is given by:

$$f(\theta) = \frac{\sqrt{3}}{2}\frac{\beta}{\sqrt{\beta^2 - \beta + 1}}\frac{1}{\cos(\Phi)} \qquad \text{where} \qquad \beta = \frac{3 - \sin(\varphi_{cs})}{3 + \sin(\varphi_{cs})} = \frac{M_e}{M_c} \tag{4.27}$$

where

$$\Phi = \begin{cases} \frac{1}{6}\cos^{-1}\left(-1 + \frac{27}{2}\frac{\beta^2(1-\beta)^2}{(\beta^2-\beta+1)^3}\sin^2(3\theta)\right) & \text{if } \theta \leq 0 \\ \frac{\pi}{3} - \frac{1}{6}\cos^{-1}\left(-1 + \frac{27}{2}\frac{\beta^2(1-\beta)^2}{(\beta^2-\beta+1)^3}\sin^2(3\theta)\right) & \text{if } \theta > 0 \end{cases} \tag{4.28}$$

In contrast to the Mohr-Coulomb criteria, this formulation yields a smooth surface. The formulation is rather complex since it must satisfied the convexity requirement for all friction angles. In contrast to the LMN dependency the Mohr-Coulomb criteria gains a more conservative failure stress and a softer stress-strain response (Bardet, 1990). A three dimensional view of the Mohr-Coulomb criteria and the LMN dependency may be seen on Figure 4.6 and Figure 4.7, respectively.

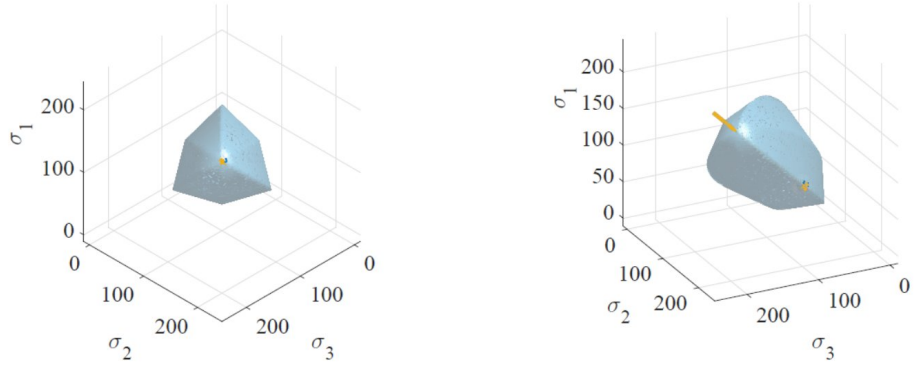

Figure 4.6: *Mohr-Coulomb criteria in the general stress space.*

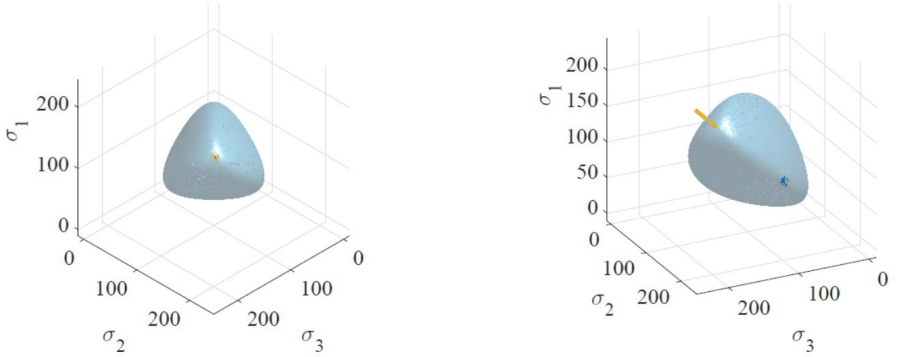

Figure 4.7: *LMN dependency in the general stress space.*

4.6.2 Effect of Fabric in the Lode angle Dependency

The fabric yields a rotation of the yield surface. Hence, the Lode angle must be defined relative to the α-line and not the isotropic axis. This correction may be introduced by following expression:

$$\boldsymbol{\sigma}_d^{\alpha} = \boldsymbol{\sigma}_d - \boldsymbol{\alpha}_d p' \tag{4.29}$$

where $\boldsymbol{\alpha}_d$ is the deviatoric fabric tensor. Introducing the deviatoric stress with respect to the fabric, the deviatoric stress invariants will be associated to the fabric as well. Thereby, the Lode angle may be determined by:

$$\theta_\alpha = \frac{1}{3}\cos^{-1}\left(\frac{3}{2}\frac{\sqrt{3}J_3^{\alpha}}{(J_2^{\alpha})^{3/2}}\right) = \frac{1}{3}\cos^{-1}\left(\frac{27}{2}\frac{J_3^{\alpha}}{(q^{\alpha})^3}\right) \tag{4.30}$$

where α refers to the fabric.

4.7 Initializing

The initial anisotropy (α_0) along with the rotation parameters (β, z, s, x) associated to the evolution may be determined through a theoretical approach. Utilizing a theoretical determination the amount of input parameters will be reduced.

4.7.1 Initial Anisotropy

Dafalias (1986) suggested a method to determine a theoretical link between the lateral earth pressure ratio in the NC-region (K_0^{NC}) and the initial rotation of the yield surface (α_0). The method is based on one-dimensional compression where the ratio between deviatoric and volumetric strains is equal to 2/3. Throughout the literature, it has been common either to neglect the elastic deviatoric strain or all elastic strains. These methods are acceptable since the plastic strains are dominant during this scenario. However, Dafalias and Herrmann (1986) suggested an expression which incorporates the elastic strains and has been implemented in the SCA-R model. The initial rotation may be determined as:

$$\alpha_{K_0^{NC}} = \frac{\eta_{K_0^{NC}}^2 + 2c\alpha_{K_0^{NC}} - M^2}{2c} \tag{4.31}$$

where:

$$c = \frac{3\left(1 - \frac{\kappa}{\lambda_i}\right)\varepsilon}{3 - \varepsilon\left(\frac{K}{G}\right)\left(\frac{\kappa}{\lambda_i}\right)\eta_{K_0^{NC}}} \quad , \quad \frac{K}{G} = \frac{2(1+\nu_{ur})}{3(1-2\nu_{ur})} \quad , \quad \underbrace{\varepsilon = \frac{3}{2}}_{\text{Oedometer conditions}} \tag{4.32}$$

where subscript *ur* refers to un-reloading. The stress ratio during one-dimensional conditions may be determined as:

$$\eta_{K_0^{NC}} = \frac{3(1 - K_0^{NC})}{1 + 2K_0^{NC}} \tag{4.33}$$

In Appendix C.8 the derivation of Eq. (4.33) along with the derivation of the expressions neglecting either elastic deviatoric strain or all elastic strains may be found. These expressions may be compared with respect to input parameters (K_0^{NC}) and the resulting initial inclination of the yield surface, see Table 4.1.

Table 4.1: *Value of K_0^{NC} to find zero initial rotation for different methods.*

Scenario	Eq.	$K_0^{NC} = 0.7481$	$K_0^{NC} = 0.7083$	$K_0^{NC} = 0.7154$
Neglecting all elastic strains	(C.77)	0	-0.076	-0.063
Neglecting deviatoric elastic strains	(C.82)	0.073	0	0.014
Neglecting none	(4.31)	0.059	-0.014	0

Utilizing $\lambda_i = 0.25$, $\kappa = 0.05$, $\nu_{ur} = 0.15$, and M=1.0.

From Table 4.1 it may be concluded that the initial inclination is slightly influenced by the elastic strain and therefore acknowledge the decision to implement Eq. (4.31). A normal Norwegian clay may have a K_0^{NC} in the range of 0.55-0.65 (Berre and Bjerrum, 1973) yielding a rotation of 0.516-0.142 with respect to Eq. (4.31).

The deviatoric fabric tensor may be initialized by assuming one-dimensional compression conditions. Hence, the deviatoric fabric tensor should obtain a different magnitude in vertical direction relative to the horizontal directions. A common approach to initialize the deviatoric fabric tensor may be formulated as:

$$\boldsymbol{\alpha}_d^{K_0^{NC}} = \alpha_{K_0^{NC}} \begin{bmatrix} \frac{-1}{3} & \frac{2}{3} & \frac{-1}{3} & 0.0 & 0.0 & 0.0 \end{bmatrix}^T \tag{4.34}$$

To satisfied the definition of a deviatoric tensor the sum of the tensor's components should be zero which is fulfilled by Eq. (4.34). A coupling between the deviatoric fabric tensor and the scalar magnitude which describes the rotation in the $(p' : q)$-space may be formulated as:

$$\alpha^2 = \frac{3}{2}\boldsymbol{\alpha}_d^T \boldsymbol{\alpha}_d \tag{4.35}$$

4.7.2 Rotational Parameter β

Wheeler et al. (2003) suggested to determine the shear rotation parameter (β) by setting the evolution of rotation to zero ($d\alpha = 0$), see Eq. (4.4). Thereby, in combination with the flow rule related to the plastic potential, the initial inclination, and the demand of zero rate for α, an expression for β may be found:

$$\beta = \frac{3(3\eta_{K_0^{NC}} - 4\alpha_{K_0^{NC}})(M^2 - \eta_{K_0^{NC}}^2)}{8(3\alpha_{K_0^{NC}} - \eta_{K_0^{NC}})(\eta_{K_0^{NC}} - \alpha_{K_0^{NC}})} \approx \frac{3(4M^2 - 4\eta_{K_0^{NC}} - 3\eta_{K_0^{NC}}^2)}{8(\eta_{K_0^{NC}} - M^2 + 2\eta_{K_0^{NC}})} \tag{4.36}$$

It should be mentioned that β is determined by utilizing the initial inclination neglecting the elastic deviatoric strains. The approximation made in Eq. (4.36) neglects all elastic strain by assuming $\kappa \approx 0$. The left hand side of Eq. (4.36) has been implemented in the SCA-R model.

The rotational parameter β may obtain unrealistic values for some input parameters. Hence, the evolution law suggested by Wheeler et al. (2003) must be investigated for its limitations. Figure 4.8 shows how β behave for different values of the friction angle (φ) and the lateral earth coefficient in NC region.

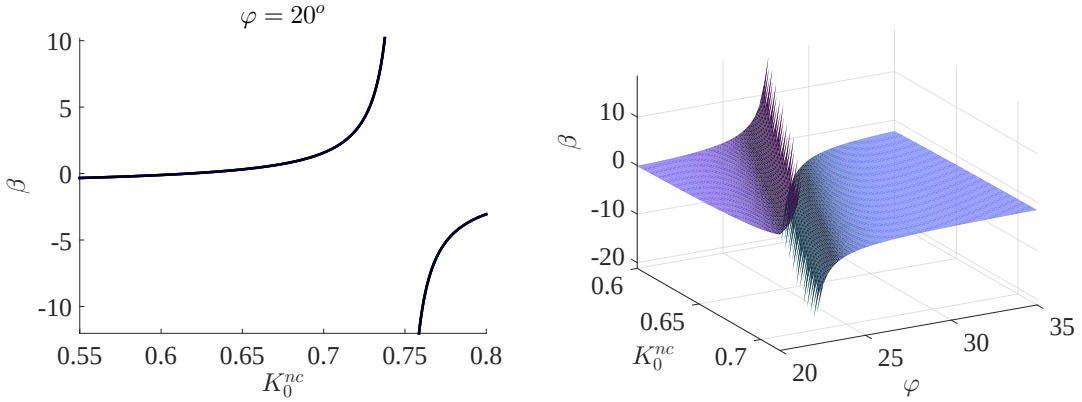

(a) β as a function of K_0^{NC} where $\varphi = 20^o$.

(b) β as a function of K_0^{NC} and frictional angle φ.

Figure 4.8: *Value of β using $\nu_{ur} = 0.20$, λ_i=0.25, and κ=0.05.*

From Figure 4.8(a) it may be concluded that β do not predict any unrealistic values since the maximum value of K_0^{NC} is 0.7154, see Table 4.1. However, changing the input parameters, the value of β may go towards a singular point, see Figure 4.8(b). During the verification of the model, a scenario is assembled where the model yields unrealistic values, see Section 6.3.2.

4.7.3 Rotational Parameter μ

The rotation parameter controlling the absolute rate of the rotation is rather complex compared to the other rotation parameters. A simple approach is suggested by Zentar et al. (2002) where the parameter is associated to the compression index (λ). Thereby, typical values of μ is found in the range of: $\mu = \frac{10}{\lambda_i}$ to $\frac{15}{\lambda_i}$. This method is based on simulations and experience where calibration is needed to ensure the correct value of μ.

Leoni et al. (2008) suggested a more theoretical approach by assuming that the anisotropy is practically erased when α decreases to $1/10^{\text{th}}$ of its initial value ($\frac{\alpha_0}{\alpha} = 10$). Leoni et al. (2008) presented the following formulation:

$$\mu = \frac{1 + e_0}{\lambda_i} \ln \left(\frac{10M^2 - 2\beta\alpha_{K_0^{NC}}}{M^2 - 2\beta\alpha_{K_0^{NC}}} \right) \tag{4.37}$$

However, the most correct method to select μ would be to generate model simulations of laboratory tests which involve a large amount of rotation (Pestana, 1999). Laboratory tests involving a large amount of rotation may be isotropic consolidation or undrained tri-axial extension tests. The determination of the rotation parameter (μ) has not been implemented in the code but the method suggested by Pestana (1999) has been utilized.

Dafalias (1986) suggested to determine the rotation parameter x^α by utilizing one-dimensional compression and the demand of zero rate of α. Thereby, the boundary inclination (α_b) should be equal to the initial inclination during one-dimensional compression. Thereby, following formulation may be assembled:

$$\alpha_b = \frac{\eta}{x^\alpha} \qquad \longrightarrow \qquad \alpha_{K_0^{NC}} = \frac{\eta_{K_0^{NC}}}{x^\alpha} \qquad \longrightarrow \qquad x^\alpha = \frac{\eta_{K_0^{NC}}}{\alpha_{K_0^{NC}}} \tag{4.38}$$

Substituting back into the general expression the boundary value of α may be defined as:

$$\alpha_b = \eta \frac{\alpha_{K_0^{NC}}}{\eta_{K_0^{NC}}} \tag{4.39}$$

4.7.4 Rotational Parameter s and z

Dafalias and Taiebat (2013) suggested to utilize the same procedure, as for the case when determining the parameter x^α, to determine s and z. Thereby, through the one-dimensional compression following expression may be assembled:

$$\alpha = \alpha_b = \alpha_{K_0^{NC}} = \pm \frac{M}{z} \left[1 - \exp \left(-s \frac{|\eta_{K_0^{NC}}|}{M} \right) \right] \tag{4.40}$$

Dafalias and Taiebat (2013) stated that one must have $s \leq z$ to satisfied Eq. (4.40) and suggested that a very good default assumption may be $z = s$. Hence, this assumption has been utilized and the parameters s and z may be determined explicitly from the initial conditions.

4.7.5 Destructuration Parameters a and b

The destructuration parameters (a, b) may be chosen through an optimisation procedure. A recommended procedure has been given by M. Koskinen, M. Karstunen (2002):

- **Selecting a value for** a: Simulations of tri-axial tests with a very low value of η.
  - Utilizing a very low value of η, the shear strains would be limited and their effect can be ignored. Hence, the parameter b was negligible.
- **Selecting a value for** b: Simulations of tri-axial tests with a high value of η
  - Utilizing a very high value of η, the volumetric strains would be limited and their effect can be ignored. Hence, the parameter a was negligible.

Through this optimisation procedure the destructuration parameters (a, b) may be selected.

4.7.6 Amount of Structure x_0

M. Koskinen, M. Karstunen (2002) recommended two approaches to determine the initial amount of bounding (x_0). The simplest and most practical approach to determine x_0 is done through the sensitivity of the soil:

$$x_0 = S_t - 1 \qquad \text{where} \qquad S_t = \frac{s_u}{s_r} \tag{4.41}$$

where s_u refers to the fully mobilised undrained shear strength and s_r represent the remoulded undrained shear strength. Hence, the initial amount of bounding x may easily be determined by standard shear vane testing. However, it should be mentioned that this approach should be referred to as a lower bound value (M. Koskinen, M. Karstunen, 2002). Regarding destruction of initial bonding when installing and testing to determine the sensitivity of the natural soft clay. The second method is based on measuring the initial void ratio (e_0) and the corresponding in situ effective mean pressure (p'_0) for the natural soft clay together with the position of the ICL. Another approach to define the initial amount of structure is presented by Grimstad and Degago (2010) through the intrinsic creep number:

$$x_0 = \frac{r_{is} - r_{is,min}}{r_{is,min}} \tag{4.42}$$

where r_{is} is the intrinsic creep number and $r_{is,min}$ is the minimum measure creep number determined by a incremental oedemeter test, see Figure 4.9.

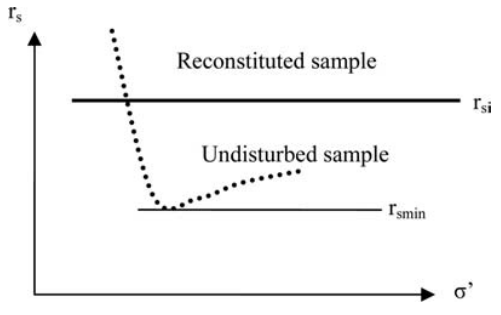

Figure 4.9: *Concept of destructuration with respect to the creep number. Taken from (Grimstad and Degago, 2010).*

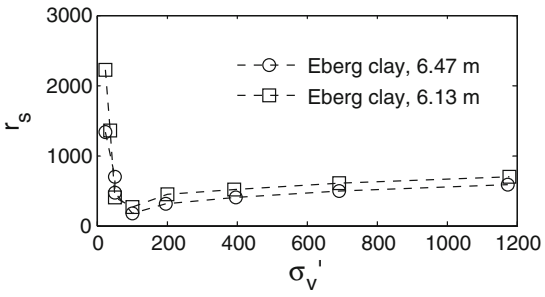

Figure 4.10: *Incremental oedometer test for Eberg clay verifying Figure 4.9. Taken from (Grimstad et al., 2010).*

The method proposed by Grimstad and Degago (2010) has been implemented in the SCA-R model. To incorporate creep the intrinsic creep number is needed. This parameter may also be determined in an incremental oedomenter. Thereby, r_{is} and $r_{is,min}$ may be determined in the same test reducing the amount of necessary laboratory testing to determine the input parameters.

4.7.7 Intrinsic Effective Pressure p'_{mi}

The intrinsic effective pressure is initialized from the amount of structure, the equivalent stress condition and the magnitude of OCR_τ:

$$p'_{mi} = \frac{p^{eq} OCR_\tau}{1 + x} \tag{4.43}$$

where OCR_τ is determined as the ratio between the equivalent stress and the stress condition representing the apparent yielding point associated with the chosen reference time (τ). For a normal consolidated sample, without any influence from bondings and strain rates effects, the intrinsic effective pressure would be equal to the equivalent stress condition:

$$p'_{mi} = p^{eq} \qquad \text{since} \qquad OCR_\tau = 1.0 \quad , \quad x = 0.0 \tag{4.44}$$

Recalling the equivalent stress condition, the fabric and critical state frictional angle will influence the intrinsic effective pressure:

$$p^{eq} = p' + \frac{\frac{3}{2}\left\{\boldsymbol{\sigma}_d - p'\boldsymbol{\alpha}_d\right\}^T \left\{\boldsymbol{\sigma}_d - p'\boldsymbol{\alpha}_d\right\}}{\left(M^2 - \frac{3}{2}\boldsymbol{\alpha}_d^T \boldsymbol{\alpha}_d\right) p'} \tag{4.45}$$

The principle when initializing the intrinsic pressure may be seen on Figure 4.11.

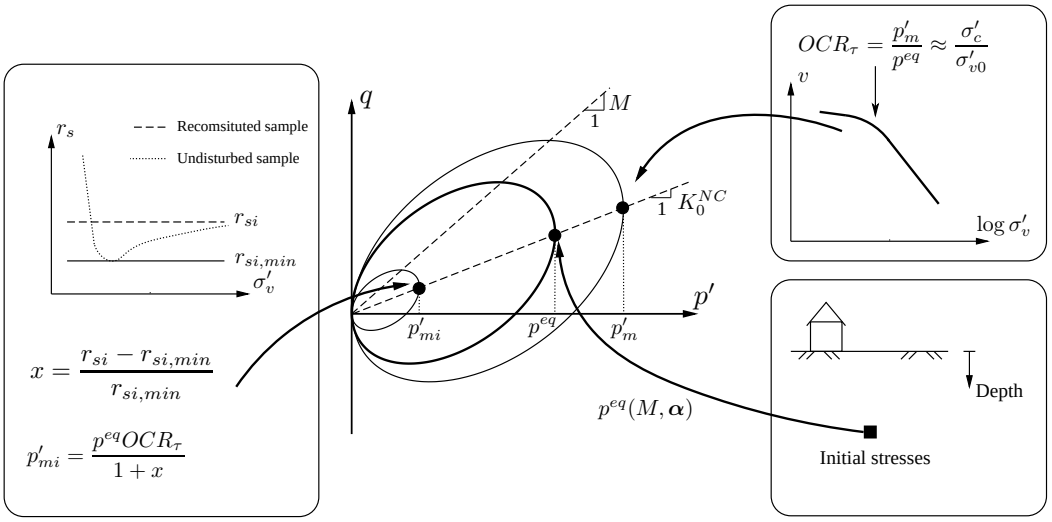

Figure 4.11: *Concept of initializing the SCA-R model. Notice that p^{eq} is a function of M,$\boldsymbol{\alpha}$ and the initial stresses.*

The concept of initializing the SCA-R model may be seen on Figure 4.11. As seen on Figure 4.11, the magnitude of OCR_τ is associated to chosen rate of strain and may be approximated to be the same as the standard definition of OCR if the strain rate effect is negligible. The initial stresses and the parameters, M and $\boldsymbol{\alpha}$, define the equivalent stress condition (p^{eq}). The intrinsic effective pressure may be determined through this information and the amount of structure.

Chapter 5

Implementation

The purpose of this chapter is to provide general information regarding the implementation of the constitutive model into commercial software. A detailed description of the procedure and alternative solution methods will be discussed. The implementation is performed by creating routines in FORTRAN supported by MATLAB coding. The general procedure is developed by Roenningen et al. (2014) related to his work with GeoFuture. The implementation is done with great assistance and effort from Roenningen (2015).

5.1 General

The main aim is to create a constitutive model which may be implemented into commercial software and take part in the Finite Element Method (FEM). Hence, the effort may be placed in the constitutive model itself instead of writing a new program which utilizes the FEM. The commercial software has been chosen to be PLAXIS caused by its long time experience with FEM with respect to geotechnical engineering. In addition, PLAXIS allows the user to implement their own constitutive models through a Digital Link Library (DLL). Explanations and examples of implementing a User Defined Soil Model (UDSM) may be found in (PLAXIS, 2015). The code may be written in different programming languages only restricted by the capability of the compiler to generate a DLL-file which establish the interface between the code and PLAXIS. PLAXIS recommends FORTRAN as the preferable programming language and libraries containing different subroutines and functions, which may be beneficial during the coding, is offered by PLAXIS (2015). Other possible programming languages could be: C, C^{++}, COMSOL ect. It has been chosen to use FORTRAN as programming language and further recommendations for utilizing FORTRAN as programming language may be found in (Grimstad and Benz, 2014).

The constitutive model estimate the soil response (stress-strain-time relationship) in a single stress point, i.e. the constitutive model returns a stress increment due to an applied strain and time increment. Hence, the constitutive model provides information regarding the current stresses and state variables and PLAXIS provides information about the previous stresses and state parameters along with the strain and time increment:

- $\sigma_{ij}^{t+\Delta t}$, $\kappa^{t+\Delta t}$ Current stresses and state variables (Constitutive model)
- σ_{ij}^{t}, κ^{t} Previous stresses and state variables (PLAXIS)
- $\Delta\varepsilon_{ij}$, Δt Strain and time increments (PLAXIS)

where the superscript $(t + \Delta t)$ refers to the current stage and (t) refers to the previous stage in PLAXIS notation. This procedure is known as the local iterative procedure. The computed stresses, in each stress point, are afterwards incorporated in the global iterative process and is governed by the FEM implementation in PLAXIS.

In order to understand the general structure of the constitutive model it would be beneficial to understand how a constitutive model is incorporated in the finite element code and how the constitutive model works together with the FEM.

5.2 PLAXIS

The concept of FEM is a numerical approach by which partial differential equations may be solved approximately (Fish and Belytschko, 2006). Thereby, complex systems may be analysed by discretizing the infinite global system into finite element representations. The principle of FEM may be seen on Figure 5.1. Notice that the the constitutive model contributes as the stress-strain relationship where time may influence the relationship.

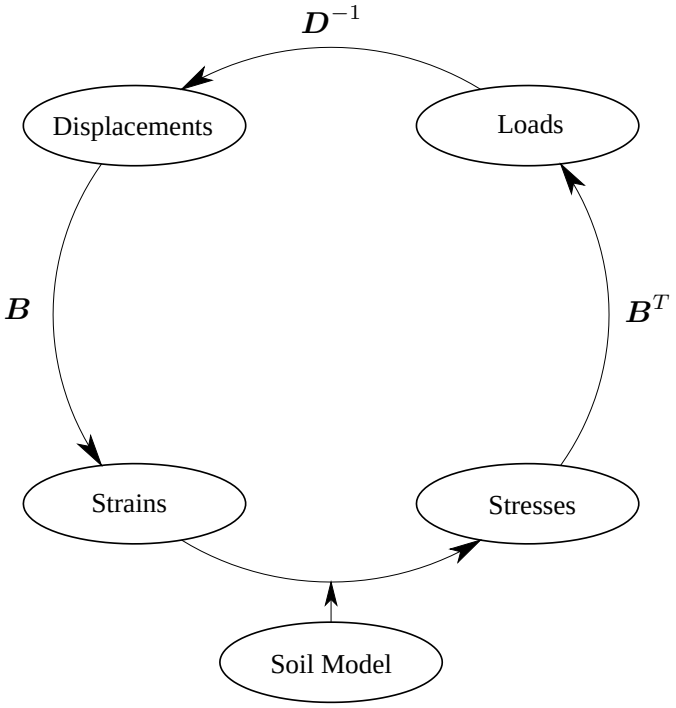

Figure 5.1: *The global iterative procedure in a FE analysis.*

where $\boldsymbol{D}$ is the stiffness matrix and $\boldsymbol{B}$ is the strain interpolation matrix. The general procedure and related equations will be highlighted in the following subsection.

5.2.1 Field Equations

Considering an arbitrary soil body as seen on Figure 5.2 where u_i refers to the displacement field, γ_i represent the three body forces, and τ_i denotes the boundary traction components. V and S refer to the volume and external surface boundary, respectively. The internal static equilibrium of this continuum, the relation between the stresses to their spatial derivatives, is given as:

$$\frac{\partial \sigma_{ij}}{\partial x_j} + \gamma_i = 0 \tag{5.1}$$

where x_j are the Cartesian coordinates and σ_{ij} denotes the Cauchy stress tensor. Notice, Einstein notation is used in consistency with the notation in the Scientific Manual given by PLAXIS (2014b).

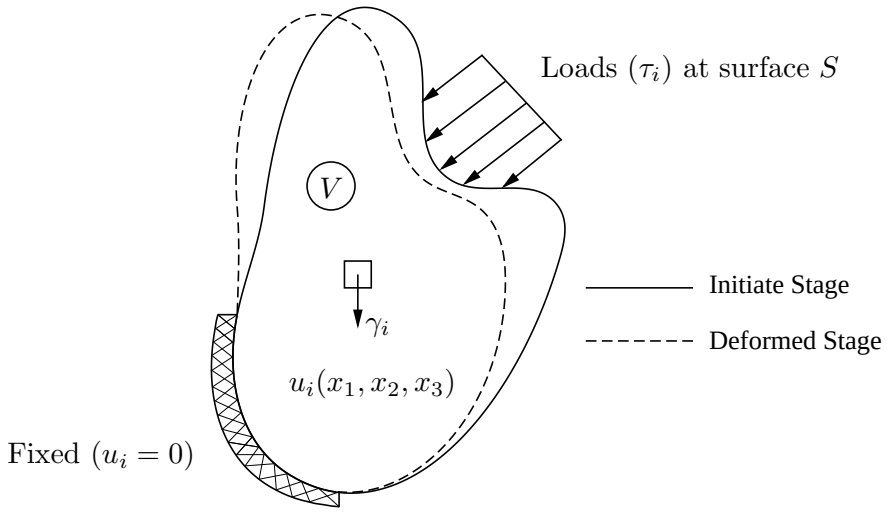

Figure 5.2: *An arbitrary body affected by a load.*

For the same body, the static equilibrium for the external boundary S is given as:

$$\tau_i = \sigma_{ij} n_j \tag{5.2}$$

where n_j represent the directions of the stresses. The equilibrium equation may be reformulated into a formulation representing the weak form by utilizing the Galerkin's variational principle followed by integration by parts (Grimstad and Benz, 2014):

$$\int_V \sigma_{ij} \frac{\partial \delta u_i}{\partial x_j} dV = \int_V \gamma_i \delta u_i dV + \int_S \tau_i \delta u_i dS \tag{5.3}$$

where δu_i represents a virtual displacement. The evolution of stresses in the body may be regarded as an incremental process ($\Delta\sigma_{ij}$) and the stress at an actual state (σ_{ij}^{n+1}) may be considered as the previous plus the incremental change:

$$\sigma_{ij}^{n+1} = \sigma_{ij}^{n} + \Delta\sigma_{ij} \qquad \text{where} \qquad \Delta\sigma_{ij} = \int \dot{\boldsymbol{\sigma}} dt \tag{5.4}$$

where σ_{ij}^{n} represent the previous state of stress. Notice that n is an integer corresponding to the load step. The mentioned procedure is known as **time stepping**. However, most quasi static problems are time independent in which case full load application is often associated with a pseudo time of 1 (Grimstad and Benz, 2014). The approach to determine $\Delta\sigma_{ij}$ in PLAXIS is done by implicit integration, see PLAXIS (2014b). Substituting Eq. (5.4) into Eq. (5.3) yields:

$$\int_V \Delta\sigma_{ij} \frac{\partial \delta u_i}{\partial x_j} dV = \int_V \gamma_i \delta u_i dV + \int_S \tau_i \delta u_i dS - \int_V \sigma_{ij}^{n} \frac{\partial \delta u_i}{\partial x_j} dV \tag{5.5}$$

According to the principle in FEM, the continuum may be divided into a number of elements where each element consists of a number of nodes. This process is called discretisation and each node has a number of degrees of freedom representing the discrete values of the unknown variables in the boundary value problem (PLAXIS, 2014b). With respect to deformation theory, the displacement field ($\boldsymbol{u}$) is determined by these discrete nodal values though interpolation functions which may be assembled in a matrix $\boldsymbol{N}$. The change in the displacement field may be formulated as:

$$\Delta\boldsymbol{u} = \boldsymbol{N}(\xi, \eta, \zeta)\Delta\boldsymbol{v} \tag{5.6}$$

where $\Delta\boldsymbol{v}$ is the nodal displacement and the matrix $\boldsymbol{N}$ consist of shape functions depending on ξ, ζ and η which are the local element coordinates. The shape functions are used to interpolate

between the nodal values and the interior of an element. A relation between the strains and nodal values may be found by substituting Eq. (5.6) into the kinematic relation:

$$\Delta\boldsymbol{\varepsilon} = \boldsymbol{L}\Delta\boldsymbol{u} = \boldsymbol{L}\boldsymbol{N}\Delta\boldsymbol{v} = \boldsymbol{B}\Delta\boldsymbol{v} \qquad \text{where} \qquad \boldsymbol{L} = \begin{bmatrix} \frac{\partial}{\partial x} & 0 & 0 & \frac{\partial}{\partial y} & 0 & \frac{\partial}{\partial z} \\ 0 & \frac{\partial}{\partial y} & 0 & \frac{\partial}{\partial x} & \frac{\partial}{\partial z} & 0 \\ 0 & 0 & \frac{\partial}{\partial z} & 0 & \frac{\partial}{\partial y} & \frac{\partial}{\partial x} \end{bmatrix} \tag{5.7}$$

where $\boldsymbol{B}$ denotes the strain interpolation matrix. Hence, the equilibrium may be reformulated into discretised form as:

$$\int_V (\boldsymbol{B}\delta\boldsymbol{v})^T \Delta\boldsymbol{\sigma} dV = \int_V (\boldsymbol{N}\delta\boldsymbol{v})^T \boldsymbol{\gamma} dV + \int_S (\boldsymbol{N}\delta\boldsymbol{v})^T \boldsymbol{\tau} - \int_V (\boldsymbol{B}\delta\boldsymbol{v})^T \boldsymbol{\sigma}^n dV \tag{5.8}$$

Eq. (5.8) is true for any virtual displacement and may thereby be simplified to:

$$\int_V \boldsymbol{B}^T \Delta\boldsymbol{\sigma} dV = \int_V \boldsymbol{N}^T \boldsymbol{\gamma} dV + \int_S \boldsymbol{N}^T \boldsymbol{\tau} - \int_V \boldsymbol{B}^T \boldsymbol{\sigma}^n dV \tag{5.9}$$

During a load application, the stress increment $\Delta\boldsymbol{\sigma}$ balances the difference between external load and internal forces within the finite element mesh. Hence, a strain increment has to be determined such that the above equation is satisfied, i.e. the global iterative procedure supplies strain and time increments for each stress point. The spatial coordinates of the stress point are defined by the mesh's geometry wherein the number of elements and the chosen element type yields the total number of stress point. The relationship between the stresses and strains may not be linear and requires a global iterative process to satisfy the equilibrium condition for all material points.

5.2.2 Global Iterative Procedure

Utilizing the relation between increment stress and strain ($\Delta\boldsymbol{\sigma} = \boldsymbol{D}\boldsymbol{\varepsilon}$), Eq. (5.9) may be formulated in terms of the response from an external force:

$$\boldsymbol{K}^i \Delta\boldsymbol{v}^i = \boldsymbol{f}_{ex}^i - \boldsymbol{f}_{in}^{i-1} \tag{5.10}$$

where $\boldsymbol{K}$ represents the global stiffness matrix, $\Delta\boldsymbol{v}$ is the incremental displacements, $\boldsymbol{f}_{ex}$ the external force and $\boldsymbol{f}_{in}$ the internal reaction vector. Furthermore, superscript i refers to the step number. In the case of non-linear relation between stresses and strains it must be treated as an iterative procedure to obtain equilibrium:

$$\boldsymbol{K}^j \delta\boldsymbol{v}^j = \boldsymbol{f}_{ex}^i - \boldsymbol{f}_{in}^{i-1} \qquad \text{where} \qquad \Delta\boldsymbol{v}^i = \sum_{j=1}^{n} \delta\boldsymbol{v}^j \tag{5.11}$$

where $\delta\boldsymbol{v}$ is a vector assembled by the sub-incremental displacements and n is the number of iterations within the step i. Notice, the stiffness matrix $\boldsymbol{K}$ is often referred to as the tangential stiffness matrix in non-linear scenarios and may be assembled by the constitutive matrix as:

$$\boldsymbol{K} = \int \boldsymbol{B}^T \boldsymbol{D} \boldsymbol{B} dV \tag{5.12}$$

Recall that $\boldsymbol{D}$ is a function of stresses and state parameters.

5.2.3 Local Iterative Procedure

The global iteration needs to incorporate the stresses in all the stress points. Therefore, in each global iteration, the stresses in at each stress point must be determined by another iteration procedure known as local integration. Hence, in a FEM two types of iterations are required:

- **Global integration** - Estimation of the displacement
- **Local integration** - Estimation of stresses and state parameters

The local integration may be solved through varies incremental updating schemes which may be divided into two general categories:

- **The explicit scheme** - Direct method
- **The implicit scheme** - Indirect method

The best approach to solve the differential equations depends on the numerical analysis. One could argue, that the explicit method is generally more stable since it always yields an answer, normally requires less computation power and is relatively simple to implement compared to the implicit method. However, this procedure may not involve any error evaluation[1] and utilizes the previous stresses and state parameters to determine the current stresses and state parameters. Hence, the explicit procedure may lead to inaccurate results associated to the step size. On the other hand, the answer given by an implicit scheme will be restricted by a chosen tolerance insuring an accuracy chosen by the user. This tolerance may be very computation demanding and the implicit scheme do not insure convergence.

Explicit Integration

The explicit integration schemes represent a direct integration procedure, where a finite strain increment ($\Delta\varepsilon$) is given as a constant value. The explicit approach utilizes a linear stress-strain-time relationship yielding an error caused by the non-linearity. However, by utilizing a small incremental step the error may be minimized to an acceptable limit. The simplest explicit method is known as the forward Euler scheme, where the stress increment is evaluated by the finite strain and time increment:

$$\Delta\boldsymbol{\sigma}_{n+1} = \boldsymbol{D}(\sigma_n, \kappa_n)\Delta\boldsymbol{\varepsilon}_{n+1} \tag{5.13}$$

where $\boldsymbol{D}(\sigma_n, \kappa_n)$ is the tangential stiffness determined by the previous iteration and n refers to the previous stage and $n+1$ refers to the current stage[2]. The accuracy of the explicit integration scheme may be increased by switching to a more advanced explicit method such as a higher order Runge-Kutta, e.g. second order (Midpoint Method) or the classic fourth order, see (Grimstad and Benz, 2014) or (Grimstad, 2009) for further details. The suggested constitutive model would simply implement the forward Euler scheme to solve the local integration.

Implicit Integration

The performance of the local integration should be analysed against other solution methods to compare its accuracy and computational demand. To deviate from the explicit integration methods it has been chosen to utilize an implicit integration scheme. Roenningen (2015) has granted access to his work related to implicit integration which utilized a modified Newton-Raphson's method to solve the differential equations. Hence, a new DLL-file may be assembled through some modifications in the MATLAB code and by utilizing the Newton-Raphson method given by Roenningen (2015). A short description of the approach will be highlighted here and further details regarding the implicit integration may be found in (Roenningen et al., 2014).

[1] In this case, control of the consistency criterion.
[2] Notice notation difference with PLAXIS: $n+1 = t + \Delta t$ and $n = t$

The implicit integration method requires the collection of the differential equations in a numerical residual which may be formulated as:

$$\boldsymbol{r} = \begin{bmatrix} \boldsymbol{r}_1 & \boldsymbol{r}_2 & r_3 \end{bmatrix}^T = 0 \tag{5.14}$$

where the physical meaning of these differential equations describes the general constitutive response whereby the update of stresses, state parameters and visco-plastic multiplier are determined through Eq (5.14). The differential equations may be formulated as:

$$\boldsymbol{r}_1 = \boldsymbol{\sigma}'_{n+1} - \sigma'_n - \boldsymbol{D}\left((\boldsymbol{\varepsilon}_{n+1} - \boldsymbol{\varepsilon}_n) - (\lambda_{n+1} - \lambda_n)\left\{\frac{\partial Q}{\partial \boldsymbol{\sigma}}\right\}_{n+1}\right) \tag{5.15a}$$

$$\boldsymbol{r}_2 = \boldsymbol{\kappa}_{n+1} - \boldsymbol{\kappa}_n - \left\{\frac{d\boldsymbol{\kappa}}{d\lambda}\right\}_{n+1} \cdot (\lambda_{n+1} - \lambda_n) \tag{5.15b}$$

$$r_3 = \lambda_{n+1} - \lambda_n - \left\{\frac{d\lambda}{dt}\right\}_{n+1} \cdot (t_{n+1} - t_n) \tag{5.15c}$$

The vector ($\boldsymbol{\kappa}$) contains the eight state variables:

$$\boldsymbol{\kappa} = \begin{bmatrix} p'_{mi} & \boldsymbol{\alpha_d} & x \end{bmatrix}^T \qquad \text{and} \qquad \frac{\boldsymbol{\kappa}}{d\lambda} = \begin{bmatrix} \frac{dp'_{mi}}{d\lambda} & \frac{d\boldsymbol{\alpha_d}}{d\lambda} & \frac{dx}{d\lambda} \end{bmatrix}^T \tag{5.16}$$

Newton-Raphson's Method

The Newton-Raphson's method is an iterative approach to solve non-linear equations. The solution for a system of equations $\Big(\boldsymbol{r}(\boldsymbol{v}) = 0\Big)$ may be formulated as:

$$\boldsymbol{v}^{i+1} = \boldsymbol{v}^i - \left(\boldsymbol{J}^i\right)^{-1} \cdot \boldsymbol{r}\left(\boldsymbol{v}^i\right) \tag{5.17}$$

where $\boldsymbol{J} = \dfrac{\partial \boldsymbol{r}}{\partial \boldsymbol{v}}$ is the Jacobian matrix and i refers to the number of iterations. The method requires a defined criterion or tolerance to stop the iteration loop. The tolerance used in Roenningen et al. (2014) is given by:

$$\boldsymbol{r}^T\boldsymbol{r} \leq \text{tol} \sim 10^{-12} \tag{5.18}$$

It should be mentioned that the Newton-Raphson's method does not guarantee convergence and a maximum number of iterations should be implemented in the coding. Inverting the Jacobian matrix given in Eq. (5.17) may be a quite computationally demanding task which may be avoided by transforming into a linear system of equations:

$$\left(\frac{\partial \boldsymbol{r}}{\partial \boldsymbol{v}_{n+1}}\bigg|\right) \Delta \boldsymbol{v}^{i+1}_{n+1} = -\boldsymbol{r}^i \tag{5.19}$$

where $\Delta \boldsymbol{v}^{i+1}_{n+1} = \boldsymbol{v}^{i+1}_{n+1} - \boldsymbol{v}^i_{n+1}$. The system of linear equations may be solved using Gauss elimination and adding the increment $\Delta \boldsymbol{v}^{i+1}_{n+1}$ to the previous iteration solution, see (Roenningen et al., 2014) for further details.

The modifications in the MATLAB code[3] are associated with assembling the numerical residual (5.14) and the Jacobian Matrix given in Eq. (5.17), see Appendix E.1.3.

[3] Required by the swap from explicit to implicit.

5.3 Constitutive Model

The constitutive model is implemented into PLAXIS using the software: MATLAB and FORTRAN and the computational framework for the chosen procedure may be seen on Figure 5.3.

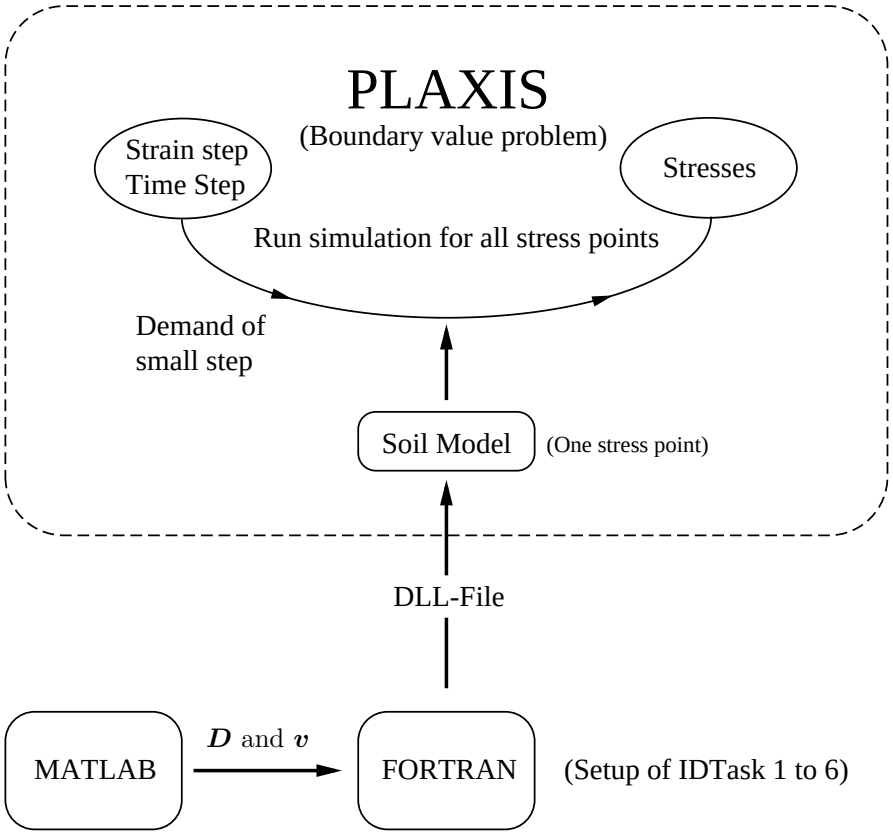

Figure 5.3: *Principle of the computational framework.*

The elastic stiffness matrix ($\boldsymbol{D}$) and the differential equations ($\boldsymbol{v}$) determining the constitutive behaviour of the soil model are assembled in MATLAB using symbolic differentiation. The code is afterwards transformed automatically into FORTRAN code and pasted into the FORTRAN framework. Through the interface between PLAXIS and FORTRAN, the FORTRAN code may be complied into a DLL-file containing the soil model. The initializing of the state parameters are defined in the FORTRAN code. The stresses are determined in the local integration through the strain and time increments restricted by an upper limit of their magnitude, see Eq. (5.27).

The elastic stiffness matrix is assembled as given in Eq. (3.6) and the vector ($\boldsymbol{v}$) contains the six Cartesian stresses, the eight state parameters and the plastic multiplier is assembled as:

$$\boldsymbol{v} = \begin{bmatrix} \sigma_{11} & \sigma_{22} & \sigma_{33} & \sigma_{12} & \sigma_{23} & \sigma_{13} & \lambda & p'_{mi} & \alpha_{d11} & \alpha_{d22} & \alpha_{d33} & \alpha_{d12} & \alpha_{d23} & \alpha_{d13} & x \end{bmatrix}^T \tag{5.20}$$

The MATLAB code for assembling these mathematical formulations may be seen in Appendix E.1.2 utilizing the theory given in Chapter 4. The local integration in the stress points is determined through a forward Euler scheme which may be formulated as:

$$\boldsymbol{v}_{n+1} = \boldsymbol{v}_n + d\boldsymbol{v} \tag{5.21}$$

where $d\boldsymbol{v}$ is the change in Eq. (5.20) and is given by:

$$d\boldsymbol{v} = \begin{bmatrix} \boldsymbol{D}\left(\Delta\boldsymbol{\varepsilon} - \Delta\lambda\dfrac{\partial Q}{\partial\boldsymbol{\sigma}}\right) \\ \Delta\lambda \\ \Delta\lambda\dfrac{\partial\boldsymbol{\kappa}}{\partial\lambda} + \Delta t\dfrac{\partial\boldsymbol{\kappa}}{\partial t} \end{bmatrix} \tag{5.22}$$

where the change in the plastic multiplier may be approximated as:

$$\Delta\lambda \approx \frac{\dot{\lambda} + \left\{\dfrac{\partial\dot{\lambda}}{\partial\boldsymbol{\sigma}}\right\}\boldsymbol{D}d\boldsymbol{\varepsilon}}{\dfrac{1}{\Delta t} - \left\{\dfrac{\partial\dot{\lambda}}{\partial\boldsymbol{\kappa}}\right\}\boldsymbol{h} + \left\{\dfrac{\partial\dot{\lambda}}{\partial\boldsymbol{\sigma}}\right\}\boldsymbol{D}\left\{\dfrac{\partial Q}{\partial\boldsymbol{\sigma}}\right\}} \tag{5.23}$$

where $\boldsymbol{D}$ refers to the elastic stiffness matrix, $\dot{\lambda} = \dfrac{\partial\lambda}{\partial t}$ and $\boldsymbol{h}$ is a vector containing the derivative state parameters with respect to the plastic multiplier:

$$\boldsymbol{h} = \left[\frac{\partial p_{mi}}{\partial\lambda} \quad \frac{\partial\boldsymbol{\alpha}_d}{\partial\lambda} \quad \frac{\partial x}{\partial\lambda} = \frac{\partial\boldsymbol{\kappa}}{\partial\lambda}\right]^T \tag{5.24}$$

Further details regarding Eq. (5.23) may be found in Appendix C.6. Notice that in contrast to an elastic-plastic model, a visco-plastic model does not need to control the yielding function (F) since the intrinsic yielding surface is sensitive to time. Hence, it would expand even if the stress condition lies inside the yield surface. An elastic-plastic model would determine the change in stresses as:

$$d\boldsymbol{\sigma} = \boldsymbol{D}_{ep}d\boldsymbol{\varepsilon} \tag{5.25}$$

where

$$\boldsymbol{D}_{ep} = \boldsymbol{D} - \frac{\boldsymbol{D}\left\{\dfrac{\partial Q}{\partial\boldsymbol{\sigma}}\right\}\left\{\dfrac{\partial F}{\partial\boldsymbol{\sigma}}\right\}^T\boldsymbol{D}}{A + \left\{\dfrac{\partial F}{\partial\boldsymbol{\sigma}}\right\}^T\boldsymbol{D}\left\{\dfrac{\partial Q}{\partial\boldsymbol{\sigma}}\right\}} \tag{5.26}$$

In an explicit integration it must be checked if $\boldsymbol{D}_{ep} = \boldsymbol{D}$ (pure elastic and inside the yield surface) or a contribution from plastic strains caused by the expansion of the yield surface should be taken into consideration during the calculation.

The next section will explain the details related to the FORTRAN framework and its interface to PLAXIS.

5.4 PLAXIS - User Defined Soil Model

In order to create an UDSM in PLAXIS, one may satisfy the requirements related to the calculation approach. The calculation procedure is defined in a subroutine called `User_Mod`, and may be divided into four main operations (PLAXIS, 2014a):

- Initialization of state variables.
- Calculation of constitutive stresses.
- Creation of effective material stiffness matrix.
- Creation of elastic material stiffness matrix.

The subroutine (`User_Mod`) is governed by its 31 input parameters where the UDSM mainly influences the first argument, the `IDTask`-parameter. The `IDTask`-parameter is associated to the above four mentioned main operations. The modified subroutine (`User_Mod`) related to this work may be found in Appendix E.2.1. A more detailed description of the general `User_Mod` subroutine and a definition of all the input parameters may be found in Appendix D.3. During a calculation phase in PLAXIS, the individual `IDTasks` may be called several times for each global iteration. It should be noted that the `IDTasks` are not chronologically called by PLAXIS and one task may be called several times during a computation.

The purpose of `IDTask 1` is related to the initializing of the state parameters: initial stresses (p^{eq}), intrinsic effective pressure (p'_{mi}), initial structure (x_0), anisotropy (α_0) and the parameters associated to the rotational hardening. These parameters are determined by the input parameters and will be stored in the vector `StVar0`. After one calculation the vector will be overwritten by the previous stresses and state parameters. The initializing procedure could be moved to `IDTask 2` but would require more computational power since the state parameters only need to be initialized once. The additional features in `IDTask 1` is related to some simple debugging aspects.

The purpose of `IDTask 2` is associated to the constitutive modelling and thereby the explicit integration. Hence, the maximum time and strain increment are chosen by a reference parameter (n) insuring a maximum time and strain increment. The time and strain increment are associated to the time reference (τ) and a chosen reference strain (x), respectively:

$$\begin{aligned} n_\varepsilon &= \texttt{nint}\left(\frac{d\varepsilon_{max}}{x}\right) & & & d\varepsilon &= \frac{d\varepsilon}{n} \\ & & \longrightarrow \quad n = \max(n_\varepsilon, n_t) \quad \longrightarrow & & & \\ n_t &= \texttt{nint}\left(\frac{dt_{max}}{\tau}\right) & & & dt &= \frac{dt}{n} \end{aligned} \tag{5.27}$$

where $x = 10^{-4}$[4] and τ is an input parameter in SCA-R model. The function `nint` is a FORTRAN command finding the closest whole number. The parameters $d\varepsilon_{max}$ and dt_{max} are the increments given by PLAXIS. The additional features in `IDTask 2` are related to some simple debugging aspects and the updating scheme of the new stresses and state parameters into the vector `StVar`. Furthermore, if the argument `IsUndr`=1 yields undrained conditions[5] and the change in excess pore pressure is determined through:

$$\underbrace{\Delta p_w}_{\texttt{Swp-Swp0}} = \underbrace{K_w \Delta \varepsilon_p}_{\texttt{BulkW*(dEps(1) + dEps(2) + dEps(3))}} \tag{5.28}$$

where K_w is the bulk modulus of water and the notation below Eq. (5.28) is FORTRAN code.

The purpose of the remaining tasks are less important for the UDSM. The only modifications in these tasks are related to `IDTask 5` where the stiffness matrix must be changed to be stress and time dependent. This is done by changing `NonSym` and `iTimeDep` from zero to one. The subroutines governing the `IDTasks` related to this work may be found in Appendix E.2.2.

5.4.1 Modular Programming

The general framework in FORTRAN may be seen on Figure 5.4. The framework consists of: `Modules, subroutines` and `functions`. Theses elements have different abilities and are utilized to obtain a modular structure of the code. The advantage of utilizing a modular structure is a relatively simple and straightforward main code which may be easier for others to read. Each task is written in subroutines and called upon when they are needed.

[4] This value has shown accurate results without any extreme computational demands.
[5] Drained conditions is equal to zero.

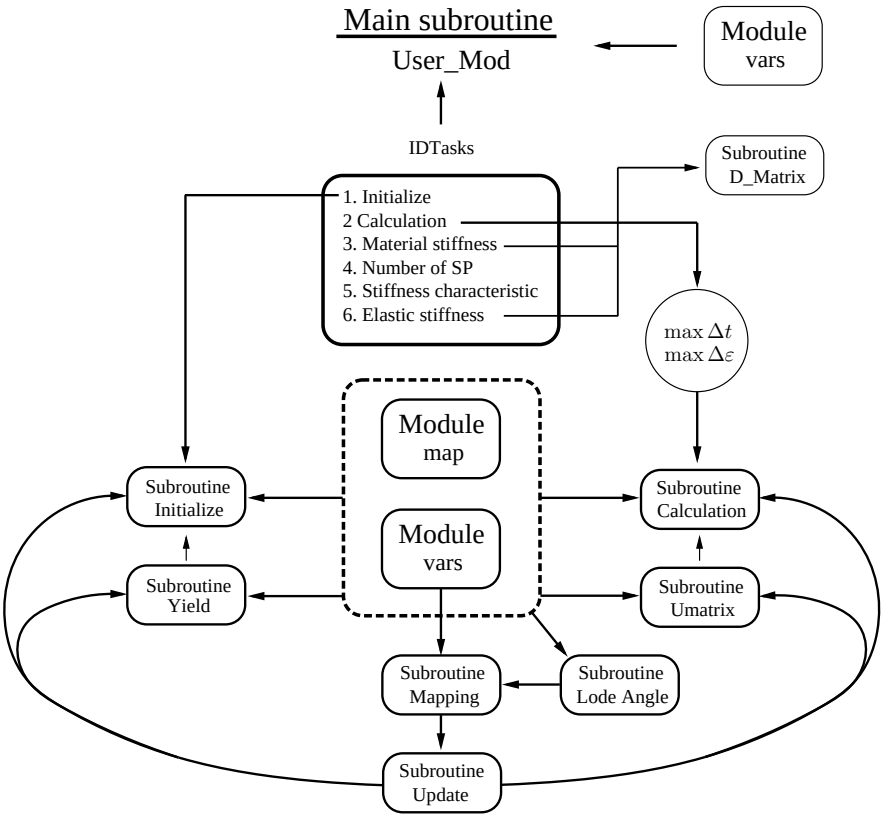

Figure 5.4: *General framework in FORTRAN. Notice that some less necessary subroutines and all the functions are left out for simplicity.*

Modules:
The framework contains two modules: Module-vars and Module-map. The Module-vars contains all the global variables presented in the main code. Hence, the subroutines which activate/call this module gain access to all the global variables. The Module-vars contains five functions which mainly are associated to the location of the input parameters, the Cartesian stresses and the state parameters along with their units. The Module-map contains the subroutines: update, mapping and Lode angle. Hence, calling the Module-map activates all these subroutines. In this module, the majority of the local variables are defined. The module also contains three other subroutines related to rotational hardening suggested by Dafalias and Taiebat (2013).

Subroutines:
Each subroutine contains a part of the total calculation process. Hence, by dividing the code into subroutines a more efficient program may be written since the subroutines only are called when they are needed. The subroutines either define the local variables they need or call the global variables through the modules.

Functions:
Functions are very small pieces of calculation which are used both in the subroutines and in the modules. Functions normally use few local variables which are defined in the function itself. The function requires a number of input parameters in order to compute the output. An example of a function may be the `Heaviside`-function yielding either: 1, $\frac{1}{2}$ or 0 depending on the input. Notice, the functions are left out from Figure 5.4 for simplicity.

The location of the DLL-file in the installation folder, issues related to the calculation kernel and choosing the DLL-file in PLAXIS are described in Appendix D.3.1.

Chapter 6

Verification of the Model

The purpose of this chapter is to provide general information regarding the verification of the SCA-R model. The verification process is necessary to guarantee high reliability and ensure that the soil model behaves according to the implemented theory. In addition, the verification process reduces the number of bugs and possible mistakes related to the coding procedure.

6.1 General

The verification process is divided into three parts. The first part will verify the basic input parameters by creating scenarios whereby the basic input parameters may be interpreted from the different graphs. The purpose of the second part is to investigate the extended features related to the mechanical response of natural soft clay to ensure that these features behave as expected. However, some of the advanced input parameters cannot be interpreted directly. Hence, different scenarios where the influence of these parameters may be observed are assembled to investigate their effect. The third part contributes with additional verification related to the MCC response.

The general verification process is mainly associated to one-dimensional compression and triaxial testing. The theoretical response during one-dimensional compression may be seen on Figure 6.1. Point A illustrates the sample before testing which has been unloaded from the in situ stresses. Point B illustrates the apparent yielding point where the stiffness response from the material changes from elastic to plastic, point C describes the new yielding surface before unloading the sample to point D. Point D represents the stress condition associated to the unloading loop. It should be noted that the effective stress path in the $(p' : q)$-space follows the K_0^{NC}-line after the apparent yielding.

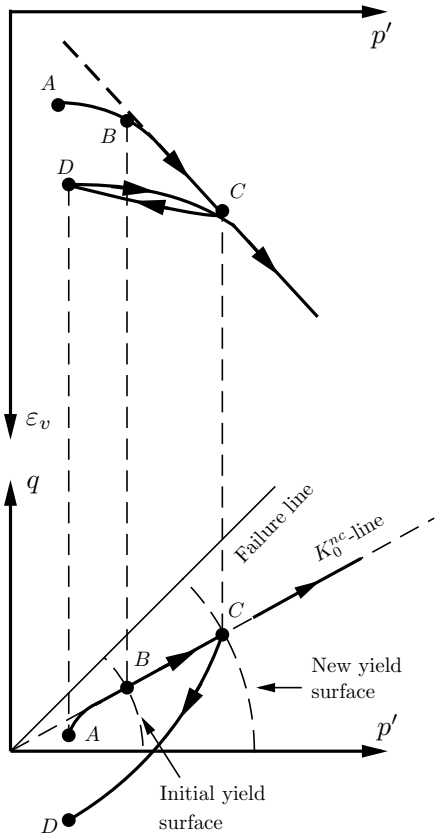

Figure 6.1: *Theoretical oedometer path. See explanation of point A, B, C and D in the paragraph to the left.*

Throughout the whole verification process, standard input parameters have been utilized to simulate all the scenarios. However, in some of the scenarios, deviations from the standard parameters are necessary. These deviations will be highlighted for the particular scenario. The verification procedure is preformed by Soil Test in PLAXIS utilizing the general option where simulations of either a one-dimensional compression or tri-axial test are preformed. Figure 6.2 shows the layout for the one-dimensional compression scenario where the standard input parameters and loading conditions are shown.

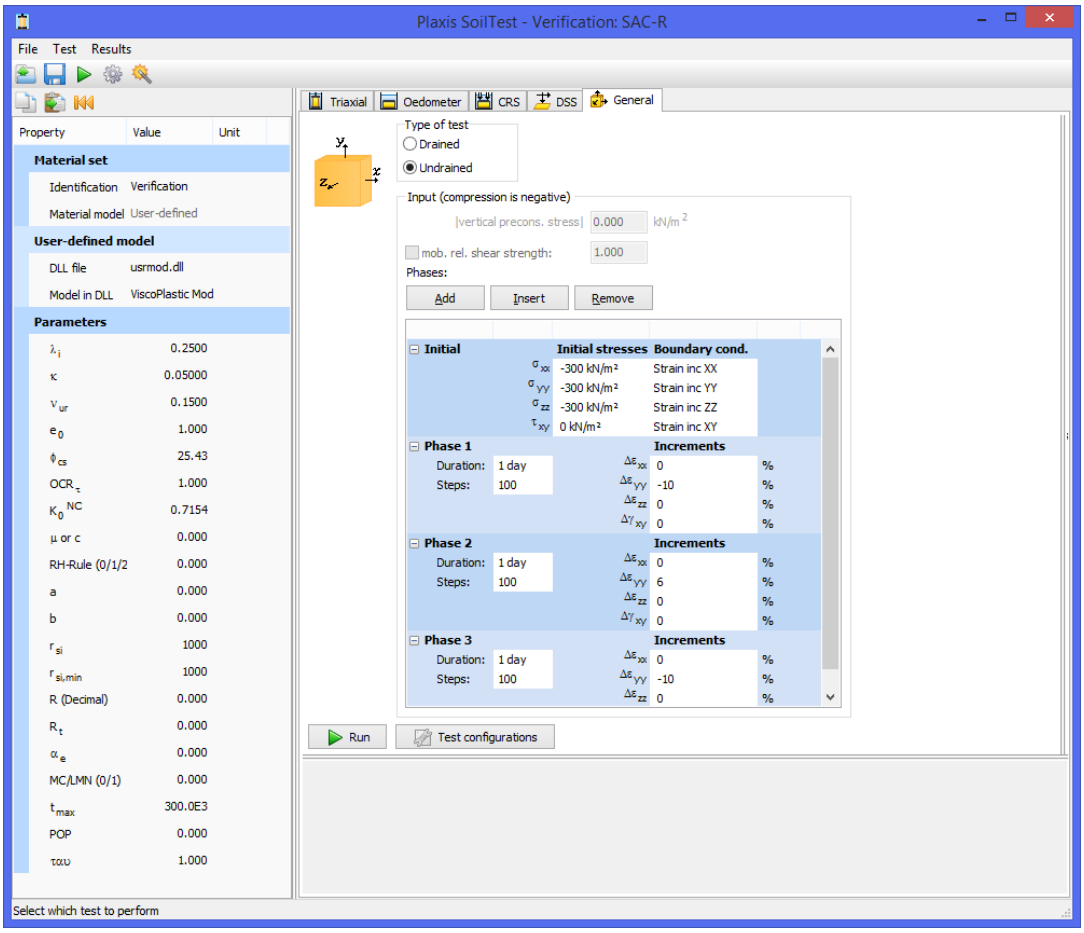

Figure 6.2: *General option in Soil Test showing the standard input parameters.*

The undrained tri-axial scenarios are performed by keeping the volume constant in each phase to avoid the default assumption of $\nu_u = 0.495$ related to the bulk modulus of the water[1].

6.2 Basic Input Parameters

The basic input parameters are related to the MCC model where five parameters are needed along with a stress history. An overview of how to interpret the parameters may be seen in Table 6.1.

Table 6.1: *Basic input parameters and methods associated to interpretation.*

Input Parameter	Scenario	Evaluated from:
λ_i, κ, and e_0	One-dimensional compression	Compression plane ($p' : \varepsilon_p$)
ν_{ur}	One-dimensional compression	Stress plane ($p' : q$) (Elastic region)
φ_{cs}, and OCR_τ	Tri-axial compression	Stress plane ($p' : q$)

The following three sections will shortly describe how these parameters are interpreted and verified.

[1] Drained tri-axial simulations are preformed by the tri-axial option available in Soil Test.

6.2.1 Inclinations of the NCL and URL

The input parameters, λ_i, κ, and e_0 may be verified through the inclination of the NCL and the URL in the compression plane with respect to a one-dimensional compression test. The one-dimensional compression scenario is simulated by utilizing the standard input parameters and the loading conditions given by Figure 6.2. The obtained NCL and URL in the compression plane may be seen on Figure 6.3.

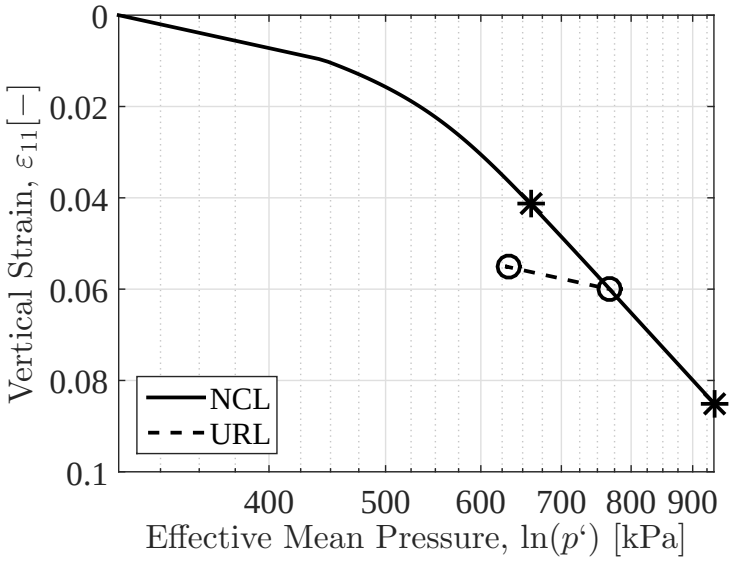

Figure 6.3: *Interpretation of the inclination of the NCL and URL to verify λ_i, κ, and e_0 from the compression plane. The standard input parameters may be seen on Figure 6.2.*

Recalling the theory given in Section 2.6.1, λ_i may be verified by the NCL and κ by the URL. Notice that the inclinations are influenced by the initial void ratio (e_0). Thereby, the observed inclinations should be reformulated as:

$$\kappa = (1 + e_0)\kappa^* \qquad \text{and} \qquad \lambda_i = (1 + e_0)\lambda_i^* \tag{6.1}$$

Using the interpreted inclinations, Eq. (6.1) and the void ratio ($e_0 = 1.0$) yields following values:

$$\kappa = (1 + 1.0) \cdot \frac{0.060 - 0.051}{\ln(752) - \ln(632)} = 0.25$$

$$\lambda = (1 + 1.0) \cdot \frac{0.085 - 0.041}{\ln(937) - \ln(660)} = 0.05$$

The interpreted values are similar to those which have been utilized in the simulation, see Figure 6.2. Hence, it may be concluded that the compression and swelling parameters may be interpreted correctly from the SCA-R model and the influence of void ratio seems correct.

6.2.2 Inclination of the Critical State Line

The Critical State Line (CSL) is a function of the critical state friction angle (φ_{cs}). Hence, the input parameter (φ_{cs}) may be verified by performing several simulations approaching the critical state. The CSL should be drawn through the end points of these simulations in the ($p' : q$)-space and thereby verify the utilized friction angle. Utilizing the standard input parameters given by Figure 6.2, several tri-axial simulations in compression have been preformed for drained and undrained

scenarios. The simulations differ from each other from each other by isotropic/anisotropic consolidation[2] along with different magnitudes of OCR_τ. Thereby, the influence of the input parameter, OCR_τ may be verified as well. Seven simulations have been performed and may be seen on Figure 6.4.

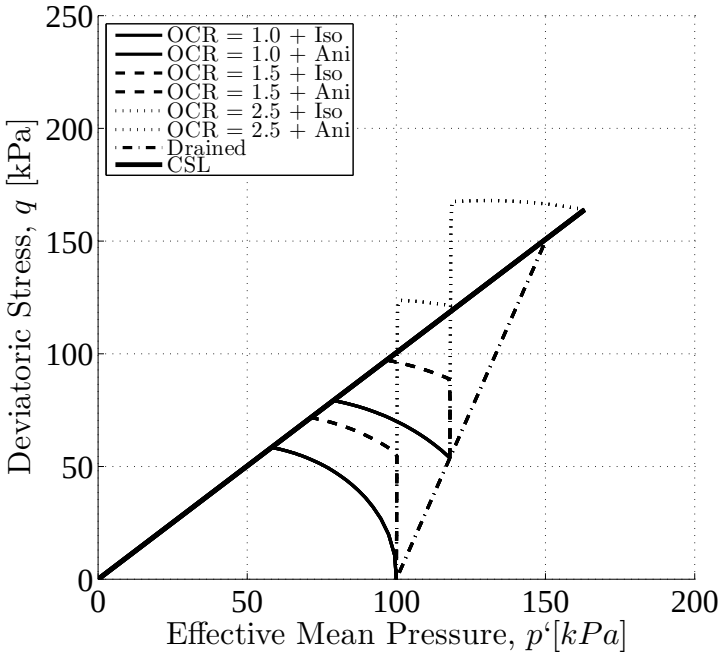

Figure 6.4: *Interpretation of the inclination of the CSL to verify φ_{cs} for tri-axial simulations in compression. The standard input parameters may be seen on Figure 6.2. Notice that $\varphi_{cs} = 25.38 \longrightarrow M = 1.0$.*

It may be observed that a straight line starting from Origo and going through all the end points of the effective stress paths may be drawn representing the CSL. The inclination of the CSL has a value of $M = 1.0$ which corresponds to the utilized critical state friction angle (φ_{cs}).

Analysing the effective stress path for the drained scenario, the well known 1:3 inclination is obtained. The undrained effective stress path for the NC and slightly NC simulations indicate the expected response towards the CSL in the wet region. The OC simulations indicate the correct pattern by going straight up into the dry region and afterwards dilate towards the CSL. Lastly, the effect of anisotropic consolidation seems to be correct but will be verified further in Section 6.4.1.

Hence, it may be concluded that the critical state friction angle may be interpreted correctly from the SCA-R model and the effect of OCR_τ and anisotropic consolidation yield the expected response.

6.2.3 Unloading Reloading

In an unloading/reloading loop the soil response is implemented to be elastic. Hence, the input parameter ν_{ur} may be verified by interpreting the inclination of the unloading/reloading[3] part of the effective stress path in the $(p' : q)$-space. The verification of ν_{ur} is performed by simulating a one-dimensional compression scenario utilizing the standard input parameters and loading conditions given by Figure 6.2. The effective stress path in the $(p' : q)$-space may be seen on Figure 6.5(b). Notice that the parameter, q, in Figure 6.5(b) deviates from the normal definition of q by being the vertical effective stress minus the horizontal effective stress which allows negative values. This is done to get a better illustrative picture of the effective stress path.

[2] In the case of anisotropic consolidation a value of $K_0' = 0.65$ is utilized.
[3] Before yielding to ensure elastic response.

Figure 6.5(a) shows the theoretical expected response during one-dimensional compression which may be used to compare the response from the SCA-R model. Point A indicates the in situ stresses, B defines the apparent yielding point and C is the K_0^{NC}-line. It may be observed that the theoretical and predicted responses are similar.

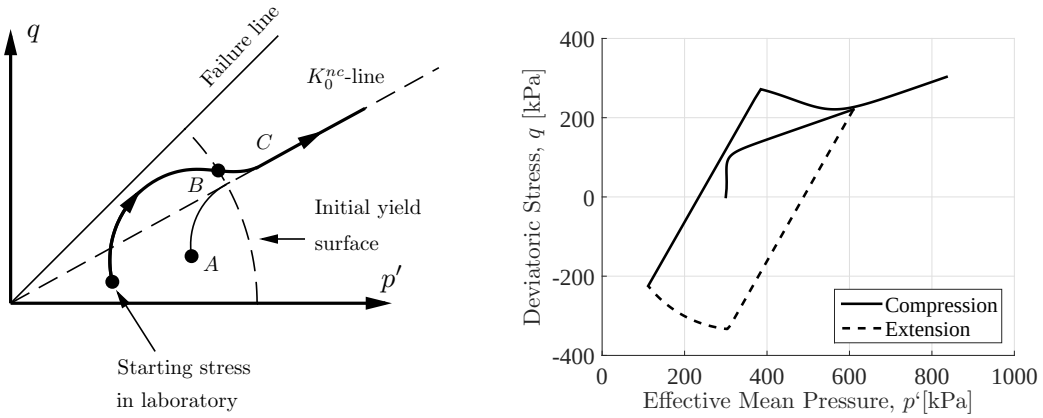

(a) Theoretical.

(b) SCA-R model.

Figure 6.5: *ESP in the $(p' : q)$-space to verify the input parameter ν_{ur} during one-dimensional compression. The standard input parameters may be seen on Figure 6.2.*

According to elastic theory, the ratio between the incremental deviatoric stress (q) and the incremental effective mean stress (p') may be determined by:

$$\frac{\Delta p}{\Delta q} = \frac{K'}{3G'} \frac{d\varepsilon_p^e}{d\varepsilon_q^e} \tag{6.3}$$

Simulating a one-dimensional compression scenario, it is known that the ratio between the deviatoric strains and volumetric strains are uniquely defined as:

$$\frac{d\varepsilon_q}{d\varepsilon_p} = \frac{d\varepsilon_q^e}{d\varepsilon_p^e} = \frac{2}{3} \tag{6.4}$$

Notice, that only elastic strains will be present since no plastic strains are created in the elastic region. Using the definition of the shear modulus and substituting Eq. (6.4) into Eq. (6.3) yields:

$$\frac{\Delta q}{\Delta p} = \frac{3(1+\nu_{ur})}{1+\nu_{ur}} \qquad \text{since} \qquad G' = \frac{3K'(1-\nu_{ur})}{2(1+\nu_{ur})} \tag{6.5}$$

The implemented value of Poisson's ratio was 0.15 which yields an inclination of:

$$\nu_{ur} = 0.15 \qquad \longrightarrow \qquad \frac{\Delta q}{\Delta p} = 1.826 \tag{6.6}$$

This is similar to the inclination found in the unloading/reloading part of the ESP, see Figure 6.5(b). Hence, it may be concluded that Poisson's ratio can be interpreted correctly by the model.

The standard input parameters have been verified and the following sections will discuss the input parameters related to the SCA-R model.

6.3 Advanced Features

The advanced features are listed in Table 6.2 with their associated input parameters.

Table 6.2: *Overview of the advanced features and related parameters.*

Feature	Parameter	Remarks
Anisotropy (Elastic)	α_e	Indirectly interpreted
Anisotropy (Plastic)[(1)]	K_0^{NC}	Indirectly interpreted
Evolution of Anisotropy	μ/c and RH	Observed behaviour
Destructuration	a, b and x_0	Observed behaviour
Creep	r_{si} and $r_{si,min}$	Indirectly interpreted[(2)]
Recovering	R and R_t	Observed behaviour

[(1)] Rotation of yield surface. [(2)] $r_{si,min}$ is related to x_0.

In addition to the highlighted aspects in Table 6.2, the coupling effect between recovering of structure and creep rate will be investigated.

6.3.1 Anisotropy in the Elastic Region

The implementation of anisotropic elastic stiffness may be verified through an undrained overconsolidated tri-axial scenario. The tri-axial simulation is simulated by utilizing the standard input parameters given by Figure 6.2 and an $OCR_\tau = 4.0$. The influence of anisotropic elastic stiffness may be seen for different magnitudes of α_e on Figure 6.6.

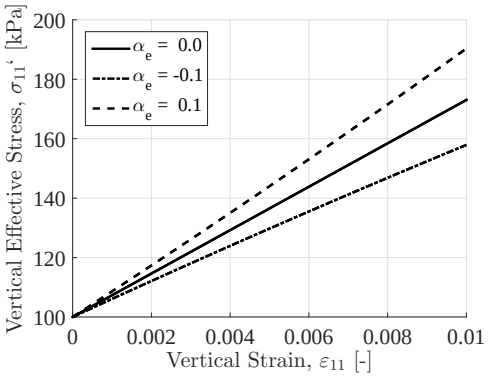

(a) Influence on vertical stress.

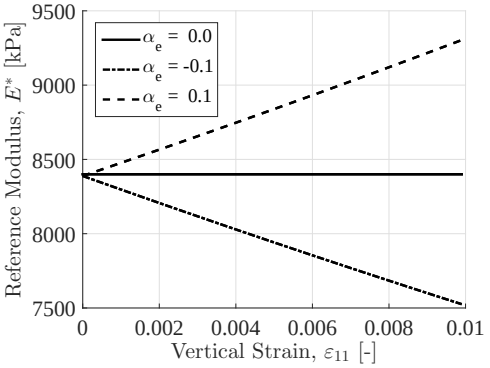

(b) Influence on reference modulus.

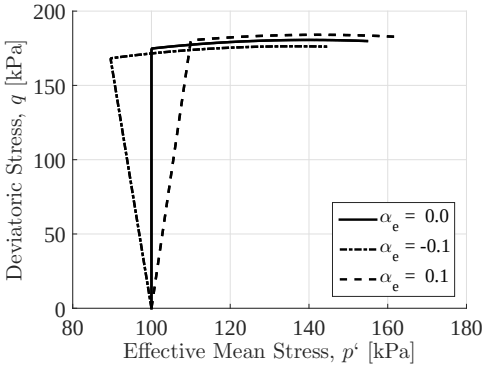

(c) Influence on effective stress path.

Figure 6.6: *Transverse anisotropic elastic response in undrained tri-axial scenario to verify the input parameter α_e. The standard input parameters may be seen on Figure 6.2 and $OCR = 4.0$ has been utilized.*

It may be observed from Figure 6.6(b) and Figure 6.6(c) that for $\alpha_e = 0.0$ yields isotropic stiffness with respect to the horizontal and vertical line, respectively. In addition, Figure 6.6(a) and Figure 6.6(b) show that a negative α_e causes a reduction in stiffness and a positive α_e is associated to an increase in stiffness as a result of changes in effective mean pressure (p'). The ESP seen in Figure 6.6(c) indicates how the effective mean pressure is affected by the anisotropy by an inclined ESP either to the left or right. It should be noted that the magnitude of q associated to the yielding point is affected by the elastic anisotropic caused by the ellipse shape of the yield surface.

The elastic stiffness parameters (α_e) may be interpreted through Figure 6.6(c) by utilizing Janbu's pore pressure parameter (D). The interpreted pore pressure parameters are determined to:

$$D_{0.1} = \frac{\Delta p'}{\Delta q} = \underbrace{\frac{109.11\,\text{kPa} - 100\,\text{kPa}}{164.09\,\text{kPa} - 0\,\text{kPa}}}_{\alpha_e = 0.1} = 0.056 \qquad \text{and} \qquad D_{-0.1} = \frac{\Delta p'}{\Delta q} = \underbrace{\frac{90.114\,\text{kPa} - 100\,\text{kPa}}{159.92\,\text{kPa} - 0\,\text{kPa}}}_{\alpha_e = -0.1} = -0.061$$

Recalling the definition on Janbu's pore pressure parameters it may be calculated as:

$$D = \frac{\alpha_e \left(K_{iso} + \frac{2}{3} G_{iso} \left(1 + \frac{1}{3}\alpha_e \right) \right)}{\alpha_e^2 K_{iso} + 3 G_{iso} \left(1 + \frac{1}{3}\alpha_e \right)^2} = \frac{\alpha_e \left(\frac{1+\nu^*}{1-2\nu^*} + 1 + \frac{1}{3}\alpha_e \right)}{\alpha_e^2 \left(\frac{1+\nu^*}{1-2\nu^*} \right) + \frac{9}{2} \left(1 + \frac{1}{3}\alpha_e \right)^2} \tag{6.7}$$

Utilizing the Poisson ratio ($\nu_{ur} = \nu^* = 0.15$) and the elastic anisotropic parameter (α_e) Janbu's pore pressure parameter may be determined analytical to:

$$D_{0.1} = 0.055 \qquad \text{and} \qquad D_{-0.1} = -0.062 \tag{6.8}$$

These values are similar to the values interpreted from the model. Hence, it may be concluded that the elastic stiffness parameter may be interpreted correctly from the SCA-R model and the change in elastic stiffness associated to the changes in effective mean pressure yields expected responses.

6.3.2 Anisotropy Evolution

The three evolution laws related to the rotational hardening of the yield surface may be relative complex to verify. A complete verification would include a control of the boundary values (the initial starting point and ending point of the rotation), the rotational path and pace of the rotation. These aspects will be controlled for different scenarios such as: critical state, isotropic compression, and one-dimensional compression. However, it has not been possible to interpret the input parameter which controls the pace of the rotation (μ or c) but it is assumed if all the other aspects satisfy the theory the pace, may be seen as reliable. Before the verification, the rotational hardening laws are recalled:

Wheeler 2003
$$\frac{d\alpha}{d\lambda} = \mu \left[\left(\frac{3\eta}{4} - \alpha \right) \langle d\varepsilon_p^p \rangle + \beta \left(\frac{\eta}{3} - \alpha \right) |d\varepsilon_q^p| \right] \tag{6.9a}$$

Dafalias 1986
$$\frac{d\alpha}{d\lambda} = c p_{at} \frac{p'}{p'_c} (\alpha_b - \alpha) \quad , \quad \alpha_b = \frac{\alpha_{K_0^{NC}}}{\eta_{K_0^{NC}}} \eta \tag{6.9b}$$

Dafalias 2013
$$\frac{d\alpha}{d\lambda} = c p_{at} \frac{p'}{p'_c} (\alpha_b - \alpha) \quad , \quad \alpha_b = \pm \frac{M}{z} \left[1 - \exp\left(-s \frac{|\eta|}{M} \right) \right] \tag{6.9c}$$

One-dimensional Compression

In a one-dimensional compression scenario the yield surface should align with the K_0^{NC}-line beyond yielding. Hence, following three requriements must be satisfied:

$$\frac{\sigma_3'}{\sigma_1'} = K_0^{NC} \quad , \quad \frac{q}{p'} = \eta = \eta_{K_0^{NC}} \quad , \quad \alpha = \alpha_{K_0^{NC}} \tag{6.10}$$

The one-dimensional compression scenario is simulated by utilizing the standard input parameters and the loading conditions given by Figure 6.2. Several simulations of each rotation law, for different magnitudes of K_0^{NC}, have been performed and the interpreted values may be seen in Table 6.3. Notice, the interpreted values are determined beyond yielding to ensure that the stress state lie on the yield surface.

Table 6.3: *Extracted values of the rotated yield surface during oedometer conditions.*

		Wheeler 2003				**Dafalias 1986**			**Dafalias 2013**		
Input:	K_0^{NC}	0.55	0.60	0.64	**0.65***	0.55	0.60	0.65	0.55	0.60	0.65
	K_0^{NC}	0.55	0.60	0.65	**0.76**	0.55	0.60	0.65	0.55	0.60	0.65
Output:	$\eta_{K_0^{NC}}$	0.642	0.546	0.474	**0.289**	0.644	0.546	0.457	0.642	0.546	0.457
	$\alpha_{K_0^{NC}}$	0.414	0.269	0.166	**0.142**	0.414	0.269	0.142	0.414	0.269	0.142

*Error: Caused by the limitations of the RH law.

The interpreted parameter, $\alpha_{K_0^{NC}}$ is taken as an output parameter in FORTRAN. The remaining parameters (K_0^{NC} and $\eta_{K_0^{NC}}$) are determined by Eq. (6.10) from each simulation. The analytical values of $\eta_{K_0^{NC}}$ and $\alpha_{K_0^{NC}}$ may be seen in Table 6.4.

Table 6.4: *Analytical values for the rotated yield surface for different K_0^{NC} related to oedometer conditions.*

K_0^{NC}	Eq.	0.55	0.60	0.65
$\eta_{K_0^{NC}}$	4.33	0.643	0.546	0.457
$\alpha_{K_0^{NC}}$	4.31	0.414	0.269	0.141

*For $\varphi_{cs} = 25.43^o \longrightarrow M = 1.0$

By comparing Table 6.3 and Table 6.4 it may be concluded that all three rotational hardening laws satisfied the oedometer scenario. The limitation with respect to evolution law suggested by Wheeler et al. (2003) at high K_0^{NC} is caused by unrealistic values of β, see Section 4.7.2.

Critical State

The critical state is defined by following statements:

$$d\varepsilon_p^p \longrightarrow 0 \qquad (dp = 0) \qquad \text{Constant Volume} \tag{6.11a}$$

$$d\varepsilon_q^p \longrightarrow \infty \qquad (dq = 0) \qquad \text{No dilatancy effect} \tag{6.11b}$$

$$d\alpha \longrightarrow 0 \qquad (d\eta = 0) \qquad \text{Unique State} \tag{6.11c}$$

The rotational hardening suggested by Wheeler (2003) utilizes all three Eqs. (6.11). Hence, the boundary value with respect to critical state may be determined as:

$$0 = \mu \left[\left(\frac{3\eta}{4} - \alpha \right) \langle 0 \rangle + \beta \left(\frac{\eta}{3} - \alpha \right) |d\varepsilon_q^p| \right] \quad \longrightarrow \quad 0 = \frac{\eta}{3} - \alpha \quad \longrightarrow \quad \alpha_b = \frac{M}{3} \tag{6.12}$$

recalling that $\eta = M$ at the critical state. The rotational hardening laws suggested by Dafalias do not obtain a unique magnitude at critical state such as the rotational hardening rule suggested by Wheeler et al. (2003). They are dependent on the stress ratio and the input parameter K_0^{NC}, see Eq. (6.9). The parameters, z and s related to the rotational hardening law suggested by Dafalias and Taiebat (2013) are assumed to be equal and are determined through an oedometer scenario[4]. Two undrained tri-axial simulations of each rotational hardening law are performed with different magnitudes of K_0^{NC} utilizing the standard input parameters given by Figure 6.2 and a loading condition ensuring critical state. The interpreted boundary values along with the analytical boundary values may be seen in Table 6.5.

Table 6.5: *Controlling the boundary value of α_b towards critical state.*

		α_b (Wheeler 2003)	α_b (Dafalias 1986)	α_b (Dafalias 2013)
Analytical$^{(1)}$**:**	$K_0^{NC} = 0.55$	0.334	0.645	0.521
	$K_0^{NC} = 0.60$	0.334	0.493	0.312
Output$^{(2)}$**:**	$K_0^{NC} = 0.55$	0.334	0.646	0.521
	$K_0^{NC} = 0.60$	0.334	0.493	0.317

$^{(1)}$See Section 4.7.1 for determination of the analytical values. $^{(2)}$See Figure 6.7.

The evolution of α may be seen for all six scenarios on Figure 6.7.

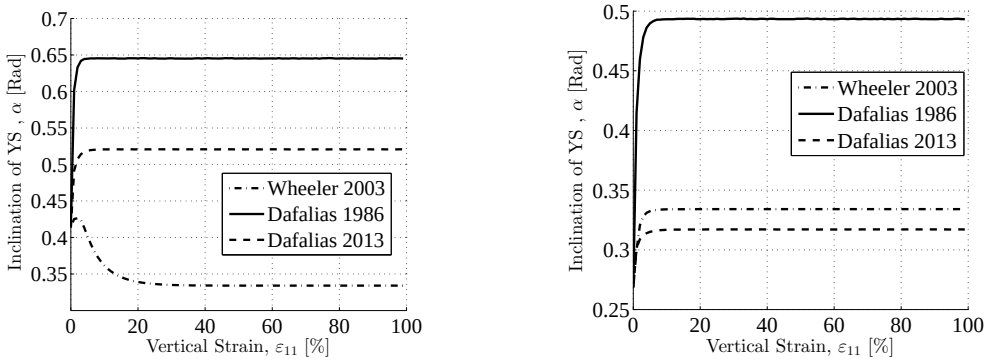

(a) For $K_0^{NC} = 0.55$ (b) For $K_0^{NC} = 0.60$

Figure 6.7: *Simulations of the rotation towards critical state in an undrained tri-axial test. Notice that the sample is compressed 100% to ensure theoretical critical state. The rate of rotation (μ and c) is set to 200. The standard input parameters may be seen on Figure 6.2.*

It may be observed from Figure 6.7 that the evolution suggested by Wheeler et al. (2003) is independent on the magnitude of K_0^{NC} regarding the boundary value but influence the initial value and thereby the path. Each law suggested by Dafalias are very sensitive to the K_0^{NC} value with respect to the boundary value. From Table 6.5 and Figure 6.7 it may be concluded that all three rotational hardening laws satisfy the implemented theory approaching critical state.

[4] $\eta = \eta_{K_0^{NC}}$

Isotropic Compression

The rotation law suggested by Wheeler (2003) may also be verified by isotropic compression. During isotropic compression, only volume change should be expected meaning $d\varepsilon_q^p \longrightarrow 0$. Hence, using the same method as in the critical state, following expression may be found for an isotropic compression:

$$\alpha_b = \frac{3\eta}{4} \qquad \longrightarrow \qquad \alpha_b = 0 \tag{6.13}$$

since $\eta \longrightarrow 0.0$ approaching isotropic conditions. The isotropic compression is simulated by the general option in Soil Test by applying the same strain increment in all directions. The same input parameters as in the critical state are utilized. The evolution of α for two different K_0^{NC} values may be seen on Figure 6.8.

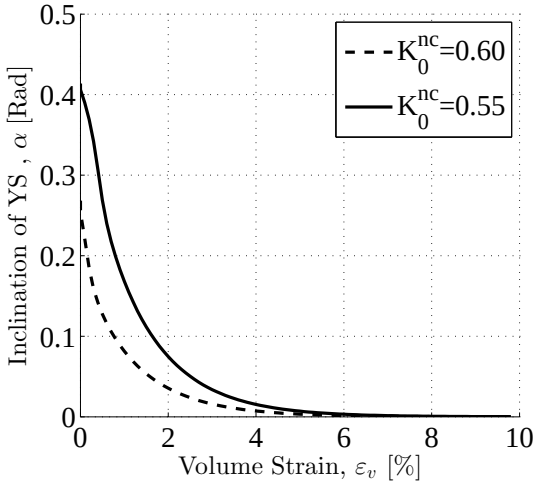

Figure 6.8: *Evolution of α during isotropic compression (Wheeler 2003).*

In each case, α approaches zero which corresponds to the theory. Hence, through these verifications of the one-dimensional compression, critical state and isotropic compression, it may be concluded that the three rotational hardening laws behave as expected regarding the limitations of the laws.

6.3.3 Destructuration

The destructuration phenomenon may be controlled by investigating the effect of changing the destructuration parameters a and b during simulations of one-dimensional compression. The one-dimensional compression scenario is simulated by utilizing the standard input parameters given by Figure 6.2 and a magnitude of $r_{si,min} = 100$ yielding an initial structure of $x_0 = 9.0$. Figure 6.9 shows different combinations of a and b for several oedometer tests.

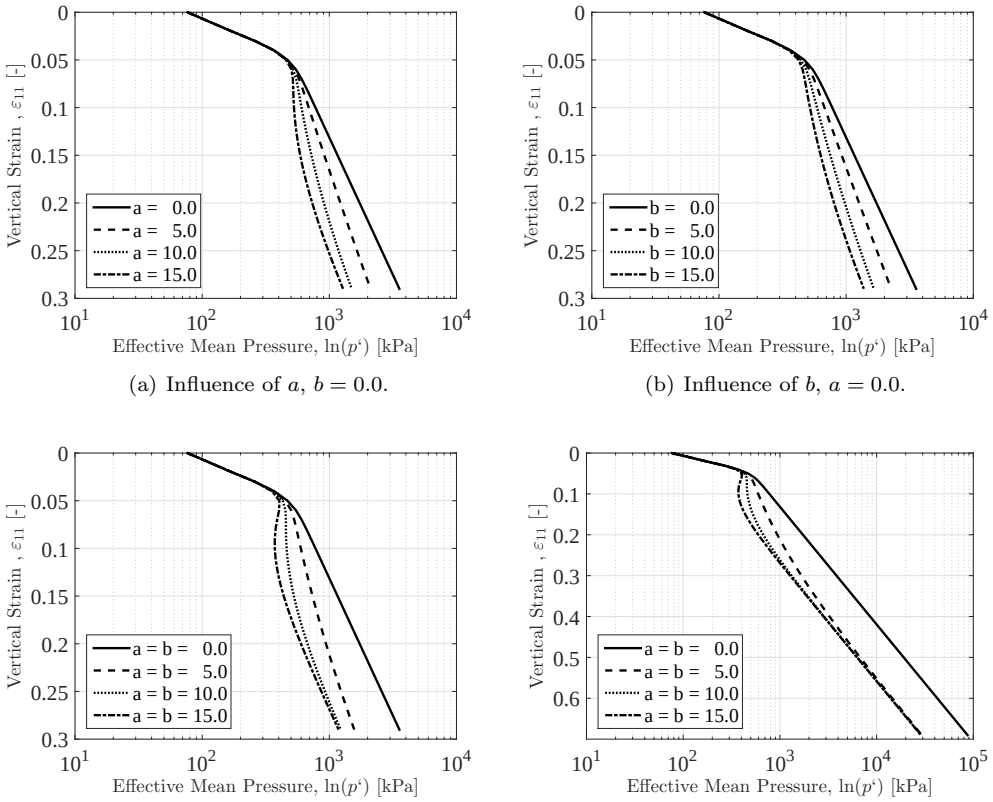

(a) Influence of a, $b = 0.0$.

(b) Influence of b, $a = 0.0$.

(c) Influence of a and b.

(d) Convergence towards the same state.

Figure 6.9: *Effect of destructuration parameters a and b during oedometer conditions. The standard soil parameters may be seen in Figure 6.2. Note, $OCR = 2.0$ and $r_{si,min} = 100$.*

It may be observed from Figure 6.9(a) and Figure 6.9(b) that the effect of changing a has larger influence compared to the same change in b. This behaviour is expected during oedometer conditions and may be explained by looking at the implementation of destructuration:

$$\frac{dx}{d\lambda} = -ax\left[|d\varepsilon_p^p| + b|d\varepsilon_q^p|\right] \tag{6.14}$$

Hence, b is associated to purely deviatoric strains and in the case of $b = 0$ yields that a will be associated to purely volumetric strains. During oedometer conditions the ratio between deviatoric and volumetric strains are given by:

$$\frac{d\varepsilon_q}{d\varepsilon_p} = \frac{2}{3} \tag{6.15}$$

The observed response of a larger destruction for the destructuration parameter a relative to the same magnitude in b may be explained by Eq. (6.15). Figure 6.9(c) shows three scenarios where the effect from both a and b in collaboration may be seen. The destructuration parameters are only associated to the pace of the destructuration. Hence, all scenarios should therefore converge towards the same intrinsic state which may be seen on Figure 6.9(d) which have similar simulations as in Figure 6.9(c) just with a higher axial strain. It may be concluded that the non-linear response after the yielding point may be simulated through the destructuration parameters a and b and the destructuration phenomenon approaches intrinsic properties.

6.3.4 Amount of Structure

The amount of structure in the soil influences the apparent yielding point relative to the intrinsic properties if the intrinsic pressure is kept constant. The intrinsic pressure is defined as:

$$p'_{mi} = \frac{p^{eq} OCR_\tau}{1+x} \qquad \longrightarrow \qquad \frac{p'_{mi}}{p^{eq}} = \frac{OCR_\tau}{1+x} \tag{6.16}$$

where p^{eq} is associated to the initial stresses and should not influence the investigation. Hence, to keep p'_{mi} constant a change in x will result in a change of OCR_τ:

$$\frac{OCR_{initial}}{1+x_{initial}} = \frac{OCR_{new}}{1+x_{new}} \tag{6.17}$$

Hence, the intrinsic pressure may be kept constant by changing the magnitude of OCR_τ. Table 6.6 shows different values of OCR_τ associated to the different amount of structure as a consequence of keeping the intrinsic pressure constant.

Table 6.6: *OCR values demanding p'_{mi} constant with a change of x. Reference: $x = 0.0$ and $OCR = 1.0$*

$r_{si,min}$ [-]	x_{new} [-]	OCR_{new} [-]
10.0	9.0	10.0
12.5	7.0	8.0
25	3.0	4.0

*For $r_{si} = 100$

The influence of structure is verified by one-dimensional compression scenarios by utilizing the standard input parameters given by Figure 6.2 and the values in Table 6.6. Four simulations have been performed and the output may be seen on Figure 6.10. Notice, the destructuration parameters (a, b) are both set to 15.0.

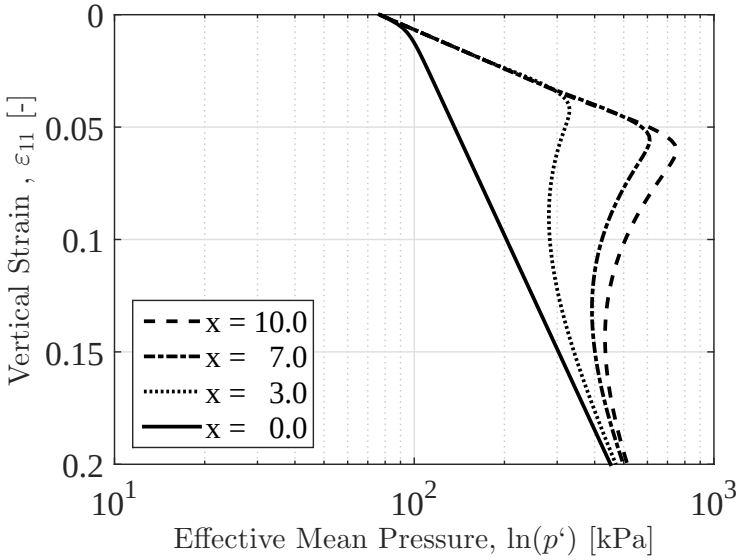

Figure 6.10: *Influence of x_0 with respect to the yielding point during oedomenter conditions keeping p'_{mi} constant. The standard soil parameters may be seen on Figure 6.2 and Table 6.6. Notice, $a = b = 15.0$.*

The solid line in Figure 6.10 corresponds to the intrinsic compression line (ICL) suggested by Burland (1990). The other three scenarios show an increase in the apparent yielding point associated to the increase in the amount of initial structure (x_0) and keeping the magnitude of p'_{mi} constant to the reference level. All three scenarios converge towards the ICL beyond yielding. The pace of

the destructuration is associated to the destructuration parameters (a, b) and the amount of initial structure (x_0). This behaviour has been confirmed in greater details in Section 6.3.3. Hence, it may be concluded that the influence of structure relative to a constant magnitude of p'_{mi} yields the expected response.

6.3.5 Creep

The input parameter associated to creep (r_{si}) may be verified by a one-dimensional compression scenario in a fixed effective stress condition (drained conditions). The one-dimensional compression test is simulated by utilizing the standard input parameters given by Figure 6.2 and keeping the stress increment in all directions constant at zero. During constant stresses, deformations would develop as a function of time. Hence, the deformation would be associated to pure creep. Eight simulations have been performed over a period of 1095 days (3 years) and may be seen on Figure 6.11.

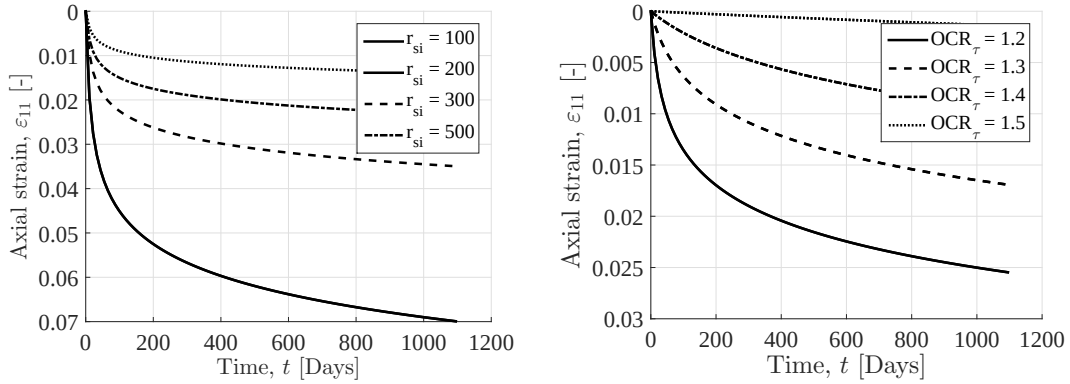

(a) Keeping $OCR_\tau = 1.0$ (b) Keeping $r_{si} = 200$

Figure 6.11: *Oedometer condition under constant effective stresses for a period of 1095 Days (3 years). Notice that $r_{si} = r_{si,min}$ and the standard input parameters may be seen on Figure 6.2.*

The tendency of increasing deformation associated to a reduction in the magnitude of r_{si} is observed on Figure 6.11(a) which corresponds to the theory. It may be seen from Figure 6.11(b) that an increase in the magnitude of OCR_τ is associated to a reduction in deformation which satisfies the theory. In addition, the r_{si} may be interpreted by plotting the resistance number (R) against the time, see Appendix C.5. Hence, a linear relationship should be formed between the time and the resistance number. The inclination of this relationship corresponds to the magnitude of r_{si}. This has been computed for the eight scenarios and may be seen in Table 6.7.

Table 6.7: *Verifying the creep parameter in oedometer scenario during constant effective stress.*

Input:	OCR_τ	1	1	1	1	1.1	1.2	1.3	1.5
	r_{si}	100	200	300	500	200	200	200	200
Output:	r_{si}	99.60	199.65	299.33	499.27	199.67	199.73	199.84	199.97

Hence, it may be concluded that the creep parameter (r_{si}) may be interpreted correctly from the model. Furthermore, the effect of OCR follows expected behaviour.

6.3.6 Influence of Creep on Yielding Point

The apparent yielding point may be influenced by the intrinsic creep number. For relative small creep numbers the intrinsic yield surface may expand so quickly with time that it will affect the apparent yielding point. The mathematical meaning of this may be explained as the intrinsic

yield surface expand so fast with time that it goes beyond the surface representing equivalent stress condition. The phenomena have been investigated by changing the intrinsic creep number and keeping the amount of structure constant by change the minimum creep number relative to intrinsic creep number. This have been done for four cases which may be seen on Figure 6.12.

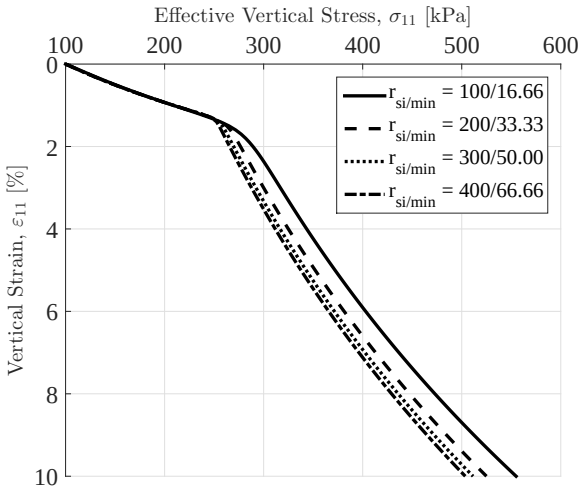

Figure 6.12: *Influence of intrinsic creep number on the apparent yielding point by keeping the structure constant ($x = 5.0$). The solid line represent a scenario where $r_{si} = 100$ and $r_{si,min} = 16.66$. The standard soil parameters may be seen in Figure 6.2 besides the initial stress condition ($\sigma'_{11} = \sigma'_{22} = \sigma'_{33} = 100$ kPa).*

It can be observed from Figure 6.12 that a lower intrinsic creep number is associated to a higher apparent yielding point. Increasing the intrinsic creep number reduces the apparent yielding point and further increase yields minor reduction in the apparent yielding pressure. This effect is similar to the strain rate effect where an increase in strain rate yields a higher apparent yielding pressure, see Section 6.3.7. Hence, the influence of small magnitudes of r_{si} yields the expected response.

6.3.7 Strain Rate

Strain rate effects may be investigated in Soil Test by changing the time step (Δt) relative to the associated deformation ($\Delta\varepsilon$). Hence, the strain rate during a simulation may be determined. The strain rate is normally given in strain/hour with respect to standard laboratory procedure. However, the time step in PLAXIS is associated with days which should be remembered when computing the strain rate. The following formulation may be used to transform a chosen deformation and strain rate into the correct time step in Soil Test:

$$\dot{\varepsilon}_{Day} = \frac{\Delta\varepsilon}{\Delta t} \qquad \longrightarrow \qquad \Delta t = \frac{\Delta\varepsilon}{\dot{\varepsilon}_{Day}} \tag{6.18}$$

This has been done for five different strain rates with a chosen deformation of 10 %, see Table 6.8.

Table 6.8: *Convention of strain rate into PLAXIS's time step for a chosen axial deformation of 10 %.*

Strain rate ($\dot{\varepsilon}$)	Time step (Δt in PLAXIS)
5.00 %/h	2.0833 days
2.00 %/h	0.8333 days
1.00 %/h*	0.4167 days
0.50 %/h	0.2083 days
0.05 %/h	0.0208 days

*Standard rate for Norwegian clays (Emdal et al., 2014).

These five strain rates have been simulated in an undrained tri-axial compression test and a one-dimensional compression test, see Figure 6.14. Notice, a simulation without creep have been plotted as a reference level. The reference level corresponds to elasto-plastic response which may be obtained from the visco-plastic model by setting to $r_{si} = 6000$. Hence, the visco-plastic model converge towards elasto-plastic response for high magnitudes of r_{si}.

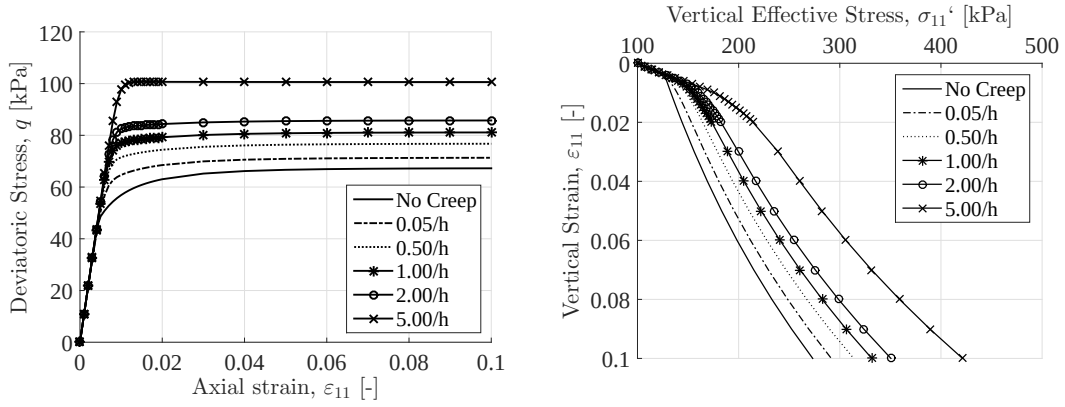

(a) Undrained tri-axial test.

(b) Oedometer test, anisotropic consolidation K_0=0.65.

Figure 6.13: *Strain rate effects from viscous-plastic response. $r_{si} = 100$ and $OCR = 1.2$. The rest of the parameters may be seen on Figure 6.2. Notice, the test without creep corresponds to elasto-plastic response.*

It may be observed that an increase in strain rate yields a larger undrained shear strength, see Figure 6.13(a). In addition, slow strain rates approach the elasto-plastic response. It may be observed from Figure 6.13(b) that higher strain rates yield an increase in the apparent yielding point. The strain rate does not influence the inclination of the one-dimensional curve before the apparent yielding point. These observations correspond well to the theory explained in Section 3.7.3. Hence, it may be concluded that the model is able to simulate strain rate effects.

6.3.8 Change Strain Rate

The phenomenon of changing the strain rate during loading should be verified. The verification has been done by simulating an undrained tri-axial compression test and a one-dimensional compression test utilizing the standard input parameters given by Figure 6.2.

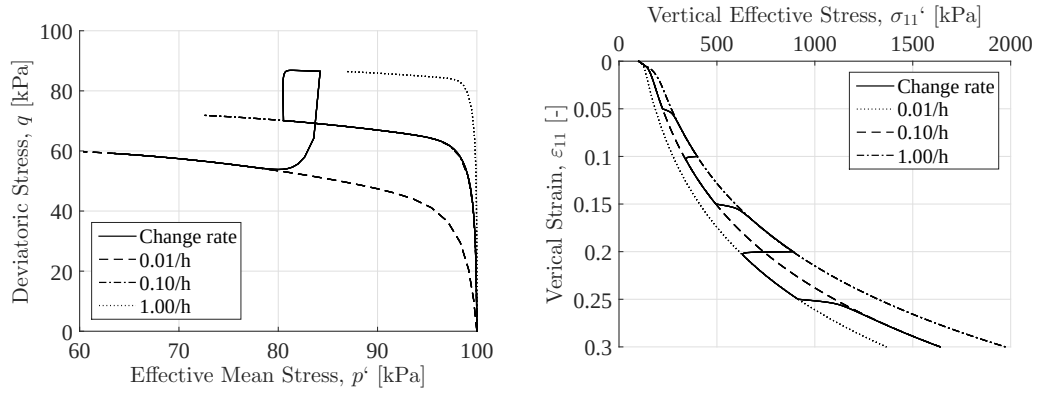

(a) Undrained tri-axial test

(b) One-dimensional compression test

Figure 6.14: *Effect of changing the strain rate in different tests. $r_{si} = 100$ and $OCR = 1.2$, the rest of the parameters may be seen on Figure 6.2.*

Figure 6.14(a) shows how a loop occurs as a result of changing the strain rate. Figure 6.14(b) shows the behaviour of changing isochors by changing the strain rate. This behaviour corresponds to the theory. Hence, it may be concluded that the model is able to simulate the effect of changing the strain rate.

6.3.9 Recovering of Structure

The verification related to the recovering of structure may be investigated through the same principle as for the verification of creep. The recovering of structure is implemented through an exponential function where the pace is controlled by the magnitude of R_t. The boundary value is dependent on the initial structure (x_0) and the allowed recovering determined by the magnitude of R. Figure 6.15 shows four scenarios for different magnitudes of the allowed recovering with the recovery pace ($R_t = 0.001$). The first part (Reference time = 0..100) of the curves symbolize a shearing phase where destroying the initial structure occurs were executed in one day. The other part (Reference time = 101..200) illustrates the recovering of structure during constant effective stresses over a period of 2000 days.

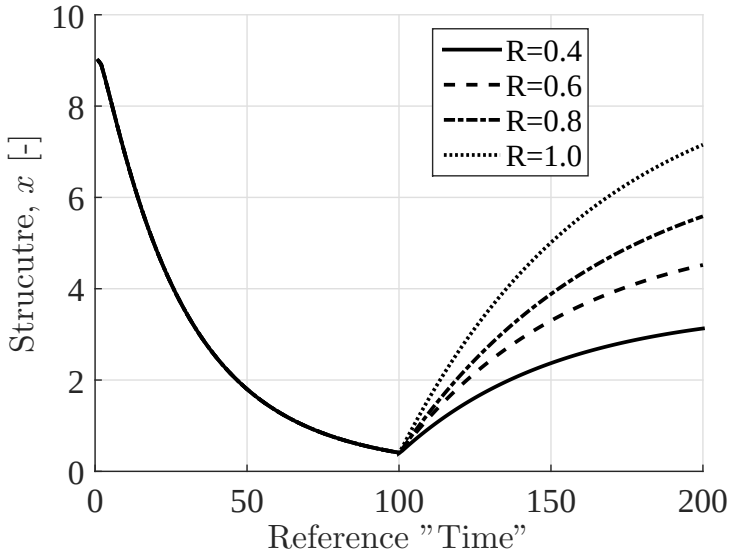

Figure 6.15: *Recovering of structure (x) over time. Notice, Reference time 0..100 symbolize a shearing phase of 1 day destroying the structure. Reference time 101..200 symbolize constant effective stresses over a period of 2000 days. For all four cases, R_t=0.001. The soil parameters may be seen in Figure 6.2.*

The behaviour of all scenarios follows the expected response of the exponential function towards the boundary value defined by R and the initial structure, see Figure 6.15. The chosen way of implementing the recovering of structure yields a different local recovering pace depending both on the recovering pace and the boundary value. This is an assumption made by the author to describe the recovery of structure.

Hence, it may be concluded that the implemented recovering of structure follow the expected response.

6.3.10 Coupling Effect

The recovering of structure induces a coupling term between the recovering of structure and implemented time evolution of the visco-plastic multiplier. Figure 6.16 shows four scenarios illustrating the coupling effect for a drained creep test at fixed effective stresses. The utilized soil parameters may be seen in Figure 6.2.

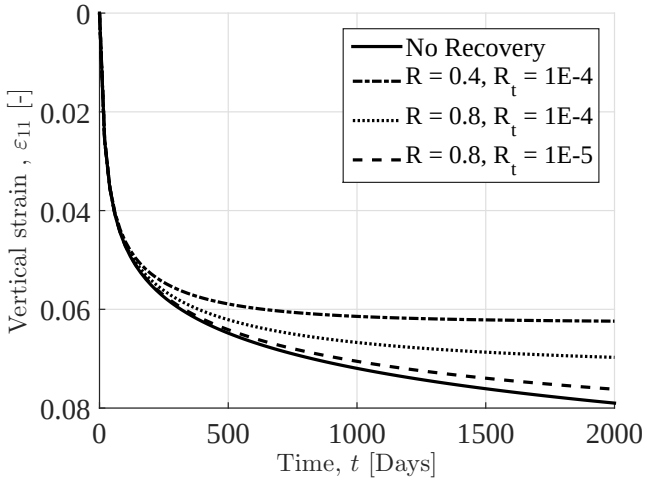

Figure 6.16: *Influence of recovering of structure with respect to creep under constant stress conditions. The standard soil parameters may be seen in Figure 6.2. The initial structure of the test is equal to* $x_0 = 1$ *going towards the boundary value of* $x_b = \frac{r_{si} - r_{si,min}}{r_{si,min}} R = 9R$*, since* $r_{si,min} = 100$ *and* $r_{si} = 1000$*.*

It may be observed that the initial part of the curves are unaffected by the recovering. Hence, it may be concluded that the destruction phenomenon dominate this phase for the given magnitude of recovering. However, after $\varepsilon_{11} \approx 0.05$ the effect shifts and a clear influence of the structure recovering may be seen. The recovering of structure contributes to an increase in OCR_τ and thereby reduces the rate of creep strains:

$$\frac{d\lambda}{dt} = \dot{\lambda} = \frac{1}{r_{si}\tau} \left(\frac{p^{eq}}{(1+x)p'_{mi}} \right)^{r_{si}\zeta_i} \frac{M^2 - \alpha_{K_0^{NC}}}{M^2 - \eta_{K_0^{NC}}} \qquad \longrightarrow \qquad OCR_\tau = \frac{(1+x)p'_{mi}}{p^{eq}} \tag{6.19}$$

It may be observed that magnitude of OCR_τ increases to a level where creep strains are negligible. Hence, introducing the recovering of structure yields an additional feature to control the creep strain rate is given. It should be mentioned that this particular test cannot be made in Soil Test without manually setting the structure (x) to a lower value than the initial structure. Hence, an initial structure of $x_0 = 1.0$ is manually chosen in FORTRAN. However, the test could be performed through a boundary value problem by creating a finite element scenario in PLAXIS which yields more degrees of freedom regarding the loading conditions.

The coupling effect influences the creep rate as expected. Hence, this concluded the verification of part 2. The next part will verify the MMC response against analytical values.

6.4 Additional Verification

The additional verification is associated to MCC behaviour during drained and undrained conditions for NC and OC scenarios. This response will be compared to a created MATLAB model, see Appendix D.1, and analytical results. In addition, the response during extension and compression will be investigated to ensure that the model yields the expected behaviour.

6.4.1 Compression vs. Extension

Testing a soil in compression or extension yields different mechanical responses. This effect is caused by the Lode angle dependence with respect to the magnitude of the intermediate principle stress. In addition, introducing an inclined yield surface, as a consequence of the anisotropic conditions of the soil, the mechanical response will be influenced.

These aspects may be verified by simulating several undrianed tri-axial simulations by utilizing the standard parameters given by Figure 6.2. An undrained tri-axial compression and tension simulation, during isotropic consolidation, may be seen on Figure 6.17. Notice, $K_0^{NC} = 0.7154$ yields isotropic stiffness which has been utilized in these simulations[5].

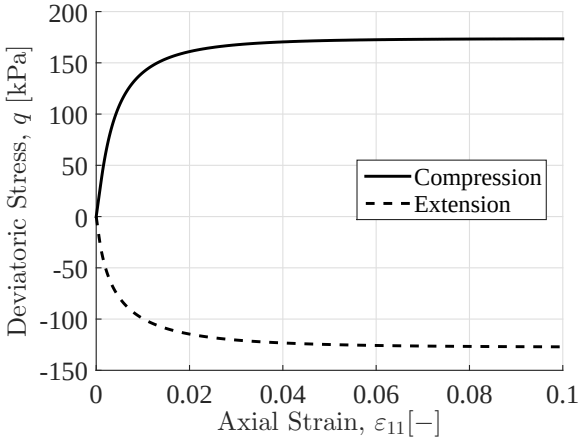

Figure 6.17: *Setup to control the soil response during compression and extension in undrained tri-axial.*

The Lode angle dependency may be seen from the difference between the compression and extension test. Hence, the ratio of the undrained shear strength may be determined to:

$$\frac{s_{u,P}}{s_{u,A}} = \frac{130.6\,\text{kPa}}{174.1\,\text{kPa}} = 0.75 \tag{6.20}$$

Notice that, A refers to **Active** and P refers to **Passive** meaning compression and extension, respectively. The inclination of the critical state line for pure compression and extension is given by Eq. (6.21)[6]. The utilized friction angle is $\varphi_{cs} = 25.43^o$ yielding a ratio between active and passive as:

$$M = \frac{6\sin(\varphi_{cs})}{3 \pm \sin(\varphi_{cs})} \qquad \longrightarrow \qquad \frac{M_{cs,P}}{M_{cs,A}} = \frac{3 - \sin(\varphi_{cs})}{3 + \sin(\varphi_{cs})} = 0.75 \tag{6.21}$$

Hence, it may be concluded that the different response regarding compression and extension during undrained tri-axial testing may be interpreted correctly from the model since the analytical ratio of the inclination of the CSL and the measured ratio of the undrained shear strength is equal.

[5] The rotation of the yield surface is zero utilizing $K_0^{NC} = 0.7154$ for $M = 1.0$. Be aware that the input parameters do not cause a negative angle of the yield surface which cause errors in the code.
[6] Positive for tension and negative for compression.

The anisotropic response may be verified by changing the magnitude of K_0^{NC}. Recalling that $K_0^{NC} = 0.7154$ yields zero inclination of the yield surface for a frictional angle of $\varphi_{cs} = 25.43^o$. Lowering the magnitude of K_0^{NC} causes a higher inclination of the yield surface. Investigating the effect of anisotropy, with respect to tri-axial testing, the initial stress condition should be changed. Hence, anisotropic consolidation must be used, $K_0^{NC} = K_0'$ meaning that the horizontal effective stresses are lower than vertical before shearing the sample. Figure 6.18 shows four undrained tri-axial simulations using the same vertical consolidation pressure (300 kPa).

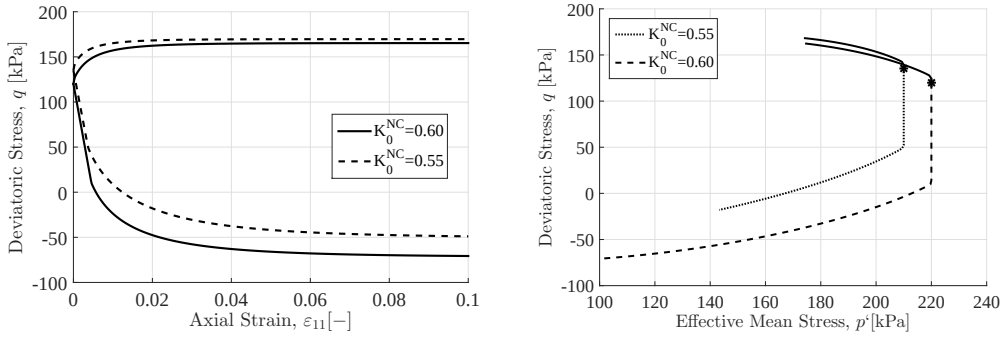

(a) $(\varepsilon_{11} : q)$-space. (b) $(p' : q)$-space, effective stress pat.h

Figure 6.18: *Influence of K_0^{NC} with respect to compression and tension during undrained tri-axial conditions. The standard soil parameters may be seen on Figure 6.2. Notice that q becomes negative since it is computed as the vertical minus the horizontal effective stress.*

In general, the compression simulations yield a stiffer response compared to their associated extension simulation. It may be observed from Figure 6.18(a) that lowering the K_0^{NC} yields a higher compression and lower extension magnitude of the undrained shear strength. This yields a more brittle response of the soil with respect to compression. Figure 6.18(b) shows the ESP for the four simulations where the vertical lines represent the less stiff response during tension. The vertical line is caused by the elastic region. Lowering the magnitude of K_0^{NC} yields a larger inclination of the yield surface which may be seen on Figure 6.18(b).

It may be observed that the size of the initial yield surface is different. This is caused by the magnitude of K_0' which influences the reference surface presenting the stress condition (p^{eq}). Thereby, the intrinsic pressure is changed through:

$$p'_{mi} = \frac{p^{eq} \cdot OCR}{1 + x} \tag{6.22}$$

Utilizing the values as for Figure 6.18 yields

$$K_0^{NC} = 0.55 \qquad p'_{mi} = 222.36\,\text{kPa}$$

$$K_0^{NC} = 0.60 \qquad p'_{mi} = 237.09\,\text{kPa}$$

The tendency of changing the K_0^{NC} may be verified from the above section. Thereby, it may be concluded that the model is able to simulate anisotropic behaviour during tri-axial conditions.

6.4.2 Modified Cam Clay Response

The purpose of this section is to compare the MCC part of the visco-plastic model programmed in FORTRAN to a constitutive model programmed in MATLAB, see Appendix D.1. In addition, during the comparison some analytical values will be determined to ensure reliability of each model.

To compare the models it is necessary to eliminate the viscous effect since it would affect the mechanical response. The visco-plastic model should converge towards an elasto-plastic model if the magnitude of r_{si} go towards infinity. Hence, using a high magnitude of r_{si}, the time effects would be negligible, see Figure 6.11. However, the model is not able to handle unrealistic numbers of r_{si}. Therefore, a value of $r_{si} = 6000$ has been chosen[7]. Furthermore, to obtain similar models, the inclination for the yield surface in the visco-plastic model must be set to zero which is done by $K_0^{NC} = 0.7154$ for the utilized friction angle. The comparison is done by a drained and an undrained tri-axial simulation of both NC and OC ($OCR = 4.0$) utilizing the standard soil parameters given by Figure 6.2. The mobilizing of shear strength may be seen on Figure 6.19

The mobilizing of shear strength:

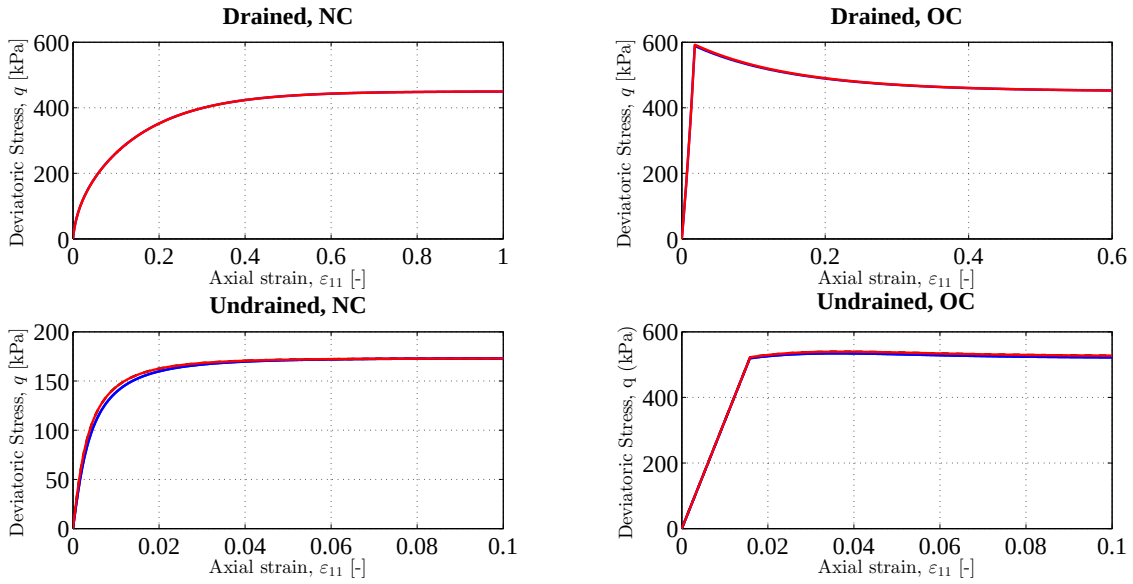

Figure 6.19: *Comparing the mobilisation of shear strength in a tri-axial test from MCC models. Red line symbolise MATLAB model, blue line symbolise visco-plastic model in PLAXIS.*

In general, an acceptable fit between the two models may be seen on Figure 6.19. In addition, the models are capable of capturing the soil response regarding NC and OC behaviour for both drained and undrained scenarios according to the theory. Table 6.9 shows the peak and end value of the mobilized shear strength.

Table 6.9: *Theoretical and numerical results to verify the MATLAB model and visco-plastic model.*

Method	Drained, NC	Drained, OC ()*	Undrained, NC	Undrained, NC
Constitutive model (MATLAB)	450.0 kPa	591.0 kPa (450.1)	172.5 kPa	525.5 kPa
Visco-plastic model (PLAXIS)	449.5 kPa	591.1 kPa (450.2)	172.2 kPa	523.7 kPa
Theoretical	450.0 kPa	591.1 kPa (450.0)	172.3 kPa	522.3 kPa

*Continue expansion after reaching the pre-consolidation surface (Softening)

It may be seen from Table 6.9 that the mobilized shear strength predicted by each model is similar to the theoretical values which have been determined in Appendix C.3.1. However, as mentioned in Chapter 5, the accuracy of the visco-plastic model could be increased by reducing the step size associated to the explicit scheme.

[7] A number of 3000 or even less would have been enough.

Volumetric strain and development of excess pore pressure:
The theoretical change in volume may be determined to $\varepsilon_p = 12\%$ and $\varepsilon_p = 1.8\%$ for NC and OC scenario, respectively. The theoretical change in excess pore pressures may be determined to $\Delta u = 185.1$ kPa and $\Delta u = 48$ kPa for NC and OC scenario, respectively. From Figure 6.20 it may be concluded that the models yield similar response with respect to the development of pore pressure and change in void ratio and the boundary values correspond to the theoretical values.

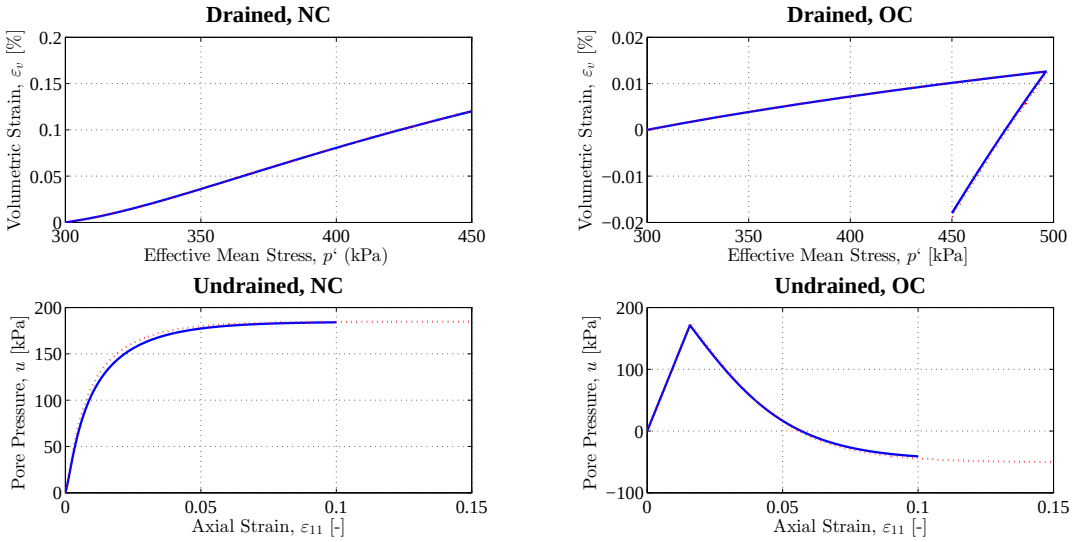

Figure 6.20: *Comparing the volumetric change and development of excess pore pressure for the drained and undrained cases in tri-axial simulation. Red line symbolise MATLAB model, blue line symbolise visco-plastic model in PLAXIS.*

Effective stress path in $(p' : q)$-space:
Figure 6.21 shows a similarity in the ESP in both models. However, some deviation may be observed in the OC undrained scenario. In the undrained scenarios, the water is assumed to be incompressible ($\nu_u = 0.5$). The numerical computation in PLAXIS cannot use the value of $\nu_u = 0.5$ caused by a division with zero when computing the bulk modulus of water. Therefore, it is set to $\nu_u = 0.495$ as default in PLAXIS unless otherwise specified which explains the deviation.

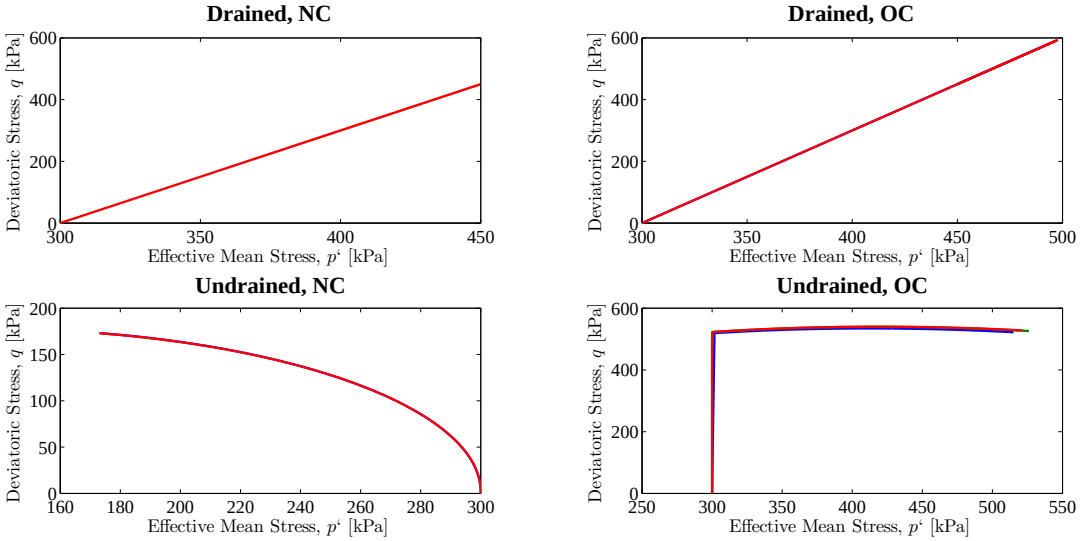

Figure 6.21: *Comparing the stress path in $(p' : q)$-space in tri-axial simulation from MCC models. Red line symbolise MATLAB model, blue line symbolise visco-plastic model in FORTRAN.*

Hence, it may be concluded that the SCA-R is capable of simulating the MCC behaviour.

Chapter 7

Soil Parameters

This chapter will clarify the selection of input parameters which have been utilized to perform the numerical simulations at the embankment located at Onsøy, Norway. The input parameters are chosen through an initial estimate determined by laboratory data and afterwards calibrated by a back-calculation procedure to obtain similar response as the laboratory tests.

7.1 General

The procedure for choosing the input parameters is based on standard practice used in Scandinavia which may be summarized as:

1. Run laboratory tests and interpret the soil parameters from relevant stress domains.
2. Simulate the laboratory tests in a numerical software. The back-calculation is used to adjust the input parameters to obtain the best fit of the laboratory results.

The soil parameters may be divided into two individual groups depending on their characteristics:

- **Stiffness parameters:** Essential for settlement calculations. Generally interpreted by oedometer tests.
- **Strength parameters:** Essential for stability calculations. Generally interpreted by triaxial tests.

The above definition deviates slightly from the truth since the soil strength determines the degree of mobilization which is associated to the deformation. Furthermore, the SCA-R model utilize input parameters which do not fit into two main groups. Hence, an additional group must be defined and will be referred to as the advanced input parameters. The SCA-R model requires 15 input parameters[1] to access all its features. An overview of the 15 input parameters, their physical meaning along with the standard method to interpret them may be seen in Table 7.1.

[1] 16 if the reference time is taken into consideration and two additional parameters added in Chapter 8.

Table 7.1: *An overview of the input parameters used in the SCA-R model and related laboratory tests associated to interpretation methods.*

Type	Test type	Parameter	Unit	Physical meaning
Settlement	**Index Test**	e_0	-	Initial void ratio
	1-D Compression test (Tri-axial, IL oedometer or CRS)	λ_i	-	Compression index evaluated from $(\ln p' : \varepsilon_v)$-space
	1-D Compression test (Tri-axial, IL oedometer or CRS)	κ	-	Swelling index evaluated from $(\ln p' : \varepsilon_v)$-space
	1-D Compression test (IL oedometer or CRS)	p'_c $(OCR_\tau)^{(1)}$	kPa -	Apparent yield pressure (Over Consolidation Ratio)
	1-D Reconstituted compression (IL oedometer)	r_{si}	-	Intrinsic creep number
	1-D Reconstituted compression (IL oedometer or CRS)	$x_0/r_{si,min}$	-	Initial amount of bonding
	$\boldsymbol{K}_0$**-oedometer** or $\boldsymbol{K}_0$**-tri-axial** (Radial strains with unloading stage)	ν_{ur}	-	Poisson´s ratio at un/reloading
		K_0^{NC}	-	K'_0, Normal consolidated region
$\mathbf{S}^{(2)}$	**Tri-axial**	φ_{cs}	^{o}	Frictional angle at critical state
Advanced	**Tri-axial** Undrained	α_e	-	Elastic anisotropy
	Tri-axial (Different stress paths)	μ or c	-	Control the volumetric and deviatoric rate of rotation
	Tri-axial Drained (Different stress paths)	a b	- -	Control the rate of degradation of bonding due to volumetric and deviatoric creep strains
	Tri-axial/Compression	R	-	Amount of recovering of x
		R_t	-	Pace of x-recovery

(1) 24 hours.

(2) S=Strength.

The parameters: a, b, R, R_t, and μ/c will not be determined through any experimental data. No experimental data is available to interpret these input parameters directly. However, the parameters a, b, and μ/c are calibrated through the back-calculation procedure. The magnitude of R and R_t will be investigated in Section 8.10.

7.2 Available Data

Norwegian Geotechnical Institute (NGI) has granted access to a great amount of high quality data consisting of several laboratory tests and some field measurements related to embankment located at Onsøy. The field measurements are presented by Berre (2013) and may be seen on Figure 7.5. The entire laboratory data is collected in one report named: *Additional Tests on Block Samples in Connection with Onsøy Test Fill* (Berre, 2010). In addition to the experimental data made by Berre (2010) his report contains additional data from four earlier reports[2,3,4,5]. An overview of available data may be seen in Table 7.2.

Table 7.2: *List of available data related to the test fill at Onsøy.*

Source	Oedometer	Tri-axial*
Berre (2010)	3	10
Wichtmann (2010)	0	5
Lunne et al. (2009)	2	2
Lunne et al. (2010)	2	3
Bamberg (2009)	2	0
*Undrained	**9**	**20**

It should be mentioned that the sampling has been done by utilizing a block sampler to obtain the highest quality samples as possible. The CRS tests have incorporated a creep period of approximately 10-24 hours between two compression stages. Thereby, a creep parameter may be interpreted. The tri-axial tests contain both compression and extension tests. The Author sends his gratitude to NGI allowing access to this high quality data.

7.3 Interpreted Parameters

The interpreted parameters will be divided into four parts: permeability, compression, initial stresses and strength parameters. For each parameter, an example of how to interpret the parameter for the sample **Block-19-A1-O1** or **Block-28-B-11** will be shown and the additional interpretations are summarized in Appendix F. Notice, in addition to the input parameters required by the SCA-R model, PLAXIS requires further input parameters which will be described in Sections 7.3.1-7.3.3.

7.3.1 Permeability Parameters

In PLAXIS, the parameters related to permeability[6] are the hydraulic conductivity in horizontal and vertical direction (k_x and k_y) along with the change in hydraulic conductivity (c_k). The permeability and its evolution during loading has been measured through the pore pressure in the CRS tests given by Berre (2010).

In a standard CRS test the dissipation of pore water would be limited to the upper part of the sample caused by the impermeable side boundaries and the requirement of measuring the pore pressure at the bottom of the sample. Hence, the initial hydraulic conductivity (k_0) and its evolution from the CRS tests are associated with the vertical hydraulic conductivity. The horizontal hydraulic conductivity may be higher with respect to the deposition process and the shape of the clay particles. The PLAXIS models related to Onsøy and made by Mehli (2015a) has utilized a factor of 1.5 between the horizontal and vertical hydraulic conductivity and for comparison reasons, the same factor has been chosen in this work.

[2] NGI project No 20092109 (Wichtmann, 2010).
[3] NGI project No 20091764 (Lunne et al., 2009).
[4] NGI project No 20081088 (Lunne et al., 2010).
[5] Master Thesis at NTNU (Bamberg, 2009).
[6] General input parameters in PLAXIS which are not related to the SCA-R model.

The change in hydraulic conductivity with respect to the formulation used in PLAXIS is given as:

$$\log\left(\frac{k}{k_0}\right) = \frac{\Delta e}{c_k} \tag{7.1}$$

where k is the changed hydraulic conductivity. PLAXIS relates the change in void ratio (Δe) to the change in volumetric strains by:

$$\Delta e = (1 + e_0)\Delta\varepsilon_p \tag{7.2}$$

where e_0 is the initial void ratio associated to stress condition under in situ stresses. The initial void ratio may be estimated by:

$$S_r = \frac{wd_s}{e} \qquad \longrightarrow \qquad \underbrace{e = wd_s}_{S_r = 100\,\%} \qquad \text{where} \qquad d_s = \frac{\rho_s}{\rho_w} \tag{7.3}$$

where S_r is the degree of saturation, w is the water content, d_s is the relative density, ρ_s and ρ_w is the solid grain and water density, respectively. The assumption of 100 % saturation is common in Norwegian clays which also appears from the data given by Berre (2010). However, it may occur due to limitations in the experimental equipment, that the magnitude of S_r exceeds 100 % and should be corrected, see Appendix F.3. Hence, the change in hydraulic conductivity may be found by substituting Eq. (7.2) and Eq. (7.3) into Eq. (7.1) which yields:

$$c_k = \frac{(1 + e_0)\Delta\varepsilon_v}{\log\left(\frac{k}{k_0}\right)} \tag{7.4}$$

Figure 7.1 shows how the change in hydraulic conductivity behaves during one-dimensional compression test (CRS) for sample **Block-28-B-11**.

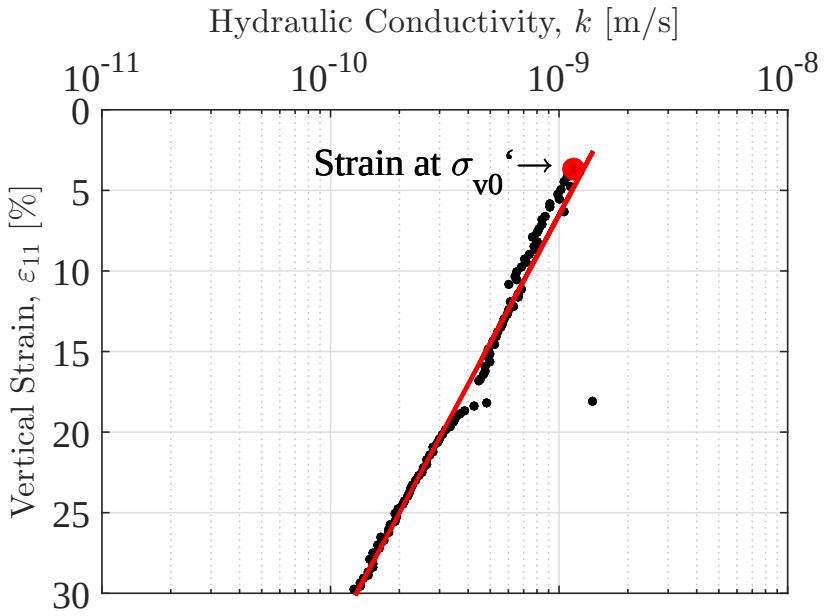

Figure 7.1: *Procedure to interpret hydraulic conductivity and its evolution from* ***Block-28-B-11****.*

The water content, degree of saturation and grain density is given by Berre (2010). The initial void ratio may be determined for sample, **Block-28-B-11** as:

$$e_0 = wd_s = \underbrace{0.6737 \cdot 2.825}_{(S_r = 101.3\%)} = 1.90 \qquad \underbrace{\longrightarrow}_{\text{Correction for } S_r} \qquad e_0 = 1.88 \tag{7.5}$$

The change in hydraulic conductivity may be determined by Eq. (7.4) as:

$$c_k = -\frac{(1+1.88)\cdot(0.30-0.024)}{\log\left(\frac{2.3\cdot10^{-10}\,\mathrm{m/s}}{1.7\cdot10^{-9}\,\mathrm{m/s}}\right)} = 0.92 \tag{7.6}$$

This procedure has been done for all available oedometer data which may be seen in Appendix F. The initial hydraulic conductivity and its evolution (c_k) may be seen in Table 7.5 along with the computed initial void ratios.

Table 7.3: *Interpreted permeability parameters from CRS tests.*

Block	Depth$^{(1)}$ [m]	σ'_{v0} $^{(1)}$ [kPa]	e_0 [-]	k_i $^{(1)}$ [$\cdot10^{-4}$ m/day]	c_k [-]
3-A1-O1	1.01	10.1	1.28 (1.28)	1.39	0.53$^{(3)}$
10-A2-O1	3.87	28.6	1.66 (1.64)	3.47	0.58$^{(3)}$
19-A1-O1	7.45	50.6	2.05 (1.99)	3.59	0.73$^{(3)}$
22-B-1-CRS	8.86	58.9	2.04 (1.99)	1.50	1.04
22-B-2-CRS	8.91	59.2	2.06 (2.03)	1.62	1.14
26-B1-0-B1-35	10.82	69.9	1.95 (-)$^{(2)}$	1.16	0.89
26-B1-0-B1-50	10.82	69.9	1.94 (-)$^{(2)}$	1.16	0.95
28-B-11	11.65	74.5	1.90 (1.88)	1.97	0.92
28-B-12	11.65	74.5	1.91 (1.88)	1.85	0.95

$^{(1)}$Taken directly from Berre (2010).

$^{(2)}$The saturation is not available from Berre (2010).

$^{(3)}$Taken from Mehli (2015a).

When interpreting c_k it should be noted that a sudden jump in the linear relationship may be expected near the pre-consolidation pressure. However, the interpretation should be made for relevant stress regions as stated by Mehli (2015a).

7.3.2 Compressibility Parameters $\boldsymbol{\lambda, \kappa}$ and $\boldsymbol{r_{si}}$

The compressibility parameters (λ_i^* and κ^*) are related to the MCC model and were defined as the slope of the NCL and the URL in the ($\ln(p')$:ε_p)-space, see Section 2.6.1. These compressibility parameters are commonly interpreted through a CRS or a 24-hour IL oedometer test. However, the modified parameters need to be transformed into the standard Cam Clay parameters (λ_i and κ) to suit the SCA-R model which may be done by:

$$\textbf{Compression index:} \qquad \lambda = \lambda^*(1+e_0) = \frac{C_c}{\ln(10)} = \frac{1}{m} \tag{7.7a}$$

$$\textbf{Swelling index:} \qquad \kappa = \kappa^*(1+e_0) \approx \frac{2C_s}{\ln(10)} \tag{7.7b}$$

where C_c and C_s are the compression and swelling index used in other literature and m is the secant modulus which may be used to determine the creep number (r_s)[7]. The CRS for **Block-19-A1-O1** may be seen on Figure 7.2 showing the method to interpret the parameters by utilizing a ($\ln(\sigma'_{11})$:ε_{11})-plot. However, the inclination of URL may be affected by using the effective vertical stress instead of the effective mean pressure. Mehli (2015a) suggested to multiply the inclination of URL by a factor of two as an assumption of isotropic state during loading. The factor of two may also be seen in Eq. (7.7).

[7] Will be explained later in this section.

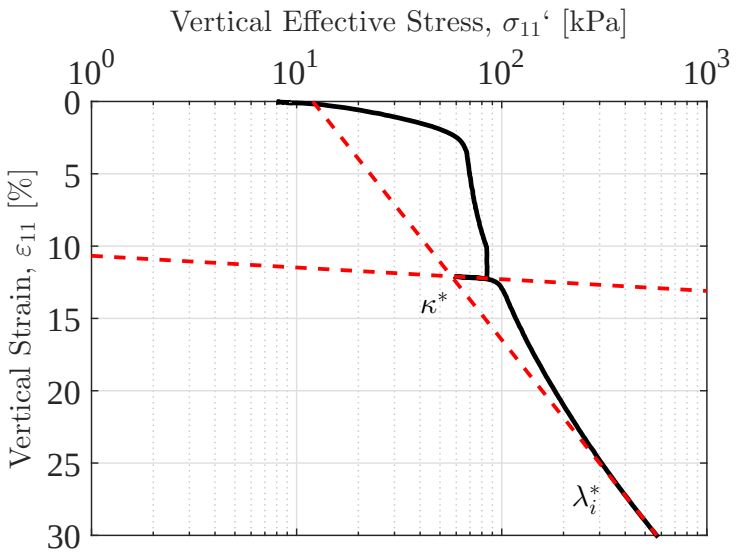

Figure 7.2: *Interpreted compression and swelling parameter from* ***Block-19-A1-O1*** *through the CRS.*

From Figure 7.2 the compression and swelling parameter may be determined by:

$$\lambda_i^* = \frac{\Delta\varepsilon_{11}}{\ln\left(\frac{\sigma'_{11,2}}{\sigma'_{11,1}}\right)} = \frac{(0.300 - 0.000)}{\ln\left(\frac{570\,\text{kPa}}{12\,\text{kPa}}\right)} = 0.078 \quad \longrightarrow \quad \lambda_i = 0.232$$

$$\kappa^* = \frac{\Delta\varepsilon_{11}}{\ln\left(\frac{\sigma'_{11,2}}{\sigma'_{11,1}}\right)} = 2 \cdot \frac{(0.131 - 0.107)}{\ln\left(\frac{1000\,\text{kPa}}{1\,\text{kPa}}\right)} = 0.007 \quad \longrightarrow \quad \kappa = 0.021$$

The swelling parameter could also be interpreted through the inclination of the initial part of the stress-strain curve towards yielding. This swelling parameter may be preferable for calculations in the elastic region where yielding has not occurred. However, one should keep in mind that sample disturbance will have a larger influence on the initial stress-strain curve compared to the unloading loop. Regarding the unloading reloading loop, it is of great importance that the loop is not too short since it may yield a too stiff response. Notice that the intrinsic compression parameter is interpreted through the inclination of stress-strain curve after all bondings are destroyed and not the inclination just beyond yielding. This procedure has been done for all available oedometer data which may be seen in Appendix F. The interpreted intrinsic compression and swelling parameters may be seen in Table 7.5.

The intrinsic creep number (r_{si}) may be interpreted through an incremental oedometer, see Section 4.7.6. However, no incremental oedometer data is available. Therefore, it may be approximated through the creep number (r_s). It has been shown through various experimental data in the literature (see for instance (Leroueil and Marques, 1996)) that the ratio between the compression parameter and creep number may be assumed as a constant:

$$\frac{\lambda}{r_s} \approx \text{Constant} \tag{7.9}$$

Thereby, knowing the creep number (r_s), and the compression parameters (λ and λ_i) the intrinsic creep number may be estimated. The creep number may be interpreted by the CRS test utilizing the time resistance concept suggested by Janbu (1969). Hence, r_s may be determined as the inclination of the curve shown in Figure 7.3 which represents the region where development of

deformation occurs as a function of time under constant effective stresses for sample **Block-19-A1-O1**, see Figure 7.2. A more detailed description of the principle suggested by Janbu (1969) may be found in Appendix C.5.

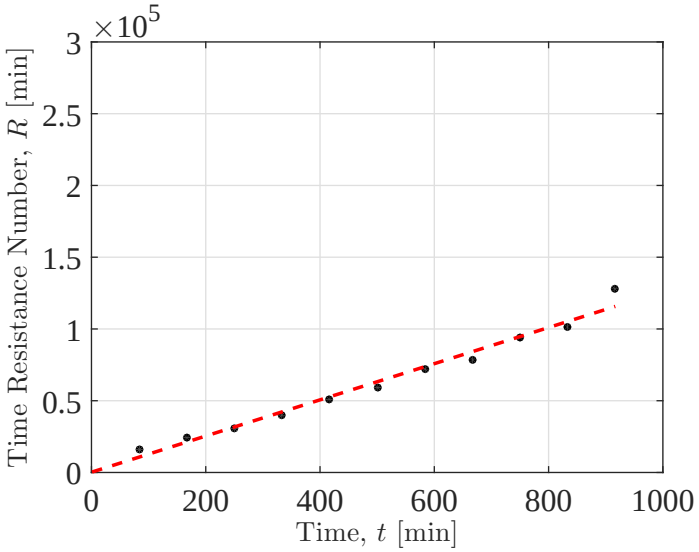

Figure 7.3: *Interpreted creep number from **Block-19-A1-O1** through the CRS.*

The creep number may be determined as:

$$r_s = \frac{\Delta R}{\Delta t} = \frac{1157\,\text{min} - 326\,\text{min}}{917\,\text{min} - 0\,\text{min}} = 126$$

The compression parameter (λ) associated to the determined creep number (r_s) and the intrinsic compression parameter (λ_i) need to be determined to approximate the magnitude of r_{si}. This may be done through the secant stiffness modulus (m)[8] concept suggested by Janbu (1969). The secant modulus may be determined as the inclination on Figure 7.4 representing the constrained stiffness (M) during the CRS test for sample **Block-19-A1-O1**. According to the theory suggested by Janbu (1969), after yielding a linear relationship between the constrained stiffness and the effective vertical stresses should be found. However, regarding the structure and the destructuration the initial part of the relationship has a larger inclination compared to the intrinsic part. Hence, secant stiffness modulus (m) with structure may be interpreted through Figure 7.4(a) and the intrinsic secant stiffness modulus (m_i) through Figure 7.4(b).

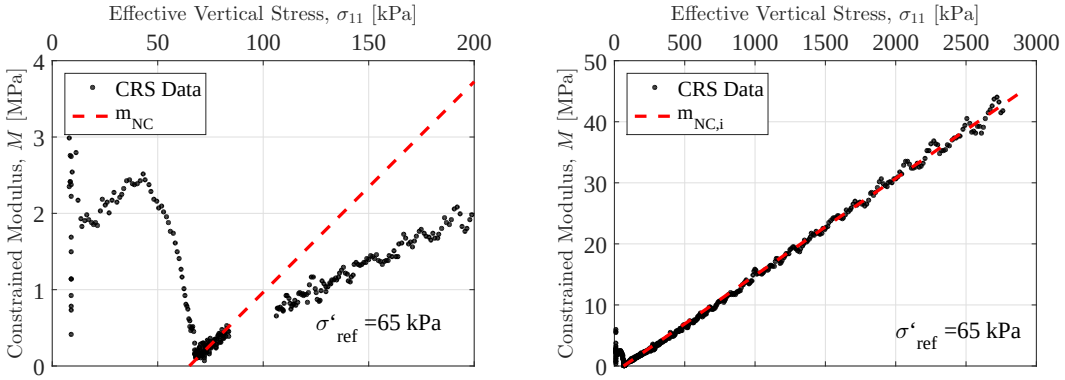

(a) **Block-19-A1-O1** zoom in.

(b) **Block-19-A1-O1** entire test.

Figure 7.4: *Interpreted compression and swelling index from CRS.*

[8] See Eq. (7.7) for how to relate m to λ.

The secant modulus may be determined as:

$$m_{NC} = \frac{\Delta M}{\Delta \sigma'} \quad \longrightarrow \quad m_{NC} = \frac{4000\,\text{kPa} - 0\,\text{kPa}}{210\,\text{kPa} - 65\,\text{kPa}} = 27.59 \quad m_{NC,i} = \frac{45000\,\text{kPa} - 0\,\text{kPa}}{2900\,\text{kPa} - 65\,\text{kPa}} = 15.87$$

The intrinsic creep number for **Block-19-A1-O1** may be approximated as:

$$r_{si} = \frac{m}{m_i} r_s = \frac{27.57}{15.87} \cdot 126 \approx 219 \tag{7.10}$$

This procedure has been done for all available oedometer data which may be seen in Appendix F[9].

The minimum creep number:
The minimum creep number ($r_{si,min}$) which determines the amount of structure relative to the value of the intrinsic creep number (r_{si}) may also be approximated. The approximation has been done through the sensitivity of the soil (S_t) which is another method to determine the amount of structure:

$$x_0 = S_t - 1 \qquad \text{and} \qquad x_0 = \frac{r_{si} - r_{si,min}}{r_{si,min}} \qquad \longrightarrow \qquad r_{si,min} = \frac{r_{si}}{S_t} \tag{7.11}$$

The sensitivity may be estimated though the bore profile shown on Figure 7.5 utilizing the undrained shear strengths (undisturbed and remoulded). Figure 7.5 may be divided into four layers and the dry crust as suggested by Mehli (2015a). For these four layers an average undisturbed and remoulded undrained shear strength may be estimated to determine the sensitivity of the soil, see Table 7.4.

Table 7.4: *Determined sensitivity of the clay at Onsøy.*

Layer	s_{ur}	s_{uu}	S_t^*
0.6 - 2.0 m	2.5 kPa	11.5 kPa	≈ 4.5
2.0 - 5.0 m	3.0 kPa	16.5 kPa	5.5
5.0 - 10.0 m	3.0 kPa	18.5 kPa	≈ 6.2
10.0 - 25.0 m	6.0 kPa	30.0 kPa	5.0

*The fallen cone has been utilized to determine S_t, see Figure 7.5.

The subscript r refers to remoulded and u refers to undistributed. The sample, **Block-19-A1-O1**, is taken at a depth of 7.45 m which yields a sensitive of 6.2. Thereby, the minimum creep number may be determined as:

$$r_{si,min} = \frac{r_{si}}{S_t} = \frac{219}{6.2} \approx 35 \tag{7.12}$$

The determined creep numbers may be seen in Table 7.5 along with other relevant information regarding each sample. Notice, the magnitude of r_{si} for **Block-22-B-1-CRS** have not been possible to interpret. The method to determine the unit weight of the soil may be seen in Appendix F.3.

[9] The secant modulus was not determined for **block**-10-A2-01 since it yields unrealistic values.

Table 7.5: *Interpreted data from the laboratory curves for the nine CRS oedometer tests.*

Test	Depth[(1)] [m]	σ'_{v0} [(1)] [kPa]	$\varepsilon_a^{(1)}$ at σ'_{v0} [%]	$\dot{\varepsilon}_a^{(1)}$ [%]	$OCR^{(2)}$ [-]	γ [kN/m^3]	λ_i [-]	$\kappa^{(3)}$ [-]	r_{si} [-]	$r_{si,min}$ [-]
3-A1-O1	1.01	10.1	0.26	0.6	4.01	17.57	0.129	0.026	270	60
10-A2-O1	3.87	28.6	2.03	0.6	1.84	16.41	0.181	0.020	295	54
19-A1-O1	7.45	50.6	1.95	0.5	1.32	15.64	0.232	0.021	350	56
22-B-1-CRS	8.86	58.9	2.08	0.4	1.32	15.68	0.233	0.034	-	-
22-B-2-CRS	8.91	59.2	1.98	0.5	1.31	15.65	0.252	0.034	219	35
26-B1-0-B1-35	10.82	69.9	2.24	0.5	1.31	15.88	0.228	0.026	153	31
26-B1-0-B1-50	10.82	69.9	2.52	0.5	1.39	15.91	0.232	0.025	419	84
28-B-11	11.65	74.5	2.59	0.5	1.17	15.98	0.221	0.026	280	56
28-B-12	11.65	74.5	1.88	0.5	1.25	15.97	0.224	0.031	334	67

(1) Taken directly from Berre (2010).

(2) The pre-consolidation pressure is determined through an average of Janbu and Cassagrande method given by Berre (2010).

(3) κ is measured at the URL part of the stress-strain curve.

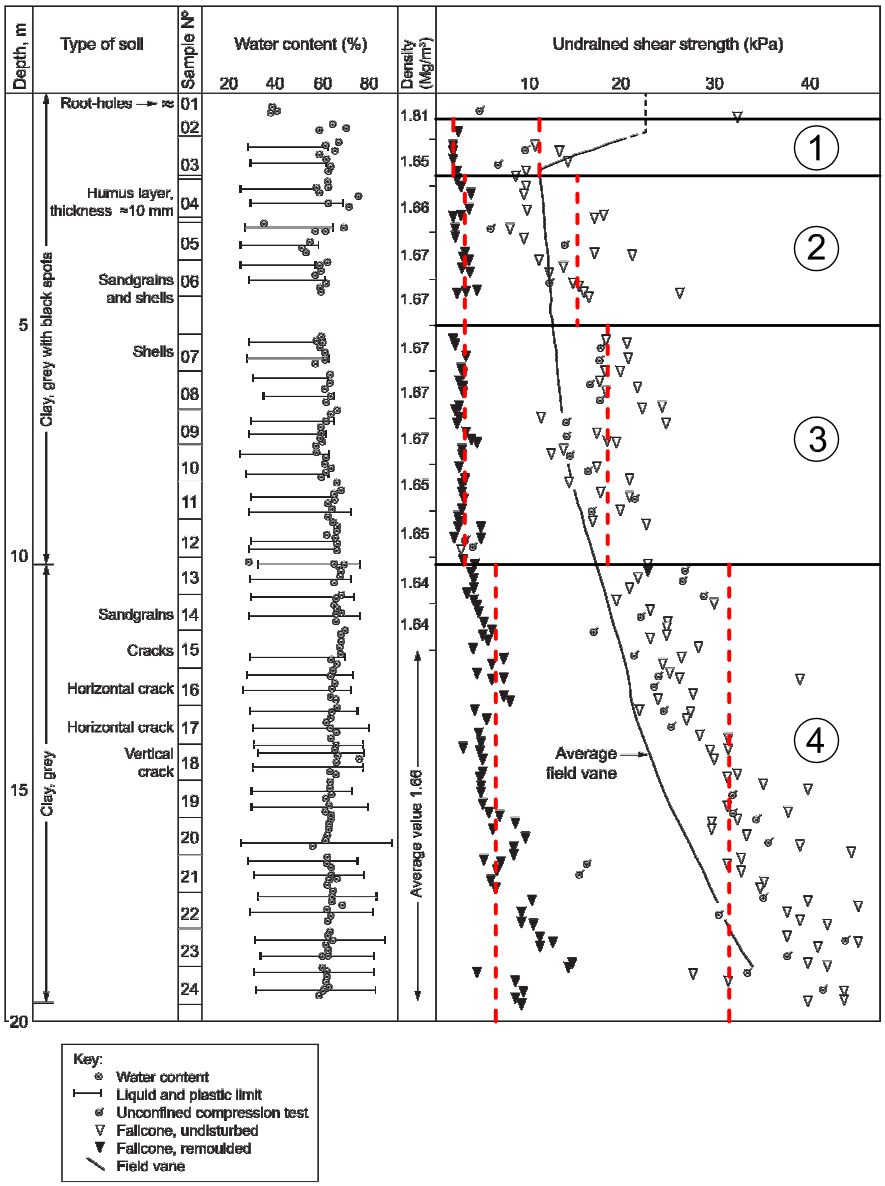

Figure 7.5: *Bore profile from a 54 mm standard tube sampler. The locations from the sampling may be seen on Figure 1.2. The bore profile is taken from (Berre, 2013). The black solid lines seperates the strata and the red dashes lines yields an average undrained remoulded and undistributed shear strength from the fallen cone in each layer.*

7.3.3 Initial Stresses

The Over Consolidation Ratio (OCR) is normally defined as the apparent yielding pressure divided with the effective in situ stresses:

$$OCR = \frac{p'_c}{\sigma'_{v0}} \tag{7.13}$$

The effective in situ stresses and the apparent yielding pressure are given by Berre (2010) for the different soil samples. The determined OCR may be seen in Table 7.5. It should be mentioned that the SCA-R utilized the OCR_τ parameter where the apparent yield surface is seen as an surface determined by an intrinsic yield surface and the structure in soil, see Section 4.4 for further details. These values is assumed to be the same. PLAXIS determines the initial horizontal stresses by the apparent lateral earth coefficient (K'_0)[10]. Utilizing a standard soil model in PLAXIS the lateral earth coefficient would automatically be determined as:

$$K'_0 = \frac{\sigma'^0_{xx}}{\sigma'^0_{yy}} = K_0^{NC} OCR - \frac{\nu_{ur}}{1-\nu_{ur}}(OCR - 1) \tag{7.14}$$

where the formulation in Eq. (7.14) may be graphically illustrated by Figure 7.6.

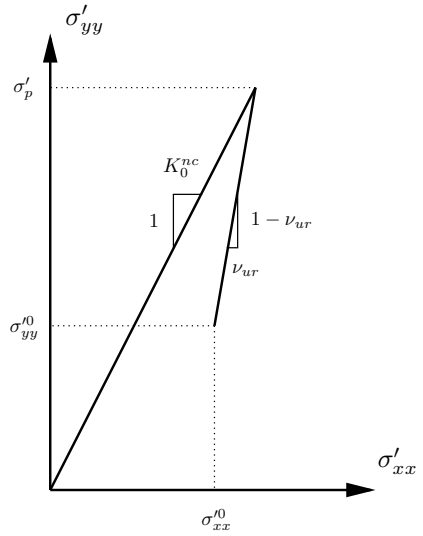

Figure 7.6: *Overconsolidation stress obtained from primary loading and unloading.*

where σ'^0_{xx} and σ'^0_{yy} are horizontal and vertical effective in situ stresses and σ_p is the yielding pressure utilizing PLAXIS notation. However, since a UDSM[11] is used the influence of OCR must be set manually. If not, PLAXIS would assume $K'_0 = K_0^{NC}$ by default settings. The magnitude of K_0^{NC} is often assumed to be determined through the frictional angle as suggested by Jaky (1944) which is also the case in PLAXIS:

$$K_0^{NC} = 1 - \sin(\varphi') \tag{7.15}$$

Utilizing the SCA-R model and default settings of K'_0 in PLAXIS it is important to know that the frictional angle controlling the magnitude of K'_0 is the frictional angle inset in the "Interfaces" window and not the frictional angle inset in the window "Parameters". The K_0^{NC} may also be determined experimentally through for instance a tri-axial compression test with a K'_0-stage. This has been done for sample **Block-19-A2-O1** and **Block-10-A3-O1** which may be seen on Figure 7.7. It may be seen that $K'_0 = 0.60$ and $K_0^{NC} = 0.53$ yielding a fiction angle of 28^o utilizing Eq. 7.15. The frictional angle from undrained tri-axial tests will be determined in Section 7.3.4.

[10] $K'_{x,0}$ in PLAXIS notation.
[11] User Defined Soil Model.

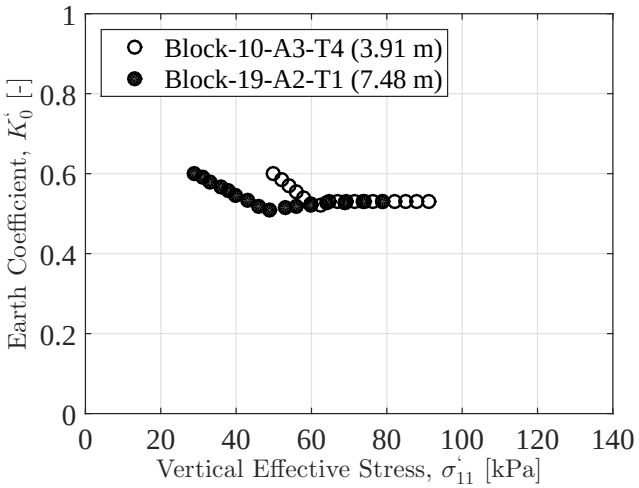

Figure 7.7: *Evolution of K_0' during CAK_0UC testing.*

No experimental data is available to determine the unloading value of Poisson's ratio. Practical experience has shown that a value of $\nu_{ur} = 0.15$ yields a good approximation (Nordal, 2014a). This value has also been suggested by Mehli (2015a) for predicting the soil response at Onsøy.

7.3.4 Strength Parameters

The strength parameter related to the SCA-R model is simply the frictional angle at critical state (φ_{cs}). The model has not been extended to incorporate the attraction (a). The frictional angle may be determined through several undrained tri-axial compression tests which are available by Berre (2010). However, the data has been modified by removing all data after passing 10% of vertical strain. It is of the Author's conviction that data beyond 10 % vertical strain is not reliable according to the unknown deformation pattern. Seven of the available tri-axial tests in compression have been used to interpret the friction angle and may be seen on Figure 7.8.

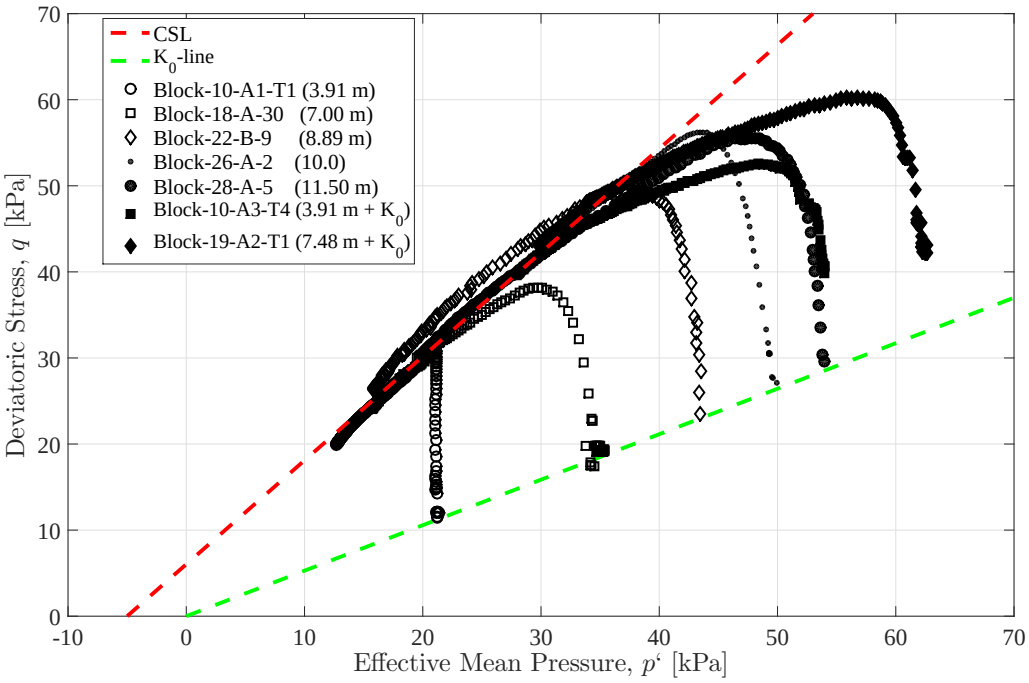

Figure 7.8: *ESP for seven tri-axial tests approaching critical state. K_0 means CAK_0UC (K_0-stage).*

A critical state line and consolidation line (K_0-line) has been drawn on Figure 7.8. Utilizing the CSL, the strength parameters may be interpreted through the inclination (M) and the intersection with the x-axis. Hence, it yields following values:

$$M_c = \frac{6\sin\varphi_{cs}}{3-\sin\varphi_{cs}} \quad \longrightarrow \quad \varphi_{cs} = 36^o \quad , \quad a = 5\,\text{kPa} \quad , \quad K_0' = 0.53 \tag{7.16}$$

Sample **block-19-A2-T1** and **block-10-A3-T4** seems to have been consolidation wrongly by deviating from the K_0-line. However, this is caused by the testing approach (CAK_0UC). Hence, the K_0' value corresponds to the value found in Section 7.3.3 where the $K_0' = 0.60$. Two undrained tri-axial tests in compression have been performed near the surface and may be seen on Figure 7.9. These tests have been omitted from Figure 7.8 due to their disturbance of the phenomena happing in or near the dry crust. It has been chosen to visualize strains beyond 10% to see if any correlation may be found.

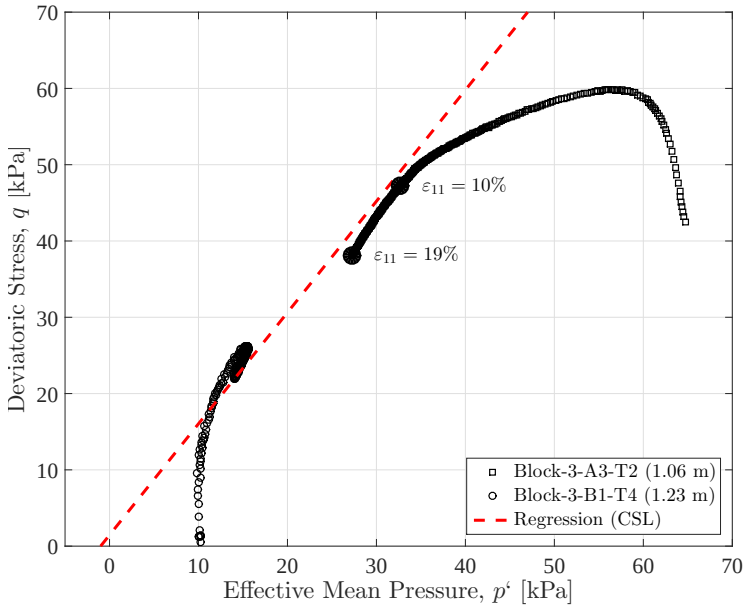

Figure 7.9: *ESP for two tri-axial tests near the surface.*

The two ESP show some relation but yields a very large frictional angle. However, the relation only occurs when showing large strains for sample **block-3-A3-T2**[12]. Furthermore, sample **block-3-A3-T2** is a CAK_0UC tri-axial test which explains the deviation from its in situ stresses. It has been chosen to use the frictional angle interpreted in Figure 7.8 since it yields a more realistic value.

In addition to the strength parameter, the elastic anisotropy parameter (α_e) may be interpreted through Janbu's pore pressure parameter (D). Thereby, the inclination of the ESP in the beginning of each test has be measured and the elastic anisotropy parameter has been determined through Eq. (3.13), see for the interpreted values Table 7.6.

Table 7.6: *Interpreted values of the elastic anisotropy parameter (α_e).*

Block		10-A1-T1	10-A3-T4	18-A-30	19-A2-T1	22-B-9	26-A-2	28-A-5
Depth	[m]	3.91	3.91	7.00	7.58	8.89	10.00	11.50
D	[-]	0.0	-0.04	-0.12	-0.16	-0.05	-0.11	-0.09
α_e	[-]	0.0	-0.07	-0.19	-0.24	-0.08	-0.17	-0.14

*Utilizing $\nu_{ur} = 0.15$.

[12] The testing for sample **block-3-B1-T4** stops at $\varepsilon_{11} = 10\%$.

7.4 Back-calculation

The next step in the procedure of selecting the final input parameters is associated to the calibration of the interpreted parameters through several back-calculation simulations of the experimental data. The performance analysis presented in Chapter 8 will mainly focus on how good the SCA-R model may predict the settlement of the embankment located at Onsøy. Therefore, the aim will be to calibrate the input parameters in a manner so that the SCA-R model may fit the CRS curves as accuracy as possible. The calibrated parameters may afterwards be utilized to simulate the tri-axial tests in the same depth as the CRS tests. Applying this approach some deviation may be expected due to the chosen calibration method with respect to the back-calculation of the tri-axial tests. However, the input parameter μ/c is mainly associated to the failure criteria and may be changed to fit the tri-axial tests as good as possible.

Back-calculation of CRS

Performing back-calculations for available soil models in PLAXIS may be done either through the oedometer option in Soil Test or through a FEM in PLAXIS. However, the SCA-R model is not capable of utilizing the oedometer option in Soil Test since the SCA-R model uses the initial stresses to generate the intrinsic pressure (p'_{mi}) where other models may use the option tab "vertical pre-consolidation stress". However, one may use the general option in Soil Test by applying the in situ stresses which results in correct pre-consolidation pressure (apparent yielding point) but initiate from a wrong stress condition (does not start from zero)[13]. Utilizing a FEM in PLAXIS would remove the limitations related to the Soil Test and the SCA-R model would be able to simulate the correct soil response in a CRS simulation.

Finite Element Model:
The boundary value problem is assembled through an axisymmetric model utilizing 15-node elements. The model dimensions are 2 x 2.5 cm referring to the height and radius, respectively. The unit weight of the sample is ignored since its influence will be negligible. The vertical boundaries are fixed against any horizontal displacement caused by axisymmetric conditions and as default in PLAXIS the bottom boundary will be fixed against any vertical and horizontal displacement. The pore water is free to dissipate through the top boundary while the other boundaries are closed for dissipation, see Figure 7.10.

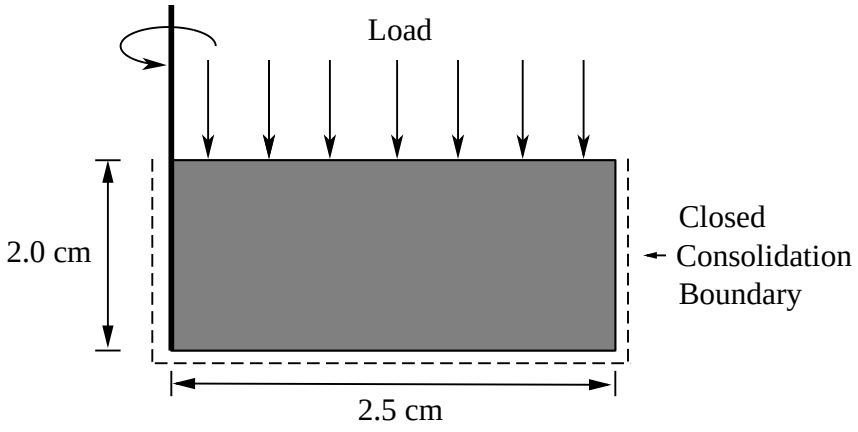

Figure 7.10: *Principal sketch of the boundary value problem setup in PLAXIS used to back-calculate the CRS oedometer tests.*

It should be mentioned that the water level is located at the bottom boundary of the sample and drained conditions are utilized.

[13] One may use the general option by initiating the test very close to zero (5-15 kPa) and by manipulation of the OCR to obtain a "correct" apparent yielding pressure.

The CRS test may be divided into four stages: 1) Loading stage, 2) Creeping stage, 3) Unloading stage, and 4) Loading stage. The procedure for the back-calculation may be assembled as:

- Create the in-situ stresses by applying a thin layer (0.01 cm) of linear elastic material above the test sample. Adjust the unit weight of the linear elastic material so it corresponds to the in situ effective stress created by the overburden soil[14]. Remember that K_0' influences the initial stress condition and should not be confused with K_0^{NC}.
- Unload the sample by changing the unit weight of the overburden material to obtain a vertical effective stress below 10 kPa.
- Reset the displacement to zero and initiate the CRS through the **described displacement** function in PLAXIS towards the creep stage.
- During the creep state, the boundary criteria must be changed to a **line load** which magnitude should correspond to the effective stresses in the soil body generated by the **described displacement**.
- The unloading phase is created by changing the magnitude of the **line load**.
- The last loading step is applied by removing the line load and activating the **described displacement** towards the final displacement.

During the whole procedure it should be remembered to adjust the time interval so it corresponds to laboratory strain rate. The calibration procedure is an iterative process since a change in material properties would change the effective stresses induced by the first described displacement. Thereby, the magnitude of the line load during the creep phase must be changed as well. Figure 7.11 shows a back-calculation curve calibrated to a laboratory curve for the sample **Block-19-A1-O1**.

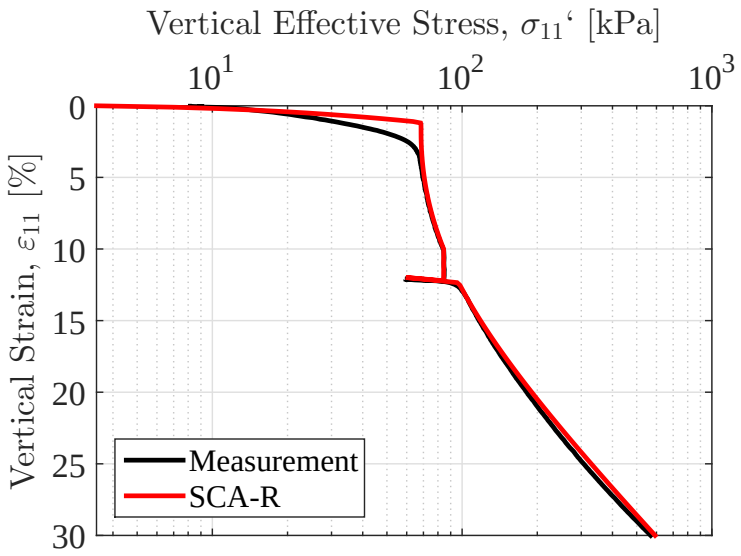

Figure 7.11: *Back-calculation of the CRS response for* ***Block-19-A1-O1****.*

From Figure 7.11 a clear deviation from the initial part of the stress-strain path approaching yielding may be observed. This is caused by the decision of fitting the curve to the unloading/reloading part instead of the initial part. The SCA-R model treats these regions by the same elastic response using the same parameter and therefore only one area can be fitted. Another reason why the unloading/reloading has been chosen is due to the fact that the sample disturbance would influence the stress-strain curve before yielding in a greater manner compared to the rest of the soil response. A more smoother bend at the apparent yielding point may be determined by increase the rate of visco-plastic strains which are associated to time step. This procedure has been done for all available oedometer data which may be seen in Appendix F.6. The utilized parameters may be seen in Table 7.7.

[14] Remember to choose a high permeability of the linear elastic material to ensure free water dissipation.

Table 7.7: *Overview of the input data used in the back-calculations of the CRS tests. The second row shows the interpreted values from laboratory tests.*

Test	Depth	$\dot{\varepsilon_{11}}^{(1)}$	$\dot{\varepsilon_{11}}^{(2)}$	λ_i	κ	e_0	OCR_τ	r_{si}	$r_{si,min}$	x	a	b
3-A1-O1	1.01 m	0.60	0.62	0.131	0.015	1.30	4.20	700	700	0	0	0
				0.129	0.026	1.28	4.10	270	60	3.50	-	-
10-A2-O1	3.87 m	0.60	0.72	0.180	0.030	1.70	1.70	550	90	5.11	12	10
				0.181	0.020	1.70	1.83	295	54	4.46	-	-
19-A1-O1	7.45 m	0.52	0.55	0.240	0.033	2.02	1.23	600	110	4.45	12	9
				0.232	0.026	1.99	1.32	350	56	5.23	-	-
22-B-1-CRS	8.86 m	0.52	0.57	0.255	0.034	1.99	1.19	575	100	4.75	12	9
				0.233	0.034	1.99	1.32	-	-	-	-	-
22-B-2-CRS	8.86 m	0.58	0.67	0.254	0.034	2.03	1.19	575	100	4.75	12	9
				0.252	0.034	2.03	1.31	219	35	5.26	-	-
26-B1-0-B1-35	10.82 m	0.51	0.53	0.219	0.034	1.95	1.18	600	104	4.77	12	10
				0.228	0.026	1.95	1.31	153	31	3.94	-	-
26-B1-0-B1-50	10.82 m	0.50	0.56	0.219	0.034	1.94	1.18	600	104	4.77	12	10
				0.232	0.025	1.94	1.39	419	84	3.99	-	-
28-B-11	11.65 m	0.34	0.58	0.220	0.027	1.88	1.01	600	110	4.45	14	9
				0.221	0.026	1.88	1.17	280	56	4.00	-	-
28-B-12	11.65 m	0.34	0.58	0.217	0.027	1.88	1.12	600	104	4.77	12	9
				0.224	0.031	1.88	1.25	334	67	3.99	-	-

(*) $K_0^{NC} = 0.53$, K_0'=0.60, $\varphi = 36^o$, $\nu_{ur} = 0.15$, $R = R_t = \mu = \alpha_e = 0.0$.
(**) Utilizing Mohr-coulomb failure criteria and RH suggested by Wheeler.
(1) First compression rate (%/h)
(2) Second compression rate (%/h)

Layer 0.6 - 2.0 m
Layer 2.0 - 5.0 m
Layer 5.0 - 10.0 m
Layer 10.0 - 25.0 m

The input parameter α_e is set to zero in these calculations. The influence of this input parameter is more clear in the $(p' : q)$-space during undrained conditions. Therefore, the parameters will be selected in Section 7.4. However, a magnitude which differs from zero will influence the stress-strain curve in the oedometer calculation. A positive α_e would reduce the inclination of κ and a negative would increase it. The effect has been investigated in Appendix F.6.1 and the effect is minimal.

It appears from Table 7.7 that most of the interpreted parameters are very similar to the input parameters used in the back-calculation. However, the intrinsic creep number deviate from this conclusion. Recalling the approximate method to interpret the r_{is} yields two reasons why this deviation occurs. Firstly, the assumption that the ratio between λ and r_s is constant is only an approximation and is not true if any organic content is present in the soil. As mentioned in Section 1.7.1 some organic content has been found down to 10 m below surface. The next reason may be caused by the r_s and the λ^*. The interpreted value of λ^* is done at a stage where the structure more or less is the same as in situ where the r_s is interpreted in a stage where some structure is destroyed. The utilized values (r_{si}) have been compared to the values used in the n-SAC model presented in (Mehli, 2015a). Comparing these values a similar magnitude may be observed.

Back-calculation of Tri-axial Tests

The back-calculations of the tri-axial tests are performed to see how accurate the SCA-R model may capture the soil response towards critical state. The same input parameters determined in the back-calculations of the CRS simulations will be used to see how good these parameters suits the soil response. However, the input parameters, μ and α_e will be chosen to obtain a better fit. The utilized input parameters may be seen in Table 7.8.

Table 7.8: *Calibrated values of μ and α_e from the tri-axial tests. Brackets are the interpreted values.*

Layer	Block	Depth	μ	α_e	
2.0 - 5.0 m	10-A1-T1	3.91 m	8.0	0.0	(0.00)
5.0 - 10.0 m	18-A-30	7.00 m	4.0	-0.12	(-0.19)
	22-B-9	8.89 m	12.0	-0.1	(-0.08)
10.0 - 25.0 m	26-A-2	10.00 m	8.0	-0.2	(-0.17)
	28-A-5	11.50 m	8.0	-0.1	(-0.14)

The back-calculations have been performed in the tri-axial option in Soil Test. To compare to the performance of the SCA-R model it has been chosen to show how accurate the Soft Soil Creep (SSC) soil model in PLAXIS may capture the response. The input parameters for the SSC have been taken from Mehli (2015a) associated to his first prediction. Figure 7.12 shows the output from the simulated undrained tri-axial test for sample **Block-18-A-30**.

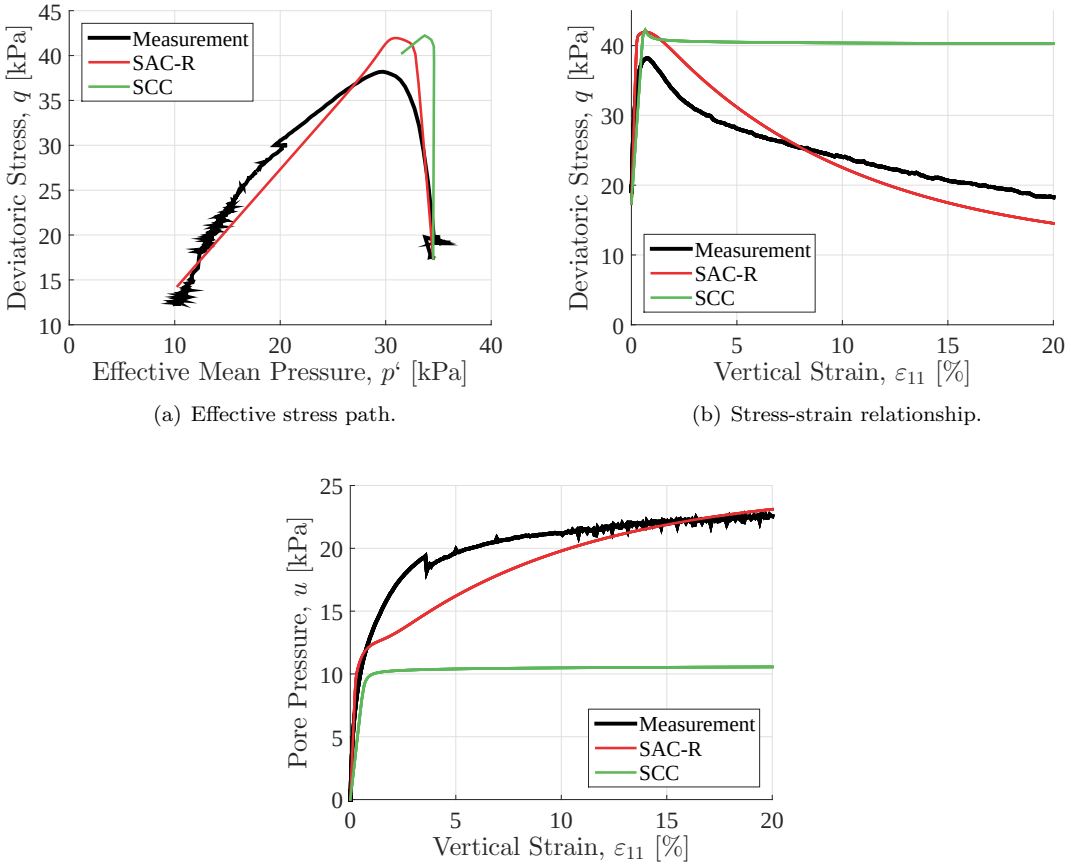

(a) Effective stress path.

(b) Stress-strain relationship.

(c) Development of pore pressure.

Figure 7.12: *Comparison of tri-axial measurements from **Block-18-A-30** to the SCA-R model and the SSC soil model. Utilizing μ = 4.0 and α_e = -0.12.*

From Figure 7.12 it can be observed that the SCA-R model predicts the soil response in a relatively accurate manner with the input parameters calibrated to the CRS laboratory curves. The SCA-R model is able to capture the inclined ESP during the first part of the ESP where the SSC only is able to simulate a vertical response, see Figure 7.12(a). Each model yields a too high apparent yielding compared to the measured values. However, this could be adjusted if the input parameters were calibrated to fit the tri-axial tests. From Figure 7.12(b) it can be seen that the SCA-R may capture the effect of destruction of structure whereas the SSC yields a response which is very inaccurate due to its limitation regarding destruction of structure. The SCA-R seems to capture the pore pressure in a fairly good manner, see Figure 7.12(c) whereas the SSC model only captures half of the maximum excess pore pressure. This procedure has been done for five tri-axial tests which may be seen in Appendix F.6.3.

It may be concluded that the SCA-R model is able to capture several of the features observed in natural soft clay with respect to the back-calculations of the CRS and tri-axial tests. This may be seen as an advantages relative to the SSC soil model which may either over- or underestimate the soil response depending on the case.

Chapter 8

Predictions and Performance

The purpose of this chapter is to present the predictions and the performance of the SCA-R model associated to the test fill located at Onsøy. A first prediction utilizing the input parameters given in Chapter 7 and a final prediction with some few modifications will be presented. The performance of the SCA-R is analysed by comparing these predictions to field measurements and similar predictions computed by other soil models. Access to similar predictions from five other soil models has been granted by Mehli (2015b) from NGI. This chapter corresponds to a combined results and discussion chapter with a discussion regarding the recovering effect in the end. It should be mentioned that the SCA-R model has been slightly modified through some early analysis which will be highlighted during this chapter.

8.1 Finite Element Model in PLAXIS

The finite element model of the embankment located at Onsøy is assembled in the same manner as suggested by Mehli (2015a). The performance of the SCA-R model will be compared to other soil models in Section 8.5. Hence, the influence from the finite element model itself should be minimal if the performance of these soil models should be compared. A detailed geometric description of the embankment and the surrounding strata, which have been used by Mehli (2015b), may be found in (Berre, 2013). The strata may be divided into four clay layers and a dry crust. Four trenches are located in the dry crust. These are man-made to speed up the dissipation of excess pore pressure. The water level is located 0.2 m below terrain, assuming constant hydrostatic head through the strata.

Only half of the embankment is modelled utilizing symmetry around the centreline of the embankment to reduce the computational time. The model is assembled by 15-noded triangular elements and assumes plane strain condition with respect to the shape of the embankment. The discretization of model is assembled through a fine mesh utilizing a higher refinement in the three upper clay layers. In total, 1629 elements (13383 nodes) are presented in the model and may be seen on Figure 8.1. The finite element model uses the default fixities in PLAXIS, i.e. fixed against any horizontal movement in the vertical boundaries and constraints for any movement in the bottom boundary. The left vertical boundary is closed for dissipation of excess pore pressure due to symmetry and the rest is left open. One could argue why the bottom boundary is left open. This discussion will not be presented here and it is chosen to open the boundary to be able to compare the different soil models, see Mehli (2015b) for further details.

The default numerical control parameters are utilized during the calculation phases. As a consequence of large deformation, it has been chosen to activate the updated mesh and water pressure function during the computation. A short discussion regarding the advantages of utilizing updated mesh and water pressure is given by Mehli (2015a) with respect to the site at Onsøy. In general, the theory behind FEM is made for small deformations. Therefore, significant deformation would violate the assumptions related to the theory used in FEM. However, an updated mesh may compensate for the significant deformation and permit to utilize the FEM for huge deformations.

Updated water pressure will consider the buoyancy effect, i.e. soil elements which move below the water level will change unit weight and the water level will follow the deformed surface.

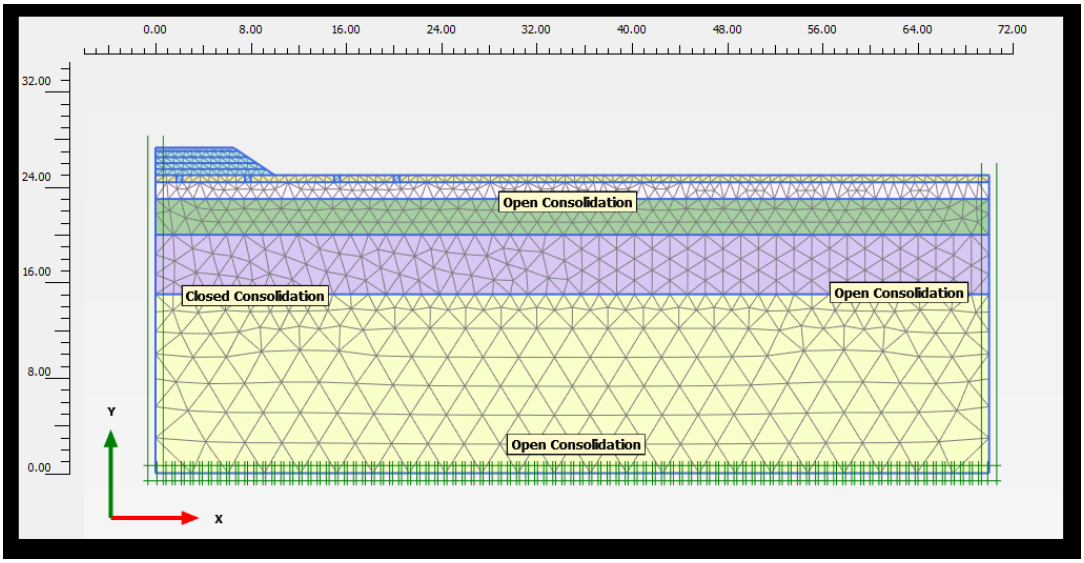

Figure 8.1: *Finite element model in PLAXIS of the embankment at Onsøy.*

8.1.1 Staged Construction

An overview of the construction phase and the associated duration of each task may be seen in Table 8.1. A "Real time" is introduced to compare the PLAXIS predictions to measured field data. The calculation types are plastic and consolidation for construction of the embankment and for the waiting phases, respectively.

Table 8.1: *Overview of the construction process and measured readings (Mehli, 2015b).*

Phase	Description	Phase duration [days]	Accumulated time [days]	Real time [days]
0	Initial phase - K_0-Procedure	-	-	22
1	Fill (0.5 m)	1	1	23
2	Wait	1	2	24
3	Fill (0.5 m)	1	3	25
4	Wait	3	6	28
5	Fill (0.5 m)	1	7	29
6	Wait	3	10	32
7	Fill (0.5 m)	1	11	33
8	Wait	2	13	35
9	Fill (0.3 m)	1	14	36
10	Wait	6	20	42
11	Wait	24	44	66
12	Wait	38	82	104
13	Wait	43	125	147
14	Wait	37	162	184
15	Wait	145	307	329
16	Wait	227	534	556
17	Wait	235	769	791
18	Wait	274	1043	1065
19	Wait	43	1086	1108
20	Wait	12	1098	1120

8.2 General Observations

Early analysis have shown that the implemented time evolution of the plastic multiplier generates visco-plastic strains in areas far away from the constructed embankment where the magnitude of visco-plastic strains should be negligible. This may be observed by analysing the development of excess pore pressure which is associated to undrained creep (undrained conditions). To avoid the unrealistic predictions, a limitation associated to the time evolution of the plastic multiplier is implemented as suggested by Grimstad and Degago (2010):

$$\dot{\lambda} = \frac{1}{\tau r_{si}} \left\langle \left(\frac{p^{eq}}{(1+x)p'_{mi}} \right)^{\zeta_i r_{si}} - \frac{\tau}{t_{\max}} \right\rangle m_{K_0^{NC}} \tag{8.1}$$

where $t_{\max}$ is a new input parameter yielding a restriction to the time evolution of the plastic multiplier through the Macaulay bracket and the reference time.

However, introducing Eq. (8.1) does not satisfy the excess pore pressure beneath the test fill with respect to the field measurements. The variation may be explained by the utilized permeability parameters k_i and c_k, which yield a dissipation pace far from field measurements, see (Berre, 2013). The permeability parameters are determined by measuring the change of pore pressure in the bottom of the oedemeter test. Hence, the permeability parameters representing the site are linked to small samples with a dimension of 20 mm x 50 mm (height and diameter, respectively) and may not capture the real permeability conditions for the site. An investigation of the ratio between the vertical and horizontal strains gives an idea of the drainage conditions associated to the constant volume during undrained conditions and may be seen on Figure 8.2.

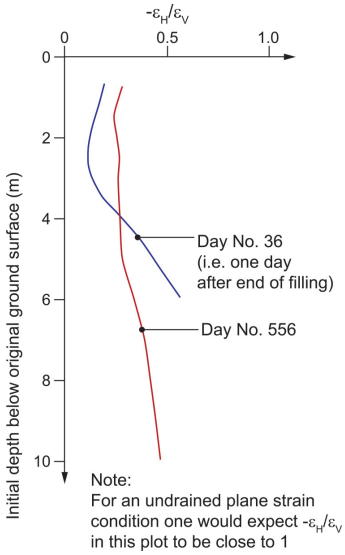

Figure 8.2: *Ratio between the horizontal and vertical strains below the centreline of the embankment from field measurements. Taken from (Berre, 2013).*

The construction of the embankment is finished at day No. 36 where undrained conditions may be expected regarding the permeability for a natural soft clay. However, it may be observed from Figure 8.2 that the upper part of the strata clearly represent a scenario where significant dissipation of pore pressure has occurred. Berre (2013) has suggested that the difference in permeability may be explained by remnants of vertical root holes which have been found in the upper part of the strata. These roots may have a large influence associated to field measurements and minor influence in a CRS test. To compensate for this phenomenon the permeability parameters suggested by Mehli (2015a) will be utilized in the first prediction.

8.3 First Prediction

The dry crust (0.00 - 0.60 m) differs from the remaining part of the strata. This is a consequence of the distance to the ground surface. The dry crust is affected by temperature fluctuations and other natural phenomena which lead to a weathering and hardening effect on the soil. Thereby, the main features associated to natural soft clay, i.e. structure, anisotropy, and creep may have minor influence to the mechanical soil response. Therefore, the soil model for the dry crust is chosen to be the Soft Soil model and utilizing the soil properties given Table 8.2 as suggested by Mehli (2015a).

Table 8.2: *Input data for material layer modelled with Soft Soil.*

Dry crust	γ [kN/m^3]	e_0 [-]	λ^* [-]	κ^* [-]	μ^* [-]	$k_y \cdot 10^{-4}$ [m/day]	$k_x \cdot 10^{-4}$ [m/day]	c_k [-]	OCR [-]	POP [kPa]
0.0 - 0.6 m	17.80	1.2	0.065	0.005	-	100.0	100.0	1	1.0	170

$\varphi = 28^o$, $c'_{\text{ref}} = 3$ kPa, $\psi' = 0^o$, $\nu_{ur} = 0.15$, $K_0^{\text{NC}} = 0.55$, and $K'_{0,x}$ = Auto.

The embankment and the trenches consist of the same material which may be classified as sand. The soil model for the fill material is chosen to be Mohr-Coulomb and the properties may be seen in Table 8.3 which have been suggested by Mehli (2015a).

Table 8.3: *Input data for material layers modelled with Mohr-Coulomb.*

Sand fill	γ [kN/m^3]	e_0 [-]	φ' [^{o}]	c'_{ref} [kPa]	$k_y \cdot 10^{-4}$ [m/day]	$k_x \cdot 10^{-4}$ [m/day]	$c_k \cdot 10^{15}$ [-]	E' [kPa]	ν' [-]	$K'_{0,x}$ [-]
	20.30	0.50	39.0	0.01	100,000	100,000	10	20 000	0.30	Auto

The remaining part of the strata is simulated through the SCA-R model. The soil parameters for the first prediction may be seen in Table 8.4 which is assembled through the information given in Chapter 7, see Table 7.1. The input parameters are chosen as an overall judgement for the interpreted values from the laboratory tests and the values used in the back calculations. Hence, the magnitude of OCR_τ in layer 2 (2.0 - 5.0 m) is relatively higher than the sample taken at level 3.91 m. This is caused by the assumption that the upper part of the layer is affected by the magnitude of OCR_τ associated to the sample taken at level 1.01 m. This procedure has been performed when selecting all the input parameters through linear interpolation.

Table 8.4: *First prediction of input data for material layers modelled with SCA-R.*

Layer	γ [kN/m^3]	λ_i [-]	κ [-]	e_0 [-]	OCR_τ [-]	r_{si} [-]	$r_{si,min}$ [-]	x [-]	a [-]	b [-]	α_e [-]	$k_x \cdot 10^{-4}$ [m/day]	$k_y \cdot 10^{-4}$ [m/day]	c_k [-]
0.6 - 2.0 m	17.80	0.130	0.025	1.29	4.00	660	150	3.40	12	9	0.00	20.0	15.0	0.50
2.0 - 5.0 m	15.60	0.180	0.030	1.70	2.10	550	90	5.11	12	9	-0.10	20.0	15.0	0.50
5.0 - 10.0 m	15.60	0.240	0.030	2.00	1.40	600	100	5.00	12	9	-0.12	2.0	1.5	1.00
10.0 - 25.0 m	16.00	0.220	0.030	1.90	1.30	900	150	5.00	12	9	-0.15	0.5	0.03	1.00

$K_0^{NC} = 0.53$, $K'_{0,x} = 0.60$, $t_{\max} = 300.000$ days, $\tau = 1$ day, $\nu_{ur} = 0.15$, $\varphi_{cs} = 36^o$, $\mu = R = R_t = 0$, and MC failure criteria.

It may be observed that the evolution of the anisotropy (μ) is set to zero caused by the high friction angle which violates the criteria from the rotational hardening suggested by Wheeler et al. (2003). The two other rotational hardening rules could have be activated but it has been chosen to investigate the performance of the SCA-R model without any evolution of anisotropy. The recovering of the structure (R) and its pace (R_t) are set to zero. It has not been possible to estimate the magnitude of these parameters. Hence, it has been chosen not to take the recovering of structure into account during the first prediction. However, if the predictions requires a reduction in creep strains they may be activated.

The settlement just beneath the center of the embankment may be seen on Figure 8.3(a). The first prediction seems to fit the measured field data in an acceptable manner. However, a tendency of undershooting the settlement in the early primary consolidation and overshooting the settlement for the long term may be observed. The settlement is directly coupled to the excess pore pressure and the settlement should be analysed simultaneously with the excess pore pressure. The undershooting may be explained by the deviation of the excess pore pressure just after finishing the embankment (day No. 36). After construction the model estimates a too high pore pressure with respect to the field measurements, see Figure 8.3(b). The overshooting of settlement may again be associated to the dissipation of pore pressure where the model estimates a smaller magnitude of the excess pore pressure with respect to the field measurements. Hence, more water has been pressed out of the clay resulting in higher deformation.

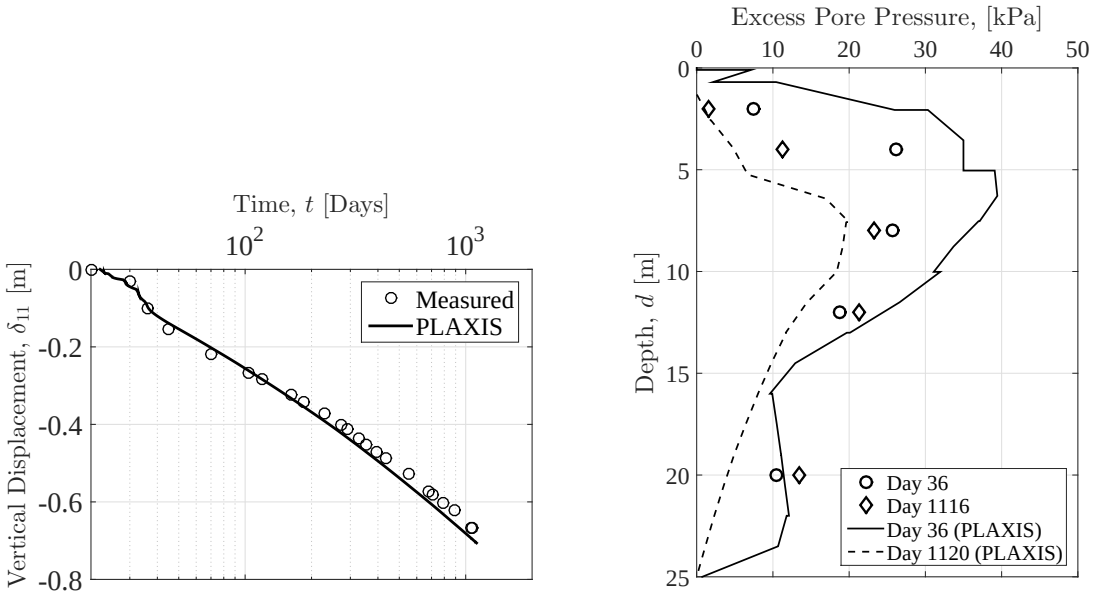

(a) Settlement just beneath the center.

(b) Excess pore pressure at the centreline.

Figure 8.3: *Measurements and predictions of the embankment (SCA-R: First prediction).*

As observed in Figure 8.3(b), the PLAXIS prediction and the measured field data for the long term deviates with four days (1116 vs. 1120). The performance of the SCA-R model will be compared to other soil models in Section 8.5. These soil models compares their predictions of day No. 1120 to the field measurements of day No. 1116. To be consistent, the same procedure is used. The deviation of four days is assumed to be insignificant for the long term.

The horizontal displacement 5.0 m away from the centreline of the embankment may be seen on Figure 8.4(a). Notice the inexplicable difference in field measurements between East and West side of the embankment, see (Berre, 2013) for further details. The SCA-R model has trouble to capture the horizontal deformation in the layers 2.0 - 14.0 m for the short term. This may be associated to the undrained deformation where the undrained stiffness is too small. However, another effect could be associated to the relative permeable layers in the upper part of the strata. Hence, the condition would deviate from the undrained condition and the volume will not be constant which

may reduce the horizontal displacement. The long term predictions seems to capture a more correct tendency in the upper part of the strata. In general for the short and long term, the model overshoots the horizontal deformation in the lower part of the strata (from 10.0 m and below). This is caused by the effect of small stiffness which is not incorporated in the SCA-R model. The vertical strain at the centreline may be seen on Figure 8.4(b).

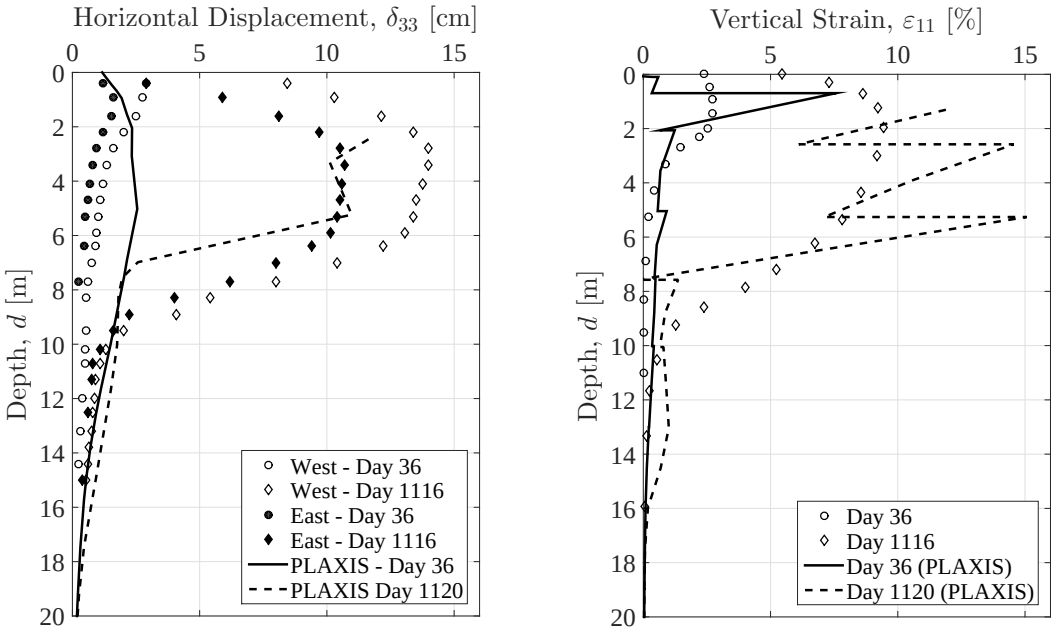

(a) Horizontal displacement 5.0 m from the centreline.

(b) Vertical strain at the centreline.

Figure 8.4: *Measurements of the embankment (SCA-R: First prediction).*

The vertical strain shows a tendency of overestimating the field measurements which may be caused by the assumption of plain strains in PLAXIS. In reality, the embankment cannot be explained by plane strains and would reduce the vertical strains if deformation into the plane was allowed. The sudden jump in the vertical strain for the short term may be explained by the stiffness in the upper layers. The restrained stiffness modulus may be determined as:

$$M = m\sigma'_v \tag{8.2}$$

where m is the secant modulus and σ'_v is the vertical effective stress. The upper part of the layer would have a lower stiffness yielding a higher strain. Another explanation could be the discretization of the finite element model. Utilizing a too coarse mesh yields predictions which are very sensitive to refinement. A mesh analysis will be given in Section 8.8 for the predictions associated to the SCA-R model.

Each plot in Figure 8.4 shows a curious tendency for the long term (day No. 1120) regarding the PLAXIS predictions by missing the top part of the data. The plotted data is taken from a vertical cross section through a chosen x-coordinate in the output window in PLAXIS for both the short and long term. The plotted data should initiate from approximately 0.7 meter below the initial surface as a result of the settlement but for some reason it initiates lower. This is most likely caused by an error in the plotting approach in PLAXIS when utilizing the updating mesh. It is concluded that the predicted data at the given level is correct and the missing upper part is caused by some communication issue internal in PLAXIS. The same tendency may be observed for standard soil models in PLAXIS and the tendency is therefore not associated to the SCA-R model, see Section 8.5.

8.4 Final Prediction

The input parameters may be calibrated to obtain a better fit of the field measurements by analysing the output of the first prediction. The calibration procedure may be relatively complex since many input parameters are linked together and an output value (for instance, settlement) may be reduced or increased though several input parameters. Hence, to obtain a clear and relatively simple optimization process, guidelines should be assembled through the knowledge of the limitations of the soil model along with the coupling between the input parameters.

8.4.1 Sensitivity Analysis of Creep

The purpose of the optimization process is to adjust the input parameters in order to minimize the difference between the field measurements and the predictions from PLAXIS without violating the input parameters or the soil model. It has been shown that the visco-plastic strains have a significant influence for the long term with respect to the deformation and excess pore pressure. Hence, the scope of this section is to investigate the sensitivity of the creep strains to obtain a better understanding of the development of creep strains. Furthermore, to analyse the contribution from each input parameter to perform at better optimization process. The development of creep is mainly controlled by three parameters, OCR_τ, r_{si} and the internal irrecoverable compressibility (ζ_i) which is defined as:

$$\zeta_i = \frac{\lambda_i - \kappa}{1 + e_0} \tag{8.3}$$

A sensitivity analysis may be performed by keeping two parameters constant and the last parameter variable. Hence, the sensitivity of visco-plastic strains may be associated to one single parameter in each analysis. Figure 8.5 shows a sensitivity analysis related to the time evolution of the plastic multiplier for the three parameters and the input parameters may be seen in Table 8.5.

Table 8.5: *Standard input parameters used in the sensitivity analysis for creep development.*

		1. Analysis	2. Analysis	3. Analysis
ζ_i	[-]	0.067	0.067	Variable
OCR	[-]	1.10	Variable	1.10
r_{is}	[-]	Variable	300	300

*In all analysis the reference is set to $\tau = 1$ day.

**$\zeta_i = 0.067$ (Typical value).

It may be observed from Figure 8.5(a) that the development of visco-plastic strains are very sensitive to changes in OCR_τ. A minor increase in OCR_τ would cause a major reduction in creep rate, see Figure 8.5(b). The intrinsic creep number may be defined as the second most dominant input parameter with respect to the sensitiveness, see Figure 8.5(a). The third parameter (ζ_i) may be a bit complex to analyse. Figure 8.5(c) indicates that the time evolution of the plastic multiplier is less sensitive to changes in ζ_i which may be changed by either, λ, κ or e_0. However, a change in each of these parameters would influence the effective stresses. Hence, a change may indirectly influence the development of visco-plastic strains which cannot be seen from Figure 8.5(c). The contribution of this parameter is still seen as less compared to the others.

It should be mentioned that the sensitivity analysis does not incorporate the destruction of the structure (x). The evolution of the plastic multiplier with time would destroy the structure and change the magnitude of OCR_τ through the change in x by:

$$\frac{1}{OCR_\tau} = \frac{p^{eq}}{(1 + x)p'_{mi}} \tag{8.4}$$

Hence, the analysis where the OCR_τ is kept constant is only true for cases where no destruction occurs. Still, the sensitivity analysis gives an idea of the input parameters related to development

of visco-plastic strains. It should be remembered that changes in ζ_i, OCR_τ and r_{is} would yield a change in the initial deformation during the construction of the embankment.

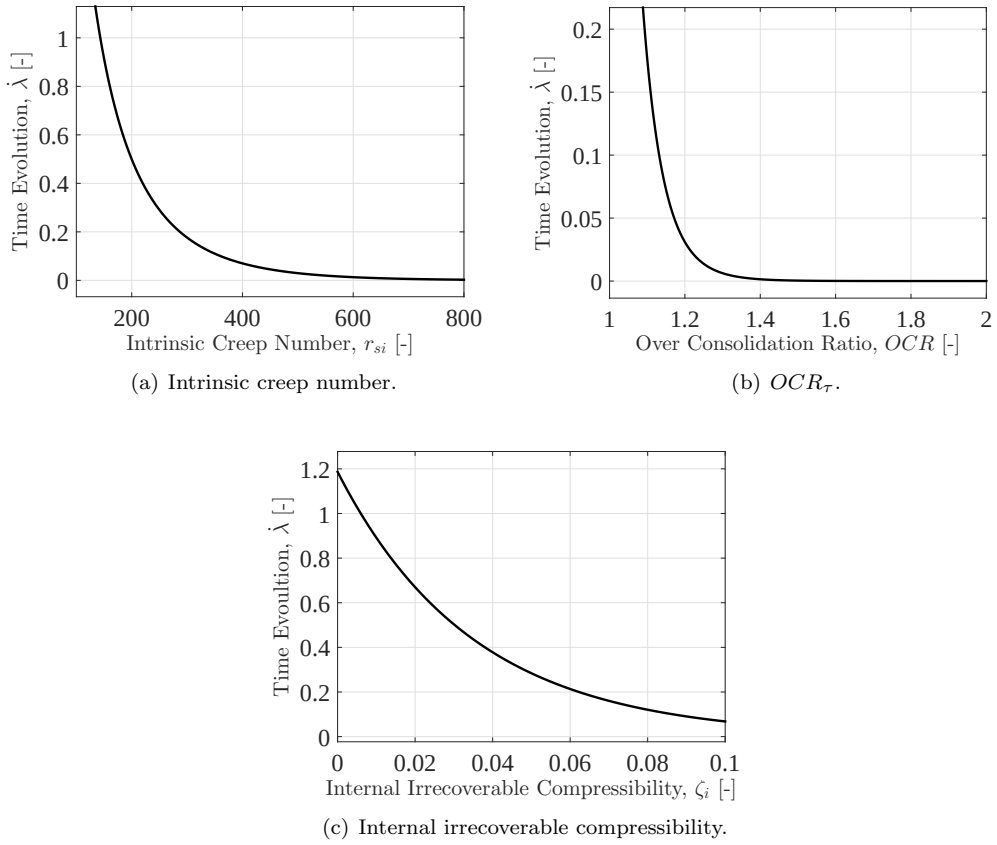

(a) Intrinsic creep number.

(b) OCR_τ.

(c) Internal irrecoverable compressibility.

Figure 8.5: *Sensitivity analysis of the input parameters related to time evolution of the plastic multiplier. The utilized parameters may be seen in Table 8.5*

8.4.2 Modifications

It has been chosen to optimize the input parameters by fitting the settlement just beneath the center of the embankment. Recalling that the settlement is directly coupled to the excess pore pressure and should be taken into consideration when fitting the settlement. The dissipation of the excess pore pressure is determined by the permeability, its evolution during volume changes and the boundary conditions (drainage path). Furthermore, undrained creep strains contribute to excess pore pressure during undrained conditions. The first modification is the vertical permeability which is increased in the two top layers to reduce the excess pore pressure after the construction phase of the embankment. In addition, the evolution in permeability is increased by reducing the value of c_k in the two top layers. Hence, a decrease of the excess pore pressure in the initial part and increase at the long term should be expected and may be seen on Figure 8.10(a). In addition, it has been chosen to close the bottom boundary for dissipation of pore water caused by the Author comprehension of reality.

The stress history and creep rate are controlled by the value of OCR_τ in each layer. By recalling the definition of OCR_τ, the layer would feel a different overburden stress throughout the layer. The top part would feel a lower overburden compared to the bottom part, see Figure 8.6. Therefore, an average value of OCR_τ has been utilized for each layer in the first prediction. As a consequence, the top part of each layer would experience a lower apparent yielding stress and the bottom part would be more resistant to creep strains. Hence, the uneven distribution of overburden stress may be handled by defining the overconsolidation through the overconsolidation pressure (POP). The difference between the OCR_τ formulation and the POP formulation may be seen in Figure 8.6.

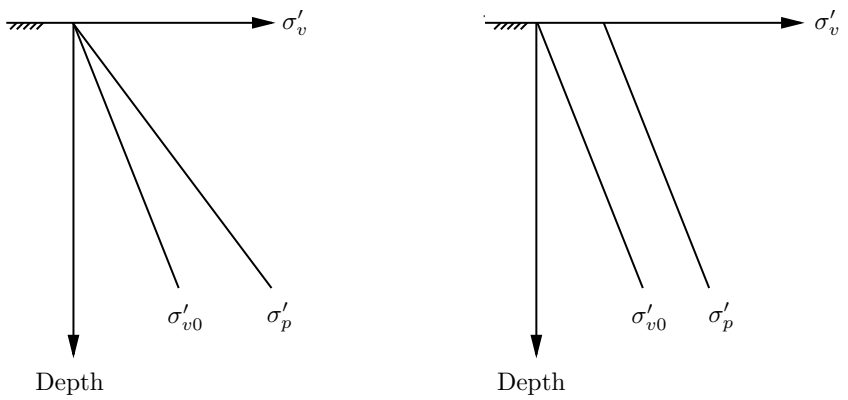

Figure 8.6: *Definition of OCR_τ and POP.*

Extending the SCA-R model to incorporate POP requires some simple modifications in the code related to the definition of the intrinsic effective pressure. The modification is performed in the initializing task where following changes are made:

$$p'_{mi} = \frac{p^{eq} OCR_\tau}{1+x} \qquad \longrightarrow \qquad p'_{mi} = \frac{p^{eq} OCR_\tau + POP}{1+x} \tag{8.5}$$

When using sing POP the SCA-R model would automatically set $OCR = 1.0$. The stress history for the three upper layers (0.6 - 10.0 m) is changed from OCR to POP to obtain a more even distribution. A $POP = 20$ kPa has been chosen to account for the previous overburden stress or the consequence of creep. However, the bottom layer would still utilize the OCR value to insure that no creep strains would occur in this layer. The removal of unwanted creep strains are ensured through the limitations incorporated by Eq. 8.1. A graphical illustration of this effect (changing the three upper layers from OCR to POP) may be seen in the magnitude of the plastic multiplier, see Figure 8.14(b) and Figure 8.17.

The model does not take small stiffness into account. This may be compromised by increasing the elastic stiffness in regions where the effect of small stiffness is significant. Hence, the value of κ is reduced in the bottom layer as an attempt to manipulate the model to take some kind of small stiffness into account. Thereby, the horizontal displacement should be reduced. In addition, the value of κ is increased in the top layer (0.6 - 2.0 m) to increase the horizontal displacement. These effects may be seen on Figure 8.9(a). Another method to control the horizontal displacement directly would be to change the value of K_0^{NC}, however it has been chosen to keep this value constant since it also would affect the amount of creep which is a function of the stress condition.

An early analysis of the first prediction states that the recovering effect would cause an unwanted effect. The recovering of structure would influence the creep strains by slowing it down at the long term. By analysing Figure 8.3(a) it may be concluded that no further reduction in creep strains are necessary if the excess pore pressure is corrected. Hence, the recovering of structure is still kept equal to zero during the final prediction as well as the evolution of anisotropy.

The κ value in layer (2.0 - 5.0 m) has been changed to fit the settlement just beneath the embankment. the parameters r_{si} and $r_{si,min}$ are changed in layer 3 to obtain the same amount of initial structure as the layer above. These modifications complete the calibration from the first to the final prediction. The chosen procedure justifies one way of calibrating the model and other parameters may be adjusted to fit the predictions to the field measurements. Another method to adjust the deformation may be done through the magnitude of λ_i. Increasing λ_i would contribute to a higher initial deformation but cause a reduction of creep strains. A sensitive analysis of the λ_i related to creep strains may be found in Section 8.4.1. The new input parameters may be seen in Table 8.6.

Table 8.6: *Final prediction of input data for material layers modelled with SCA-R. Number in brackets shows earlier values.*

Layer	λ_i [-]	κ [-]	OCR_τ [-]	POP [kPa]	r_{si} [-]	$r_{si,min}$ [-]	x [-]	$k_x \cdot 10^{-4}$ [m/day]	$k_y \cdot 10^{-4}$ [m/day]	c_k [-]
0.6 - 2.0 m	0.130	0.035 (0.025)	1.00 (4.00)	20.0	660	150	3.40	20.0	30.0 (15.0)	0.19 (0.50)
2.0 - 5.0 m	0.180	0.035 (0.030)	1.00 (2.10)	20.0	550	90	5.11	20.0	30.0 (15.0)	0.19 (0.50)
5.0 - 10.0 m	0.240	0.030	1.00 (1.40)	20.0	550 (600)	90 (100)	5.11	2.0	1.5	1.00
10.0 - 25.0 m	0.220	0.02 (0.030)	1.30	0.0	900	150	5.00	0.5	0.03	1.00

*$K_0^{NC} = 0.53$, $K'_{0,x} = 0.60$, $t_{\max} = 300.000$ days, $\tau = 1$ day, $\nu_{ur} = 0.15$, $\varphi_{cs} = 36^o$, and $R = R_t = \mu = 0.0$.

**Notice, the magnitude of e_0, a, b and α_e is the same and the failure criteria, see Table 8.4.

The following three subsections contain the final predictions of the SCA-R model: 1) Settlement and displacement 2) Pore pressure 3) State parameters.

8.4.3 Settlement and Displacement

The settlement just beneath the center of the embankment may be seen on Figure 8.7, and the surface settlement may be seen on Figure 8.8.

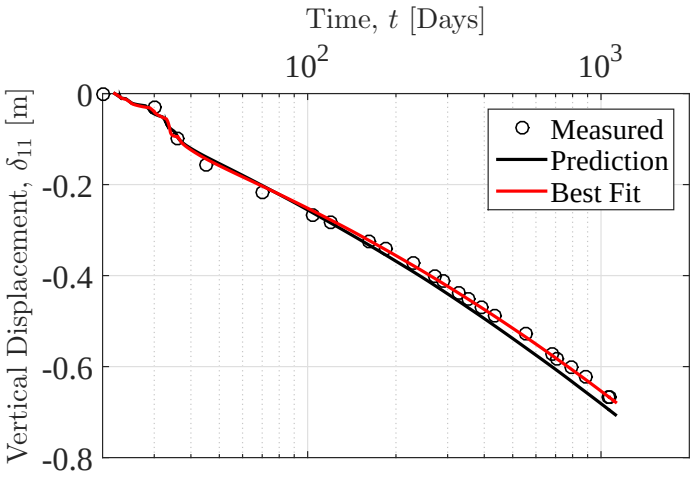

Figure 8.7: *Estimated settlement just beneath the center of the embankment (SCA-R: Best-fit).*

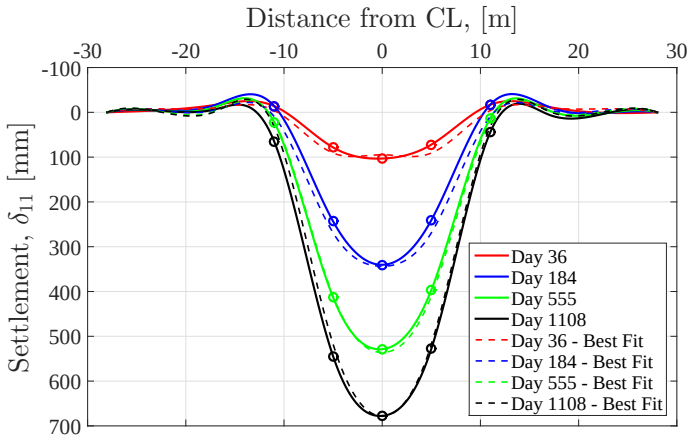

Figure 8.8: *Estimated surface settlement of the embankment (SCA-R model best-fit).*

The modified input parameters yield a prediction of the settlement just beneath the center of the embankment which is very similar to the field measurements. Hence, through some simple corrections the SCA-R model may estimate the settlement in a relatively accurate manner. A slight deviation from the field measurements may still be observed between 45 to 80 days. However, the excess pore pressure is too high after the construction and further modifications of permeability parameters could reduce this deviation, see Section 8.4.4. The predictions of the surface settlement fits fairly good with respect to the field measurements. Notice that the dots symbolize measured values.

Figure 8.9(a) shows the horizontal displacement 5.0 m away from the centreline and Figure 8.9(b) shows the vertical strain at the centreline of the embankment. The modifications of κ to adjust for the missing capacity of the small stiffness seems to give better estimate of the horizontal displacement in the bottom layer (10.0 - 25.0 m) for the short and long term. Increasing κ in the top layer (0.0 - 2.0 m) also yields a better fit since it is location between the East and West measurements. However, the layer (2.0 - 5.0 m) yields a slightly worse estimate which could be changed through another modification of κ.

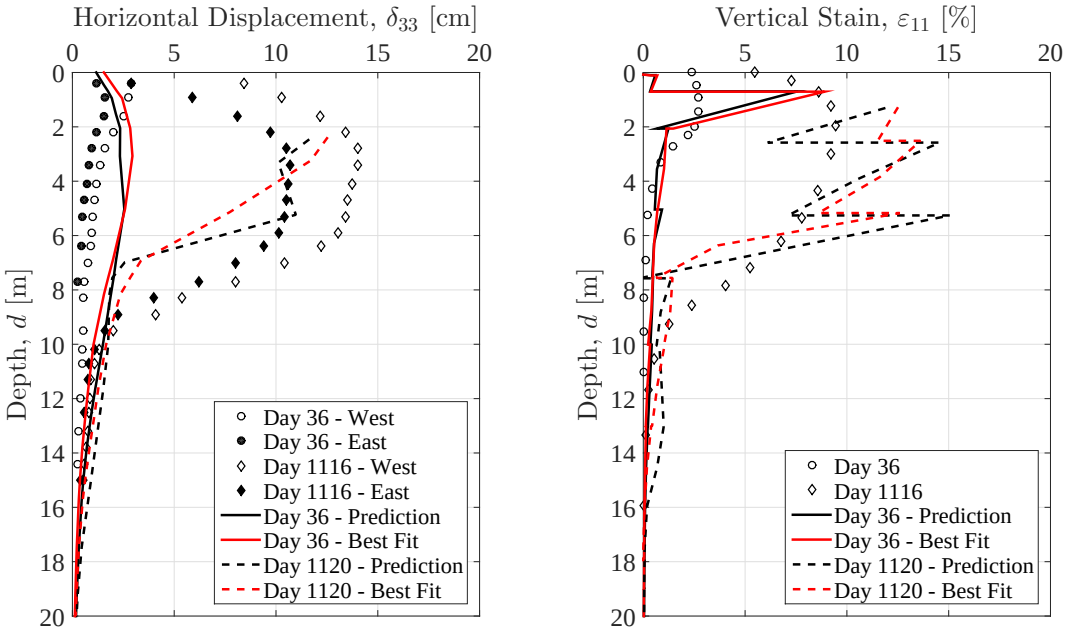

(a) Horizontal displacement 5.0 m from the centreline.

(b) Vertical strain at the centreline.

Figure 8.9: *Estimated displacement and strain of the embankment (SCA-R: Best-fit).*

The modifications only cause slight changes for the vertical strain for the short term. However, the sudden jumps going from one soil layer to another soil layer are reduced for the long term. This is caused by the change from OCR_τ to POP which yields a more even distribution of creep strains. Figure 8.14(b) and Figure 8.17 show the magnitude of the plastic multiplier at day No. 1120 for the first and final prediction. Recalling that the plastic multiplier is associated to visco-plastic strain it may be concluded that the final prediction yields a more even distribution of the magnitude of the visco-plastic strains compared to the first prediction.

8.4.4 Pore Pressure

The excess pore pressure at the centreline of the embankment may be seen on Figure 8.10(a). Through the modifications of the permeability parameters and the change of how to initialize the stress history, a slightly better prediction in the short term is obtained. The model still overshoots in the upper part (0.0 - 8.0 m) of the strata which may be associated to undershooting in settlements. The long time prediction yields a fairly good estimate which is very close to the measured field data. The effect of changing the bottom boundary from open to closed may be discussed. It most likely has an insignificant impact in the short term. However, in the long term it may have large influence. Utilizing the new input parameters the excess pore pressure in the bottom part of the strata is captured quite accurately and the decision of closing the boundary is assumed to be more realistic.

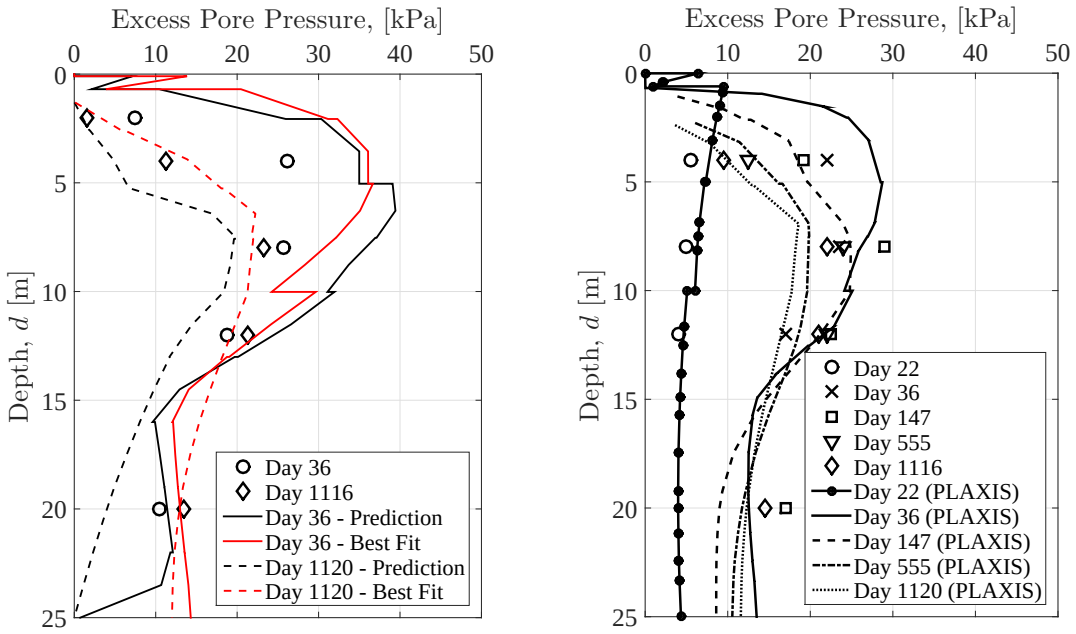

(a) At the centreline.

(b) 5.0 meters from the centreline.

Figure 8.10: *Estimated excess pore pressure of the embankment (SCA-R: Best-fit).*

The excess pore pressure 5.0 m away from the centreline may be seen on Figure 8.10(b). Again it may be concluded that the SCA-R model overshoots the pore pressure at this location of the short term. However, the general pattern of the pore pressure distribution seems to follow the field measurements. An interesting observation of the field measurements are related to the maximum excess pore pressure which is measured for day No. 147 at a depth of 8.0 m. This is most likely caused by undrained creep strains and it would have been interesting to have more observations near this time. Another tendency which should be observed is how measurements behave in each layer. The maximum excess pore pressure and the reducing tendency may be listed as:

4 m	:	36 day	$\longrightarrow$	147 day	$\longrightarrow$	555 day	$\longrightarrow$	1116 day
8 m	:	147 day	$\longrightarrow$	555 day	$\longrightarrow$	36 day	$\longrightarrow$	1116 day
12 m	:	147 day	$\longrightarrow$	555 day	$\longrightarrow$	36 day	$\longrightarrow$	1116 day

This observation may justify the very permeable layer in the upper part of the strata since the excess pore pressure generated by creep strains is dissipated and the maximum excess pore pressure is measured just after construction of the embankment in contrast to the other layers. Figure 8.11 shows the excess pore pressure 8.0 m below the surface. It can be observed that the model shows the correct pattern but deviates from the field measurements.

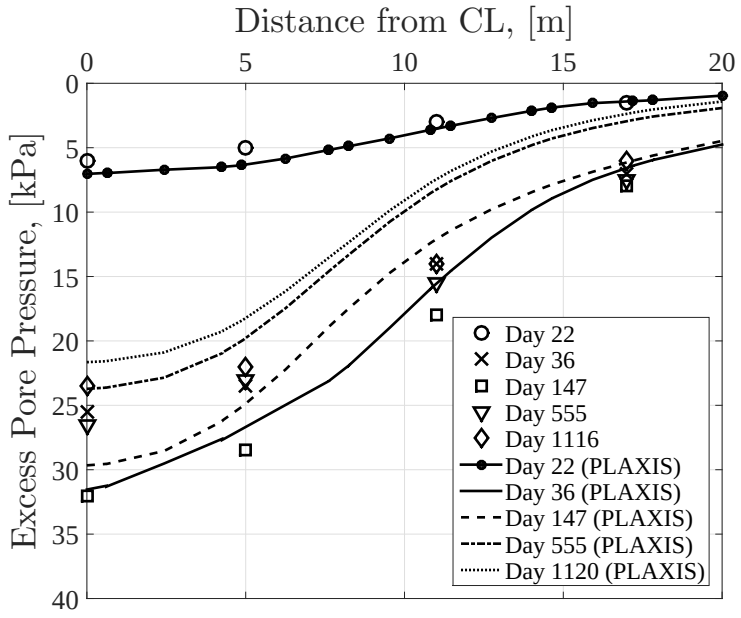

Figure 8.11: *Excess pore pressure 8.0 meters below the ground surface (SCA-R: Best-fit).*

Figure 8.12 and Figure 8.13 shows the excess pore pressure distribution for the whole finite element model for day No. 36 and No. 1200, respectively. These plots indicate a reasonable distribution of the excess pore pressure with a concentration a few meters below the center of the embankment which is moving down with time.

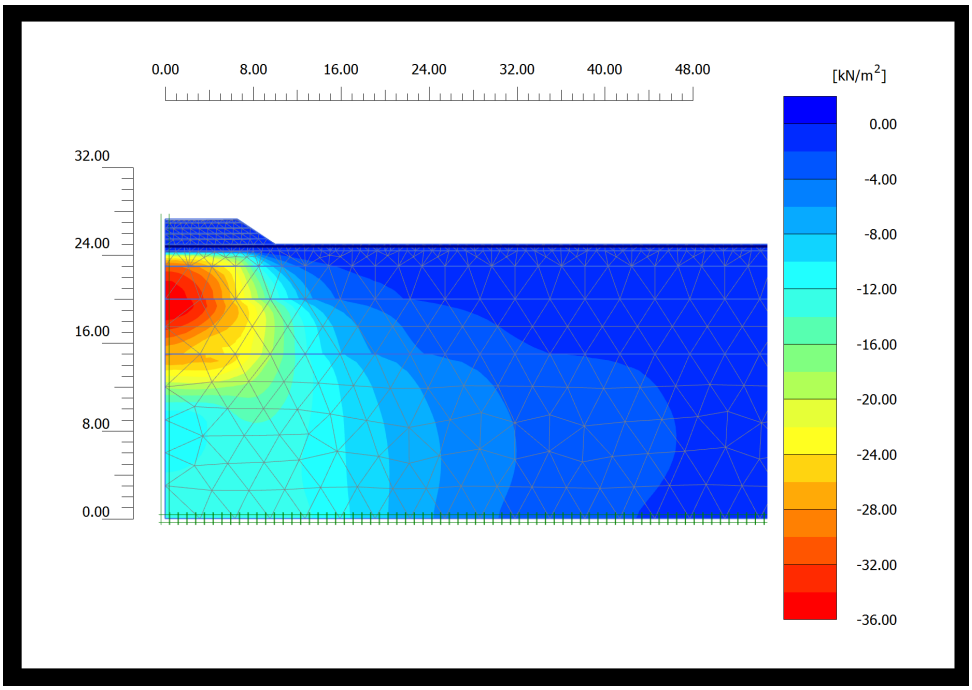

Figure 8.12: *Excess pore pressure distribution at day No. 36 (SCA-R: Best-fit).*

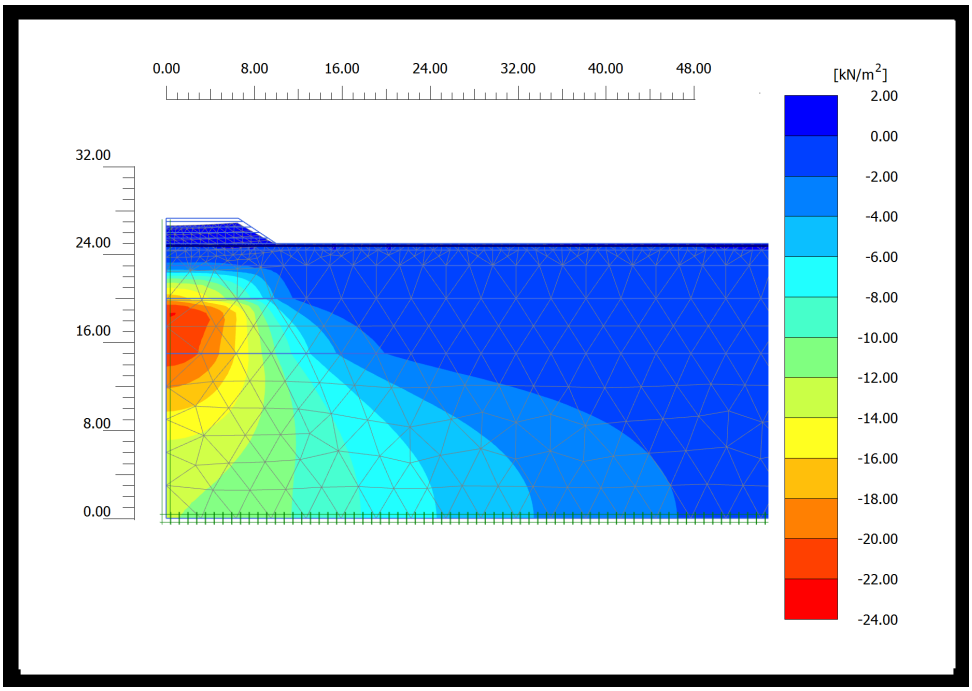

Figure 8.13: *Excess pore pressure distribution at day No. 1220 (SCA-R: Best-fit).*

8.4.5 State Parameters

The state parameters[1] are plotted as 2-D plots in the area of interest for day No. 36 and day No. 1120. Figure 8.14 shows the evolution of the plastic multiplier, Figure 8.15 the destruction of the structure and Figure 8.16 the increase in the intrinsic pressure.

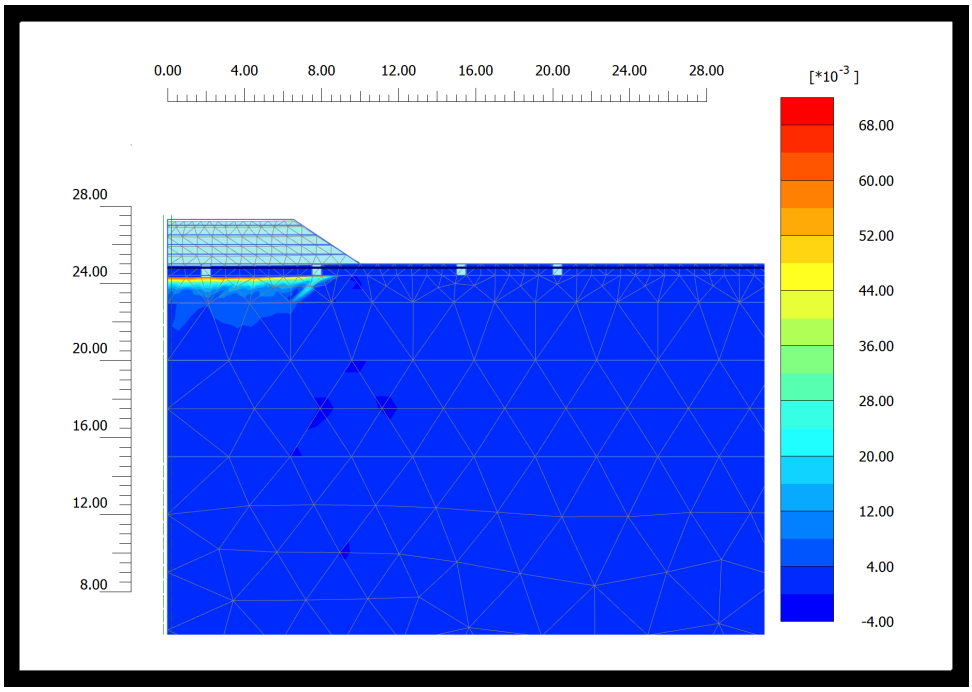

(a) Day No. 36

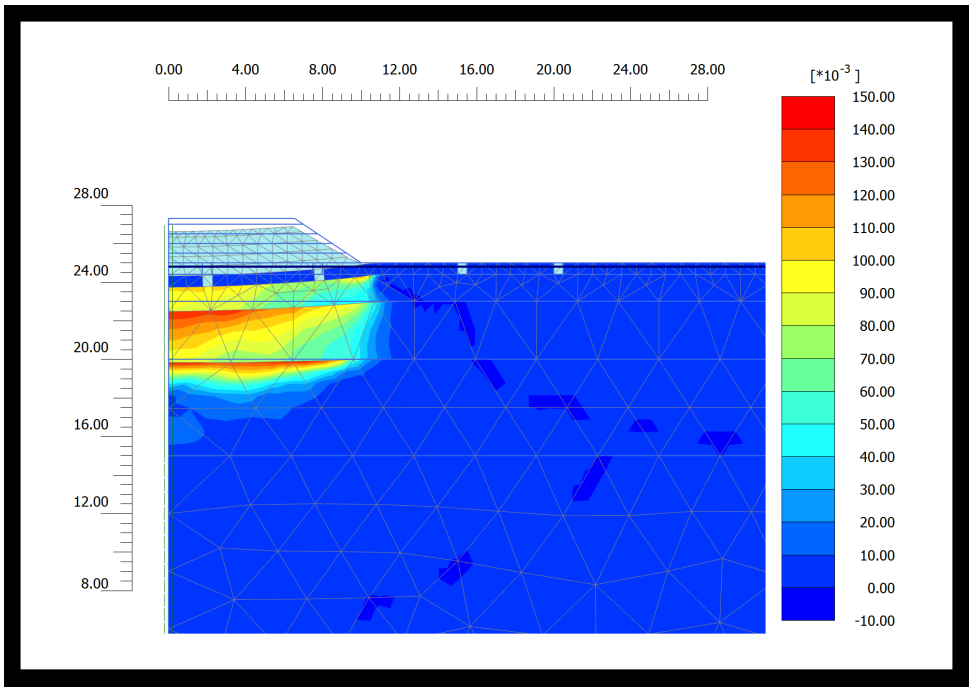

(b) Day No. 1120

Figure 8.14: *Evolution of plastic multiplier (dλ) - (SCA-R: Best-fit).*

[1] The state parameters related to the fabric are left out since the evolution is set to zero.

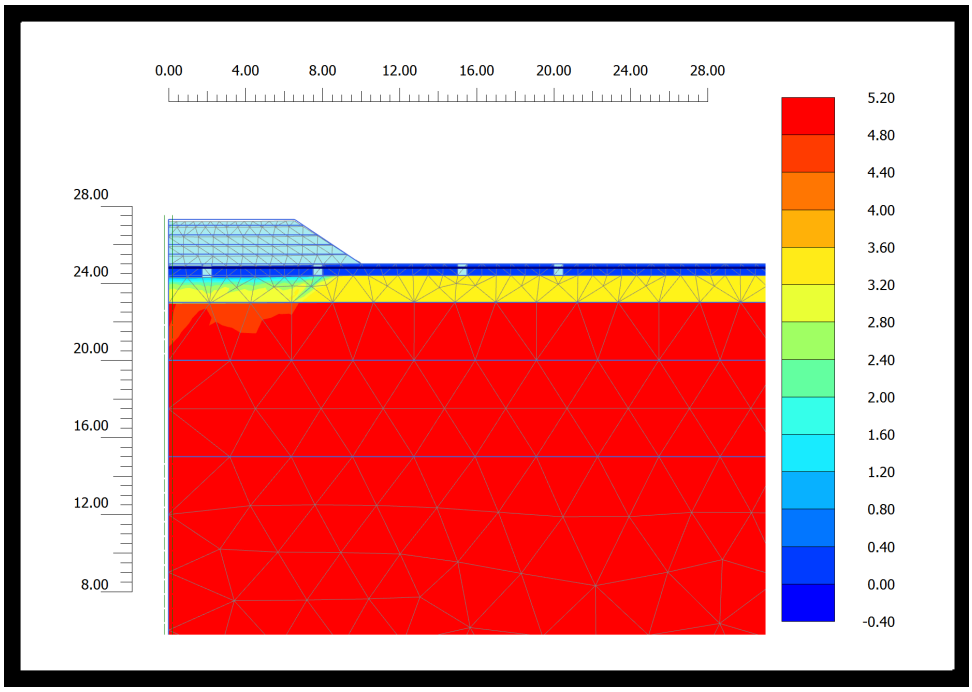

(a) Day No. 36

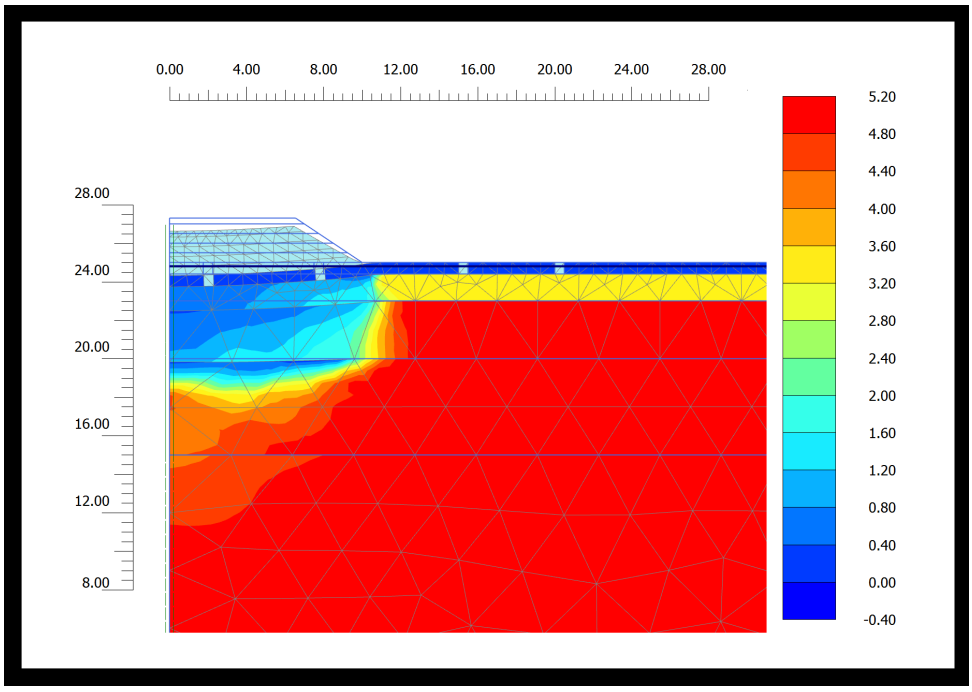

(b) Day No. 1120

Figure 8.15: *Destruction of structure (x) - (SCA-R: Best-fit).*

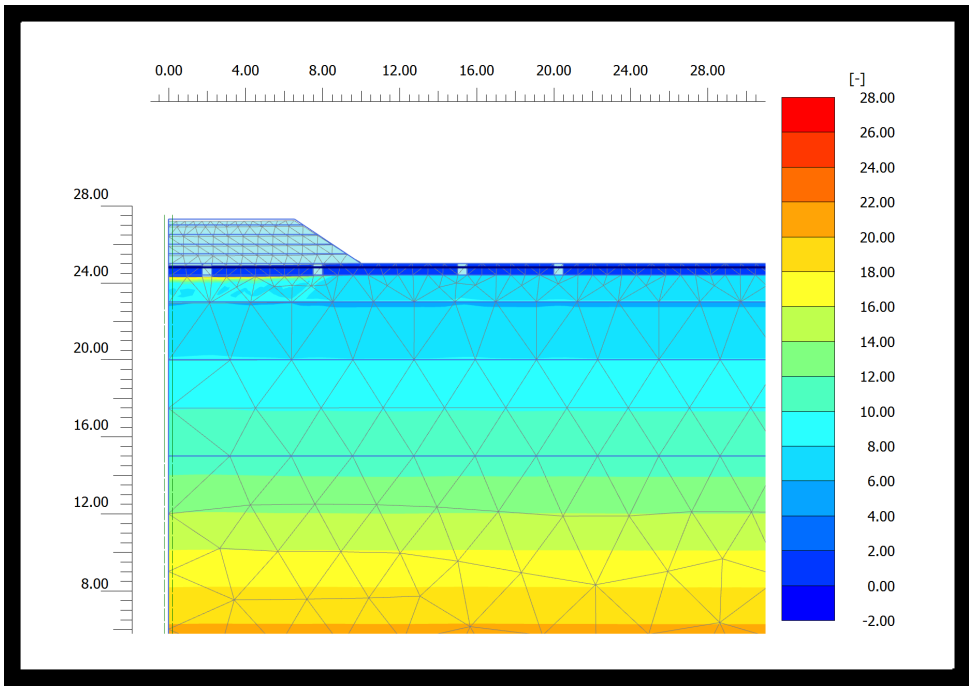

(a) Day No. 36

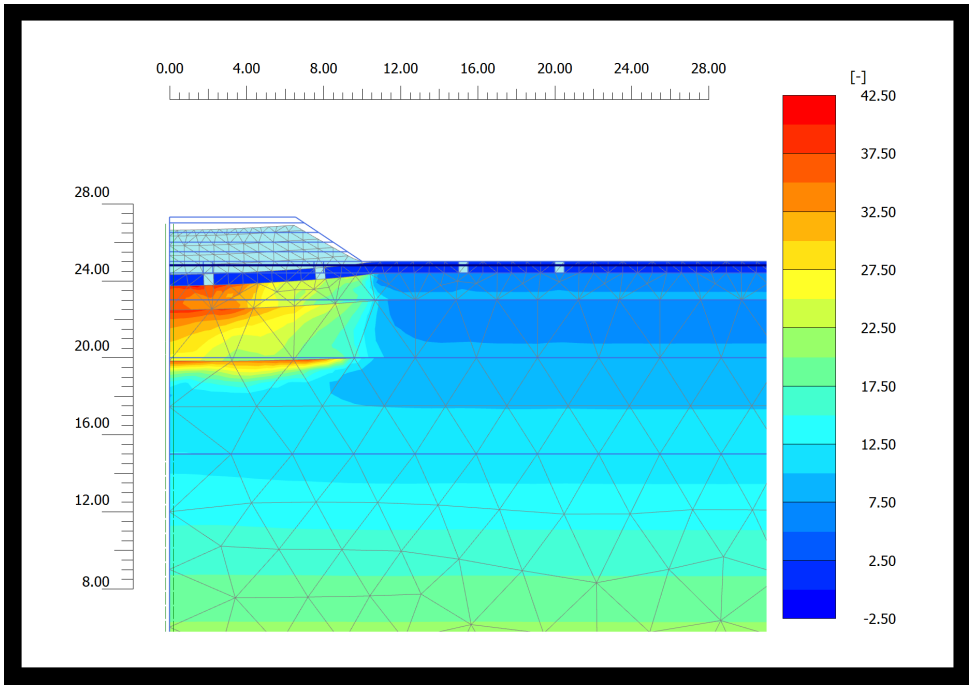

(b) Day No. 1120

Figure 8.16: *Increase in intrinsic pressure (p'_{mi}) - (SCA-R: Best-fit).*

These state parameters are linked together and the same pattern should be expected which may be seen on the above Figures 8.14-8.16. The link between the state parameters is as follows: The magnitude of the plastic multiplier indicates the development of visco-plastic strains. The visco-plastic strains will result in a destruction of the structure and an increase in the intrinsic pressure for this case. Notice that the embankment, the trenches and the dry crust do not incorporate any state parameters since other soil models are utilized.

The plastic multiplier at day No. 36 may be seen on Figure 8.14. Firstly, it may be concluded that no unwanted creep strains are generated in areas far away from the embankment. Secondly, the largest evolution is associated to the upper part of the layer (0.6 - 2.0 m) with a maximum magnitude of $68{\cdot}10^{-3}$ which is reduced towards the middle of the layer below. Notice, that the magnitude of the plastic multiplier is not influenced by the magnitude of elastic strains. Figure 8.14(b) shows the magnitude at day No. 1120. The additional development of creep strains may be investigated by comparing the magnitude of the plastic multiplier at day No. 36 and No. 1120. Hence, the development of visco-plastic strains during construction of the embankment may be subtracted. The majority of creep strains are generated in the second layer (2.0 - 5.0 m) with a maximum value of $150{\cdot}10^{-3}$. This development of visco-plastic strains may be associated to the excess pore pressure which obtains largest value in the lower part of this layer for the long term.

Figure 8.15(a) shows the amount of structure at day No. 36. It can be observed that the structure only is destroyed in the first layer which is reduced to half of the initial magnitude in the upper part of this layer. Recalling that the structure is only destroyed by visco-plastic strains. One could argue that this assumption may be relatively crucial since the top layer is deformed approximately 12 cm at the centreline after construction of the embankment and only half of the structure is destroyed. The structure is almost completely destroyed beneath the embankment towards the long term as a function of creep strains, see Figure 8.15(b).

The evolution of the intrinsic pressure may be seen on Figure 8.16(a) and Figure 8.16(b). It may be concluded that the intrinsic yield surface is expanded in the same regions where the magnitude of the plastic multiplier is high and the largest values are found just beneath the center of the embankment as expected.

Figure 8.14(b) and Figure 8.17 show the plastic multiplier for the first and final prediction. The influence of using POP instead of OCR may clearly be seen by a concentration of the plastic multiplier yielding a more realistic pattern.

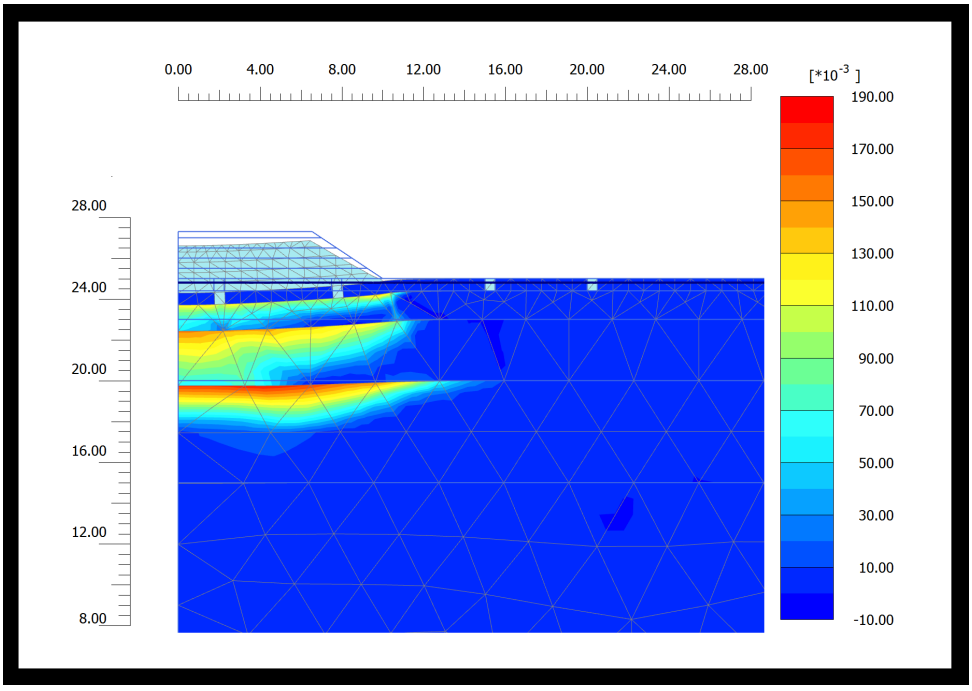

Figure 8.17: *Plastic multiplier at day No. 1120 using* OCR_τ.

The general performance of the SCA-R seems quite accurate, although the model has a slight difficulty in capturing the excess pore pressure after construction of the embankment (day No. 36). However, the performance should be compared to other available soil models to investigate its advantages and disadvantages.

8.5 Comparison with other Soil Models

The performance of the SCA-R model has been compared to other available soil models to identify its advantages and disadvantages with respect to capturing the soil response in a full scale boundary value problem. Previous performance analyses for different soil models have been performed by Mehli (2015a) with respect to the embankment at Onsøy. Access to this previous work has been granted and the Author of this thesis sends his gratitude. The constitutive models and their main characteristics may be seen in Table 8.7.

Table 8.7: *Constitutive models and their characteristics. Modified version of (Ashrafi, 2014).*

Model	Author	Elasticity	Plasticity			
		Small Strain Shear Stiffness	Creep	Anisotropy	Destructuration	Lode Angle
SS	Roscoe and Burland (1968)	-	-	-	-	-
SSC	Stolle et al. (1999)	-	Vol. Creep	-	-	-
CS-SSCG	Ashrafi (2014)	√	Pl. Multiplier	-	-	-
n-SAC	Grimstad and Degago (2010)	-	Pl. Multiplier	√	√	√
Kryton	Svanoe (1986)	-	"Vol. Creep"	-	"√"	-
SCA-R		-	Pl. Multiplier	√*	√	√

*In elastic and plastic domain.

A short description of the listed soil models in Table 8.7 is given by Mehli (2015a) where further details of these performance analysis may be found. Hence, information regarding the utilized parameters, calibration of the models and general model set-up will not be highlighted here. It should be mentioned that some models are left out in particular plots in the following section due to missing data. The performance analysis will contain following elements:

- **Figure 8.18**: The settlement just beneath the center of the embankment.
- **Figure 8.19**: The surface settlement at different time stages.
- **Figure 8.20**: Pore pressure distribution beneath the centreline at different time stages.
- **Figure 8.21:** Horizontal displacement 5.0 m away for the centreline at different time stages.
- **Figure 8.22:** Vertical strain at the centreline at different time stages.

Figure 8.18 shows the settlement just beneath the center of the embankment.

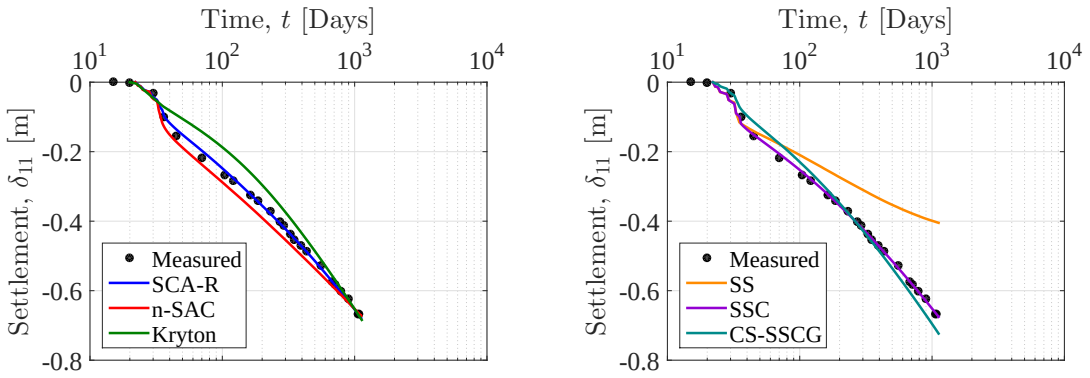

Figure 8.18: *Comparison of soil models to estimate the settlement just beneath the center of the embankment.*

Four models are able to capture the final settlement: SCA-R, n-SAC, Kryton and SSC. However, only the SCA-R and the SSC models are able to capture the path towards the final settlement. Notice, the SS model does incorporate any creep. An approximation of creep strains may be found by comparing the SS to the other models caused by the same framework of utilizing MCC. It may be observed that the contribution from creep strains are significant. The amount of visco-plastic strains are investigated in Section 8.7 for the SCA-R model.

Figure 8.19 shows the surface settlement at different time stages. In general every model capture the surface settlement in a fairly good manner. However, trouble of estimating the settlement after the construction of the embankment (day No. 36) may be observed.

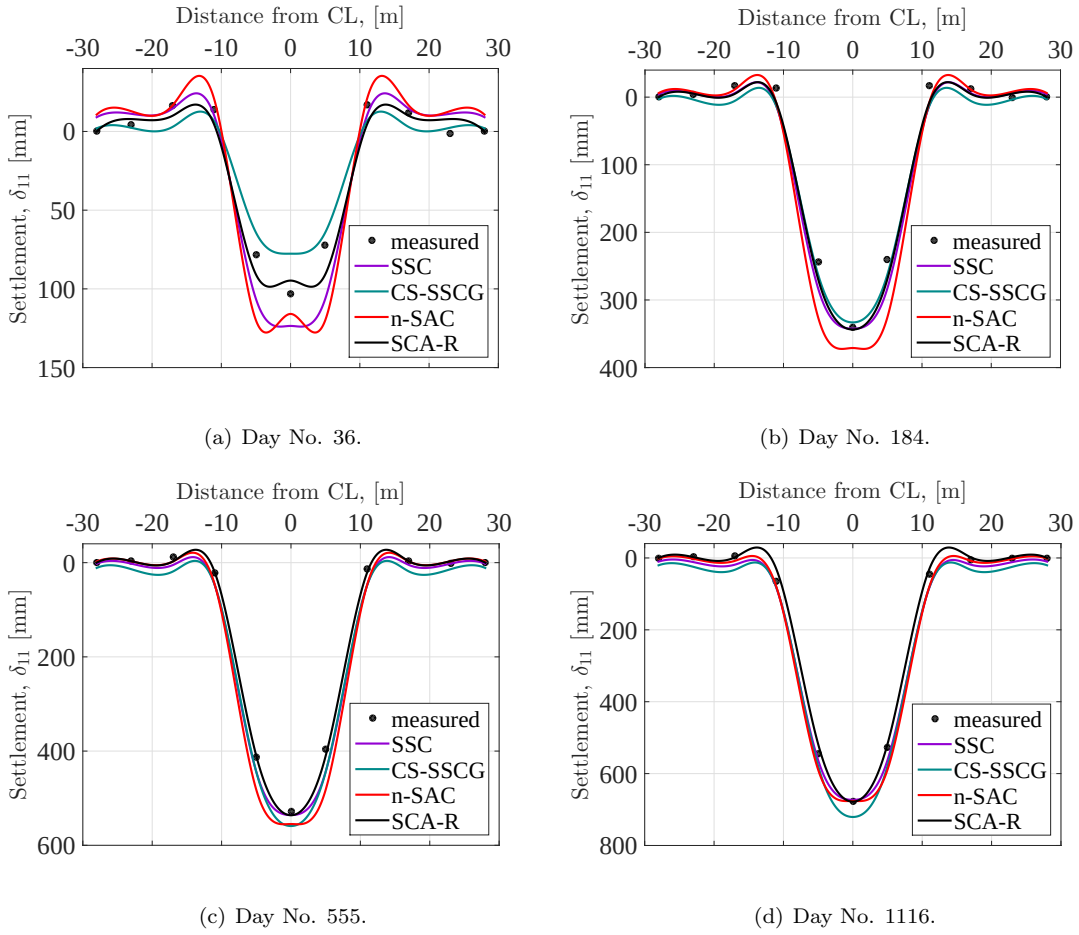

(a) Day No. 36.

(b) Day No. 184.

(c) Day No. 555.

(d) Day No. 1116.

Figure 8.19: *Comparison of different soil models ability to estimate the surface settlement.*

It should be mentioned that the solid lines on Figure 8.19 are drawn by the `spline`-function in MATLAB. This function fits a line to particular points though piecewise polynomial interpolations. Hence, the regions where the curves are bending should be analysed by knowing this particular fitting method.

The excess pore pressure at the centreline of the embankment may be seen on Figure 8.20. In general, each soil model overshoots the excess pore pressure in the upper part of the strata after the construction phase. However, the models still capture the correct pattern of the excess pore pressure distribution. Notice that, the SCA-R uses a closed boundary for dissipation in the bottom compared to an open one used in the other models. All models seems to capture the excess pore pressure fairly good for the long term besides the SS caused by the missing creep strains. The SCA-R captures the pore pressure in the upper layer slightly better caused by other permeability parameters.

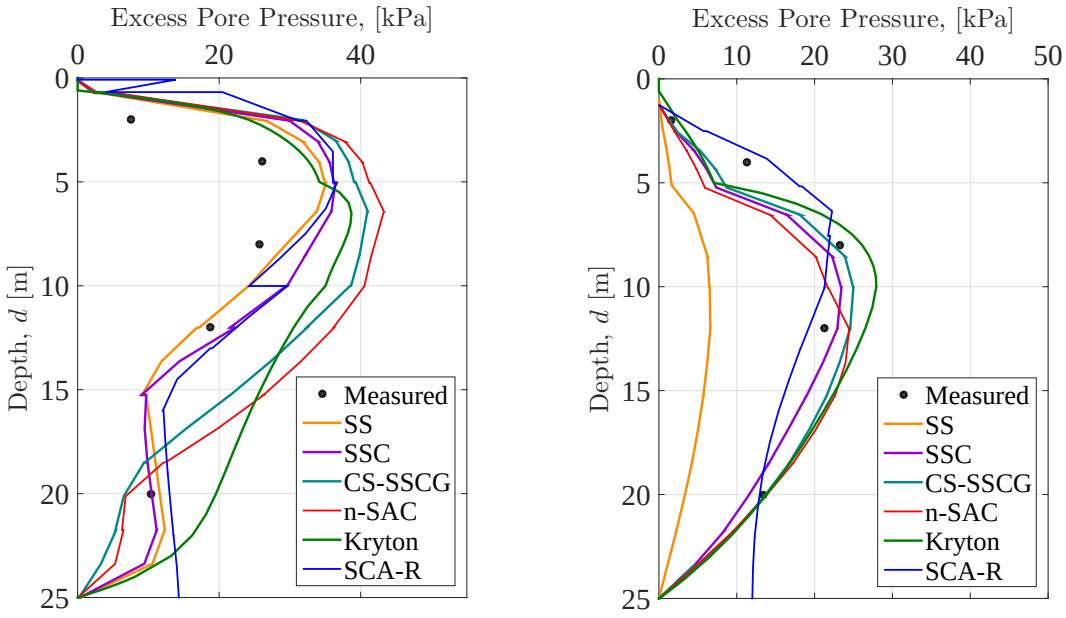

(a) Day No. 36. (b) Day No. 1120.

Figure 8.20: *Comparison of different soil models ability to estimate the excess pore pressure at the centreline of the embankment.*

The horizontal displacement may be seen on Figure 8.21. The CS-SSCG model, which incorporates small stiffness, yields fairly accurate estimations of the horizontal displacement. The other models tend to overshoot the early stages where the SCA-R model yields better estimations compared to the other models. At the long term the accuracy of the models improve.

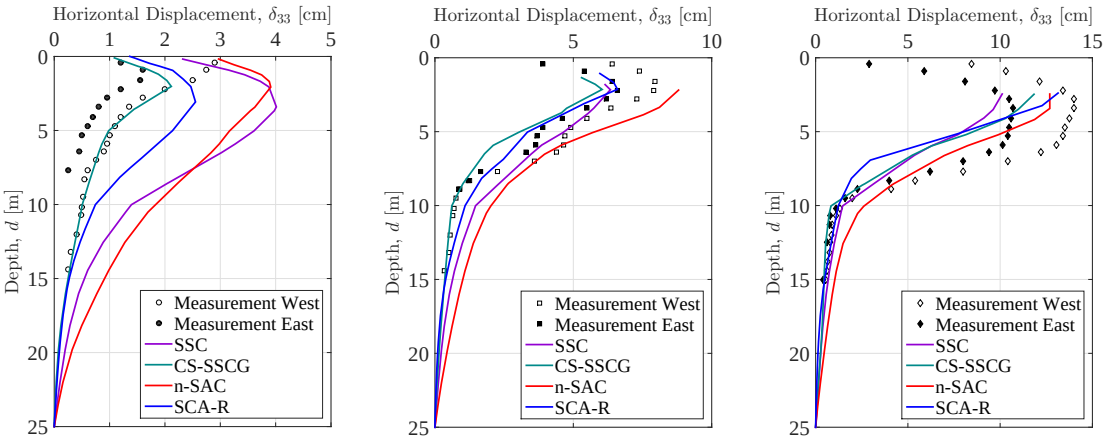

(a) Day No. 36. (b) Day No. 147. (c) Day No. 1116.

Figure 8.21: *Comparison of different soil models ability to estimate the horizontal displacement 5.0 m from the centreline of the embankment.*

The vertical strain at the centreline of the embankment may be seen on Figure 8.22. The early stage of each model shows a peak value. The CS-SSCG again prove quite accurate responses in the lower part of the strata where the Kryton also yields fairly good response. The models tend to improve in the long term. In general, the SCA-R yields slightly less accurate estimations compared to the other models.

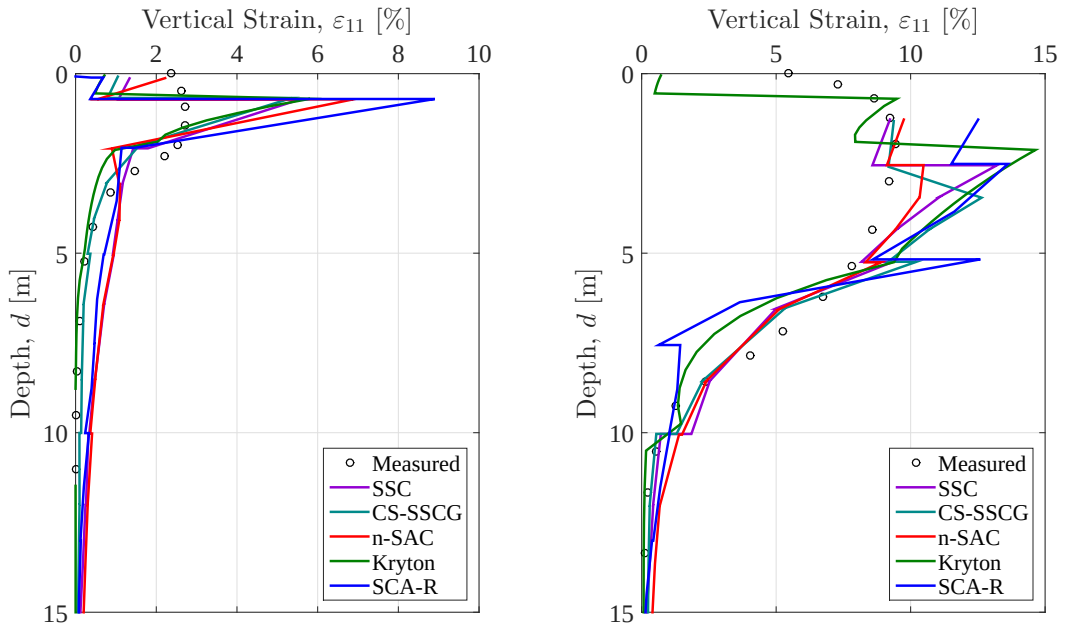

(a) Day No. 36.

(b) Day No. 1116.

Figure 8.22: *Comparison of different soil models ability to estimate the vertical strain at the centreline of the embankment.*

In general, each model produces quite accurate predictions with respect to the field measurements. The SCA-R model shows relatively high performance with respect to the settlement compared to several of the other models. It may be argued that the SCA-R captures the excess pore pressure and the horizontal displacement[2] in a slightly more accurate manner, although it is very similar to the best predictions of the other models. However, the SCA-R is less accurate at predicting the vertical strain than the other models.

[2] Besides the CS-SSCG.

8.6 Evolution of OCR_τ

The magnitude of OCR_τ is associated with the development of visco-plastic strains over time. Hence, the evolution of OCR_τ is interesting to investigate to see if the magnitude corresponds to the development of visco-plastic strains and to obtain a general understanding of the model behaviour. OCR_τ is defined as the ratio between the reference surface, representing the stress condition (p^{eq}), and the surface associated to the intrinsic pressure through the amount of structure, see Figure 4.3.

$$OCR_\tau = \frac{p'_m}{p^{eq}} \qquad \text{where} \qquad p'_m = (1+x)p'_{mi} \tag{8.6}$$

The magnitude of OCR_τ is sensitive to state parameters x, p'_{mi}, and $\boldsymbol{\alpha}$[3] and to the excess pore pressure through the reference surface. Hence, an increase in the excess pore pressure caused by undrained creep strains can result in an increase in OCR_τ by reducing p^{eq}.

The FORTRAN code needs to be modified to visualize the magnitude of OCR_τ during a PLAXIS simulation. The vector containing the state parameters ($\boldsymbol{v}$) is extended by adding two rows (number 16+17) containing OCR_τ and p^{eq} at each stage[4]. Figure 8.24 shows the evolution of OCR_τ, x, p'_{mi}, p^{eq}, the excess pore pressure, and the total mean pressure (p) during the construction phase for the centreline of the embankment.

The investigation of OCR_τ is made for the final prediction. It may be observed that for the in situ case, a steady decrease in OCR_τ occurs in the three upper layers towards layer 4 which has a constant magnitude, see Figure 8.23(a). This is caused by the initializing of p'_{mi} by POP in the three upper layers and by OCR_τ in the bottom layer.

During construction of the fill layers, the total stress increases which is mainly carried by an increase in the excess pore pressure, see Figure 8.23(e) and Figure 8.23(f). The effective stresses increase as a consequence of dissipation of the excess pore pressure. Hence, the magnitude of p^{eq} increases as seen on Figure 8.23(d). However, an increase in the excess pore pressure caused by visco-plastic strains would not increase the total stresses and reduce the magnitude of p^{eq}. Therefore, it should be investigated if any development of visco-plastic strains occurs during construction. The development of visco-plastic strains are associated with time evolution of the visco-plastic multiplier and changes in the stress condition bringing the soil outside of the elastic domain. An investigation may be done through an analysis of the structure (x), see Figure 8.23(b). A small change in the upper part of layer 1, with respect to in situ structure, occurs after raising the height of the embankment to 1.5 m. This is caused by the time evolution. This has not occurred before due to the restriction of time evolution caused by t_{max}. Raising the height to 2.3 m yields a major change in the structure of layer 1 mostly caused by leaving the elastic domain but also the time evolution. The changes in x in the remaining part of the strata is caused by the time evolution. Leaving the elastic domain affects the intrinsic pressure significantly which may be seen on Figure 8.23(c). Notice, small changes in p'_{mi} occurs in the same location as where the reduction of structure occurs but is relatively small compared to the magnitude of p'_{mi}. Thereby, it may be concluded that some of the excess pore pressure is caused by visco-plastic strains but are counteracted by the dissipation yielding no net reduction in p^{eq}.

The magnitude of OCR_τ is reduced placing the first two layers caused by the increase in p^{eq}. Raising the embankment to 1.0 m yields a significant change in the peak value of OCR_τ. Placing the next layer (1.5 m in total) yields further reducing in OCR_τ and the evolution with time in the strata initiates. Hence, the reduction in x and increase in p'_{mi} contributes to minor changes in OCR_τ. Raising the height to 2.3 m yields approximately an $OCR_\tau \approx 1.0$ from the surface to level 12.0 m.

[3] Recalling that $\boldsymbol{\alpha}$ is utilized to determine p^{eq}.

[4] These values are determined in each step where the remaining part of vector $\boldsymbol{v}$ is added from the current and previous step.

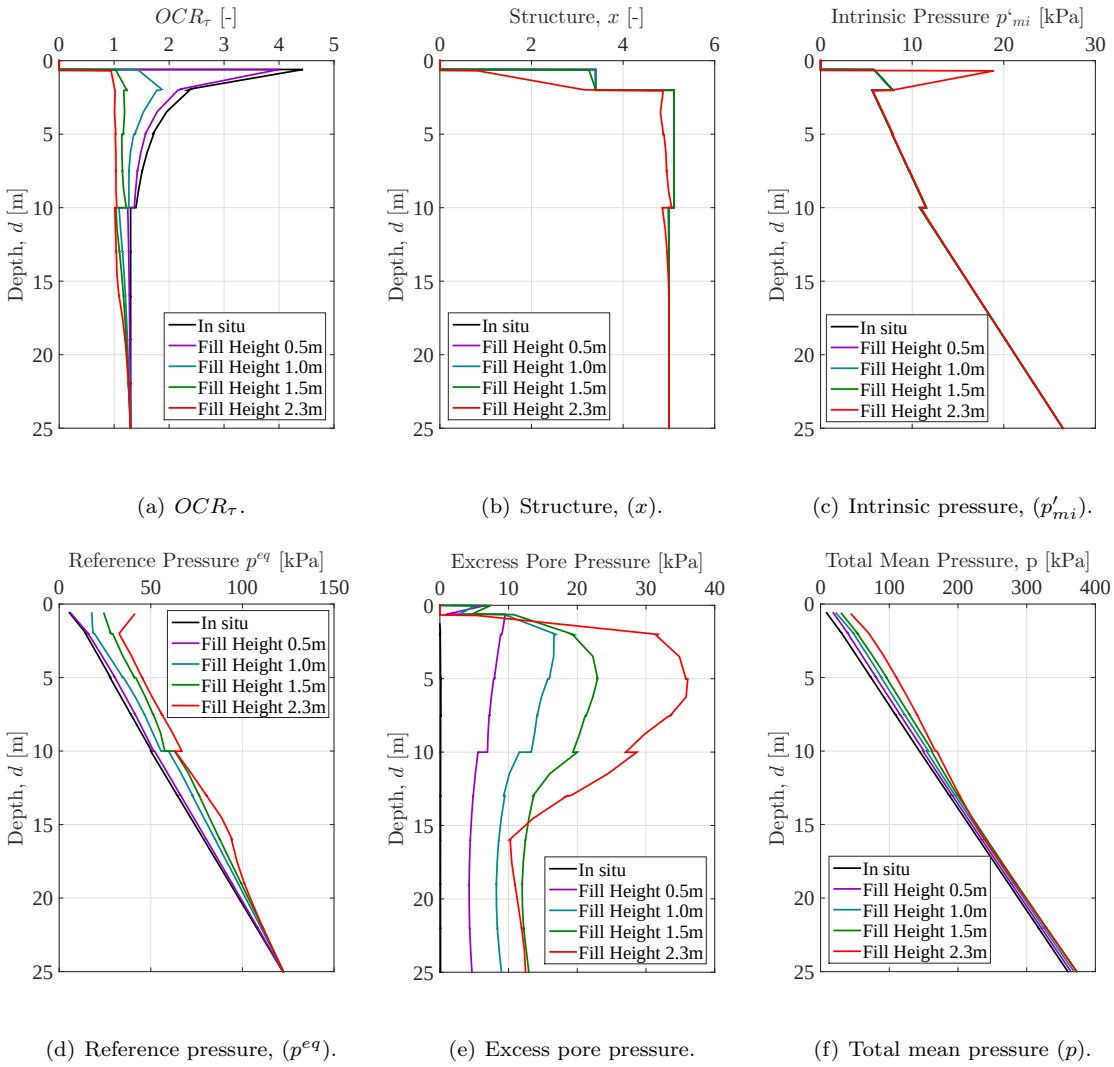

(a) OCR_τ. (b) Structure, (x). (c) Intrinsic pressure, (p'_{mi}).

(d) Reference pressure, (p^{eq}). (e) Excess pore pressure. (f) Total mean pressure (p).

Figure 8.23: *Evolution of OCR_τ and its associated parameters during construction of the fill (centreline). Note the black, violet, cyan, and green are located on top of each other or very close in Figure b and c.*

It should be noted that OCR_τ reaches values below 1.0. in the upper part of layer 1. This is possible according to the theory and depends on the magnitude of the chosen reference time (τ). The mathematical meaning yields that the reference surface (p^{eq}) is larger than the surface represented by the intrinsic pressure and the amount of structure.

The same investigation is executed for the long term which may be seen on Figure 8.24. The excess pore pressure decreases as a function of time even though visco-plasticity is generated, see Figure 8.24(e). This is caused by higher dissipation relative to the generated pore pressure from the undrained creep strains. However, the excess pore pressure increases in the bottom part of the strata as a consequence of the lower hydraulic head. This increase influences the reference pressure which takes a value below the original in situ stresses, see Figure 8.24(d). This results in an artificial and apparent increase in OCR_τ which disappears with time. The evolution in x (reduction) and p'_{mi} (increase) are very similar and major changes occurs from level 8.0 m and above. Visco-plastic strains develop over time from level 18.0 m and above which may be seen on the destruction of the structure, see Figure 8.24(b). The strata below is restricted by t_{max}. The significant difference in x and p'_{mi} at level 5.0 m is caused by switching from layer 2 to layer 3. Each layer has the same intrinsic creep parameter (r_{si}) but the internal irrecoverable compressibility (ζ_i) is different (0.055 vs. 0.070, respectively). Hence, a larger amount of visco-plastic strain develops over time in layer 3 which causes larger destruction of x and expansion in p'_{mi} relative to the layer above. The sudden jump at level 8.0 m in p^{eq}, x and p'_{mi} has not been possible to explain in a physical manner.

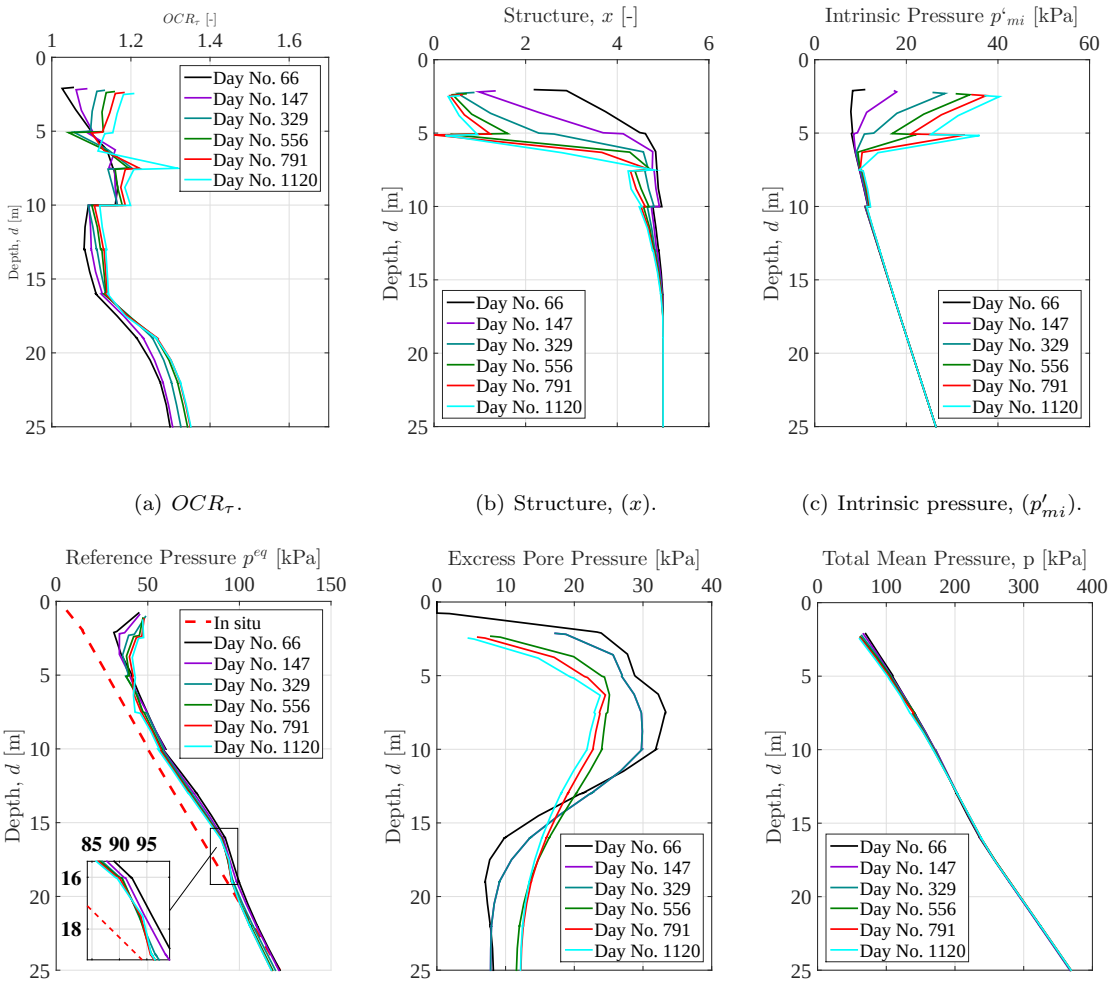

(a) OCR_τ. (b) Structure, (x). (c) Intrinsic pressure, (p'_{mi}).

(d) Reference pressure, (p^{eq}). (e) Excess pore pressure. (f) Total mean pressure, (p).

Figure 8.24: *Evolution of OCR_τ and its associated parameters at the long term.*

The magnitude of OCR_τ steadily increases as a function of time. This is a consequence of a higher increase in p'_{mi} relative to the reduction in x with respect to Eq. (8.6). The rate of OCR_τ may be associated to the rate of visco-plastic strains.

The above analysis of the model response in a boundary value problem describes the behaviour of the SCA-R model during a loading and time perspective. The observed response verify the expected behaviour of the SCA-R model.

8.7 Visco-Plastic Strains

The amount of visco-plastic strains may be investigated by increasing the magnitude of r_{si}. According to the theory, when $r_{is} \longrightarrow \infty$ the visco-plastic model yields elasto-plastic response. The model is restricted to an upper magnitude of r_{is} depending on the combination of the other input parameters. However, simulating the soil response of the embankment utilizing a magnitude of $r_{is} = 5000$ in each layer the major part of the visco behaviour should be removed. The settlement just beneath the center of the embankment may be seen on Figure 8.25(a) utilizing the input parameters related to the final prediction, $r_{is} = 5000$ and a magnitude of $r_{is,min}$ yielding the same structure in each layer as in the final prediction.

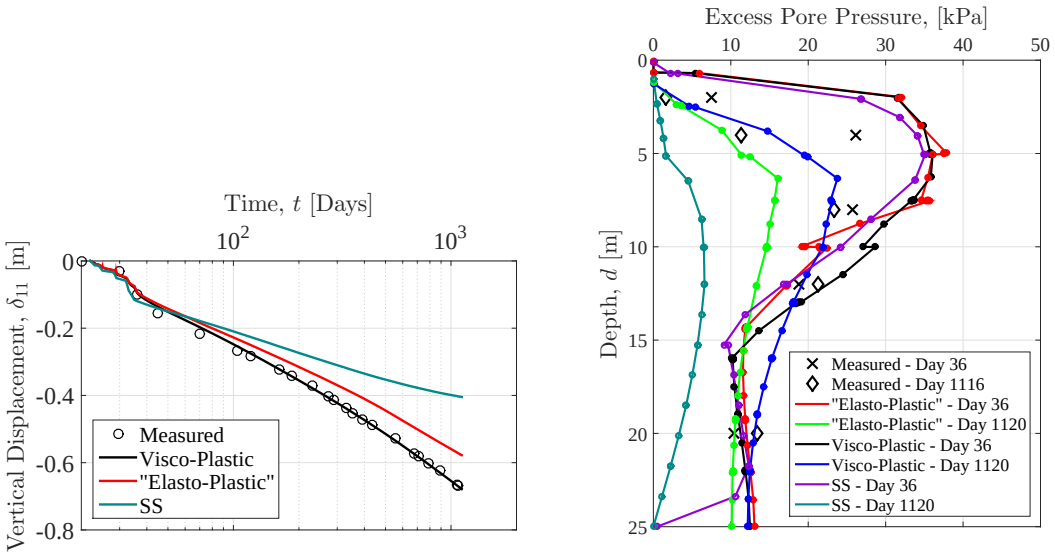

(a) Settlement just beneath the center of the embankment.

(b) Excess pore pressure at the centreline.

Figure 8.25: *Comparing elasto-plastic and visco-plastic response (SCA-R: Best-fit).*

It may be observed that the soil response during the construction phases is approximately the same for the two predictions. The deviation of the settlement increases when approaching the long term with a final difference of 15 %[5] lesser deformation for the elasto-plastic response. This should be compared to the associated excess pore pressure which may be seen on Figure 8.25(b). The excess pore pressure is quite identical for both models in the short term which confirms the similar settlement response during the construction. A small deviation may be seen in level 8.0 - 15.0 m showing a smaller magnitude of the excess pore pressure for the elasto-plastic response caused by minor contribution of the visco-plastic strains. A greater deviation for the whole strata may been seen for the long term. The development of visco-plastic strains over time are associated to excess pore pressure and a minor contribution may be seen as smaller excess pore pressure for the elasto-plastic response. Hence, the difference of 15 % lesser settlement will increase as a function of dissipation of the excess pore pressure. The predictions for the SS model are shown on Figure 8.25 to compare the predictions for the models. It may be concluded that the SS model yields a response which is very different with respect to the elasto-plastic response when comparing the settlement and excess pore pressure at the same time. This may be caused by the additional features which are incorporated in the SCA-R model and the utilized input parameters where the difference in permeability in the upper part of the strata may have a major influence.

It may be concluded for the short term that the visco-plastic impact is minor for this particular case. However, the magnitude of r_{si} may influence the apparent yielding point and may have a greater influence in other cases. The visco-plastic strains have a major impact on the long term where neglecting the creep strains would be a crucial simplification with respect to the predictions of the soil response performed by the SCA-R model.

[5] $\left(\frac{678.4-577.8}{678.4}\right) \cdot 100 \approx 15\%$

8.8 Mesh Analysis

The mesh utilized in the first and final prediction has been chosen to match the finite element model suggested by Mehli (2015a) to make the predictions comparable to other soil models. However, a mesh analysis should be performed to investigate the sensitivity of the predictions related to the chosen mesh. A new mesh containing 3086 elements (25017 nodes) has been created and may be seen on Figure 8.26.

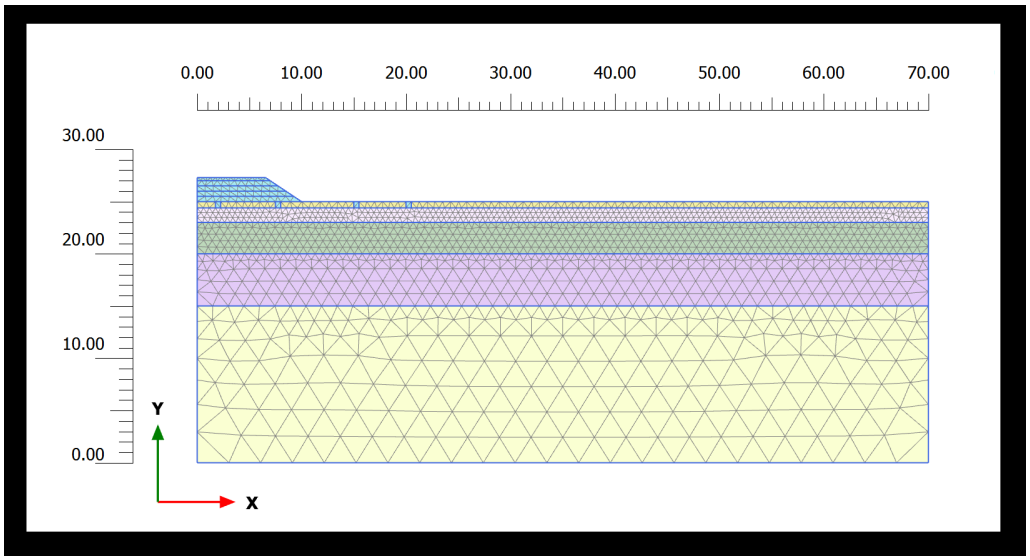

Figure 8.26: *New mesh for the finite element model used to model the embankment at Onsøy.*

The mesh dependency will be analysed through the old and new mesh by utilizing the input parameters associated to the final prediction. The settlement settlement just beneath the center of the embankment may be seen on Figure 8.27(a), the excess pore pressure at the centreline may be seen on Figure 8.27(b), the vertical strain at the centreline may be seen on Figure 8.28(a), and the horizontal displacement 5.0 m away from the centreline may be seen on Figure 8.28(b).

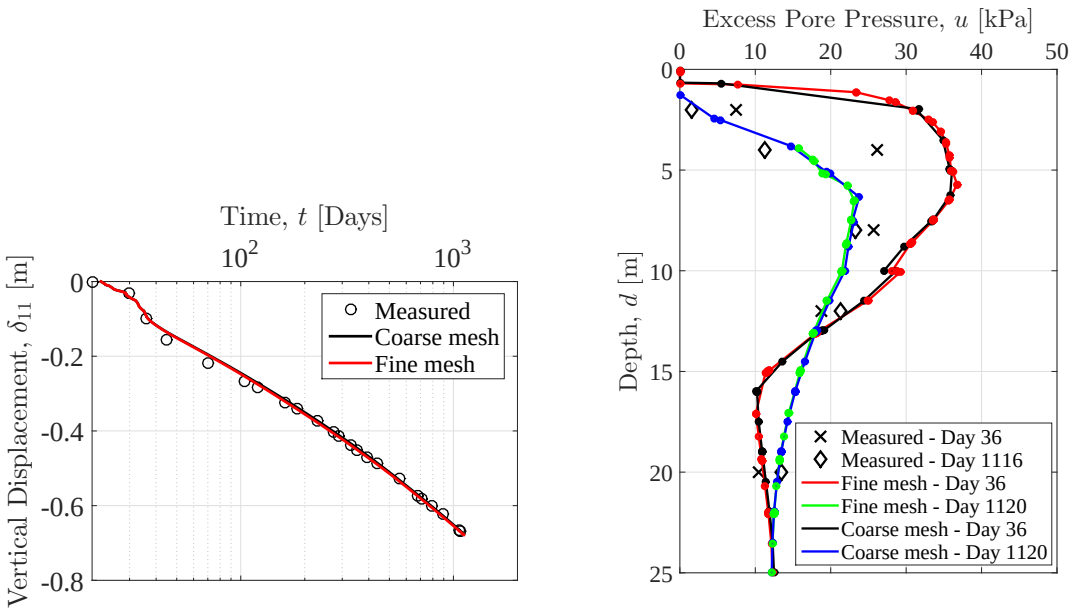

(a) Predictions of settlements just beneath the center.

(b) Excess pore pressure at the centreline.

Figure 8.27: *Mesh analysis I of the embankment.*

The settlement and the excess pore pressure yields very similar predictions and an insignificant mesh dependency can be observed relative to the mesh used in the final prediction. It should be mentioned that the prediction of the settlement for the course mesh is so identical to the fine mesh that it is hard to distinguish between them. The same conclusion can be drawn for the horizontal displacement, although a slight deviation can be seen in the upper 7.0 m of the strata for day No. 147 and day No. 1120. The vertical strain shows the biggest mesh dependency, especially for the long time. The deviation in the vertical strain may be explained through the small stiffness in the top of each layer.

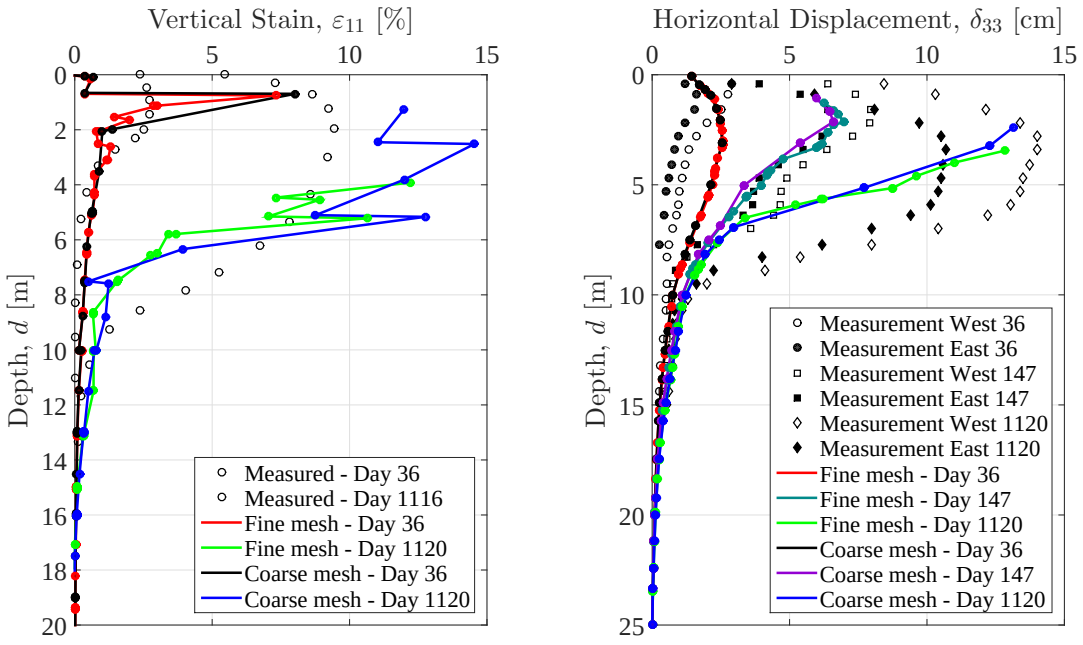

(a) Vertical strain at the centreline.

(b) Horizontal displacement 5.0 m away from the CL.

Figure 8.28: *Mesh analysis II for the embankment.*

It may be concluded that further refinement of the mesh utilized in the final prediction does not make any significant changes with respect to the predictions shown in this section. Therefore, the predictions given in Section 8.4 and Section 8.5 may be considered as mesh "independent", i.e. further refinement only yields minor changes.

8.9 Implicit vs. Explicit

The SCA-R has incorporated an explicit scheme to solve the differential equations in the local iteration. The performance of this method will be analysed through an implicit Newton Raphson's method developed by Roenningen (2015), see Chapter 5 for further details. To clarify, the FORTRAN code which has been used to generate the dll-file has been made by Roenningen (2015) with some modifications to handle the input from the MATLAB code developed to the explicit scheme. The Author sends his gratitude to Roenningen (2015) for sharing this part of his work.

The performance is investigated by comparing the settlement just beneath the center of the embankment utilizing the input parameters for the final prediction. The computational time was approximately the same for the two approaches with respect to the chosen step size, tolerance and maximum number of iterations, see Chapter 5 for exact values. The settlement may be seen on Figure 8.29(a) and the associated excess pore pressure on Figure 8.29(b).

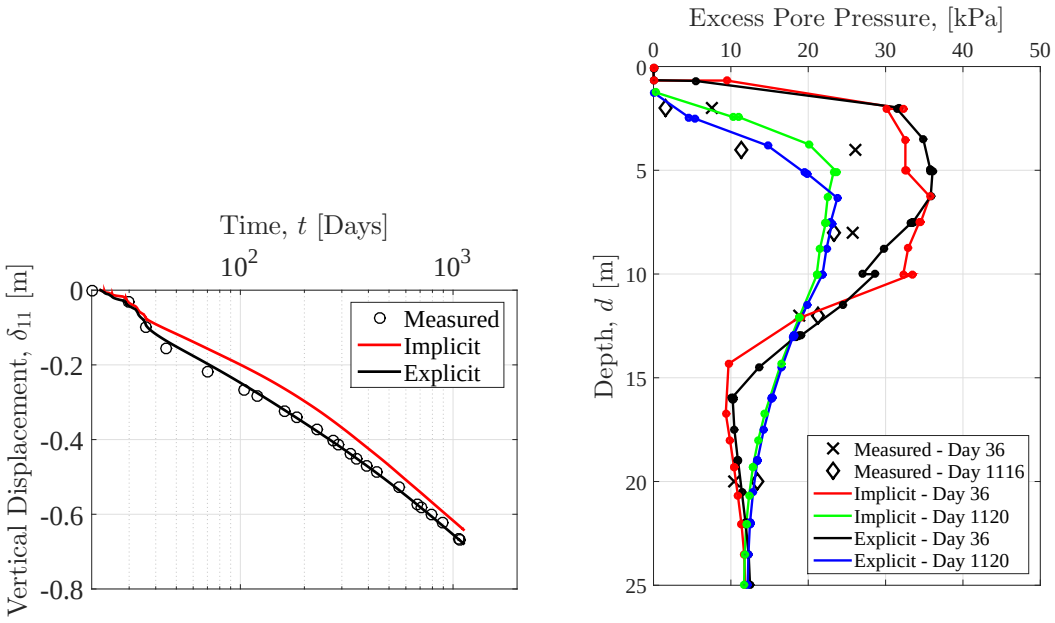

(a) Settlement just beneath the center of the embankment.

(b) Excess pore pressure at the CL.

Figure 8.29: *Performance for an explicit and implicit scheme in the local iteration.*

A significant difference may be observed in the settlement with respect to the two approaches. The long term settlement yields a difference of 3.7 cm where 1.8 cm is associated to the construction phase. The excess pore pressure has some similarities in the strata. This observation yields a hypothesis that the amount of visco-plastic strains which are generated are approximate the same. The implicit method has a larger excess pore pressure in the upper part of the strata for the long term which may explain some of the deviation in settlement for the long term. However, this cannot explain the general difference in the response and an investigation of the accuracy of each method should be performed.

The explicit scheme may be investigated through a sensitivity analysis of the predictions associated with the utilized step size. Recalling the restrictions on the step size in the explicit method, the reference time τ and a chosen parameter x are associated with the time and strain increment, respectively. A combination of these parameters control the utilized step size. However, reducing or increasing the magnitude of x by one order of magnitude has not shown any improvement or reduction in the prediction of settlement. Neither has changes by one order of magnitude in the reference time showed any sensitivity. Notice, the modifications of τ related to the time increment has been modified in FORTRAN so the evolution time of the plastic multiplier was not effected by changes in τ. Hence, it may be concluded that the explicit method uses a too conservative step size with respect to the simulation of the embankment.

The implicit scheme utilizes a chosen tolerance and only yields an output if the error is below the chosen tolerance with respect to a maximum number of iterations. The utilized tolerance is chosen to be: $\boldsymbol{r}\boldsymbol{r}^T = 10^{-12}$ where $\boldsymbol{r}$ is the residual vector. This tolerance should insure a high accuracy with respect to the predictions if the implicit scheme converge. Hence, no obvious evidence related to the accuracy of each method may explain the difference. Further investigation may be done by assembling different test scenarios and analysing the estimate soil response. Four scenarios in Soil Test are assembled to investigate the soil response:

1. **Undrained tri-axial compression** $\underbrace{\sigma'_{11} = \sigma'_{22} = \sigma'_{33} = 99\,\text{kPa}}_{\text{Initial stress}}$
   - **a.** $\Delta\varepsilon_{11} = 10$ %
2. **One-dimensional compression** $\underbrace{\sigma'_{11} = 100\sigma'_{22} = \sigma'_{33} = 99\,\text{kPa}}_{\text{Initial stress}}$
   - **a.** $\Delta\varepsilon_{11} = 10$ %
   - **b.** $\Delta\varepsilon_{11} = 50$ % and $a = b = 30$
3. **One-dimensional compression + creep** $\underbrace{\sigma'_{11} = 100\sigma'_{22} = \sigma'_{33} = 99\,\text{kPa}}_{\text{Initial stress}}$
   - **a.** $\Delta\sigma'_{11} = 100\,\text{kPa}$ $\Delta\sigma'_{22} = \Delta\sigma'_{33} = 50$ kPa
   - **b.** $\Delta\sigma'_{11} = \Delta\sigma'_{22} = \Delta\sigma'_{33} = 0$ kPa
4. **Drained creep** $\underbrace{\sigma'_{11} = 200\,\text{kPa},\ \sigma'_{22} = \sigma'_{33} = 149\,\text{kPa}}_{\text{Initial stress}}$
   - **b.** $\Delta\sigma'_{11} = \Delta\sigma'_{22} = \Delta\sigma'_{33} = 0$ kPa

All compression phases are performed in 1 day and the creep phases are simulated for 1000 days. Furthermore, test four is assembled in a manner so that the development of creep strains occur for the same stress condition as for the creep test in scenario three after the compression. These scenarios have been tested for all four layers in the strata associated with final prediction. The response from layer 2 may be seen on Figure 8.30 and the response of the other layers in the strata may be seen in Appendix G.3.

Tri-axial: The undrained tri-axial scenario yields approximately the same response for all four cases and may be seen on Figure 8.30(a) for layer 2. The explicit method shows a tendency of a slightly smaller residual strength for all cases. However, the method which determines the maximum peak strength depends on each layer. Similar response has been observed in extension and drained conditions. The same conclusion may be drawn if the simulation was continued to 100 % vertical strain.

One-dimensional compression: The elastic response and the location of the apparent yield point are similar for the one-dimensional compression test for all cases and may be seen on Figure 8.30(c) for layer 2. However, beyond the yielding point the soil response deviates. The explicit method can be distinguish from the implicit method by a tendency of smaller void ratio for a given effective stress. This behaviour may be investigated through the compression index which should approach the intrinsic input parameter (λ_i) as a function of destruction of the structure. Hence, extending the compression to $\varepsilon_{11} = 50$ % and increasing the destruction parameters $a = b = 30$ should ensure $x \longrightarrow 0.0$. Hence, the interpreted compression index should converge towards the intrinsic compression index. This has been done for all layers in the strata and may be seen on Figure 8.30(d) for layer 2 where the compression index has been determined for each increment strain step. Notice, only the evolution beyond yielding is shown and the x-axis symbolizes each increment step. It may be observed that each method shows the expected behaviour of reducing λ as a function of compression. Each method shows a steady decrease towards a boundary value close to the input. The explicit method shows a tendency of overestimating the magnitude which is the consequence of utilizing the previous stresses and state parameters. The implicit method shows a tendency of undershooting the magnitude where a reduction in the tolerance to $\boldsymbol{rr}^T = 10^{-24}$ will move the magnitude slightly closer to the input value but still on the opposite side to the input parameter relative to the explicit. Hence, it may be concluded that some of the difference in settlement during the construction phase is caused by a lower compression index for the implicit method causing a stiffer response.

Drained creep: The drained creep simulation may be see on Figure 8.30(b) for layer 2. The initial part of the curve shows similar response. The explicit method shows a general tendency of a larger development of visco-plastic strains for the long term. One explanation may be found in the amount of structure at a given time. As seen in the one-dimensional compression, the destruction process seems to be faster for the explicit method which will influence the rate of

visco-plastic strains through the magnitude of OCR_τ. However, further investigation has shown the same tendency for simulations without any structure.

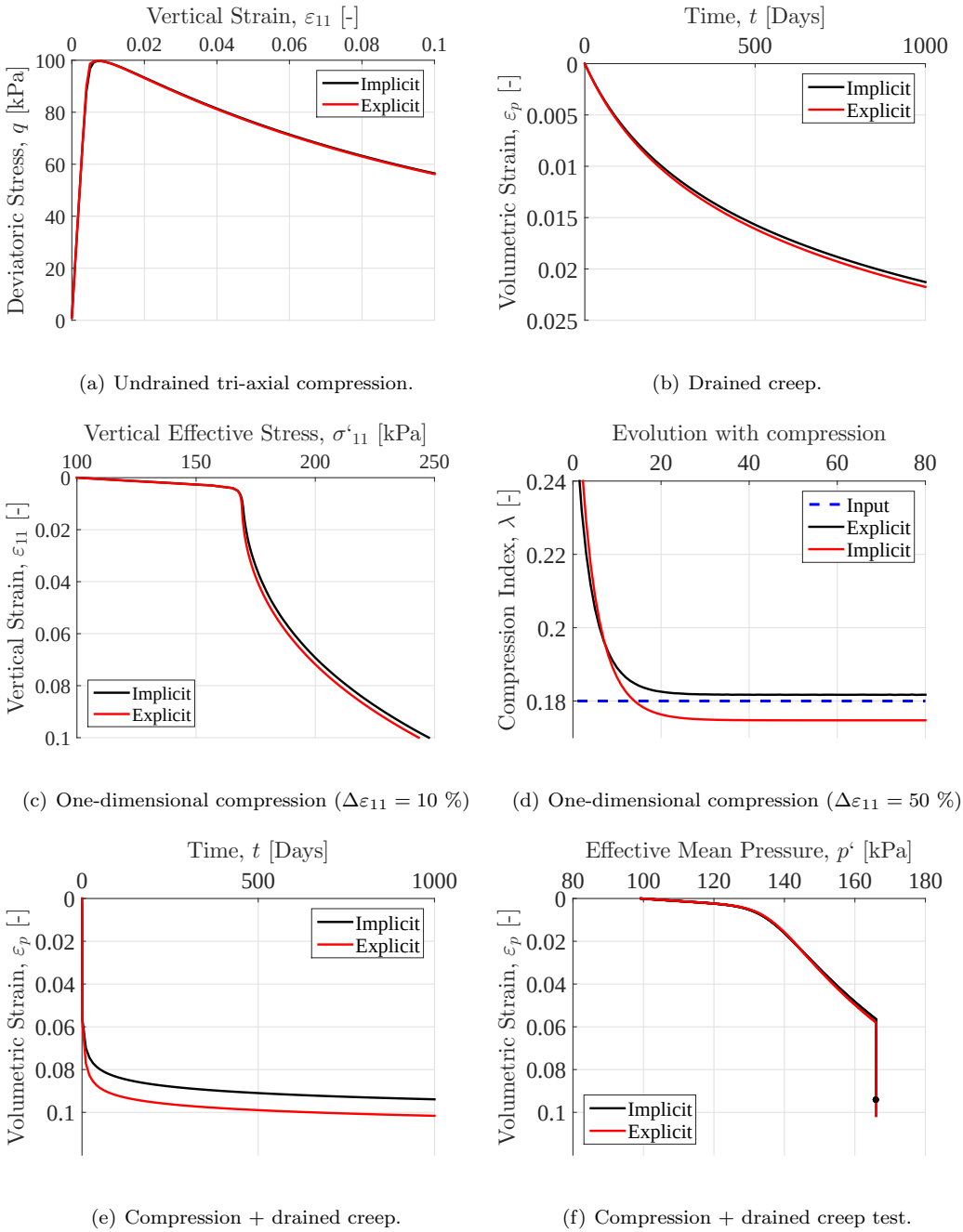

(a) Undrained tri-axial compression.

(b) Drained creep.

(c) One-dimensional compression ($\Delta\varepsilon_{11} = 10$ %)

(d) One-dimensional compression ($\Delta\varepsilon_{11} = 50$ %)

(e) Compression + drained creep.

(f) Compression + drained creep test.

Figure 8.30: *Investigation of explicit and implicit scheme for layer 2 (2.0 - 5.0 m).*

One-dimensional compression + creep: This scenario is assembled since it illustrates a more similar loading scenario as in the boundary value problem. It may be observed on Figure 8.30(e) that the explicit method yields a larger deformation relative to the implicit method. The difference in volumetric strain between the explicit and the implicit method is 0.37 % after the compression phase. However, the first step in the creep test (10 days step) yields a difference of 4.46 % and the difference will reduce towards the long term to a final difference of 2.66 %. The explanation for the difference during the compression was a consequence of a lower magnitude of λ in the implicit method. The significant difference during the creep test could be found by investigating the stress level. According to the set-up in Soil Test the stress level should be constant during the simulation which is verified by Figure 8.30(f). Hence, it has not been possible to explain the difference.

The general performance for the explicit scheme and the credibility of the predictions presented earlier in this chapter may be discussed as a consequence of Figure 8.29(a). The settlement prediction has shown insignificant sensitivity when changing the magnitude of the x parameter associated to the maximum step size by one order of magnitude. This may be a consequence of the strain and time increment given by PLAXIS which may have a magnitude yielding a high accuracy without the restrictions to the step size in the code. The explicit scheme shows similar response during undrained tri-axial simulations as for the case when utilizing the implicit scheme. The evolution of λ during one-dimensional compression follows the expected behaviour towards the intrinsic input value. These aspects acknowledge the reliability of the explicit scheme. However, the difference between the schemes during the creep tests requires more investigation before it may be concluded that the explicit scheme yields the correct response. It should be recalled that the incremental change in the plastic multiplier is assembled through a Taylor expansion in the explicit method, see Eq. (5.23). This may lead to minor deviations and may be associated to some of the deviation between the methods. This aspect will not be investigated in this thesis. Further investigation of the implicit method, related to the boundary value problem, has shown negative values of x. According to the theory, the structure should decrease exponentially towards zero as a function of visco-plastic strains and never become zero or below. This may be seen as an error in the implicit scheme and increase the uncertainty of this method. Hence, it is concluded that this tendency occurs as a consequence of combining the coding from the explicit scheme with the Newton Raphson's scheme made by Roenningen (2015) which causes some kind of numerical errors. However, due to time limitations it has not been possible to investigate this phenomenon in greater details.

To sum up, the deviation in the settlement predictions is quite interesting since several of the scenarios in Soil Test states that the soil response yields the correct pattern and are approximately the same for both methods. It may be concluded that a careful and detailed verification of the constitutive model is required to ensure that the model yields the correct response. Furthermore, the utilized soil parameters, in the first and final prediction, have been calibrated by the explicit scheme. Hence, if further investigations indicate that the explicit scheme yields an incorrect response the calibrated parameters would have obtained others values through the implicit scheme. It is assumed that the implicit model would be able to simulate a similar response with some modifications in the input parameters if its shows to be correct.

8.10 Prediction - Recovery

The recovery of x over time should be investigated to see its influence in a boundary value problem. The effect has been discussed for a single stress point in Section 6.3.9 but further investigation will be shown here. Recalling, R refers to maximum recovery of the initial structure and R_t refers to the pace of the recovery. Seven creep tests are executed utilizing the input parameters similar to soil layer 2 (2.0 - 5.0 m) at an isotropic stress condition of $\sigma' = 100$ kPa, see Figure 8.31.

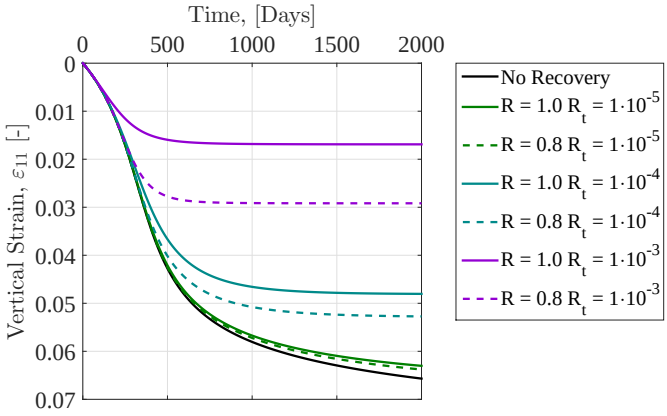

Figure 8.31: *Effect of recovery of structure during creep test. The utilized input parameters are similar to the properties of layer 2 (2.0 - 5.0 m) and an isotropic stress condition of $\sigma' = 100$ kPa.*

It may be observed that high values of R and R_t yields a significant reduction in the rate of creep strains and may completely stop the development of creep strains for the long term. This is caused by a high recovery of x which may be associated to a higher value of OCR_τ. The initial path for all the scenarios is similar to the test without recovery. The deviation from the test without recovery depends on the magnitude of R and R_t. The case, $R = 0.8$ and $R_t = 1 \cdot 10^{-5}$, yields approximately the same response as for the case without recovery. This case has been controlled for each layer in the strata related to the final prediction and the same conclusion may be drawn. The same behaviour should be expected during a boundary value problem. Three scenarios are assembled and may be seen in Table 8.8.

Table 8.8: *Different scenarios with recovery of structure. The input parameters (R and R_t) are used for all layers.*

Scenario	R_t [-]	R [-]	**Comments**(1)
1	$1 \cdot 10^{-5}$	0.8	Minor deviation (approx. same creep).
2	$1 \cdot 10^{-4}$	1.0	Influence of recovery (less creep).
3	$1 \cdot 10^{-3}$	1.0	High influence for recovery (lesser creep).

(1) According to Figure 8.31.

The effect of recovery will be compared to the settlement just beneath the center of the embankment and may be seen on Figure 8.32. Notice, the other input parameters which are not presented in Table 8.8 are similar to those utilized in the final prediction. The excess pore pressure for day No. 36 and No. 1220 along with the state parameters x, p'_{mi} and the plastic multiplier for day No. 1120 may be seen in Appendix G.2 for the three scenarios.

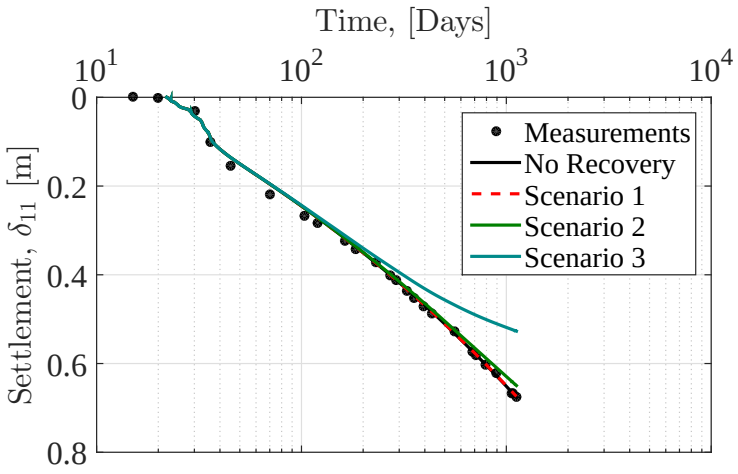

Figure 8.32: *Influence of recovery on the settlement just beneath the center for the embankment.*

The boundary value problem yields the same conclusion of the single stress point. Scenario 1 yields a final settlement of 674 mm which should be compared to the final prediction without recovery of 676 mm and the field measured value of 676 mm. Increasing the rate of recovery (R_t), as in scenario 2, yields a final settlement of 650 mm and a further increase yields an even lower settlement, see Figure 8.32. The recovery effect is associated to the development of visco-plastic strains. Hence, the effect may be coupled to the excess pore pressure of each scenario where scenario 3 has the lowest magnitude. The phenomenon regarding the initial path, as for the single stress point, is also present in the boundary value problem. Scenario 3 yields the largest recovery of x and its evolution of x may be investigated. The lowest amount of x may be observed at day No. 329, see Figure 8.33. After this day, the structure initiate to regain itself as a function of time, and day No. 329 may be defined as the transition where the recovery feature overtakes the destruction feature. The final amount of structure may be seen on Figure 8.33(b) where a significant amount of structure is regained with respect to day No. 329. However, it should be noted that the affected area is increased. Hence, some regions have suffered a loss in structure. This effect may be explained by

the equilibrium criteria between the destruction and recovery phenomena where recovering cannot initiate until after some structure has been destroyed.

It may be concluded that the recovery element in the SCA-R model yields an extra parameter to control the creep strains at the long term. The recovery effect works as expected for a single stress point as well as for a boundary value problem. The final prediction does not benefit when activating the recovery effect for the given time. However, one should keep in mind that the input parameters have been calibrated to fit the settlement without the recovery effect. Another argument could be that the influence of recovery is minor for a period of 1200 days for this particular case. The structure observed in natural soft clay is developed over thousands of years. Hence, the regaining during 1120 days could be insignificant.

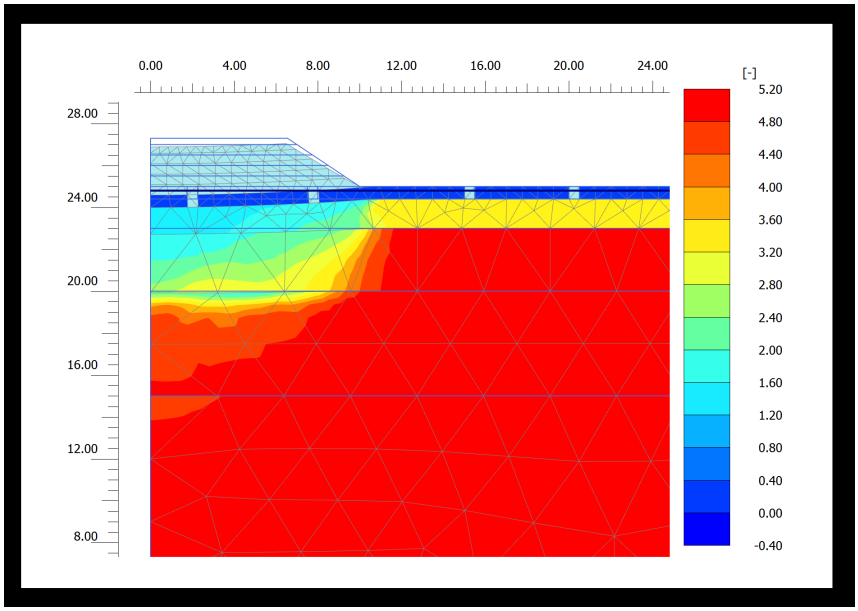

(a) Day No. 329.

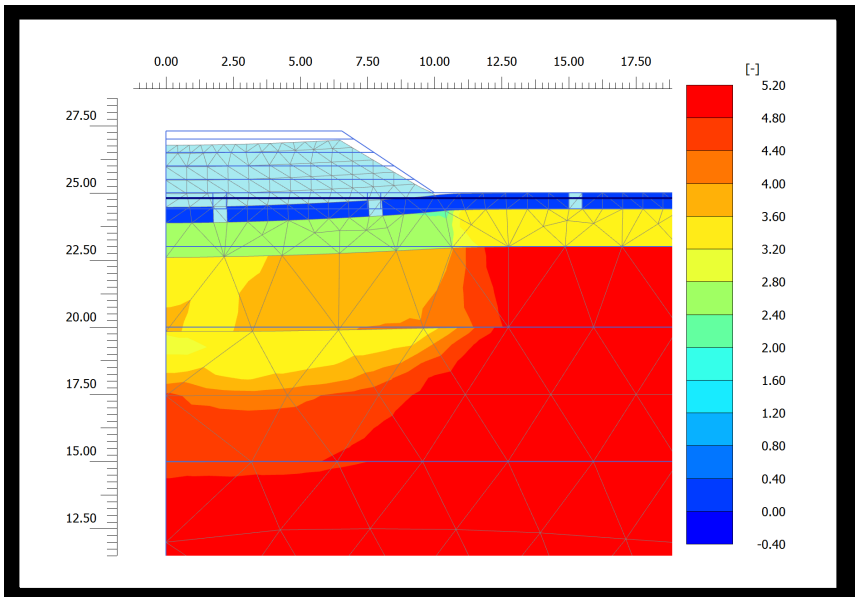

(b) Day No. 1120.

Figure 8.33: *Structure (x) for scenario 3.*

8.11 Coupling Effect - Reconstituted Response

The coupling effect between the recovery of structure and the evolution of the plastic multiplier with respect to time may be further investigated through a reconstituted sample. A reconstituted sample represent a stress history and structure (bonding) which are completely removed ($x = 0.0$, $OCR_\tau = 1.0$ and $POP = 0.0$). Utilizing these specifications to simulate a compression scenario in continuation of a drained creep test the coupling effect may be analysed. The drained creep phase is executed in 30 days with an associated stress condition of: $\sigma'_{11} = \sigma'_{22} = \sigma'_{33} = 100$ kPa and the compression phase is executed in 1 day by the stress change of: $\Delta\sigma'_{11} = 100$ kPa and $\Delta\sigma'_{22} = \Delta\sigma'_{33} = 50$ kPa. The remaining soil parameters are similar to soil layer 3 (5.0 - 10.0 m) in the final prediction. Five simulations may be seen on Figure 8.34(a) for different magnitudes of the recovery pace (R_t) and a constant value of $R = 1.0$.

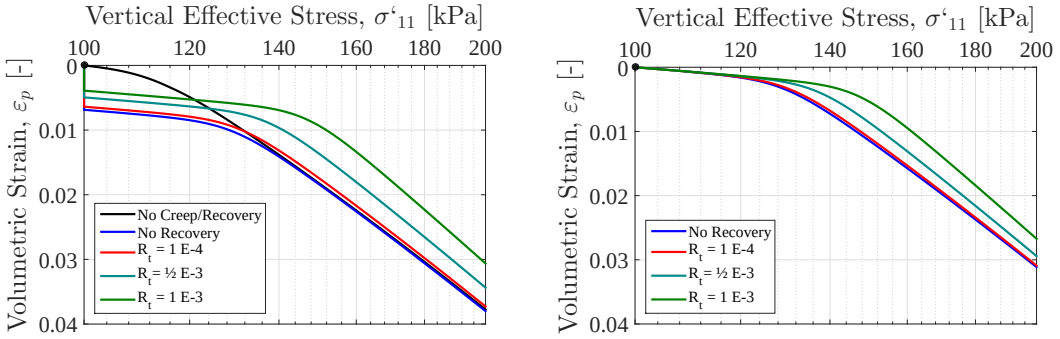

(a) Coupling effect between recovery of x and creep.

(b) Reset volumetric strain after creep period.

Figure 8.34: *Reconstituted response during drained creep and compression affected by recovery. The utilized input parameters are similar to soil layer 3 (5.0 - 10.0 m) in the final prediction.*

Notice, the initial amount of bonding (x_0) is manually set to zero in FORTRAN to activate the recovery without any destruction. Analysing the drained creep part, it may be observed that the visco-plastic strains causes an apparent yield point relative to the elasto-plastic response ()no creep. The consequence of the coupling effect may be observed through change in volume where the magnitude of the recovery pace is directly associated to the visco-plastic strain. Hence, a higher recovery pace give rise to a smaller amount of visco-plastic strains. Figure 8.34(b) shows the additional strength gained by recovery where the volume change caused by creep is removed. The recovery of x induces a higher apparent yielding point with respect to simulation without recovery. The evolution of x may be seen on Figure 8.35.

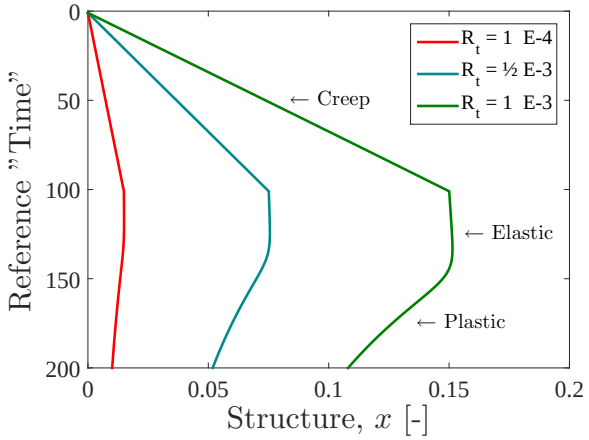

Figure 8.35: *Evolution of x during drained creep and compression for a reconstituted sample. The soil parameters is similar to layer 3 (5.0 - 10.0 m) in the final prediction and $POP = x = 0.0$.*

Notice that the "Reference Time = 0..100" symbolize the drained creep phase and "Reference Time = 101..200" symbolize the compression phase. As marked on Figure 8.35, the structure increases during the creep phase as a function of time and the magnitude of R_t. During the compression, the structure slightly increase in the elastic region. The destruction is pure associated visco-plastic strains. Hence, the recovery is larger than the destruction of x in the elastic region for the compression phase. However, other scenarios could show an opposite phenomenon if the loading condition and the combination of input parameters causes a higher rate of visco-plastic strains. Beyond the yielding point, the structure is destructed where the pace is controlled by the destruction parameters a and b along with the magnitude of x. Hence, the destruction rate of x is larger for the green curve on Figure 8.35 caused by a higher magnitude of x even though it has the largest recovery pace.

This analysis shows that the SCA-R model is capable to of simulating creep as the proposed time line suggested by Bjerrum (1967) and how the recovery effect reduces the creep rate and influence the apparent yield point.

8.11.1 Ageing Effect during Loading

As presented in Section 3.8, a CRS test with a strain rate of $\dot{\varepsilon}_p = 1.0 \cdot 10^{-7}\text{s}^{-1}$ was affected by ageing effects relative to a conventional 24 hrs incremental loading. The feature of recovering the structure in the SCA-R model may influence the compression path and show some of the observed behaviour as presented in Section 3.8. Figure 8.36(a) shows six compression simulations executed over 50 days for different values of R_t on a reconstituted sample ($OCR = 1.0$ and $POP = x_0 = 0.0$). The remaining soil parameters are similar to soil layer 3 (5.0 - 10.0 m) in the final prediction and $R = 1.0$.

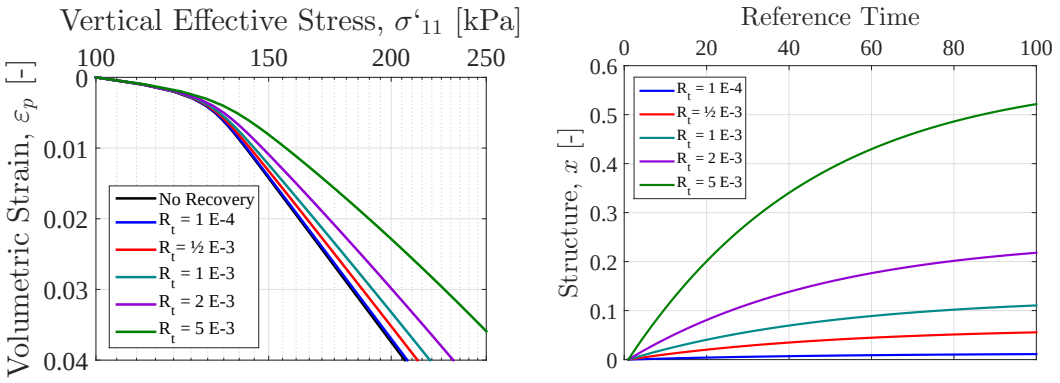

(a) Coupling effect between recovery of x and creep.

(b) Reset volumetric strain after creep period.

Figure 8.36: *Reconstituted response during compression affected by recovery. The utilized input parameters are similar to soil layer 3 (5.0 - 10.0 m) in the final prediction.*

It may be observed that a higher recovery is associated to a stiffer soil response. The evolution of x may be seen on Figure 8.36(b) which shows the expected exponential patten. Notice that destruction of x also occurs during the simulation but the net evolution of x is positive. However, x converged towards a lower boundary value than $\left(\frac{r_{si} - r_{si,min}}{r_{si,min}} \cdot\right)$ caused by the destruction. The boundary value would be an equilibrium between the recovery and destruction effects.

From this analysis it may be concluded the SCA-R model is able to effect the compression path through the recovery of x. However, further investigation is necessary to decide if the observed response from the SCA-R model is similar to the observed behaviour in laboratory tests.

In general, further research and testing is required before the recovery effect may be dismissed or acknowledged. The mathematical formulation, see Eq. (4.23), should also be reconsidered to see if another approach yields better predictions. The investigation of the recovery of structure will end here due to time limitations.

Chapter 9

Conclusion

This chapter contains the final conclusion of the work related to this master's thesis. Suggestions for further work will be given at the end of this chapter.

9.1 Summary and Conclusion

The objective of this master's thesis has been related to natural soft clay and the characteristic features which dominate its mechanical behaviour.

The mechanical behaviour of natural soft clay has been studied through a literature study to identify the characteristic features which have been observed in the field and in the laboratory. These features are mainly associated to viscous and ageing effects and may dominate the mechanical response with respect to natural soft clay. The main characteristics have been outlined as:

- Structure
- Creep
- Rate-dependency

Where the term, **structure**, consist of the fabric representing the arrangement of the particles and pore space, and the bonding representing the inter-particle forces between the clay particles and the water. These characteristics have created the framework for a new constitutive model known as the SCA-R which stands for: Structure Creep Anisotropy – Recovering. The constitutive model is based on effective stresses, utilizes the Modified Cam Clay (MCC) model and invariants as a framework. The MCC response may be obtained by setting the additional input parameters, related to the natural soft clay response, to zero.

The anisotropy is introduced as an initial rotated and skewed yield surface. The evolution in anisotropy corresponds to rotation of the inclined yield surface. The elastic anisotropy is implemented through an elastic anisotropic parameter which increase or decrease the stiffness in vertical or horizontal direction similar to a modified version of Houlsby and Graham (1983) anisotropy factor. The creep and rate-dependency are simulated through a time evolution of the plastic multiplier suggested by Grimstad (2009). The evolution is based on a time resistance concept suggested by Janbu (1969) which utilizes one-dimensional evolution in the general three-dimensional space. The bonding between the clay particles is implemented through an intrinsic yield surface and an associated surface represented by the intrinsic properties and the amount of bonding. The model introduces a method to regain the lost structure (bonding) over time. This feature yields an additional parameter to control the visco-plastic strains through a induced coupling term. However, more testing is required to ensure its capability to capture real soil response.

The model requires 17 input parameters to access all of its implemented features. Three additional input parameters are available to switch between different methods of simulating the stress history, evolution of anisotropy, and failure criteria in the general stress space. The model assumes associated flow and thereby introduces eight state (hardening) parameters in total. The SCA-R model is implemented as a user defined soil model in PLAXIS through the interface between PLAXIS and FORTRAN. It utilizes a simple forward Euler scheme to solve the local integration required by PLAXIS.

The necessary soil parameters associated to the SCA-R model have been interpreted from several laboratory tests with respect to the relevant stress domain. These parameters have been calibrated by performing several back-calculations of the CRS and undrained tri-axial tests which have been used to interpret the initial input parameters. These back-calculations have shown that the SCA-R model is capable of capturing the main characteristics which have been observed in natural soft clay and only minor modifications of the interpreted laboratory parameters were necessary.

As a final test, a full scale boundary value problem for the embankment located at Onsøy in Norway has been performed. The SCA-R model has shown capability to capture the soil response and the dissipation of excess pore water as expected and yields fairly acceptable results compared to field measurements. The predictions of the settlement, excess pore pressure and horizontal displacement have been compared to predictions from five other soil models. The main conclusion states that the SCA-R model yields quite accurate results according to the predictions of settlement and excess pore pressure. However, because of its limitation to small stiffness, the SCA-R model yield less accurate results compared to soil models which have incorporated this feature. However, the prediction is still relatively fair compared to the field measurements.

The performance of the forward Euler scheme has been tested against an implicit scheme utilizing a Newton-Raphson iteration to solve the differential equations in the local integration. During the performance investigation complications arose and the predictions of the two integration schemes were not similar. However, it is believed that this is a consequence of an error when combining the code from the explicit scheme to the implicit scheme. This conclusion is supported by unrealistic predictions of the structure in the implicit scheme. The step size associated to the explicit scheme has been investigated. Changing the restrictions, which control the maximum time and strain increment, by one order of magnitude have showed no sensitivity in the final predictions of the embankment. It is believed that PLAXIS applied a time and strain increment, for the given case, which yields an accurate result without the restrictions. However, more verification is needed because of some unexplained observations when comparing the explicit and implicit schemes.

The recovery of structure has not been activated in the final prediction of the embankment. However, the effect of activating the recovery on the final prediction has been investigated. It may be concluded that lesser visco-plastic strains were generated and a higher amount of structure were left at the long term, as expected. In addition, the recovery of structure has been investigated on a reconstituted sample. The implemented feature is able to simulate a similar response as observed by laboratory tests. However, this has not been compared to any specific laboratory test and further research and testing are required before the recovery effect may be dismissed or acknowledged.

It may be concluded that a user friendly soil model which is able to capture the main characteristic features in natural soft clay has been created. The models seems quite robust with similar computational time as for other available soil models in PLAXIS. However, further verification is necessary before the model finally can be acknowledged.

9.2 Suggestions for Further work

The implemented feature, related to the recovering of structure, should be investigated in greater detail to verify whether the model is capable of capturing more of the behaviour observed in the laboratory and in the field. For the short term, laboratory tests performed on reconstituted clays

have shown that a waiting period of a few days change the mechanical behaviour during tri-axial testing which is not associated to creep (Sorensen, 2006). Regarding the long term, during larger infrastructure projects a huge amount of natural soft clay may be removed and seen as a waste of material. However, this material could be utilized if the initial mechanical properties and its evolution over time were known.

The SCA-R model may be further extended to capture the soil response in greater details:

- Predictions from the embankment located at Onsøy have shown that the lack of small stiffness causes large strains in areas where the strains should have a minor magnitude. Hence, the performance in the small strain domain (i.e. shear strains below 10^{-5}) should be optimized to obtain more realistic predictions. In addition, the SCA-R assumes a constant Poisson's ratio which may trigger a too large stiffness during cyclic loading.
- The assumption of associated flow could be changed so that the SCA-R model uses non-associated flow as e.g. the n-SAC or the SANICLAY model. Hence, the model will contain a separate yield and plastic potential surface which are controlled by different inclinations and evolution laws, see Figure 9.1(a). Hence, one may apply the rotational hardening suggested by Wheeler et al. (2003), which is restricted by high friction angles, to the plastic potential and utilize another approach for the yield surface.
- With respect to the recovery of structure for the long term, the model could be extended to simulate ground improvement in form of cementing the soil. This has been done in the MCC model by (Horpibulsuk and Liu, 2009) and the principle may be seen on Figure 9.1(b).

Other improvements or extensions of the SCA-R may be suggested. However, one should keep in mind that the majority of these aspects require additional input parameters. Increasing the number of input parameters would most likely not be beneficial if the SCA-R should be utilized outside the research society.

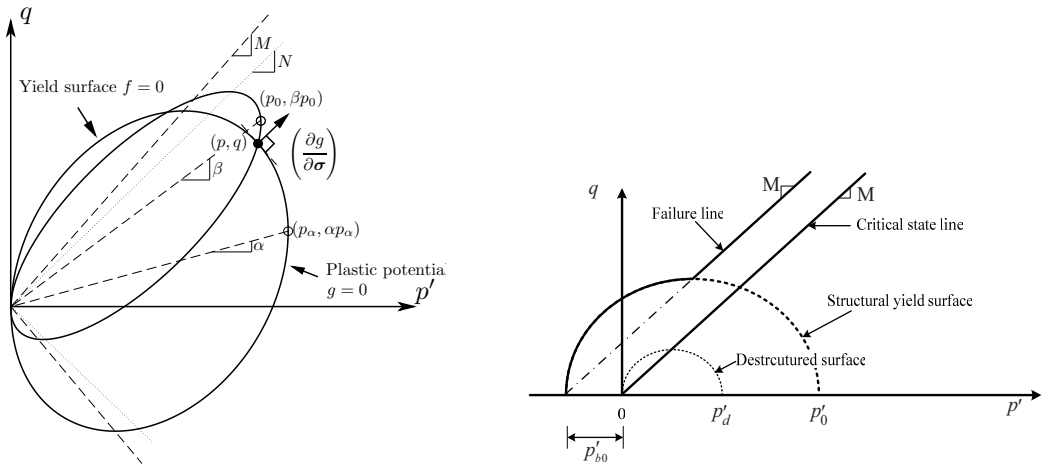

(a) Effect of non-associated flow. Note: the plastic potential is not equal to the yield surface

(b) Material idealization for the MCC model suggested by (Horpibulsuk and Liu, 2009)

Figure 9.1: *Suggested extensions to the SCA-R model.*

Another improvement, which does not requires any additional input parameters, is related to the solution technique of the local integration. The forward Euler scheme could be changed to a more advanced explicit scheme or the implicit approach suggested by Roenningen et al. (2014). In addition, it is suggested to develop a software which may be used to interpret and calibrate the input parameters since it may be confusing for people who are inexperienced in natural soft clay and how these features are modeled.

Bibliography

M. Ashrafi. Implementation of a Critical State Soft Soil Creep Model with Shear Stiffnes. Technical report, NTNU, 2014.

A. H. Augustesen. *The Effects of Time on Soil Behaviour and Pile Capacity*. PhD thesis, Aalborg Universitet, 2006.

L. Bamberg. *Master Thesis at NTNU*. 2009.

J. P. Bardet. Lode Dependences for Isotropic Pressure-Sensitive Elastoplastic Materials. *Journal of Applied Mechanics*, 57:498–506, 1990. doi: 10.1115/1.2897051.

T. Berre. Additional Tests on Block Samples in Connection with the Onsøy Test Fill. Technical report, Norwegian Geotechnical Institute (NGI), Oslo, 2010.

T. Berre. Test Fill on Soft Plastic Marine Clay at Onsøy, Norway. *Canadian Geotechnical Journal*, 50:30–50, 2013. doi: 10.1139/cgj-2012-0479.

T. Berre and L. Bjerrum. Shear Strength of Normally Consolidated Clays. In *Proceedings of the 8th International Conference on Soil Mechanics and Foundation Engineering*, volume 1, pages 39–49, Moscow, Russia, 1973.

L. Bjerrum. Engineering Geology of Norwegian Normally-Consolidated Marine Clays as Related to Settlements of Buildings. *Géotechnique*, 17:83–118, 1967. doi: 10.1680/geot.1967.17.2.83.

L. Bjerrum. Problems of Soil Mechanics and Construction on Soft Clays. Technical report, Norwegian Geotechnical Institute (NGI), Oslo, 1973.

L. Bjerrum and K. Y. Lo. Effect of Aging on the Shear-strength Properties of a Normally Consolidated Clay. *Géotechnique*, 13(2):147–157, 1963.

J. B. Burland. On the Compressibility and Shear Strength of Natural clays. *Géotechnique*, 40: 329–378, 1990. doi: 10.1680/geot.1990.40.3.329.

J. P. Carter and M. D. Liu. Virgin Compression of Structured Soils. *Géotechnique*, 49:43–57, 1999. doi: 10.1680/geot.1999.49.1.43.

A. Casagrande and S. D. Wilson. Effect of Rate of Loading on the Strength of Clays and Shales at Constant Water Content. *Géotechnique*, 2(3):251–263, 1951.

W. Coombs, R. Crouch, and C. Augarde. Influence of Lode Angle Dependency on the Critical State for Rotational Plasticity. In *International Conference on Computational Plasticity*, Barcelona, Spain, 2009.

Y. Dafalias. An Anisotropic Critical State Soil Plasticity Model. *Mechanics Research Communications*, 13(6):341–347, 1986. doi: 10.1016/0093-6413(86)90047-9.

Y. Dafalias and M. Taiebat. Anatomy of Rotational Hardening in Clay Plasticity. *Géotechnique*, 63(16):1406–1418, 2013. doi: 10.1680/geot.12.P.197.

Y. Dafalias, M. T. Manzari, and A. G. Padadimitriou. SANICLAY: Simple Anisotropic Clay Plasticity Model. *International Journal for Numerical and Analytical Methods in Geomechanics*, 30:1231–1257, 2006. doi: 10.1002/nag.

Y. F. Dafalias and L. R. Herrmann. Bounding Surface Plasticity. III: Application to Anisotropic Cohesive Soils. *Journal of Engineering Mechanics*, 112(12):1292–1318, 1986. ISSN 0733-9399. doi: 10.1061/(ASCE)0733-9399(1986)112:12(1292).

A. Emdal, R. Sandben, K. Sennest, S. Nordal, N. Janbu, L. Grande, and H. A. Kornbrekke. *Lecture Notes, Geotechnics Field and Laboratory Investigations (TBA4110)*. NTNU, Geotechnical division, Trondheim, 1. edition, 2014.

J. Fish and T. Belytschko. *First Course in Finite Elements (Book)*. JohnWiley & Sons, Ltd, 2006. ISBN 9780470035801.

A. Gasparre. *Advanced Laboratory of London Clay*. PhD thesis, Imperial College London, 2005.

A. Gens and R. Nova. Conceptual bases for a Constitutive Model for Bonded Soils and Weak Rocks. *Geological Features, Investigation and Classification: Mechnical ProperTIES and Behaviour*, 1: 485–494, 1993.

H. Ghiabi and A. Selvadurai. Laboratory Testing of a Soft Silty Clay. *Soft Soil Engineering*, (978-0-415-42280-2):447–456, 2007.

J. Graham, R. B. Pinkney, K. V. Lew, and P. G. S. Trainor. Curve-fitting and Laboratory Data. *Canadian Geotechnical Journal*, 19:201–205, 1982. doi: 10.1139/t82-023.

J. Graham, M. L. Noonan, and K. V. Lew. Yield States and Stress–Strain Relationships in a Natural Plastic Clay. *Canadian Geotechnical Journal*, 21:598–599, 1984. doi: 10.1139/t84-064.

G. Grimstad. *Development of Effective Stress Based Anisotropic Models for Soft Clays*. PhD thesis, Norwegian University of Science and Technology, 2009.

G. Grimstad and T. Benz. *Lecture Notes, Soil Modeling (BA8104) - Implementation of Soil Models*. NTNU, Geotechnical division, Trondheim, 1. edition, 2014.

G. Grimstad and S. Degago. *Numerical Methods in Geotechnical Engineering (NUMGE 2010): A Non-Associated Creep Model for Structured Anisotropic (n-SAC)*. Taylor & Francis Group, London, England, 2010. ISBN 9780415592390. doi: 10.1201/b10551-1.

G. Grimstad, S. A. Degago, S. Nordal, and M. Karstunen. Modeling Creep and Rate Effects in Structured Anisotropic Soft Clays. *Acta Geotechnica*, 5:69–81, 2010. doi: 10.1007/s11440-010-0119-y.

L. Hight, D. W., Potts, D. M., Zdravkovic. The Effect of Strength Anisotropy on the Behaviour of Embankments on Soft Ground. *Géotechnique*, 52(6):447–457, 2002.

Hokkaido. Elasto-Plastic Description of Soil Behaviour. URL `http://www.eng.hokudai.ac.jp/labo/soilmech/lectures/SM_nishimura/Week5.pdf`.

S. Horpibulsuk and M. D. Liu. Behavior of Cemented Soft Clays in Undrained Situations. In *The Australian Earthquake Engineering Society*, pages 1–9, 2009.

G. T. Houlsby and J. Graham. Anisotropic Elasticity of a Natural Clay. *Géotechnique*, 33(2): 354–354, 1983. doi: 10.1680/geot.1983.33.3.354.

G. T. Houlsby, A. Amorosi, and E. Rojas. Elastic Noduli of Soils Dependent on Pressure: A Hyperelastic Formulation. *Géotechnique*, 55(5):383–392, 2005.

J. Jaky. The Coefficient of Earth Pressure at Rest. *Journal of the Society of Hungarian Architects and Engineering*, 78(22):355–358, 1944.

N. Janbu. *The Resistance Concept Applied to Deformations of Soils (Bulletin 3)*, volume 1. NTNU, Geotechnical division, Trondheim, 1 edition, 1969.

N. Janbu. Soil Models in Offshore Engineering. *Géotechnique*, 35(3):241–282, 1985.

N. Janbu. *Sediment Deformations. A Classical Approach to Stress-Strain-Time Behaviour of Granular Media as Developed at NTH over a 50 Year Period*. NTNU, Geotechnical division, Trondheim, 1. edition, 1998.

M. Karstunen, H. Krenn, S. Wheeler, M. Koskinen, and R. Zentar. The Effect of Anisotropy and Destructuration on the Behaviour of Murro Test Embankment. *Soil Mechanics and Foundations Division*, 5(2):87–97, 2005. doi: 10.1061/(ASCE)1532-3641(2005)5:2(87).

M. Karstunen, M. Koskinen, and U. of Strathclyde. Plastic Anisotropy of Soft Reconstituted Clays. *Canadian Geotechnical Journal*, 45(3):314–328, 2008. doi: 10.1139/T07-073.

Y. T. Kim and T. H. Do. Effect of Leaching on the Compressibility of Busan Clay. *KSCE Journal of Civil Engineering*, 14:291–297, 2010. doi: 10.1007/s12205-010-0291-5.

S. Krenk and J. Hoegsberg. *Statics and Mechanics of Structures (Book)*. 2013. ISBN 978-94-007-6112-4. doi: 10.1007/978-94-007-6113-1.

S. Lacasse, T. Berre, and G. Lefebvre. Block Sampling of Sensitive Clay. In *Eleventh International Conference on Soil Mechanics and Foundation Engineering*, volume 2 and 3, pages 887–892, 907–912, 1003–1006 and 1401–1406 , 1589–1, 1985.

P. V. Lade and J. M. Duncan. Elastoplastic Stress-Strain Theory for Cohesionless Soil. *Geotechnical Engineering Division, ASCE*, 101:1037–1053, 1975.

L. Laloui, S. Leroueil, and S. Chalindar. Modelling the Combined Effect of Strain Rate and Temperature on One-Dimensional Compression of Soils. *Canadian Geotechnical Journal*, 45: 1765–1777, 2008. doi: 10.1139/T08-093.

T. Länsivaara. *A Study of the Mechanical Behavior of Soft Clay*. PhD thesis, Norwegian University of Science and Technology, 1999.

M. Leoni, M. Karstunen, and P. Vermeer. Anisotropic Creep Model for Soft Soils. *Géotechnique*, 58(3):215–226, 2008. doi: 10.1680/geot.2008.58.3.215.

S. Leroueil and M. E. S. Marques. Importance of Strain Rate and Temperature Effects in Geotechnical Engineering. *Geotechnical Special Publication by ASCE*, 61, 1996.

S. Leroueil and P. R. Vaughan. The General and Congruent Effects of Strucure in Natural Soil and Weak Rocks. *Géotechnique*, 40(3):467–488, 1993.

S. Leroueil, M. Kabbaj, F. Tavenas, and R. Bouchard. Stress-Strain-Strain Rate Relation for the Compressibility of Sensitive Natural Clay. *Géotechnique*, 35(2):159–180, 1985.

M. Liingaard, A. Augustesen, and P. V. Lade. Characterization of Models for Time-Dependent Behavior of Soils. *International Journal of Geomechanics*, 4(3):157–177, 2004.

M. D. Liu and J. P. Carter. A Structured Cam Clay Model. *Canadian Geotechnical Journal*, 39: 1313–1332, 2002. doi: 10.1139/t02-069.

J. Locat and D. Demers. Viscosity, Yield Stress, Remolded Strength, and Liquidity Index Relationships for Sensitive Clays. *Canadian Geotechnical Journal*, 25(4):799–806, 1988. ISSN 0008-3674. doi: 10.1139/t88-088.

T. Lunne, T. Berre, K. H. Andersen, S. Strandvik, and M. Sjursen. Erratum: Effects of Sample Disturbance and Consolidation Procedures on Measured Shear Strength of Soft Marine Norwegian Clays. *Canadian Geotechnical Journal*, 43:726–750, 2006. doi: 10.1139/t07-008.

T. Lunne, S. Perkins, and C. S. Chang. NGI Report No. 20081088-1: Temperature Effects on Laboratory Strength Measured on Soft Clay Sampled in Deep Water and Cold Environment - Literature Survey and Results of Laboratory Tests. Technical report, 2009.

T. Lunne, Y. Shaoli, G. Forsberg, and C. S. Chang. NGI Report No. 20091784-00-3-R: Soil Investigation. Technical report, 2010.

S. W. M. Koskinen, M. Karstunen. Modelling Destructuration and Anisotropy of a Natural Soft Clay. In *5th European Conference on Numerical Methods in Geotechnical Engineering*, pages 11–20, Paris, France, 2002.

H. Matsuoka and T. Nakai. Stress-Deformation and Strength Characteristics of Soil under Three Difference Principal Stresses. *Proceedings of the Japan Society of Civil Engineers (JSCE)*, 232: 59–70, 1974.

M. Mehli. NGI Report: EU Creep (PIAG-GA-2011-286397). Technical report, 2015a.

M. Mehli. NGI: Norwegian Geotechnical Institute, 2015b.

J. K. Mitchell. Fundamentak Aspects of Thixotropy in Soil. *Soil Mechanics and Foundations Design*, 86(3):19–52, 1960.

D. Muir Wood. General Report: Evaluation of Material Properties, Pre-Failure Deformation on Geomaterials. Technical report, Rotterdam, Netherlands, 1994.

A. Näätänen, S. Wheeler, M. Karstunen, and M. Lojander. Experimental Investigation of an Anisotropic Hardening Model for Soft Clays. In *Proceedings of the 2nd International Symposium on Pre-failure Deformation Characteristics of Geomaterials*, pages 28–30, Torino, Italy, 1999.

S. Nordal. *Lecture Notes, Geotechnical Engineering, Advanced Course (TBA4116).* NTNU, Geotechnical division, Trondheim, 1. edition, 2014a.

S. Nordal. *Lecture Slides, Geotechnical Engineering, Advanced Course (TBA4116).* NTNU, Geotechnical division, Trondheim, 1. edition, 2014b.

S. Nordal. *Lecture Notes, Soil Modeling (BA8104).* NTNU, Geotechnical division, Trondheim, 1. edition, 2014c.

H. Ohta. Comparison of Original and Modified Cam-Clay Models Extended For K0-Consolidated Clays. In *Proceedings of the Sri Lankan Geotechnical Society's First International Conference on Soil & Rock Engineering*, pages 1–5, 2007.

M. Olsson. *On Rate-Dependency of Gothenburg Clay.* PhD thesis, Chalmers University of Technology, 2013.

D. Perret, J. Locat, and S. Leroueil. Strength Development with Burial in Fine-Granied Sediments from the Sqguenay Fjord, Quebec. *Canadian Geotechnical Journal*, 32:247–262, 1995.

P. Perzyna. The Constitutive Equations for Rate Sensitive Plastic Materials. *Quarterly of Applied Mathematics*, 20:321–322, 1963.

J. M. Pestana. Formulation of a Unified Constitutive Model for Clays and Sands. *International Journal For Numerical and Analytical Methods in Geomechanics*, 23:1215–1243, 1999.

. PLAXIS. PLAXIS - User Defined Soil Models (2015-02-08). URL `http://kb.plaxis.nl/models/plaxis-user-defined-soil-models`.

PLAXIS. PLAXIS 2D - AE Material Models Manual 2014. Technical report, 2014a.

PLAXIS. PLAXIS 2D - Scientific Manual 2014. Technical report, 2014b.

PLAXIS. PLAXIS - User Defined Soil Models, 2015. URL `http://kb.plaxis.nl/models/plaxis-user-defined-soil-models`.

D. Potts and L. Zdravkovic. Some Pitfalls when using Modified Cam Clay. In *Proceedings of the Workshop on Soil and Structure Interaction (COST C7)*, pages 1–14, Thessaloniki, Greece, 1999.

A. M. Richardson and R. V. Whitman. Effect of Strain-Rate upon Undrained Shear Resistance of a Saturated Remoulded Fat Clay. *Géotechnique*, 13(4):310–324, 1963.

J. A. Roenningen. Ph.D. Candidate at Norwegian University of Science and Technolgy - Personal Correpondance., 2015.

J. A. Roenningen, V. Gavel-Solberg, and G. Grimstad. Effective Stress Model for Soft Scandinavian Clays. In *European Young Geotechnical Engineers Conference*, pages 1–4, Barcelona, Spain, 2014.

K. Roscoe and J. Burland. On The Generalised Stress-Strain Behaviour of 'Wet' Clay. *Eng. plasticity*, pages 535–609, 1968.

M. Rouainia and D. Muir Wood. A Kinematic Hardening Constitutive Model for Natural Clays with Loss of Structure. *Géotechnique*, 50(2):153–164, 2000. doi: 10.1680/geot.2000.50.2.153.

H. Sekiguchi and H. Ohta. Induced Anisotropy and Time Dependency in Clays, Constitutive Equation of Soils. In *Soil Mechanics and Foundations Engineering*, volume 9, pages 229–238, Tokyo, Japan, 1977.

S. Seng and H. Tanaka. Properties of Very Soft Clays: A Study of Thixotropic Hardening and Behavior under Low Consolidation Pressure. *Soils and Foundations*, 52(2):335–345, 2012. doi: 10.1016/j.sandf.2012.02.010.

G. Sides and L. Barden. The Microstructure of Dispersed and Flocculated Samples of Kaolinite, Illite, and Montmorillonite. *Canadian Geotechnical Journal*, 8:391–399, 1970.

A. Singh and J. K. Mitchell. General Stress-Strain-Time Function for Soils. *ASCE Soil Mechanics and Foundations Division*, 94(1):21–46, 1968.

A. W. Skempton and R. D. Northey. The Sensitivity of Clay. *Géotechnique*, 3(1):30–53, 1952.

K. Soga, J. K. Mitchell, and M. Hon. Rate-Dependent Deformation of Structured Natural Clays. *Geotechnical Special Publication by ASCE*, 62, 1996.

K. K. Sorensen. *Influence of Viscosity and Aging on the Behaviour of Clays*. PhD thesis, University College London, 2006.

D. Stolle, P. A. Vermeer, and P. G. Bonnier. A Consolidation Model for a Creeping Clay. *Canadian Geotechnical Journal*, 36:754–759, 1999. doi: 10.1139/t99-034.

G. Svanoe. KRYKON, Documentation and Manual (The "Soft Clay Deformation" Project.), 1986.

F. Tavenas, S. Leroueil, P. L. Rochelle, and M. Roy. Creep Behaviour of an Undisturbed Lightly Overconsolidated Clay. *Canadian Geotechnical Journal*, 15(3):402–423, 1978.

K. Terzaghi. The Shearing Resistance of Saturated Soils and the Angle between Planes of Shear. In *Proceedings of the 1st International Conference on Soil Mechanics and Foundation Engineering*, volume 1, pages 54–56, 1936.

A. Tsutsumi and H. Tanaka. Combined Effects of Strain Rate and Temperature on Consolidation Behavior of Clayey Soils. *Soils and Foundations*, 52(2):207–215, 2012. doi: 10.1016/j.sandf.2012.02.001.

P. A. Vermeer and H. Neher. A soft soil model that accounts for creep. In *Beyond 2000 in Computational Geotechnics*, Rotterdam, Netherlands, 1999.

S. J. Wheeler, A. Naatanen, M. Karstunen, and M. Lojander. An Anisotropic Elastoplastic Model for Soft Clays. *Canadian Geotechnical Journal*, 40:403–418, 2003. doi: 10.1139/T02-119.

T. Wichtmann. NGI Report No. 20092109: Verhalten bindiger Böden unter hochzyklisher Belastung: Experimentelle Untersuchungen und constitutive Beschreibung. Technical report, 2010.

P. K. K. Wong. Yielding and Plastic Flow of Sensitive Cemented Clay. *Géotechnique*, 25(4):763–782, 1975. doi: 10.1680/geot.1975.25.4.763.

D. M. Wood. *Soil Behaviour and Critical State Soil Mechanics (Book)*. Cambridge University Press, 1. edition, 1990. ISBN 9780521332491.

D. M. Wood. *Geotechnical Modelling (Book)*. Spon Press, 1. edition, 2004. ISBN 9780203477977.

P. Yoginder, G. Richard, and G. Campanella. Time-Dependent Behaviour of Undisturbed Clay. *Soil Mechanics and Foundations Division, ASCE*, 103(7):693–709, 1977.

R. Zentar, M. Karstunen, and S. J. Wheeler. Influence of Anisotropy and Destructuration on Undrained Shearing of Natural Clays. In *5th European Conference Numerical Methods in Geotechnical Engineering*, volume 21, pages 21–26, Paris, France, 2002.

NTNU – Trondheim
Norwegian University of
Science and Technology

Technical University
of Denmark

Development and Evaluation of an Effective Stress Based Model for Soft Clays

Appendix Report

Jesper Bjerre (s102905)

Supervisors:

Assistant Professor Varvara Zania	(DTU)
Professor Steinar Nordal	(NTNU)
Professor Gustav Grimstad	(NTNU)
Ph.D. Candidate Jon A. Rønningen	(NTNU)

Master Thesis in Geotechnical Engineering
Norwegian University of Science and Technology
Technical University of Denmark
June 10, 2015

Contents

List of Figures **iv**

List of Tables **vi**

A Task Description **1**

B Test fill - Onsøy **5**

B.1 Instrumentation 5

C Mathematical Derivations **7**

C.1 Continuum Mechanics 7

C.1.1 Stress State 7

C.1.2 Principal Stresses 8

C.1.3 Mean and Deviatoric Stresses 9

C.1.4 Stress Spaces 10

C.1.5 Strains and Strain Invariants 10

C.1.6 The Lode Angle 11

C.1.7 Bulk and Shear modulus 12

C.1.8 Tensors 13

C.2 CC vs. MCC 14

C.2.1 Derivation of Yield Surface 14

C.3 Critical State 16

C.3.1 Hand Calculations to Verify the MCC in MATLAB 19

C.4 Constitutive matrix 21

C.5 Time Resistance Concept 22

C.6 Talyor Expansion - Plasitic Multiplier 23

C.7 Elastic Anisotropy 24

C.8 Initial Anisotropy 25

C.8.1 Stress Ratio during One-dimensional Condition 25

C.8.2 Neglecting Elastic Strains 26

C.8.3 Neglecting Elastic Shear Strains 27

C.9 Rotational Hardening 28

D Programming **33**
D.1 Algorithm for the MCC Model . . . 33
D.1.1 Determination of Strains . . . 35
D.2 Simulations of Tri-axial Tests . . . 35
D.3 Subroutine User_Mod . . . 38
D.3.1 DLL File - Location . . . 39
D.3.2 Finding the UDSM in PLAXIS . . . 40
D.4 Macauley Brackets . . . 41

E Code **43**
E.1 MATLAB . . . 43
E.1.1 MCC in MATLAB . . . 43
E.1.2 Generate FORTRAN Code . . . 46
E.1.3 Changes to Implicit Integration . . . 50
E.2 FORTRAN . . . 51
E.2.1 User_Mod . . . 51
E.2.2 Constitutive Model . . . 53
E.2.3 Additional Coding . . . 60

F Soil Parameters **61**
F.1 Compression and Swelling Parameters . . . 61
F.2 Permeability and Its Evolution . . . 63
F.3 Unit Weight . . . 64
F.4 Creep Number . . . 64
F.5 Transformation of $\boldsymbol{r_s}$ to $\boldsymbol{r_{is}}$. . . . 66
F.6 Back Calculation . . . 69
F.6.1 Effect of $\boldsymbol{\alpha_e}$ . . . 69
F.6.2 CRS Tests . . . 69
F.6.3 Tri-axial Tests . . . 71

G Documentation of Calculations **73**
G.1 NGI Data . . . 73
G.2 Recovering . . . 74
G.2.1 Scenario 1 . . . 74
G.2.2 Scenario 2 . . . 76
G.2.3 Scenario 3 . . . 79
G.3 Investigation of Implicit vs. Explicit . . . 82

List of Figures

B.1 Overview of the instrumentation in the test fill located at Onsøy, see legend on the next page. Taken from (Berre, 2013). 5

B.2 Legend for Figure B.1. Taken from (Berre, 2013). 6

C.1 Stresses acting on a unit cube of soil orientated according to a Cartesian reference system 8

C.2 Stress spaces. 10

C.3 Difference between CC and MCC. Notice notation difference, $p_0 = p'_c$. 14

C.4 Difference between the original CC and the MCC. Notice notation difference, $\varepsilon_v = \varepsilon_p$. 14

C.5 Elliptical yield surface for the MCC. 15

C.6 State boundary surface. Taken from (Hokkaido). 16

C.7 Theoretical MCC: Drained tri-axial compression. 18

C.8 Theoretical MCC: Undrained tri-axial compression. 18

C.9 Hand calculation MCC: Drained, normal consolidated 19

C.10 Hand calculation MCC: Drained, over consolidated 19

C.11 Hand calculation MCC: Undrained, normal consolidated 20

C.12 Hand calculation MCC: Undrained, over consolidated 20

C.13 Janbu's stress-strain-time concept. Taken from (Janbu, 1998). 22

C.14 Concept of Eq. (C.54). Taken from (Grimstad et al., 2010). Notice, $\varepsilon_v = \varepsilon_p$. . . . 23

C.15 Equilibrium values of α/M for radial stress path with various η/M. Taken from (Dafalias and Taiebat, 2013) 29

C.16 Undrained stress path in compression and extension after K_0 consolidation, indicating uniqueness or lack of it of CSL. a) Eq. (C.83) b) Eq. (C.84) c) Eq. (C.85) d) Eq. (C.86) in Appendix C.9. Taken from (Dafalias and Taiebat, 2013). 31

D.1 MATLAB MCC: Drained normal consolidated. 36

D.2 MATLAB MCC: Drained over consolidated. 36

D.3 MATLAB MCC: Undrained normal consolidated. 37

D.4 MATLAB MCC: Undrained over consolidated. 37

D.5 Selecting the UDSM. 40

D.6 Choosing the correct DLL file. 40

D.7 Selecting the wanted soil model in the DLL file. 41

F.1 Interpreted compression and swelling index from CRS. The data is taken from Bamberg (2009) and Lunne et al. (2009). 61

F.2 Interpreted compression and swelling index from CRS. The data is taken from Lunne et al. (2010) and Berre (2010). 62

F.3 Interpreted permeability and change in permeability from CRS. The data is taken from Lunne et al. (2010), Lunne et al. (2009), and Bamberg (2009). 63
F.4 Interpreted creep number from CRS. The data is taken from Bamberg (2009) and Lunne et al. (2009). 64
F.5 Interpreted creep number from CRS. The data is taken from Lunne et al. (2010) and Berre (2010). 65
F.6 Interpreted compression and swelling index from CRS. The data is taken from Lunne et al. (2010) and Berre (2010). 66
F.7 Interpreted compression and swelling index from CRS. The data is taken from Bamberg (2009) and Lunne et al. (2009). 67
F.8 Interpreted compression and swelling index from CRS. Taken from Bamberg (2009) and Lunne et al. (2009). 68
F.9 Back calculations of the CRS for **Block**-19-A1-O1. Investigating the effect of α_e . 69
F.10 Back calculation of CRS. 69
F.11 Back calculation of CRS. 70
F.12 Back calculation of tri-axial test I. ESP and vertical strain vs. deviatoric stress. . . 71
F.13 Back calculation of tri-axial test II. Vertical strain vs. deviatoric stress and pore pressure. 72

G.1 Comparison of assembled finite element models through the SSC soil model. The graph shows the vertical displacement just beneath the center of the embankment. 73
G.2 Scenario 1 - State parameters. 74
G.3 Scenario 1 - Excess pore pressure. 75
G.4 Scenario 1 - Plastic multiplier ($d\lambda$), Day No. 1120. 76
G.5 Scenario 2 - Plastic multiplier ($d\lambda$), Day No. 1120. 76
G.6 Scenario 2 - State parameters. 77
G.7 Scenario 2 - Excess Pore Pressure. 78
G.8 Scenario 3 - Plastic Multiplier ($d\lambda$), Day No. 1120. 79
G.9 Scenario 3 - State parameters. 80
G.10 Scenario 3 - Excess pore pressure. 81
G.11 Investigation explicit and implicit scheme for layer 1 (0.6 - 2.0 m). 82
G.12 Investigation explicit and implicit scheme for layer 3 (5.0 - 10.0 m). 83
G.13 Investigation explicit and implicit scheme for layer 4 (10.0 - 25.0 m). 84

List of Tables

D.1 Soil parameters used in the MCC model programmed in MATLAB. Used in Figures D.1-D.4 35

F.1 Interpreted creep numbers (r_s) from Figure F.4 and Figure F.5. 65

F.2 Transforming r_s to r_{si} from Figure F.6 and Figure F.8. 66

Appendix A

Task Description

A signed description of the thesis statement is inserted on the following page.

NTNU
Faculty of Engineering Science and Technology
Institute of Civil and Transport Engineering

MASTER DEGREE THESIS

Spring 2015
for

Jesper Bjerre

DEVELOPMENT AND EVALUATION OF AN EFFECTIVE STRESS BASED MODEL FOR SOFT CLAYS

BACKGROUND
As part of the ongoing research project GeoFuture, the development of an effective stress soil model for soft Scandinavian clays is being carried out at NTNU. In this development various formulations are considered with the objective of obtaining a close fit between simulated behavior and actual measurements.

The Onsøy test fill, Norway was a heavily instrumented fill with measurements showing the effects of time on strength and deformation characteristics (Berre T., 2013). It was built on very soft marine clay and was subjected to stages of loading until finally brought to failure.

TASK
The task is to develop an effective stress based soil model which is able to capture some of the observed characteristic features in natural clay. The model should be evaluated based on simulations of the Onsøy test fill and the results discussed.

The candidate shall first through literature study obtain the necessary knowledge of natural soft clay behavior and how constitutive models can model such features. Effects that may be incorporated in soft clay models include anisotropy, destructuration, small-strain elastic stiffness and creep. Based on the literature study, the student shall develop a user friendly effective stress based soil model which is able to capture some of the features observed in natural clay. The soil model should be implemented in a commercial software as PLAXIS. The performance of the soil model should be verified through a F.E. model of the Onsøy clay test fill. The predictions can then be compared with recorded measurements and potential improvements to the material model formulation may be pointed out.

Professor in charge:
Steinar Nordal (NTNU), Gustav Grimstad (NTNU) and Varvara Zania (DTU)

Other supervisors:
Jon A. Rønningen (NTNU)

Department of Civil and Transport Engineering, NTNU
Date: 10.06.2015

Professor in charge

References:
Berre, T. (2013): Test fill on soft plastic marine clay at Onsøy, Norway. Canadian Geotechnical Journal. 1-22

Appendix B

Test fill - Onsøy

This appendix contains additional information regarding the test fill located at Onsøy.

B.1 Instrumentation

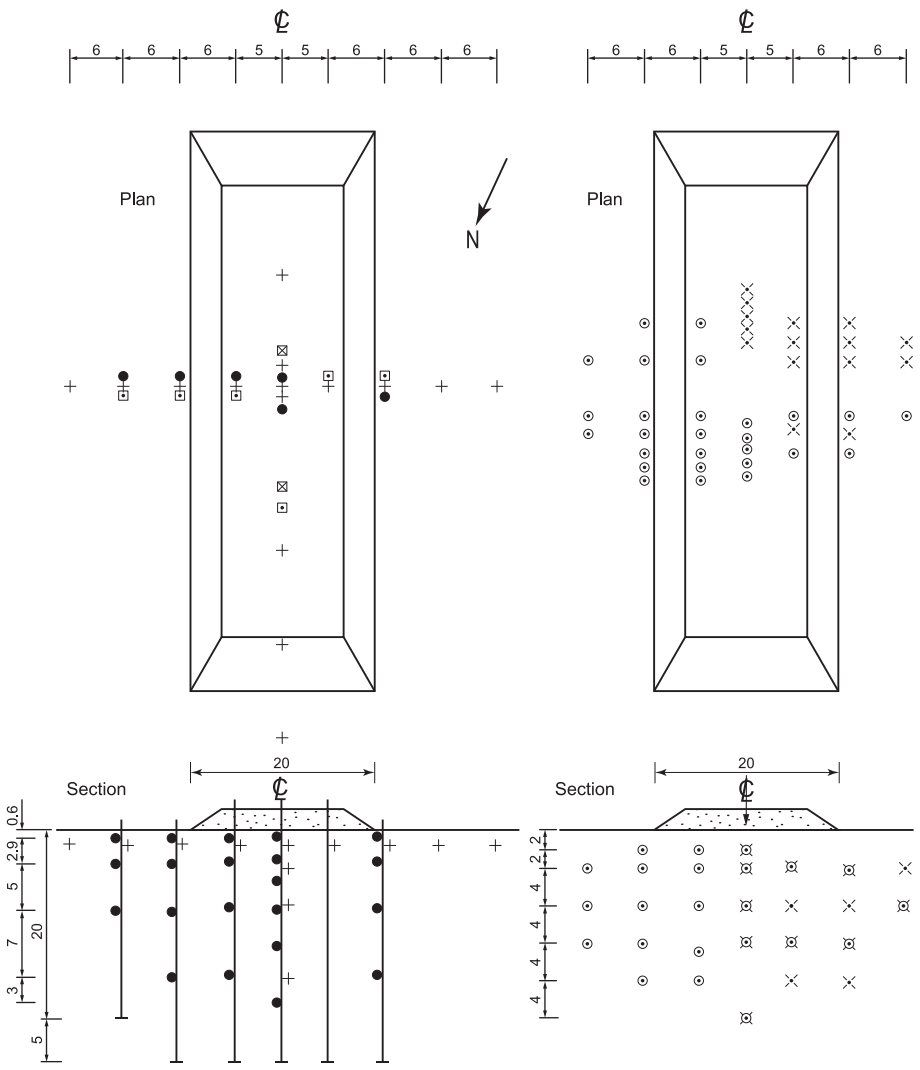

Figure B.1: *Overview of the instrumentation in the test fill located at Onsøy, see legend on the next page. Taken from (Berre, 2013).*

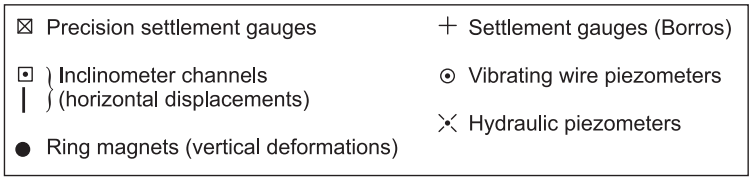

Figure B.2: *Legend for Figure B.1. Taken from (Berre, 2013).*

Appendix C

Mathematical Derivations

This appendix contains additional theory and derivations which have been left out of the main report.

C.1 Continuum Mechanics

A short introduction to continuum mechanics will be given to minimise the confusion regarding the utilized notation, references and definitions which may vary with respect to the field of knowledge and the background of the reader. For instance, in geotechnical engineering compression will be considered as positive compared to structural engineering where tension normally is considered as positive.

Soil as a material may be regarded as a relatively complex material. For simplicity reasons, soil is divided into two phases: solid particles and pores. However, soil is often considered as a three phases material since the pores may contain water and/or gas (normally air). The saturation degree in the soil may vary and three states are commonly defined as: dry, partly saturated or fully saturated. These states are very important with respect to stiffness and strength of the soil since these properties are associated with the effective stresses (stiffness of the grain skeleton). The concept of effective stresses was introduced by Terzaghi in 1923 (Nordal, 2014c) and relates the total stresses (σ), pore pressure (u) and effective stresses (σ') for fully saturated soils as:

$$\sigma_{ij} = \sigma'_{ij} + \delta_{ij} u \qquad \text{where} \qquad \delta_{ij} = \begin{cases} 1 & \text{if } i = j \\ 0 & \text{if } i \neq j. \end{cases} \qquad i, j = 1, 2, 3 \tag{C.1}$$

Notice, the water only influences the principle directions through Kronecker's delta (δ_{ij}) since water cannot withstand any shear forces. The indices in Eq. (C.1) refers to the three Cartesian axes (x_1, x_2, x_3).

C.1.1 Stress State

Regarding the stress state in a soil body, it is common to analyse an infinitesimal cubic element orientated with respect to a Cartesian coordinate system, see Figure C.1. Hence, the stress components may be written in matrix from as:

$$\boldsymbol{\sigma} = \begin{bmatrix} \sigma'_{11} & \sigma'_{12} & \sigma'_{13} \\ \sigma'_{21} & \sigma'_{22} & \sigma'_{23} \\ \sigma'_{31} & \sigma'_{32} & \sigma'_{33} \end{bmatrix} \tag{C.2}$$

where the first index refers to the surface where the stress component acts and the second index refers to the direction of the stress component according to the Cartesian coordinate system. Eq. (C.2) becomes symmetrical with six independent stress components with respect to moment equilibrium around the three axes.

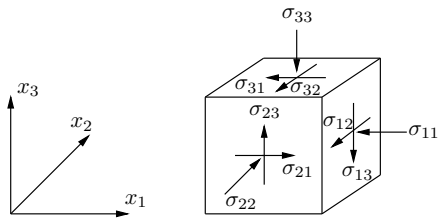

Figure C.1: *Stresses acting on a unit cube of soil orientated according to a Cartesian reference system*

C.1.2 Principal Stresses

Principal stresses represent a stress situation where stresses acting perpendicular (as normal vectors) to the plane without any shear stresses ($\sigma'_{12} = \sigma'_{23} = \sigma'_{13} = 0$). Hence, considering a unit cube exposed to an arbitrary stress field it is possible to determine the principle stresses by use of Cauchy's law through an Eigenvalue problem:

$$(\boldsymbol{\sigma} - \sigma' \boldsymbol{I})\, \boldsymbol{n} = 0 \qquad \text{or} \tag{C.3a}$$

$$(\sigma'_{ij} + \sigma' \delta_{ij})\boldsymbol{n} = 0 \qquad \text{where} \qquad \delta_{ij} = \begin{cases} 1 & \text{if } i = j \\ 0 & \text{if } i \neq j. \end{cases} \qquad i, j = 1, 2, 3 \tag{C.3b}$$

where $\boldsymbol{I}$ is the identity matrix and $\boldsymbol{n}$ is a normal vector ($\boldsymbol{n} = [n_1, n_2, n_3]$). To obtain non-trivial solutions from Eq. (C.3) it requires:

$$det\,(\boldsymbol{\sigma} - \sigma' \boldsymbol{I}) = 0 \tag{C.4}$$

which may be rewritten to:

$$\sigma'^3 - I_1 \sigma'^2 - I_2 \sigma' - I_3 = 0 \tag{C.5}$$

where:

$$I_1 = \sigma'_{11} + \sigma'_{22} + \sigma'_{33} \tag{C.6a}$$

$$I_2 = -\sigma'_{11}\sigma'_{22} - \sigma'_{11}\sigma'_{33} - \sigma'_{22}\sigma'_{33} + \sigma'^2_{12} + \sigma'^2_{13} + \sigma'^2_{23} \tag{C.6b}$$

$$I_3 = det(\boldsymbol{\sigma'}) = \sigma'_{11}\left(\sigma'_{22}\sigma'_{33} - \sigma'^2_{23}\right) - \sigma'_{12}\left(\sigma'_{12}\sigma'_{33} - \sigma'_{13}\sigma'_{23}\right) + \sigma'_{13}\left(\sigma'_{12}\sigma'_{23} - \sigma'_{13}\sigma'_{22}\right) \tag{C.6c}$$

It can be proved that Eq. (C.5) has three real roots since the matrix is real and symmetric. Therefore, the solution yields three eigenvalues with three orthogonal eigenvectors ($\boldsymbol{n_1}, \boldsymbol{n_2}, \boldsymbol{n_3}$). These eigenvalues are the principle stresses denoted as $\sigma'_1, \sigma'_2, \sigma'_3$ and are often referred to as the major, intermediate and minor principle stress, respectively. The coefficients in Eq. (C.5) are often called the stress invariants. In the principal directions, the stress invariants can be rewritten as

$$\begin{aligned} I_1 &= \sigma'_1 + \sigma'_2 + \sigma'_3 \\ I_2 &= -\sigma'_1\sigma'_2 - \sigma'_1\sigma'_3 - \sigma'_2\sigma'_3 \\ I_3 &= det(\boldsymbol{\sigma}) = \sigma'_1\sigma'_2\sigma'_3 \end{aligned}$$

It should be mentioned that the stress matrix ($\boldsymbol{\sigma}$) will vary depending on the chosen reference system or basis but the principle stresses will remain the same for a given stress condition.

C.1.3 Mean and Deviatoric Stresses

The deviatoric stress is defines as:

$$\boldsymbol{s} = \boldsymbol{\sigma} - \boldsymbol{p} \qquad \text{or} \tag{C.7a}$$

$$s_{ij} = (\sigma'_{ij} - p\delta_{ij}) \qquad \text{where} \qquad \delta_{ij} = \begin{cases} 1 & \text{if } i = j \\ 0 & \text{if } i \neq j. \end{cases} \qquad i, j = 1, 2, 3 \tag{C.7b}$$

where $\boldsymbol{p}$ is the mean stress tensor containing the mean stress in the diagonal. The mean stress is defined by:

$$p = \frac{1}{3}\left(\sigma'_{11} + \sigma'_{22} + \sigma'_{33}\right) = \frac{1}{3}\left(\sigma'_1 + \sigma'_2 + \sigma'_3\right) = \frac{I_1}{3} \tag{C.8}$$

As for the principle stresses, the deviatoric stresses can be solved by an Eigenvalue problem:

$$\left(\boldsymbol{s} - s\boldsymbol{I}\right)\boldsymbol{n} = 0 \tag{C.9}$$

Yielding a third order equation:

$$s^3 - J_1 s^2 - J_2 s - I_3 = 0 \tag{C.10}$$

where:

$$\begin{aligned} J_1 &= s_{11} + s_{22} + s_{33} = s_1 + s_2 + s_3 = 0 \\ J_2 &= -s_{11}s_{22} - s_{11}s_{33} - s_{22}s_{33} + s_{12}^2 + s_{13}^2 + s_{23}^2 \\ J_3 &= det(\boldsymbol{s}) = s_{11}\left(s_{22}s_{33} - s_{23}^2\right) - s_{12}\left(s_{12}s_{33} - s_{13}s_{23}\right) + s_{13}\left(s_{12}s_{23} - s_{13}s_{22}\right) \end{aligned}$$

As for the principal stresses, the principle deviatoric stresses are independent of the reference system. Therefore, J_1, J_2 and J_3 are often referred to as the deviatoric stress invariants. It can be shown that

$$\begin{aligned} J_1 &= 0 \\ J_2 &= \left(\frac{1}{6}\right)\left\{(\sigma'_1 - \sigma'_2)^2 + (\sigma'_1 - \sigma'_3)^2 + (\sigma'_2 - \sigma'_3)^2\right\} \\ J_2 &= I_2 + \frac{I_1^2}{3} \\ J_3 &= I_3 + \left(\frac{1}{3}\right) I_2 I_1 + \left(\frac{2}{27}\right) I_1^3 \end{aligned}$$

Note, the deviatoric stresses are functions of the full stresses and can therefore be written as shown above. Furthermore, the principle deviatoric stresses are called: s_1, s_2, s_3.

C.1.4 Stress Spaces

As mentioned in section C.1.1 the stress tensor consists of 6 independent components. To visualize the stress state one may use one of following planes indicated in Figure C.2(a).

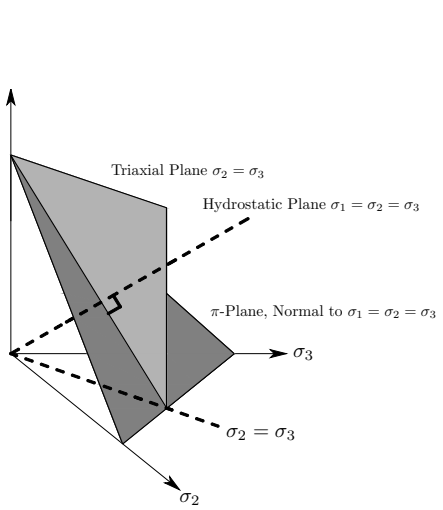

(a) Principal stress space indicating location of: Triaxial, hydrostatic and π-plane.

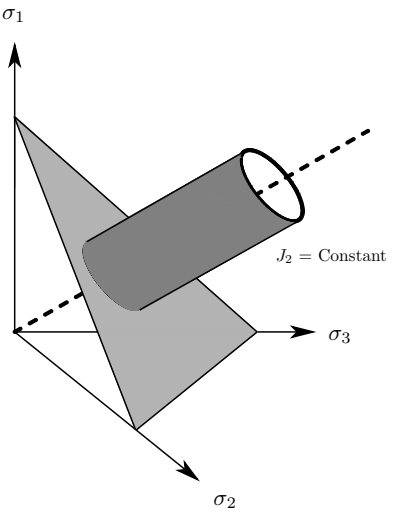

(b) The second deviatoric stress invariant forming a cylinder in the principle space with $\sqrt{2J_2}$ as radius.

Figure C.2: *Stress spaces.*

Utilizing these planes, a three-dimensional stress state is easier to imagine. A geometric interpretation of a stress state can be done through the hydrostatic and the deviatoric contribution. The hydrostatic contribution will locate the π-plane and the deviatoric contribution would determine the size of a circle as a function of J_2. Furthermore, it can be shown that the second deviatoric stress invariant (J_2) simply will form a circle on the π-plane and a cylinder in the principle coordinate system, see Figure C.2(b).

C.1.5 Strains and Strain Invariants

Utilizing the conventional engineering strain, the infinitesimal strain tensor for a unit cube exposed to the displacement field (u) with the reference system (x) is given as:

$$\varepsilon_{ij} = -\frac{1}{2}\left(\frac{\partial u_i}{\partial x_j} + \frac{\partial u_j}{\partial x_i}\right) \qquad i,j = 1,2,3 \qquad \text{or} \qquad \boldsymbol{\varepsilon} = \begin{bmatrix} \varepsilon_{11} & \varepsilon_{12} & \varepsilon_{13} \\ \varepsilon_{21} & \varepsilon_{22} & \varepsilon_{23} \\ \varepsilon_{31} & \varepsilon_{32} & \varepsilon_{33} \end{bmatrix} \tag{C.11}$$

Where u_i is the displacement in the direction x_i. The negative sign is a consequence of considering compression as positive. As for the strain tensor, an eigenvalue problem may be assembled as:

$$(\boldsymbol{\varepsilon} - \varepsilon \boldsymbol{I})\overline{\boldsymbol{x}} = 0 \tag{C.12a}$$

$$det(\boldsymbol{\varepsilon} - \varepsilon \boldsymbol{I}) = 0 \qquad \text{Non trivial solutions} \tag{C.12b}$$

where $\overline{\boldsymbol{x}}$ is the orthonormal bases for the eigenvectors. In other words, the principal axes of the strains. As for the principle and deviatoric stresses, it yields a third order equation:

$$\varepsilon - I_1^{\varepsilon}\varepsilon^2 - I_2^{\varepsilon}\varepsilon - I_3^{\varepsilon} = 0 \tag{C.13}$$

where the strains invariants are defined as:

$$I_1^\varepsilon = \varepsilon_{11} + \varepsilon_{22} + \varepsilon_{33} = \varepsilon_p \tag{C.14a}$$
$$I_2^\varepsilon = -\varepsilon_{11}\varepsilon_{22} - \varepsilon_{11}\varepsilon_{33} - \varepsilon_{22}\varepsilon_{33} + \varepsilon_{12}^2 + \varepsilon_{13}^2 + \varepsilon_{23}^2 \tag{C.14b}$$
$$I_3^\varepsilon = det(\boldsymbol{\varepsilon}) = \varepsilon_{11}\left(\varepsilon_{22}\varepsilon_{33} - \varepsilon_{23}^2\right) - \varepsilon_{12}\left(\varepsilon_{12}\varepsilon_{33} - \varepsilon_{13}\varepsilon_{23}\right) + \varepsilon_{13}\left(\varepsilon_{12}\varepsilon_{23} - \varepsilon_{13}\varepsilon_{22}\right) \tag{C.14c}$$

Notice, the first strain invariant is the same as the volumetric strain. This is an assumption caused by neglecting the multiplication of the three principle strains. The deviatoric strain tensor is defined as:

$$\boldsymbol{e} = \boldsymbol{\varepsilon} - \frac{\varepsilon_p}{3} I \qquad \text{or} \tag{C.15a}$$
$$e_{ij} = \varepsilon_{ij} - \frac{\varepsilon_p}{3}\delta_{ij} \qquad \text{where} \qquad \delta_{ij} = \begin{cases} 1 & \text{if } i = j \\ 0 & \text{if } i \neq j. \end{cases} \qquad i, j = 1, 2, 3 \tag{C.15b}$$

Where the deviatoric strain invariants are defined as:

$$J_1^e = e_{11} + e_{22} + e_{33} = e_1 + e_2 + e_3 = 0 \tag{C.16a}$$
$$J_2^e = -e_{11}e_{22} - e_{11}e_{33} - e_{22}e_{33} + e_{12}^2 + e_{13}^2 + e_{23}^2 \tag{C.16b}$$
$$J_3^e = det(\boldsymbol{e}) = e_{11}\left(e_{22}e_{33} - e_{23}^2\right) - e_{12}\left(e_{12}e_{33} - e_{13}e_{23}\right) + e_{13}\left(e_{12}e_{23} - e_{13}e_{22}\right) \tag{C.16c}$$

Notice that $J_1^\varepsilon \equiv 0$ by the definition of the deviatoric strains.

C.1.6 The Lode Angle

As shown in Section C.1.2 the principal stresses (Eq. (C.5)) is a third order equation making an explicit solution impossible. However, using the definition of the deviatoric stresses the first deviatoric invariant is zero and can be used to find an explicit solution. From Eq. (C.10) and using $J_1 \equiv 0$ yields:

$$s^3 - J_2 s - J_3 = 0 \tag{C.17}$$

The explicit solution is found by use of trigonometric relations. It can be shown that the sine and cosine relations are given by:

$$\sin(\alpha \pm \beta) = \sin\alpha\cos\beta \pm \cos\alpha\sin\beta \tag{C.18a}$$
$$\cos(\alpha \pm \beta) = \cos\alpha\sin\beta \mp \sin\alpha\cos\beta \tag{C.18b}$$

Using trigonometric identity and some algebra it may be shown that a relation (function of θ) can be obtained in the same form as the deviatoric principal stress in Eq. (C.17):

$$\cos(\theta 2 + \theta) = \cos\theta\cos(\theta + \theta) - \sin\theta\sin(\theta + \theta) \tag{C.19a}$$
$$= \cos\theta\left(\cos\theta\cos\theta - \sin\theta\sin\theta\right) - 2\sin\theta\sin\theta\cos\theta \tag{C.19b}$$
$$= \cos^2\theta - 3\sin^2\theta\cos\theta \tag{C.19c}$$
$$= 4\cos^2\theta - 3\cos\theta \tag{C.19d}$$

The last step is to remove the constant in front of the term $(\cos^2\theta)$ by division:

$$\cos^2\theta - \frac{3}{4}\cos\theta - \frac{1}{4}\cos(3\theta) = 0 \tag{C.20}$$

Recalling the definition of the π-plane. Any vector drawn in this particular plane will represent the deviaoric part of a given stress state. Defining a vector ρ in the π-plane the length (magnitude) can be found by:

$$\rho = \sqrt{\boldsymbol{ss}} = \sqrt{s_1^2 + s_2^2 + s_3^3} = \sqrt{2J_2} \tag{C.21}$$

A relationship between Eq. (C.17) and Eq. (C.21) may be done utilizing polar coordinates which is done by $s = r\cos\theta$. By use of some algebra it can be shown that:

$$\cos^3\theta - \frac{J_2}{r^2}\cos\theta - \frac{J_3}{r^3} = 0 \tag{C.22}$$

Now, by substituting an expression of J_2 from Eq. (C.21) into Eq. (C.22) and combining this with Eq. (C.20) yields:

$$\cos(3\theta) = \frac{4J_3}{r^3} = \frac{3\sqrt{3}J_3}{2\sqrt{J_2^3}} \qquad \text{where} \qquad r = 2\sqrt{\frac{J_2}{3}} = \sqrt{\frac{2}{3}}\rho \tag{C.23}$$

According to (Nordal, 2014c), it may be verified that the term: $\cos 3\theta$ or $d\frac{3\sqrt{3}J_3}{2\sqrt{J_2^3}}$ varies between -1 to 1 for all values of J_2 and J_3. Since cosine is a periodic function there will be more than one solution to Eq. (C.24). Hence, all solutions may be found by any angle equal to $3\theta + 2\pi n$ where n is a positive integer with the increment of 1. According to the definition of the major and minor stresses ($\sigma_1' > \sigma_2' > \sigma_3'$) and substituting the relation of $s = r\cos$ following expression for the principle stresses may be found for $n = 1, 2$ and 3:

$$\begin{bmatrix}\sigma_1'\\ \sigma_2'\\ \sigma_3'\end{bmatrix} = 2\sqrt{\frac{J_2}{3}}\begin{bmatrix}\cos\theta\\ \cos\left(\theta - \frac{2\pi}{3}\right)\\ \cos\left(\theta + \frac{2\pi}{3}\right)\end{bmatrix} + \frac{I_3}{3}\begin{bmatrix}1\\1\\1\end{bmatrix} \qquad \text{for} \qquad \theta \in \left[0, \frac{\pi}{3}\right] \tag{C.24}$$

It is possible to find the corresponding tri-axial plane in terms of the Lode angle. If implementing an angle of $\theta = 0^o$ it corresponds to compression and an angle of $\theta = 60^o$ corresponds to extension.

C.1.7 Bulk and Shear modulus

Bulk Modulus: The reason for using the bulk modulus (K) in soil mechanicss, during isotropic elasticity, can be seen by introducing the mean stress:

$$p' = \frac{1}{3}\left(\sigma_{11}' + \sigma_{22}' + \sigma_{33}'\right) \tag{C.25}$$

Utilizing the constitutive matrix the stresses can be rewritten into stiffness and strains and by some algebra it can be shown that:

$$p' = K\left(\varepsilon_{11} + \varepsilon_{22} + \varepsilon_{33}\right) = K\varepsilon_p \tag{C.26}$$

Hence, it can be seen that the volumetric strain is proportional to the mean effective stress through the bulk modulus for isotropic elastic conditions.

Shear Modulus: The shear modulus (G) can be determined by looking at the definition of the deviatoric stresses:

$$\boldsymbol{s} = \boldsymbol{\sigma} - \boldsymbol{I}p' = \boldsymbol{D}(\boldsymbol{\varepsilon} + \frac{\boldsymbol{\varepsilon_p}}{3}) - \boldsymbol{I}p' \tag{C.27}$$

where $\boldsymbol{\varepsilon}$ is the strain tensor and D the elastic stiffness matrix. By some algebra it can be shown that

$$s_{ij} = 2Ge_{ij} \tag{C.28}$$

Meaning, the deviatoric stress (s_{ij}) is proportional to the deviator strain (e_{ij}) by a factor of 2.

C.1.8 Tensors

It is common to write the tensors presented in Section C.1 in vector format as:

Stress and strain tensor:

$$\boldsymbol{\sigma} = \begin{bmatrix} \sigma'_{11} \\ \sigma'_{22} \\ \sigma'_{33} \\ \sigma'_{12} \\ \sigma'_{23} \\ \sigma'_{13} \end{bmatrix} \quad , \quad \boldsymbol{\varepsilon} = \begin{bmatrix} \varepsilon_{11} \\ \varepsilon_{22} \\ \varepsilon_{33} \\ \varepsilon_{12} \\ \varepsilon_{23} \\ \varepsilon_{13} \end{bmatrix}$$

Deviatoric stress, strain, and fabric tensor:

$$\boldsymbol{\sigma}_d = \begin{bmatrix} \sigma'_{11} - p \\ \sigma'_{22} - p \\ \sigma'_{33} - p \\ \sqrt{2}\sigma'_{12} \\ \sqrt{2}\sigma'_{23} \\ \sqrt{2}\sigma'_{13} \end{bmatrix} = \begin{bmatrix} \frac{1}{3}\left(2\sigma'_{11} - \sigma'_{22} - \sigma'_{33}\right) \\ \frac{1}{3}\left(-\sigma'_{11} + 2\sigma'_{22} - \sigma'_{33}\right) \\ \frac{1}{3}\left(-\sigma'_{11} - \sigma'_{22} + 2\sigma'_{33}\right) \\ \sqrt{2}\sigma'_{12} \\ \sqrt{2}\sigma'_{23} \\ \sqrt{2}\sigma'_{13} \end{bmatrix} \quad , \quad \boldsymbol{\varepsilon}_d = \begin{bmatrix} \varepsilon_{11} - 1 \\ \varepsilon_{22} - 1 \\ \varepsilon_{33} - 1 \\ \sqrt{2}\varepsilon_{12} \\ \sqrt{2}\varepsilon_{23} \\ \sqrt{2}\varepsilon_{13} \end{bmatrix} \quad , \quad \boldsymbol{\alpha}_d = \begin{bmatrix} \alpha_{11} - 1 \\ \alpha_{22} - 1 \\ \alpha_{33} - 1 \\ \sqrt{2}\alpha_{12} \\ \sqrt{2}\alpha_{23} \\ \sqrt{2}\alpha_{13} \end{bmatrix} = \begin{bmatrix} \alpha_{d11} \\ \alpha_{d22} \\ \alpha_{d33} \\ \alpha_{d12} \\ \alpha_{d23} \\ \alpha_{d13} \end{bmatrix}$$

Note that the fabric tensor has not been presented in Section C.1 but follows the same principle. The deviatoric tensors may be presented by the second deviatoric invariant as:

$$J_2 = \frac{1}{2}\boldsymbol{\sigma}_d^T\boldsymbol{\sigma}_d \quad , \quad J_2^{\varepsilon} = \frac{1}{2}\boldsymbol{\varepsilon}_d^T\boldsymbol{\varepsilon}_d \quad , \quad J_2^{\alpha} = \frac{1}{2}\left(\boldsymbol{\sigma}_d - p'\boldsymbol{\alpha}_d\right)^T\left(\boldsymbol{\sigma}_d - p'\boldsymbol{\alpha}_d\right) \tag{C.29}$$

The fabric may also be presented by a single factor as:

$$\boldsymbol{\alpha} = \sqrt{\frac{3}{2}\alpha_d^T\alpha_d} \tag{C.30}$$

C.2 CC vs. MCC

The difference between the original and the Modified Cam Clay (MCC) is the shape of the yield surface. In the original formulation the yield surface was theoretically derived based on an energy equation. The shape has a logarithmic spiral format compared to the ellipse shape in the MCC, see Figure C.3. However, the inconvenient shape in the CC model leads to numerical issues at the tip of the yield surface where unrealistic plastic shear strain increments during isotropic compression were predicted (Hokkaido).

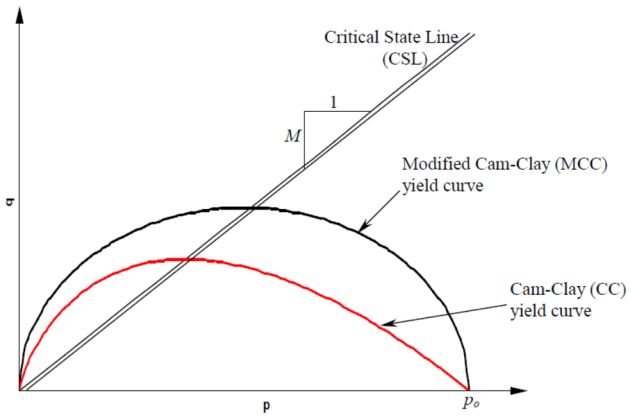

Figure C.3: *Difference between CC and MCC. Notice notation difference,* $p_0 = p'_c$.

The evolution of the dilatation is associated to a linear relationship between the volumetric strain and the stress ratio in the original whereas the MCC uses a logarithmic behaviour, see Figure C.4 (Ohta, 2007).

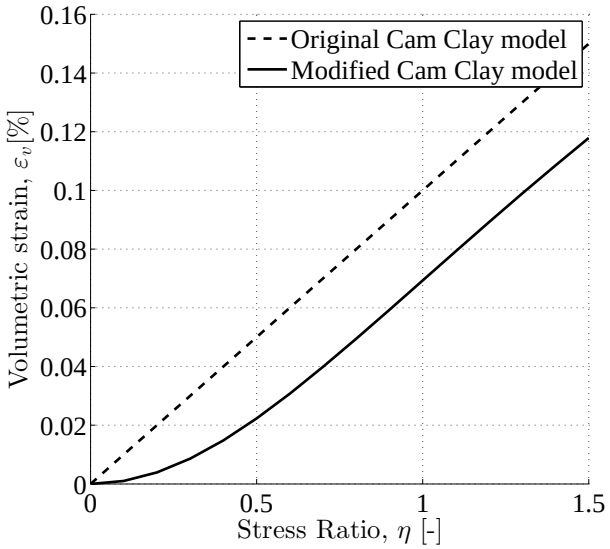

Figure C.4: *Difference between the original CC and the MCC. Notice notation difference,* $\varepsilon_v = \varepsilon_p$.

C.2.1 Derivation of Yield Surface

The shape of the yield surface in the MCC model is defined as an ellipse in the $(p : q)$-space (Ellipsoid in the principle space). The yield surface is governed by the material parameter M which defines the Critical State Line (CSL). The CSL is associated to the Critical State (CS). For more details about the CS see Appendix C.3. As a characteristic feature, the top point of the ellipse would always touch through the CSL, see Figure C.5.

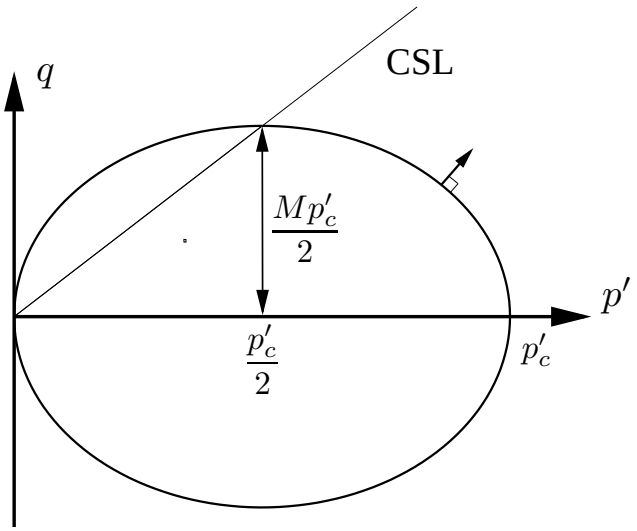

Figure C.5: *Elliptical yield surface for the MCC.*

Notice, the ellipse is passing through zero regarding that cohesion is assumed to be negligible. It has been stated that this assumption is reasonable to propose except for soil particles which have been cemented together. Soil itself cannot withstand an all round effective tensile stress which will develop irrecoverable volumetric deformation (Wood, 1990). A formulation of the yield surface may be assembled as a function of: p', q, M and p'_c. The first step is to recall the mathematical expression of an ellipse which is given by:

$$\left(\frac{x}{a}\right)^2 \left(\frac{y}{b}\right)^2 - 1 = 0 \tag{C.31}$$

Eq. (C.31) can be rewritten by substituting x and y with p' and q, respectively, and choose values for a and b corresponding to the dimension of the ellipse:

$$F = \left(\frac{p'}{\frac{p'_c}{2}}\right)^2 + \left(\frac{q}{M\frac{p'_c}{2}}\right)^2 - 1 = 0 \tag{C.32}$$

It may be observed in Eq. (C.32) that the center of the ellipse is located at origo. In order to eliminate the tension part the ellipse must be moved to the right to obtain the location as shown in Figure C.5. The translation is done by subtracting a from x in Eq. (C.32). Furthermore, to achieve a more simplified solution, Eq. (C.32) is multiplied by $b = (Mp'_c/2)^2$. Utilizing some algebra it may be reduced to the known form given in Eq. (C.33c).

$$0 = \left(\left(\frac{x-a}{a}\right)^2 + \left(\frac{y}{b}\right)^2 - 1\right) b^2 \tag{C.33a}$$

$$0 = F = \left(\left(\frac{p' - \frac{p'_c}{2}}{\frac{p'_c}{2}}\right) + \left(\frac{q}{M\frac{p'_c}{2}}\right)^2 - 1\right) \left(M\frac{p'_c}{2}\right)^2 \tag{C.33b}$$

$$0 = F = q^2 - M^2(p'(p'_c - p')) \tag{C.33c}$$

With respect to the MCC model, it is common to express the yield surface in another manner, see Eq. (2.56).

C.3 Critical State

The Critical State (CS) may be formulated as suggested by (Nordal, 2014a):

Definition 10. *A Critical State (CS) is a state where large shear strains may be applied without any change in effective stresses or in volume.*

The CS represents a state where the soil is completely remoulded and may be seen as homogeneous. The state is emerged since the plastic potentials are assumed to have a slope in the $(p' : q)$-plane of $dq/dp' = 0$, at the a particular stress ratio (Wood, 1990):

$$q_{cs} = M p_{cs} \qquad \text{and} \qquad \eta_{cs} = \frac{q_{cs}}{p'_{cs}} \tag{C.34}$$

To each specific volume (v), a critical state may be found by the effective mean pressure at CS:

$$v_{cs} = \Gamma - \lambda \ln p'_{cs} \tag{C.35}$$

where:

$$\Gamma = N - (\lambda - \kappa)\ln(2) \tag{C.36}$$

The soil response is associated to the OCR when approaching the CSL. For large OCR the soil will show dilate behaviour and the contractive behaviour for small OCR. Introducing the CSL it may be drawn in a three-dimensional space along with the NCL, see Figure C.6.

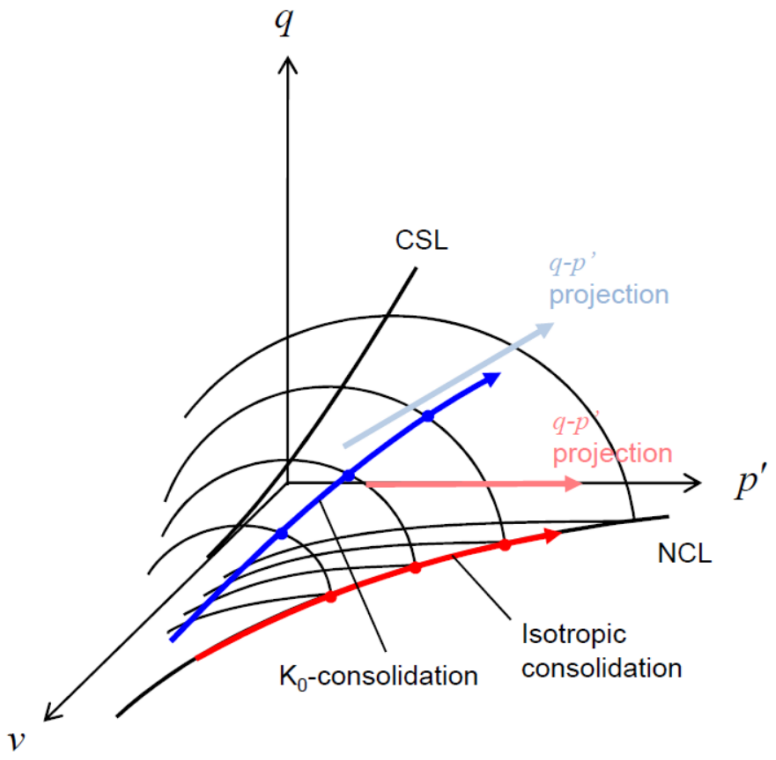

Figure C.6: *State boundary surface. Taken from (Hokkaido).*

As illustrated in Figure C.6, the CSL and the yield surfaces generate a boundary surface, often known as the State Boundary Surface (SBS). The inside of SBS represent the elastic domain and on the surface of SBS the plastic domain is represented. Notice, outside of the SBS is impossible. Furthermore, the plastic potential will be normal to the SBS. The SBS may be used as a graphical tool to easily see the effect of compacting regarding to the shear strength of a soil.

Drained vs. Undrained

A drained or undrained condition are two very different scenarios which will dominate the soil response. Hence, general understanding of how the constitutive model behave in these conditions must be assembled.

Drained
In a conventional drained tri-axial test, the Effective Stress Part (ESP) and the Total Stress Path (TSP), in the $p' : q$ space, will be known since the cell pressure will be kept constant during the test. According to the definition of drained condition, the ESP and TSP will be equal. It may be derived that the inclination would be 1:3 in the $(p' : q)$-space. Thereby, the stress increment can be formulated as:

$$\frac{1}{3} = \frac{dp'}{dq} \quad , \quad d\boldsymbol{\sigma} = \begin{bmatrix} \frac{dq}{3} \\ dq \end{bmatrix} \tag{C.37}$$

When the ESP approaches the yield surface the following two situations may occur:

- **Approaching in the dry region**: Plastic expansion will occur resulting in a shrinking yield surface. The ESP will follow the same path back until it reaches the CSL.
- **Approaching in the wet region**: Plastic compression will occur resulting in a expansion of the yield surface. The expansion will stop approaching the CSL.

The demanding criteria, if the ESP will approach the yield surface in the wet or dry region, is determined by the OCR. These two scenarios may be seen in Figure C.7(a) and C.7(b).

Undrained
In a conventional undrained tri-axial test no dissipation of pore water will occur since the pore water will be trapped inside the sample by closing the valve during shearing. Thereby, the volume will be kept constant and no volumetric strain will occur:

$$d\varepsilon_p = 0 \tag{C.38}$$

Notice that it has been assumed that full saturation is achieved prior to shearing, and water and soil particles are incompressible. According to Eq. (2.57) and Eq. (C.38) the incremental stress will only be dependent on the incremental shear strain:

$$d\varepsilon = \begin{bmatrix} 0 \\ d\varepsilon_q \end{bmatrix} \tag{C.39}$$

The ESP may be estimated utilizing the criterion of constant volume. In the elastic domain the volumetric change will only be related to effective mean stress. Hence, no volumetric change will result in a vertical ESP until it reaches the yield surface. As in the drained case, the TSP will still have an inclination on 1:3 and the difference between ESP and TSP corresponds to the developed excess pore pressure. In the plastic domain a change in effective mean pressure may occur since a change does not result in a change in volume in contrast to the elastic domain. Recalling the definition of change in strain caused by effective mean pressure:

$$d\varepsilon_p = d\varepsilon_p^e + d\varepsilon_p^p = \left(\kappa \frac{dp'}{vp'}\right) + \left((\lambda - \kappa)\frac{dp'_c}{vp'_c}\right) = 0 \tag{C.40}$$

From the definition of strain it is observed that a change in p'_c yields a change in p' in the opposite direction to satisfy the equation. Utilizing Eq. (C.40) the following conclusion may be drawn:

- **Approaching in the dry region**: Plastic expansion will occur resulting in a shrinking yield surface (decrease in p'_c and increase in p'). The ESP will be directed to the right until it reach the CSL.

- **Approaching in the wet region**: Plastic compression will occur resulting in an expansion of the yield surface (increase in p'_c and decrease in p'). The ESP will be directed to the left until it reaches the CSL.

The ESP for these two cases may be seen on Figure C.8(a) and C.8(b).

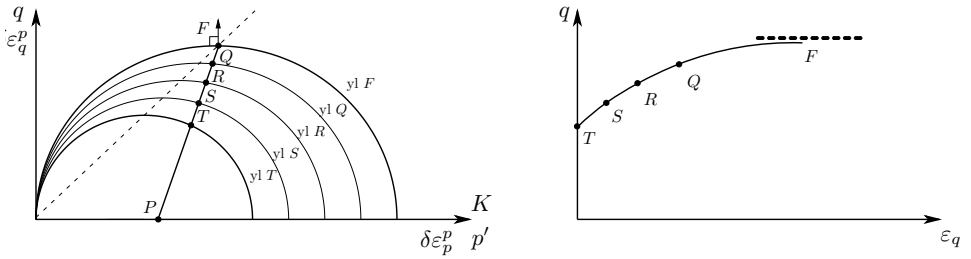

(a) Slightly over consolidated.

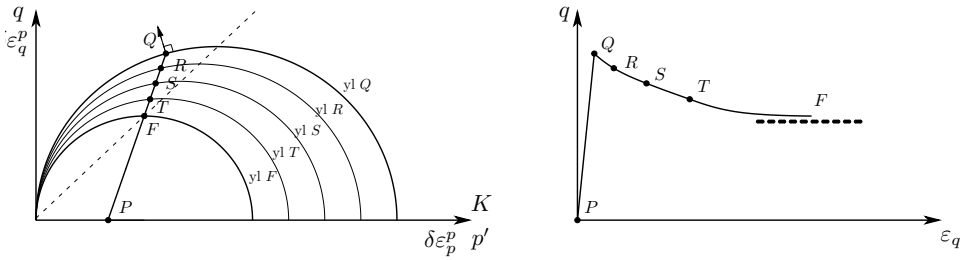

(b) Over Consolidated.

Figure C.7: *Theoretical MCC: Drained tri-axial compression.*

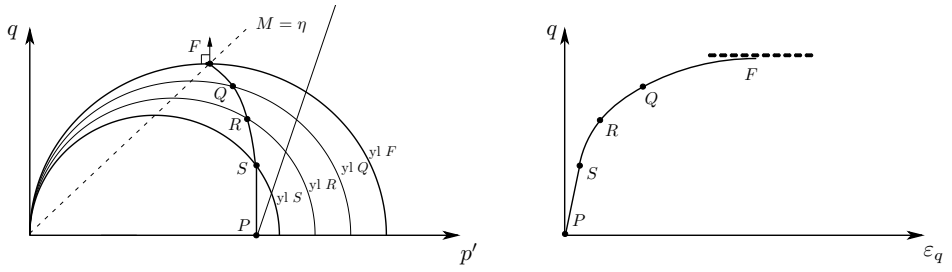

(a) Slightly over consolidated.

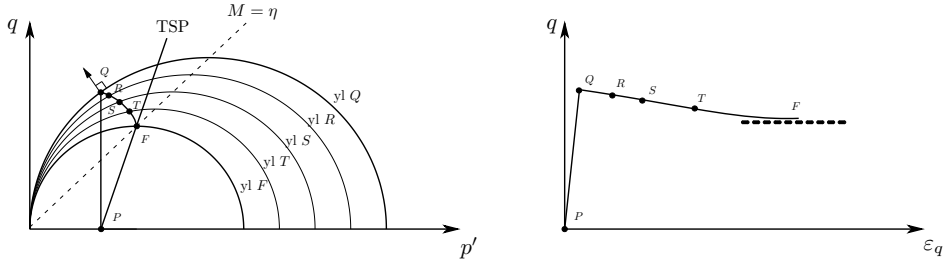

(b) Over consolidated.

Figure C.8: *Theoretical MCC: Undrained tri-axial compression.*

C.3.1 Hand Calculations to Verify the MCC in MATLAB

Theoretical calculation of the four scenarios given in Section 6.4.2.

Drained scenarios

The drained shear strength:

$$\tau_f = \frac{p'_c}{2} = \frac{900kPa}{2} = 450\text{kPa}$$

The change in volume in each step:

$$\Delta\nu_{AB} = \lambda \ln \frac{p'_c + \Delta p'_0}{p'_c}$$
$$= 0.25 \cdot \ln\left(\frac{900\text{kPa}}{300\text{kPa}}\right) = -0.275$$
$$\Delta\nu_{BF} = -\kappa \ln \frac{p' + \Delta p'}{p'}$$
$$= 0.05 \cdot \ln\left(\frac{450\text{kPa}}{900\text{kPa}}\right) = 0.035$$

The final specific volume:

$$v_F = 2 - 0.275 + 0.035 = 1.76$$

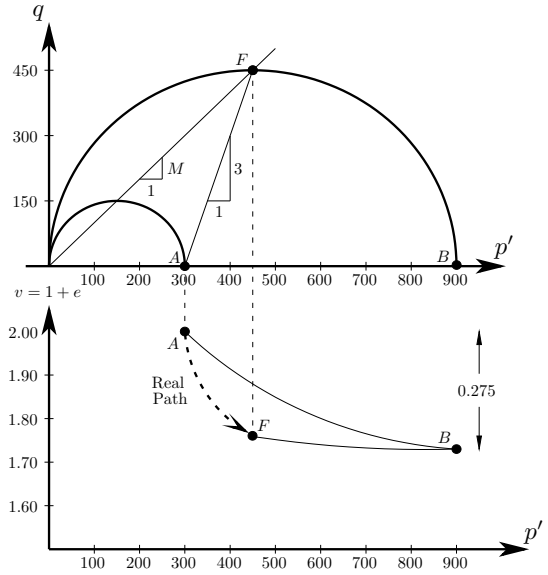

Figure C.9: *Hand calculation MCC: Drained, normal consolidated*

The maximum shear strength:

$$q = \sqrt{(p'(1200\text{kPa} - p'))} = 591.1\text{kPa}$$

The residual shear strength:

$$\tau_f = \frac{900\text{kPa}}{2} = 450\text{kPa}$$

The change in volume in each step:

$$\Delta v_{AB} = -0.05 \ln\left(\frac{1200\text{kPa}}{300\text{kPa}}\right) = -0.069$$
$$\Delta v_{BC} = -0.25 \ln\left(\frac{900\text{kPa}}{1200\text{kPa}}\right) = 0.072$$
$$\Delta v_{CF} = -0.05 \ln\left(\frac{450\text{kPa}}{900\text{kPa}}\right) = 0.035$$

The final specific volume:

$$v_F = 2.000 - 0.069 + 0.072 + 0.035 = 2.0373$$
$$\varepsilon_p = \frac{\Delta V}{V_0} = \frac{0.0373}{2.0} = 1.87\%$$

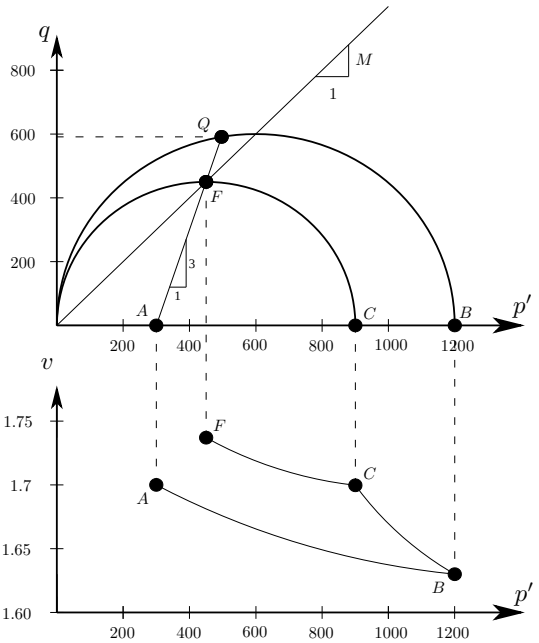

Figure C.10: *Hand calculation MCC: Drained, over consolidated*

Undrained scenarios

Change in volume during each step:

$$\Delta v = \Delta v_{AB} + \Delta v_{BF} = 0$$

$$0 = -\lambda \ln\left(\frac{p'_{0,A} + \Delta p'_{0,A\longrightarrow B}}{p'_{0,A}}\right) - \kappa \ln\left(\frac{p'_{0,B} + \Delta p'_{0,B\longrightarrow F}}{p'_{0,B}}\right)$$

The new preconsolidation pressure:

$$0 = -0,25 \ln\frac{P'_x}{300} - 0.05 \ln\frac{P'_x/2}{P'_x}$$

$$P'_x = 344.6\text{kPa}$$

The undrained shear strength:

$$s_u = \frac{P'_x}{2} = 172.3\text{kPa}$$

$$\Delta u = \left(300 - \frac{344.6}{2}\right) + \frac{1}{3}\frac{344.6}{2} = 185.1\,\text{kPa}$$

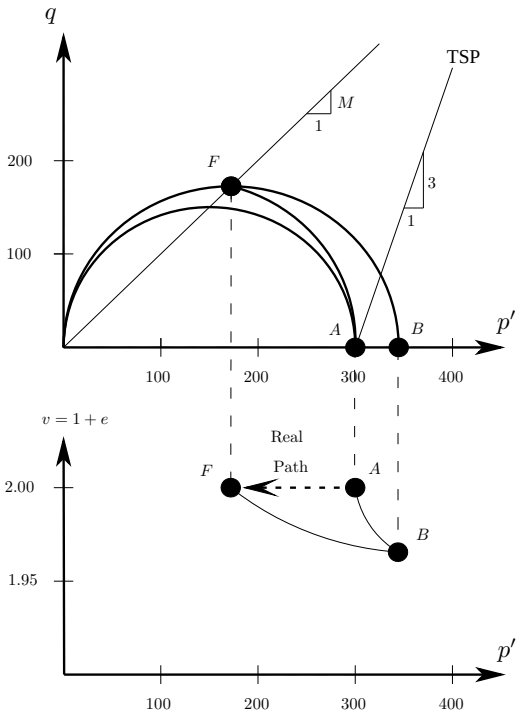

Figure C.11: *Hand calculation MCC: Undrained, normal consolidated*

No change in volume:

$$\Delta v = \Delta v_{AB} + \Delta v_{BC} + \Delta v_{CF} = 0$$

The change in volume from $A \longrightarrow B$:

$$\Delta v_{AB} = -0.05 \ln\frac{1200\text{kPa}}{300\text{kPa}} = -0.0069315$$

$$v_B = 2 - 0.069315 = 1.93069$$

New consolidation pressure:

$$0 = -0.069315 - 0.25 \ln\left(\frac{P'_x}{1200\text{kPa}}\right) - \kappa \ln\left(\frac{P'_x/2}{P'_x}\right)$$

$$P'_x = 1044.66\text{kPa}$$

$$\Delta u = 522 - 300 - \frac{522}{3} = 48\,\text{kPa}$$

The change in volume from $B \longrightarrow C$:

$$\Delta V_{BC} = -0.25 \ln\left(\frac{1044.66\text{kPa}}{1200\text{kPa}}\right) = 0.034658$$

$$V_C = 1.93069 + 0.034658 = 1.95535$$

$$\Delta V_{CF} = -0.25 \ln\left(\frac{1044.66\text{kPa}}{1200\text{kPa}}\right) = 0.034658$$

$$V_F = 1.95535 + 0.034658 = 2$$

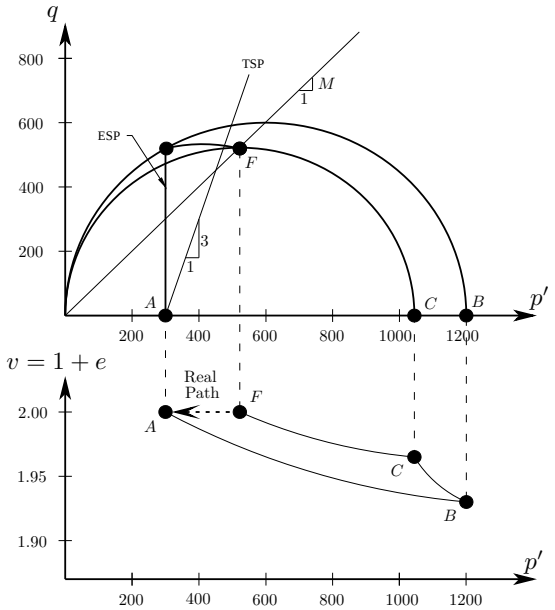

Figure C.12: *Hand calculation MCC: Undrained, over consolidated*

C.4 Constitutive matrix

The theory to assemble the constitutive matrix has been given in Section 2.3-2.7.3. The first step is to recall the reformulated expression of the strain given in Eq. (2.43):

$$d\boldsymbol{\varepsilon} = \boldsymbol{D}^{-1} d\boldsymbol{\sigma} + d\lambda \frac{\partial Q}{\partial \boldsymbol{\sigma}} \tag{C.41}$$

Next step is to multiply by, $\left\{\frac{\partial F}{\partial \boldsymbol{\sigma}}\right\}^T \boldsymbol{D}$, which yields:

$$\left\{\frac{\partial F}{\partial \boldsymbol{\sigma}}\right\}^T \boldsymbol{D} d\boldsymbol{\varepsilon} = \left\{\frac{\partial F}{\partial \boldsymbol{\sigma}}\right\}^T \boldsymbol{D}\boldsymbol{D}^{-1} d\boldsymbol{\sigma} + \left\{\frac{\partial F}{\partial \boldsymbol{\sigma}}\right\}^T \boldsymbol{D} \left\{\frac{\partial Q}{\partial \boldsymbol{\sigma}}\right\} d\lambda \tag{C.42}$$

Utilizing the relationship between stresses and strains in Eq. (C.42) it may be reduced to:

$$\underbrace{\left\{\frac{\partial F}{\partial \boldsymbol{\sigma}}\right\}^T d\boldsymbol{\sigma}}_{A d\lambda} = \left\{\frac{\partial F}{\partial \boldsymbol{\sigma}}\right\}^T \boldsymbol{D} d\boldsymbol{\varepsilon} + \left\{\frac{\partial F}{\partial \boldsymbol{\sigma}}\right\}^T \boldsymbol{D} \left\{\frac{\partial Q}{\partial \boldsymbol{\sigma}}\right\} d\lambda \tag{C.43}$$

Using the consistency equation as shown in (C.43) it may be further reduced to:

$$0 = \left(\left\{\frac{\partial F}{\partial \boldsymbol{\sigma}}\right\}^T \boldsymbol{D} d\boldsymbol{\varepsilon} + \left\{\frac{\partial F}{\partial \boldsymbol{\sigma}}\right\}^T \boldsymbol{D} \left\{\frac{\partial Q}{\partial \boldsymbol{\sigma}}\right\} d\lambda \right) - A d\lambda \tag{C.44}$$

Where the plastic multiplier may be found by:

$$d\lambda = \frac{\left\{\frac{\partial F}{\partial \boldsymbol{\sigma}}\right\}^T \boldsymbol{D} d\boldsymbol{\varepsilon}}{A + \left\{\frac{\partial F}{\partial \boldsymbol{\sigma}}\right\}^T \boldsymbol{D} \left\{\frac{\partial Q}{\partial \boldsymbol{\sigma}}\right\}} \tag{C.45}$$

Substituting back into Eq. (C.41), the general stress strain relationship may be expressed by:

$$d\boldsymbol{\sigma'} = \left(\boldsymbol{D} - \frac{\boldsymbol{D} \left\{\frac{\partial Q}{\partial \boldsymbol{\sigma}}\right\} \left\{\frac{\partial F}{\partial \boldsymbol{\sigma}}\right\}^T \boldsymbol{D}}{A + \left\{\frac{\partial F}{\partial \boldsymbol{\sigma}}\right\} \boldsymbol{D} \left\{\frac{\partial Q}{\partial \boldsymbol{\sigma}}\right\}} \right) d\boldsymbol{\varepsilon} \tag{C.46}$$

Which may be written in compact form by:

$$d\boldsymbol{\sigma} = \boldsymbol{D}_{ep} d\boldsymbol{\varepsilon} \tag{C.47}$$

where

$$\boldsymbol{D}_{ep} = \boldsymbol{D} - \frac{\boldsymbol{D} \left\{\frac{\partial Q}{\partial \boldsymbol{\sigma}}\right\} \left\{\frac{\partial F}{\partial \boldsymbol{\sigma}}\right\}^T \boldsymbol{D}}{A + \left\{\frac{\partial F}{\partial \boldsymbol{\sigma}}\right\}^T \boldsymbol{D} \left\{\frac{\partial Q}{\partial \boldsymbol{\sigma}}\right\}} \tag{C.48}$$

Notice that the term $\left(\left\{\frac{\partial Q}{\partial \boldsymbol{\sigma}}\right\} \left\{\frac{\partial F}{\partial \boldsymbol{\sigma}}\right\}^T \right)$ yields a full symmetric matrix for associated plasticity and a non symmetric matrix for non associated flow.

C.5 Time Resistance Concept

The time resistance concept was suggested by Janbu (1969) which is a method to determine the influence of creep by a single creep parameter. The definition of resistance is normally defined as:

$$\text{Resistance} = \frac{\text{Cause}}{\text{Effect}}$$

Transforming this principle into creep methodology, the resistance parameter may be defined as:

$$R = \frac{dt}{d\varepsilon} = \frac{\text{Increment in time}}{\text{Increment in strain}} \tag{C.49}$$

Recalling that creep is associated to deformation over time corresponding to effect and cause, respectively. The time resistance concept is a simplification of the reality since the method assumes one-dimensional compression. However, the majority of deformation caused by creep occurs vertically during normal scenarios (ageing of young deposits). Through the assumption of one-dimensional, the magnitude of creep may be determined by one single parameter determined from a one-dimensional testing equipment. The principle of Janbu's stress-strain-time behaviour may be seen on Figure C.13.

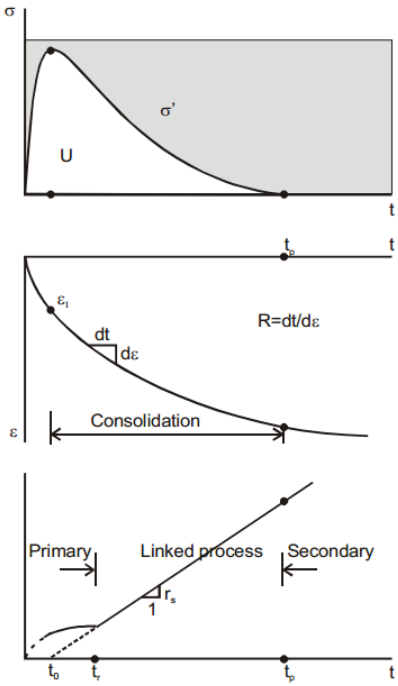

Figure C.13: *Janbu's stress-strain-time concept. Taken from (Janbu, 1998).*

As seen on Figure C.13, the time resistance number (r_s) may be determined as the inclination during the secondary compression.

$$r_s = \frac{dR}{dt} = \frac{d\left(\dfrac{\partial t}{\partial \varepsilon_{11}}\right)}{dt} = \frac{\dfrac{\partial t}{\partial \varepsilon_{11}(t)} - R_{\text{ref}}}{t - \tau} \tag{C.50}$$

where ε_{11} is the axial strain in an oedometer and R_{ref} is the time resistance at a certain reference time, τ. Eq. (C.50) may be rewritten into:

$$\frac{dt}{d\varepsilon}(t) = r_s(t - \tau) + R_{ref} = r_s t \qquad \text{since} \qquad r_s \tau = R \tag{C.51}$$

Time Evolution in Volumetric Strain

To determine the change in volume with respect to time Eq. (C.51) may be formulated as:

$$\frac{d\varepsilon_p^{vp}}{dt} = \frac{1}{r_s t} \qquad \longrightarrow \qquad \Delta\varepsilon_p^{vp} = \frac{1}{r_s} \ln\left(\frac{t}{\tau}\right) \tag{C.52}$$

The change in the equivalent one-dimensional pre-consolidation stress (p_c) caused by a change in volumetric strain ($\Delta\varepsilon_p$) may be found through an integration of the isotropic hardening rule:

$$\frac{dp_c}{d\varepsilon_p^{vp}} = \frac{vp_c}{\lambda - \kappa} \longrightarrow \Delta\varepsilon_p^{vp} = \frac{\lambda - \kappa}{v} \ln\left(\frac{p_{c,ref}}{p^{eq}}\right) \tag{C.53}$$

where $p_{c,ref}$ is the effective one-dimensional reference preconsolidation stress for the corresponding R_{ref}. Combining Eqs. C.51, C.52, and C.53 where the t is eliminated yields:

$$\frac{d\varepsilon_p^{vp}}{dt} = \frac{1}{R_{ref}} \left(\frac{p^{eq}}{p_{c,ref}}\right)^{r_s \zeta} \qquad \text{where} \qquad \zeta = \frac{\lambda - \kappa}{v} \tag{C.54}$$

The concept of Eq. (C.54) has been suggested by Grimstad et al. (2010) and may be illustrated graphically as seen on Figure C.14.

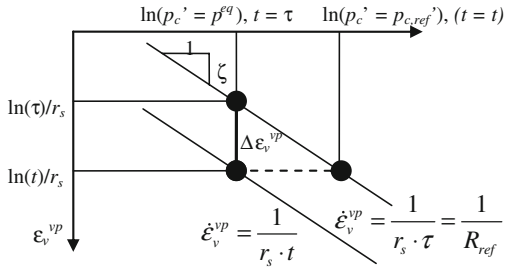

Figure C.14: *Concept of Eq.* (C.54). *Taken from (Grimstad et al., 2010). Notice,* $\varepsilon_v = \varepsilon_p$.

C.6 Talyor Expansion - Plasitic Multiplier

As shown by Grimstad and Benz (2014), the change in the plastic multiplier with respect to time may be found through a Taylor series as:

$$\Delta\lambda \approx \left(\dot{\lambda} + \left\{\frac{\partial\dot{\lambda}}{\partial\boldsymbol{\sigma}}\right\}\Delta\boldsymbol{\sigma} + \left\{\frac{\partial\dot{\lambda}}{\partial\boldsymbol{\kappa}}\right\}\Delta\boldsymbol{\kappa}\right)\Delta t \tag{C.55}$$

where the change in stresses may be approximated to:

$$\Delta\boldsymbol{\sigma} \approx \boldsymbol{D}\left(\Delta\boldsymbol{\varepsilon} - \frac{\partial Q}{\partial\boldsymbol{\sigma}}\Delta\lambda\right) \tag{C.56}$$

The change in state parameter may be approximated to:

$$\Delta\boldsymbol{\kappa} \approx \boldsymbol{h}\Delta\lambda \qquad \text{where} \qquad \boldsymbol{h} = \frac{d\boldsymbol{\kappa}}{d\lambda} \tag{C.57}$$

Solving Eq. (C.55) for the change in the plastic multiplier following formulation may be found:

$$\Delta\lambda = \frac{\dot{\lambda} + \left\{\frac{\partial\dot{\lambda}}{\partial\boldsymbol{\sigma}}\right\}\boldsymbol{D}d\boldsymbol{\varepsilon}}{\frac{1}{\Delta t} - \left\{\frac{\partial\dot{\lambda}}{\partial\boldsymbol{\kappa}}\right\}\boldsymbol{h} + \left\{\frac{\partial\dot{\lambda}}{\partial\boldsymbol{\sigma}}\right\}\boldsymbol{D}\left\{\frac{\partial Q}{\partial\boldsymbol{\sigma}}\right\}} \tag{C.58}$$

C.7 Elastic Anisotropy

This section shortly summaries the mathematical expressions to obtain elastic anisotropic response through a general rotated orthotropic stiffness matrix as presented by Grimstad (2009).

The diagonal matrix $\boldsymbol{\alpha}$ is defined as:

$$\boldsymbol{\alpha} = \begin{bmatrix} \alpha_x & 0 & 0 & 0 & 0 & 0 \\ 0 & \alpha_y & 0 & 0 & 0 & 0 \\ 0 & 0 & \alpha_z & 0 & 0 & 0 \\ 0 & 0 & 0 & \sqrt{\alpha_x \alpha_y} & 0 & 0 \\ 0 & 0 & 0 & 0 & \sqrt{\alpha_x \alpha_z} & 0 \\ 0 & 0 & 0 & 0 & 0 & \sqrt{\alpha_y \alpha_z} \end{bmatrix} \tag{C.59}$$

where x, y and z refers to Cartesian coordinates and α to the fabric. To obtain consistency of the fabric the following expression should be satisfied:

$$tr(\boldsymbol{\alpha}) = \alpha_x + \alpha_y + \alpha_z = 3 \tag{C.60}$$

The isotropic ($\boldsymbol{D}_{iso}$) stiffness may be formulated as:

$$\begin{bmatrix} \sigma'_{11} \\ \sigma'_{22} \\ \sigma'_{33} \\ \sigma'_{12} \\ \sigma'_{13} \\ \sigma'_{23} \end{bmatrix} = \begin{bmatrix} \frac{1}{E} & \frac{-\nu}{E} & \frac{-\nu}{E} & 0 & 0 & 0 \\ \frac{-\nu}{E} & \frac{1}{E} & \frac{-\nu}{E} & 0 & 0 & 0 \\ \frac{-\nu}{E} & \frac{-\nu}{E} & \frac{1}{E} & 0 & 0 & 0 \\ 0 & 0 & 0 & \frac{1}{2}(D_{11} - D_{12}) & 0 & 0 \\ 0 & 0 & 0 & 0 & \frac{1}{2}(D_{11} - D_{12}) & 0 \\ 0 & 0 & 0 & 0 & 0 & \frac{1}{2}(D_{11} - D_{12}) \end{bmatrix} \begin{bmatrix} \varepsilon_{11} \\ \varepsilon_{22} \\ \varepsilon_{33} \\ 2\varepsilon_{12} \\ 2\varepsilon_{13} \\ 2\varepsilon_{23} \end{bmatrix} \tag{C.61}$$

Thereby, the orthotropic stiffness matrix may be written as:

$$\boldsymbol{D}_{ort} = \boldsymbol{\alpha} \boldsymbol{D}_{iso} \boldsymbol{\alpha} \tag{C.62}$$

and in full format:

$$\boldsymbol{D}_{ort} = \begin{bmatrix} \alpha_x^2 D_{11} & \alpha_x \alpha_y D_{12} & \alpha_x \alpha_z D_{13} & 0 & 0 & 0 \\ \alpha_y \alpha_x D_{21} & \alpha_y^2 D_{22} & \alpha_y \alpha_z D_{23} & 0 & 0 & 0 \\ \alpha_z \alpha_x D_{31} & \alpha_z \alpha_y D_{32} & \alpha_z^2 D_{33} & 0 & 0 & 0 \\ 0 & 0 & 0 & \alpha_x \alpha_y \frac{1}{2}(D_{11} - D_{12}) & 0 & 0 \\ 0 & 0 & 0 & 0 & \alpha_x \alpha_z \frac{1}{2}(D_{11} - D_{12}) & 0 \\ o & 0 & 0 & 0 & 0 & \alpha_y \alpha_z \frac{1}{2}(D_{11} - D_{12}) \end{bmatrix} \tag{C.63}$$

As indicated in Eq. (C.63) the principle axis was assumed to coincide with the Cartesian coordinates. Expressing the orthotropic material with respect to the axis of orthotropy may be done through a fabric tensor. The eigenvectors and eigenvalues of the second order fabric tensor ($\boldsymbol{\alpha}$) yields the orthotropic axis.

$$\boldsymbol{\alpha} = \begin{bmatrix} \alpha_{xx} & \alpha_{xy} & \alpha_{xz} \\ \alpha_{yx} & \alpha_{yy} & \alpha_{yz} \\ \alpha_{zx} & \alpha_{zy} & \alpha_{zz} \end{bmatrix} \tag{C.64}$$

The eigenvalues, α_1, α_2 and α_3 with the corresponding eigenvectors x_1, x_2 and x_3. One may now define a second order tensor, called the transformation tensor, as:

$$\boldsymbol{a} = \begin{bmatrix} x_1^T \\ x_2^T \\ x_3^T \end{bmatrix} \tag{C.65}$$

The elements of the rotation tensor $\boldsymbol{a}$ will then be used in a rotational matrix A^{-1}:

$$\boldsymbol{A}^{-1} = \begin{bmatrix} a_{11}^2 & a_{21}^2 & a_{31}^2 & 2a_{11}a_{21} & 2a_{11}a_{31} & 2a_{21}a_{31} \\ a_{12}^2 & a_{22}^2 & a_{32}^2 & 2a_{12}a_{22} & 2a_{12}a_{32} & 2a_{22}a_{32} \\ a_{13}^2 & a_{23}^2 & a_{33}^2 & 2a_{13}a_{23} & 2a_{13}a_{33} & 2a_{23}a_{33} \\ a_{11}a_{12} & a_{21}a_{22} & a_{31}a_{32} & \begin{pmatrix} a_{11}a_{22} \\ +a_{12}a_{21} \end{pmatrix} & \begin{pmatrix} a_{11}a_{32} \\ +a_{12}a_{31} \end{pmatrix} & \begin{pmatrix} a_{21}a_{32} \\ +a_{22}a_{31} \end{pmatrix} \\ a_{11}a_{13} & a_{21}a_{23} & a_{31}a_{33} & \begin{pmatrix} a_{11}a_{23} \\ +a_{13}a_{21} \end{pmatrix} & \begin{pmatrix} a_{11}a_{33} \\ +a_{13}a_{31} \end{pmatrix} & \begin{pmatrix} a_{21}a_{33} \\ +a_{23}a_{31} \end{pmatrix} \\ a_{12}a_{13} & a_{22}a_{23} & a_{32}a_{33} & \begin{pmatrix} a_{12}a_{23} \\ +a_{13}a_{22} \end{pmatrix} & \begin{pmatrix} a_{12}a_{33} \\ +a_{13}a_{32} \end{pmatrix} & \begin{pmatrix} a_{22}a_{33} \\ +a_{23}a_{32} \end{pmatrix} \end{bmatrix} \tag{C.66}$$

The elastic material stiffness matrix, for the full three dimensional orthopic material (extended Houlsby and Graham (1983)), may now be presented for a Cartesian coordinate system as:

$$\boldsymbol{D} = \boldsymbol{A}^{-1}\boldsymbol{D}_{ort}\boldsymbol{A}^T \tag{C.67}$$

C.8 Initial Anisotropy

This section will describe the initial anisotropy related to plasticity, i.e. the rotation of the yield surface. Two different approaches to initialize the rotation of the yield surface will be determined. Furthermore, the stress ratio in one-dimensional compression will be defined.

C.8.1 Stress Ratio during One-dimensional Condition

The stress ratio may be determined as:

$$\eta = \frac{q}{p'} = \frac{\sigma'_{11} - \sigma'_{33}}{\frac{1}{3}\left(\sigma'_{11} + \sigma'_{22} + \sigma'_{33}\right)} \tag{C.68}$$

During one-dimensional conditions $\sigma'_{22} = \sigma'_{33}$ and ${}^{\sigma'_{33}}/_{\sigma'_{11}} = K'_0$. Hence, following formulation of the stress ratio may be found:

$$\eta_{K_0^{NC}} = \frac{3(1 - K_0^{NC})}{1 + 2K_0^{NC}} \tag{C.69}$$

C.8.2 Neglecting Elastic Strains

Assuming that plastic strains are dominant and thereby neglecting the elastic contribution the ratio between deviatoric and volumetric strains is equal to:

$$\frac{2}{3} = \frac{d\varepsilon_d}{d\varepsilon_p} \approx \frac{d\varepsilon_d^p}{d\varepsilon_p^p} \tag{C.70}$$

Utilizing associated flow the deviatoric and volumetric plastic strains may be determined from Eq. (4.2) as:

$$d\varepsilon_d^p = \frac{\partial Q}{\partial q} = 2q - 2\alpha p' \tag{C.71a}$$

$$d\varepsilon_p^p = \frac{\partial Q}{\partial p'} = \alpha^2 p_c' + 2M^2 p - M^2 p_c' - 2 \tag{C.71b}$$

The ratio of deviatoric and volumetric plastic strains may be arranged as:

$$\frac{d\varepsilon_d^p}{d\varepsilon_p^p} = \frac{2q - 2\alpha p'}{\alpha^2 p_c' + 2M^2 p - M^2 p_c' - 2q\alpha} = \frac{2(\eta - \alpha)}{2M^2 + \alpha^2 \dfrac{p_c'}{p} - M^2 \dfrac{p_c'}{p} - 2\eta\alpha} \tag{C.72}$$

Recalling the definition of the yield function:

$$(q - \alpha p')^2 - (M^2 - \alpha^2)(p_c' - p')p' = 0 \tag{C.73}$$

The yield function may be rearranged as:

$$\frac{q^2}{p^2} = 2\eta\alpha + M^2 + \alpha^2 \frac{p_c'}{p'} - M^2 \frac{p_c'}{p'} \qquad \longrightarrow \qquad -M^2 - \eta^2 = \underbrace{\alpha^2 \frac{p_c'}{p'} - M^2 \frac{p_c'}{p'} - 2\eta\alpha}_{\text{Same as denominator in Eq. (C.72)}} \tag{C.74}$$

Substituting Eq. (C.74) into Eq. (C.72) yields:

$$\frac{d\varepsilon_d^p}{d\varepsilon_p^p} = \frac{2\,(\eta - \alpha)}{2M^2 - M - \alpha^2} = \frac{2\,(\eta - \alpha)}{M^2 - \alpha^2} \tag{C.75}$$

Utilizing Eq. (C.71) following expression for the ratio between the volumetric and plastic deviatoric strains may be assembled:

$$\frac{d\varepsilon_d}{d\varepsilon_p} = \frac{2}{3} = \frac{2\left(\eta_{K_0^{NC}} - \alpha_{K_0^{NC}}\right)}{M^2 - \alpha_{K_0^{NC}}^2} \tag{C.76}$$

Notice that $\alpha = \alpha_{K_0^{NC}}$ and $\eta = \eta_{K_0^{NC}}$ since the one-dimensional condition is utilized. Hence, an expression for $\alpha_{K_0^{NC}}$ may now be determined:

$$\alpha_{K_0^{NC}} = \frac{\eta_{K_0^{NC}}^2 + 3\alpha_{K_0^{NC}} - M^2}{3} \tag{C.77}$$

where $\eta_{K_0^{NC}}^2$ can be found from K_0^{NC}.

C.8.3 Neglecting Elastic Shear Strains

The expression for the initial rotation only neglecting the elastic shear strain may be found by recalling the definition of the dilatancy angle:

$$\Psi = \frac{d\varepsilon_p^p}{d\varepsilon_q^p} \tag{C.78}$$

Utilizing the $(\ln p' : e)$-plane an expression for the change in volumetric strain may be found as:

$$d\varepsilon_p = \left(\frac{\lambda}{\lambda - \kappa}\right) d\varepsilon_p^p \tag{C.79}$$

The shear strain can be found by neglecting the elastic contribution, meaning $d\varepsilon_q \approx d\varepsilon_q^p$. Hence, using the standard relation of strains ($\varepsilon = d\varepsilon_p / d\varepsilon_q$) an expression for the dilatancy angle can be found:

$$\Psi = \left(1 - \left(\frac{\lambda}{\kappa}\right)\right) \varepsilon \tag{C.80}$$

According to the flow rule the ratio between the deviatoric and volumetric plastic strains may be written as:

$$\frac{d\varepsilon_p^p}{d\varepsilon_q^p} = \frac{M^2 - \eta^2}{2(\eta - \alpha)} \tag{C.81}$$

Using Eq. (C.80) and Eq. (C.81) and solving for α with respect to one-dimensional conditions following expression may be assembled:

$$\alpha_{K_0^{NC}} = \frac{\eta_{K_0^{NC}}^2 + 3\left(1 - \frac{\kappa}{\lambda}\right)\alpha_{K_0^{NC}} - M^2}{3\left(1 - \frac{\lambda}{\kappa}\right)} \tag{C.82}$$

C.9 Rotational Hardening

The evolution of anisotropy is a complex phenomenon where the grains in the soil are reorganized. The main aim will be to highlight some of the different formulations which have been suggested to describe the rotational hardening. The benefits and drawbacks of these formulations will be pointed out and it will be shortly discussed where the main conclusions are taken from (Dafalias and Taiebat, 2013).

The corresponding rotational hardening law to the yield surface ((4.2)) presented by (Dafalias, 1986) may be formulated as

$$d\alpha = \langle d\lambda \rangle c \left| \frac{\partial Q}{\partial p'} \right| \frac{p'}{p'_c}(\alpha_b - \alpha) \qquad \text{where} \qquad \alpha_b = \frac{\eta}{x^\alpha} \tag{C.83}$$

where c is a model parameter controlling the pace of evolution, Q is the plastic potential surface, and x^α is another model parameter defining the equilibrium or bonding value (α_b) under fixed stress-ratio η loading. Later Dafalias changed the evolution rule slightly due to the $\left|\frac{\partial Q}{\partial p'}\right|$ term in (C.83) to following expression:

$$d\alpha = \langle d\lambda \rangle c p_{at} \frac{p'}{p'_c}(\alpha_b - \alpha) \qquad \text{where} \qquad \alpha_b = \frac{\eta}{x^\alpha} \tag{C.84}$$

where p_{at} is the atmospheric pressure introduced for dimensional consistency. The third evolution rule was presented by (Wheeler et al., 2003) assuming associated flow:

$$d\alpha = \mu \left[\left(\frac{3\eta}{4} - \alpha \right) \langle d\varepsilon_p^p \rangle + \beta \left(\frac{\eta}{3} - \alpha \right) |d\varepsilon_q^p| \right] \tag{C.85a}$$

$$= \mu \langle d\lambda \rangle p' \left[\left(\frac{3\eta}{4} - \alpha \right) \langle M^2 - \eta^2 \rangle + \beta \left(\frac{\eta}{3} - \alpha \right) |2(\eta - \alpha)| \right] \tag{C.85b}$$

where μ and β are model constants. The fourth and last presented evolution law is a further development of Eq. (C.84) presented by Dafalias and Taiebat (2013) and is formulated as:

$$d\alpha = \langle d\lambda \rangle c p_{at} \frac{p'}{p'_c}(\alpha_b - \alpha) \qquad \text{where} \qquad \alpha_b = \pm \frac{M}{z} \left[1 - \exp\left(-s \frac{|\eta|}{M} \right) \right] \tag{C.86}$$

where z and s are positive model constants. Notice that, M will take the value of either M_c or M_e and the $\pm$ sign becomes positive or negative for $\eta \geq 0$ or $\eta \leq 0$, respectively.

Comparing Eqs. (C.83)-(C.86) it can be seen that the formulation proposed by Dafalias suggests a bounding value of α denoted as α_b. The formulation given by Wheeler uses an implicit approach by setting the bracketed term equal to zero and thereby determining a bounding value of α. The soil parameter presented in the four formulations may be divided into two categories: 1. Control of the equilibrium values of α under constant-stress-ratio (η) and is represented by x^α, β and z, s. 2. control the pace of rotation and is represented by c and μ.

Model Parameters during Constant-Stress-Ratio

Utilizing the fact that a specific constant-strain-rate ratio will have a corresponding constant stress ratio, the model parameters that control the equilibrium value of α may be determined. In such a determination, it is required that experimental data for the equilibrium values of α are available. This procedure has been done for the four rotational laws by Dafalias and Taiebat (2013).

The first step is to determine an analytical value of the bounding value of α which is done by the following expressions and may be derived from Eqs. C.84-C.86, respectively:

$$\alpha = \alpha_b = \frac{\eta}{x^\alpha} \tag{C.87a}$$

$$\alpha = \begin{cases} \sqrt{8\beta(3\alpha - \eta)(\eta - \alpha) - 3(3\eta - 4\alpha)(M^2 - \eta^2)} = 0 & \text{if } \eta < M \\ \frac{\eta}{3} & \text{if } \eta > M \end{cases} \tag{C.87b}$$

$$\alpha = \alpha_b = \pm\frac{M}{z}\left[1 - \exp\left(-s\frac{|\eta|}{M}\right)\right] \tag{C.87c}$$

The Eqs. ((C.87a), (C.87b), and (C.87a)) are plotted in Figure C.16 where the model parameters x^α, β, z and s are chosen to fit the experimental data in the compression zone. Note that $z = s$ in the particular case, see Dafalias and Taiebat (2013) for further details.

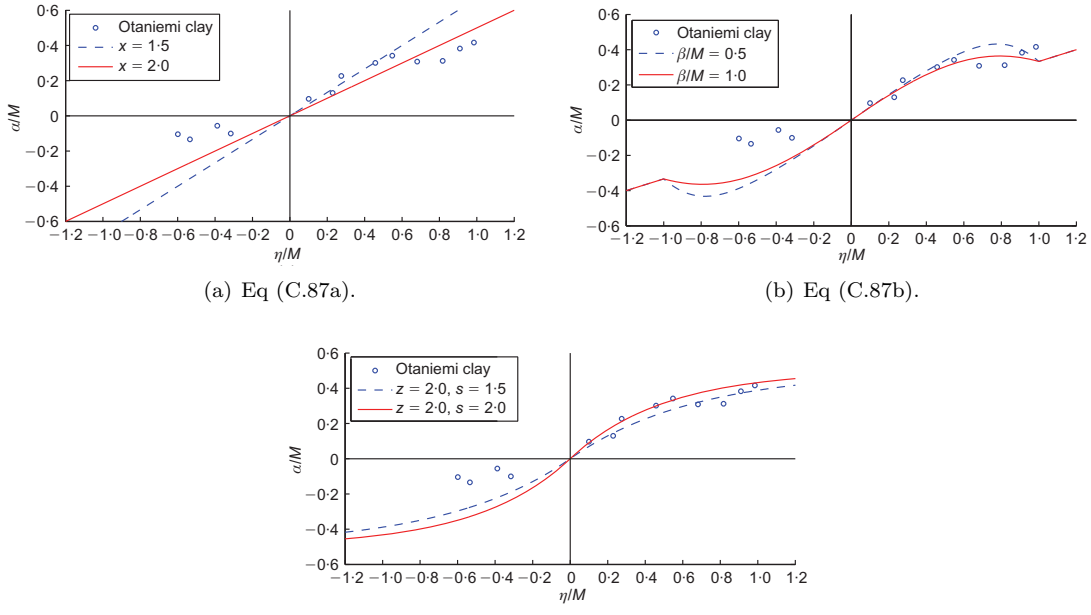

(a) Eq (C.87a).

(b) Eq (C.87b).

(c) Eq (C.87c).

Figure C.15: *Equilibrium values of α/M for radial stress path with various η/M. Taken from (Dafalias and Taiebat, 2013)*

All three Eqs fit the data point reasonably well, but Eq. (C.87b) and Eq. (C.87c) fits better compared to Eq. (C.87a) due to the benefit of the shape of the functions. The soil parameters have been chosen to fit the compression data points and it has been suggested by (Dafalias and Taiebat, 2013) to calibrate the parameter either to a compression or a tension test.

Loading to critical state and uniqueness of CSL:

In the main essence of critical state theory it requires that the critical state ratio $\eta = \eta_c = M$ at the state where $\frac{\partial Q}{\partial p} = 0$ meaning that the rate of p'_c is zero. Therefore, by incorporating an evolution law the same requirement should be fulfilled. To do this the bounding value of α should approach a critical value simultaneously with isotropic hardening and the combination of α_c and η_c guarantees a unique critical state line in the $(e : \ln p')$-space.

The first step in this analyses process is to rewrite the formulation for the yield surface to obtain a relationship between the stress conditions and rotation parameter in the critical state:

$$\frac{p'_{cs}}{p'_c} = \frac{1}{2}\left(1 + \frac{\alpha_c}{M}\right) \qquad \text{where} \qquad q_{cs} = M p'_{cs} \tag{C.88}$$

According to Eq. (C.88), a unique CSL represented by the change of the pre-consolidation pressure in the $(e : \ln)$-space will be dependent on the ratio of α_c/M. The uniqueness of the CSL may be confirmed if the ratio α_c/M remains the same for any loading at any mean pressure p' and yielding the same predictions of the critical state.

Going back to the four evolution laws the first would never yield a unique critical state line due to the term of $|\partial G/\partial p|$. As stated in Dafalias and Taiebat (2013), this term would freeze the evolution of both α and p'_c approaching the stress point $\eta = M$. The tree other laws do not show the same lack of uniqueness and would approach equilibrium at $\eta = M$. The ratio for this particular state is given below for Eqs. (C.87), respectively:

$$\frac{\alpha_c}{M} = \frac{1}{x^\alpha} \qquad \text{and} \qquad \frac{p'_{cs}}{p'_c} = \frac{1 + x^\alpha}{2x^\alpha} \tag{C.89a}$$

$$\frac{\alpha_c}{M} = \frac{1}{3} \qquad \text{and} \qquad \frac{p'_{cs}}{p'_c} = \frac{2}{3} \tag{C.89b}$$

$$\frac{\alpha_c}{M} = \frac{1}{z}\left[1 - \exp\left(-s\right)\right] \qquad \text{and} \qquad \frac{p'_{cs}}{p'_c} = \frac{1}{2}\left[1 + \frac{1}{z}\left(1 - \exp\left(-s\right)\right)\right] \tag{C.89c}$$

Notice, to obtain a uniqueness of the CSL it requires independence of the ratio $\frac{p'_{cs}}{p'_c}$ and the parameters x^α, z and s from the Lode angle. Uniqueness of the CSL should still be obtained in a multiaxial space. The lack of uniqueness may best be illustrated by plotting the undrained stress path in a $(p' : q)$-space and can be seen on Figure C.16 associated to the test made by Dafalias and Taiebat (2013).

In Figure C.16 two main conclusions may be drawn. Regarding the first rotation law suggested Dafalias (1986), the yield surface has not rotated enough towards extension region comparing to the other cases. Furthermore, the critical state in compression and extension is found at different mean pressures caused by the term $|\partial Q/\partial p|$. Comparing the three other rotation laws, a "hook-type" shape appears approaching failure where extension paths are more dominant in this behaviour.

This indicates continuous rotation of the yield surface at a constant p'_c. Dafalias and Taiebat (2013) has stated that the three rotational rules yield very similar results despite the fact that all the rotational rules approach a different critical state and location on the unique CSL. In addition, by applying non-associated flow the simulation capability is improved dramatically.

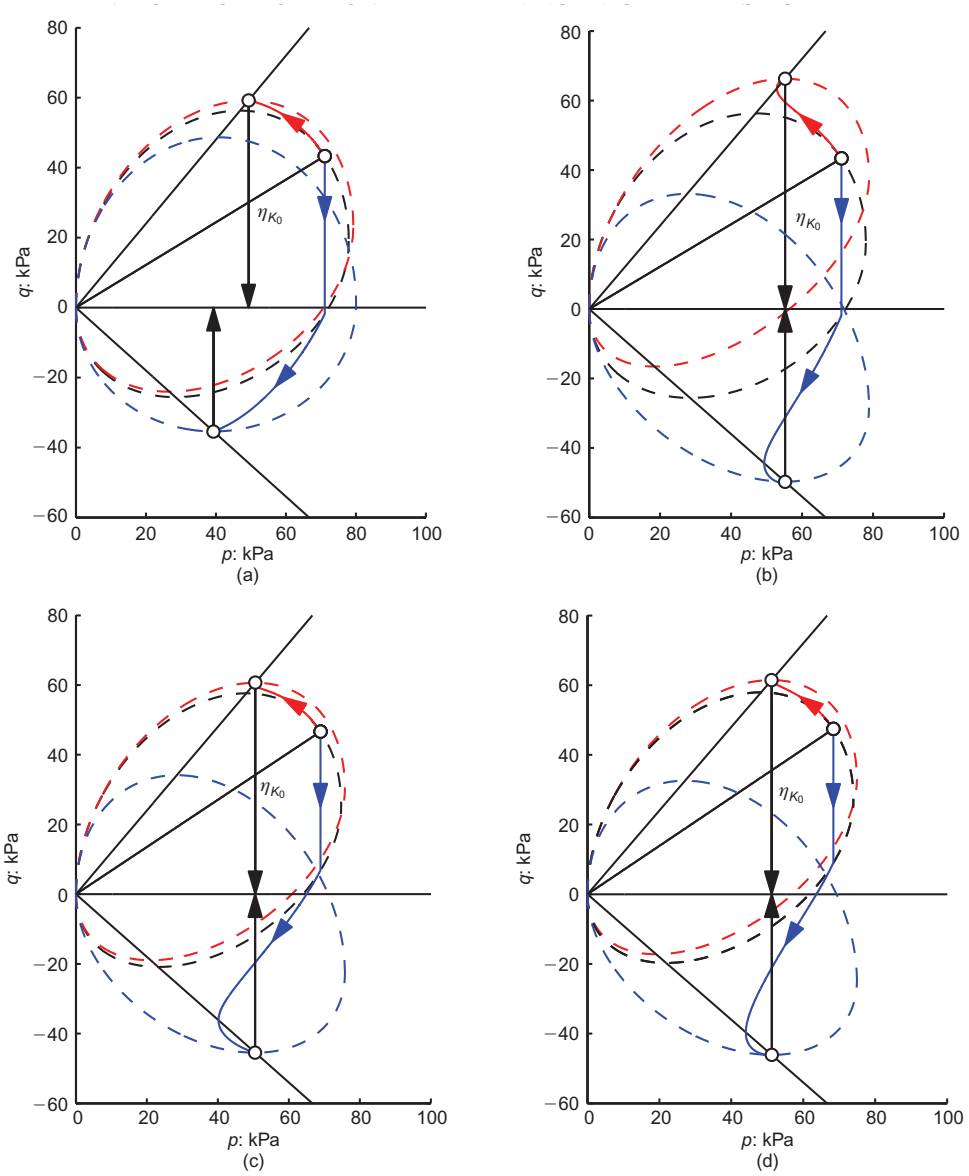

Figure C.16: *Undrained stress path in compression and extension after K_0 consolidation, indicating uniqueness or lack of it of CSL. a) Eq.* (C.83) *b) Eq.* (C.84) *c) Eq.* (C.85) *d) Eq.* (C.86) *in Appendix C.9. Taken from (Dafalias and Taiebat, 2013).*

Appendix D

Programming

The purpose of this appendix is to provide information regarding the constitutive model. The first part will introduce the algorithm and the procedure related to the MCC model which has been programmed in MATLAB. The second part will present the FORTRAN framework.

D.1 Algorithm for the MCC Model

The MCC model in MATLAB is an iterative procedure where stresses are determined by a known vertical deformation. A pseudo code may be seen in Algorithm 1.

Data: $\kappa, \lambda, \nu, e_0, M$ and p'_c
Result: $p'_{cs}, q_{cs}, u, \varepsilon_{11}, \varepsilon_p$ and ε_d
Initialization by assembling the initial contributions in vectors and matrices
while *Counter < Max number of iterations* **do**
  if $F = 0$ **then**
    Determine new p'_0 by the previous stresses
  else
    No change in p'_c
  end
  if *yield = 0* **then**
    Compute $d\lambda$
  else
    $d\lambda = 0$
  end
  -Assemble the constitutive stiffness matrix
  -Determine Incremental strains
  -Determine Incremental stress
  -Updating stresses, strains and state parameters
end

Algorithm 1: MCC in MATLAB

The MATLAB code can be found in Appendix E.1.1. In general, the code has been assembled by the elastic and plastic theory given by Chapter 2. The assembling of the constitutive stiffness matrix will be explained in the following section.

Assembled Constitutive Matrix

Recalling the definition on the yield function:

$$F = q^2 - M^2 p'(2p' - p'_c) \tag{D.1}$$

To assemble the constitutive matrix the partial derivatives of the yield surface with respect to the

stress tensor are needed. The derivative with respect to tri-axial conditions may be given as:

$$\begin{aligned}
\frac{\partial F}{\partial \sigma'_{11}} &= 2\sigma'_{11} - \sigma'_{22} - \sigma'_{33} + \frac{1}{3}p' - \frac{1}{3}(p'_c - p')M^2 \quad \longrightarrow \quad \frac{2}{3}(p' - p'_c) + \frac{2\sigma'_{11} - \sigma'_{22} - \sigma'_{33}}{M^2} \\
\frac{\partial F}{\partial \sigma'_{22}} &= -\sigma'_{11} + 2\sigma'_{22} - \sigma'_{33} + \frac{1}{3}p' - \frac{1}{3}(p'_c - p')M^2 \quad \longrightarrow \quad \frac{2}{3}(p' - p'_c) + \frac{2\sigma'_{22} - \sigma'_{11} - \sigma'_{33}}{M^2} \\
\frac{\partial F}{\partial \sigma'_{33}} &= -\sigma'_{11} - \sigma'_{22} + 2\sigma'_{33} + \frac{1}{3}p' - \frac{1}{3}(p'_c - p')M^2 \quad \longrightarrow \quad \frac{2}{3}(p' - p'_c) + \frac{2\sigma'_{33} - \sigma'_{11} - \sigma'_{22}}{M^2} \\
\frac{\partial F}{\partial \sigma'_{12}} &= 0 \\
\frac{\partial F}{\partial \sigma'_{13}} &= 0 \\
\frac{\partial F}{\partial \sigma'_{23}} &= 0
\end{aligned}$$

which may be rewritten into:

$$\begin{aligned}
\frac{\partial F}{\partial \sigma'_{11}} &= \frac{2}{3}(p' - p'_c) + \frac{2\sigma'_{11} - \sigma'_{22} - \sigma'_{33}}{M^2} \quad \longrightarrow \quad \frac{2}{3}(p' - p'_c) + 3(\sigma'_{11} - p') \\
\frac{\partial F}{\partial \sigma'_{22}} &= \frac{2}{3}(p' - p'_c) + \frac{2\sigma'_{22} - \sigma'_{11} - \sigma'_{33}}{M^2} \quad \longrightarrow \quad \frac{2}{3}(p' - p'_c) + 3(\sigma'_{22} - p') \\
\frac{\partial F}{\partial \sigma'_{33}} &= \frac{2}{3}(p' - p'_c) + \frac{2\sigma'_{33} - \sigma'_{11} - \sigma'_{22}}{M^2} \quad \longrightarrow \quad \frac{2}{3}(p' - p'_c) + 3(\sigma'_{33} - p') \\
\frac{\partial F}{\partial \sigma'_{12}} &= 0 \\
\frac{\partial F}{\partial \sigma'_{13}} &= 0 \\
\frac{\partial F}{\partial \sigma'_{23}} &= 0
\end{aligned}$$

In MATLAB a general expression may be formulated in a for loop as:

$$\frac{\partial F}{\partial \boldsymbol{\sigma}} = \frac{(2p(a) - p'_c)) + 3(\sigma'(n) - p(i))}{M^2} \tag{D.2}$$

where n is a counter ($n = 1:6$)[1] to represent the principle stresses, and i is the iteration number.

Plastic resistance number:

The plastic resistance number may be determined by:

$$A = -\left(\frac{\partial F}{\partial \boldsymbol{\sigma}}\right)\frac{d\boldsymbol{\sigma}}{d\lambda} \tag{D.3}$$

The first term has been determined by the above divination of the yield function and the second term may be found by using the flow rule utilizing associated flow:

$$d\varepsilon_p^p = d\lambda \frac{\partial Q}{\partial \boldsymbol{\sigma}} \quad \longrightarrow \quad \frac{\partial F}{d\varepsilon_p^p} = \frac{\partial \boldsymbol{\sigma}}{d\lambda} \tag{D.4}$$

The partial derivative of the yield surface with respect to the plastic volumetric strain yields:

$$\frac{\partial F}{d\varepsilon_p^p} = -M^2 p' p'_c \frac{v}{\lambda - \kappa} \quad \text{since} \quad d\varepsilon_p^p = \frac{\lambda - \kappa}{v}\frac{dp'_c}{p'_c} \tag{D.5}$$

Hence, the plastic number may be determined. The constitutive matrix may be assembled by:

[1] It goes up to 6 but yields zero for 4-6.

$$\boldsymbol{D}_{ep} = \boldsymbol{D} - \frac{\boldsymbol{D}\left\{\frac{\partial F}{\partial \boldsymbol{\sigma}}\right\}\left\{\frac{\partial F}{\partial \boldsymbol{\sigma}}\right\}^T \boldsymbol{D}}{A + \left\{\frac{\partial F}{\partial \boldsymbol{\sigma}}\right\}^T \boldsymbol{D}\left\{\frac{\partial F}{\partial \boldsymbol{\sigma}}\right\}} \tag{D.6}$$

D.1.1 Determination of Strains

The strains may be divided into drained and undrained with respect to tri-axial conditions:

- In undrained conditions the strains in the horizontal direction would be equal ($\varepsilon_{22} = \varepsilon_{33}$) and obtain the half of the vertical strain since no volume change is allowed.
- In drained conditions the horizontal strain is determined by utilizing the fact that no change in stresses will occur on a free surface.

Drained condition: For elastic conditions the change in stresses may be formulated as:

$$\Delta\sigma'_{11} = \Delta\varepsilon_{11}D_{11} + \Delta\varepsilon_{22}D_{12} + \Delta\varepsilon_{33}D_{13} \tag{D.7a}$$

$$\Delta\sigma'_{22} = \Delta\varepsilon_{11}D_{21} + \Delta\varepsilon_{22}D_{22} + \Delta\varepsilon_{33}D_{23} \tag{D.7b}$$

$$\Delta\sigma'_{33} = \Delta\varepsilon_{11}D_{31} + \Delta\varepsilon_{22}D_{32} + \Delta\varepsilon_{33}D_{33} \tag{D.7c}$$

Under triaxial conditions following relations can be assumed.

$$\Delta\sigma_{22} = \Delta\sigma_{33} = 0 \qquad \text{and} \qquad \Delta\varepsilon_{22} = \Delta\varepsilon_{33} \tag{D.8}$$

Thereby, expressions for the horizontal strains may be formulated as:

$$\Delta\varepsilon_{22} = \frac{-\Delta\varepsilon_{11}D_{21}}{D_{22} + D_{23}} \qquad \text{and} \qquad \Delta\varepsilon_{33} = \frac{-\Delta\varepsilon_{11}D_{31}}{D_{33} + D_{31}} \tag{D.9}$$

Notice that the elastic relationship is used. This approximation is only valid if very small steps are utilized:

D.2 Simulations of Tri-axial Tests

The MCC model has been used to simulate four scenarios for tri-axial conditions. Two drained and two undrained simulations. The results can be seen in Figures D.1-D.4. The initial soil parameters and stress history used to simulate the output are given in Table D.1.

Table D.1: *Soil parameters used in the MCC model programmed in MATLAB. Used in Figures D.1-D.4*

Parameter		Value	Unit
Confining pressure	p'_0	300	kPa
Consolidation pressure (NC)	p'_c	300	kPa
Consolidation pressure (OC)	p'_c	1200	kPa
Inclination of CSL	M	1.0	-
Initial specific volume	v	2.0	-
Compression coefficient	λ	0.25	-
Swelling coefficients	κ	0.05	-
Poisson's ratio	ν	0.15	-

The output from the MCC model during a drained normal consolidated scenario may be seen in Figure D.1.

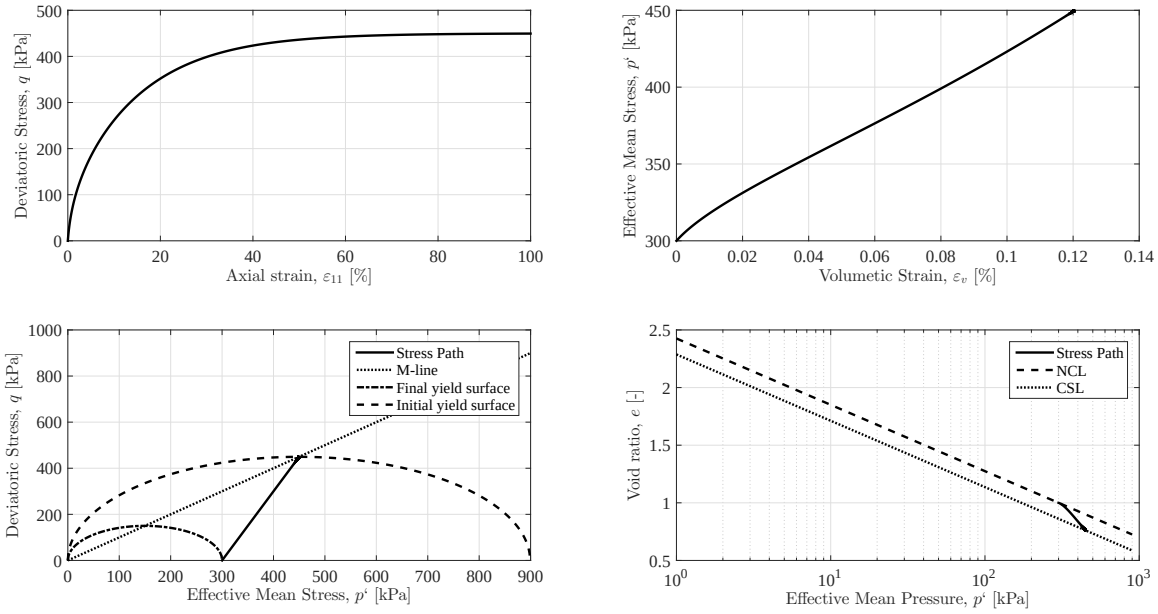

Figure D.1: *MATLAB MCC: Drained normal consolidated.*

The output from the MCC model during a drained over consolidated scenario may be seen in Figure D.2.

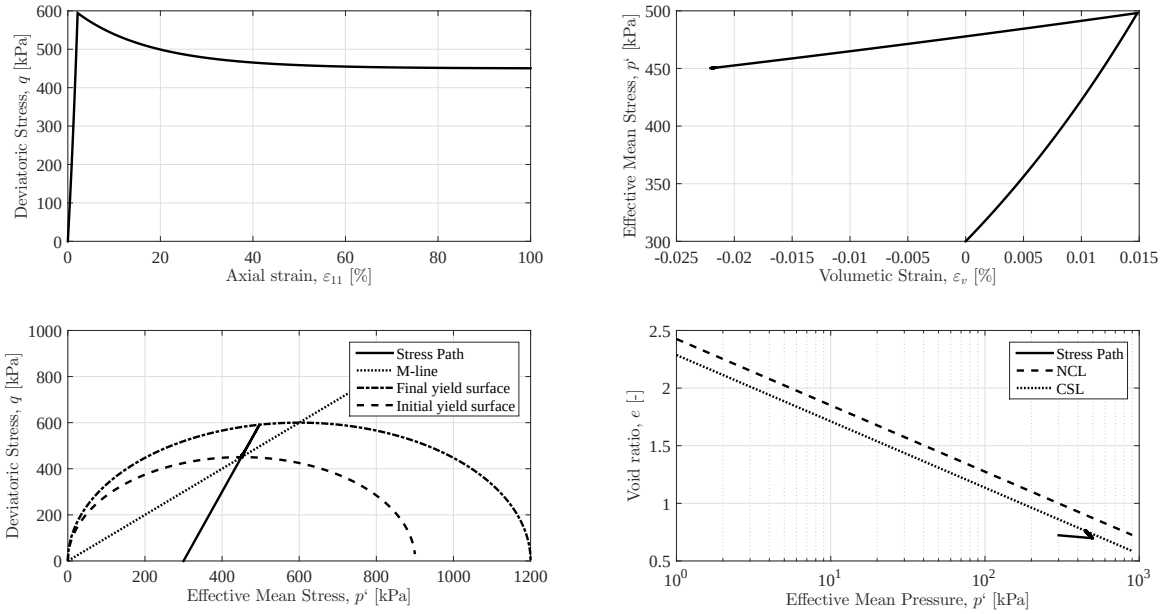

Figure D.2: *MATLAB MCC: Drained over consolidated.*

The output from the MCC model during an undrained normal consolidated scenario may be seen in Figure D.4.

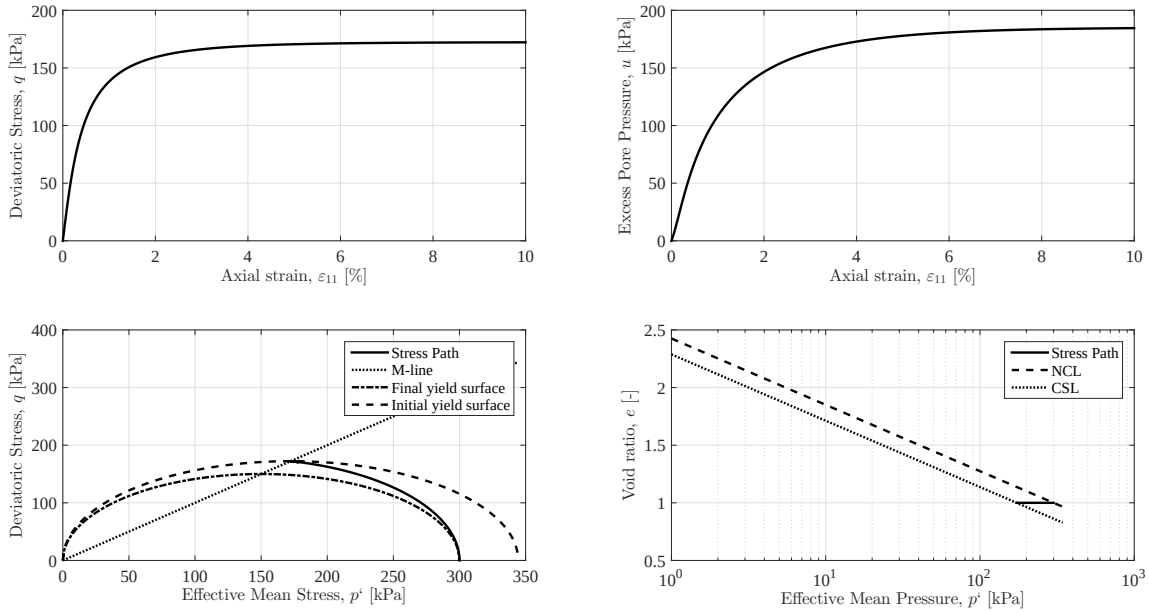

Figure D.3: *MATLAB MCC: Undrained normal consolidated.*

The output from the MCC model during an undrained over consolidated scenario may be seen in Figure D.4.

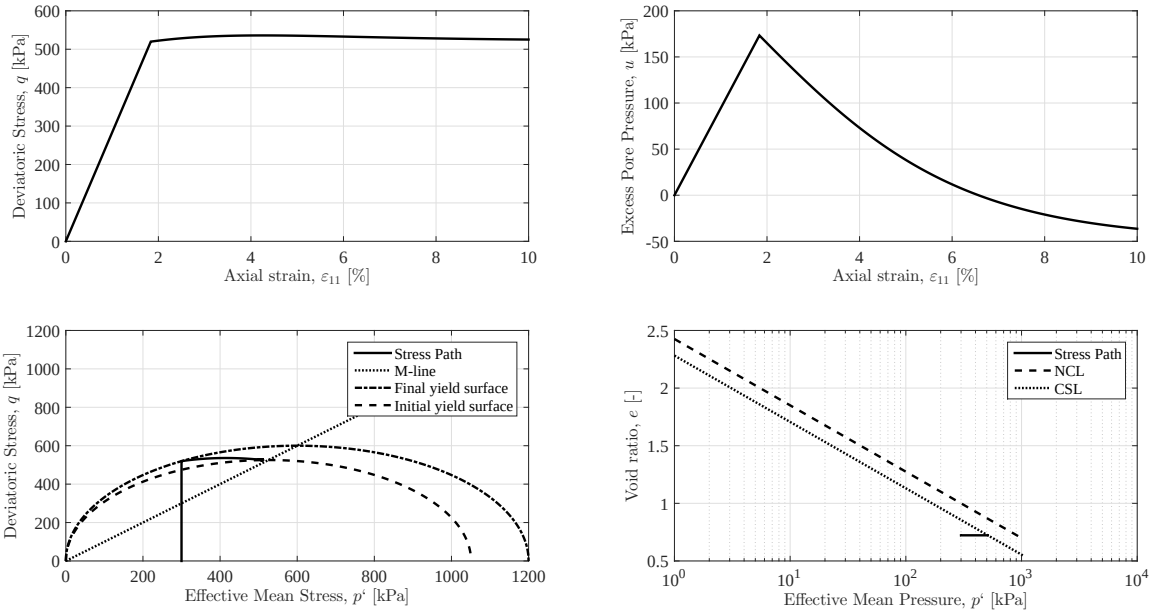

Figure D.4: *MATLAB MCC: Undrained over consolidated.*

D.3 Subroutine User_Mod

This appendix will describe the subroutine `User_Mod` in greater details. The subroutine contains 31 arguments and should have the following structure:

```
Subroutime User_Mod  =  IDTask, iMod, IsUndr, iStep, iTer, Ier, Int, X, Y,
                        Z, Time0, dTime, Props, Sig0, Swp0, StVar0, dEps, D,
                        Bulk\W, Sig, Swp, StVar, ipl, nStat, NonSym, iStrsDep,
                        iTimeDep, iTang, iPrjDir, iPrjLen, iAbort
```

where:

`IDTask` = Identification of the task
- 1= Initialise state variables
- 2 = Calculate constitutive stresses
- 3 = Create effective material stiffness matrix
- 4 = Return the number of state variables
- 5 = Return matrix attributes (NonSym, iStrsDep, iTimeDep, iTang)
- 6 = Create elastic material stiffness matrix

`iMod` = User-defined soil model number (Allows more than one UD model, up to 10.)

`IsUndr` = Drained condition (IsUndr = 0) or undrained condition (IsUndr = 1). In the latter case, PLAXIS will add a large bulk stiffness for water.

`iStep` = Current calculation step number

`iter` = Current iteration number

`Iel` = Current element number

`Int` = Current local stress point number (1..3 for 6- noded elements, or 1..12 for 15-noded elements

`X,Y,Z` = Global coordinates of current stress point

`Time0` = Time at the start of the current step

`dTime` = Time increment of current step

`Props` = Array (1..50) with User-defined model parameters for the current stress point

`Sig0` = Array (1..20) with previous (= at the start of the current step) effective stress components for the current stress point (σ'^0_{xx} , σ'^0_{yy} , σ'^0_{zz} , σ'^0_{xy} , σ'^0_{yz} , σ'^0_{zx} , p_{steady} , $\sum Mstage^0$, $\sum Mstage$, Sat, Sat^0, Suc, Suc^0, $\sum Msf^0$, $\sum Msf$, 0 , 0 , 0 , 0) In 2D calculations σ_{yz} and σ_{zx} should be zero.)

`Swp0` = Previous excess pore pressure of the current stress point

`StVar0` = Array (1..nStat) with previous values of state variables of the current stress point

`dEps` = Array (1..12) with strain increments of the current stress point in the current step ($\Delta\varepsilon_{11}, \Delta\varepsilon_{22}, \Delta\varepsilon_{33}, \Delta\gamma_{12}, \Delta\gamma_{23}, \Delta\gamma_{13}, \Delta\varepsilon^0_{11}, \Delta\varepsilon^0_{22}, \Delta\varepsilon^0_{33}, \Delta\gamma^0_{12}, \Delta\gamma^0_{23}, \Delta\gamma^0_{13}$). In 2D calculations $\Delta\gamma_{yz}, \Delta\gamma_{zx}, \Delta\gamma^0_{yz}, \Delta\gamma^0_{zx}$ should be zero.

`D` = Effective material stiffness matrix of the current stress point (1..6, 1..6).

`Bulk_W` = Bulk modulus of water for the current stress point (for undrained calculations and consolidation)

`Sig` = Array (1..6) with resulting constitutive stresses of the current stress point ($\sigma'_{11}, \sigma'_{22}, \sigma'_{33}, \sigma'_{12}, \sigma'_{23}, \sigma'_{13}$).

`Swp` = Resulting excess pore pressure of the current stress point

`StVar` = Array (1..nStat) with resulting values of state variables for the current stress point

`ipl` = Plasticity indicator

0 = No plasticity
1 = Mohr-Coulomb (failure) point
2 = Tension cut-off point
3 = Cap hardening point
4 = Cap friction point
5 = Friction hardening point

`nStat` = Number of state variables (unlimited)

`NonSym` = Parameter indicating whether the material stiffness matrix is non-symmetric (NonSym = 1) or not (NonSym = 0) (required for matrix storage and solution).

`iStrsDep` = Parameter indicating whether the material stiffness matrix is stress-dependent (iStrsDep = 1) or not (iStrsDep = 9).

`iTimeDep` = Parameter indicating whether the material stiffness matrix is a tangent stiffness matrix, to be used in a full Newton-Raphson iteration process (iTang = 1) or not (iTang = 0).

`iPrjDir` = Project directory (for debugging purposes)

`iPrjLen` = Length of project directory name (for debugging purposes)

`iAbort` = Parameter forcing the calculation to stop (iAbort = 1)

All the arguments above consists of standard type, i.e. parameters starting with the letters A-H and O-Z are associated to double (8-byte) floating points. The parameters may be divided into:

- **Input:** `IDTask, iMod, IsUndr, iStep, iTer, Ier, Int, X, Y, Z, Time0, dTime, Props, Sig0, Swp0, StVar0, dEps uPrjDir` and `iPrjLen`.
- **Output:** `D, Bulk_W, Sig, Swp, StVar, ipl, nStat, NonSym, iStrsDep, iTimeDep, iTang` and `iAbort`.

The input parameters are provided by PLAXIS and should be within the subroutine where the output parameters should be chosen by the user. Note, in the case of `IDTask = 1` then `StVar0` becomes an output parameter.

D.3.1 DLL File - Location

The created DLL file must be placed in the correct directory to be able to be used in PLAXIS. Depending on the version of PLAXIS the file must be placed at different locations in the installation folder. As mentioned in Section 1.6 the PLAXIS version is PLAXIS 2D AE 2.0. The correct location of this version is:

- `C:\Program Files\Plaxis\Plaxis 2D\udsm\` *Your DLL file*

Beware of other locations of the installation folder. Using other versions of PLAXIS please look at the PLAXIS homepage at: `http://kb.plaxis.nl/models/plaxis-user-defined-soil-models`.

The bit version of the DLL file may cause issues when trying to run the UDSM in PLAXIS. The calculation kernel in PLAXIS uses 64-bit applications which are not able to communicate with a 32-bit DLL file. The problem cannot be solved by creating a 64-bit DLL file since the Graphical User Interface (GUI) is only available as a 32-bit application. Therefore, a 32-bit and 64-bit DLL file must be created and placed in the folder mentioned above. This approach has been used to run the UDSM in PLAXIS. Otherwise, it is possible to force PLAXIS to use the 32-bit kernel by removing or renaming the 64-bit kernel from the installation folder. For more information about changing to a 32-bit kernel, please look at the PLAXIS homepage: `http://kb.plaxis.nl/tips-and-tricks/64-bit-user-defined-soil-model`.

D.3.2 Finding the UDSM in PLAXIS

When the UDSM is created and the DLL files (32-bit and 64-bit) are located at the correct location the UDSM can be selected as a soil model in PLAXIS. This is done by choosing the User-defined option in the Material model combo box in the *General* tabsheet when defining new soils, see Figure D.5.

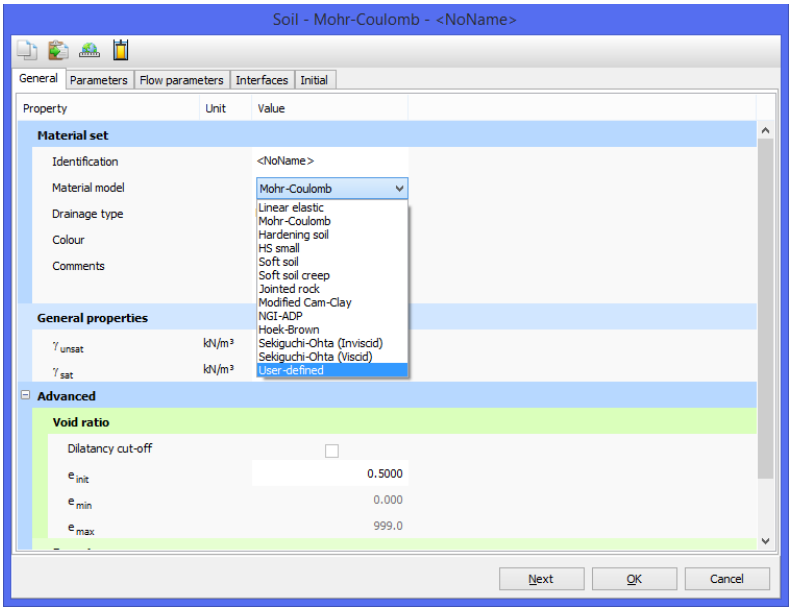

Figure D.5: *Selecting the UDSM.*

Next step is done in the *Parameters* tabsheet. At the combo box "DLL file" the created DLL file is selected, see Figure D.6. Note that only one DLL file will be available even if both a 32-bit and a 64 bit DLL file are created.

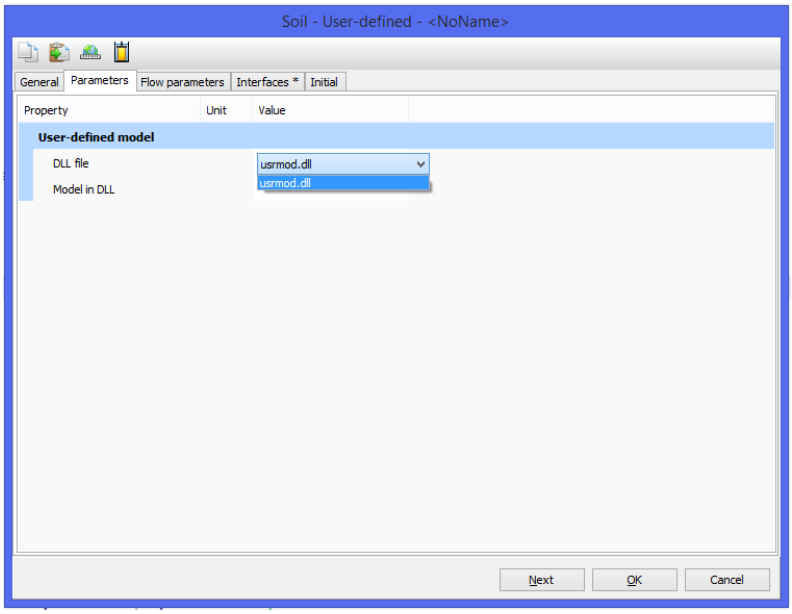

Figure D.6: *Choosing the correct DLL file.*

The DLL file may contain more soil models. Therefore the wanted UDSM (if more are available) needs to be chosen which is done in the *Model in DLL* combo box, see Figure D.7. Note that some PLAXIS versions have a bug and do not show the combo box clearly. If the user just clicks where it should be, a drop down window should appear.

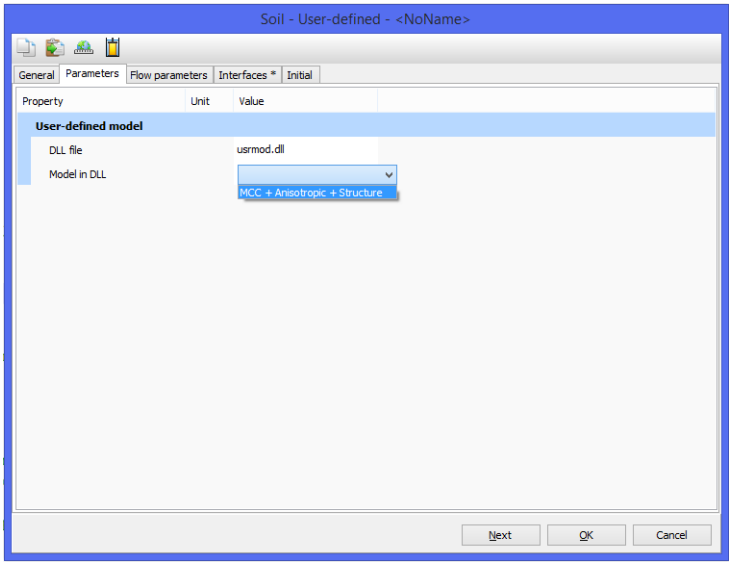

Figure D.7: *Selecting the wanted soil model in the DLL file.*

PLAXIS will automatically read the input parameters from the DLL file and they should be visible in the *Parameters* tabsheet just below the *Model in DLL* combo box. The rest of the soil properties can be added to the soil model. Note that the Interfaces are slightly different in a UDSM. It contains the oedometers modulus ($E_{\text{oed}}^{\text{ref}}$), the interface strength parameters $c_{\text{inter}}, \varphi_{\text{inter}}$ and ψ_{inter}. Hence the interface shear strength is directly given in strength parameters instead of using a factor relating the interface shear strength to the soil shear strength (PLAXIS, 2015).

D.4 Macauley Brackets

The Macauley brackets is a mathematical tool which yields the same magnitude as input if the input is positive and zero if the input is negative or zero.

MATLAB: The `heaviside`-function is used to describe the Macauley bracket. This is a built-in function in MATLAB returning following output:

$$\langle x \rangle = x \cdot \text{heaviside}(x) \qquad \text{where} \qquad \text{heaviside}(x) = \begin{cases} 0 & \text{if } x < 0 \\ \frac{1}{2} & \text{if } x = 0 \\ 1 & \text{if } x > 0 \end{cases} \tag{D.10}$$

As observed in Eq. (D.10) one could expect errors when the input value is zero caused by the `heaviside`-function yielding a value of $\frac{1}{2}$. Hence, it deviates from the definition of the Macauley brackets. However, the `heaviside`-function is multiplied by the input value which solve the issue.

FORTRAN: Converting to FORTRAN code, the built-in functions in MATLAB will not be transferred. Therefore, in the generated code from MATLAB an unknown function call `heaviside` is present. This function is created in FORTRAN by the following procedure:

if $x > 0.0$ **then**
  $y = 1.0$
else if x == 0.0 **then**
  y = 0.5
else
  $y = 0.0$
end if

Appendix E

Code

This appendix consists of the MATLAB and FORTRAN code which has been developed during the master thesis.

E.1 MATLAB

This section contains the MATLAB files which generate the FORTRAN code for vector $\boldsymbol{v}$ and matrix $\boldsymbol{D}$ along with the associated functions. In addition, a file containing the additional coding for utilizing implicit integration and a simple MCC model in MATLAB may be found.

E.1.1 MCC in MATLAB

```
%%%%%%%%%%%%%%%%%%%%%%%%%%%%%%%%%%%%%%%%%%%%%%%%%%%%%%%%%%%%%%%%%%%%%%%%%%%%%%%%
%%% Modificd Cam Clay (MCC)                                                    %%%
%%% Tri-Axial                                                                   %%%
%%% By Jesper Bjerre - s102905                                                  %%%
%%% Master Thesis                                                               %%%
%%% DTU and NTNU                                                                %%%
%%% Spring 2015                                                                 %%%
%%%%%%%%%%%%%%%%%%%%%%%%%%%%%%%%%%%%%%%%%%%%%%%%%%%%%%%%%%%%%%%%%%%%%%%%%%%%%%%%
clear all
close all
clc

font = 14;
set(0,'DefaultAxesFontName','Times')
set(0,'DefaultAxesFontAngle','Normal')
set(0,'DefaultAxesFontSize',font)
set(0,'DefaultTextFontName','Times')
set(0,'DefaultTextFontAngle','Normal')
set(0,'DefaultTextFontSize',font)

%============================ Input Parameters ============================%
k = 0.05;                               % Swelling index
l = 0.25;                               % Compression index
nu = 0.15;                              % Poissons ratio
M = 1;                                  % Stress ratio (critical state)
N = 3.4259;                             % Location of isotrop0c normal

pcc = 300;                              % Preconsolidation pressure
p0 = 300;                               % Initial pressure

%========================= Initial Calculations ==========================%
%% Determine following initial parameters V,e0 and OCR
pc = pcc;                               % Renaming
v = N-(l*log(pc))-(k*log(p0/pc));       % Specific Volume
e0 = v-1;                               % Initial Void Ratio
OCR = pcc/p0;                           % Over Consolidation Ratio
```

```
%============================ Numerical setup ==============================%
%% Number of iterations and vertical strain]
iteration = 10000;                      % Number of iterations
                                        % (should not be lower than 10000)
ide  =0.01;                             % In decimal
de = ide/100;                           % Determining the procentence
es = 0:ide:(iteration-1)*ide;           % Determine the vertical strains
n = 1;                                  % Iterator

%====================== Initial vectors and matrice ======================%
%% Setup of the dimension og necessary vectors and matrice.
D = zeros(6,6);                         % Stiffness Matrix
p = zeros(iteration,1);                 % Mean Effective Stress
q = zeros(iteration,1);                 % Deviatoric Stress
u = zeros(iteration,1);                 % Pore Water Pressure
void = zeros(iteration,1);              % Void ratio
dStrain = zeros(6,1);                   % Increamental Strain
eps_p = zeros(iteration,1);             % Volumetic Strain
eps_d = zeros(iteration,1);             % Deviatoric Strain

% Vector for subcalculation yield function different with respect to:

dfdep=zeros(6,1);                       % The Plastic Strains
dfds=zeros(6,1);                        % The Stress Tensor
%============================ Initialize ===================================%
%% Stresses, Strains, Yield Surface and Void Ratio
Sig=p0*[1;1;1;0;0;0];                   % Stress
p(n)=(Sig(1)+2*Sig(3))/3;               % Effective Mean Stress
q(n)=(Sig(1)-Sig(3));                   % Deviatoric Stress
yield=(q(n)^2/M^2+p(n)^2)-p(n)*pc;      % Defining the yield surface
strain=[0;0;0;0;0;0];                   % Strain
void(n)=e0;                             % Void Ratio

%% Plotting the initial yield surface
p_ini_yield=(0:pc);                     % Effective Mean pressure
qy = (M^2*(pc*p_ini_yield-...
    p_ini_yield.^2)).^0.5;              % Deviatoric Stress

%====================== While loop (Iteration process) ===================%
% While loop creates the elastic stiffness matrix and constitutive matrix.
% Checking if the yield condition i fulfilled and if yes computing the
% stresses with respect to the constitutive matrix. If the yield criteria
% is below zero when only the elastic part is taken. Furhtermore, updating
% all parameters which changes in each increment.

while n<iteration
    K=v*p(n)/k;                                 % Bulk Modulus
    G=(3*K*(1-2*nu))/(2*(1+nu));                % Shear Modulus
    if yield==0, pc=(q(n)^2/M^2+p(n)^2)/p(n);   % New preconsolidation
    else pc=pcc;                                % No yielding --> no change
    end

%% Determine the Elastic Stiffness, plastic stiffness and subcalculations.
    for i=1:6                                   % The stiffness matrix 6x6
        for j=1:6                               % The stiffness matrix 6x6
            if i<=3
                if yield <0, dfds(i,1)=0;dfdep(i,1)=0; % No platicity!
                else                                   % Platicity ! -->
                    dfds(i,1)=(2*p(n)-pc)/3 + 3*(Sig(i)-p(n))/M^2;  % dfds
                    dfdep(i,1)=(-p(n))*pc*(1+e0)/(l-k)*M^2;         % dfdep
                end
                if i==j                         % First 3 in the diagonal
                    D(i,j)= K+4/3*G;            % Elastic Stiffness 1/3
                else if i<=3, D(i,j)=K-2/3*G;   % Elastic stiffness 2/3 % obs
                    end
                end
            end
            if i>3, dfds(i,1)=0; dfdep(i,1)=0;  % df/ds',df/dep (tri-Axial)
                if i==j, D(i,j)= G;             % Elastic Stiffness 3/3
                else  D(i,j)=0;                 % Setting rest to zero
                end
            end
```

```
        end
    end

%% Constrution the Stiffness Matrix, either elastic or platic
    if yield<0, Dep=D;                                      % Elastic
    else Dep=D-((D*dfds*(dfds')*D)/...
            ((-(dfdep')*dfds+(dfds')*D*dfds)));             % Plastic
    end

%============================== Updating ================================%
%% Incremental strains, Note first line Undrained, second drained!
 %  dStrain = [de;-de/2.;-de/2.;0.;0.;0.];                    % (Tri-Axial)
    dStrain = [de;-1*Dep(2,1)/(Dep(2,2)+Dep(2,3))*de;-1*Dep(3,1)/...
        (Dep(3,2)+Dep(3,3))*de;0.;0.;0.];

%% Incremental stress
    dS = Dep*dStrain;

%% New strain and stresses
    Sig = Sig+dS;
    strain = strain+dStrain;

%% Incremental volumetric and deviatoric strains
    deps_p = dStrain(1) + dStrain (2) + dStrain (3); % Volumetric
    deps_d = 2./3. * (dStrain(1) - dStrain(3));      % Deviatoric

%% Update Specific Volume
    v = N-((k*log(p(n)/pc))+l*log(pc));

%% Updating Iteration, Effective Mean Stress, Shear stress, Pore Pressure
    n = n+1;
    p(n) = (Sig(1)+Sig(2)+Sig(3))/3;
    q(n) = Sig(1)-Sig(3);
    u(n) = p0+q(n)/3-p(n);

%% Updating Void Ratio, Final Strain Volume, Deviator Strain
    void(n) = v-1.0;
    eps_p(n) = deps_p + eps_p(n-1);
    eps_d(n) = deps_d + eps_d(n-1);

%% Defining the yield surface at the partical increment
    if yield<0, yield=q(n)^2+M^2*p(n)^2-M^2*p(n)*pc;
    else yield=0;
    end
end

%============== Determining stuff for plotting ============================%
%% Final Yield Surface
p_fyield = (0:pc);                              % Effective Mean Pressure
q_fyield = M*p_fyield;
q_yf = (M^2*(pc*p_fyield-p_fyield.^2)).^0.5; % Deviatoric Stress

%% Normal Consolidation Line (NCL)
p_NCL = (1:pc);                                  % Effective Mean Pressure
q_NCL = p_NCL*M;                                 % Deviatoric Stress
e_NCL = (N - l*log(p_NCL)) - 1;                  % Void Ratio

%% Critical State Line (CSL)
p_CSL = p_NCL;                                   % Effective Mean Pressure
Gamma = 1+l*log(p(n))+void(n);                   % Deviatoric Stress
e_CSL = (Gamma - l*log(p_CSL)) - 1;              % Void Ratio

%========================== Results and Plots ============================%
figure(1)
hold on
subplot(2,2,1)
plot(es,q,'k','LineWidth',2)
grid on
xlabel('Axial strain, $\varepsilon_{11} $ [\%]','Interpreter','latex','fontsize',font)
ylabel('Deviatoric Stress, $q $ [kPa]','Interpreter','latex','fontsize',font)
subplot(2,2,3),
plot(p,q,'k-','LineWidth',2);
grid on
```

```
hold on
plot(p_fyield,q_fyield,'k:','LineWidth',2);
plot(p_ini_yield,qy,'k-.','LineWidth',2);
plot(p_fyield,q_yf,'k--','LineWidth',2);
legend('Stress Path', 'M-line', 'Final yield surface', 'Initial yield surface')
xlabel('Effective Mean Stress, $   p` $ [kPa]','Interpreter','latex','fontsize',font)
ylabel('Deviatoric Stress, $q $ [kPa]','Interpreter','latex','fontsize',font)
subplot(2,2,2);
plot(eps_p,p,'k','LineWidth',2);                    % Drained
grid on
xlabel('Volumetic Strain, $\varepsilon_v$ [\%]','Interpreter','latex','fontsize',font)
ylabel('Effective Mean Stress, $   p` $ [kPa]','Interpreter','latex','fontsize',font)
%plot(es,u,'k-','LineWidth',2);                     % Undrianed
%grid on
%xlabel('Axial strain, $\varepsilon_{11} $ [\%]','Interpreter','latex','fontsize',font)
%ylabel('Excess Pore Pressure, $u $ [kPa]','Interpreter','latex','fontsize',font)
subplot(2,2,4);
semilogx(p,void,'k-','LineWidth',2);
grid on
hold on
semilogx(p_NCL,e_NCL,'k--','LineWidth',2);
semilogx(p_CSL,e_CSL,'k:','LineWidth',2);
xlabel('Effective Mean Pressure, $p` $ [kPa]','Interpreter','latex','fontsize',font)
ylabel('Void ratio, $e $ [-]','Interpreter','latex','fontsize',font)
legend('Stress Path','NCL','CSL')
hold off
```

E.1.2 Generate FORTRAN Code

```
%%%%%%%%%%%%%%%%%%%%%%%%%%%%%%%%%%%%%%%%%%%%%%%%%%%%%%%%%%%%%%%%%%%%%%%%%%%%%%%
%%% MCC + Anisotropic + Structure                                             %%%
%%% General --> Generate Fortran code --> PLAXIS                               %%%
%%% By Jesper Bjerre - s102905                                                 %%%
%%% Master Thesis                                                              %%%
%%% DTU and NTNU                                                               %%%
%%% Spring 2015                                                                %%%
%%%%%%%%%%%%%%%%%%%%%%%%%%%%%%%%%%%%%%%%%%%%%%%%%%%%%%%%%%%%%%%%%%%%%%%%%%%%%%%
clear all
close all
clc

global Sig alpha_d dF_ds F1 F2 c p0 v p  M  % For 3D plotting (Plotsurf)

%======================== Basic Input Parameters ========================&
%% General MCC
k = sym('k', 'real');                       % Swelling Index
l= sym('l', 'real');                        % Compression Index
nu = sym('nu', 'real');                     % Poissons Ratio
e0 = sym('e0', 'real');                     % Initial Void Ratio
M = sym('M', 'real');                       % Stress Ratio (Critical State)
p0 = sym('p0', 'real');                     % Preconsolidation Pressure
OCR = sym('OCR', 'real');                   % Over Consolidation rRatio
K0nc= sym('K0nc', 'real');                  % Lateral coefficient in NC

%================================ Lode Angle ================================&
phi = sym('phi', 'real');                   % Angle of Friction
MC_LMN = sym('MC_LMN', 'real');             % Select rule

%================================ Tensors ================================&
%% Symbolics - Stresses.
s11 = sym('s11', 'real');                   % Sigma_11
s22 = sym('s22', 'real');                   % Sigma_22
s33 = sym('s33', 'real');                   % Sigma_33
s12 = sym('s12', 'real');                   % Sigma_12
s23 = sym('s23', 'real');                   % Sigma_23
s13 = sym('s13', 'real');                   % Sigma_13

p = (s11+s22+s33)/3;                        % Mean Effective Stress
Sig = [s11;s22;s33;s12;s23;s13];            % Stress Tensor
q = sqrt(3/2*dev_Sig'*dev_Sig);             % Deviatoric stress (q)
dev_Sig = Sig - p*[1;1;1;0;0;0];            % Deviatoric Stress (sigma)
```

```
dev_Sig(4:6) = sqrt(2)*dev_Sig(4:6);        % Deviat. Stress Tensor

%% Symbolics - Strains.
e11 = sym('e11', 'real');                   % Strain_11
e22 = sym('e22', 'real');                   % Strain_22
e33 = sym('e33', 'real');                   % Strain_33
e12 = sym('e12', 'real');                   % Strain_12
e23 = sym('e23', 'real');                   % Strain_23
e13 = sym('e13', 'real');                   % Strain_13

strain = [e11;e22;e33;e12;e23;e13];         % Strain Tensor

%% Symbolics - Fabric
alphad11 = sym('alphad11', 'real');         % Deviatoric strain_11
alphad22 = sym('alphad22', 'real');         % Deviatoric strain_22
alphad33 = sym('alphad33', 'real');         % Deviatoric strain_33
alphad12 = sym('alphad12', 'real');         % Deviatoric strain_12
alphad23 = sym('alphad23', 'real');         % Deviatoric strain_23
alphad13 = sym('alphad13', 'real');         % Deviatoric strain_13

alpha_d = [alphad11;alphad22;alphad33;...   % Fabric Tensor
    alphad12;alphad23;alphad13];

%======================= Advanced Input Parameters ======================&
%% Symbolics - Structure for soil.
x = sym('x', 'real');                       % Structure for soil
a = sym('a', 'real');                       % Absolute rate of destructuation
b = sym('b', 'real');                       % Relatece effectiveness of strains
                                            % in destruying the bonding
%% Symbolics - Recovery of structure
R = sym('R', 'real');                       % Recovery of structure
Rtime = sym('Rtime', 'real');               % Rate of recovery
rsi_min = sym('rsi_min', 'real');           % Should to defined x_b and x

%% Symbolics - Creep.
rsi = sym('rsi', 'real');                   % Creep parameter
aK0NC = sym('aK0NC', 'real');               % Initial rotation
etaK0NC = sym('etaK0NC', 'real');           % Stress Ratio corresponding to K0
tau = sym('tau', 'real');                   % Reference Time
dt = sym('dt', 'real');                     % Time
t_max = sym('t_max', 'real');               % Maximum Time for creep
lambda = sym('lambda', 'real');             % Plastic multiplier

% Symbolics - Rotation Hardening
beta = sym('beta', 'real');                 % Wheeler 2003
mu = sym('mu', 'real');                     % Wheeler 2003
z = sym('z', 'real');                       % Dafalias 2013
s = sym('s', 'real');                       % Dafalias 2013
rule = sym('rule', 'real');                 % Evalution rule 1, 2 or 3


%======================= Defining Stiffness matrix ======================%
% Houlsby treansversely isotropic constant
E = sym('E', 'real');                       % Elastic Modulus
alpha_e = sym('alpha_e', 'real');           % Houlsby anisotropy
alpha1 = sym('alpha1', 'real');             % Houlsby anisotropy
alpha2 = sym('alpha2', 'real');             % Houlsby anisotropy
alpha3 = sym('alpha3', 'real');             % Houlsby anisotropy

De = E/((1+nu)*(1-2*nu))*...
    [(1-nu) nu nu 0 0 0;
      nu (1-nu) nu 0 0 0;
      nu nu (1-nu) 0 0 0;
      0 0 0 1/2*(1-2*nu) 0 0;
      0 0 0 0 1/2*(1-2*nu) 0;
      0 0 0 0 0 1/2*(1-2*nu)]               % Linear Elastic Stiffness Matrix

transverse = [alpha1*alpha1 alpha1*alpha2 alpha1*alpha3 0 0 0;
              alpha2*alpha1 alpha2*alpha2 alpha2*alpha3 0 0 0;
              alpha3*alpha1 alpha3*alpha2 alpha3*alpha3 0 0 0;
              0 0 0 alpha1*alpha2 0 0;
              0 0 0 0 alpha1*alpha3 0;
              0 0 0 0 0 alpha2*alpha3]; % Transversely Transforming Matrix
```

```
De = De.*transverse                    % Transversely Isotropic Stiffness

%======================== Equivalent Pressure ============================%
peq = p + ((3/2)*(dev_Sig-p*alpha_d)'*(dev_Sig-p*alpha_d))/...
    ((M^2-(3/2)*alpha_d'*alpha_d)*p);

%% Derivative of Equivalent Pressure
dpeq_dp = (M^2-((3/2)*dev_Sig'*dev_Sig)/p^2)/...    % Respect to
    (M^2-(3/2)*alpha_d'*alpha_d);                   % Effective Mean Stress
dpeq_dsigd = 3*(dev_Sig-p*alpha_d)/...              % Respect to
    ((M^2-(3/2)*(alpha_d'*alpha_d))*p);             % Stress Tensor

%========================= Defining Yield surface ========================%
pm = (1+x)*p0;                         % Intrinsic Yield Surface (Structure)
F = peq - pm                           % Yield Surface

%============================ Plastic Potential ==========================%
Q = F;                                 % Assumed Associated flow
dQ_ds = diffvec(Sig,Q);                % Respect to Stress Tensor
dF_ds = dQ_ds;                         % Renaming

%% Derivative of Plastic Potential
dQ_dp = dpeq_dp;                       % Respect to Effective Mean Stress
dQ_dq = sqrt(2/3*...                   % "Equivalent" Deviatoric Plastic
    dpeq_dsigd'*dpeq_dsigd);           % Strain Measure

%=================== Defining Constants for Anisotropic ==================%
c2 = mu;                               % Renaming
c3 = beta;                             % Renaming
c4 = 3/4;                              % Taken from Wheeler 2003
c5 = 1/3;                              % Taken from Wheeler 2003
c6 = z;                                % Taken for Dafalias 2013
c7 = s;                                % Taken for Dafalias 2013
c8 = mu;                               % Remaning (Dafalias vs. Wheeler)
patm = 101;                            % Atmospheric Pressure

% Evolution Rule 1 - Wheeler 2003
y1 = c2/(1+x)*((c4*(dev_Sig/p)-alpha_d)*macaulay_brackets(dQ_dp)+c3*...
    (c5*(dev_Sig/p)-alpha_d)*dQ_dq);

% Evolution Rule 2 - Dafalais 1986
alpha_b_2 = aK0NC/etaK0NC*dev_Sig/p;
y2 =  c8*patm*p/peq*(alpha_b_2-alpha_d);

% Evolution Rule 3 - Dafailis 2013
sig_norm = norm(dev_Sig/p);
eta = sqrt(3/2*(dev_Sig/p)'*dev_Sig/p);
n_r = (dev_Sig/p)/(norm(dev_Sig/p));
alpha_b_3 = M/c6*(1-exp(-c7*abs(eta)/M))*n_r;

y3 =  c8*patm*p/peq*(alpha_b_3-alpha_d);

% Chosing the evolution rule
dalpha_dlam =(1-rule)*(2-rule)*1/2*y1+rule*(2-rule)*y2-rule/2*(1-rule)*y3;

%=================== Defining Constants for Structrure ===================%
c6 = a;                                          % Renaming
c7 = b;                                          % Renaming
c8 = R;                                          % Recovering of structure
c9 = Rtime;                                      % Renaming
x_b = (rsi-rsi_min)/rsi_min;                     % Defining boundary value of x

dx_dlam = -x*(c6*abs(dQ_dp)+c7*abs(dQ_dq));  % Destructuration
dx_dt = heaviside(c8*x_b-x)*(c8*x_b-x)*c9*dt;% Recovering of structure

%======================== Plastic resistance number ======================%
%% Determine parameters in A (Differentiate)
dF_dp0 = -(1+x);                                 % Yield Surface by p0
dp0_dlam = (1+e0)/(1-k)*p0*dQ_dp;                % p0 by Plastic Multiplier
dF_dalpha = diffvec(alpha_d, F);                 % Yield Surface by Fabric
dF_dx = diffvec(x, F);                           % Yield Surface by Structure
```

```
%======================== State Parameters  ==============================%
dkappa_dlam = [dp0_dlam; dalpha_dlam; dx_dlam];
dkappa_dt = [0;0;0;0;0;0;0;dx_dt];

%============================ Creep ======================================%
kappa = [p0; alpha_d; x];                                % State parameters
zetai = (1-k)/(1+e0);                                    % Coefficient
m_K0NC = (M^2-aK0NC^2)/(M^2-etaK0NC^2);                  % Inclination
dlam_dt = 1/(rsi*tau)*macaulay_brackets((peq/pm)^(rsi*zetai)-tau/t_max)*m_K0NC;
dlam_dsig = diffvec(Sig,dlam_dt);                        % (Differentiate)
dlam_dkappa = diffvec(kappa,dlam_dt);                    % (Differentiate)

%======================== Plastic Multipliers  ===========================%
dLambda_VP = (dlam_dt+dlam_dsig'*De*strain)/...          % Visco-Plastic
             (1/dt-dlam_dkappa'*dkappa_dlam+dlam_dsig'*De*dF_ds);
%====================== Output to Fortran framework ======================%
U_VP = [De*(strain-dQ_ds*dLambda_VP);
        dLambda_VP;
        dkappa_dlam*dLambda_VP + dkappa_dt*dt];          % Visco Plastic

% ============================= Fortran ================================== %
De = fortran([De;De]);
fortran(U_VP, 'file', 'UJB_t_max2.f');
fortran(peq, 'file', 'peq.f');

%======================== Defining vectors for plotting ==================%
v = [Sig;lambda;p0;alpha_d;x];                          % State parameters
c = [l;k;nu;e0;phi;OCR;K0nc;mu;rule;a;b;rsi;rsi_min;R;Rtime;alpha_e;MC_LMN];
```

Associated Functions

```
%%%%%%%%%%%%%%%%%%%%%%%%%%%%%%%%%%%%%%%%%%%%%%%%%%%%%%%%%%%%%%%%%%%%%%%%%%%%
%%% Function                                                              %%%
%%% macaulay_brackets(x)                                                  %%%
%%% By Jesper Bjerre - s102905                                            %%%
%%% Master Thesis                                                         %%%
%%% DTU and NTNU                                                          %%%
%%% Spring 2015                                                           %%%
%%%%%%%%%%%%%%%%%%%%%%%%%%%%%%%%%%%%%%%%%%%%%%%%%%%%%%%%%%%%%%%%%%%%%%%%%%%%
function out = macaulay_brackets(x)
out = x*heaviside(x);
end
```

```
%%%%%%%%%%%%%%%%%%%%%%%%%%%%%%%%%%%%%%%%%%%%%%%%%%%%%%%%%%%%%%%%%%%%%%%%%%%%
%%% Function                                                              %%%
%%% diffvec(Sig, Q)                                                       %%%
%%% By Jesper Bjerre - s102905                                            %%%
%%% Master Thesis                                                         %%%
%%% DTU and NTNU                                                          %%%
%%% Spring 2015                                                           %%%
%%%%%%%%%%%%%%%%%%%%%%%%%%%%%%%%%%%%%%%%%%%%%%%%%%%%%%%%%%%%%%%%%%%%%%%%%%%%
function out = diffvec(Sig, Q)
 for i = 1:1:length(Sig)
     dfdv(i) = simplify(diff(Q,Sig(i)));
 end
out = dfdv';
```

E.1.3 Changes to Implicit Integration

```
%%%%%%%%%%%%%%%%%%%%%%%%%%%%%%%%%%%%%%%%%%%%%%%%%%%%%%%%%%%%%%%%%%%%%%%%%%%%%%%%
%%% Modifications for utilizing implicit integration                          %%%
%%% Assembling the residual and the Jacobi matrix                              %%%
%%% By Jesper Bjerre - s102905                                                 %%%
%%% Master Thesis                                                              %%%
%%% DTU and NTNU                                                               %%%
%%% Spring 2015                                                                %%%
%%%%%%%%%%%%%%%%%%%%%%%%%%%%%%%%%%%%%%%%%%%%%%%%%%%%%%%%%%%%%%%%%%%%%%%%%%%%%%%%
% Vector containing unknowns
v = [Sig;Lambda;p0;alpha_d;x];
% State parameters in previous and current stage
kappa = [p0;alpha_d;x];
kappa0 = [p00; alpha_d0; x0];
% Evolution in state parameters
dkappa_dlamda = [dp0_dlamda; dalpha_d_dlamda; dx_dlamda];
dkappa_dt = [0;0;dx_dt];
% Formulating the differential equaitions
r1 = Sig - Sig0 - De*de + De*diffvec(Q,Sig)*(lam-lam0);
r2 = kappa-kappa0 - dkappa_dlamda*(lam-lam0) + dkappa_dt*dt;
r3 = (lam-lam0) - dlamdt*dt; % For elasto-plastic: F
% Assembling the residual
r = [r1;r2;r3];
% Generate the FORTRAN code
fortran(r, 'file', 'Residuals.f');
matlabFunction(r, 'file', 'Residuals.m');
% Jacobian matrix - 15x15 matrix
J = jacobian(r,v);
fortran(J, 'file', 'Jacobian.f');
```

E.2 FORTRAN

This section contains the FORTRAN code for generating the DLL-file. The file-`usrlin.f90` is left out since it is offered by PLAXIS, see (PLAXIS, 2015).

E.2.1 User_Mod

```
%%%%%%%%%%%%%%%%%%%%%%%%%%%%%%%%%%%%%%%%%%%%%%%%%%%%%%%%%%%%%%%%%%%%%%%%%%%%%%%%
%%% Main subroutine - User_Mod                                                  %%%
%%% By Jesper Bjerre - s102905                                                  %%%
%%% Supporeted by Jon Roenningen (NTNU)  - Realted to  GeoFuture                %%%
%%% Master Thesis                                                               %%%
%%% DTU and NTNU                                                                %%%
%%% Spring 2015                                                                 %%%
%%%%%%%%%%%%%%%%%%%%%%%%%%%%%%%%%%%%%%%%%%%%%%%%%%%%%%%%%%%%%%%%%%%%%%%%%%%%%%%%

include 'Constitutive Model'
subroutine User_Mod(IDTask, iMod, IsUndr,iStep, iTer, iEl, Int,X, Y, Z,Time0,
                    dTime,Props, Sig0, Swp0, StVar0,dEps, D, BulkW,Sig, Swp,
                    StVar, ipl,nStat, NonSym, iStrsDep, iTimeDep,iTang,iPrjDir,
                    iPrjLen, iAbort)

      %  iMod     I   I    : model number (1..10)
      %  IsUndr   I   I    : =1 for undrained, 0 otherwise
      %  iStep    I   I    : Global step number
      %  iter     I   I    : Global iteration number
      %  iel      I   I    : Global element number
      %  Int      I   I    : Global integration point number
      %  X        I   R    : X-Position of integration point
      %  Y        I   R    : Y-Position of integration point
      %  Z        I   R    : Z-Position of integration point
      %  Time0    I   R    : Time at start of step
      %  dTime    I   R    : Time increment
      %  Props    I   R()  : List with model parameters
      %  Sig0     I   R()  : Stresses at start of step
      %  Swp0     I   R    : Excess pore pressure start of step
      %  StVar0   I   R()  : State variable at start of step
      %  dEps     I   R()  : Strain increment
      %  D       I/O  R(,) : Material stiffness matrix
      %  BulkW   I/O  R    : Bulkmodulus for water (undrained only)
      %  Sig      O   R()  : Resulting stresses
      %  Swp      O   R    : Resulting excess pore pressure
      %  StVar    O   R()  : Resulting values state variables
      %  ipl      O   I    : Plasticity indicator
      %  nStat    O   I    : Number of state variables
      %  NonSym   O   I    : Non-Symmetric D-matrix ?
      %  iStrsDep O   I    : =1 for stress dependent D-matrix
      %  iTimeDep O   I    : =1 for time dependent D-matrix
      %  iTang    O   I    : =1 for tangent matrix
      %  iAbort   O   I    : =1 to force stopping of calculation

      use vars
      Implicit Double Precision (A-H,O-Z)
      Dimension iPrjDir(*)
      Character*255 PrjDir, Dbg_Name
      Integer IDTask, ne, nt, n
      double precision, dimension(6) :: Sig0, Sig, dEps, deabs
      double precision, dimension(size(v)) :: StVar0, StVar
      double precision, dimension(size(c)) :: Props
      double precision :: demax, dtmax

       if (IDTask.eq.1) then ! Initialize state variables
         c(:) = props(:)                % Emtry vector
         v(:) = 0                       % Emtry vector
         v0(:) = 0                      % Emtry vector

         v(1:6) = -1.0*Sig0(1:6)        % Changing notation
         I1 = v(1) + v(2) + v(3)
```

```
    if (I1.le.0) then
     v(1:3) = 1.0e-3              % Debugging
    end if
    call initialize()             % Initialize state patameters (SP)
    if (lvec(StVar0, size(v)).eq.0) then
         StVar0 = v
    end if
  end if ! End IDTask 1

 if (IDTask.eq.2) then ! Calculate stresses
   c(:) = props(:)                % Emtry vector
   v = StVar0                     % Redefine previous SP
   v(1:6) = -1*Sig0(1:6)          % Add the new stresses
   v0 = v                         % Rename the time
   dt = dTime
   dn = 0
   de(:) = 0
   de(1:6) = -1.0*Deps(1:6)       % Changing notation

   I1 = v(1) + v(2) + v(3)

   If (IsUndr.Eq.1) Then
     Swp   = Swp0 + BulkW*(dEps(1) + dEps(2) + dEps(3))
   Else
     Swp = Swp0
   End If

   ! Check if time increment or strain increment is too large
   deabs = abs(de)
   demax = max(deabs(1), deabs(2), deabs(3), deabs(4), deabs(5), deabs(6))
   dtmax = dt
   ne = nint(demax/1.0e-4)
   nt = nint(dtmax/1.0)

   if (ne.eq.0) then
     ne = 1
   end if

   if (nt.eq.0) then
     nt = 1
   end if

   n = max(ne,nt)

   de = de/n*1.0
   dt = dt/n*1.0

   do i = 1,n
     call calcondition()
   end do

   if (checkv() == .true.) then
     v = StVar0
   else
     Sig(1:6) = -1.0*v(1:6)
   end if

   StVar = v
 end if ! End IDTask 2

 if (IDTask.eq.3) then ! Material stiffness matrix
   v = StVar0
   v(1:6) = -1*Sig0(1:6)
   call Dematrix(D)
 end if ! End IDTask 3

 if (IDTask.eq.4) then ! Return number of state variables
   nStat = size(v);
 end if ! End IDTask 4

 if (IDTask.eq.5) then ! Inquire matrix properties
   NonSym   = 0                % 1 for non-symmetric D-matrix
   iStrsDep = 1                % 1 for stress dependent D-matrix
```

```
        iTang    = 0                % 1 for tangent D-matrix
        iTimeDep = 1                % 1 for time dependent D-matrix
      end if ! End IDTask 5

      if (IDTask.eq.6) then ! Dependent material stiffness matrix
        v = StVar0
        v(1:6) = -1*Sig0(1:6)
        call Dematrix(D)
      end if ! End IDTask 6

      return
End subroutine
```

E.2.2 Constitutive Model

```
%%%%%%%%%%%%%%%%%%%%%%%%%%%%%%%%%%%%%%%%%%%%%%%%%%%%%%%%%%%%%%%%%%%%%%%%%%%%%%%
%%% FORTRAN                                                                  %%%
%%% Constitutive Model                                                       %%%
%%% By Jesper Bjerre - s102905                                               %%%
%%% Supporeted by Jon Roenningen (NTNU) - Realted to  GeoFuture              %%%
%%% Master Thesis                                                            %%%
%%% DTU and NTNU                                                             %%%
%%% Spring 2015                                                              %%%
%%%%%%%%%%%%%%%%%%%%%%%%%%%%%%%%%%%%%%%%%%%%%%%%%%%%%%%%%%%%%%%%%%%%%%%%%%%%%%%
module vars
include Additional_code.f90
include usrlib.f90
%%%%%%%%%%%%%%%%%%%%%%%%%%%%%%%%%%%%%%%%%%%%%%%%%%%%%%%%%%%%%%%%%%%%%%%%%%%%%%%
% Create vectors with state parameters (v,v0)
% Input parameters (c) and strain vector (de)
  double precision, dimension(17) :: v, v0
  double precision, dimension(20) :: c
  double precision, dimension(6)  :: de
  integer                         :: dn
  double precision                :: dt
  logical                         :: op

% Making following function local. See the functions below.
public :: desc, pardesc, undesc, statpardesc, statundesc

contains
function desc() result(y)
  implicit none
  Character (Len=255) :: y
  y = 'ViscoPlastic Model (Explicit)'   % Name in PLAXIS
end function desc

function pardesc(i) result(y)           % Input parameters in PLAXIS
  implicit none
  Character (Len=255), dimension(size(c)) :: u
  Character (Len=255) :: y
  Integer i
  u = (/'@l#_i', '@k#', '@n#_ur', 'e_0', '@f#_cs', 'OCR_@t#', 'K_0#^NC# ',
        '@m# or c','RH-Rule 1/2/3 (0/1/2)', 'a', 'b','r_si','r_si,min','R',
        'R_T','@a#_e','MC/LMN (0/1)','t_max','POP','@tau'/)
  y = u(i)
end function pardesc

function undesc(i) result(y)            % Unit of the input parameters
  implicit none
  Character (Len=255), dimension(size(c)) :: u
  Character (Len=255) :: y
  Integer i
  u = (/'-', '-', '-', '-', '-', '-', '-', '-', '-', '-', '-', '-', '-',
        '-', '-', '-', '-', '-', '-', '-'/)
  y = u(i)
end function undesc

function statpardesc(i) result(y)       % Naming the state variables
  implicit none
  Character (Len=255), dimension(size(v)) :: u
```

```
  Character (Len=255) :: y
  Integer i
  u = (/'S11', 'S22', 'S33', 'S12', 'S23', 'S13', 'lambda', 'p0', 'ad11',
        'ad22', 'ad33', 'ad12', 'ad23', 'ad13', 'x','OCR_1'/)
  y = u(i)
end function statpardesc

function statundesc(i) result(y)        % Unit of the state variables
                                        % F for force unit
                                        % L for length unit
                                        % T for time unit
  implicit none
  Character (Len=255), dimension(size(v)) :: u
  Character (Len=255) :: y
  Integer i
  u = (/'F/L^2#', 'F/L^2#', 'F/L^2#', 'F/L^2#', 'F/L^2#', 'F/L^2#', '-',
        'F/L^2#', '-', '-', '-', '-', '-', '-', '-', '-'/)
  y = u(i)
end function statundesc
end module vars

module map                              % Mapping the state varialbes

double precision :: OCR_1,M,M1,a,alphad11,alphad12,alphad13,alphad22,alphad23,
                    alphad33,b,beta_Var,e0,k,l,mu,nu,p0,s11,s12,s13,s22,s23,s33,
                    x, etak0nc, ak0nc, OCR, K0nc, epst, kdivg, atemp,e11,e12,e13,
                    e22,e23,e33,tau,rsi,eta_K0NC,alpha_K0NC,rule,Recovery,rsimin,
                    Rtime,R,theta,J2,J3,q,PI,phi,LMN_beta,LMN_theta,x1,x2,LMN,rsi_min,
                    s,z,alpha_e,Ke,G,MC_LMN,fvalue,dfdxx,p,alpha1,alpha2,alpha3,zz,ss,
                    z0,xx,E_var,ss2,sinTHETA,costheta,t_max,POP,peq,peqq

contains
%%%%%%%%%%%%%%%%%%%%%%%%%%% subroutine update %%%%%%%%%%%%%%%%%%%%%%%%%%%%%
subroutine update()                     % Update state variables
  use vars
  call mapping()
end subroutine
%%%%%%%%%%%%%%%%%%%%%%%%%%% subroutine mapping %%%%%%%%%%%%%%%%%%%%%%%%%%%%%
subroutine mapping()                    % Map state variables
  use vars
         l        = c(1)
         k        = c(2)
         nu       = c(3)
         e0       = c(4)
         phi      = c(5)
         OCR      = c(6)
         K0nc     = c(7)
         mu       = c(8)
         rule     = c(9)
         a        = c(10)
         b        = c(11)
         rsi      = c(12)
         rsi_min  = c(13)
         R        = c(14)
         Rtime    = c(15)
         alpha_e  = c(16)
         MC_LMN   = c(17)
         t_max    = c(18)
         POP      = c(19)
         tau      = c(20)

         p0       = v(8)
         x        = v(15)
         OCR_1    = v(16)
         ppeq     = v(17)

% Debugging for zero

if (rsi_min == 0.0) then
      rsi_min = c(12)
  else
      rsi_min = c(13)
end if
```

```
if (tau == 0.0) then
      tau = 1.0
  else
      tau = c(20)
end if

if (OCR == 0.0) then
      OCR = 1.0
  else
      OCR = c(6)
end if

% Defining Stresses
         s11 = v(1)
         s12 = v(4)
         s13 = v(6)
         s22 = v(2)
         s23 = v(5)
         s33 = v(3)

% Defining Strains
         e11 = de(1)
         e12 = de(4)
         e13 = de(6)
         e22 = de(2)
         e23 = de(5)
         e33 = de(3)

% Defining Fabric
         alphad11 = v(9)
         alphad12 = v(12)
         alphad13 = v(14)
         alphad22 = v(10)
         alphad23 = v(13)
         alphad33 = v(11)

% Determine J2, J3, q and defining Pi for Lode Angle
          Pi  = 4.D0*DATAN(1.D0) ! Define Pi in Fortran

          J2 = 0.0
          t2 = s22*(1.0D0/3.0D0)
          t3 = s33*(1.0D0/3.0D0)
          t4 = s11*(1.0D0/3.0D0)
          t5 = t2+t3+t4
          t6 = s33*(1.0D0/6.0D0)
          t7 = s11*(1.0D0/6.0D0)
          t8 = s22*(1.0D0/6.0D0)
          t9 = sqrt(2.0D0)

  J2 = (alphad12*t5-s12*t9)*(alphad12*t5*(1.0D0/2.0D0)-s12*t9*(1.0D0/2.0D0))+
       (alphad13*t5-s13*t9)*(alphad13*t5*(1.0D0/2.0D0)-s13*t9*(1.0D0/2.0D0))+
       (alphad23*t5-s23*t9)*(alphad23*t5*(1.0D0/2.0D0)-s23*t9*(1.0D0/2.0D0))+
       (s11*(-2.0D0/3.0D0)+t2+t3+alphad11*t5)*(-t4+t6+t8+alphad11*t5*(1.0D0/2.0D0))+
       (s22*(-2.0D0/3.0D0)+t3+t4+alphad22*t5)*(-t2+t6+t7+alphad22*t5*(1.0D0/2.0D0))+
       (s33*(-2.0D0/3.0D0)+t2+t4+alphad33*t5)*(-t3+t7+t8+alphad33*t5*(1.0D0/2.0D0))

          J3  = 0.0
          t3  = s11*(1.0D0/3.0D0)
          t4  = s33*(1.0D0/3.0D0)
          t5  = s22*(1.0D0/3.0D0)
          t6  = t3+t4+t5
          t7  = sqrt(2.0D0)
          t16 = s13*t7
          t17 = alphad13*t6
          t2  = t16-t17
          t8  = alphad12*t6-s12*t7
          t18 = s23*t7
          t19 = alphad23*t6
          t9  = -t18+t19
          t10 = alphad11*t6
          t11 = s11*(-2.0D0/3.0D0)+t4+t5+t10
          t12 = alphad22*t6
```

```
          t13 = s22*(-2.0D0/3.0D0)+t3+t4+t12
          t14 = alphad33*t6
          t15 = s33*(-2.0D0/3.0D0)+t3+t5+t14
  J3  = t2**2.0*t13+t9**2.0*t11+t8**2.0*t15-t2*(t18-t19)*(alphad12*t6*2.0D0-s12*t7*2.0D0)-
        t11*t13*t15

          q   = 0.0
          t2  = s22*(1.0D0/3.0D0)
          t3  = s33*(1.0D0/3.0D0)
          t4  = s11*(1.0D0/3.0D0)
          t5  = t2+t3+t4
          t6  = s33*(1.0D0/2.0D0)
          t7  = s11*(1.0D0/2.0D0)
          t8  = s22*(1.0D0/2.0D0)
          t9  = sqrt(2.0D0)
  q   = sqrt((alphad12*t5-s12*t9)*(alphad12*t5*(3.0D0/2.0D0)-s12*t9*(3.0D0/2.0D0))+
        (alphad13*t5-s13*t9)*(alphad13*t5*(3.0D0/2.0D0)-s13*t9*(3.0D0/2.0D0))+
        (alphad23*t5-s23*t9)*(alphad23*t5*(3.0D0/2.0D0)-s23*t9*(3.0D0/2.0D0))+
        (s11*(-2.0D0/3.0D0)+t2+t3+alphad11*t5)*(-s11+t6+t8+alphad11*t5*(3.0D0/
        2.0D0))+(s22*(-2.0D0/3.0D0)+t3+t4+alphad22*t5)*(-s22+t6+t7+alphad22*t5*
        (3.0D0/2.0D0))+(s33*(-2.0D0/3.0D0)+t2+t4+alphad33*t5)*(-s33+t7+t8+
        alphad33*t5*(3.0D0/2.0D0)))

% Setting yield criteria

if (MC_LMN  == 0.0) then
    call Lode_Angle()               % Mohr Coulomb Criteria
  else
    call Lode_Angle_LMN()           % LMN Denpendency
end if

% Calculate alpha_k0nc
         etak0nc  = 3.0*(1.0-K0nc)/(1.0+2.0*K0nc)
         epst     = 3.0/2.0
         kdivg    = 2.0*(1.0+nu)/3.0/(1.0-2.0*nu)
         ak0nc    = (etak0nc**2 + 2*etak0nc*atemp-M**2)/2.0/atemp
         beta_Var = 3.0*(3.0*etak0nc-4.0*ak0nc)*(M**2.0-etak0nc**2.0)/(8.0*
                    (3.0*ak0nc-etak0nc)*(etak0nc-ak0nc)) % Dafalias 2013
end subroutine
end module map

%%%%%%%%%%%%%%%%%%%%%%%%%%%% subroutine initialize %%%%%%%%%%%%%%%%%%%%%%%%%%
subroutine initialize()             % Initialize parameters
  use vars
  use map
    implicit none
    double precision f90
    double precision f
    call update()

% Initial anisotropy
         v(9:14) = (/-1.0/3.0*ak0nc,2.0/3.0*ak0nc,-1.0/3.0*ak0nc,
                     0.0d0,0.0d0,0.0d0/)
% Plastic multiplier
         v(7) = 0
% Initial structure
         if (c(13) == 0.0) then
         v(15) = 0
         else
         v(15) =  (c(12)-c(13))/c(13)
         end if
% Set p0
         call yield(f)
         v(8) = (f*OCR+POP)/(1+v(15))
end subroutine

%%%%%%%%%%%%%%%%%%%%%%%%%%%% subroutine Lode_Angle %%%%%%%%%%%%%%%%%%%%%%%%%%
subroutine Lode_Angle()            % Mohr Coulomb Criteria
  use vars
  use map
    Implicit Double Precision (A-Z)
    double precision, dimension(6) :: St
```

```
  % Stresses
         St(1) = v(1)
         St(4) = v(4)
         St(6) = v(6)
         St(2) = v(2)
         St(5) = v(5)
         St(3) = v(3)

  call Eig_3a(St,SS2)             % Determine principle stresses

  if (q == 0.0 ) then
          M =  6.0*sin(phi*PI/180)/(3.0-sin(phi*PI/180))
  else
          theta = -1.0/3.0*asin(checkSINA(27.0/2.0*J3/(q**3.0)))
          M =  3.0*sin(phi*PI/180)/(sqrt(3.0)*cos(theta)+sin(THETA)*sin(phi*PI/180))
  end if
  end subroutine

%%%%%%%%%%%%%%%%%%%%%%%%%% subroutine Lode_Angle_LMN %%%%%%%%%%%%%%%%%%%%%%%%
subroutine Lode_Angle_LMN()       % Incorreborate the Lode Angle by LMN
  use vars
  use map
    Implicit Double Precision (A-Z)

  if (q == 0.0) then
          M =  6.0*sin(phi*PI/180)/(3.0-sin(phi*PI/180))
  else
          theta = -1.0/3.0*asin(checkSINA(27.0/2.0*J3/(q**3.0)))
          LMN_beta = (3.0-sin(phi*PI/180))/(3+sin(phi*PI/180))
          x1 = 1.0/6.0*acos(-1.0+27.0/2.0*(LMN_beta**2.0*(1.0-LMN_beta)**2.0)/
              ((LMN_beta**2.0-LMN_beta+1.0)**3.0)*sin(3.0*theta)**2.0)
          x2 = PI/3.0-1.0/6.0*acos(-1.0+27.0/2.0*(LMN_beta**2.0*(1.0-LMN_beta)**
              2.0)/(LMN_beta**2.0-LMN_beta+1.0)**3.0*sin(3.0*theta)**2.0)
          LMN_theta = heaviside(theta)*x1 + heaviside(-theta)*x2
          LMN = sqrt(3.0)/2.0*LMN_beta/(sqrt(LMN_beta**2.0-LMN_beta+1.0))*1.0/
                (cos(LMN_theta))
          M =  (6*sin(phi*PI/180)/(3-sin(phi*PI/180)))*LMN
  end if
end subroutine


%%%%%%%%%%%%%%%%%%%%%%%%%% subroutine Umatrix %%%%%%%%%%%%%%%%%%%%%%%%%%%%%%
 subroutine Umatrix(A0)
  use vars
  use map
    Implicit Double Precision (A-Z)
    double precision, dimension(size(v),size(de)) :: A0
      call update()
      call Newton_Raphson_s_z()
      call yield(f)
      A0(:,:) = 0.0d0

% Redefining some terms from MATLAB
      p      = (s11+s22+s33)/3.0
      alpha2 = 1.0+2.0/3.0*alpha_e
      alpha1 = 1.0-alpha_e/3.0
      alpha3 = 1.0-alpha_e/3.0
      E_VAR  = 27.0*(1.0+e0)*p*(-1.0+2.0*nu)*(1.0+nu)/(k*(4.0*alpha_e**2.0*nu
              -2.0*alpha_e**2-9.0*nu-9.0))

      INPUT VECTOR V FROM MATLAB and added these two line to the vector:

      A0(16,1) = p0*(1.0+x)/f
      A0(17,1) = f

end subroutine
%%%%%%%%%%%%%%%%%%%%%%%%%% subroutine Dematrix %%%%%%%%%%%%%%%%%%%%%%%%%%%%%%
  subroutine Dematrix(A0)           % Elastic stiffness matrix
    use vars
    use map
      Implicit Double Precision (A-Z)
      double precision, dimension(6,6) :: A0
        call update()
```

```
% Redefining parameters from MATLAB
        p      = (s11+s22+s33)/3.0
        alpha2 = 1.0+2.0/3.0*alpha_e
        alpha1 = 1.0-alpha_e/3.0
        alpha3 = 1.0-alpha_e/3.0
        E_VAR = 27.0*(1.0+e0)*p*(-1.0+2.0*nu)*(1.0+nu)/(k*(4.0*alpha_e**2.0*nu
                -2.0*alpha_e**2-9.0*nu-9.0))

        INPUT MATRIX D FROM MATLAB

  end subroutine
%%%%%%%%%%%%%%%%%%%%%%%%% subroutine calcondition %%%%%%%%%%%%%%%%%%%%%%%%%
  subroutine calcondition()           % Calculate the new stresses
    use vars
    use map
      Implicit Double Precision (A-Z)
      double precision, dimension(size(v)) :: dv
        call update()
        dv(:) = 0.0d0
        call UMatrix(dv)
        v(1:15) = v(1:15) + dv(1:15)
        v(16) = dv(16)
        v(17) = dv(17)

  end subroutine
%%%%%%%%%%%%%%%%%%%%%%%%%%%% subroutine yield %%%%%%%%%%%%%%%%%%%%%%%%%%%%
 subroutine yield(f)                  % Defining the yield function
  use vars
  use map
    Implicit Double Precision (A-Z)
    double precision f
      call update()

        f = 0
        t2 = s11*(1.0D0/3.0D0)
        t3 = s22*(1.0D0/3.0D0)
        t4 = s33*(1.0D0/3.0D0)
        t5 = t2+t3+t4
        t6 = s33*(1.0D0/2.0D0)
        t7 = s11*(1.0D0/2.0D0)
        t8 = s22*(1.0D0/2.0D0)
        t9 = sqrt(2.0D0)
      f= t2+t3+t4-((alphad12*t5-s12*t9)*(alphad12*t5*(3.0D0/2.0D0)-s12*t9*(3.0D0/
          2.0D0))+(alphad13*t5-s13*t9)*(alphad13*t5*(3.0D0/2.0D0)-s13*t9*(3.0D0/
          2.0D0))+(alphad23*t5-s23*t9)*(alphad23*t5*(3.0D0/2.0D0)-s23*t9*(3.0D0/
          2.0D0))+(s11*(-2.0D0/3.0D0)+t3+t4+alphad11*t5)*(-s11+t6+t8+alphad11*
          t5*(3.0D0/2.0D0))+(s22*(-2.0D0/3.0D0)+t2+t4+alphad22*t5)*(-s22+t6+t7+
          alphad22*t5*(3.0D0/2.0D0))+(s33*(-2.0D0/3.0D0)+t2+t3+alphad33*t5)*
          (-s33+t7+t8+alphad33*t5*(3.0D0/2.0D0)))/(t5*(-M**2+alphad11**2*(3.0D0/
            2.0D0)+alphad12**2*(3.0D0/2.0D0)+alphad13**2*(3.0D0/2.0D0)+alphad22**
          2*(3.0D0/2.0D0)+alphad23**2*(3.0D0/2.0D0)+alphad33**2*(3.0D0/2.0D0)))

end subroutine

%-------------------------------------------------------------------------%
function lvec(v, l) result(y)
        integer i,l
        double precision :: y
        double precision, dimension(l) :: v
        y = 0.0
        do i=1,l
           y = y + v(i)*v(i)
         end do
end function
%-------------------------------------------------------------------------%
 function checkv() result(u) % Control that p cannot be negative
  use vars
    Integer i
    logical u
    double precision I1

      do i = 1,size(v)
        if (isNan(v(i))) then
```

```
          u = .true.
        end if
      end do

      I1 = v(1) + v(2) + v(3)
      if (I1.le.0) then
        u = .true.
      end if
end function
%-------------------------------------------------------------------------%
function heaviside(x) result(y) % Function from MATLAB
  double precision x,y
      if (x > 0.0) then
        y = 1.0d0
      else if (x == 0.0) then
        y = 0.5d0
        else
        y = 0.0d0
      end if
end function

%-------------------------------------------------------------------------%
% Ensure that sina(1.0) and sina*(-1.0) gives a real number
function checkSINA(x) result(y)
  double precision x,y
      if (x > 1.0) then
        y =  1.0d0
        else if (x < -1.0) then
        y = -1.0d0
      else
        y = x
      end if
end function
%-------------------------------------------------------------------------%
function ifzero(x) result(y) ! Check for division with zero
  double precision x,y
       if (x == 0.0) then
          y =  0.999999999999999
        else
          y = x
        end if
end function
%-------------------------------------------------------------------------%
```

E.2.3 Additional Coding

```
%%%%%%%%%%%%%%%%%%%%%%%%%%%%%%%%%%%%%%%%%%%%%%%%%%%%%%%%%%%%%%%%%%%%%%%%%%%%%%%
%%% FORTRAN                                                                   %%%
%%% Additional_coding                                                         %%%
%%% By Jesper Bjerre - s102905                                                %%%
%%% Master Thesis                                                             %%%
%%% DTU and NTNU                                                              %%%
%%% Spring 2015                                                               %%%
%%%%%%%%%%%%%%%%%%%%%%%%%%%%%%%%%%%%%%%%%%%%%%%%%%%%%%%%%%%%%%%%%%%%%%%%%%%%%%%


%%%%%%%%%%%%%%%%%%%%%%%%%%%% Newton_Raphson_s_z() %%%%%%%%%%%%%%%%%%%%%%%%%%%
% NR to determine Dafalias 2013 evoluation rule of rotation (z and s)
subroutine Newton_Raphson_s_z()
    implicit none
    real(kind=8), parameter :: tol = 1.d-14
    real(kind=8) :: res= 1.0
    integer :: itere = 0
    integer:: maxiter = 20
    double precision xx, ff, dff, deltaxx
       xx = 2.0                  % Initial guess of xx

do while (res.gt.tol)
    if(itere.gt.maxiter) stop
      call fff(xx,ff)
      call dfff (xx,dff)
      deltaxx = ff/dff           % Compute Newton increment xx
      xx = xx - deltaxx          % Update xx
      call fff(xx,ff)
      res = abs(ff)
      itere = itere + 1
end do

if (xx  == 2.0) then
    xx = xx
  else
    s = xx
    z = xx
end if

end subroutine

%%%%%%%%%%%%%%%%%%%%%%%%%%%%%%%%% fff() %%%%%%%%%%%%%%%%%%%%%%%%%%%%%%%%%%%%
% Function I for Dafalias 2013 evoluation rule of rotation (z and s)
subroutine fff(xx,ff)
    real(kind=8), intent(in) :: xx
    real(kind=8), intent(out) :: ff
    call mapping()
          M1 = 6.0*sin(phi*PI/180)/(3-sin(phi*PI/180))
          ff = aK0NC - M1/xx*(1-exp(-xx*abs(etaK0NC)/M1))
end subroutine

%%%%%%%%%%%%%%%%%%%%%%%%%%%%%%%%% dfff() %%%%%%%%%%%%%%%%%%%%%%%%%%%%%%%%%%%%
% Function II for Dafalias 2013 evoluation rule of rotation (z and s)
subroutine dfff(xx,dff)
    real(kind=8), intent(in) :: xx
    real(kind=8), intent(out) :: dff
      call mapping()
          M1 = 6.0*sin(phi*PI/180)/(3-sin(phi*PI/180))
          dff = M1*(1.0-exp(-xx*etak0nc/M1))/xx**2.0-etak0nc*exp(-xx*etak0nc/M1)/xx
end subroutine
```

Appendix F

Soil Parameters

This appendix contains the interpretation of soil parameters which have not been presented in the main report. The interpreted parameters are related to the predictions of the embankment located at Onsøy which have been performed with the SCA-R model.

F.1 Compression and Swelling Parameters

The interpreted intrinsic compression and swelling parameters may be seen in Table 7.5 in the main report.

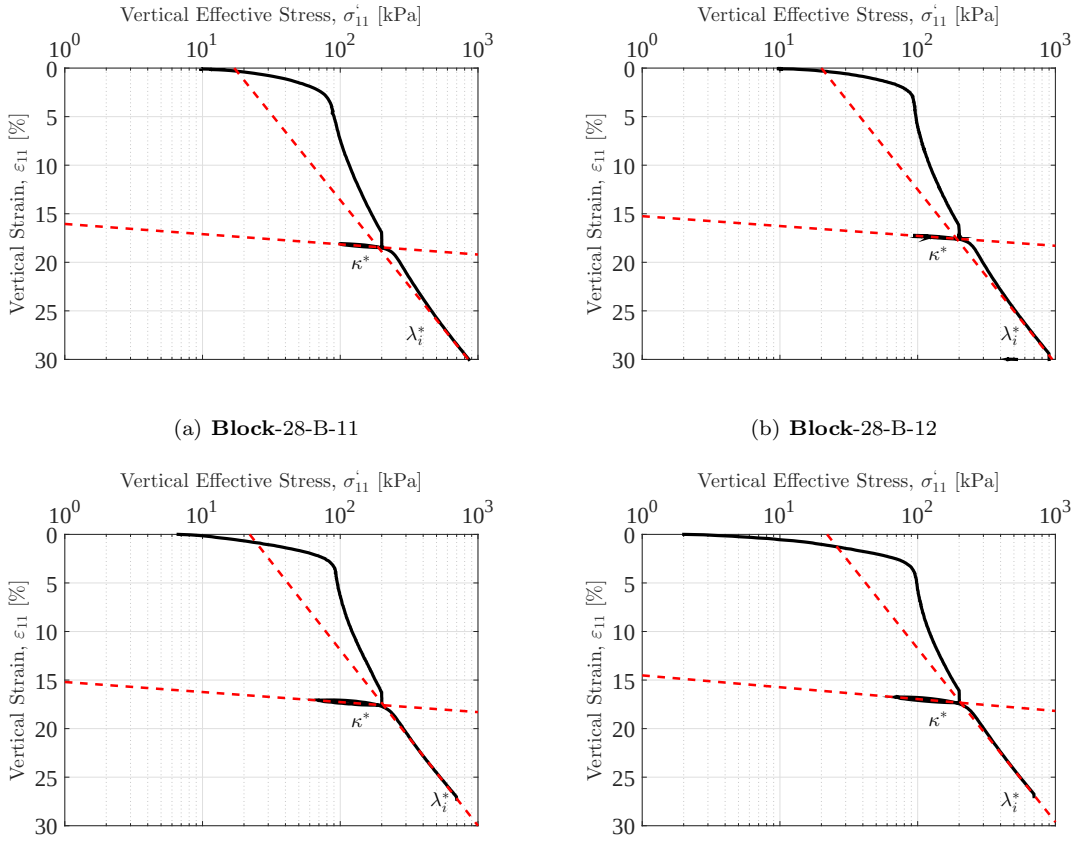

(a) **Block**-28-B-11

(b) **Block**-28-B-12

(c) **Block**-26-B1-19-35

(d) **Block**-26-B1-20-50

Figure F.1: *Interpreted compression and swelling index from CRS. The data is taken from Bamberg (2009) and Lunne et al. (2009).*

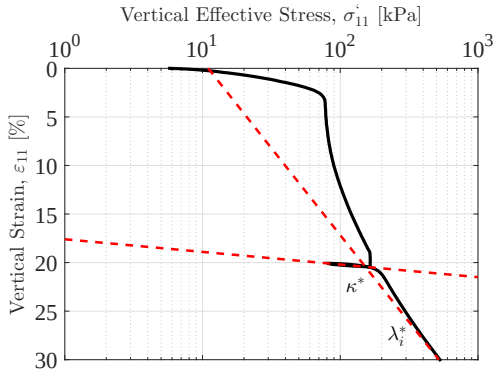

(a) **Block**-22-B-1-CRS

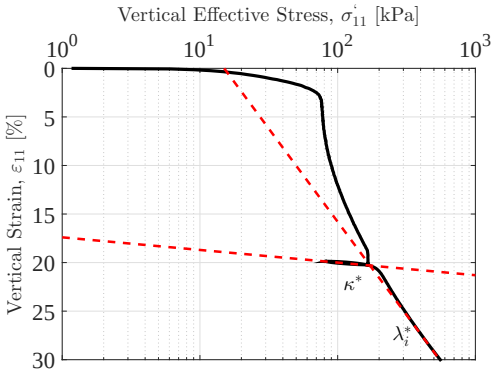

(b) **Block**-22-B-2-CRS

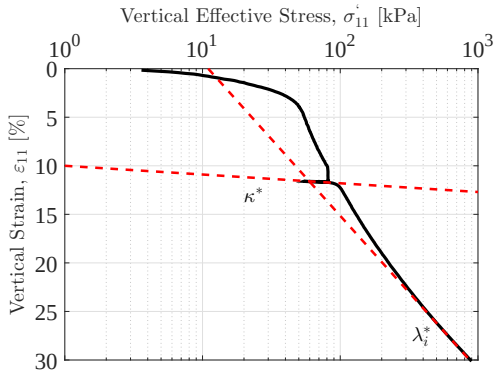

(c) **Block**-3-A1-O1

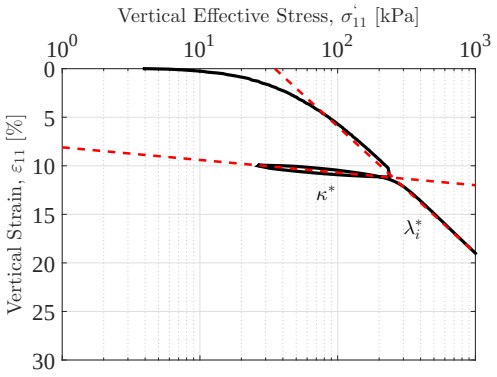

(d) **Block**-10-A2-O1

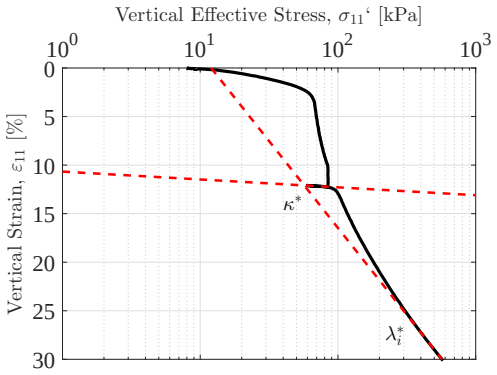

(e) **Block**-19-A1-O1

Figure F.2: *Interpreted compression and swelling index from CRS. The data is taken from Lunne et al. (2010) and Berre (2010).*

F.2 Permeability and Its Evolution

Only six CRS tests are presented in the appendix. This is a consequence of missing the data for the remaining CRS tests. The interpreted parameters may be seen in Table 7.3 in the main report.

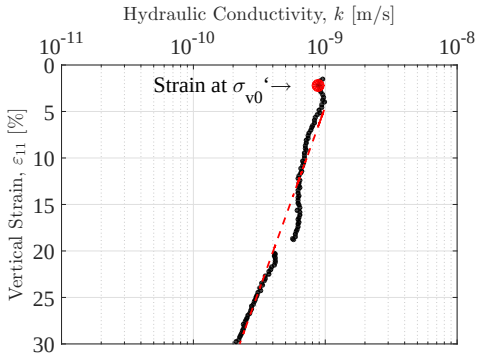

(a) **Block**-22-B-1-CRS

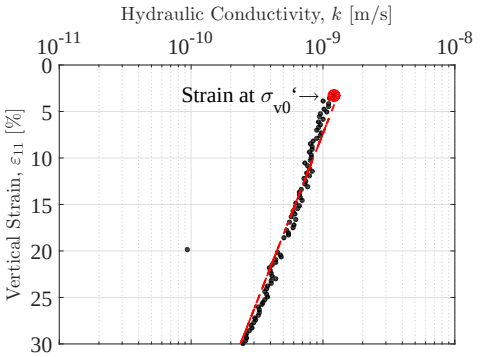

(b) **Block**-22-B-2-CRS

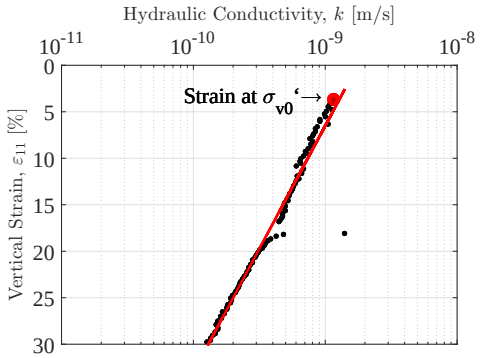

(c) **Block**-28-B-11

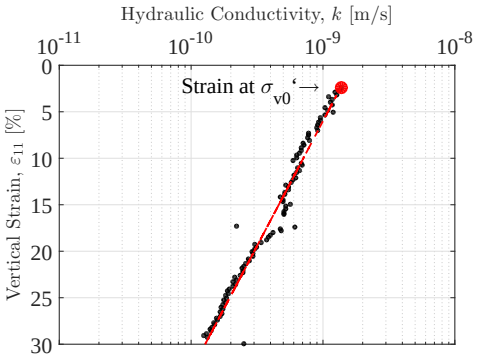

(d) **Block**-28-B-12

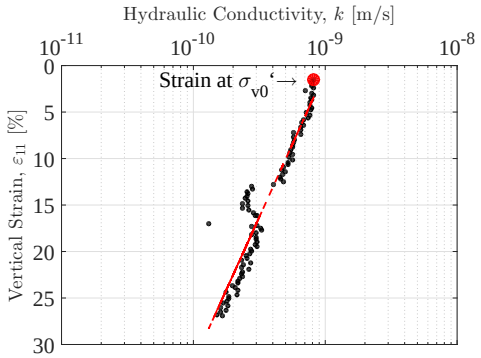

(e) **Block**-26-B1-19-35

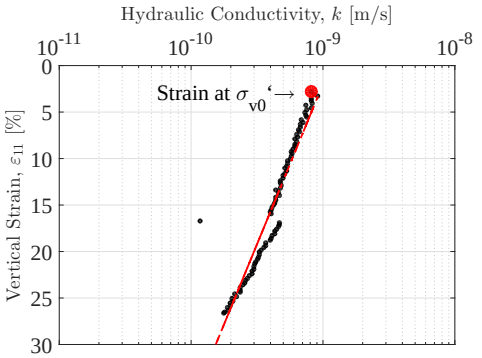

(f) **Block**-26-B1-19-50

Figure F.3: *Interpreted permeability and change in permeability from CRS. The data is taken from Lunne et al. (2010), Lunne et al. (2009), and Bamberg (2009).*

F.3 Unit Weight

The unit weight has been determined through the following method:

$$\gamma = \frac{(1+w)S_w d_s}{wd_s + S_w}\gamma_w \tag{F.1}$$

where γ_w is the unit weight of water, S_w is the degree of saturation, w is the water content and d_s is the relative density which may be determined by:

$$d_s = \frac{\rho_s}{\rho_w} \tag{F.2}$$

where ρ_s is the grain density of the soil and ρ_w is the density of the water. Notice, S_r is modified if the magnitude if higher than 100 %. This is done by adjusting the initial void ratio.

F.4 Creep Number

A summary of all the interpreted creep numbers may be seen in Table F.1. The creep number may be interpreted through the principle suggested by Janbu (1969). Hence, r_s may be determined through the inclination of the curves shown in Figure F.4 and Figure F.5 representing the development of deformations under constant effective stress.

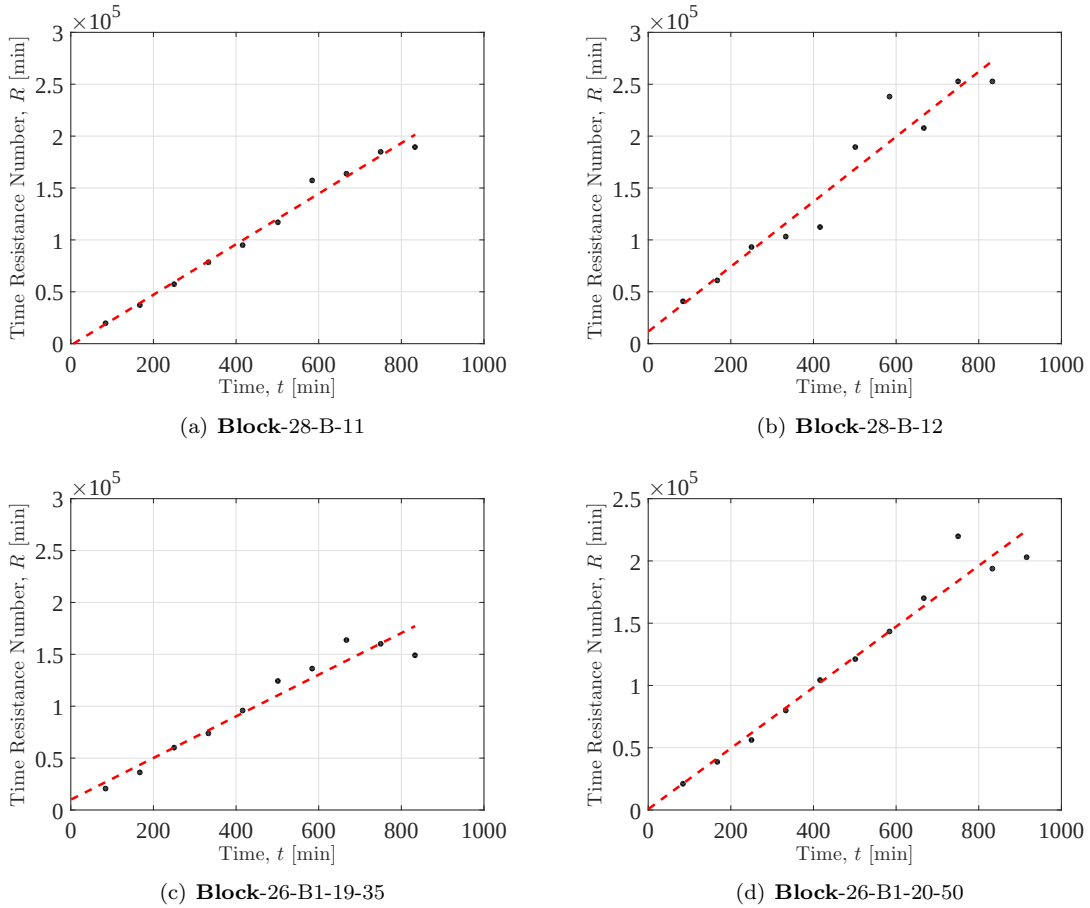

(a) **Block**-28-B-11

(b) **Block**-28-B-12

(c) **Block**-26-B1-19-35

(d) **Block**-26-B1-20-50

Figure F.4: *Interpreted creep number from CRS. The data is taken from Bamberg (2009) and Lunne et al. (2009).*

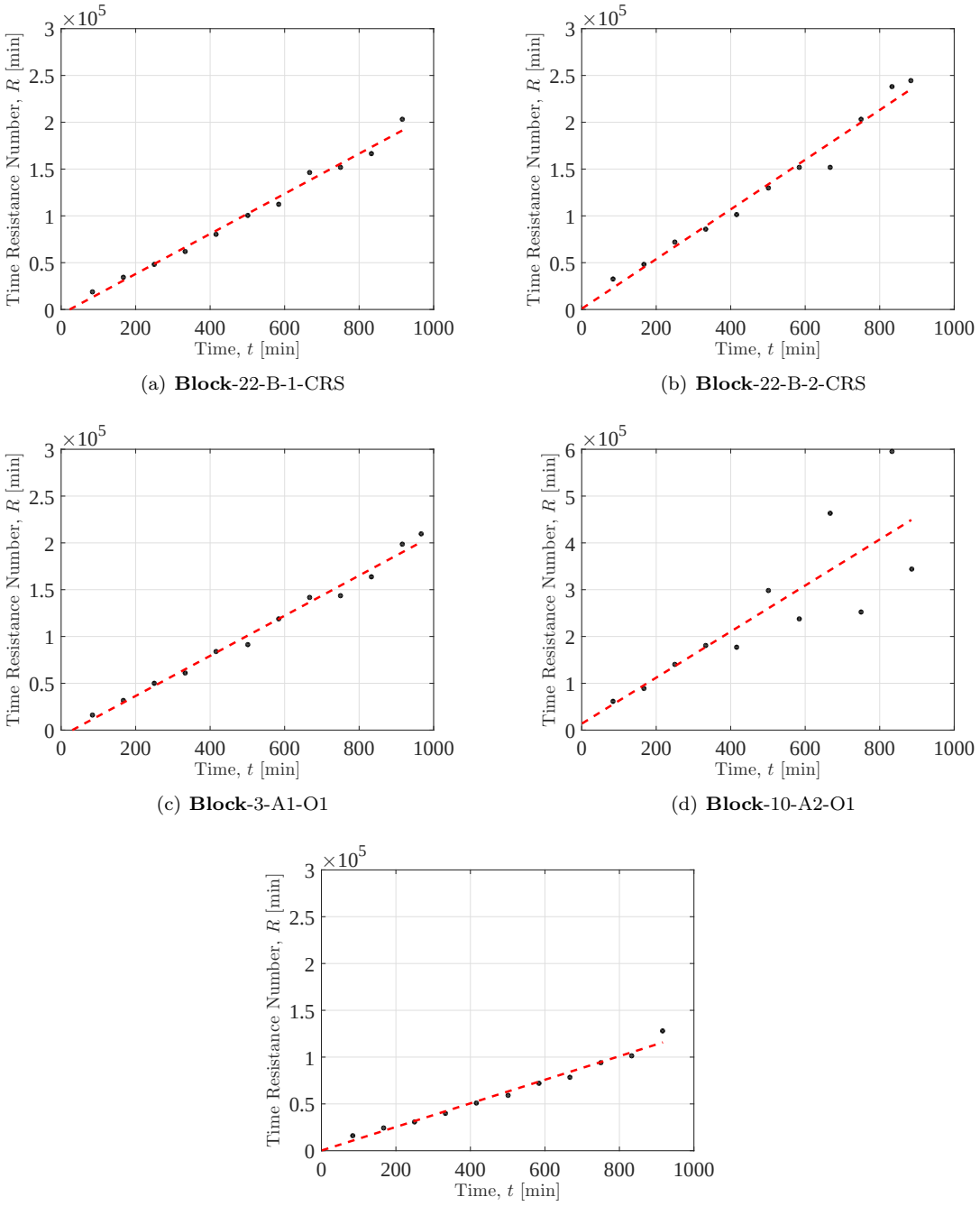

(a) **Block**-22-B-1-CRS

(b) **Block**-22-B-2-CRS

(c) **Block**-3-A1-O1

(d) **Block**-10-A2-O1

(e) **Block**-19-A1-O1

Figure F.5: *Interpreted creep number from CRS. The data is taken from Lunne et al. (2010) and Berre (2010).*

Table F.1: *Interpreted creep numbers (r_s) from Figure F.4 and Figure F.5.*

22-B-1-CRS	22-B-2-CRS	3-A1-O1	10-A2-O1	19-A1-O1	28-B-11	28-B-12	26-B1-19-35	26-B1-19-50
214	214	265	492	126	244	313	201	244.4

F.5 Transformation of r_s to r_{is}.

The intrinsic creep number is normally found by an incremental oedometer. However, no incremental data is available and may be approximated through the CRS data. The intrinsic creep number (r_{is}) may be found through the creep number (r_s). It may be assumed that the ratio between the compression parameter and creep number is a constant:

$$\frac{\lambda}{r_s} \approx \text{Constant} \tag{F.3}$$

Hence, knowing the creep number (r_s), and the compression parameters (λ and λ_i) the intrinsic creep number may be found through:

$$r_{si} = r_s \frac{m_i}{m} \tag{F.4}$$

Notice that the secant modulus has been utilized and may be rewritten into the compression modulus through Eq. (7.7). The secant modulus is determined as suggested by Janbu (1969). Hence, it may be found through the inclination of the curves shown in Figure F.6-F.7.

Table F.2: *Transforming r_s to r_{si} from Figure F.6 and Figure F.8.*

		22-B-1-CRS	22-B-2-CRS	3-A1-O1	10-A2-O1	19-A1-O1	28-B-11	28-B-12	26-B1-19-35	26-B1-19-50
m_{nc}	[-]	19.42	18.73	5.68	-*	14.27	14.29	14.46	15.15	15.27
$m_{nc,i}$	[-]	20.41	21.83	6.55	-*	19.67	15.38	15.58	17.09	17.24
r_{si}	[-]	225	250	306	-	174	136	337	226	276

* Not able to interpret data.

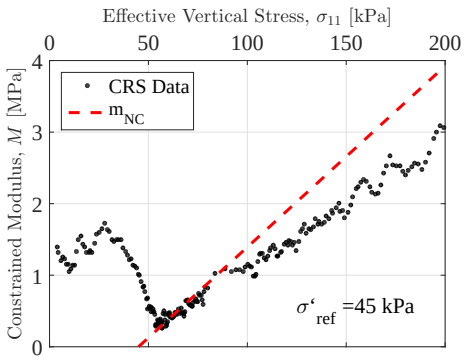

(a) **Block**-3-A1-O1

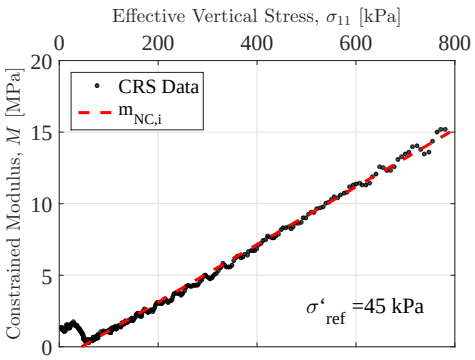

(b) **Block**-3-A1-O1

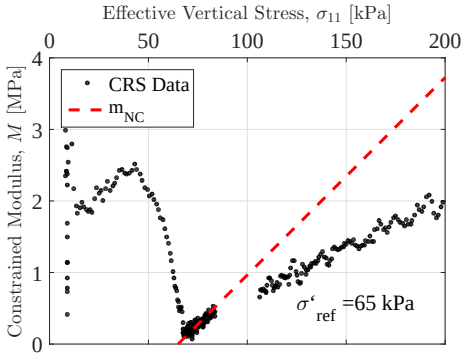

(c) **Block**-19-A1-O1

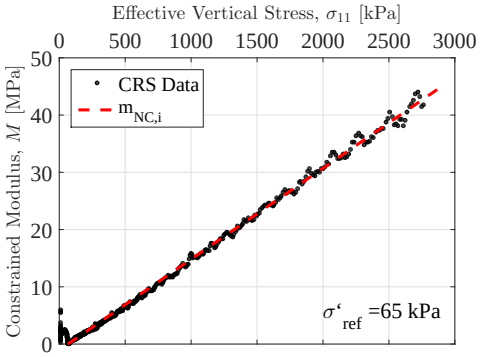

(d) **Block**-19-A1-O1

Figure F.6: *Interpreted compression and swelling index from CRS. The data is taken from Lunne et al. (2010) and Berre (2010).*

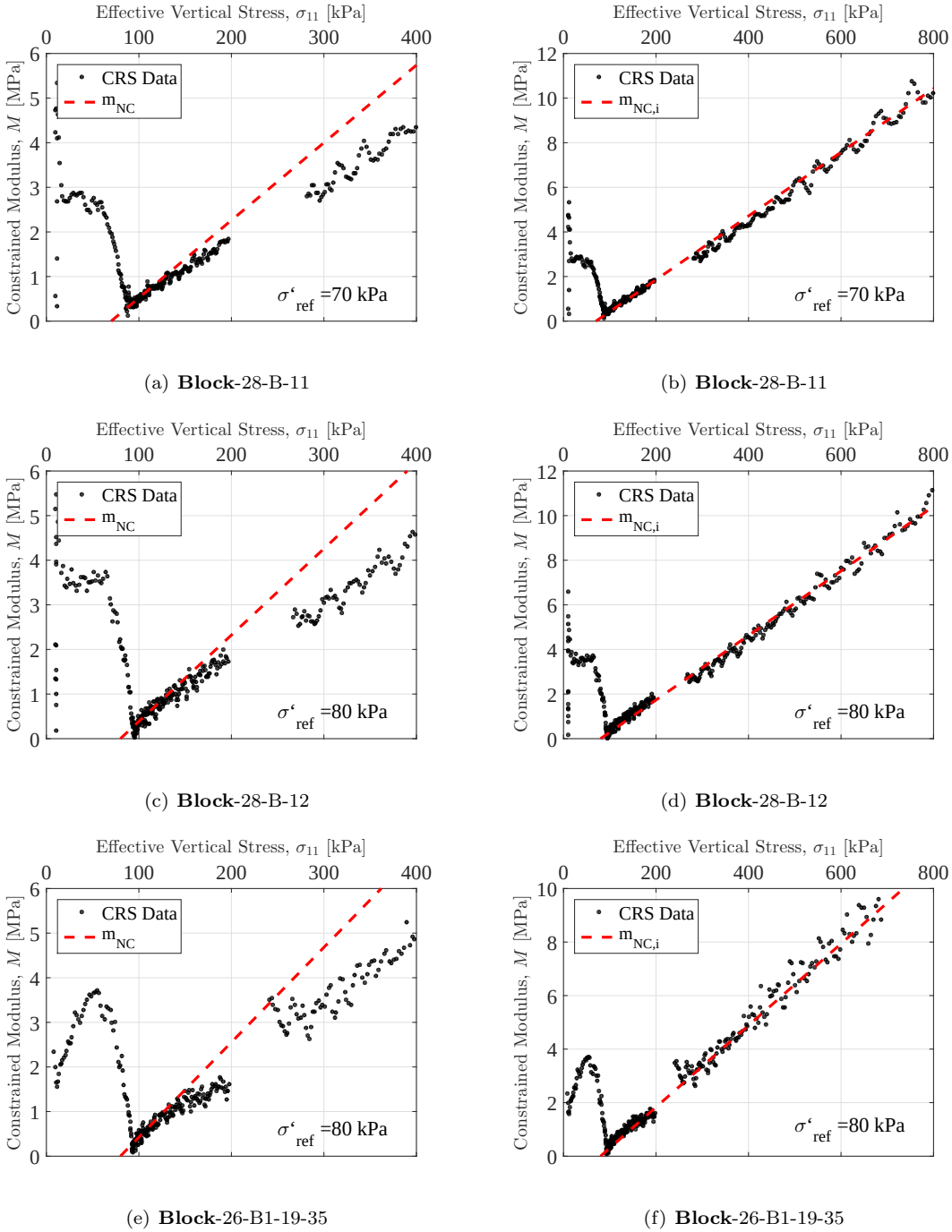

(a) **Block**-28-B-11

(b) **Block**-28-B-11

(c) **Block**-28-B-12

(d) **Block**-28-B-12

(e) **Block**-26-B1-19-35

(f) **Block**-26-B1-19-35

Figure F.7: *Interpreted compression and swelling index from CRS. The data is taken from Bamberg (2009) and Lunne et al. (2009).*

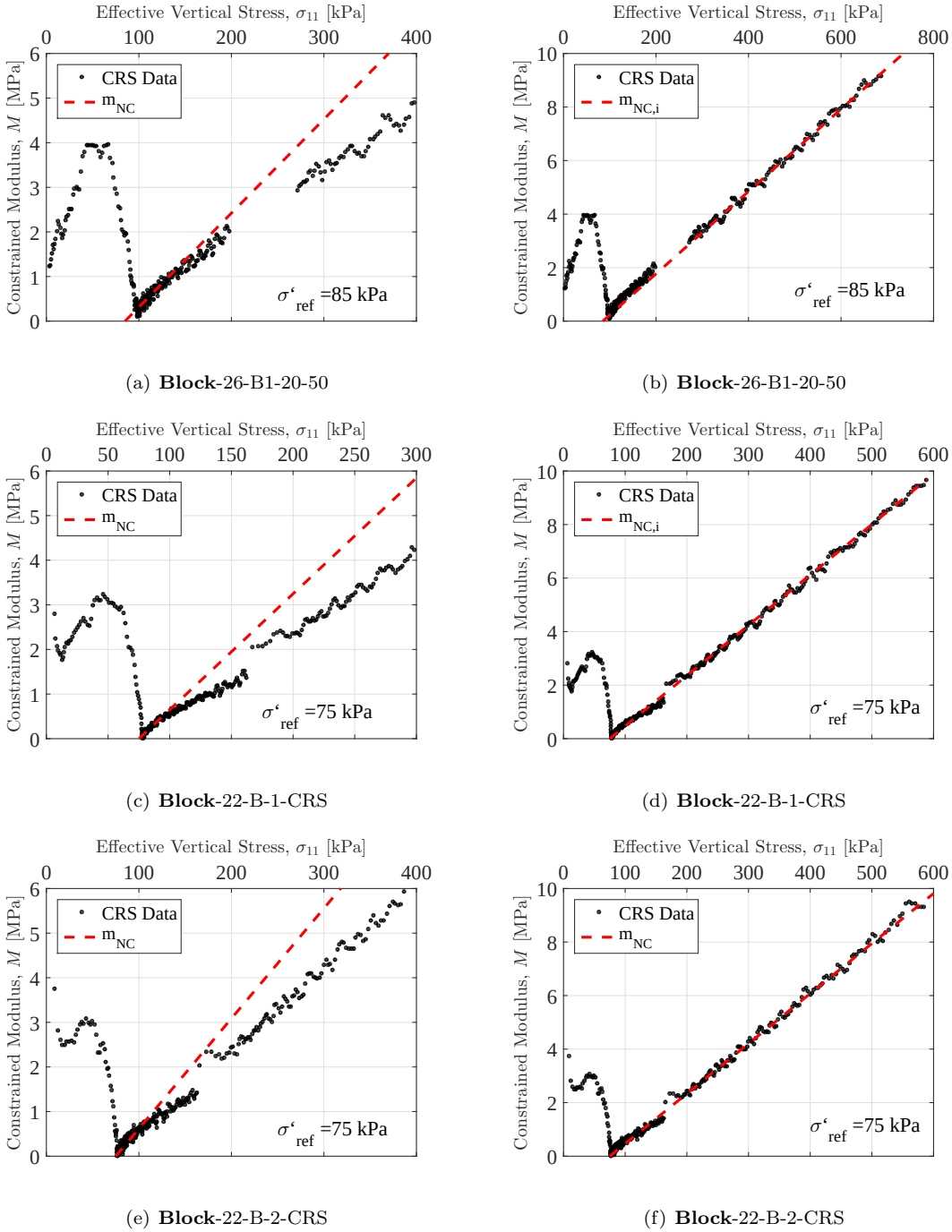

(a) **Block**-26-B1-20-50

(b) **Block**-26-B1-20-50

(c) **Block**-22-B-1-CRS

(d) **Block**-22-B-1-CRS

(e) **Block**-22-B-2-CRS

(f) **Block**-22-B-2-CRS

Figure F.8: *Interpreted compression and swelling index from CRS. Taken from Bamberg (2009) and Lunne et al. (2009).*

F.6 Back Calculation

This section contains the back calculation curves of the CRS and tri-axial tests. The utilized input parameters are presented in the main report, see Table 7.7. In addition, the section contains the investigation of neglecting the influence of α_e during the CRS simulations.

F.6.1 Effect of α_e

In Section 7.4 the input parameter, α_e, was set to zero during the back calculation of the CRS tests. Hence, the influence on the stress-strain relationship must be investigated. A typical value of the elastic stiffness parameter is $\alpha_e = -0.1$, see Section 7.4. A back calculation of the stress-strain path for sample **Block**-19-A1-O1 may be seen on Figure F.9 with and without the influence from α_e.

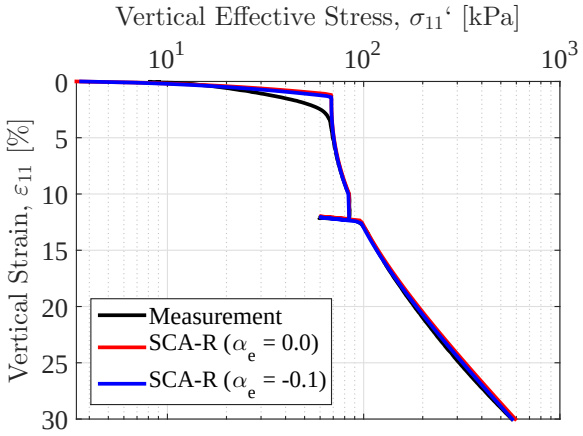

Figure F.9: *Back calculations of the CRS for **Block**-19-A1-O1. Investigating the effect of α_e*

It may be seen that $\alpha_e = -0.1$ affected the stress-strain path by lowering the curve. However the lowering is not significant and would not cause major changes in the soil response. Hence, the utilized approach in Section 7.4 is assumed to be acceptable.

F.6.2 CRS Tests

The back calculation of the CRS tests may be seen on Figure F.10-F.11.

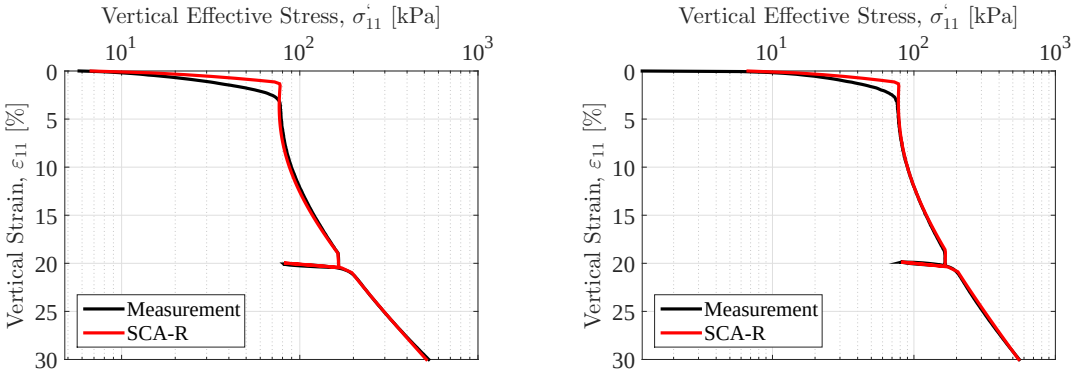

(a) **Block**-22-B-1-CRS

(b) **Block**-22-B-2-CRS

Figure F.10: *Back calculation of CRS.*

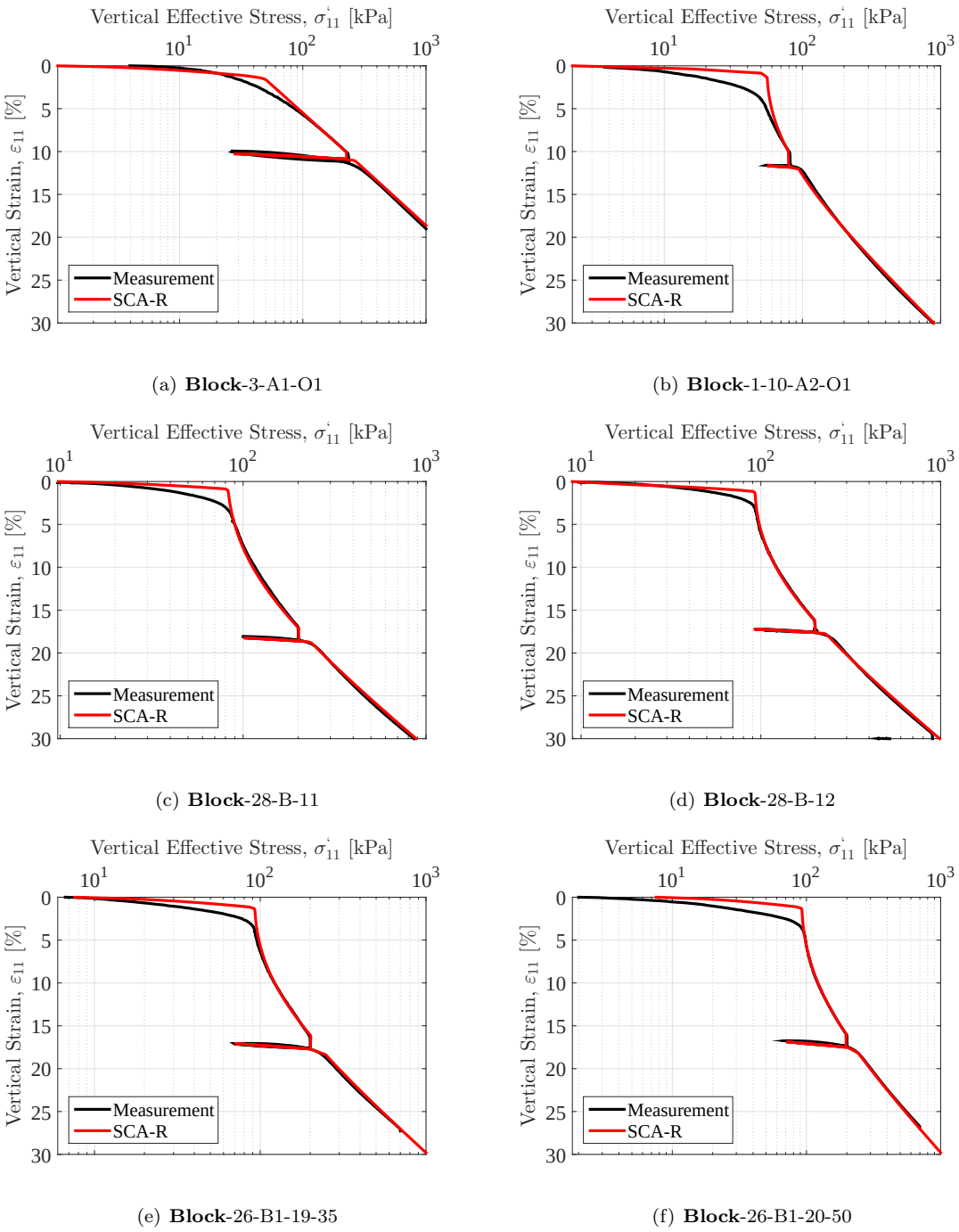

(a) **Block**-3-A1-O1

(b) **Block**-1-10-A2-O1

(c) **Block**-28-B-11

(d) **Block**-28-B-12

(e) **Block**-26-B1-19-35

(f) **Block**-26-B1-20-50

Figure F.11: *Back calculation of CRS.*

F.6.3 Tri-axial Tests

The back calculation of the tri-axial tests may be seen on Figure F.12-F.13. Notice that a modified version of **Block**-10-A1-T1 using a OCR_τ=1.5 has added to avoid the loop in the ESP as seen on Figure F.12(a).

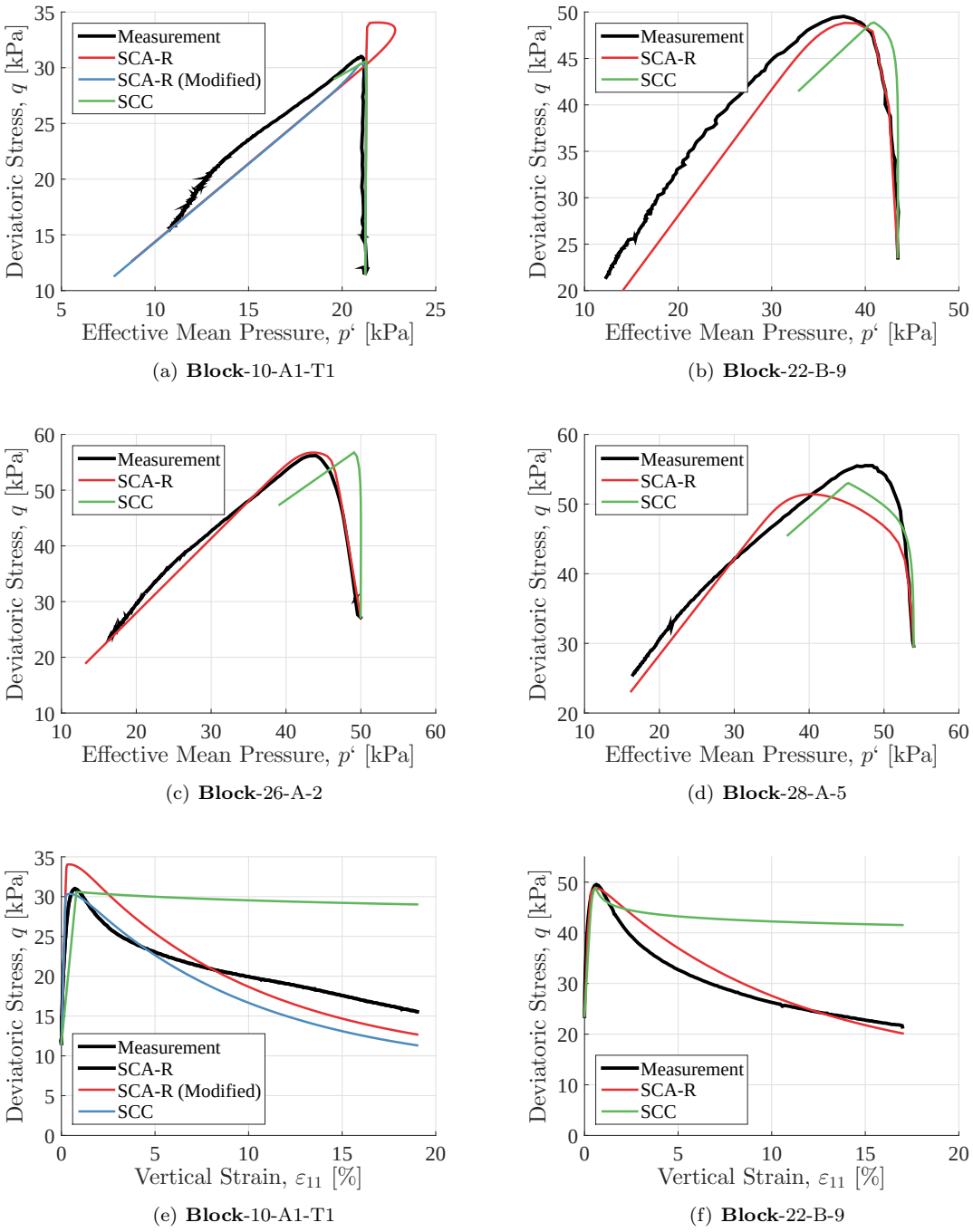

(a) **Block**-10-A1-T1

(b) **Block**-22-B-9

(c) **Block**-26-A-2

(d) **Block**-28-A-5

(e) **Block**-10-A1-T1

(f) **Block**-22-B-9

Figure F.12: *Back calculation of tri-axial test I. ESP and vertical strain vs. deviatoric stress.*

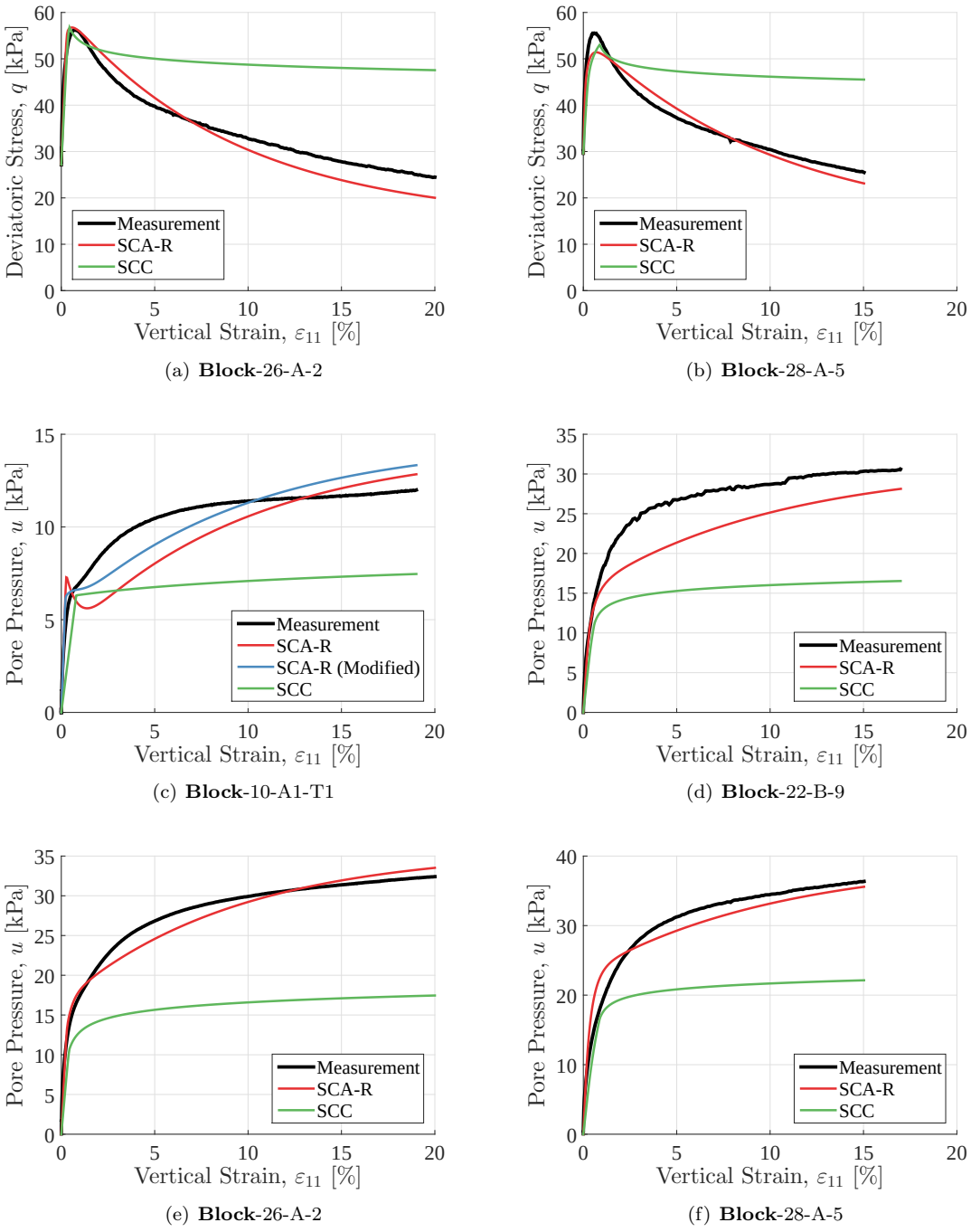

(a) **Block**-26-A-2 (b) **Block**-28-A-5

(c) **Block**-10-A1-T1 (d) **Block**-22-B-9

(e) **Block**-26-A-2 (f) **Block**-28-A-5

Figure F.13: *Back calculation of tri-axial test II. Vertical strain vs. deviatoric stress and pore pressure.*

Appendix G

Documentation of Calculations

This appendix contains additional predictions related to the embankment located at Onsøy which have not been highlighted in the main report.

G.1 NGI Data

The performance of the SCA-R model has been compared to other soil models in Section 8. To ensure a reliable comparison, the influence of the finite element model itself should be investigated. Hence, the utilized finite element model should be controlled to see if similar predictions, as for the finite element model assembled by Mehli (2015b), may be achieved. The SSC model is an available soil model in PLAXIS and may be used in such a verification. Figure G.1 shows two simulations, one performed by the finite element model suggested by the Author and one by Mehli (2015b).

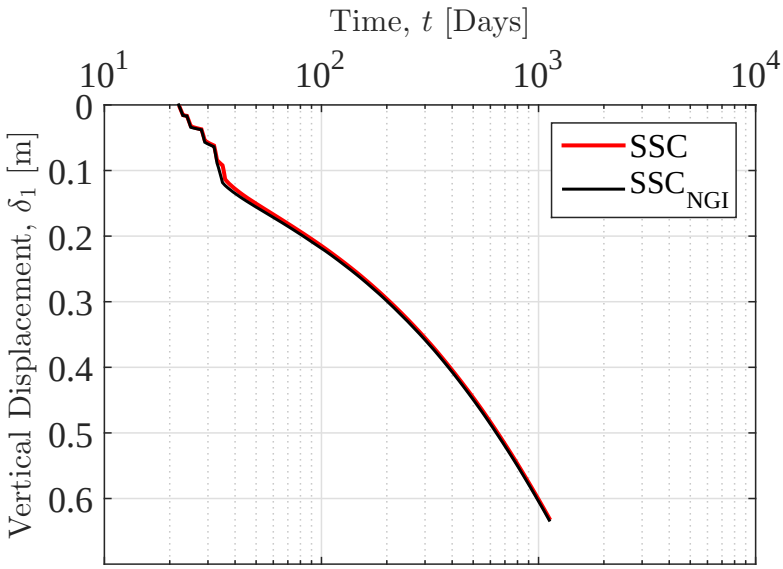

Figure G.1: *Comparison of assembled finite element models through the SSC soil model. The graph shows the vertical displacement just beneath the center of the embankment.*

A small deviation near 0.1 m of vertical displacement may be observed on Figure G.1. This may be a consequence of how the fill layers are activated. By investigating the path closely it looks as if the two last fill layers are activated on the same time for the NGI model. However, the rest of the curve is very similar. Hence, it may be concluded that the assembled finite element model yields a similar response as for the finite element model suggested by Mehli (2015b).

G.2 Recovering

This section contains the investigation of how the recovery effect influences the final predictions of the embankment located at Onsøy.

G.2.1 Scenario 1

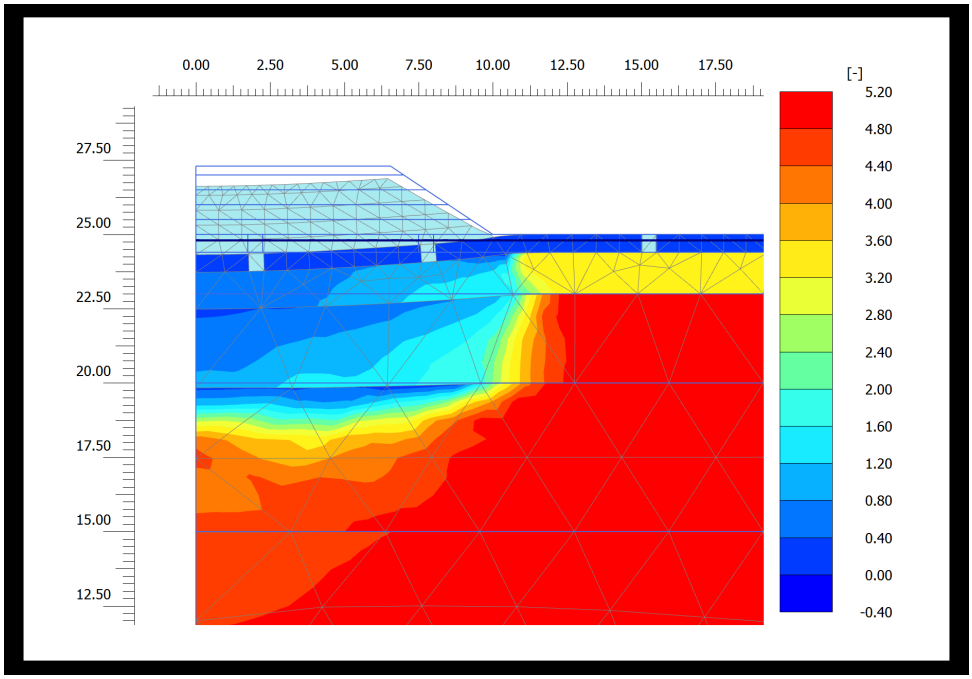

(a) Structure (x), Day No. 1120.

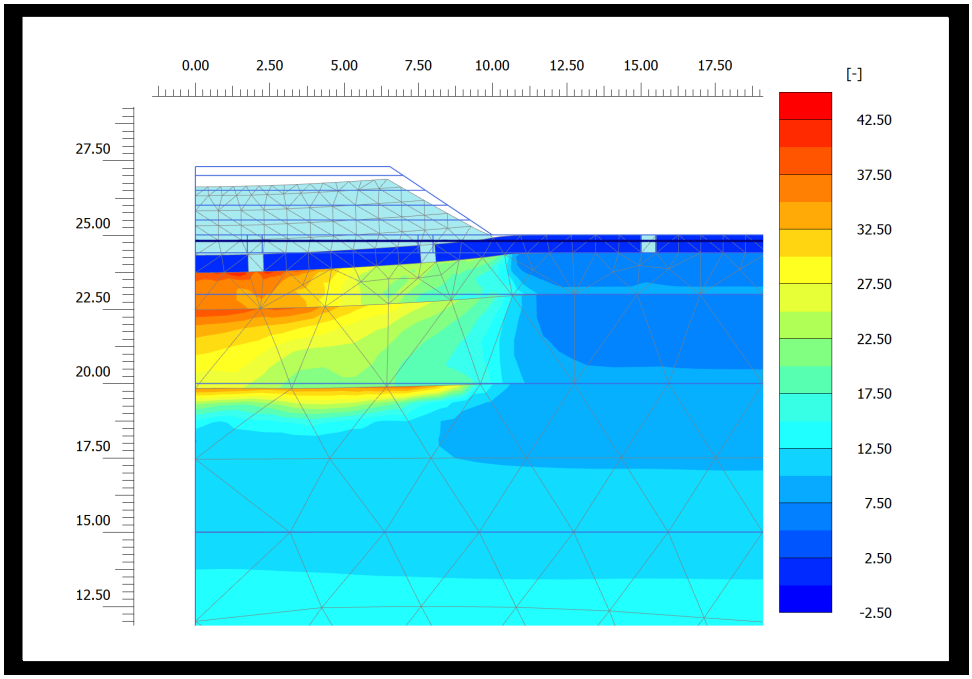

(b) Intrinsic Pressure (p'_{mi}), Day No. 1120.

Figure G.2: *Scenario 1 - State parameters.*

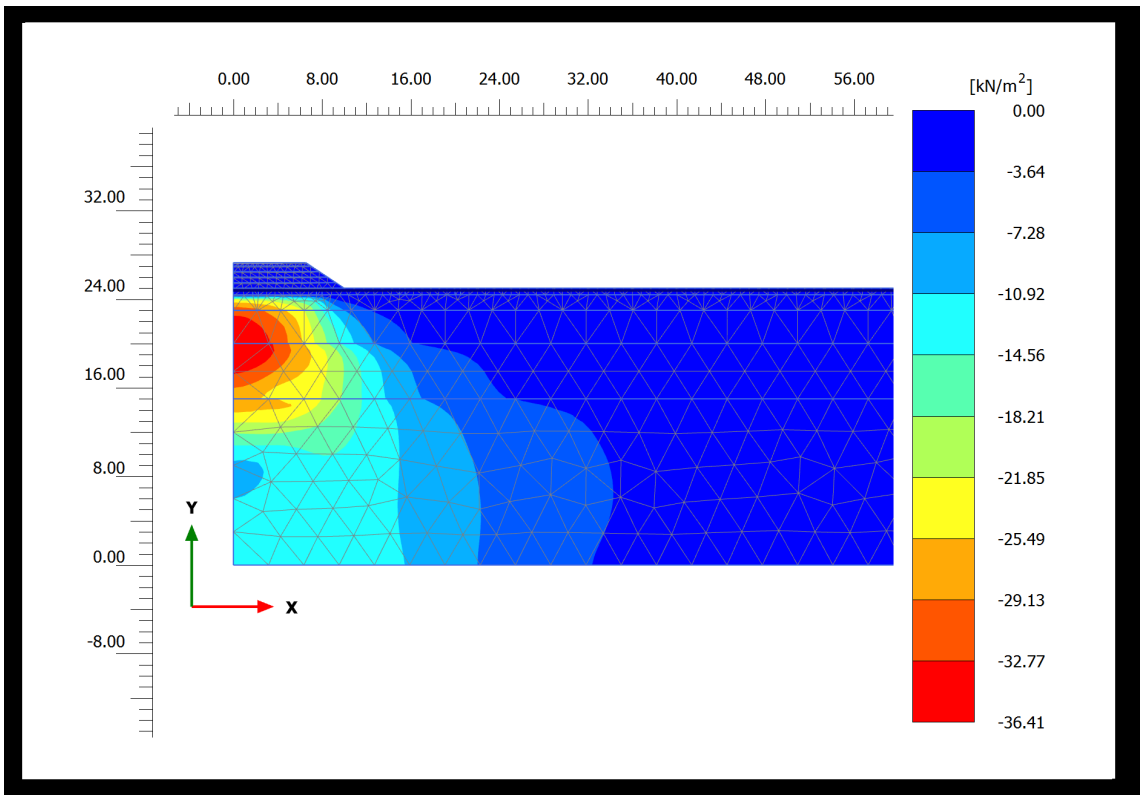

(a) Day No. 36.

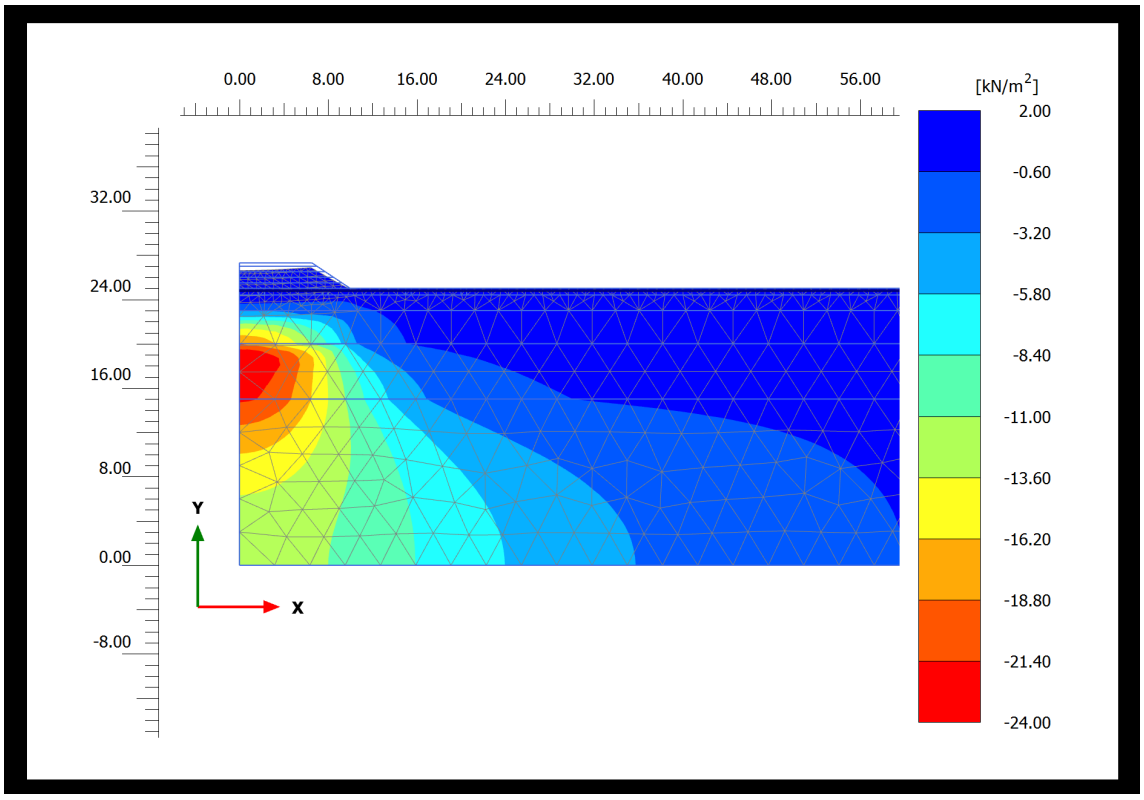

(b) Day No. 1120.

Figure G.3: *Scenario 1 - Excess pore pressure.*

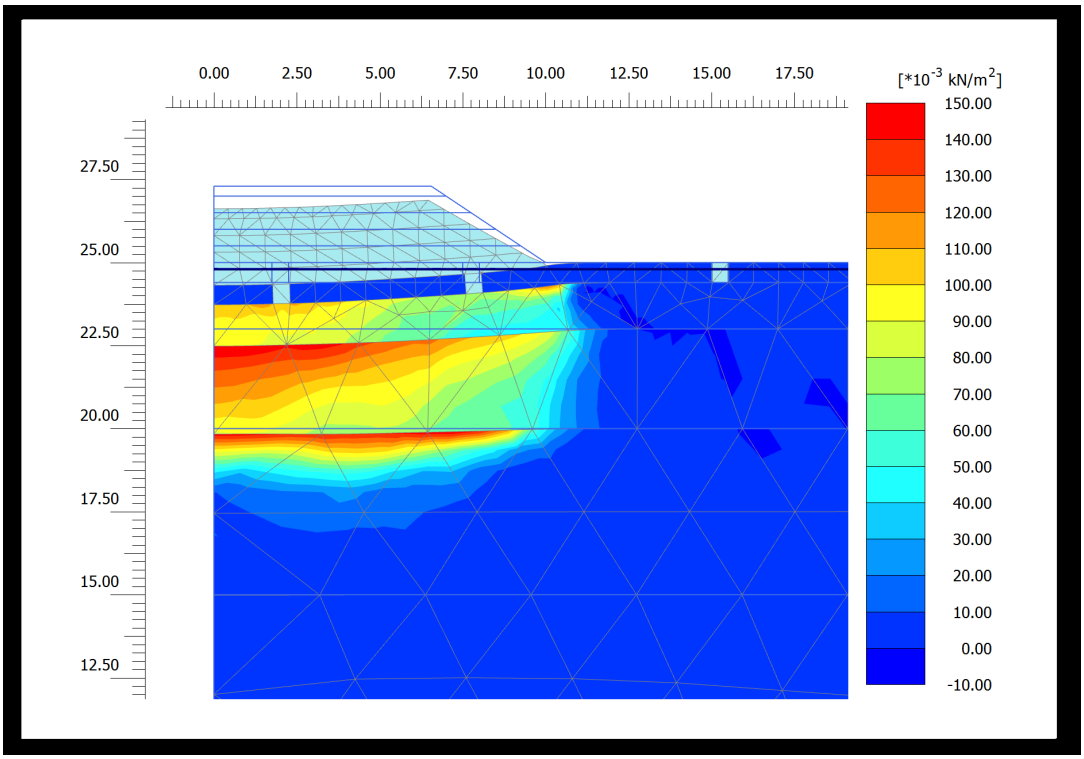

Figure G.4: *Scenario 1 - Plastic multiplier (dλ), Day No. 1120.*

G.2.2 Scenario 2

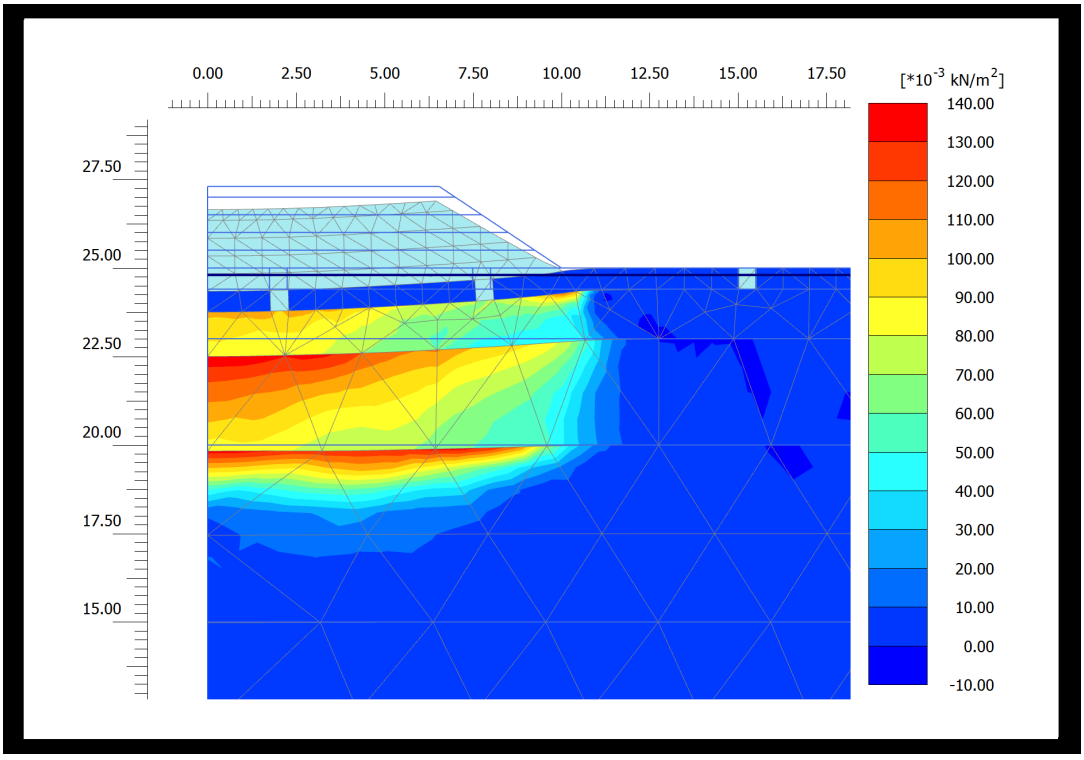

Figure G.5: *Scenario 2 - Plastic multiplier (dλ), Day No. 1120.*

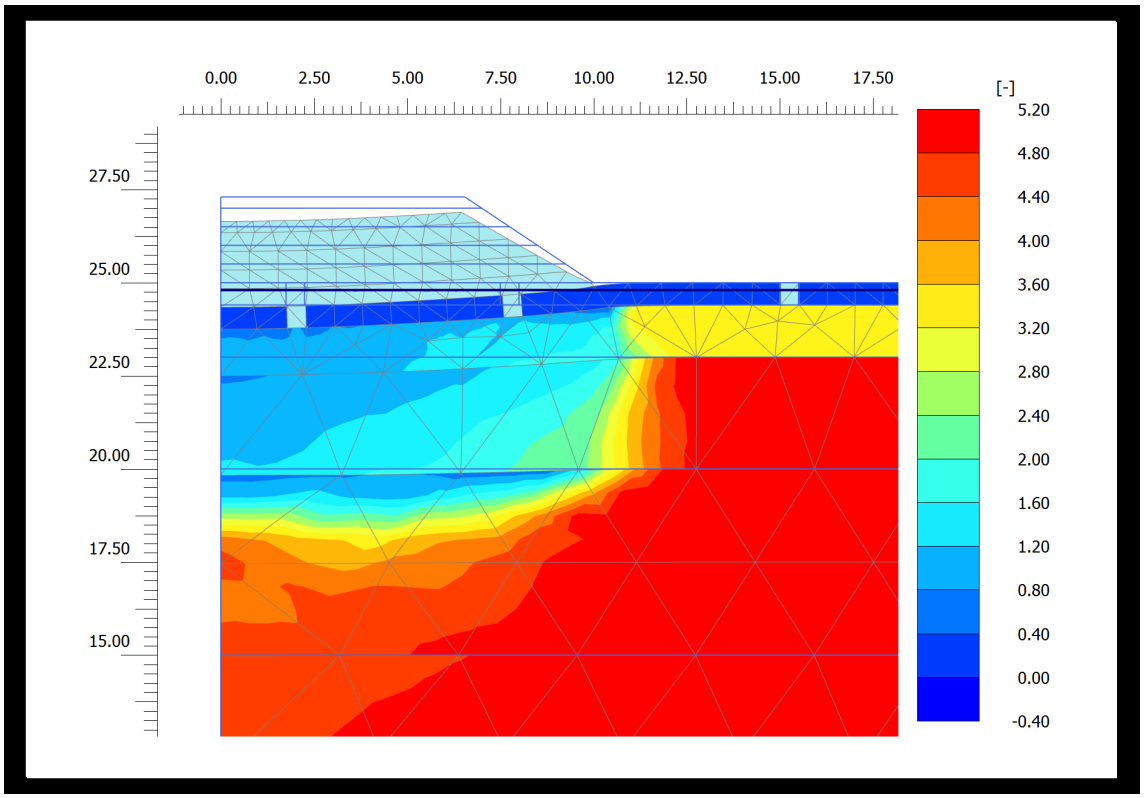

(a) Structure (x), Day No. 1120.

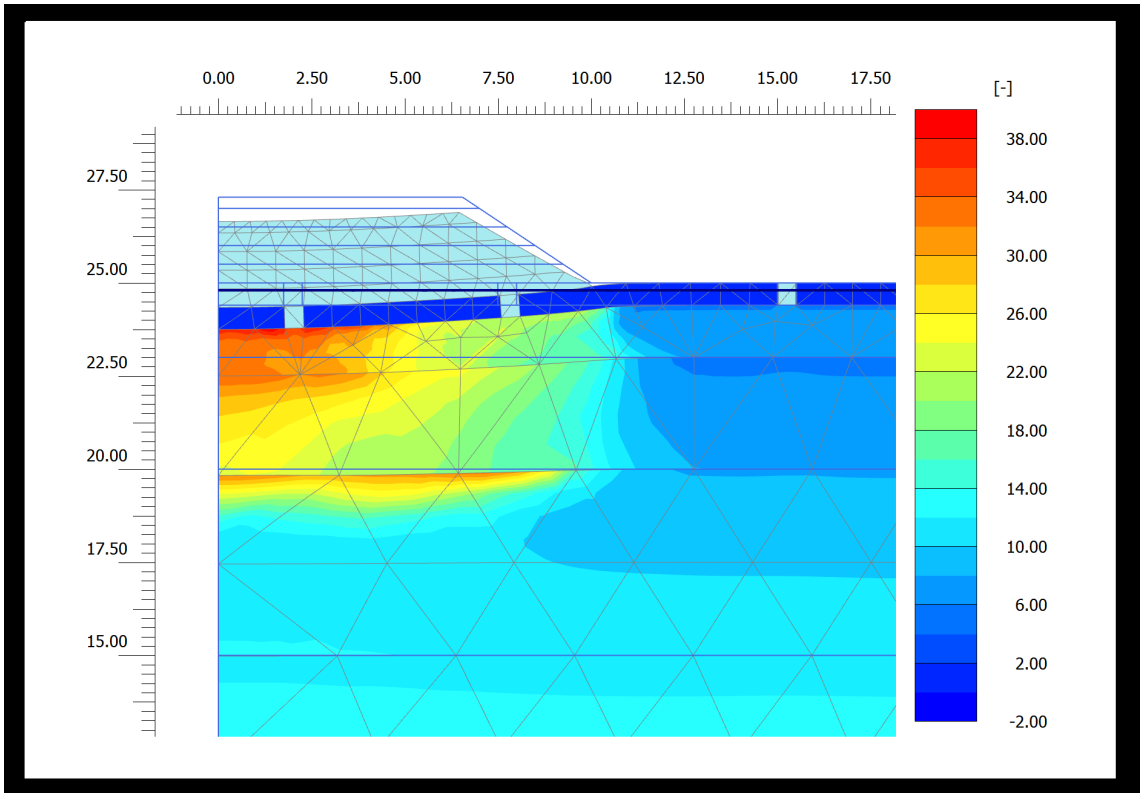

(b) Intrinsic Pressure (p'_{mi}), Day No. 1120.

Figure G.6: *Scenario 2 - State parameters.*

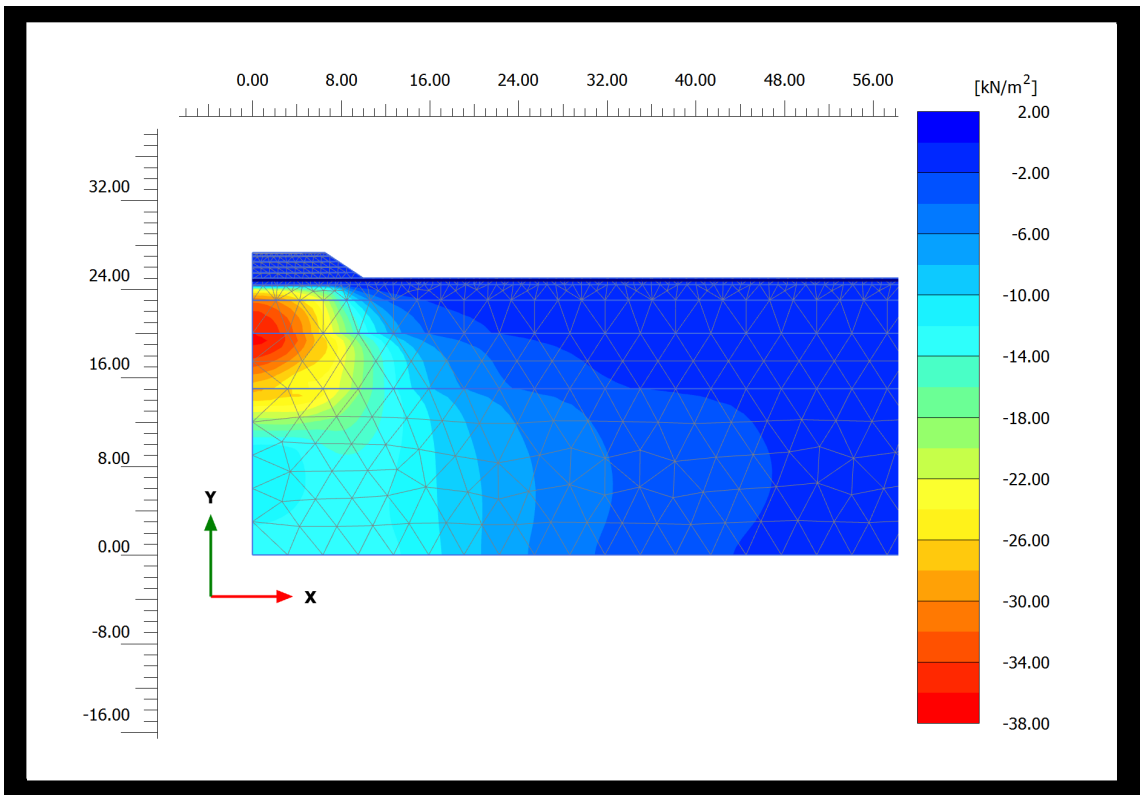

(a) Day No. 36.

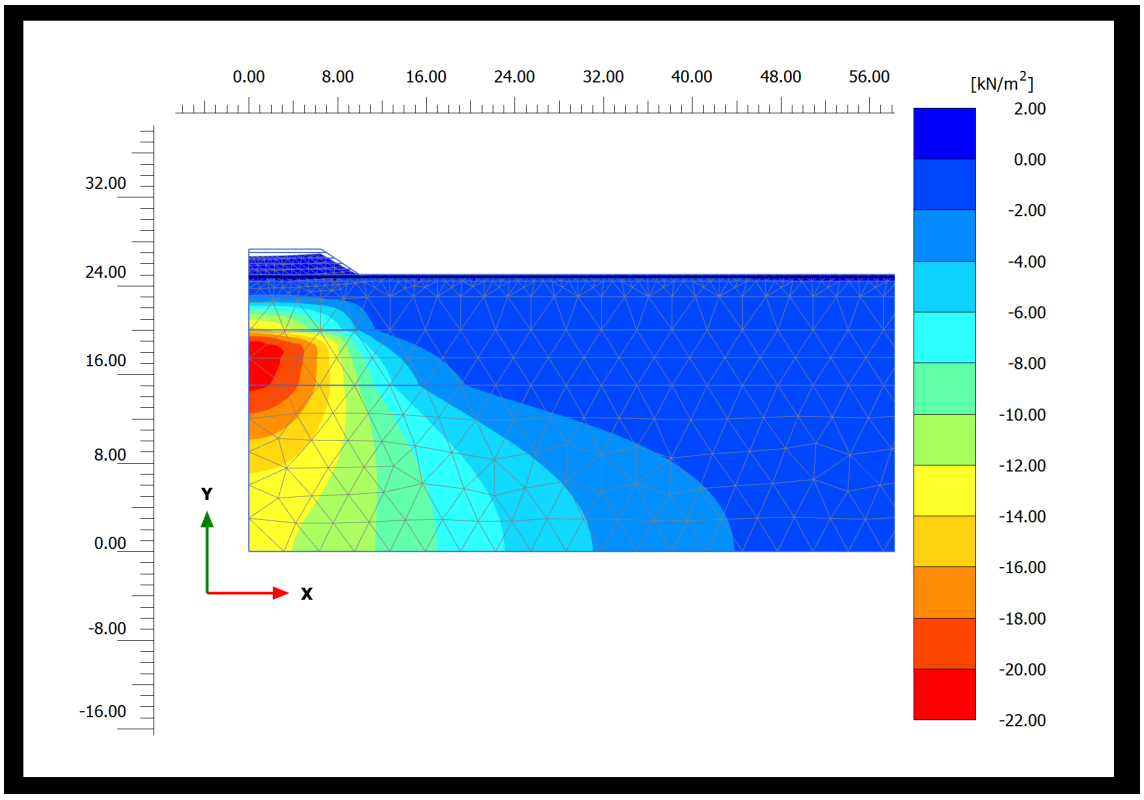

(b) Day No. 1120.

Figure G.7: *Scenario 2 - Excess Pore Pressure.*

G.2.3 Scenario 3

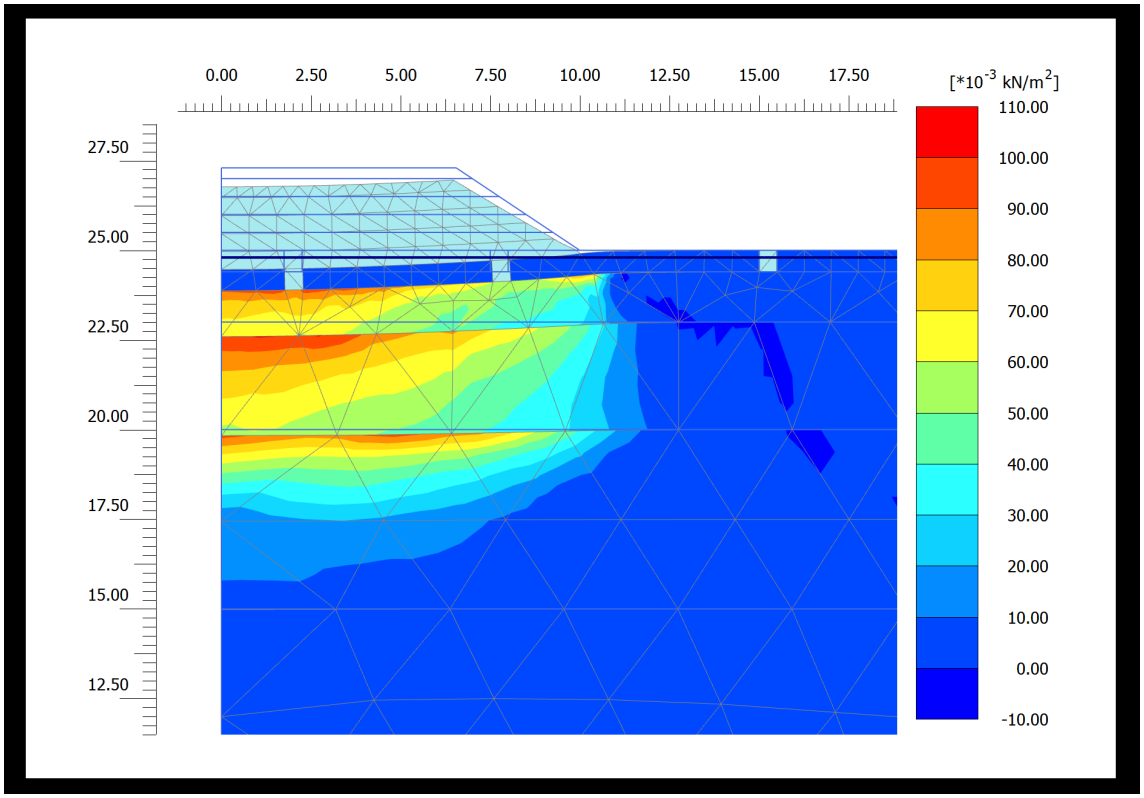

Figure G.8: *Scenario 3 - Plastic Multiplier (dλ), Day No. 1120.*

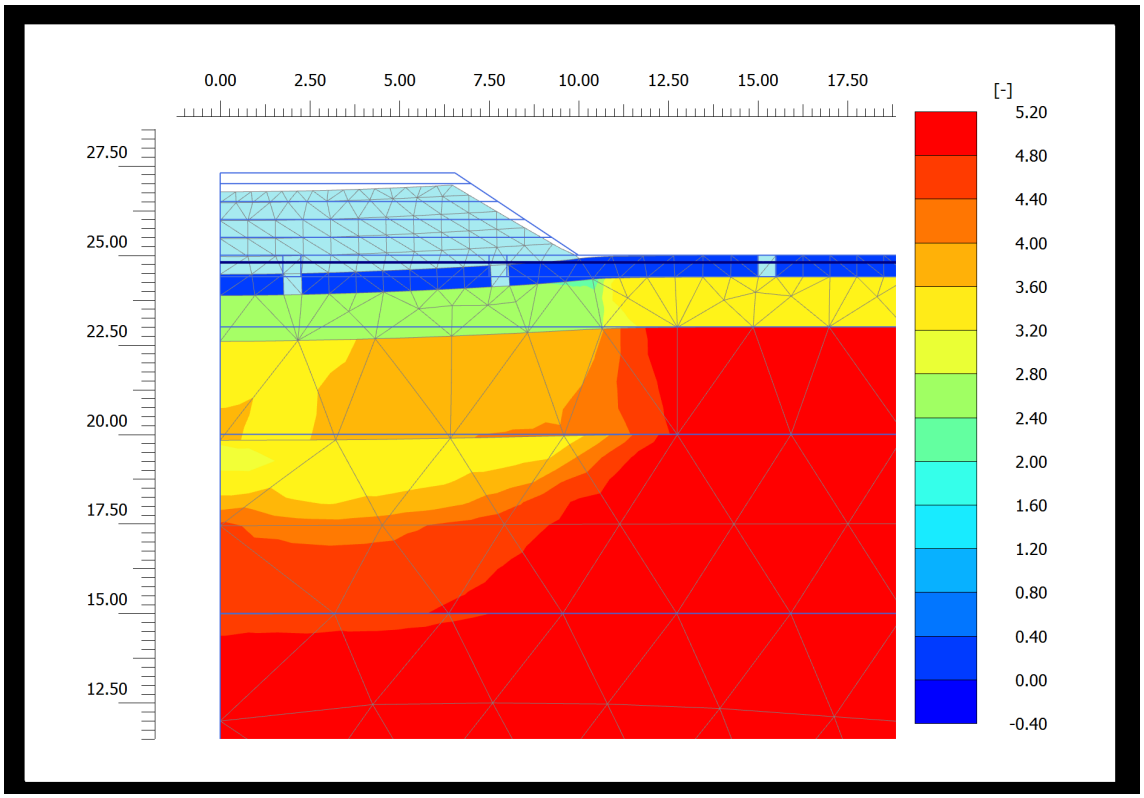

(a) Structure (x), Day No. 1120.

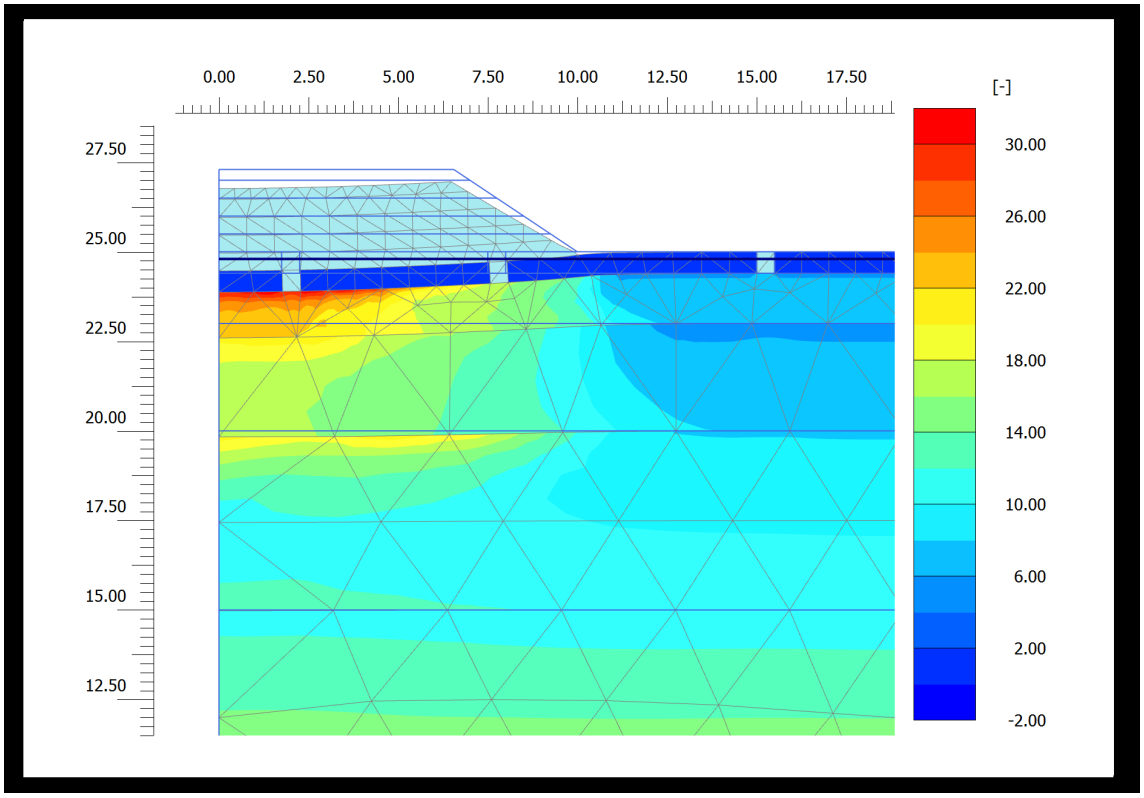

(b) Intrinsic Pressure (p'_{mi}), Day No. 1120.

Figure G.9: *Scenario 3 - State parameters.*

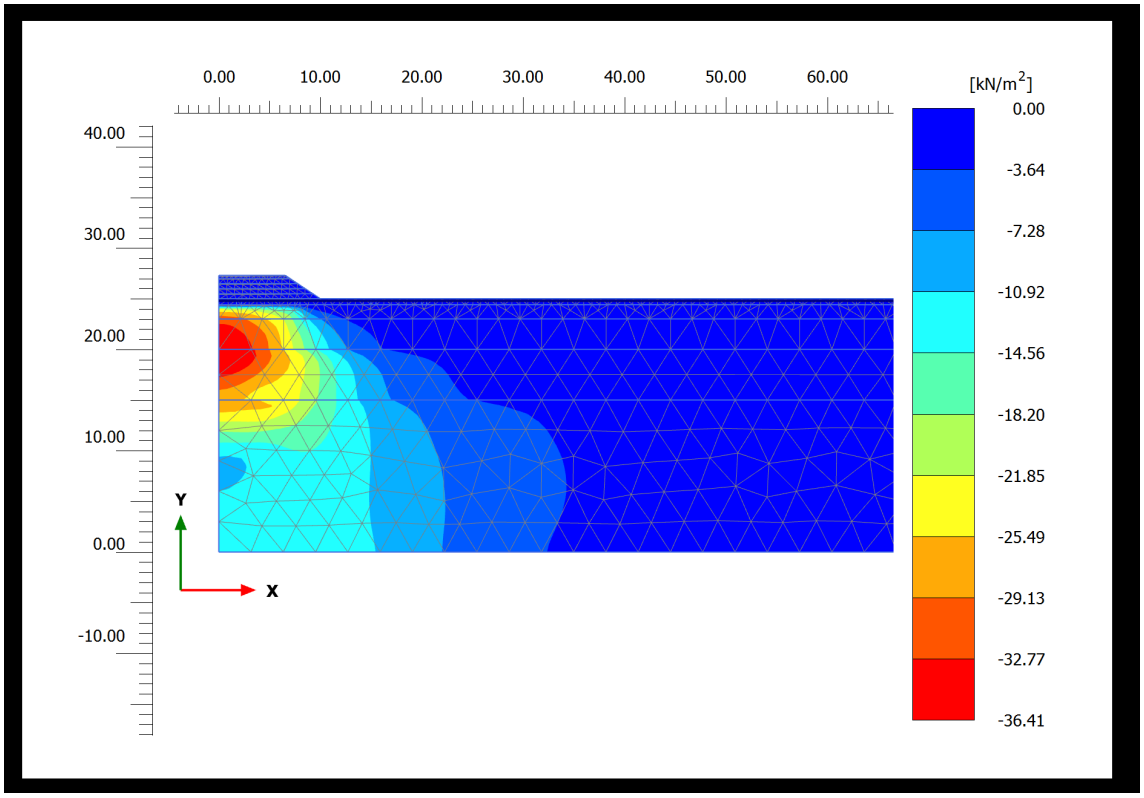

(a) Day No. 36

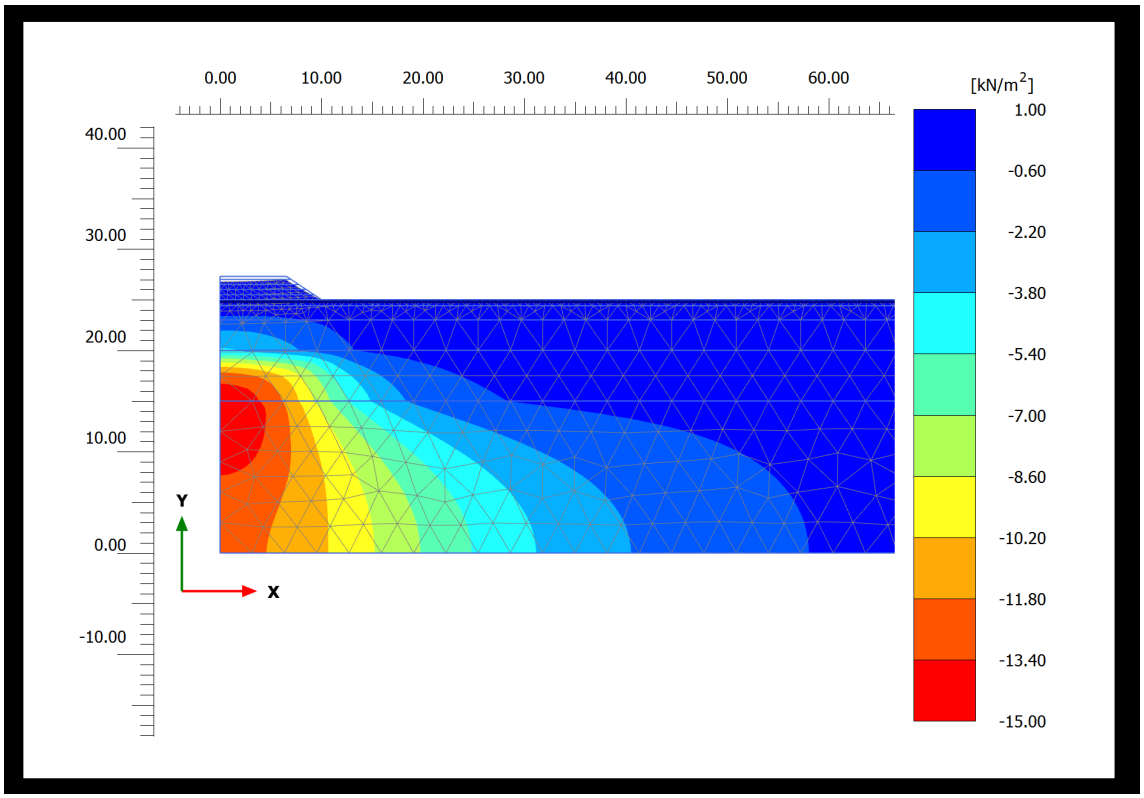

(b) Day No. 1120.

Figure G.10: *Scenario 3 - Excess pore pressure.*

G.3 Investigation of Implicit vs. Explicit

This section contains the predictions of layer 1 (0.6 - 2.0 m), layer 3 (5.0 - 10.0 m) and layer 4 (10.0 - 25.0 m) related to the investigation of the explicit and implicit scheme described in Section 8.9.

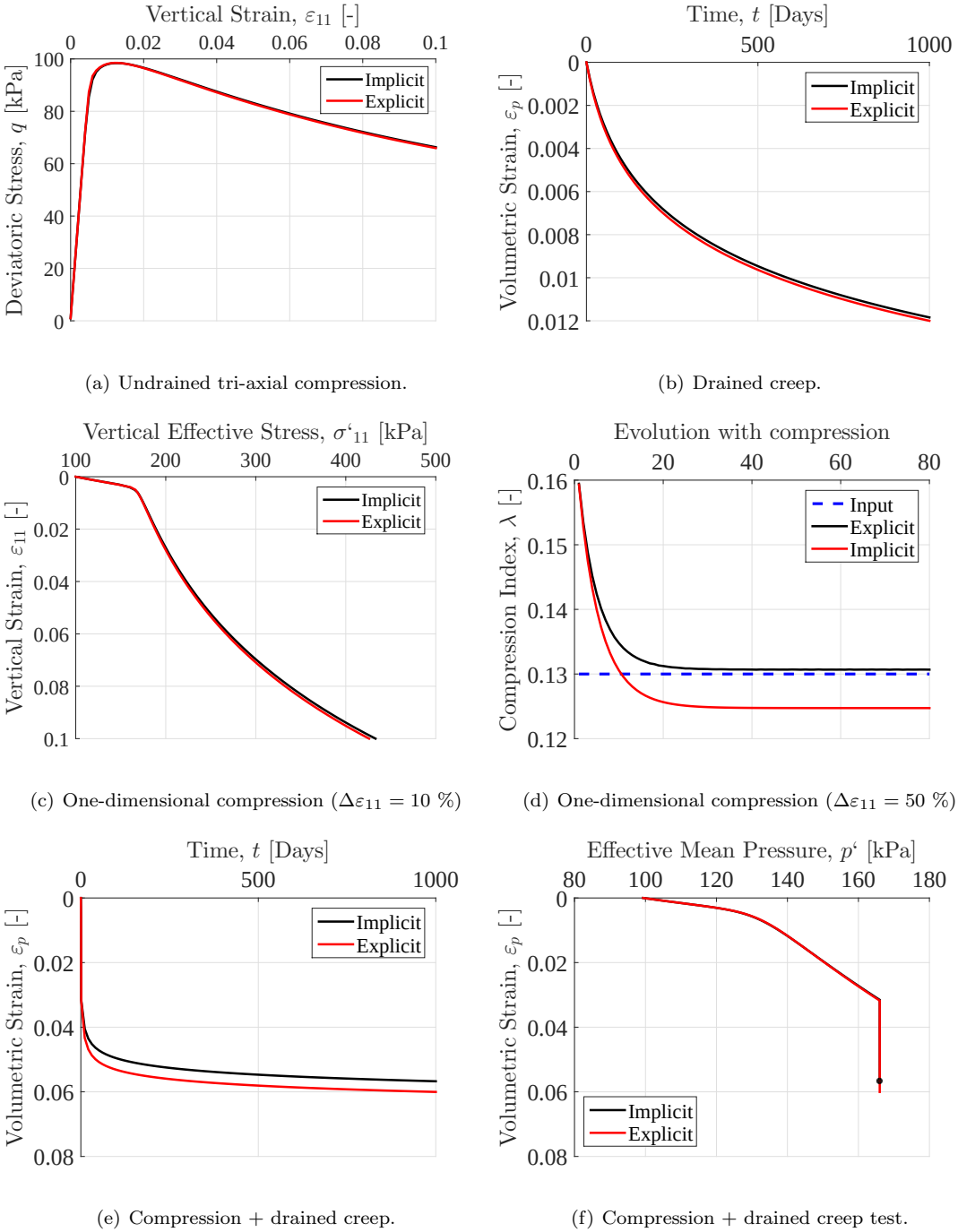

(a) Undrained tri-axial compression.

(b) Drained creep.

(c) One-dimensional compression ($\Delta\varepsilon_{11} = 10$ %)

(d) One-dimensional compression ($\Delta\varepsilon_{11} = 50$ %)

(e) Compression + drained creep.

(f) Compression + drained creep test.

Figure G.11: *Investigation explicit and implicit scheme for layer 1 (0.6 - 2.0 m).*

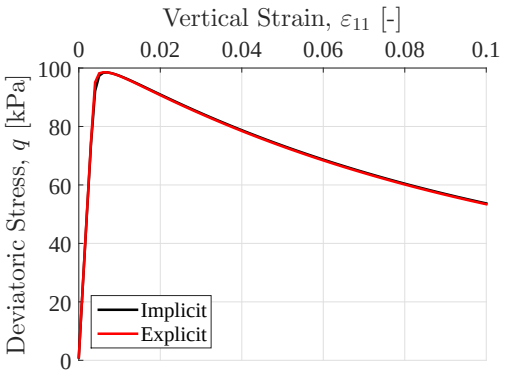

(a) Undrained tri-axial compression.

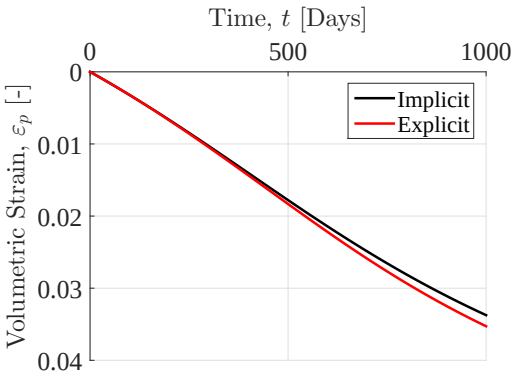

(b) Drained creep.

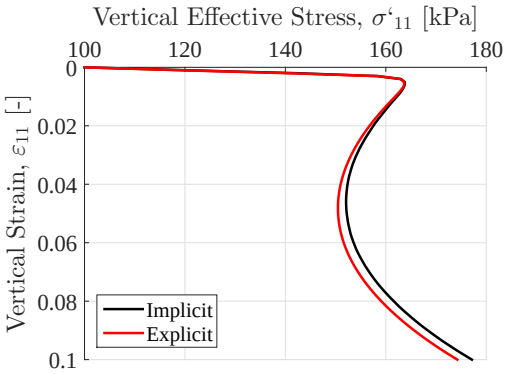

(c) One-dimensional compression ($\Delta\varepsilon_{11} = 10$ %)

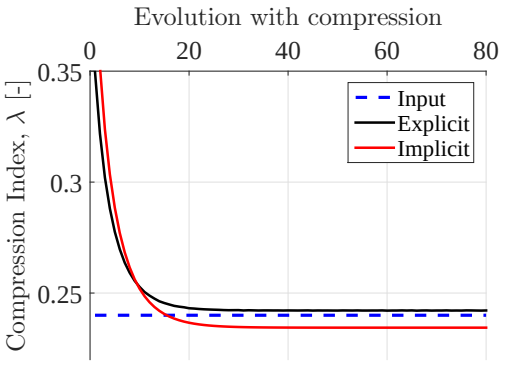

(d) One-dimensional compression ($\Delta\varepsilon_{11} = 50$ %)

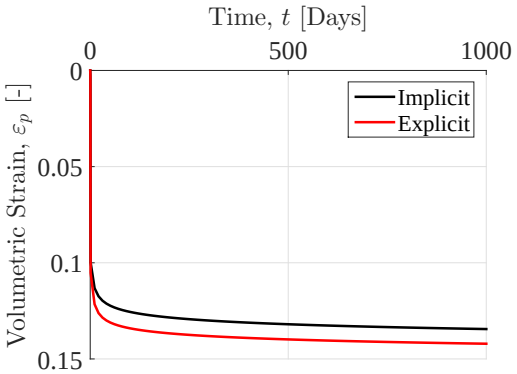

(e) Compression + drained creep.

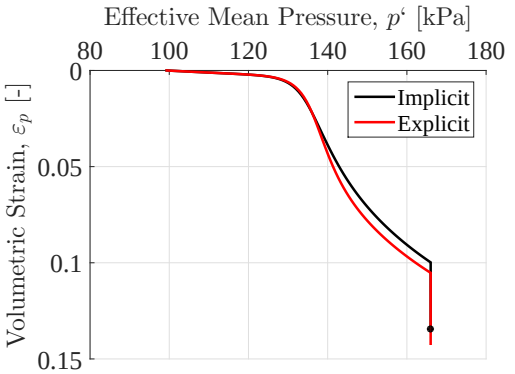

(f) Compression + drained creep test.

Figure G.12: *Investigation explicit and implicit scheme for layer 3 (5.0 - 10.0 m).*

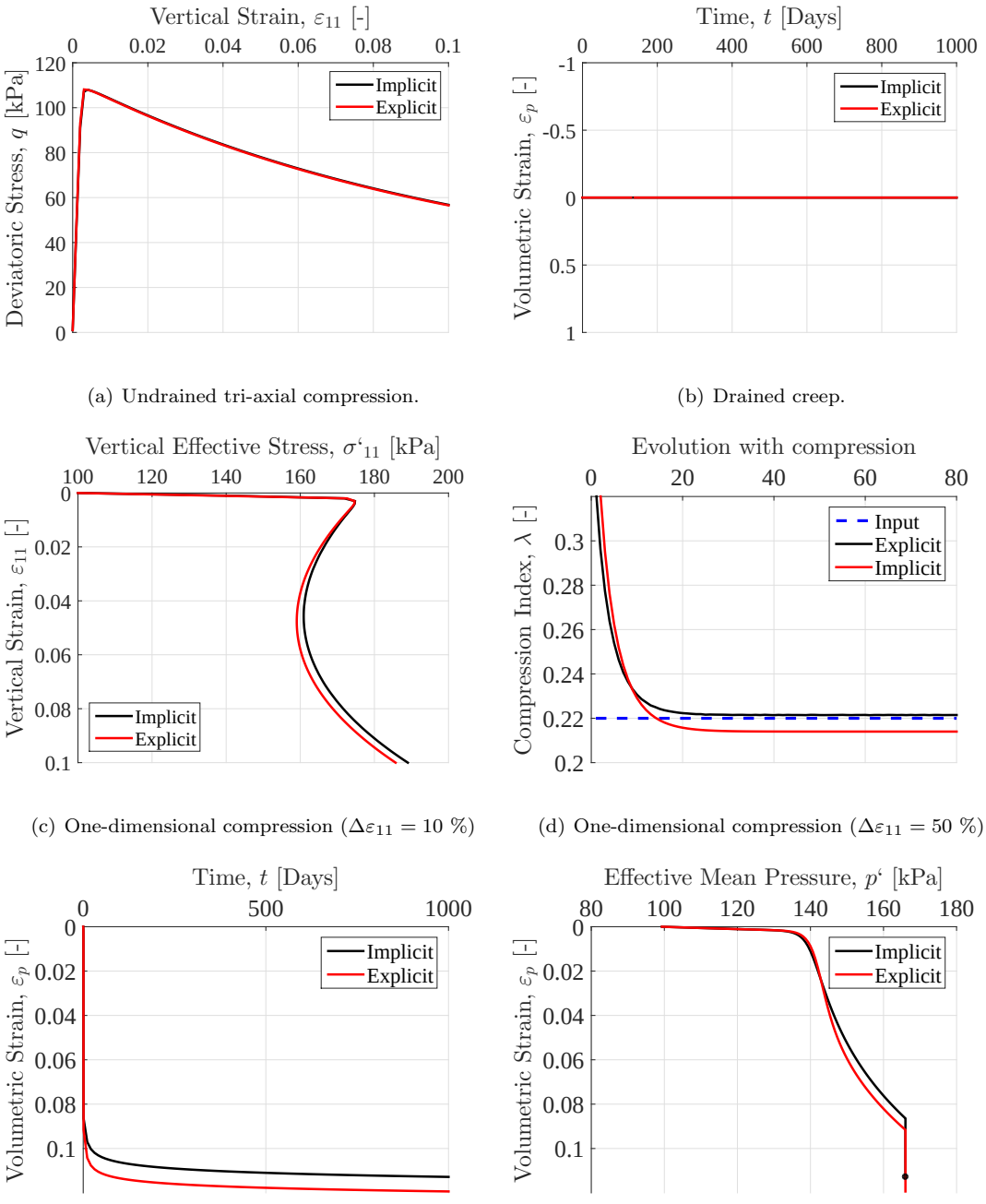

(a) Undrained tri-axial compression.

(b) Drained creep.

(c) One-dimensional compression ($\Delta\varepsilon_{11} = 10$ %)

(d) One-dimensional compression ($\Delta\varepsilon_{11} = 50$ %)

(e) Compression + drained creep.

(f) Compression + drained creep test.

Figure G.13: *Investigation explicit and implicit scheme for layer 4 (10.0 - 25.0 m).*